Polarised Raman spectroscopy as a quantitative probe of interfacial molecular orientation

RAMMELOO, RAYMOND,XAVEER

Polarised Raman Spectroscopy as a Quantitative Probe of Interfacial Molecular Orientation

Raymond Xaveer Rammeloo

Submitted for the degree of Doctor of Philosophy

Department of Chemistry

Durham University

2019

Abstract

Polarised Raman Spectroscopy as a Quantitative Probe of Interfacial Molecular Orientation – by R.X. Rammeloo

Raman scattering is an ubiquitous phenomenon that can be used to great effect to study molecules near interfaces. It has traditionally been used as an analytical tool to identify materials, but by using polarised light, the degree of order within that material can be assessed simultaneously. This thesis seeks to enhance this technique by accurately quantifying interfacial molecular orientation from peak intensities in polarised Raman spectra. This requires a joint modelling and experimental approach.

The experimental system, previously developed in our group, obtains surface selectivity through total internal reflection (TIR) of an incident laser beam at the interface under investigation. The evanescent wave generated by TIR causes Raman scattering by the molecules of interest. This system enables investigation of molecular layers at solid-air, solid-liquid and solid-solid interfaces.

A numerical model is constructed to predict Raman scattering intensities based on a generalised experimental geometry, the Raman tensor of the vibrational mode under investigation and the orientation of the scattering molecule. A local field correction is implemented for incident as well as emitted radiation. The scattered intensity is calculated with Lorentz reciprocity and integration over the microscope objective that collects the Raman signal. The modelling outcomes are fitted to experimental Raman scattering intensities to deduce molecular orientation. The electrodynamic model of the scattering process is complemented with Raman tensors, polarisabilities and molecular radii obtained by *ab initio* computation.

The novel methodology is validated with isotropic scatterers and a supported monolayer of zinc arachidate. Analysis of Raman spectra of zinc arachidate in a contact under static load reveals a variation in alkyl chain tilt of $(4.8\pm0.5)^\circ$ per 100 MPa around $(27\pm4)^\circ$ at 500 MPa. The exact tilt angle depends on the intensity and fitting metrics used.

The model further allows quantitative interpretation of Raman spectra as well as optimisation of experimental design. Limitations as well as future applications of this approach are discussed.

This version is submitted after minor corrections following the *viva voce* of 27 March 2020.

Thesis supervisor	Professor Colin D. Bain (Durham University)
Thesis examiners	Professor Ioan Notingher (Nottingham University)
	Professor Andrew Beeby (Durham University)

Copyright statement

The author may be contacted by email through r.x.rammeloo *at* dunelm.org.uk.

How to cite this work:
Rammeloo, R.X. (2019) *Polarised Raman spectroscopy as a quantitative probe of interfacial molecular orientation.* Doctoral thesis, Durham University.

Contents

APPENDICES

Acknowledgements

Though a doctoral thesis only bears one name as its author, it is usually not merely the result of the efforts of an individual. This project was no exception. I therefore want to thank and acknowledge the following people and organisations.

First of all, thanks are due to Professor Colin Bain, without whom this project would not have existed. Since recruiting me to his research group, he has shared his knowledge and experience freely. I am grateful for his support and commitment throughout the project. I have grown both scientifically and personally under his guidance.

I am grateful to Dr Eric Tyrode of Kungliga Tekniska Högskolan (KTH) in Stockholm, Sweden for in-depth discussions and for welcoming me to his lab to run a series of experiments. Working with his Raman system has been a pleasure, not least for his meticulous approach to scientific research and his enthusiasm.

I warmly thank Dr Mark Fox for performing the GAUSSIAN computations on the Hamilton cluster of Durham University. Though the computations had to be adjusted and redone multiple times, he has been patient and supportive throughout. I also thank him for reviewing chapter 4.

I thank Dr Simon Beaumont as second supervisor of my studentship. I am glad to have contributed to the start of his project on Raman spectroscopy of heterogeneous catalysis and to see that it has developed since.*

Though the above academics have been important in shaping the research project, the daily experience was dominated by the interaction with (past and present) undergraduate, postgraduate and post-doctoral members of the Bain research group. I am happy to have met such a diverse group of people during my years amongst you and hope you will continue to welcome many more in the future. Though it is usually not polite to single out someone in particular, I believe all will understand and appreciate me making special mention of Dr Lisong Yang. Thank you.

My doctoral studentship was embedded in the NanoS3 initial training network of the Marie Curie Actions in Framework Programme 7 of the European Commission. I thank the principal investigators of the network for setting up this network and sharing their expertise so freely. Particular thanks go to Dr Imre Varga of Eötvös Loránd Tudományegyetem

*The interested reader may find my contribution in: Bingham, Laura Maria (2017) *Development of nanoparticle catalysts and total internal reflection (TIR) Raman spectroscopy for improved understanding of heterogeneous catalysis.* Doctoral thesis, Durham University.

(ELTE) in Budapest, Hungary as initiator and coordinator of the network and a great supporter of all 'his' researchers. It has always been a joy to meet my fellow Early Stage Researchers at our training courses and meetings throughout Europe. The burden was shared and lightened.

I would like to give thanks to the dedicated staff of the Department of Chemistry, from Lab Attendants to Head of Department, for their support and providing the infrastructure essential to scientific work such as this. I greatly appreciate the understanding and patience shown by the administrative team as my personal circumstances developed during the course of my studentship.

I would also like to thank the examiners of this thesis for their valuable comments and thorough questioning during my viva, even though it had to be held by video conference.

An important part of my life at Durham revolved around Hatfield College. It has been a home for me literally as well as figuratively. I wish to thank the College Officers and Staff, (past) members of the Middle Common Room as well as the Senior Common Room for memorable moments, people and opportunities that have enriched its community and my life.

Hatfield College
Durham University

I warmly thank my current manager and co-workers at Arnold & Siedsma for their collegiality during the final phases of writing and correcting this thesis.

Finally, I am extremely grateful to my fiancée Jana and our son Remi for being a source of inspiration, happiness and love.

This project has received funding from the European Unions Seventh Framework Programme for research, technological development and demonstration under grant agreement no. 290251.

Chapter 1

Introduction

This thesis is concerned with interfaces and with Raman spectroscopy as a tool to gain insight into molecular behaviour at interfaces. Molecules often behave strikingly different at an interface compared to their behaviour in the bulk of a material. Various techniques have been developed to investigate interfaces, each probing certain characteristic of the studied material. Raman scattering is particularly promising as an interfacial technique to complement existing methods.

1.1 Interfaces

Interfaces form between two materials of disparate properties. This includes outer surfaces of a macroscopic material, such as an aeroplane wing with the surrounding atmosphere, as well as interactions between molecular structures, such as an anti-icing coating applied to the airplane wing to prevent sublimation of water molecules at the interface. Other highly relevant microscopic interfaces include proteins, in which biochemical functionality is driven by surface binding characteristics of molecules, and heterogeneous catalysis, where a solid catalyst facilitates chemical transformation at its surface.

In this work, tribological interfaces are presented. In the field of tribology, friction and wear is studied [1, 2]. As two surfaces make contact, pressure is exerted on the mating surfaces and any molecules in between, which gives rise to friction, deformation and possibly damage. This is relevant for mechanical contacts as well as physiological, pathological and artificial joints [3]. Understanding molecular structure and dynamics in such contacts would greatly facilitate development of better lubricants and aid in developing therapies for joint-related pathologies. However, studying material in a contact is challenging because these are generally buried between the two mating parts and most experimental techniques can only be applied to open, accessible surfaces. A technique is desired that provides access to such buried interfaces *in situ*, *i.e.* while undergoing pressure and shear forces, and that provides time-resolved measurements of molecular behaviour without altering the system to obtain this information.

Ideally, knowledge is desired of what molecular species are present in the contact

and how these are distributed, what their order is or in what phases these occur, what orientation these molecules posses with respect to the plane of the interface and how these properties change with external stimuli, such as increased load and shear of the contact, modifications of the mating surfaces and changing composition of the lubricant.

Reduction of friction and wear is an age-old problem. Molecular behaviour in a contact has so far been studied by various techniques, most of which provide measurements of mechanical characteristics such as forces, surface profiles, amount of wear and thickness of the lubricant layer [1]. For a molecular understanding, chemical information is also desired since these physical characteristics arise from surface forces generated by molecular interactions [4].

Other fields in which detailed understanding of molecular mechanisms at interfaces is desired include the study of functional interfaces, such as heterogeneous catalysis, absorption and release of active agents, coatings and (bio)sensors. In each of these applications, a desired functional property arises from molecular characteristics. Elucidating structure-function relations in these systems allows functionalisation by design.

1.2 Interface analytical techniques

Various techniques have been developed to study interfaces, a selection of which are briefly discussed here. Raman scattering is also introduced and compared to existing methods.

1.2.1 Optical techniques

Optical microscopy provides access to surfaces and to interfaces bound by at least one optically transparent medium. Lubricant film thickness can be determined via interference fringes (Newton rings, also applied in chapter 7) as long as the interface remains transparent [5]. However, imaging resolution is limited by the wavelength of light and thus molecules cannot be observed nor their properties measured.

Higher resolution is obtained by (scanning) electron microscopy, which is however limited to *ex situ* analysis and requires a conductive substrate. Great resolution can be obtained at long exposure times but dynamic effects can not be measured at relevant time scales. Combination with elemental analysis provides insight into the composition of wear particles and thus which contact surface abrades [6].

In Brewster angle microscopy (BAM), a smooth surface is illuminated by polarised light under the Brewster angle so that no reflection is detected (this effect is explained and employed in section 3.3.1). At locations where the surface is covered by a (mono)layer, the polarisation changes and reflections are detected. The method shows presence and distribution of a layer but not its thickness or chemical composition.

Spatial distribution of molecules may be observed by fluorescence microscopy. It requires labelling with a fluorophore, which may affect the behaviour of the materials involved. Label-free techniques are therefore desirable. However, fluorescence generally

gives a strong signal, thus allowing detection of minute quantities of a fluorescent material. The technique may be made surface-selective by the application of supercritical angle fluorescence (SAF) [7, 8], in which fluorescence is detected by an annulus of grazing angles around the microscope focus. Velocity profiles in a contact under shear have been measured by photobleaching the lubricant and observing the return of fluorescence at a spatially removed location [9].

Ellipsometry employs the change in polarisation of laser light caused by a film to determine its thickness in combination with in-plane and out-of-plane dielectric constants. A second measurement is generally required to disentangle the two, such as X-ray diffraction. In stead, it is also possible to collect a series of measurements while varying the dielectric constant of the liquid subphase [10]. No chemical information is obtained and the technique is generally applied to exposed surfaces to obtain layer thickness on the nanometer scale.

1.2.2 Force measurements

Interactions at interfaces are driven by surface forces, which arise from molecular attraction and repulsion as well as macroscopically applied pressures. The response of an interface to an applied force is a measure of the molecular interactions. Chemical specificity can not be obtained.

The surface-force apparatus (SFA) [11] measures the response of a buried interface formed between two mica surface to which pressure and shear are applied. Surface separation, contact area (typically in the order of 0.1 mm^2) as well as static and dynamic forces can be determined. The pressure range of the apparatus is limited by a mechanical spring, which is relatively weak to allow accurate force measurements. Friction is generated in a reciprocating manner at typically 1 $\mu m\ s^{-1}$. This technique provides insight into lubricant function, such as models for joint lubrication [12].

Forces are also measured in atomic force microscopy (AFM) at an atomic resolution. Mounting a colloidal probe to the AFM cantilever allows an increased interaction area of about 1 μm^2. Attainable sliding speeds remain low while contact pressures are in the order of 10 GPa. Buried interfaces can be produces between a substrate and the colloidal probe. This technique has been applied succesfully to study lubricating properties of soft matter [13, 14].

1.2.3 X-ray and neutron scattering

X-ray and neutron scattering techniques are the scientific workhorses of structure determination. These can equally be applied to interfaces. Scattering of X-ray and neutrons arises from scattering length densities of the electron cloud and atomic nucleus, respectively. These techniques are sensitive to atomic species and molecular properties are inferred from the deduced distributions of atoms.

Small-angle scattering is used to obtain nanometer scale dimensions of a film, such as

molecular spacing, film thickness and ordering length scales in crystalline domains of the film. Reflectivity at grazing incidence can be used to infer an effective or average molecular tilt from the layer thickness. Though small-angle X-ray scattering can be performed with a laboratory-based instrument, neutron scattering experiments can only be performed in dedicated facilities. All require relatively long exposure times due to the small amount of material probed.

1.2.4 Spectroscopic techniques

Vibrational spectroscopy of interfaces provides direct access to information on what compounds are present and in what configuration without disturbing the materials. In a contact, at least one of the mating solids has to be transparent for the incident as well as outgoing radiation.

Infra-red (IR) spectroscopy on interfaces generally uses Fourier-transform techniques with broadband pulsed illumination. Surface sensitivity is obtained by multiple total internal reflections through a crystal on which the interface is formed. The attenuated total reflection (ATR) of the IR beam is evaluated. When using polarisation, the spectra provide information on the conformation and orientation of the IR absorbing molecules, which may be quantified [15].

With IR absorbing substrates, such as glass and water, spectra may be recorded at multiple incidence angles to obtain a relatively neat spectrum of the film [16].

On various substrates, reflection-absorption infrared spectroscopy (RAIRS also known as IRRAS) can be employed, in which the infrared beam is incident on the interfacial film under a grazing angle [17]. The absorption of the molecule depends on its orientation with respect to the polarisation of the incident IR beam. Polarised spectra or the ratio of their absorbances (the dichroic ratio) can thus be linked to molecular order and orientation. On metals, this technique only detects vibrational modes that result in a change of the molecular dipole moment perpendicular to the metal surface. In this case, it is thus intrinsically sensitive to molecular orientation. A tribological interface was studied *ex situ* with this technique by Kahtri *et al.* [18].

All IR techniques are based on absorption and thus face the limitation that it measures a fluctuation in a signal on a high background, which is intrinsically less sensitive then measuring a small fluctuation on a zero background as is the case in sum-frequency generation or Raman scattering.

An alternative spectroscopic technique is vibrational sum-frequency spectroscopy (VSFS). It is intrinsically surface selective as the sum-frequency effect only occurs in a non-centrosymmetrical environment while ordered structures do not give a signal [19]. In this technique, both a visible and IR pulsed laser beam are overlapped onto the interface and light is emitted (as a beam) at the summed frequency, which is strongest when the IR laser is resonant with an appropriate vibrational mode of the molecules as the interface.

The sum-frequency intensity also depends on the optical geometry [20]. The linear

polarisations of each beam can be set to in-plane or out-of-plane, providing eight combinations that allow analysis of the orientation of the molecule (or functional group) that gives rise to the sum-frequency signal.

VSFS has been used to obtain molecular orientation [21, 22] though this knowledge is restricted to those parts of the interface that are sum-frequency active. For example, the orientation of terminal methyl groups of surfactants at the liquid-vapour interface was determined [23] and order within the monolayer can be assessed by observation of *gauche* defects in otherwise stretched alkyl chains. Water structure at interfaces has also be assessed [24, 25]. Interpretation of sum-frequency spectra from interfaces is complicated by non-resonant contributions [26] as well as interference effects in thin films [27–29].

This technique has also been applied to monolayers in a contact, starting with a publication from Bain *et al.* in 1998 [30] with details later published in [31, 32]. Later studies of Ghalgaoui *et al.* [33] also included variation of load and shear on an octadecyltrichlorosilane monolayer, showing irreversible changes in the order of the monolayer after shear was applied. Meltzer *et al.* studied indentation of a octadecylphosphonic acid monolayer by a glass sphere [34]. From both spectra and molecular dynamics simulations of the system, the authors showed that *gauche* defects increase to a saturation value when pressure is increased while the monolayer fully recovers after pressure again reduced.

Though VSFS has proven a fruitful technique in studied buried interface, the number of published studies is still small, likely because its implementation requires significant effort and experienced researchers to obtain good spectra.

1.2.5 Raman scattering

Raman spectroscopy is the use of Raman scattering for chemical analysis of a material. Generally, continuous-wave lasers are used as a source of monochromatic light to illuminate the sample under investigation. The incoherently scattered light is collected and analysed in a spectrograph. Peaks in the spectrum are linked to specific molecular transitions which allows identification of molecules and their constituent groups. Selective sampling of an interfacial layer, as opposed to bulk material, can be achieved through total internal reflection (TIR) of the laser beam [35, 36].

As infrared and sum-frequency spectroscopy, Raman spectroscopy probes molecular vibrations. Raman spectra are presented as intensity *versus* Raman shift in wavenumbers (cm^{-1}) from the frequency of the incident laser light. The fundamental Raman lines in a spectrum of a molecule are numbered ν_1, ν_2, ... according to their shift and the symmetry species of the vibrational mode from which they arise. Starting with the fully symmetric modes, all bands are numbered from high to low frequency, before considering bands from modes of increasingly lower symmetry. Normally degenerate modes receive an additional label when they become distinguishable.

Selection rules apply, resulting in more distinct Raman bands compared to IR spectroscopy with weaker glass, carbon dioxide or water background features. Compared to

VSFS, Raman spectra provide more peaks as the strict symmetry requirements of non-linear sum-frequency effect do not apply. This means that all parts of the molecule and all molecules contribute to the Raman spectrum in an additive way. A detailed explanation of the Raman effect is given in chapter 2.

Raman scattering is sensitive to polarisation and can thus be used to assess molecular orientation. This has been used in establishing molecular orientation of dyes in films [37] and alignment of (parts of) peptides [38, 39], for example. At interfaces, polarised Raman spectroscopy has long been used to assess order in surface films qualitatively and is a subject of ongoing research as this thesis and references herein show.

To enhance spatial resolution in the sampled interface, a confocal arrangement can be used of illumination and collection of scattered light in a microscope.

In order to overcome the intrinsically weak nature of the Raman effect, various schemes have been developed to enhance its signal. These include a waveguide geometry [40], the TIR configuration as well as generation of surface plasmons [41]. This last method is surface-enhanced Raman scattering (SERS), in which plasmonic hot spots give rise to extreme amplification of the local electric field between two nanoparticles through a surface plasmon resonance at the wavelength of the incident laser. Due to this enhanced field, the intensity of Raman scattering increases dramatically. SERS may be combined with TIR illumination to further increase the Raman signal in addition to ensuring surface selectivity [42]. Surface-plasmons can also be generated in metal coatings, such as gold, to amplify Raman scattering from molecules absorbing to such interface [43].

Another method employing plasmon enhancement is tip-enhanced Raman scattering (TERS), in which an AFM probe is combined with Raman spectroscopy. Combining scanning probe microscopy with confocal microscopy, to deliver laser light and collect Raman scattering, allows chemical mapping of even single molecules [44]. The polarisation of the incident laser is set parallel to the AFM tip to excite a plasmon resonance that strongly enhances the Raman scattering of molecules between tip and substrate. Moving the sample below the tip and through the laser spot produces an image of the surface. A spatial resolutions below 2 nm has been reported [45]. Such techniques can be used to image static samples, including cell membranes [46].

In the above plasmon-resonance enhanced techniques, Raman scattering arises from very few molecules that may be modified by the close proximity of the tip, colloid or surface with which the plasmon is generated. A more expansive area of the interface can be probed when illuminating the interface with a laser beam and collecting Raman scattering through a microscopy objective as used in our research group (detailed in chapter 3). This also allows variation of the angle of incidence, which determines the sampling depth in TIR. Scanning the laser incidence angle can thus provide layer thickness and depths of layers in a multilayered system, as experimentally demonstrated by Emily Smith's group in a series of papers [47–50]. Another recent application of this was Ota's study of water structure at hydrophobic and hydrophilic interfaces [51].

The TIR geometry thus ensures surface-selective Raman scattering. Another advan-

tage of this geometry is the enhancement of the field at the interface over any background signal from the substrate. For example, the TIR arrangment has been used to increase sensitivity of a Raman detector of volatile organic compounds [52]. More information can be obtained by using polarised TIR Raman scattering. Polarisations are well-defined with respect to incoming laser beam and plane of the interface, thus in principle allowing analysis of molecular orientation with respect to the interface.

TIR Raman spectroscopy has been applied to confined films in our research group for over a decade [53, 54]. It proved a more versatile technique than VSFS, previously used, as all material in the contact is probed and its application is generally less cumbersome. In combination with a tribometer, TIR Raman spectra can be collected from lubricants as these undergo load and shear forces [55, 56]. Molecular distribution, order and orientation can then be assessed *in situ* and dynamically. However, interpretation of these spectra has so far been qualitative.

In summary, a range of interface analytical techniques are currently available to investigate interfaces. Raman spectroscopy is particularly appealing as it provides a vibrational spectrum that includes detailed chemical information, allows for polarisation control to determine molecular orientation, can be made surface selective through TIR, can be employed with common substrates such as glass, water and air while providing signals that are strong enough to perform sub-second time resolution experiments *in situ* and not requiring labelling or other interference with the sample. However, like other spectroscopic techniques, it requires an optically transparent substrate to access buried interfaces. Furthermore, fluorescence of samples should be avoided, though choosing different lasers and time-gating can minimise this. Finally, the experimental system is relatively inexpensive compared to the other techniques and easy to use.

1.3 Research focus

We seek to quantitatively deduce molecular orientation from experimentally obtained Raman scattering intensities. A numerical model based on the experimental geometry used in our laboratory could provide (relative) intensities as a function of the orientation of the scattering molecule and other parameters of the interface. The strategy is to fit the experimental data with these modelling outcomes and extract the orientation of the scatterer, having ruled out all other variables.

With such a model, peak intensities in Raman spectra can be predicted for various linear polarisations. Quantitative analysis of experimental spectra would then be possible to provide insight in the molecular response to externally applied stimuli, such as pressure and shear in a tribological contact. It is believed that the current qualitative, limited interpretations of available data may be improved to place Raman spectroscopy on a more equal footing with some of the well-established techniques of interface analysis.

The focus of this thesis is on developing a consist framework for the interpretation of Raman spectra, comprising a model to predict scattering intensities as a function of exper-

imental and molecular parameters. It is further desired that these molecular parameters, including Raman tensors, can be obtained by computation to predict Raman spectra. The model should then be validated and applied to relevant interfaces to demonstrate its applicability. In doing so, we aim to establish polarised Raman spectroscopy as a quantitative probe for interfacial molecular orientation.

1.4 Thesis outline

The remainder of this thesis is structured as follows. Chapter 2 introduces and develops theoretical aspects of Raman scattering. Experimental aspects are described in chapter 3. These include the Raman systems and procedures for preparation of the experiments. Material properties, in particular refractive indices, are also included.

Chapter 4 deals with the form of Raman tensors and derivation of its numerical values by *ab initio* computation.

Theory and experiment are combined in the model developed in chapter 5. Detailed electromagnetic considerations are presented as well as a discussion of its applicability, limitations and assumptions.

The new model is applied to apparently simple interfaces in chapter 6 in order to validate the model description of the Raman scattering process. Here, the *ab intio* computations of chapter 4 are employed.

In chapter 7, the model is applied to Raman spectra of zinc arachidate monolayers in a solid-solid contact under static pressure. This presents an application of the developed approach to a system of tribological interest.

Chapter 8 concludes this thesis with a summary of conclusions from the preceding chapters and suggestions for further work. Additional material is provided in appendices.

Parts of this work include rather rudimentary aspects. These are nevertheless included to ensure a self-contained source of information that is accessible to the uninitiated coming to the field of Raman spectroscopy from various scientific backgrounds, such as future doctoral students in our research group or elsewhere. They form the primary audience I have kept in mind while writing this thesis.

All data presented in this thesis is labelled with a chronological data key, with which it may be traced in the digital data archive of Professor Bain's research group. Every figure where raw experimental data is first introduced, includes such a data key in its caption.

Chapter 2

Elements of Raman scattering theory

This chapter brings together various theories relevant to the Raman effect. It is meant to provide a complete and coherent framework for this thesis and seeks to spare the reader from having to consult disparate sources that focus on particular aspects of theory only, include hidden assumptions or contain inconsistent definitions. An effective modelling approach needs a rigorous internal consistency built from a thorough understanding of its elementary concepts.

2.1 Introduction

The Raman effect is named after Chandrasekhara Venkata Raman (1888-1970), who published the discovery of a new kind of radiation from molecules in 1928 [57]. Light scattering experiments on some 80 transparent liquids conducted with Kariamanickam Srinivasa Krishnan (1898-1961) at Calcutta University revealed that some of the scattered light was of a wavelength different from the wavelengths of the incident light [58]. They demonstrated that this radiation was not the same as fluorescence as its intensity was of an "entirely different order" and it was as strongly polarised as ordinary light scattering, whereas fluorescence from a bulk liquid was known to be unpolarised [59]. This effect had not been observed before. Raman was awarded the 1930 Nobel prize in physics "for his work on the scattering of light and for the discovery of the effect named after him" [60] with nominations from Bohr, Rutherford, Stark and de Broglie, amongst others.

Due to the intrinsic weakness of the Raman effect, a strong light source is needed to observe Raman scattering. The advent of lasers as stable monochromatic sources of light has increased the ease of performing Raman spectroscopy. Raman himself demonstrated the effect with a pure toluene sample, using a strong mercury arc lamp (or a focussed beam of Southern Indian Summer sunlight in his first experiments) with a blue-violet filter to illuminate the sample and a green filter to observe the ray traversing the liquid. This can be replicated in a modern lab with ease, using a laser to illuminate a transparent

sample and wearing the appropriate safety goggles to look at the opalescent track within the liquid. Using a green laser and goggles that block this colour, an orange-red line is observed where the laser beam traverses liquid toluene.

Molecular light scattering is distinct from scattering by particulate matter such as dust in the atmosphere or colloidal particles in a suspension. The latter is known as Mie scattering and arises from spherical particles in a medium of different refractive index. Fluorescence and phosphorescence are two other effects that result in a scattered wavelength different from that of the incident light. However, such photoluminescence has a different molecular origin involving both electronic and vibrational transitions leading to red-shifted emitted light whereas Raman scattering commonly involves vibrational transitions only and can result in both red and blue-shifted spectral lines. Raman scattering occurs with any incident frequency, whereas photoluminescence only occurs at an electronic absorption band. Furthermore, the time delay and intensities at which these effects occur is of a different order of magnitude. Fluorescence delays are typically on the order of $1-10$ ns and those in phosphorescence range from from ms to hours. Raman scattering is instantaneous and much weaker.

2.2 Tensors, bases and transformations

The following mathematical definitions are used in the treatment of Raman scattering. As multiple conventions exist, a full specification is necessary.

2.2.1 Tensor conventions

Light scattering by molecules, including the Raman effect, is generally described with a combination of classical electrodynamics and quantum mechanics: the first is used to describe the electromagnetic radiation, while the latter describes the molecular properties of the scattering material [61, 62]. In the description that follows, extensive use will be made of tensors of rank zero, one and two.

A tensor of rank zero is a scalar, a single number unrelated to any frame of reference.

A tensor of the first rank is specified by three components, each associated with one of the axes of the frame of reference. It is represented as a column vector within a particular frame of reference, such as

$$\mathbf{b} = b_x\hat{\mathbf{x}} + b_y\hat{\mathbf{y}} + b_z\hat{\mathbf{z}} = \begin{pmatrix} b_x & b_y & b_z \end{pmatrix} \begin{pmatrix} \hat{\mathbf{x}} \\ \hat{\mathbf{y}} \\ \hat{\mathbf{z}} \end{pmatrix} \equiv \begin{pmatrix} b_x \\ b_y \\ b_z \end{pmatrix} \tag{2.1}$$

with vector $\mathbf{b}$ given in the basis $\{\hat{\mathbf{x}}, \hat{\mathbf{y}}, \hat{\mathbf{z}}\}$.

A second-rank tensor is specified by nine components, each of which is associated with a pair of axes taken in a particular order. This forms a matrix represented as a square

array of 3×3 elements, for example

$$\begin{aligned}\mathbf{M} &= \hat{\mathbf{x}}M_{xx}\hat{\mathbf{x}} + \hat{\mathbf{x}}M_{xy}\hat{\mathbf{y}} + \hat{\mathbf{x}}M_{xz}\hat{\mathbf{z}} \\ &\quad + \hat{\mathbf{y}}M_{yx}\hat{\mathbf{x}} + \hat{\mathbf{y}}M_{yy}\hat{\mathbf{y}} + \hat{\mathbf{y}}M_{yz}\hat{\mathbf{z}} + \hat{\mathbf{z}}M_{zx}\hat{\mathbf{x}} + \hat{\mathbf{z}}M_{zy}\hat{\mathbf{y}} + \hat{\mathbf{z}}M_{zz}\hat{\mathbf{z}} \\ &= \begin{pmatrix}\hat{\mathbf{x}} & \hat{\mathbf{y}} & \hat{\mathbf{z}}\end{pmatrix} \begin{pmatrix}M_{xx} & M_{xy} & M_{xz} \\ M_{yx} & M_{yy} & M_{yz} \\ M_{zx} & M_{zy} & M_{zz}\end{pmatrix} \begin{pmatrix}\hat{\mathbf{x}} \\ \hat{\mathbf{y}} \\ \hat{\mathbf{z}}\end{pmatrix} \\ &\equiv \begin{pmatrix}M_{xx} & M_{xy} & M_{xz} \\ M_{yx} & M_{yy} & M_{yz} \\ M_{zx} & M_{zy} & M_{zz}\end{pmatrix}\end{aligned} \tag{2.2}$$

in which each element M_{kl} is a scalar. The basis vectors are usually omitted in the notation of tensors. These are implied in the matrices used throughout this work. Note that a matrix is only an array of numbers, whereas a tensor is defined with respect to a complete, orthonormal basis. A second-rank tensor has eigenvalues and can be diagonalised, while this is not possible for all 3×3 matrices.

Multiplication of two vectors follows three distinct types. First, the direct product, without particular symbolism, results in a tensor of second rank

$$\mathbf{ab} = \begin{pmatrix}a_x \\ a_y \\ a_z\end{pmatrix} \begin{pmatrix}b_x & b_y & b_z\end{pmatrix} = \begin{pmatrix}a_x b_x & a_x b_y & a_x b_z \\ a_y b_x & a_y b_y & a_y b_z \\ a_z b_x & a_z b_y & a_z b_z\end{pmatrix} \tag{2.3}$$

Second, the dot product results in a scalar and is indicated by a centred dot $\cdot$ as in

$$\mathbf{a} \cdot \mathbf{b} = \begin{pmatrix}a_x & a_y & a_z\end{pmatrix} \begin{pmatrix}b_x \\ b_y \\ b_z\end{pmatrix} = a_x b_x + a_y b_y + a_z b_z \tag{2.4}$$

Third, the cross product results in another vector, orthogonal to the original pair and is indicated with a cross $\times$. In matrix notation, this follows

$$\mathbf{a} \times \mathbf{b} = \begin{pmatrix}a_x \\ a_y \\ a_z\end{pmatrix} \times \begin{pmatrix}b_x \\ b_y \\ b_z\end{pmatrix} = \begin{pmatrix}a_y b_z - a_z b_y \\ a_z b_x - a_x b_z \\ a_x b_y - a_y b_x\end{pmatrix} \tag{2.5}$$

Multiplication between tensors of second rank and multiplication of a second-rank and a first-rank tensor are performed according to pre-multiplication (or left multiplication) of matrices. This approach is used throughout this work and no multiplication symbols are used when second-rank tensors are involved. Applying a tensor of second rank to one

of first rank is represented in a matrix multiplication as

$$\begin{aligned} \mathbf{b} &= \mathbf{M}\,\mathbf{a} \\ \begin{pmatrix} b_x \\ b_y \\ b_z \end{pmatrix} &= \begin{pmatrix} M_{xx} & M_{xy} & M_{xz} \\ M_{yx} & M_{yy} & M_{yz} \\ M_{zx} & M_{zy} & M_{zz} \end{pmatrix} \begin{pmatrix} a_x \\ a_y \\ a_z \end{pmatrix} \\ &= \begin{pmatrix} M_{xx}a_x & M_{xy}a_y & M_{xz}a_z \\ M_{yx}a_x & M_{yy}a_y & M_{yz}a_z \\ M_{zx}a_x & M_{zy}a_y & M_{zz}a_z \end{pmatrix} \end{aligned} \tag{2.6}$$

where the matrix element M_{kl} relates component l of $\mathbf{a}$ to component k of $\mathbf{b}$. The multiplication of two matrices $\mathbf{L}\,\mathbf{M}$ gives a third matrix $\mathbf{K}$ as

$$\begin{aligned} \mathbf{K} &= \mathbf{L}\,\mathbf{M} \\ \begin{pmatrix} K_{xx} & K_{xy} & K_{xz} \\ K_{yx} & K_{yy} & K_{yz} \\ K_{zx} & K_{zy} & K_{zz} \end{pmatrix} &= \begin{pmatrix} L_{xx} & L_{xy} & L_{xz} \\ L_{yx} & L_{yy} & L_{yz} \\ L_{zx} & L_{zy} & L_{zz} \end{pmatrix} \begin{pmatrix} M_{xx} & M_{xy} & M_{xz} \\ M_{yx} & M_{yy} & M_{yz} \\ M_{zx} & M_{zy} & M_{zz} \end{pmatrix} \end{aligned} \tag{2.7}$$

$$= \begin{pmatrix} L_{xx}M_{xx} + L_{xy}M_{yx} + L_{xz}M_{zx} & L_{xx}M_{xy} + L_{xy}M_{yy} + L_{xz}M_{zy} & L_{xx}M_{xz} + L_{xy}M_{yz} + L_{xz}M_{zz} \\ L_{yx}M_{xx} + L_{yy}M_{yx} + L_{yz}M_{zx} & L_{yx}M_{xy} + L_{yy}M_{yy} + L_{yz}M_{zy} & L_{yx}M_{xz} + L_{yy}M_{yz} + L_{yz}M_{zz} \\ L_{zx}M_{xx} + L_{zy}M_{yx} + L_{zz}M_{zx} & L_{zx}M_{xy} + L_{zy}M_{yy} + L_{zz}M_{zy} & L_{zx}M_{xz} + L_{zy}M_{yz} + L_{zz}M_{zz} \end{pmatrix}$$

and is generally not equal to the matrix product $\mathbf{M}\,\mathbf{L}$. If the order of multiplication does not matter, the matrices are said to commute. Matrices and vectors are given in bold typeface while tensor components, scalars and coordinates are given in italics. This notation also holds for the norm of a vector

$$b = ||\mathbf{b}|| = \sqrt{{b_x}^2 + {b_y}^2 + {b_y}^2} \tag{2.8}$$

which is a scalar and gives the Euclidean length of a vector in three dimensions. Basis vectors are of unit length and are given in bold type and carry a hat, *e.g.* $\hat{\mathbf{x}}$. A label in superscript is used to indicate the frame of reference and basis in which a quantity is given, while subscript labels are used for other specifications, such as vector components or matrix elements as in equations 2.6 and 2.7. Except where noted, SI units are used.

2.2.2 Cartesian and spherical basis

The scattering process is described in a right-handed Cartesian coordinate basis $\{\hat{\mathbf{x}}, \hat{\mathbf{y}}, \hat{\mathbf{z}}\}$. A spherical basis $\{\hat{\boldsymbol{\rho}}, \hat{\boldsymbol{\theta}}, \hat{\boldsymbol{\phi}}\}$ is sometimes convenient to express the same vector or a point in space. Figure 2.1 defines each basis (or coordinate system) in the same frame of reference.

The transformation from Cartesian to spherical coordinates for a point in space within

a particular frame of reference is given by

$$\begin{aligned} \rho &= \sqrt{x^2 + y^2 + z^2} \\ \theta &= \arccos\left(\frac{z}{\sqrt{x^2 + y^2 + z^2}}\right) \\ \phi &= \text{arctan2}\left(\frac{y}{x}\right) \end{aligned} \tag{2.9}$$

where the arctan2 function is the four-quadrant inverse tangent, which takes the signs of the x and y coordinates into account to determine the angle ϕ in the interval $0° \leq \phi < 360°$. As the angle θ only ranges from $0°leq\theta \leq 180°$, the direct arccosine suffices to find that angle. The radial distance $\rho \geq 0$. Equations 2.10 are used to find the Cartesian coordinates of a point, given its spherical coordinates in the same frame of reference.

$$\begin{aligned} x &= \rho \sin\theta \cos\phi \\ y &= \rho \sin\theta \sin\phi \\ z &= \rho \cos\theta \end{aligned} \tag{2.10}$$

These expressions can be deduced readily from the dashed line projections in figure 2.1.

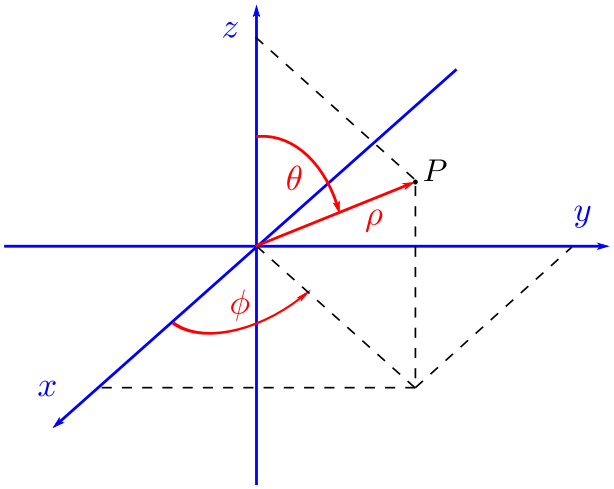

Figure 2.1: A three-dimensional frame of reference in which the location of point P is specified in coordinates of a Cartesian (x, y, z) (blue) as well as a spherical (ρ, θ, ϕ) (red) basis.

2.2.3 Transformation matrices

If the matrix $\mathbf{M}$ in equation 2.6 represents a transformation matrix $\mathbf{T}_{A\to B}$, it transforms the Cartesian basis of vector $\mathbf{a}^A$ with coordinates specified in frame of reference A to the vector $\mathbf{a}^B$, which is the same vector fixed in space but now described in the Cartesian basis

of frame of reference B. Equation 2.11 summarises this passive (or *alias*) transformation.

$$\begin{aligned} \mathbf{a}^B &= \mathbf{T}_{A\to B}\,\mathbf{a}^A \\ \begin{pmatrix} a_{x^B} \\ a_{y^B} \\ a_{z^B} \end{pmatrix} &= \begin{pmatrix} T_{x^Ax^B} & T_{x^Ay^B} & T_{x^Az^B} \\ T_{y^Ax^B} & T_{y^Ay^B} & T_{y^Az^B} \\ T_{z^Ax^B} & T_{z^Ay^B} & T_{z^Az^B} \end{pmatrix} \begin{pmatrix} a_{x^A} \\ a_{y^A} \\ a_{z^A} \end{pmatrix} \end{aligned} \tag{2.11}$$

If a vector has to be transformed within a fixed frame of reference, an active (or *alibi*) transformation is required. For rotations, this means that the inverse transformation matrix should be applied, as is demonstrated below. This definition is not trivial, as the rotation matrices to effect a rotation of the frame of reference for a vector fixed in space is mathematically identical to the inverse rotation of a vector expressed in the original frame of reference.

Transformations between several frames of reference are required to describe the scattering process. By choosing a common origin, only rotations are needed to effect transformations between Cartesian frames of reference. Choosing axes conveniently can further reduce the complexity of the transformations involved. A coordinate transformation is then completed by sequentially performing no more than three elemental rotations, each given by a 3×3 rotation matrix as presented in equations 2.12. Each rotation matrix $\mathbf{R}_a(\theta)$ specifies a rotation of the frame of reference about one of the three Cartesian axes a over angle θ in an anticlockwise direction looking down axis a from its positive end towards the origin. This definition conforms to an anticlockwise rotation of a frame of reference with a point or vector fixed in space (an *alias* transformation), as well as a clockwise rotation of a vector within a fixed coordinate system (an *alibi* transformation).

$$\begin{aligned} \mathbf{R}_x(\theta) &= \begin{pmatrix} 1 & 0 & 0 \\ 0 & \cos\theta & \sin\theta \\ 0 & -\sin\theta & \cos\theta \end{pmatrix} \\ \mathbf{R}_y(\theta) &= \begin{pmatrix} \cos\theta & 0 & -\sin\theta \\ 0 & 1 & 0 \\ \sin\theta & 0 & \cos\theta \end{pmatrix} \\ \mathbf{R}_z(\theta) &= \begin{pmatrix} \cos\theta & \sin\theta & 0 \\ -\sin\theta & \cos\theta & 0 \\ 0 & 0 & 1 \end{pmatrix} \end{aligned} \tag{2.12}$$

The classical (or proper) Euler angles α, β and γ are used to rotate one frame of reference into another. These angles are defined in figure 2.2 for a general transformation from frame of reference $\{\hat{\mathbf{x}}^A, \hat{\mathbf{y}}^A, \hat{\mathbf{z}}^A\}$ to $\{\hat{\mathbf{x}}^B, \hat{\mathbf{y}}^B, \hat{\mathbf{z}}^B\}$. Rotation matrices in three dimensions do not commute. The three elemental rotations must be performed in a particular order, as the direction of two of the axes change at each step.

First, a rotation of angle $0 \le \alpha < 360^\circ$ about the $\hat{\mathbf{z}}^A$ axis (which is the original z

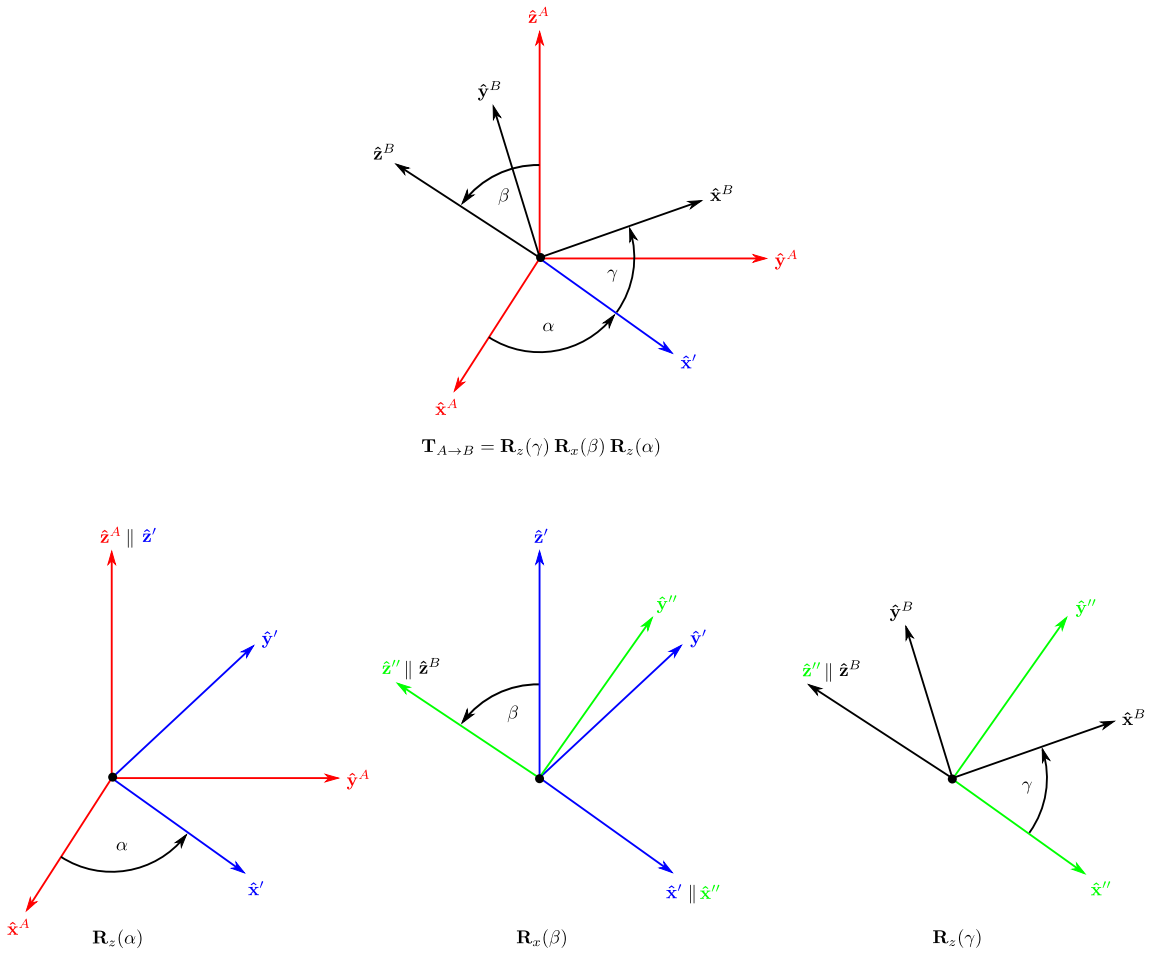

Figure 2.2: The proper Euler angles α, β and γ give the rotation angles to transform the frame of reference $\{\hat{\mathbf{x}}^A, \hat{\mathbf{y}}^A, \hat{\mathbf{z}}^A\}$ (red) to $\{\hat{\mathbf{x}}^B, \hat{\mathbf{y}}^B, \hat{\mathbf{z}}^B\}$ (black). The three elemental rotations in the bottom row are subsequently executed from left to right about the $\hat{\mathbf{z}}^A$, $\hat{\mathbf{x}}'$ and $\hat{\mathbf{z}}^B$ axes following the right-hand rule to effect the transformation summarised in the top figure. The two intermediate coordinate systems are $\{\hat{\mathbf{x}}', \hat{\mathbf{y}}', \hat{\mathbf{z}}'\}$ (blue) and $\{\hat{\mathbf{x}}'', \hat{\mathbf{y}}'', \hat{\mathbf{z}}''\}$ (green).

axis);

second, a rotation of angle $0 \leq \beta < 180°$ about the $\hat{\mathbf{x}}'$ axis (the line of intersection between the $x^A y^A$ and $x^B y^B$ planes, which is the x axis after the first rotation);

third, a rotation of angle $0 \leq \gamma < 180°$ about the $\hat{\mathbf{z}}^B$ axis (which is the z axis after the second rotation).

All rotations follow the right-hand rule: looking down the rotation axis towards the origin, a positive angle describes an anticlockwise rotation of the two remaining axes. If an angle is negative, the direction of the rotation is inverted. The angles α, β and γ correspond to the azimuthal position from the x^A axis, the tilt angle from the z^A axis and the negative twist angle from the x^B axis, respectively. These have been chosen for their straightforward physical interpretation. Note that other definitions of these Euler angles are in use that result in different transformation matrices.

The general transformation matrix $\mathbf{T}_{A\to B}$ from equation 2.11 can now be specified following the definitions given above as

$$\begin{aligned}
\mathbf{T}_{A\to B} &= \mathbf{R}_z(\gamma)\,\mathbf{R}_x(\beta)\,\mathbf{R}_z(\alpha) \\
&= \begin{pmatrix} \cos\gamma & \sin\gamma & 0 \\ -\sin\gamma & \cos\gamma & 0 \\ 0 & 0 & 1 \end{pmatrix} \begin{pmatrix} 1 & 0 & 0 \\ 0 & \cos\beta & \sin\beta \\ 0 & -\sin\beta & \cos\beta \end{pmatrix} \begin{pmatrix} \cos\alpha & \sin\alpha & 0 \\ -\sin\alpha & \cos\alpha & 0 \\ 0 & 0 & 1 \end{pmatrix} \\
&= \begin{pmatrix} \cos\gamma\cos\alpha - \sin\gamma\cos\beta\sin\alpha & \cos\gamma\sin\alpha + \sin\gamma\cos\beta\cos\alpha & \sin\gamma\sin\beta \\ -\sin\gamma\cos\alpha - \cos\gamma\cos\beta\sin\alpha & \cos\gamma\cos\beta\cos\alpha - \sin\gamma\sin\alpha & \cos\gamma\sin\beta \\ \sin\beta\sin\alpha & -\sin\beta\cos\alpha & \cos\beta \end{pmatrix}
\end{aligned} \tag{2.13}$$

It expresses a vector or the coordinates of a point fixed in space in the coordinates of frame or reference B from the original coordinates specified in frame of reference A. The opposite rotation is effected by performing the elementary rotations in inverse order and rotating in the opposite direction, thus

$$\mathbf{T}_{B\to A} = \mathbf{R}_z(-\alpha)\,\mathbf{R}_x(-\beta)\,\mathbf{R}_z(-\gamma) \tag{2.14}$$

gives the transformation matrix $\mathbf{T}_{B\to A}$ which brings a vector specified in frame of reference B into the coordinate system of frame of reference A. For the general form of equation 2.13,

this results in

$$\begin{aligned}\mathbf{T}_{B\to A} &= \begin{pmatrix} \cos(-\alpha) & \sin(-\alpha) & 0 \\ -\sin(-\alpha) & \cos(-\alpha) & 0 \\ 0 & 0 & 1 \end{pmatrix} \begin{pmatrix} 1 & 0 & 0 \\ 0 & \cos(-\beta) & \sin(-\beta) \\ 0 & -\sin(-\beta) & \cos(-\beta) \end{pmatrix} \begin{pmatrix} \cos(-\gamma) & \sin(-\gamma) & 0 \\ -\sin(-\gamma) & \cos(-\gamma) & 0 \\ 0 & 0 & 1 \end{pmatrix} \\ &= \begin{pmatrix} \cos\alpha & -\sin\alpha & 0 \\ \sin\alpha & \cos\alpha & 0 \\ 0 & 0 & 1 \end{pmatrix} \begin{pmatrix} 1 & 0 & 0 \\ 0 & \cos\beta & -\sin\beta \\ 0 & \sin\beta & \cos\beta \end{pmatrix} \begin{pmatrix} \cos\gamma & -\sin\gamma & 0 \\ \sin\gamma & \cos\gamma & 0 \\ 0 & 0 & 1 \end{pmatrix} \\ &= \begin{pmatrix} \cos\gamma\cos\alpha - \sin\gamma\cos\beta\sin\alpha & -\sin\gamma\cos\alpha - \cos\gamma\cos\beta\sin\alpha & \sin\beta\sin\alpha \\ \cos\gamma\sin\alpha + \sin\gamma\cos\beta\cos\alpha & \cos\gamma\cos\beta\cos\alpha - \sin\gamma\sin\alpha & -\sin\beta\cos\alpha \\ \sin\gamma\sin\beta & \cos\gamma\sin\beta & \cos\beta \end{pmatrix}\end{aligned} \tag{2.15}$$

which is readily identified as the inverse of $\mathbf{T}_{A\to B}$ when comparing the result to equation 2.13. The identity

$$\mathbf{T}_{B\to A} = {\mathbf{T}_{A\to B}}^{\mathrm{T}} = {\mathbf{T}_{A\to B}}^{-1} \tag{2.16}$$

is a result of the orthogonal nature of the elementary rotation matrices. Their transpose and inverse are identical, which thus also holds for the transformation matrices involving subsequent elementary rotations.

2.3 Light scattering by molecules

Molecules scatter light through various processes. In classical physics, the scattered light is treated as radiation from an induced electric dipole $\mathbf{p}$, which is generated in the scattering molecule by incident electromagnetic waves. This interaction is described by tensors and can be linear or non-linear in the time-dependent electric field vector $\mathbf{E}$ at the location of the scattering molecule. The induced dipole is the sum of these terms, which form a rapidly converging series. The first three terms

$$\begin{aligned}\mathbf{p} &= \mathbf{p}^{(1)} + \mathbf{p}^{(2)} + \mathbf{p}^{(3)} + \dots \\ &= \boldsymbol{\alpha}\,\mathbf{E} + \frac{1}{2}\boldsymbol{\beta}\,\mathbf{E}\,\mathbf{E} + \frac{1}{6}\boldsymbol{\gamma}\,\mathbf{E}\,\mathbf{E}\,\mathbf{E} + \dots\end{aligned} \tag{2.17}$$

contain the polarisability $\boldsymbol{\alpha}$ (a second rank tensor), the hyperpolarisability $\boldsymbol{\beta}$ (a third rank tensor) and the second hyperpolarisability tensor $\boldsymbol{\gamma}$ (a fourth rank tensor), respectively. Multiple electric fields (*e.g.* lasers of different wavelengths) can be used to give rise to the non-linear terms. The interaction between the incoming light and the molecule under investigation thus depends on multiple elements of the appropriate tensors, which vary with the wavelengths of the incoming light as dictated by the molecular properties. A quantum mechanical treatment and symmetry arguments are required to explain how the internal transitions of the scattering molecule affect the induced dipole and what selection

rules apply to the scattering process.

A typical order of magnitude for the components of $\boldsymbol{\alpha}$ is 10^{-40} C V^{-1} m^2, while this is 10^{-50} C V^{-2} m^3 for components of $\boldsymbol{\beta}$ and 10^{-61} C V^{-3} m^4 for components of $\boldsymbol{\gamma}$ [61]. Values for $\boldsymbol{\alpha}$ are also given in units of volume (with a typical magnitude of 10^{-30} m^3 or 1 Å^3), in which case a multiplication by $4\pi\epsilon_0$ will correct the units.

The scattering process can be coherent or incoherent, depending on the experimental system used. When one monochromatic light source is used that produces a single field, the scattered light is incoherent: each molecule radiates independently. There is no phase relation between the incoming and scattered light. This linear process is described by the term $\mathbf{p}^{(1)}$ of equation 2.17. The scattered light is emitted in all directions with varying intensity. This includes Rayleigh and Raman scattering, treated in more detail below.

Non-linear effects occur in materials without inversion symmetry, such as at interfaces or defects in an otherwise ordered system. These can be probed by a single intense laser beam, leading to second harmonic generation, or by using two overlapping beams (one of which is variable) for sum-frequency generation. In such cases, the scattered light is coherent: scattering at particular combinations of the two wavelengths is enhanced and a fixed phase relation exists between the incoming and scattered light, which will be emitted from the sample in a particular direction. This process is contained in the non-linear term $\mathbf{p}^{(2)}$ of equation 2.17 with two different electric fields. Examples include coherent Stokes Raman scattering (CSRS), its anti-Stokes variant CARS and sum-frequency spectroscopy. As the scattered light is coherent, the radiation from multiple scattering molecules interferes and a directional beam of light is emitted by the sample.

Three overlapping electric fields give rise to the second non-linear term $\mathbf{p}^{(3)}$ and so on.

2.3.1 Rayleigh and Raman scattering

The linear term $\mathbf{p}^{(1)}$ of equation 2.17 includes both Rayleigh and Raman scattering. Rayleigh scattering is a ubiquitous phenomenon: the scattered light is of the same frequency as the incident light, *i.e.* the light scatters elastically. Raman scattering is inelastic: the frequencies of the scattered radiation are shifted from the incident frequency. The magnitude of these shifts is characteristic of the internal transitions of the scattering molecule. This work focusses on vibrational transitions in the molecules under investigation, which serve as a signature of the presence of the scattering molecule and its spatial orientation.

Figure 2.3 presents a general energy diagram for the three linear scattering processes that molecules can give rise to. For a single molecule, the incoming and scattered light are coherent, but for an ensemble of molecules, the total scattering is incoherent because of the random phases of the vibrational state of each molecule. Rayleigh scattering is much stronger than Raman scattering and does not alter the energy of the scattered photon. Raman scattering results in the transition from one internal molecular state to another. If the scattered light is red-shifted with respect to the incoming light (*i.e.* it is of lower frequency), part of the incoming light has been taken up by the molecule. This has

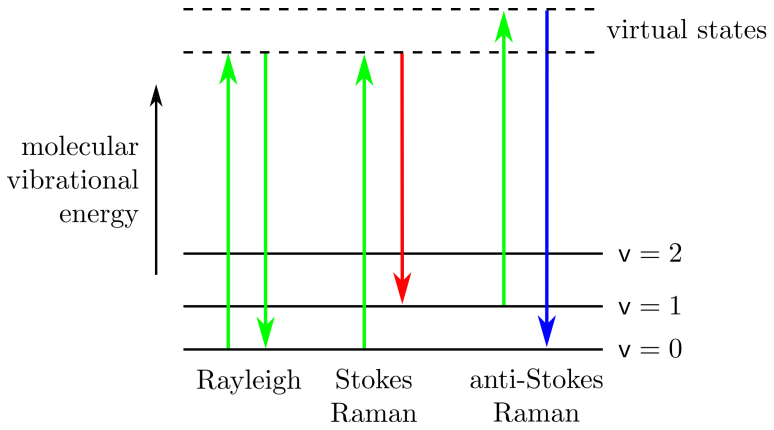

Figure 2.3: Schematic energy diagram for linear scattering processes in a molecule with internal vibrational states v. The coloured arrows designate transitions between molecular vibrational states, the colour representing the energy associated with each transition.

increased its internal energy and it now occupies a higher quantum-mechanical state. This process is called Stokes Raman scattering, because it follows Stokes' law, which states that the wavelength of fluorescence is always longer than that of absorbed light. (Even though the Raman scattering process is entirely different from fluorescence, the same nomenclature has traditionally been applied.) Anti-Stokes Raman scattering is the opposite effect: the molecule loses internal energy in the scattering process by falling to a lower internal state. The energy lost by the molecule is added to the scattering photon causing the scattered radiation to be blue-shifted with respect to the incoming radiation. As the population of high-energy states is usually lower than that of states with low internal energy (as described by the Boltzmann distribution), anti-Stokes Raman scattering is weaker in general than Stokes Raman scattering.

The virtual states in figure 2.3 are not actual energy levels of the molecule. These are included to make a distinction between an apparently absorbed and emitted photon. In normal vibrational Raman scattering, the energy of these virtual states is far below the first electronic excited state. If the photon energy of the incident light is close to that of an internal transition (*i.e.* the virtual states become real), resonant Raman scattering occurs. This is stronger than normal Raman scattering and requires a quantum mechanical description of the intermediate state as well as of the initial and final states. In this work, normal vibrational Raman scattering is employed, though many of the concepts also apply to other forms of Raman scattering.

The polarisability tensor $\boldsymbol{\alpha}$ incorporates both Rayleigh and Raman scattering. It can expanded in a Taylor series with respect to the vibrational normal coordinate Q_{v} of vibrational mode v as

$$\boldsymbol{\alpha} = \boldsymbol{\alpha}_0 + \left(\frac{\partial \boldsymbol{\alpha}}{\partial Q_{\mathsf{v}}}\right)_0 Q_{\mathsf{v}} + \frac{1}{2}\left(\frac{\partial^2 \boldsymbol{\alpha}}{\partial {Q_{\mathsf{v}}}^2}\right)_0 {Q_{\mathsf{v}}}^2 + \ldots \tag{2.18}$$

where $\boldsymbol{\alpha}_0$ is a constant polarisability that is independent of the vibrational mode. The subscript 0 at the derivative denotes the equilibrium configuration of the molecule, at which $Q_{\mathsf{v}} = 0$ for all vibrational modes. The vibrational normal coordinate represents the motion of the nuclei of the molecule in a pattern given by the vibrational mode. As the nuclear positions oscillate, the polarisability changes due to the rearrangement of the electron density. Taking only the first order term in Q_{v} (known as the electrical harmonicity approximation), equation 2.18 can be rewritten as

$$\boldsymbol{\alpha} = \boldsymbol{\alpha}_0 + \boldsymbol{\alpha}_{\mathsf{v}} \tag{2.19}$$

where

$$\boldsymbol{\alpha}_{\mathsf{v}} = Q_{\mathsf{v}} \left(\frac{\delta \boldsymbol{\alpha}}{\delta Q_{\mathsf{v}}} \right)_0 . \tag{2.20}$$

The notation of the derivative is generally shortened to

$$\boldsymbol{\alpha'}_{\mathsf{v}} \equiv \left(\frac{\delta \boldsymbol{\alpha}}{\delta Q_{\mathsf{v}}} \right)_0 \tag{2.21}$$

which the linear polarisability derivative at the equilibrium configuration of the molecule for a vibrational normal mode v. Its unit is C V^{-1} m.

We now introduce the time-dependence of the scattering process. Assuming a harmonic oscillation of the nuclei in the molecule, the time dependence of Q_{v} can be given as

$$Q_{\mathsf{v}}(t) = Q_{\mathsf{v}0} \cos(\omega_{\mathsf{v}} t + \delta_{\mathsf{v}}) \tag{2.22}$$

where $Q_{\mathsf{v}0}$ is the normal coordinate amplitude in m, ω_{v} is the angular frequency of the vibration and δ_{v} is the phase of the vibration at $t = 0$ for a particular molecule. The electric field at the molecule that gives rise to the induced dipole is also time-dependent with frequency ω

$$\mathbf{E}(t) = \mathbf{E}_0 \cos(\omega t) . \tag{2.23}$$

Introducing equations 2.22 and 2.23 into the linear expression for the induced dipole $\mathbf{p}^{(1)}$ from equation 2.17 results in

$$\begin{aligned}
\mathbf{p}^{(1)}(t) &= \boldsymbol{\alpha}(t)\, \mathbf{E}(t) \\
&= \left(\boldsymbol{\alpha}_0 + \boldsymbol{\alpha'}_{\mathsf{v}} Q_{\mathsf{v}}(t)\right) \mathbf{E}_0 \cos(\omega t) \\
&= \boldsymbol{\alpha}_0 \mathbf{E}_0 \cos(\omega t) + \boldsymbol{\alpha'}_{\mathsf{v}} Q_{\mathsf{v}0} \cos(\omega_{\mathsf{v}} t + \delta_{\mathsf{v}}) \mathbf{E}_0 \cos(\omega t) \\
&= \boldsymbol{\alpha}_0 \mathbf{E}_0 \cos(\omega t) + \frac{1}{2} \boldsymbol{\alpha'}_{\mathsf{v}} Q_{\mathsf{v}0} \mathbf{E}_0 \cos((\omega_{\mathsf{v}} + \omega) t + \delta_{\mathsf{v}}) + \frac{1}{2} \boldsymbol{\alpha'}_{\mathsf{v}} Q_{\mathsf{v}0} \mathbf{E}_0 \cos((\omega_{\mathsf{v}} - \omega) t + \delta_{\mathsf{v}})
\end{aligned} \tag{2.24}$$

where we used the trigonometric identity

$$\cos(x)\cos(y) = \frac{1}{2} \left(\cos(x + y) + \cos(x - y) \right) . \tag{2.25}$$

The three terms of equation 2.24 represent three induced dipoles that give rise to radiation of frequencies ω through Rayleigh scattering, $(\omega+\omega_{\mathsf{v}})$ through anti-Stokes Raman scattering and $(\omega-\omega_{\mathsf{v}})$ through Stokes Raman scattering. Moreover, the Raman scattered light suffers a phase shift of δ_{v}. It is also evident that Raman scattering can only occur if the polarisability derivative with respect to the vibrational normal coordinate at the equilibrium position ($\boldsymbol{\alpha'}_{\mathsf{v}}$) is non-zero.

The Rayleigh and Raman polarisability tensors can now be defined as

$$\boldsymbol{\alpha}_{\mathsf{Rayleigh}} \equiv \boldsymbol{\alpha}_0 \tag{2.26}$$

$$\boldsymbol{\alpha}_{\mathsf{Raman}} \equiv \boldsymbol{\alpha}_{\mathsf{v}} = Q_{\mathsf{v}0}\boldsymbol{\alpha'}_{\mathsf{v}} \tag{2.27}$$

where $\boldsymbol{\alpha}_{\mathsf{Raman}}$ is equally valid for Stokes as well as for anti-Stokes Raman scattering. In the classical treatment, both Stokes and anti-Stokes Raman scattering are equally likely. Quantum-mechanical considerations show that these are distinct processes and that $Q_{\mathsf{v}0}$ depends on the vibrational levels involved in the transition.

The Rayleigh polarisability tensor is a static molecular property, while the Raman tensor additionally depends on the particular vibrational mode of the molecule. Note that this definition excludes the time dependence in the Raman tensor that was introduced through $Q_{\mathsf{v}}(t)$ as our main interest is in time-averaged quantities. The Rayleigh as well as Raman tensor is a polarisability tensor. These can be distinguished from each other through the different frequencies of the dipole fields that the scattering processes generate. The tensor $\boldsymbol{\alpha'}_{\mathsf{v}}$ is colloquially also known as 'the Raman tensor', though strictly speaking it is the tensorial linear polarisability derivative with respect to the vibrational normal coordinate at the equilibrium position, which explains why the short-hand is often used, notwithstanding the potential for confusion with the Raman polarisability tensor.

2.3.2 A quantum mechanical description

So far, the linear scattering process has been treated classically. In a conventional quantum mechanical description, the molecular system is described through wave functions while only the electromagnetic radiation is described classically [61–63]. The quantum-mechanical theory of Raman scattering was derived by Placzek in the 1930's [64] and is summarised in chapters 2 and 4 of Long's work [61]. The incident light perturbs the (vibrational) states of a molecule. The total transition electric dipole vector $(\mathbf{p})_{fi}$ is calculated using the perturbed wave functions Ψ' for the initial i and final f states of the molecule through

$$(\mathbf{p})_{fi} = \langle \Psi'_f | \hat{\mathbf{p}} | \Psi'_i \rangle \tag{2.28}$$

where Dirac notation is used. $\hat{\mathbf{p}}$ is the electric dipole moment operator and has a component in each of the three spatial dimensions. It depends on the distribution of electric charge within the molecule (due to both electrons and nuclei) around its centre of mass. For a collection of point charges, the dipole moment is given by a sum over all electric

charges c of charge e_c located at $\mathbf{r}_c$ relative to the location of the centre of mass $\mathbf{r}_{\mathsf{cm}}$

$$\hat{\mathbf{p}} = \sum_c e_c(\mathbf{r}_c - \mathbf{r}_{\mathsf{cm}}) \tag{2.29}$$

The choice of the origin affects the dipole moment in ionic species. It is conventional to take the centre of mass as the origin for the molecular frame of reference, even if the net charge is zero. The charge distribution within a molecule changes during vibrational motion while the incident electric field also oscillates. $\hat{\mathbf{p}}$ thus depends on the quantum-mechanical state of the molecule and on time.

The integral of equation 2.28 further includes time-dependent wavefunctions that are perturbed by an incident electromagnetic field $\mathbf{E}$ of a certain angular frequency ω. The perturbed wave functions of the system can be expressed as the unperturbed wave function plus a series of modifications that depend on increasing powers of $\mathbf{E}(\omega)$. The wave functions of the unperturbed and first order perturbed states

$$\Psi' = \Psi^{(0)} + \Psi^{(1)} \tag{2.30}$$

determine the first order transition electric dipole moment $(\mathbf{p}^{(1)})_{fi}$ that gives rise to Rayleigh ($i = f$, which may be degenerate) and Raman ($i \neq f$) scattering. The zeroth-order dipole arises from transitions between unperturbed states, so does not involve light scattering. Higher-order terms in the electric dipole moment give rise to hyper-Rayleigh and hyper-Raman scattering. The first-order induced dipole moment can be written as

$$(\mathbf{p}^{(1)})_{fi} = \langle \Psi_f^{(0)} | \hat{\mathbf{p}} | \Psi_i^{(1)} \rangle + \langle \Psi_f^{(1)} | \hat{\mathbf{p}} | \Psi_i^{(0)} \rangle \tag{2.31}$$

where the first-order perturbed wavefunctions of the initial and final states may be expressed as a linear combination of all unperturbed wavefunctions of the molecule. The coefficients are linear in $\mathbf{E}(\omega)$ and so is $(\mathbf{p}^{(1)})_{fi}$. The electric field can then be taken out of the integrals of equation 2.31.

In addition to the electric dipole moment, the magnetic dipole moment and the electric quadrupole moment are also linearly dependent on the electric field. Only $\hat{\mathbf{p}}$ is considered here, assuming that the gradient of the electric field is zero over the extend of the wavefunctions. This approximation is known as the electric dipole approximation and is valid as long as the size of the molecule is negligible compared to the wavelength of the electric field. In the visible range, this approximation is usually justified.

The induced dipole contains more than one frequency component, which is the basis of Rayleigh and Raman scattering. At these frequencies, time-independent unperturbed wavefunctions ψ can be used to describe the system. The amplitudes of the electric transition dipole moment $(\mathbf{p}^{(1)})_{fi}$ can then be expressed similar to the classical description (equation 2.17) as

$$(\mathbf{p}^{(1)})_{fi} = (\boldsymbol{\alpha})_{fi}\, \mathbf{E} \tag{2.32}$$

with $(\boldsymbol{\alpha})_{fi}$ the transition polarisability tensor. In time-independent perturbation theory, the elements kl of the transition polarisability are a result of summing over all possible transitions

$$(\alpha_{kl})_{fi} = \frac{2\pi}{h} \sum_{\mathsf{v} \neq i,f} \left(\frac{\langle \psi_f | \hat{p}_k | \psi_\mathsf{v} \rangle \langle \psi_\mathsf{v} | \hat{p}_l | \psi_i \rangle}{\omega_\mathsf{v} - \omega_i - \omega - \mathrm{j}\Gamma_\mathsf{v}} + \frac{\langle \psi_f | \hat{p}_l | \psi_\mathsf{v} \rangle \langle \psi_\mathsf{v} | \hat{p}_k | \psi_i \rangle}{\omega_\mathsf{v} - \omega_f + \omega + \mathrm{j}\Gamma_\mathsf{v}} \right) \tag{2.33}$$

which is a function of ω, the angular frequency of the incident field $\mathbf{E}$. The wavefunctions ψ are time-independent and angular frequency Γ_v is inversely proportional to the lifetime of state v. For the initial and final states, these are assumed to be zero (*i.e.* stable states with an infinite lifetime) and therefore do not appear in the equation. The differences $\omega_\mathsf{v} - \omega_i$ and $\omega_\mathsf{v} - \omega_f$ are proportional to the energy differences between pairs of states. A quantum-mechanical analysis of Raman scattering thus includes a sum over all internal states of the scattering molecule and can predict the tensor elements involved based on the molecular structure as described through unperturbed time-independent wavefunctions.

If the incident angular frequency ω matches an internal transition $\omega_\mathsf{v} - \omega_i$, the denominator of the first term in equation 2.33 depends on Γ_v only. This gives rise to resonance Raman scattering and $(\alpha_{kl})_{fi}$ increases dramatically. In normal Raman scattering, employed in this work, $\omega \ll \omega_\mathsf{v} - \omega_i$ and the intermediate state v is a non-stable virtual state as illustrated in figure 2.3.

The numerators of equation 2.33 include two transition electric dipole moments: first a transition from state i to v and next from v to f. This represents an absorption followed by an emission (as ω_v is greater than both ω_i and ω_f). The scattering process from a particular state i, via v to f thus only contributes to $(\alpha_{kl})_{fi}$ if both transition electric dipole moments involved are non-zero. This property gives rise to selection rules discussed below.

Through $(\boldsymbol{\alpha})_{fi}$, the induced dipole contains multiple frequencies that follow from the internal states of the scattering molecule. It can be shown that [61]

$$(\mathbf{p}^{(1)})_{ii}(\omega) = (\boldsymbol{\alpha})_{ii}\, \mathbf{E}(\omega) \tag{2.34}$$

for Rayleigh scattering (explicitly including the frequency dependence) and

$$(\mathbf{p}^{(1)})_{fi}(\omega \pm \omega_\mathsf{m}) = (\boldsymbol{\alpha})_{fi}\, \mathbf{E}(\omega) \tag{2.35}$$

for Raman scattering, with $\omega_\mathsf{m} = \omega_f - \omega_i$ matching a transition between internal states of the scattering molecule. However, not all transitions result in Raman scattering. For harmonic vibrational wave functions with quantum number v, the quantum-mechanically allowed transitions are limited to $\Delta\mathsf{v} = \mathsf{v_f} - \mathsf{v_i} = \pm 1$. Anharmonicity of the vibrational energy potential relaxes this selection rule. If the energy of the incoming photons matches a specific transition in the molecule, absorption or resonances result in more intricate spectral features not discussed here. Such effects generally obscure normal Raman scattering.

2.4 Classical electrodynamics

The previous section described Rayleigh and Raman scattering mathematically as

$$\mathbf{p} = \boldsymbol{\alpha}\, \mathbf{E} \tag{2.36}$$

both classically and quantum-mechanically. An incident electric field $\mathbf{E}$ induces an oscillating dipole $\mathbf{p}$ and the relation is incorporated in the polarisability tensor $\boldsymbol{\alpha}$. We now derive an electromagnetic description of $\mathbf{E}$ as a plane electromagnetic wave and of $\mathbf{p}$ as a source of a dipole field.

2.4.1 Plane electromagnetic waves

A propagating ray of light can be described as a monochromatic harmonic plane electromagnetic wave. The wave is specified by a frequency, a direction of propagation, a transverse amplitude in two orthogonal directions and a phase relation between these two. We discuss each of those aspects before coming to a complete expression for a plane electromagnetic wave. We consider isotropic materials, in which the optical properties do not vary with the propagation direction of the wave.

The angular frequency ω is the number of oscillations in 2π seconds

$$\omega = 2\pi\nu \tag{2.37}$$

which is related to the frequency ν that specifies the number of oscillations per second. The period of oscillation T is its reciprocal

$$T = \frac{1}{\nu} = \frac{2\pi}{\omega}\ . \tag{2.38}$$

The wavelength λ of the wave depends on the speed of the wave v (more correctly its phase velocity) and its period as

$$\lambda = vT = \frac{2\pi c}{n\omega} \tag{2.39}$$

where we have used equation 2.38 and introduced the refractive index n which is a property of the material in which the wave is propagating

$$n \equiv \frac{c}{v} \tag{2.40}$$

with c the speed of light in vacuum ($2.998 \cdot 10^8$ m s^{-1}). The refractive index of a material is a function of ω while it is unity in vacuum. Note that the frequency of the wave is the same in different materials, but the wavelength is not: the latter is a manifestation of the refractive index of the material, as

$$n(\lambda) = \frac{c}{v} = \frac{cT}{\lambda} = \frac{\lambda_0}{\lambda} \tag{2.41}$$

where λ_0 is the wavelength for a wave of the same frequency propagating in vacuum. n is related to the relative permittivity (or dielectric constant) ϵ_r and the relative permeability μ_r of the material through

$$n = \sqrt{\epsilon_r \mu_r} \tag{2.42}$$

and is a complex refractive index $\tilde{n}$ for materials and wavelengths at which absorption takes place

$$\tilde{n} = n + \mathrm{j}\kappa \tag{2.43}$$

where j is the complex number $\sqrt{-1}$ and κ is the extinction coefficient. For non-magnetic materials $\mu_r = 1$, while many materials exhibit $\mu_r \approx 1$ for optical frequencies and the approximation

$$n \approx \sqrt{\epsilon_r} \tag{2.44}$$

is often used. The permittivity and permeability of vacuum are $\epsilon_0 = 8.854{\cdot}10^{-12}$ C^2 N^{-1} m^{-2} and $\mu_0 = 4\pi \cdot 10^{-7}$ N A^{-2}, respectively. These are also termed the electric and magnetic constant and are related to c as

$$c = \frac{1}{\sqrt{\epsilon_0 \mu_0}} \, . \tag{2.45}$$

The absolute permittivity ϵ and absolute permeability μ of a material are given through

$$\epsilon = \epsilon_r \epsilon_0 \tag{2.46}$$

and

$$\mu = \mu_r \mu_0 \, . \tag{2.47}$$

The number of wavelengths per unit length is termed the wavenumber $\bar{\nu}$

$$\bar{\nu} = \frac{1}{\lambda} \tag{2.48}$$

which is usually given in units of cm^{-1} while λ is often specified in nm in the visible range of the electromagnetic spectrum (400-700 nm in vacuum). The frequency of an electromagnetic oscillation in a medium is thus specified through ω, ν, T, λ or $\bar{\nu}$, where n has to be specified with the last two quantities.

The propagation direction of the wave is specified by the unit vector $\hat{\boldsymbol{k}}$. The wave vector $\mathbf{k}$ is defined as

$$\mathbf{k} = \frac{2\pi}{\lambda} \hat{\boldsymbol{k}} \tag{2.49}$$

and incorporates both the propagation direction of the plane electromagnetic wave as well as its wavelength in the particular medium it is propagating through.

The wave oscillates in two mutually orthogonal transverse directions $\hat{\boldsymbol{p}}$ and $\hat{\boldsymbol{s}}$. These form the right-handed orthonormal Cartesian basis $\{\hat{\boldsymbol{p}}, \hat{\boldsymbol{s}}, \hat{\boldsymbol{k}}\}$, related through

$$\hat{\boldsymbol{k}} = \hat{\boldsymbol{p}} \times \hat{\boldsymbol{s}} \, . \tag{2.50}$$

The electric vector of a plane wave has a complex component E_p, E_s along each of the directions $\hat{\boldsymbol{p}}$ and $\hat{\boldsymbol{s}}$ while the third component along $\hat{\boldsymbol{k}}$ is zero. E_p and E_s include real amplitudes A_p, A_s and phases δ_p, δ_s in radians

$$\begin{cases} E_p \propto A_p \Re\{\mathrm{e}^{-\mathrm{j}\delta_p}\} \\ E_s \propto A_s \Re\{\mathrm{e}^{-\mathrm{j}\delta_s}\} \\ E_k = 0 \end{cases} \tag{2.51}$$

where $\Re$ designates that the real part of the exponent should be taken. However, this is generally implied without explicitly stating so. Euler's formula

$$\mathrm{e}^{\mathrm{j}\varphi} = \cos\varphi + \mathrm{j}\sin\varphi \tag{2.52}$$

gives the real and imaginary parts as the cosine and sine of the phase angle φ. The exponential notation simplifies the calculation of phases when dealing with multiple waves. The phases δ_p and δ_s are the phase angles of each component at the origin at $t = 0$.

The time and space domains are also incorporated in exponential notation (implying cosine functions that satisfy the wave equation). These apply equally to all three components of the electric vector $\mathbf{E}$ of the plane wave so that

$$\mathbf{E}(t) \propto \mathrm{e}^{-\mathrm{j}\omega t} \tag{2.53}$$

where t is the time. As the wave travels from the origin to a point in space $\mathbf{r}$, it takes a time interval of duration r/v seconds to arrive there. The retarded time t' at location $\mathbf{r}$ relative to time t at the origin is given as

$$t' = t - \frac{r}{v} \tag{2.54}$$

which combines with equation 2.53 to yield

$$\mathbf{E}(\mathbf{r}, t) \propto \mathrm{e}^{-\mathrm{j}\omega t'} = \mathrm{e}^{-\mathrm{j}\omega t + \omega \frac{r}{v}} = \mathrm{e}^{-\mathrm{j}(\omega t - kr)} \tag{2.55}$$

where the exponent has been arranged using

$$k = \frac{\omega}{v} \tag{2.56}$$

derived from equations 2.38, 2.39 and 2.49. The product kr in the exponent of equation 2.55 holds if both k and r are parallel, but in general the dot product $\mathbf{k} \cdot \mathbf{r}$ is used to give the distance from the origin projected onto the propagation direction of the wave.

Having derived the various factors, the electric field of a plane wave can now be given

as

$$\mathbf{E}(\mathbf{r},t) = \begin{pmatrix} E_p \\ E_s \\ E_k \end{pmatrix} = \begin{pmatrix} A_p \mathrm{e}^{-\mathrm{j}\delta_p} \\ A_s \mathrm{e}^{-\mathrm{j}\delta_s} \\ 0 \end{pmatrix} \mathrm{e}^{-\mathrm{j}(\omega t - \mathbf{k}\cdot\mathbf{r})} \tag{2.57}$$

in units of N C^{-1}. A full specification of a plane wave thus includes ω (or one of its equivalents) with n of the medium (these two provide $\mathbf{k}$), as well as A_p, A_s, δ_p and δ_s. Chapter 5 discusses how this description changes in a frame of reference that does not conform to the $\{\hat{\boldsymbol{p}}, \hat{\boldsymbol{s}}, \hat{\boldsymbol{k}}\}$ basis as given here.

The magnetic field vector $\mathbf{B}$ associated with the electromagnetic plane wave is derived from the relation

$$\mathbf{B} = \frac{1}{v}\hat{\boldsymbol{k}} \times \mathbf{E} \tag{2.58}$$

which results in

$$\mathbf{B} = \begin{pmatrix} B_p \\ B_s \\ B_k \end{pmatrix} = \frac{1}{v}\begin{pmatrix} 0 \\ 0 \\ 1 \end{pmatrix} \times \begin{pmatrix} E_p \\ E_s \\ 0 \end{pmatrix} = \frac{1}{v}\begin{pmatrix} -E_s \\ E_p \\ 0 \end{pmatrix} = \begin{pmatrix} -A_s \mathrm{e}^{-\mathrm{j}\delta_s} \\ A_p \mathrm{e}^{-\mathrm{j}\delta_p} \\ 0 \end{pmatrix} \frac{\mathrm{e}^{-\mathrm{j}(\omega t - \mathbf{k}\cdot\mathbf{r})}}{v} \tag{2.59}$$

where the frame of reference $\{\hat{\boldsymbol{p}}, \hat{\boldsymbol{s}}, \hat{\boldsymbol{k}}\}$ is unchanged. It remains defined as for the electric field vector. The magnetic field is given in units of N m^{-1} A^{-1}.

Polarisation

The polarisation state of a plane wave is determined by the real amplitudes A_p and A_s and the phase difference δ of the electric vector components E_p and E_s, where

$$\delta = \delta_s - \delta_p \; . \tag{2.60}$$

In general, E_p and E_s describe an ellipse

$$\left(\frac{E_p}{A_p}\right)^2 + \left(\frac{E_s}{A_s}\right)^2 - 2\frac{E_p E_s}{A_p A_s}\cos\delta = \sin^2\delta \tag{2.61}$$

that is inscribed in a rectangle of $2A_p$ by $2A_s$ along $\hat{\boldsymbol{p}}$ and $\hat{\boldsymbol{s}}$, respectively. Figure 2.4 illustrates the orientation of this polarisation ellipse. Its major and minor axes $\hat{\mathbf{a}}$ and $\hat{\mathbf{b}}$ do not necessarily coincide with the directions $\hat{\boldsymbol{p}}$ and $\hat{\boldsymbol{s}}$ as defined before. The angle ψ between the two is the polarisation angle that can be computed from E_p and E_s using

$$\tan(2\psi) = \frac{2A_pA_s}{A_p^2 + A_s^2}\cos\delta \; . \tag{2.62}$$

(A derivation of the last two equations can be found in [65].) The electric vector components along the axes of the ellipse E_a and E_b can then be expressed with this angle

as

$$\begin{cases} E_a = E_p \cos\psi + E_s \sin\psi \\ E_b = -E_p \sin\psi + E_s \cos\psi \ . \end{cases} \tag{2.63}$$

The electric vector may describe the ellipse in two senses: clockwise or anticlockwise. These directions are relative to the point of view and are specified for a viewer facing the direction where the radiation is coming from. This is the case in figure 2.4 with $\hat{\boldsymbol{k}}$ coming out of the page towards the reader. If the ratio

$$\frac{E_s}{E_p} = \frac{A_s}{A_p} \mathrm{e}^{-\mathrm{j}\delta} \tag{2.64}$$

has a positive imaginary part, the polarisation direction is anticlockwise (also traditionally termed left-handed polarisation or simply left-polarised, though it conforms to the right-hand-rule). For clockwise or right-handed polarisation, the ratio has a negative imaginary part.

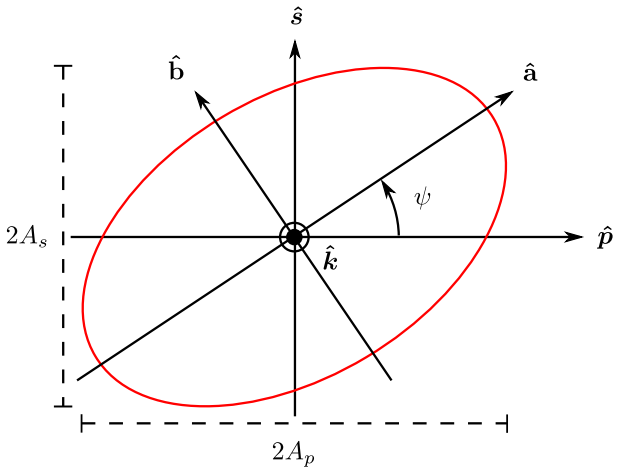

Figure 2.4: The polarisation ellipse (in red) for the electric vector of a plane wave is given in its basis $\{\hat{\boldsymbol{p}}, \hat{\boldsymbol{s}}, \hat{\boldsymbol{k}}\}$. The major ($\hat{\mathbf{a}}$) and minor ($\hat{\mathbf{b}}$) axes of the ellipse are in general rotated from this basis by ψ.

When the polarisation ellipse reduces to a circle, circular polarisation is achieved. Equation 2.61 reduces to the expression of a circle

$$E_p^2 + E_s^2 = A^2 \tag{2.65}$$

if

$$A = A_p = A_s \tag{2.66}$$

and if the phase difference is such that one of the components is zero when the other reaches its extreme value. This is the case if

$$\delta = \pm\frac{\pi}{2} + 2m\pi \qquad (m = 0, \pm1, \pm2, \dots) \tag{2.67}$$

which results in right-handed polarised light when the + sign is used and in left-handed polarised light when the − sign is used. The ratio E_s/E_p is −j in the first case and j in the latter.

Linear polarisation is achieved when the polarisation ellipse reduces to a straight line. This is the case if

$$\delta = m\pi \qquad (m = 0, \pm 1, \pm 2, \ldots) \tag{2.68}$$

so that

$$\frac{E_s}{E_p} = (-1)^m \, \frac{A_s}{A_p} \, . \tag{2.69}$$

The general expression for a plane wave was given in equation 2.57. This reduces to the following expressions for right and left-circularly polarised light

$$\mathbf{E} = A\mathrm{e}^{-\mathrm{j}(\omega t - \mathbf{k}\cdot\mathbf{r})} \left\{ \begin{array}{ll} \begin{pmatrix} \mathrm{e}^{-\mathrm{j}\delta_p} \\ \mathrm{e}^{-\mathrm{j}\left(\delta_p + \frac{\pi}{2}\right)} \\ 0 \end{pmatrix} & \text{for right-circular polarisation} \\ \begin{pmatrix} \mathrm{e}^{-\mathrm{j}\delta_p} \\ \mathrm{e}^{-\mathrm{j}\left(\delta_p - \frac{\pi}{2}\right)} \\ 0 \end{pmatrix} & \text{for left-circular polarisation} \end{array} \right. \tag{2.70}$$

while a linearly polarised wave is given through

$$\mathbf{E} = \begin{pmatrix} A_p \\ A_s \\ 0 \end{pmatrix} \mathrm{e}^{-\mathrm{j}(\omega t - \mathbf{k}\cdot\mathbf{r} + \delta_p)} \qquad \text{for linear polarisation} \tag{2.71}$$

where we have used $m = 0$ in both equations. As the current work is concerned with time-averaged fields the absolute instantaneous phases of the fields are irrelevant. Only the relative phase δ is of importance and the value of δ_p is chosen to be zero, simplifying the above expressions.

Flow of electromagnetic energy

The instantaneous flow of energy per unit area per unit time is given by the Poynting vector $\mathbf{S}$ as

$$\mathbf{S} = \frac{1}{\mu}\mathbf{E} \times \mathbf{B} \, . \tag{2.72}$$

Substitution of $\mathbf{E}$ and $\mathbf{B}$ from equations 2.57 and 2.59 gives the Poynting vector for a plane electromagnetic wave propagating in an isotropic medium

$$\mathbf{S} = \frac{1}{\mu v} \left({E_p}^2 + {E_s}^2 \right) \hat{\boldsymbol{k}} \tag{2.73}$$

which is propagating along $\mathbf{k}$. Note that $\mathbf{S}$ is a function of time. In practice, however, this variation is not observed. For example, an optical wavelength of 500 nm in air has a period of $1.67 \cdot 10^{-15}$ s, which is orders of magnitude shorter than conventional detectors can measure. Experiments therefore record a time-averaged energy flow.

The time average of the Poynting vector $\mathbf{S}$ follows from the time average of the squared real parts of E_p and E_s. Averaging these over one period (or many) results in

$$\langle E_p \rangle = \langle \Re\{A_p \mathrm{e}^{-\mathrm{j}(\omega t - \mathbf{k}\cdot\mathbf{r} + \delta_p)}\}^2 \rangle = {A_p}^2 \langle \cos^2(\omega t - \mathbf{k}\cdot\mathbf{r} + \delta_p) \rangle = \frac{1}{2}{A_p}^2 \tag{2.74}$$

and a similar expression holds for $\langle E_s \rangle$. Thus

$$\langle \mathbf{S} \rangle = \frac{1}{2\mu v}\left({A_p}^2 + {A_s}^2\right)\ \hat{\boldsymbol{k}} \tag{2.75}$$

which is independent of δ and the exact nature of the polarisation. Its magnitude is called the irradiance I, the average energy per unit area per unit time

$$I \equiv ||\langle \mathbf{S} \rangle|| \tag{2.76}$$

in units of J s^{-1} m^{-2}. For a plane wave, this results in

$$I = \frac{n\epsilon_0 c}{2\mu_r}\left({A_p}^2 + {A_s}^2\right) \tag{2.77}$$

where equations 2.40 and 2.45 have been used to rearrange the proportionality. The irradiance refers to a unit area perpendicular to $\mathbf{S}$ which in turn is parallel to $\mathbf{k}$. Approximation 2.44 ($\mu_r = 1$) can further simplify the equation.

Light detectors such as charge-coupled devices and photomultipliers do not record the irradiance, but count the number of photons N arriving on each of its pixels. The photon flux Φ is the number of photons arriving per unit time on detector area $\mathrm{d}A$, which is usually kept constant throughout an experiment. It is given through

$$\Phi = \frac{\mathrm{d}N}{\mathrm{d}t} = \frac{I\ \mathrm{d}A}{\varepsilon} \tag{2.78}$$

where ε is the energy of a single photon, which is proportional to its frequency

$$\varepsilon = h\nu \tag{2.79}$$

with Planck's constant $h = 6.626 \cdot 10^{-34}$ J s. The photon count N is accumulated over the exposure time, so that

$$N = \int_{\text{exposure}} \Phi\ \mathrm{d}t \propto \frac{I}{h\nu}\ . \tag{2.80}$$

The lower the wavelength of the wave (towards blue colour in the visual range of the electromagnetic spectrum), the higher the frequency and the higher the energy per photon.

Less 'blue' photons are thus needed than 'red' ones to reach the same irradiance.

Finally, the power P of electromagnetic radiation (in J s^{-1}) is the irradiance integrated over an area A normal to the Poynting vector

$$P = \int I \, \mathrm{d}A \tag{2.81}$$

where I in general depends on the location of integration element $\mathrm{d}A$. A projection is needed if the area of interest is not normal to $\mathbf{S}$. Equation 2.81 thus holds for any surface and radiation profile shape. In particular, the optical power of a light beam is the irradiance integrated over its cross-sectional area.

2.4.2 Dipole radiation

An oscillating electric dipole is a source of electromagnetic radiation. The Rayleigh or Raman scattered light is modelled through computation of that dipole $\mathbf{p}$ as outlined above. We employ the magnetic vector potential $\mathbf{A}$ (in part based on the suggestion in [66]) to deduce the magnetic field $\mathbf{B}$ due to an oscillating electric dipole and subsequently its electric field $\mathbf{E}$ in a linear homogeneous non-absorbing medium. Standard electromagnetic and optics texts (including [65, 67, 68]) only provide derivations of the dipole far-field in vacuum, which does not apply in our system.

Oscillating infinitesimal dipole

Consider an oscillating infinitesimal dipole $\mathbf{p}$ of constant frequency ω (known as a Hertzian or perfect dipole) positioned at the origin of a Cartesian basis and directed along the $\hat{\mathbf{z}}$ axis

$$\mathbf{p}(t) = \begin{pmatrix} 0 \\ 0 \\ p \end{pmatrix} \mathrm{e}^{-\mathrm{j}\omega t} \tag{2.82}$$

where p is the electric dipole moment in units of C m. As before, the real part of this wave is implied so that $\mathbf{p}(t) = p\cos(\omega t)\hat{\mathbf{z}}$. The frequency ω depends on the frequency of the incident radiation ω_{in} and the energy associated with the vibrational transition $h\omega_{\mathsf{m}}$ as

$$\omega = \omega_{\mathrm{in}} \pm \omega_{\mathsf{m}} \tag{2.83}$$

for Raman scattering (with + in case of anti-Stokes and − for Stokes), while $\omega = \omega_{\mathrm{in}}$ for Rayleigh scattering. This dipole can be described as a charge q at $z = l/2$ and a charge $-q$ at $z = -l/2$ that oscillate as

$$q(t) = q_0 \mathrm{e}^{-\mathrm{j}\omega t} \tag{2.84}$$

so that the dipole moment is

$$\mathbf{p}(t) = \left(q(t)\frac{l}{2} - q(t)\frac{-l}{2} \right) \hat{\mathbf{z}} = q(t)l \, \hat{\mathbf{z}} = q_0 l \mathrm{e}^{-\mathrm{j}\omega t} \, \hat{\mathbf{z}} = p\mathrm{e}^{-\mathrm{j}\omega t} \, \hat{\mathbf{z}} \tag{2.85}$$

with $p = q_0 l$ a constant. An oscillating current $I(t)$ is then found at the centre of the dipole

$$I(t) = \frac{dq}{dt} = -\mathrm{j}\omega q_0 \mathrm{e}^{-\mathrm{j}\omega t} \, . \tag{2.86}$$

Magnetic vector potential

In linear media, the electric $\mathbf{E}$ and magnetic $\mathbf{B}$ fields are related to the auxiliary fields $\mathbf{D}$ (the electric displacement) and $\mathbf{H}$ through

$$\mathbf{D} = \epsilon \mathbf{E} \tag{2.87}$$

and

$$\mathbf{H} = \frac{1}{\mu}\mathbf{B} \, . \tag{2.88}$$

The magnetic field $\mathbf{B}$ can be derived from the magnetic vector potential $\mathbf{A}$ though

$$\mathbf{B} = \nabla \times \mathbf{A} \tag{2.89}$$

which in turn provides the electric field $\mathbf{E}$ through one of Maxwell's equations in matter

$$\nabla \times \mathbf{H} = \mathbf{J}_f + \frac{\partial \mathbf{D}}{\partial t} \tag{2.90}$$

which combines with equations 2.88 and 2.87 to form

$$\frac{1}{\epsilon\mu} \nabla \times \mathbf{B} = \frac{\partial \mathbf{E}}{\partial t} \tag{2.91}$$

where the free current $\mathbf{J}_f = 0$, which holds for $r > 0$ as the dipole is located in the exact origin (at $r = 0$) and no further currents exist in the dielectric medium.

The general solution for the magnetic vector potential of a localised line current (that is, assuming that the current $I(t)$ goes to zero at infinity) is given through [68]

$$\mathbf{A}(\mathbf{r}, t) = \frac{\mu}{4\pi} \int \frac{I(t')\hat{\mathbf{z}}}{r} dl \tag{2.92}$$

where t is the time at the origin and t' is the retarded time at location $\mathbf{r}$ as given in equation 2.54. The integral is taken over a single point only (namely the origin where all current is located) with the current given in equation 2.86. This results in

$$\mathbf{A}(\mathbf{r}, t) = \frac{\mu}{4\pi} \left(-\mathrm{j}\omega q_0 \mathrm{e}^{-\mathrm{j}\omega t'} l \right) = \frac{-\mathrm{j}\mu\omega p}{4\pi r} \mathrm{e}^{-\mathrm{j}(\omega t - kr)} \hat{\mathbf{z}} \tag{2.93}$$

where we assume that as $l \to 0$, q_0 increases to keep p constant. This vector potential only

depends on r and is therefore conveniently described in spherical coordinates $\{\hat{\boldsymbol{\rho}}, \hat{\boldsymbol{\theta}}, \hat{\boldsymbol{\phi}}\}$ by

$$\mathbf{A}(\mathbf{r},t) = \begin{pmatrix} A_\rho \\ A_\theta \\ A_\phi \end{pmatrix} = \begin{pmatrix} A_z \cos\theta \\ -A_z \sin\theta \\ 0 \end{pmatrix} \tag{2.94}$$

with

$$A_z = \frac{-\mathrm{j}\mu\omega p}{4\pi r} \mathrm{e}^{-\mathrm{j}(\omega t - kr)} \tag{2.95}$$

from equation 2.93 and with the radial component $\rho = ||\mathbf{r}|| = r$. $\mathbf{A}$ is independent of the azimuthal angle ϕ due to the rotational symmetry around the dipole axis chosen to be along $\hat{\mathbf{z}}$.

Magnetic and electric fields of a dipole

The magnetic field $\mathbf{B}$ due to the dipole can now be found in spherical coordinates through equation 2.89, which provides

$$\begin{aligned} \mathbf{B}(\mathbf{r},t) &= \nabla \times \mathbf{A}(\mathbf{r},t) \\ &= \begin{pmatrix} B_\rho \\ B_\theta \\ B_\phi \end{pmatrix} = \begin{pmatrix} \frac{1}{r\sin\theta}\frac{\partial A_\phi \sin\theta}{\partial\theta} - \frac{1}{r\sin\theta}\frac{\partial A_\theta}{\partial\phi} \\ \frac{1}{r\sin\theta}\frac{\partial A_r}{\partial\phi} - \frac{1}{r}\frac{\partial A_\phi r}{\partial r} \\ \frac{1}{r}\frac{\partial A_\theta r}{\partial r} - \frac{1}{r}\frac{\partial A_r}{\partial\theta} \end{pmatrix} \end{aligned} \tag{2.96}$$

where all A_ϕ terms are zero through equation 2.94, as well as those involving partial derivatives with respect to ϕ, as $\mathbf{A}$ is independent of ϕ for the dipole along $\hat{\boldsymbol{z}}$. This causes $B_\rho = 0$ and $B_\theta = 0$ while

$$\begin{aligned} B_\phi &= \frac{1}{r}\frac{\partial A_\theta r}{\partial r} - \frac{1}{r}\frac{\partial A_r}{\partial\theta} \\ &= \frac{1}{r}\frac{-\mu\omega p k \sin\theta}{4\pi}\mathrm{e}^{-\mathrm{j}(\omega t - kr)} - \frac{1}{r}\frac{\mathrm{j}\mu\omega p \sin\theta}{4\pi r}\mathrm{e}^{-\mathrm{j}(\omega t - kr)} \\ &= \frac{-\mu\omega p k \sin\theta}{4\pi r}\left(1 + \frac{\mathrm{j}}{kr}\right)\mathrm{e}^{-\mathrm{j}(\omega t - kr)} . \end{aligned} \tag{2.97}$$

The electric field due to the dipole is derived through equation 2.91, where the time-dependence of $\mathbf{E}$ is given through $\mathrm{e}^{-\mathrm{j}\omega t}$ as with all quantities in this analysis, so that

$$\frac{\partial \mathbf{E}(\mathbf{r},t)}{\partial t} = -\mathrm{j}\omega \mathbf{E}(\mathbf{r},t) \tag{2.98}$$

which results in

$$\begin{aligned} \mathbf{E} &= \frac{\mathrm{j}}{\omega\epsilon\mu}\nabla \times \mathbf{B}(\mathbf{r},t) \\ &= \begin{pmatrix} E_\rho \\ E_\theta \\ E_\phi \end{pmatrix} = \frac{\mathrm{j}}{\omega\epsilon\mu} \begin{pmatrix} \frac{1}{r\sin\theta}\frac{\partial B_\phi \sin\theta}{\partial\theta} - \frac{1}{r\sin\theta}\frac{\partial B_\theta}{\partial\phi} \\ \frac{1}{r\sin\theta}\frac{\partial B_r}{\partial\phi} - \frac{1}{r}\frac{\partial B_\phi r}{\partial r} \\ \frac{1}{r}\frac{\partial B_\theta r}{\partial r} - \frac{1}{r}\frac{\partial B_r}{\partial\theta} \end{pmatrix} \end{aligned} \tag{2.99}$$

in spherical coordinates. The terms involving B_ρ, B_θ and $\partial/\partial\phi$ are zero, so that $E_\phi = 0$ while E_ρ and E_θ are derived as follows.

$$\begin{aligned} E_\rho &= \frac{\mathrm{j}}{\omega\epsilon\mu}\frac{1}{r\sin\theta}\frac{\partial B_\phi \sin\theta}{\partial\theta} \\ &= \frac{\mathrm{j}}{\omega\epsilon\mu}\frac{1}{r\sin\theta}\frac{-2\mu\omega pk\sin\theta\cos\theta}{4\pi r}\left(1+\frac{\mathrm{j}}{kr}\right)\mathrm{e}^{-\mathrm{j}(\omega t-kr)} \\ &= \frac{-\mathrm{j}pk\cos\theta}{2\pi\epsilon r^2}\left(1+\frac{\mathrm{j}}{kr}\right)\mathrm{e}^{-\mathrm{j}(\omega t-kr)} \end{aligned} \tag{2.100}$$

$$\begin{aligned} E_\theta &= \frac{\mathrm{j}}{\omega\epsilon\mu}\frac{-1}{r}\frac{\partial B_\phi r}{\partial r} \\ &= \frac{\mathrm{j}}{\omega\epsilon\mu}\frac{-1}{r}\frac{-\mu\omega pk\sin\theta}{4\pi}\left(\mathrm{j}k-\frac{1}{r}-\frac{\mathrm{j}}{kr^2}\right)\mathrm{e}^{-\mathrm{j}(\omega t-kr)} \\ &= \frac{-pk^2\sin\theta}{4\pi\epsilon r}\left(1+\frac{\mathrm{j}}{kr}-\frac{1}{k^2r^2}\right)\mathrm{e}^{-\mathrm{j}(\omega t-kr)} \end{aligned} \tag{2.101}$$

In summary, an infinitesimal oscillating electric dipole of magnitude p and angular frequency ω is directed along $\hat{\boldsymbol{z}}$ and located at the origin. It produces an electromagnetic field at location $\mathbf{r} = (r, \theta, \phi)$, with $r > 0$, given in spherical coordinates and at time t as

$$\mathbf{B}(\mathbf{r},t) = \frac{-\mu cpk^3\sin\theta}{4\pi n}\begin{pmatrix} 0 \\ 0 \\ \frac{1}{kr}+\frac{\mathrm{j}}{k^2r^2}\end{pmatrix}\mathrm{e}^{-\mathrm{j}(\omega t-kr)} \tag{2.102}$$

with

$$\mathbf{E}(\mathbf{r},t) = \frac{-pk^3}{4\pi\epsilon}\begin{pmatrix} 2\mathrm{j}\cos\theta\left(\frac{1}{k^2r^2}+\frac{\mathrm{j}}{k^3r^3}\right) \\ \sin\theta\left(\frac{1}{kr}+\frac{\mathrm{j}}{k^2r^2}-\frac{1}{k^3r^3}\right) \\ 0\end{pmatrix}\mathrm{e}^{-\mathrm{j}(\omega t-kr)} \tag{2.103}$$

where equation 2.56 was used to eliminate ω from the pre-factor in $\mathbf{B}$ and k has been grouped with r throughout. The product

$$kr = 2\pi\frac{r}{\lambda} \tag{2.104}$$

is a measure of the distance from the dipole that takes into account the refractive index of the material in which it is embedded relative to the wavelength of the emitted radiation. None of the field components depend on azimuthal coordinate ϕ due to the symmetry of the system. The dipole field is symmetric around z but depends on the position (r, θ). The terms of $\mathbf{B}$ and $\mathbf{E}$ are dependent on different powers of kr. At $kr \gg 1$ increases, the higher reciprocal powers become negligible, whereas these dominate at $kr \ll 1$.

Radiated energy

Before looking into limiting regimes of kr, we derive the instantaneous energy flux. The real parts of the non-zero components of the dipole field are

$$\Re\{B_\phi\} = \frac{-\mu c p k^3 \sin\theta}{4\pi n}\left(\frac{\cos(\omega t - kr)}{kr} + \frac{\sin(\omega t - kr)}{k^2 r^2}\right) \tag{2.105}$$

$$\Re\{E_\rho\} = \frac{-p k^3 \cos\theta}{2\pi\epsilon}\left(\frac{\sin(\omega t - kr)}{k^2 r^2} - \frac{\cos(\omega t - kr)}{k^3 r^3}\right) \tag{2.106}$$

$$\Re\{E_\theta\} = \frac{-p k^3 \sin\theta}{4\pi\epsilon}\left(\frac{\cos(\omega t - kr)}{kr} + \frac{\sin(\omega t - kr)}{k^2 r^2} - \frac{\cos(\omega t - kr)}{k^3 r^3}\right) \tag{2.107}$$

which are used in computing the Poynting vector $\mathbf{S}$ of the dipole field as function of place and time. From equation 2.72 and using the real parts of the field components

$$\begin{aligned}\mathbf{S}(\mathbf{r},t) &= \frac{1}{\mu}\mathbf{E}\times\mathbf{B} \\ &= \frac{1}{\mu}\begin{pmatrix}E_\rho\\E_\theta\\E_\phi\end{pmatrix}\times\begin{pmatrix}B_\rho\\B_\theta\\B_\phi\end{pmatrix} = \frac{1}{\mu}\begin{pmatrix}E_\rho\\E_\theta\\0\end{pmatrix}\times\begin{pmatrix}0\\0\\B_\phi\end{pmatrix} \\ &= \frac{1}{\mu}\begin{pmatrix}E_\theta B_\phi\\-E_\rho B_\phi\\0\end{pmatrix}\end{aligned} \tag{2.108}$$

which results in

$$\begin{aligned}S_\rho &= \frac{c p^2 k^6 \sin^2\theta}{16\pi^2\epsilon n}\left(\frac{1}{k^2 r^2}\cos^2(\omega t - kr) + \frac{2}{k^3 r^3}\cos(\omega t - kr)\sin(\omega t - kr)\right. \\ &\quad \left. + \frac{1}{k^4 r^4}\left(\sin^2(\omega t - kr) - \cos^2(\omega t - kr)\right) - \frac{1}{k^5 r^5}\cos(\omega t - kr)\sin(\omega t - kr)\right) \\ &= \frac{c p^2 k^4 \sin^2\theta}{16\pi^2\epsilon n r^2}\left(\cos^2(\omega t - kr) + \frac{1}{kr}\sin(2\omega t - 2kr)\right. \\ &\quad \left. - \frac{1}{k^2 r^2}\cos(2\omega t - 2kr) - \frac{1}{2k^3 r^3}\sin(2\omega t - 2kr)\right)\end{aligned} \tag{2.109}$$

and

$$\begin{aligned}S_\theta &= \frac{-c p^2 k^6 \cos\theta\sin\theta}{8\pi^2\epsilon n}\left(\frac{1}{k^3 r^3}\sin(\omega t - kr)\cos(\omega t - kr)\right. \\ &\quad \left. + \frac{1}{k^4 r^4}\left(\sin^2(\omega t - kr) - \cos^2(\omega t - kr)\right) - \frac{1}{k^5 r^5}\sin(\omega t - kr)\cos(\omega t - kr)\right) \\ &= \frac{-c p^2 k^3 \sin(2\theta)}{16\pi^2\epsilon n r^3}\left(\left(\frac{1}{2} - \frac{1}{2k^2 r^2}\right)\sin(2\omega t - 2kr) - \frac{1}{kr}\cos(2\omega t - 2kr)\right)\end{aligned} \tag{2.110}$$

where the trigonometric identities

$$2\cos x \sin x = \sin(2x) \tag{2.111}$$

and

$$\cos^2 x - \sin^2 x = \cos(2x) \tag{2.112}$$

have been employed.

The time-average of the sine and cosine terms is zero, while

$$\langle \sin^2(\omega t - kr)\rangle = \langle \cos^2(\omega t - kr)\rangle = \frac{1}{2} \tag{2.113}$$

so that $\langle \mathbf{S} \rangle$ is found to be

$$\langle \mathbf{S} \rangle = \begin{pmatrix} S_\rho \\ S_\theta \\ S_\phi \end{pmatrix} = \begin{pmatrix} 1 \\ 0 \\ 0 \end{pmatrix} \frac{cp^2k^4 \sin^2\theta}{32\pi^2\epsilon n r^2} \tag{2.114}$$

which demonstrates that the oscillating dipole is emitting radially outward only, even though it generates an instantaneous energy flux S_θ along $\hat{\boldsymbol{\theta}}$ through the radially fluctuating electric field E_ρ. The irradiance $I_{\mathsf{dip}}(r,\theta)$ from a dipole depends on the radial and angular position relative to the orientation of the dipole. It is presented in figure 2.5 and given through equation 2.76 as

$$\begin{aligned} I_{\mathsf{dip}}(r,\theta) &= \frac{cp^2k^4\sin^2\theta}{32\pi^2\epsilon n r^2} \\ &= \frac{\sqrt{\epsilon_r\mu_r}\mu_r\pi^2p^2\nu^4\sin^2\theta}{2c^3\epsilon_0 r^2} \end{aligned} \tag{2.115}$$

where the latter expression is obtained by substitution of equations 2.56, 2.37 and 2.42. In the approximation given as equation 2.44 ($\mu_r = 1$ and thus $n = \sqrt{\epsilon_r}$), this simplifies to

$$I_{\mathsf{dip}}(r,\theta) = \frac{n\pi^2p^2\nu^4\sin^2\theta}{2c^3\epsilon_0 r^2} \tag{2.116}$$

which depends linearly on the refractive index of the material. A dipole in an optically dense material thus radiates more energy than an identical dipole in vacuum. Conversely, the energy required to induce a dipole increases with the refractive index of the surrounding material at the frequency of the radiation.

The irradiance from a dipole depends on the distance r from the dipole as r^{-2}. This is a manifestation of the conservation of the total energy in the radiated field. The total energy from a point source emitting radiation in all directions towards infinity is conserved. This implies that the energy flux $\mathbf{S}$ as a function of the distance to the source r decreases in the same proportion as the increase of the spherical surface area through which this flux passes. The spherical surface area is given as $4\pi r^2$, so $\mathbf{S} \propto r^{-2}$.

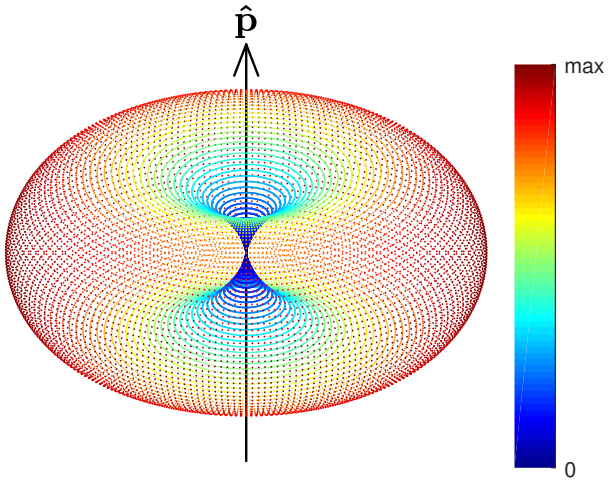

Figure 2.5: The irradiance from a dipole directed along $\hat{\mathbf{p}}$ in a homogeneous linear dielectric computed with equation 2.115 for a three-dimensional grid of angular directions. No energy is transmitted along the dipole axis while the maximum irradiance is perpendicular to it.

Furthermore, the irradiance from the dipole is directional. Due to the term $\sin^2\theta$, no energy is emitted on average along the axis of the dipole ($\theta = 0°$ and $180°$) while the maximum irradiance is found perpendicular to it at $\theta = 90°$. This implies that one can discern the orientation of a dipole through measuring its irradiance at various angular positions.

Total radiated power

The total power P radiated by a dipole can be found by integrating $I_{\mathsf{dip}}(r,\theta)$ over a sphere around the origin, where the dipole is located. Starting from equations 2.81 and 2.115 and using spherical coordinates to integrate over a sphere of radius r

$$\begin{aligned} P &= \int\limits_{\text{sphere}} I_{\mathsf{dip}}(r,\theta)\mathrm{d}A = \int_{\theta=0}^{\theta=\pi}\int_{\phi=0}^{\phi=2\pi} \frac{\sqrt{\epsilon_r\mu_r}\mu_r\pi^2p^2\nu^4\sin^2\theta}{2c^3\epsilon_0 r^2} r^2\sin\theta\mathrm{d}\phi\mathrm{d}\theta \\ &= \frac{\sqrt{\epsilon_r\mu_r}\mu_r\pi^2p^2\nu^4}{2c^3\epsilon_0}\int_{\theta=0}^{\theta=\pi}\int_{\phi=0}^{\phi=2\pi}\sin^3\theta\mathrm{d}\phi\mathrm{d}\theta = \frac{\sqrt{\epsilon_r\mu_r}\mu_r\pi^2p^2\nu^4}{2c^3\epsilon_0}\frac{3}{4}\cdot 2\pi \\ &= \frac{3\sqrt{\epsilon_r\mu_r}\mu_r\pi^3p^2\nu^4}{4c^3\epsilon_0} \end{aligned} \tag{2.117}$$

which is independent of r as expected from the conservation of energy. The total photon count from the dipole is then given by

$$N = \frac{P}{h\nu} = \frac{3\sqrt{\epsilon_r\mu_r}\mu_r\pi^3p^2\nu^3}{4c^3\epsilon_0 h} \tag{2.118}$$

where $h\nu$ is the energy carried by a single photon.

Both the total power of a dipole and its irradiance depend on the frequency of the

dipole oscillation, and thus the frequency of the radiation, as ν^4. In terms of the number of photons, this factor reduces to ν^3. This implies that energy is radiated much more effectively at higher frequencies (or shorter wavelengths). A well-known example of this is the blue colour of the sky: more blue than red light from the solar spectrum is Rayleigh scattered to an earth-bound observer. This also holds for Raman scattering, which is strongest for Raman bands at high frequency. Through equation 2.83, it is clear that this is obtained by using high-frequency incident radiation with low Raman shift in Stokes Raman scattering or high Raman shift in anti-Stokes Raman scattering. However, this argument does not include the effective scattering cross-section of the molecule under investigation (*i.e.* the absolute values of the Raman tensor elements and the vibrational normal mode amplitude) nor the occupation of the initial vibrational state which may overshadow the differences expected on the basis of frequency alone.

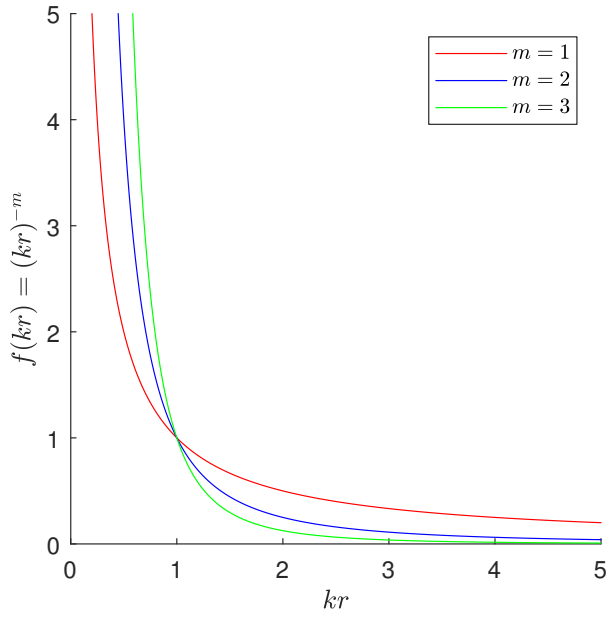

Figure 2.6: The functions $f(kr) = (kr)^{-m}$ with $m = 1, 2, 3$.

Dipole near and far-fields

We now return to the **E** and **B** fields due to the dipole and analyse their behaviour in the near-field and far-field limits. The three non-zero field components B_ϕ, E_r and E_θ have terms that depend on kr as $(kr)^{-1}$, $(kr)^{-2}$ and $(kr)^{-3}$. Figure 2.6 presents these functions to compare the relevance of each term as a function of kr. All are equal at $kr = 1$. Below that value, the higher inverse powers of kr dominate. The lower inverse powers decay slower with increasing kr and dominate at higher values of kr.

The near-field is defined as $kr \ll 1$ which spans the range of $r \ll \lambda$. All except the highest inverse power of kr in **E** and **B** become negligible. In this case, the non-zero

components of the magnetic and electric fields are

$$\begin{aligned} B_{\phi,\text{near}} &= \frac{-\mathrm{j}\mu kcp\sin\theta}{4\pi nr^2}\mathrm{e}^{-\mathrm{j}(\omega t-kr)} \\ E_{\rho,\text{near}} &= \frac{p\cos\theta}{4\pi\epsilon r^3}\mathrm{e}^{-\mathrm{j}(\omega t-kr)} \\ E_{\theta,\text{near}} &= \frac{p\sin\theta}{4\pi\epsilon r^3}\mathrm{e}^{-\mathrm{j}(\omega t-kr)} \end{aligned} \tag{2.119}$$

where the magnetic component is $\pi/2$ out of phase with the two electric components. The frequency-dependence that is prominent in the energy flux is absent in the electric near-field. Furthermore, the $\cos\theta$ term in $E_{\rho,\text{near}}$ implies that this component is strongest at $\theta = 0°$ and $180°$, which is in the direction of the dipole. This again contrasts with the energy flux that is zero in those directions.

In the far-field region, defined as $kr \gg 1$, the distance from the dipole $r \gg \lambda$, the $(kr)^{-1}$ terms dominate equations 2.102 and 2.103 to give

$$\begin{aligned} B_{\phi,\text{far}} &= \frac{-\mu k^2 cp\sin\theta}{4\pi nr}\mathrm{e}^{-\mathrm{j}(\omega t-kr)} \\ E_{\rho,\text{far}} &\approx 0 \\ E_{\theta,\text{far}} &= \frac{-pk^2\sin\theta}{4\pi\epsilon r}\mathrm{e}^{-\mathrm{j}(\omega t-kr)} \end{aligned} \tag{2.120}$$

in which E_ρ has been approximated to zero as $E_\rho \ll E_\theta$ at large r. In this far-field region, the electromagnetic field at each position (r, θ, ϕ) reduces to a plane wave as described in the beginning of this section. It is a transverse wave, propagating along $\hat{\boldsymbol{\rho}}$ with its electric and magnetic components in phase. This field is linearly polarised, with the direction of polarisation along $\hat{\boldsymbol{\theta}}$. In particular, it meets equation 2.58 and the ratio

$$\frac{E_\theta}{B_\phi} = \frac{1}{\sqrt{\epsilon\mu}} = v\ . \tag{2.121}$$

The time-averaged energy flux of the far-field

$$\langle\mathbf{S}\rangle(r,\theta) = \frac{1}{2\mu}E_\theta B_\phi\hat{\boldsymbol{\rho}} = \frac{cp^2k^4\sin^2\theta}{32\pi^2\epsilon nr^2}\hat{\boldsymbol{\rho}} \tag{2.122}$$

is exactly what we found previously in equation 2.114 for the whole dipole field. It is therefore clear that the near-field does not contribute to the energy flux. The field due to a dipole can thus be regarded as the combination of an evanescent field localised around the dipole and a propagative field that radiates outwards.

The dipole radiation as described in this section holds for a dipole embedded in a homogeneous linear medium. This may no longer be valid for dipoles close to an interface between two materials as the close-ranged terms of the dipole field come into play. In addition to the proximity of such an interface, the radiation will depend on the orientation of the dipole with respect to the plane of the interface. Emission of dipole radiation in

the vicinity of a surface has indeed been shown to differ from that in bulk material [69]. Chapter 5 addresses how the distance from a planar dielectric and the orientation of a dipole affect the detected Raman scattering intensities in our system.

2.5 The Raman tensor

We now focus on the properties of the Raman tensor. The Raman tensor $\boldsymbol{\alpha}_{\mathsf{v}}$ was defined in equation 2.27. The proportionality factor Q_{v_0} can be dropped when relative values suffice, which reduces the Raman tensor to $\boldsymbol{\alpha'}_{\mathsf{v}}$, the polarisability derivative. The tensorial properties of $\boldsymbol{\alpha}_{\mathsf{v}}$ and $\boldsymbol{\alpha'}_{\mathsf{v}}$ are identical. Most mathematical arguments in this work hold for the polarisability tensor as a whole as well as for the polarisability derivative tensor in particular. The notation is simplified by using $\boldsymbol{\alpha}$ in those cases while $\boldsymbol{\alpha'}$ is used for the Raman tensor when it is discussed more exclusively.

2.5.1 Tensorial properties

The polarisability $\boldsymbol{\alpha}$ is a second rank tensor and given in a Cartesian basis $\{\hat{\mathbf{x}}, \hat{\mathbf{y}}, \hat{\mathbf{z}}\}$ as

$$\boldsymbol{\alpha} = \begin{pmatrix} \alpha_{xx} & \alpha_{xy} & \alpha_{xz} \\ \alpha_{yx} & \alpha_{yy} & \alpha_{yz} \\ \alpha_{zx} & \alpha_{zy} & \alpha_{zz} \end{pmatrix} \tag{2.123}$$

which can generally be decomposed into a sum of three irreducible parts [61, 70] being a diagonal isotropic tensor $\boldsymbol{\alpha}_{\text{iso}}$, a symmetric traceless tensor $\boldsymbol{\alpha}_{\text{sym}}$ and an antisymmetric traceless tensor $\boldsymbol{\alpha}_{\text{anti}}$ as

$$\boldsymbol{\alpha} = \boldsymbol{\alpha}_{\text{iso}} + \boldsymbol{\alpha}_{\text{symm}} + \boldsymbol{\alpha}_{\text{anti}} \, . \tag{2.124}$$

These irreducible matrices are given by linear combinations of the original nine elements in $\boldsymbol{\alpha}$ through

$$\begin{aligned} \boldsymbol{\alpha}_{\text{iso}} &= \begin{pmatrix} \bar{\alpha} & 0 & 0 \\ 0 & \bar{\alpha} & 0 \\ 0 & 0 & \bar{\alpha} \end{pmatrix} \\ \boldsymbol{\alpha}_{\text{sym}} &= \frac{1}{2} \begin{pmatrix} 2(\alpha_{xx} - \bar{\alpha}) & \alpha_{xy} + \alpha_{yx} & \alpha_{xz} + \alpha_{zx} \\ \alpha_{xy} + \alpha_{yx} & 2(\alpha_{yy} - \bar{\alpha}) & \alpha_{yz} + \alpha_{zy} \\ \alpha_{xz} + \alpha_{zx} & \alpha_{yz} + \alpha_{zy} & 2(\alpha_{zz} - \bar{\alpha}) \end{pmatrix} \\ \boldsymbol{\alpha}_{\text{anti}} &= \frac{1}{2} \begin{pmatrix} 0 & \alpha_{xy} - \alpha_{yx} & \alpha_{xz} - \alpha_{zx} \\ \alpha_{yx} - \alpha_{xy} & 0 & \alpha_{yz} - \alpha_{zy} \\ \alpha_{zx} - \alpha_{xz} & \alpha_{zy} - \alpha_{yz} & 0 \end{pmatrix} \end{aligned} \tag{2.125}$$

where $\bar{\alpha}$ is defined as a third of the trace of the diagonal tensor. The decomposition into tensors containing only symmetric or antisymmetric off-diagonal elements can be

understood from the identity

$$\alpha_{xy}\hat{\mathbf{x}}\hat{\mathbf{y}} + \alpha_{yx}\hat{\mathbf{y}}\hat{\mathbf{x}} = \frac{1}{2}\left(\alpha_{xy} + \alpha_{yx}\right)\left(\hat{\mathbf{x}}\hat{\mathbf{y}} + \hat{\mathbf{y}}\hat{\mathbf{x}}\right) + \frac{1}{2}\left(\alpha_{xy} - \alpha_{yx}\right)\left(\hat{\mathbf{x}}\hat{\mathbf{y}} - \hat{\mathbf{y}}\hat{\mathbf{x}}\right) \tag{2.126}$$

with identical relations for the pair of xz, zx and of yz, zy elements.

The trace of a matrix is unaffected by a rotation of the coordinate system in which its elements are defined. Thus, the trace is one of its rotational invariants. The polarisability tensor has three rotational invariants: the mean polarisability $\bar{\alpha}$, the anisotropy γ and the antisymmetric anisotropy δ. Their general definitions are

$$\bar{\alpha} = \frac{1}{3}\left(\alpha_{xx} + \alpha_{yy} + \alpha_{zz}\right) \tag{2.127}$$

$$\begin{aligned}\gamma^2 = {} & \frac{1}{2}\left(|\alpha_{xx} - \alpha_{yy}|^2 + |\alpha_{yy} - \alpha_{zz}|^2 + |\alpha_{zz} - \alpha_{xx}|^2\right) \\ & + \frac{3}{4}\left(|\alpha_{xy} + \alpha_{yx}|^2 + |\alpha_{yz} + \alpha_{zy}|^2 + |\alpha_{zx} + \alpha_{xz}|^2\right)\end{aligned} \tag{2.128}$$

$$\delta^2 = \frac{3}{4}\left(|\alpha_{xy} - \alpha_{yx}|^2 + |\alpha_{yz} - \alpha_{zy}|^2 + |\alpha_{zx} - \alpha_{xz}|^2\right) \tag{2.129}$$

which reduce to simpler expressions if the tensor elements have some symmetry (for example, if $\boldsymbol{\alpha}$ is symmetric along its main diagonal, $\boldsymbol{\alpha}_{\text{anti}}$ vanishes and $\delta = 0$). These definitions also apply to the invariants of the polarisability derivative tensor $\bar{\alpha}'$, γ' and δ', keeping in mind that these are a function of the frequency of the scattered light. The invariants of the Raman tensor are relevant in traditional Raman scattering experiments on bulk liquids and gases using a well-defined illumination-observation geometry. Such samples are usually isotropic, including all possible orientations of the scattering moiety. The individual components of the Raman tensor can not always be resolved in such experiments, but its invariants can be deduced analytically from a set of polarised spectra [61].

The polarisability and Raman tensors have no meaning on their own but are specified in a particular frame of reference within which they can be applied. This frame can be relative to the illumination-observation geometry of the experiment or can be chosen along symmetry axes within the scattering molecule, for example. Though Raman scattering is always recorded with respect to a particular laboratory frame of reference, it is due to a molecular property that is best described within a molecular frame of reference. Analysis of how the latter affects the former (and *vice versa*) requires the use of coordinate transformations. In this work, the emphasis is on molecular orientation with respect to such a fixed laboratory frame. The relation between these frames of reference is fully addressed in chapter5 and only a general introduction is given here.

As scattered light is recorded relative to the laboratory frame, the experimentalist measures scattering due to an effective polarisability tensor $\boldsymbol{\alpha}^{\text{lab}}$ relative to that frame of reference, which generally differs from the polarisability tensor given in a molecular frame of reference $\boldsymbol{\alpha}^{\text{mol}}$ [61, 71]. The two tensors are related through the orientation of the molecule in the laboratory frame, which is expressed through a coordinate transformation

matrix $\mathbf{T}_{\text{mol}\to\text{lab}}$ and applies as

$$\boldsymbol{\alpha}^{\text{lab}} = \mathbf{T}_{\text{mol}\to\text{lab}}\, \boldsymbol{\alpha}^{\text{mol}}\, \mathbf{T}_{\text{mol}\to\text{lab}}{}^{\text{T}} \tag{2.130}$$

where the superscript T stands for the transpose of the matrix. Writing out the components of these tensors results in

$$\begin{pmatrix} \alpha_{xx}^{\text{lab}} & \alpha_{xy}^{\text{lab}} & \alpha_{xz}^{\text{lab}} \\ \alpha_{yx}^{\text{lab}} & \alpha_{yy}^{\text{lab}} & \alpha_{yz}^{\text{lab}} \\ \alpha_{zx}^{\text{lab}} & \alpha_{zy}^{\text{lab}} & \alpha_{zz}^{\text{lab}} \end{pmatrix} = \begin{pmatrix} T_{11} & T_{12} & T_{13} \\ T_{21} & T_{22} & T_{23} \\ T_{31} & T_{32} & T_{33} \end{pmatrix} \begin{pmatrix} \alpha_{xx}^{\text{mol}} & \alpha_{xy}^{\text{mol}} & \alpha_{xz}^{\text{mol}} \\ \alpha_{yx}^{\text{mol}} & \alpha_{yy}^{\text{mol}} & \alpha_{yz}^{\text{mol}} \\ \alpha_{zx}^{\text{mol}} & \alpha_{zy}^{\text{mol}} & \alpha_{zz}^{\text{mol}} \end{pmatrix} \begin{pmatrix} T_{11} & T_{21} & T_{31} \\ T_{12} & T_{22} & T_{32} \\ T_{13} & T_{23} & T_{33} \end{pmatrix} \tag{2.131}$$

where, as an example, the element α_{xx}^{lab} is given as

$$\begin{aligned} \alpha_{xx}^{\text{lab}} = &\left(\alpha_{xx}^{\text{mol}} T_{11} + \alpha_{xy}^{\text{mol}} T_{12} + \alpha_{xz}^{\text{mol}} T_{13}\right) T_{11} \\ &+ \left(\alpha_{yx}^{\text{mol}} T_{11} + \alpha_{yy}^{\text{mol}} T_{12} + \alpha_{yz}^{\text{mol}} T_{13}\right) T_{12} \\ &+ \left(\alpha_{zx}^{\text{mol}} T_{11} + \alpha_{zy}^{\text{mol}} T_{12} + \alpha_{zz}^{\text{mol}} T_{13}\right) T_{13} \end{aligned} \tag{2.132}$$

which is a combination of all nine elements of the Raman tensor in the molecular frame of reference.

The polarisability tensor in the laboratory frame can thus be derived in a straightforward fashion from the molecular polarisability and the transformation matrix that applies to its orientation. This is readily implemented in a modelling approach. However, the inverse problem faced in an experiment does not yield unique solutions. It is clear from equation 2.132 that multiple combinations of $\mathbf{T}_{\text{mol}\to\text{lab}}$ and $\boldsymbol{\alpha}^{\text{mol}}$ may give rise to the same $\boldsymbol{\alpha}^{\text{lab}}$, which cannot be distinguished. Furthermore, the radiation pattern of a dipole is symmetric upon inversion of its orientation, so that $\mathbf{p}$ appears identical to $-\mathbf{p}$ in an experiment. Therefore, $\boldsymbol{\alpha}^{\text{lab}}$ and $-\boldsymbol{\alpha}^{\text{lab}}$ will give the same result. This means, for instance, that a scattering molecule in a particular orientation and its exact opposite, *e.g.* $(x, y, z) = (1, 1, 1)$ and $(x, y, z) = -(1, 1, 1)$, give rise to the same scattered intensity. This is intrinsic to both Rayleigh and Raman scattering and explains why tensor invariants are used to describe the effect. From an experimental point of view, it would be better not to speak of the orientation of a scatter as no unique value for it can be deduced without prior assumptions, but rather of its alignment or directionality relative to the laboratory frame. However, in modelling efforts the exact orientation can be given as an input parameter. The use of the word is therefore appropriate in that context.

2.5.2 Molecular ensembles

In an experiment, the observed light scattering arises from the collection of molecules in the sampled volume. A dipole is induced in a number of these molecules and each gives rise to scattered light. Following equation 2.24, the phase shift δ_{ν} of this radiation relative to the incident electric field is different for every molecule. Spatial spread of the scatterers

further contributes to the random nature of their phase relation. Scattering from an ensemble of molecules is therefore intrinsically incoherent. This implies that the total intensity of scattered light $I_{\mathsf{scat}}(r,\theta,\phi)$ is the sum over the irradiance from each induced dipole $I_{\mathsf{dip}}(r,\theta)$. The first is specified at a particular point of observation in the laboratory frame, using spherical coordinates, while the latter is given relative to the induced dipole, such as in equation 2.115. In the case of induced dipoles embedded in a homogeneous non-absorbing medium, these expressions combine to form

$$I^{\mathsf{lab}}_{\mathsf{scat}}(r,\theta,\phi) = \sum_{\mathsf{scatterers}} I^{\mathsf{lab}}_{\mathsf{dip}}(r,\theta) = \sum_{p,\theta} \frac{\sqrt{\epsilon_r \mu_r}\mu_r \pi^2 p^2 \nu^4 \sin^2\theta}{2c^3\epsilon_0 r^2} \tag{2.133}$$

where only p^2 and θ are different for each scatterer (θ now being the angular position in the laboratory frame, differing from θ in equation 2.115, which is relative to the dipole axis). All other quantities are constant, in particular ν when considering a single spectral line and r for a given distant experimental point of observation ($r \gg$ extend of the scattering ensemble). Using this and invoking equation 2.24 to substitute $p = ||\mathbf{p}||$ gives

$$I^{\mathsf{lab}}_{\mathsf{scat}}(\theta,\phi) = \frac{\sqrt{\epsilon_r \mu_r}\mu_r \pi^2 \nu^4}{2c^3\epsilon_0 r^2} \left(\sum_{\mathsf{orientations}} ||\boldsymbol{\alpha}^{\mathsf{lab}}\mathbf{E}^{\mathsf{lab}}||^2 \sin^2\theta \right) \tag{2.134}$$

in which the summation is over the orientations of the scattering molecules relative to the laboratory frame of reference where the intensity measurement is conducted. The quantities θ (arising from the relative orientation of $\mathbf{p}$), $\mathbf{E}^{\mathsf{lab}}$ and $\boldsymbol{\alpha}^{\mathsf{lab}}$ are all expressed in that laboratory frame. $\boldsymbol{\alpha}^{\mathsf{lab}}$ is obtained through transformations depending on the orientation of the scattering molecule.

From equation 2.134, we can conclude that only the orientation distribution of the scatterers and the incident field $\mathbf{E}$ affect the total scattered intensity for a particular Raman transition. This transition is specified by a Raman tensor $\boldsymbol{\alpha}^{\mathsf{mol}}$ in the molecular frame of reference. Changing the incident electric vector $\mathbf{E}$ in either intensity, polarisation or both, will also affect the total intensity $I_{\mathsf{scat}}(\theta,\phi)$ of the scattering.

As the irradiance scales with $||\mathbf{E}||^2$ (see equation 2.73), the scattered intensity scales linearly with the incident irradiance I_{in}. The proportionality is the differential scattering cross-section σ' for that particular frequency which depends on the angular position of detection (θ,ϕ) as

$$\sigma'(\theta,\phi) = \frac{I_{\mathsf{scat}}(\theta,\phi)\, r^2}{I_{\mathsf{in}}} \tag{2.135}$$

where the product $I_{\mathsf{scat}}(\theta,\phi)\, r^2$ is the radiant intensity of the scattering, which is independent of r. The total scattering cross-section σ is obtained by integrating the differential cross-section over all θ and ϕ, which amounts to integrating $I_{\mathsf{scat}}(\theta,\phi)\, r^2$ to give the total scattering power P_{scat}

$$\sigma = \frac{P_{\mathsf{scat}}}{I_{\mathsf{in}}} \tag{2.136}$$

which is given in units of m^2. This captures the effectiveness with which the molecules remove energy from the incident beam through scattering and corresponds to the radiation incident on an area σ. The values of σ and σ' thus relate to the probability of scattering occurring and thus to the strength of spectral lines. For normal vibrational Raman scattering, σ is on the order of 10^{-34} m^2 $molecule^{-1}$ which is a factor 10^{16} smaller than the physical size of a 1 nm^2 molecule. One could therefore say that only one in ten million billion photons undergoes Raman scattering and that the Raman effect is a weak phenomenon.

Aligned scatterers

If all scattering molecules have the same orientation, the sum in equation 2.133 reduces to the same expression for each scatterer, so that

$$I_{\mathsf{scat}}(r,\theta,\phi) = N_{\mathsf{v}} I_{\mathsf{dip}}(r,\theta) \tag{2.137}$$

where N_{v} is the number of scatterers. This number relates to the number of scatterers in the correct initial quantum state v, which is proportional to the total number of molecules of the scattering species through the Boltzmann distribution, taking into account any degeneracies. At constant temperature, the total intensity of the scattered light thus scales linearly with the number of scatterers in the illuminated volume of the sample.

To compute the scattering intensity pattern on the detector, $I_{\mathsf{dip}}(r,\theta)$ has to be found in laboratory frame coordinates. This comes down to finding

$$I^{\mathsf{lab}}_{\mathsf{dip}}(\theta) \propto ||\boldsymbol{\alpha}^{\mathsf{lab}}\mathbf{E}^{\mathsf{lab}}||^2 \sin^2\theta = ||\mathbf{T}_{\mathrm{mol}\to\mathrm{lab}}\, \boldsymbol{\alpha}^{\mathrm{mol}}\, {\mathbf{T}_{\mathrm{mol}\to\mathrm{lab}}}^{\mathrm{T}} \mathbf{E}^{\mathsf{lab}}||^2 \sin^2\theta \tag{2.138}$$

where $\mathbf{E}^{\mathsf{lab}}$ is computed from the experimental illumination geometry in the laboratory frame, $\mathbf{T}_{\mathrm{mol}\to\mathrm{lab}}$ includes the orientation of the scattering molecules with respect to the laboratory frame, θ is the angle between $\mathbf{p}$ and $\hat{\mathbf{z}}$ in the laboratory frame while $\boldsymbol{\alpha}^{\mathrm{mol}}$ is deduced independently from the molecular properties.

As we have used the irradiance from a dipole in a homogeneous material, the expression holds for scattering molecules in such system. If the sample is of a different structure, appropriate expressions for I_{dip} need to be derived.

Isotropic average

An isotropic orientation distribution holds for gases and many liquids. The scattering molecules possess all possible angles (θ,ϕ) with respect to the laboratory frame of reference. Equation 2.134 is then solved by taking an isotropic average of the Raman tensor $\langle\boldsymbol{\alpha}^{\mathsf{lab}}\rangle$, given the illumination-observation geometry. The isotropic average of the sine term is

$$\langle\sin^2\theta\rangle = \frac{1}{2} \tag{2.139}$$

as we have seen before for the time-average of a squared cosine.

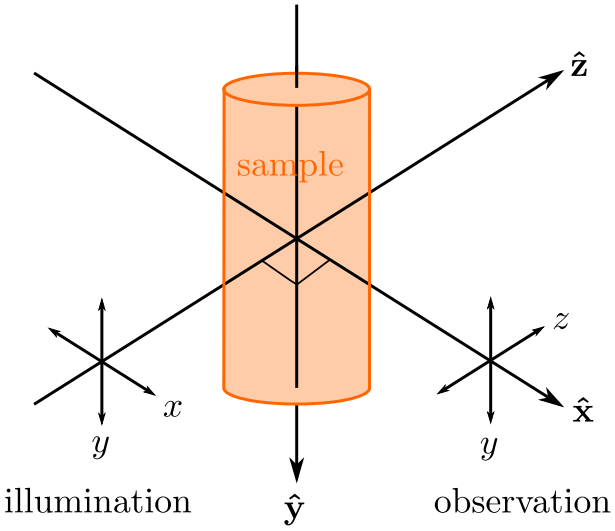

Figure 2.7: Illumination-observation geometry in traditional Raman spectroscopy on a bulk liquid or gas sample. The incident laser light is linearly polarised along x or y and the scattered light is collected in a spectrograph through another linear polariser oriented along y or z.

In traditional Raman spectroscopy, bulk liquids or gases are illuminated with a linearly polarised laser beam and their scattering is collected at an angle to the incident beam, usually at right angles. Both directions span the scatter plane and each is chosen as one of the laboratory frame axes as illustrated in figure 2.7. In that case, $\mathbf{E}^{\mathsf{lab}}$ simplifies to one component only, say along $\hat{\mathbf{y}}$. It interacts with three components of the laboratory-frame Raman tensor as

$$\begin{pmatrix} \alpha_{xx}^{\mathrm{lab}} & \alpha_{xy}^{\mathrm{lab}} & \alpha_{xz}^{\mathrm{lab}} \\ \alpha_{yx}^{\mathrm{lab}} & \alpha_{yy}^{\mathrm{lab}} & \alpha_{yz}^{\mathrm{lab}} \\ \alpha_{zx}^{\mathrm{lab}} & \alpha_{zy}^{\mathrm{lab}} & \alpha_{zz}^{\mathrm{lab}} \end{pmatrix} \begin{pmatrix} 0 \\ E_y^{\mathrm{lab}} \\ 0 \end{pmatrix} = \begin{pmatrix} \alpha_{xy}^{\mathrm{lab}} \\ \alpha_{yy}^{\mathrm{lab}} \\ \alpha_{zy}^{\mathrm{lab}} \end{pmatrix} E_y^{\mathrm{lab}} \tag{2.140}$$

The scattered light also passes through a linear polariser, allowing further selection of the three vector components. By setting this observation polariser along $\hat{\mathbf{y}}$, only light scattered with polarisation along this direction reaches the detector. Such radiation is the far-field of dipoles oriented along $\hat{\mathbf{y}}$. Only the $\alpha_{yy}^{\mathrm{lab}} E_y^{\mathsf{lab}}$ term of the above expression is thus actually measured in the experiment.

The detected intensity for this experimental geometry is now given through the isotropic average of $\alpha_{yy}^{\mathrm{lab}} E_y^{\mathsf{lab}}$ and equation 2.134 reduces to

$$I_{\mathsf{scat}}(\mathsf{polarised}) \propto \langle {\alpha_{yy}^{\mathrm{lab}}}^2 \rangle {E_y^{\mathrm{lab}}}^2 \tag{2.141}$$

which is the intensity of polarised scattering (*i.e.* the direction of polarisation of illumination and observation is in the same plane). Alternatively, the observation polarisation

is set along $\hat{\mathbf{z}}$ and the depolarised intensity is recorded

$$I_{\mathsf{scat}}(\mathsf{depolarised}) \propto \langle {\alpha_{zy}^{\mathrm{lab}}}^2 \rangle E_y^{\mathrm{lab}\,2} \tag{2.142}$$

which again reduces to a calculation of the isotropic average of a squared Raman tensor element. Isotropic averages of squared polarisability tensor elements have been deduced for various experimental geometries and are tabulated in [61, 62, 70, 72] amongst other works. The isotropic averages turn out to be functions of the tensor invariants $\bar{\alpha}$, γ and δ only. In our case

$$\begin{aligned} \langle {\alpha_{yy}^{\mathrm{lab}}}^2 \rangle &= \frac{45\bar{\alpha}^2 + 4\gamma^2}{45} \\ \langle {\alpha_{zy}^{\mathrm{lab}}}^2 \rangle &= \frac{\gamma^2}{15} \end{aligned} \tag{2.143}$$

where the numerical values depend on the Raman tensor involved. Note that the superscript lab can be dropped from the isotropic averages as these are given through invariants that are not affected by rotations of the frame of reference. It is found that the isotropic average of the squared Raman tensor elements are related by

$$\begin{aligned} \langle {\alpha'_{xy}}^2 \rangle &= \langle {\alpha'_{yx}}^2 \rangle \\ \langle {\alpha'_{yz}}^2 \rangle &= \langle {\alpha'_{zy}}^2 \rangle \\ \langle {\alpha'_{zx}}^2 \rangle &= \langle {\alpha'_{xz}}^2 \rangle \, . \end{aligned} \tag{2.144}$$

Furthermore, in the normal vibrational Raman effect where all tensor elements are real, the isotropic averages also satisfy

$$\begin{aligned} \langle {\alpha'_{xx}}^2 \rangle = \langle {\alpha'_{yy}}^2 \rangle = \langle {\alpha'_{zz}}^2 \rangle \\ \langle {\alpha'_{xy}}^2 \rangle = \langle {\alpha'_{yz}}^2 \rangle = \langle {\alpha'_{zx}}^2 \rangle \\ \langle |\alpha'_{xx}\alpha'_{yy}| \rangle = \langle |\alpha'_{yy}\alpha'_{zz}| \rangle = \langle |\alpha'_{zz}\alpha'_{xx}| \rangle \end{aligned} \tag{2.145}$$

while all other averages are zero.

The ratio of the intensities recorded with the different polarisation combinations is a measure of the symmetry properties of the Raman band in question. The depolarisation ratio ρ is defined as

$$\rho = \frac{I_{\mathsf{scat}}(\mathsf{depolarised})}{I_{\mathsf{scat}}(\mathsf{polarised})} \tag{2.146}$$

and for the case we have discussed above

$$\rho = \frac{3{\gamma'}^2}{45\bar{\alpha'}^2 + 4{\gamma'}^2} \tag{2.147}$$

which has a maximum of 3/4 when the mean polarisability derivative $\bar{\alpha'}$ and thus the irreducible diagonal tensor $\boldsymbol{\alpha'}_{\mathsf{iso}}$ are zero. Such a Raman line is said to be depolarised. All

other transitions have $\rho < 3/4$ in this case and are polarised to some extend. It is said to be completely polarised if $\rho = 0$, which is the case if $\gamma' = 0$. A depolarised Raman spectrum thus only includes fully depolarised bands, while a polarised one includes both fully and partly polarised bands. Whether a Raman band is polarised or depolarised depends on the symmetry of the Raman tensor, which in turn depends on the symmetry properties of the vibrational mode that gives rise to the scattering.

2.5.3 Symmetry

The isotropic averages of the Raman tensor elements demonstrate symmetry properties arising from the nature of the averaging. The Raman tensor itself also shows symmetry, which depends on the vibrational transition it relates to. We now consider its tensorial symmetry and the molecular and vibrational symmetries it originates from.

Tensorial symmetry

The tensors $\boldsymbol{\alpha}$ and $\boldsymbol{\alpha'}$ have intrinsic symmetry properties that derive from the Hermitian nature of the operator $\hat{H}$. For real and time-independent wave functions, the transition dipole operator ensures that $\mathbf{p}$ is the same, whether a transitions is from state i to f or the other way round. This implies that the polarisability and Raman tensors have symmetry properties irrespective of the frame of reference used [61].

For Rayleigh scattering, $f = i$ and the tensor elements kl are fully symmetric around the main diagonal of the polarisability tensor

$$\alpha_{\mathsf{Rayleigh}\,kl} = \alpha_{\mathsf{Rayleigh}\,lk} \tag{2.148}$$

while an antisymmetric part can be present for scattering from and to degenerate states.

The Raman tensor $\boldsymbol{\alpha'}$ is not symmetric in general and can be expressed similarly to the three terms of equation 2.124 as

$$\boldsymbol{\alpha'} = \boldsymbol{\alpha'}_{\mathrm{iso}} + \boldsymbol{\alpha'}_{\mathrm{sym}} + \boldsymbol{\alpha'}_{\mathrm{anti}} \tag{2.149}$$

which follow the definitions of equation 2.125. The diagonal and symmetric tensors have

$$\alpha'_{\mathsf{sym}\,kl} = \alpha'_{\mathsf{sym}\,lk} \tag{2.150}$$

and the antisymmetric tensor has

$$\alpha'_{\mathsf{anti}\,kl} = -\alpha'_{\mathsf{anti}\,lk} \tag{2.151}$$

which reduces the number of independent component in each tensor of equation 2.149. The isotropic tensor has one such component (and could be reduced to a 1×1 matrix representing a tensor of rank zero), while the symmetric tensor has five (the isotropic

tensor specifying one of its diagonal elements) and the antisymmetric tensor has three. In normal vibrational Raman scattering, the antisymmetric tensor vanishes and a maximum of six independent tensor elements occur for each vibrational mode: three for the diagonal and three for the off-diagonal. The general definition of the Raman tensor for normal vibrational scattering can now be given in tensorial form as

$$\boldsymbol{\alpha'} = \begin{pmatrix} \alpha'_{xx} & \alpha'_{xy} & \alpha'_{xz} \\ \alpha'_{xy} & \alpha'_{yy} & \alpha'_{yz} \\ \alpha'_{xz} & \alpha'_{yz} & \alpha'_{zz} \end{pmatrix} \tag{2.152}$$

The values of the six elements α'_{xx}, α'_{yy}, α'_{zz}, α'_{xy}, α'_{xz} and α'_{yz} depend on the vibrational transition involved in the Raman scattering. As we will see below, the symmetry of the vibrational transition dictates which elements are finite or zero and which are of equal value. The level of symmetry in a Raman tensor is classified following the placement of these elements. We now establish some of its nomenclature for use later on.

All Raman tensors in normal vibrational Raman scattering are symmetric, thus satisfy equation 2.152 and contain real elements. The Raman tensor invariants $\bar{\alpha}'$, γ' and δ' (defined analogous to equations 2.127, 2.128 and 2.129) are given by

$$a' = \frac{1}{3}(\alpha'_{xx} + \alpha'_{yy} + \alpha'_{zz}) \tag{2.153}$$

$$\gamma'^2 = \frac{1}{2}\left((\alpha_{xx} - \alpha_{yy})^2 + (\alpha_{yy} - \alpha_{zz})^2 + (\alpha_{zz} - \alpha_{xx})^2\right) + 3\left({\alpha_{xy}}^2 + {\alpha_{yz}}^2 + {\alpha_{zx}}^2\right) \tag{2.154}$$

$$\delta' = 0 \tag{2.155}$$

If a symmetric tensor is traceless, *i.e.* $\alpha'_{xx} + \alpha'_{yy} + \alpha'_{zz} = 0$, the invariant $\bar{\alpha}' = 0$. The antisymmetric anisotropy δ' is always zero in symmetric tensors.

A diagonal tensor has non-zero elements on its main diagonal only, $\alpha'_{kl} = 0$ for all $k \neq l$, so that

$$\boldsymbol{\alpha'} = \begin{pmatrix} \alpha'_{xx} & 0 & 0 \\ 0 & \alpha'_{yy} & 0 \\ 0 & 0 & \alpha'_{zz} \end{pmatrix} \tag{2.156}$$

which is termed an anisotropic tensor or a tensor of elliptical symmetry. The Raman activity for such a tensor can be seen as describing an ellipsoid with its axes along x, y and z. A 3×3 tensor that has a complete basis of eigenvectors can be rotated in three dimensions to reduce to a diagonal tensor, though it is then defined relative to that frame, which may not be the simplest one for a physical interpretation. Off-diagonal element are therefore relevant and need not be avoided.

The Raman activity ellipsoid reduces to a sphere if $\alpha'_{xx} = \alpha'_{yy} = \alpha'_{zz}$ in a diagonal tensor. This is therefore termed spherical symmetry as the effect of applying the tensor is

the same in all spatial directions. The two relevant tensor invariants reduce to

$$\begin{cases} \bar{\alpha}' = \alpha'_{xx} \\ \gamma' = 0 \end{cases} \tag{2.157}$$

and the Raman tensor is $\boldsymbol{\alpha'} = \boldsymbol{\alpha'}_{\mathsf{iso}}$ which is fully specified by the scalar $\bar{\alpha}'$. Such a vibrational mode would present a completely polarised band in the Raman spectrum. If only $\alpha_{xx} = \alpha_{yy}$ and α_{zz} has a different non-zero value, the tensor is said to be cylindrically symmetric about the z axis. The tensor invariants then simplify to

$$\begin{cases} \bar{\alpha}' = \frac{1}{3}(2\alpha'_{xx} + \alpha'_{zz}) \\ \gamma' = |\alpha'_{xx} - \alpha'_{zz}| \end{cases} \tag{2.158}$$

If $\alpha_{zz} = 0$ in addition, the tensorial symmetry is said to be planar and effectively reduces the Raman tensor to two dimensions. Its invariants become

$$\begin{cases} \bar{\alpha}' = \frac{2}{3}\alpha'_{xx} \\ \gamma' = |\alpha'_{xx}| \end{cases} \tag{2.159}$$

The molecular Cartesian axes are chosen with the symmetry of the molecule in mind, the z-axis being the principal symmetry axis. Binary combinations of the molecular axes form the basis

$$\{\hat{\mathbf{x}}\hat{\mathbf{x}}, \hat{\mathbf{y}}\hat{\mathbf{y}}, \hat{\mathbf{z}}\hat{\mathbf{z}}, \hat{\mathbf{x}}\hat{\mathbf{y}}, \hat{\mathbf{x}}\hat{\mathbf{z}}, \hat{\mathbf{y}}\hat{\mathbf{z}}\}$$

in which the elements of the Raman tensor are defined. Only six basis vectors are needed for the six independent elements of the Raman tensor. However, this basis (and thus the Raman tensor) do not always match the symmetry species of the vibrational modes of the molecule. Linear combinations of the six basis vectors are therefore used as new basis vectors that give rise to a decomposition of the Raman tensor into symmetry-adapted tensors. These are still expressed in the molecular frame of reference and contain a reduced number of independent elements. Only a limited number of tensor decompositions is relevant, as the assignment of molecular axes follows strictly from the symmetry of the molecular equilibrium structure.

The three diagonal elements of the tensor can be decomposed into three linear combinations, using the identity

$$\begin{aligned} \alpha'_{xx}\hat{\mathbf{x}}\hat{\mathbf{x}} + \alpha'_{yy}\hat{\mathbf{y}}\hat{\mathbf{y}} + \alpha'_{zz}\hat{\mathbf{z}}\hat{\mathbf{z}} = {} & \frac{1}{3}\left(\alpha'_{xx} + \alpha'_{yy} + \alpha'_{zz}\right)\left(\hat{\mathbf{x}}\hat{\mathbf{x}} + \hat{\mathbf{y}}\hat{\mathbf{y}} + \hat{\mathbf{z}}\hat{\mathbf{z}}\right) \\ & + \frac{1}{6}\left(2\alpha'_{zz} - \alpha'_{xx} - \alpha'_{yy}\right)\left(2\hat{\mathbf{z}}\hat{\mathbf{z}} - \hat{\mathbf{x}}\hat{\mathbf{x}} - \hat{\mathbf{y}}\hat{\mathbf{y}}\right) \\ & + \frac{1}{2}\left(\alpha'_{xx} - \alpha'_{yy}\right)\left(\hat{\mathbf{x}}\hat{\mathbf{x}} - \hat{\mathbf{y}}\hat{\mathbf{y}}\right) \end{aligned} \tag{2.160}$$

which decomposes the basis $\{\hat{\mathbf{x}}\hat{\mathbf{x}}, \hat{\mathbf{y}}\hat{\mathbf{y}}, \hat{\mathbf{z}}\hat{\mathbf{z}}\}$ into a set of three symmetry-adapted linear

combinations

$$\left\{\begin{array}{c} \frac{1}{\sqrt{3}}\left(\hat{\mathbf{x}}\hat{\mathbf{x}}+\hat{\mathbf{y}}\hat{\mathbf{y}}+\hat{\mathbf{z}}\hat{\mathbf{z}}\right) \\ \frac{1}{\sqrt{6}}\left(2\hat{\mathbf{z}}\hat{\mathbf{z}}-\hat{\mathbf{x}}\hat{\mathbf{x}}-\hat{\mathbf{y}}\hat{\mathbf{y}}\right) \\ \frac{1}{\sqrt{2}}\left(\hat{\mathbf{x}}\hat{\mathbf{x}}-\hat{\mathbf{y}}\hat{\mathbf{y}}\right) \end{array}\right\}$$

where the numerical factors ensure normalisation of the new basis vectors. In matrix notation this decomposition is represented as

$$\begin{pmatrix} \alpha'_{xx} & \cdot & \cdot \\ \cdot & \alpha'_{yy} & \cdot \\ \cdot & \cdot & \alpha'_{zz} \end{pmatrix} = \begin{pmatrix} a & \cdot & \cdot \\ \cdot & a & \cdot \\ \cdot & \cdot & a \end{pmatrix} + \begin{pmatrix} -b & \cdot & \cdot \\ \cdot & -b & \cdot \\ \cdot & \cdot & 2b \end{pmatrix} + \begin{pmatrix} c & \cdot & \cdot \\ \cdot & -c & \cdot \\ \cdot & \cdot & 0 \end{pmatrix} \tag{2.161}$$

irrespective of the off-diagonal elements. Any diagonal tensor can thus be decomposed into tensors of spherical, cylindrical and planar symmetry. The off-diagonal elements can be decomposed trivially as

$$\begin{pmatrix} \cdot & \alpha_{xy} & \alpha_{xz} \\ \alpha_{xy} & \cdot & \alpha_{yz} \\ \alpha_{xz} & \alpha_{yz} & \cdot \end{pmatrix} = \begin{pmatrix} \cdot & d & 0 \\ d & \cdot & 0 \\ 0 & 0 & \cdot \end{pmatrix} + \begin{pmatrix} \cdot & 0 & e \\ 0 & \cdot & 0 \\ e & 0 & \cdot \end{pmatrix} + \begin{pmatrix} \cdot & 0 & 0 \\ 0 & \cdot & f \\ 0 & f & \cdot \end{pmatrix} \tag{2.162}$$

with the six independent tensor elements labelled a through f for the complete decomposition of the Raman tensor. As the choice of axes is dictated by symmetry, the off-diagonal elements do not require symmetry adaptation. We recognise the first matrix on the right-hand-side of equation 2.161 as the isotropic Raman tensor $\boldsymbol{\alpha'}_{\mathsf{iso}}$, while the second and third term combine to form the diagonal of $\boldsymbol{\alpha'}_{\mathsf{sym}}$.

For tensors of cylindrical and planar symmetry, a suitable decomposition of the diagonal results from the identity

$$\alpha'_{xx}\hat{\mathbf{x}}\hat{\mathbf{x}}+\alpha'_{yy}\hat{\mathbf{y}}\hat{\mathbf{y}} = \frac{1}{2}\left(\alpha'_{xx}+\alpha'_{yy}\right)\left(\hat{\mathbf{x}}\hat{\mathbf{x}}+\hat{\mathbf{y}}\hat{\mathbf{y}}\right)+\frac{1}{2}\left(\alpha'_{xx}-\alpha'_{yy}\right)\left(\hat{\mathbf{x}}\hat{\mathbf{x}}-\hat{\mathbf{y}}\hat{\mathbf{y}}\right) \tag{2.163}$$

which has the same form as equation 2.126. In matrix notation, the diagonal components are

$$\begin{pmatrix} \alpha'_{xx} & \cdot & \cdot \\ \cdot & \alpha'_{yy} & \cdot \\ \cdot & \cdot & \alpha'_{zz} \end{pmatrix} = \begin{pmatrix} a & \cdot & \cdot \\ \cdot & a & \cdot \\ \cdot & \cdot & 0 \end{pmatrix} + \begin{pmatrix} b & \cdot & \cdot \\ \cdot & -b & \cdot \\ \cdot & \cdot & 0 \end{pmatrix} + \begin{pmatrix} 0 & \cdot & \cdot \\ \cdot & 0 & \cdot \\ \cdot & \cdot & c \end{pmatrix} \tag{2.164}$$

illustrating that it is essentially a two dimensional decomposition. The values of a, b and c are different from those of equation 2.161. Decomposition of the Raman tensor does not reduce the number of six unknowns *per se*, but in combination with symmetry arguments (developed below), the number of unique non-zero elements can be reduced below that number.

The elements of the Raman tensor mix upon multiplication by a vector as in equation 2.32 or through a transformation that includes off-diagonal elements, such as the coordinate transformation of equation 2.132 or upon taking an isotropic average. The

individual Raman tensor elements in the molecular frame of reference are therefore only observed in crystalline samples using polarised intensity measurements. However, by decomposing the Raman tensor, the number of unknown elements can be reduced and the Raman tensors for individual vibrational transitions can be deduced. We will now consider how this follows from the symmetry of the molecule.

Molecular symmetry

Symmetry in the Raman tensor arises from the symmetry properties of the vibrational transition it describes. In turn, the vibrational modes and their symmetries depend on the molecular structure. The symmetry of the molecule thus determines what vibrational modes are Raman active.

Group theory is used to analyse the symmetry and vibrational modes of a molecule. A limited number of relevant concepts is presented here, detailed texts can be found in [72–74]. Starting from an assumed molecular structure, its point group is determined by systematically testing what symmetry operations R project the molecule onto itself. These include rotations, reflections, inversion and rotation-reflections, all performed with respect to a set of symmetry elements in the molecular frame of reference. The effect of symmetry operations is represented by square matrices that apply to a particular choice of basis vectors. This basis is called a representation Γ. The trace of these matrices is invariant (as we have seen for the polarisability tensor) and is the same for all symmetry operations that constitute a class. It is therefore used to characterise the symmetry operations. In this context, the trace is called the character $\chi(R)$ of operation R. Its value is listed in a character table for each point group.

A representation Γ (such as a set of basis vectors to describe molecular vibrations) can often be decomposed into a sum of irreducible representations P

$$\Gamma = \sum_{\mathrm{P}} a_{\mathrm{P}} \mathrm{P} \tag{2.165}$$

which each occur a_{P} times. The character table for the point group of the molecule of interest is used to deduce a_{P} through the reduction formula

$$a_{\mathrm{P}} = \frac{1}{g} \sum_{\mathsf{classes}} n_R \chi_\Gamma(R) \chi_{\mathrm{P}}(R) \tag{2.166}$$

that gives the contribution of each irreducible representation P to the reducible representation Γ under consideration. Here, g is the order of the point group, which is the total number of symmetry operations R in that point group, and n_R is the number of symmetry operators in each class. The number of irreducible representations in a point group is equal to the number of classes of symmetry operations in that point group.

Each irreducible representation has a distinct pattern of behaviour with respect to the symmetry operations of its point group. The base vectors of each irreducible repre-

sentation only transform amongst themselves, *i.e.* they form a symmetry-adapted choice of base vectors that are orthogonal to base vectors of other irreducible representations. An irreducible representation is also called a symmetry species, to which the symmetry-adapted vectors belong. The same is true for translations, rotations and vibrations of the molecule. Each vibrational mode belongs to a particular symmetry species and the symmetry-adapted basis in which it is described belongs exclusively to that symmetry species. These facts are used to deduce the symmetry properties of the vibrational modes of a molecule.

Vibrational normal modes

The polarisability tensor is generally given in a Cartesian basis $\{\hat{\mathbf{x}}, \hat{\mathbf{y}}, \hat{\mathbf{z}}\}$, with the choice of axes following from the symmetry of the molecule as given in appendix A. The symmetry species to which each of these basis vectors belong are listed in the character tables. These describe the symmetry behaviour of translations. The three orthogonal rotations (two in a linear molecule) are also included and describe the symmetry behaviour of molecular rotations and angular momenta. This information permits an analysis of the vibrational normal modes of a molecule or a molecular group on the basis of an assumed equilibrium structure.

Considering a molecule consisting of N atoms, it has $3N$ degrees of freedom to move in the three dimensions of space. This can be decoupled into a translation of the molecule as a whole, which requires 3 degrees of freedom for a full description, a rotation of the molecule about its three principal axes and the internal motions. The latter thus have $(3N - 6)$ degrees of freedom, which is the number of vibrational normal modes of the molecule (also termed the fundamental vibrations). A linear molecule only has two distinct rotation axes, so that the number of vibrational modes is $(3N - 5)$ in such a case.

The symmetry species of each vibrational normal mode can be derived by assessing the effect of the symmetry operations of the molecular point group on the reducible representation Γ_{3N}, that includes the $\hat{\mathbf{x}}$, $\hat{\mathbf{y}}$ and $\hat{\mathbf{z}}$ axes on each atom of the molecule. This representation is the combination of the representation of translations Γ_{trans}, rotations Γ_{rot} and vibrations Γ_{vib} as

$$\Gamma_{3N} = \Gamma_{\mathsf{trans}} + \Gamma_{\mathsf{rot}} + \Gamma_{\mathsf{vib}} \tag{2.167}$$

in which each representation can be reduced to a sum of irreducible representations. Having reduced Γ_{3N} with equation 2.166, the irreducible representations that compose Γ_{trans} and Γ_{rot} can be taken from the relevant character table so that the remaining irreducible representations can be assigned to Γ_{vib}. These irreducible representations form the vibrational normal modes of the molecule. Not all vibrational normal modes are observed in infrared or Raman spectra: only the active modes satisfy particular selection rules and give rise to non-zero intensities.

Subsets of vibrational modes can be deduced by choosing basis vectors that describe *e.g.* bond stretching or bending motions. Analysing the symmetry behaviour of such a

basis gives rise to another representation, which can in turn be reduced to the irreducible representations that give the number and symmetry species of the vibrational normal modes in question. Examples of this procedure are given in group theory and spectroscopy textbooks [62, 70, 72, 73] and is summarised in appendix A for molecules relevant to this work.

2.5.4 Vibrational selection rules

All molecules are polarisable to some extend ($\boldsymbol{\alpha}_0 \neq 0$) as these contain electrons and therefore give rise to Rayleigh scattering, however strong or weak. From the classical description of the Raman effect (equation 2.27), it is clear that Raman scattering only occurs for vibrational modes with

$$\boldsymbol{\alpha'} = \left(\frac{\partial \boldsymbol{\alpha}}{\partial Q_{\mathsf{v}}}\right)_0 \neq 0 \tag{2.168}$$

which should hold for at least one of the elements of the polarisability tensor. (Equally but trivially, $Q_{\mathsf{v}0} \neq 0$ as is the case for all vibrational modes or they would not exist.) A vibrational mode is thus Raman active if the electric polarisability is changing when the vibrational motion passes through the equilibrium configuration of the molecule.

From the quantum mechanical description presented in equation 2.28, it is evident that Raman scattering only occurs if the expectation value for the transition dipole moment is non-zero. In turn, component kl of the Raman tensor $(\alpha'_{kl})_{fi}$ is non-zero if the integrals of equation 2.33 are non-zero. The selection rule for Raman scattering in a quantum-mechanical description thus comes down to

$$(\alpha'_{kl})_{fi} \propto \langle \Psi_f | kl | \Psi_i \rangle \neq 0 \tag{2.169}$$

where k and l are one of the three Cartesian components x, y or z. This integral is zero if the functions $|\Psi_f\rangle$ and $|kl|\Psi_i\rangle$ are orthogonal. This is the case if each belong to a different irreducible representation of the point group, *i.e.* a different symmetry species. The components of the polarisability tensor transform in the same way as binary combinations of the Cartesian basis vectors, which means that the symmetry species of kl is the same as that of α'_{kl}. Such binary combinations of the Cartesian axes in the molecular frame of reference are included with the character tables. Similarly, the basis vectors of a vibrational normal mode, as analysed in the preceding section, belong to the symmetry species of the wavefunction that describes the normal mode. The selection rule in equation 2.169 thus turns into a question of symmetry.

A transition is only Raman active if the direct product of the representations of Ψ_f, kl and Ψ_i includes the totally symmetric species A of the point group

$$A \subset \Gamma_{\Psi_f} \times \Gamma_{kl} \times \Gamma_{\Psi_i} \tag{2.170}$$

which is the symmetry species with $\chi(R) = 1$ for all symmetry operators R. If the product is antisymmetric, the integral will reduce to zero. The direct product of representations is computed by multiplying the characters for each and reducing the result into irreducible representations as described above. This is simplified if the initial state is the vibrational ground state of the molecule, which is always non-degenerate and symmetric. It then suffices to assess whether $\Gamma_{\Psi_f} \times \Gamma_{kl}$ includes the totally symmetric species, which is the case if both representations contain the same symmetry species.

The form of the Raman tensor reflects the symmetry species of the vibrational motion to which it belongs. The non-zero tensor elements are derived through symmetry analysis of the fundamental vibrations and are included in the character table of the point group. Every element listed with a particular symmetry species (α'_{xx}, α'_{xy}, α'_{xz}, α'_{yy}, α'_{yz} and α'_{zz} or linear combinations thereof) is non-zero in the Raman tensor while all other elements are zero. Chapter 4 develops this further. The tensor can then be classified as symmetric, elliptical, cylindrical or spherical as discussed above. This determines the tensor invariants and the expected depolarisation ratio. Totally symmetric vibrations result in highly polarised Raman bands, whereas vibrational modes of lower symmetry give depolarised bands.

Note that, even though a transition is classified as Raman active on the basis of symmetry, it may not be visible in an experimental spectrum due to its low scattering cross-section compared to the sensitivity of detection.

Overtones and combinations

Vibrational normal modes describe transitions from the vibrational ground state to an excited state by gaining one photon. The quantum number v of a particular vibrational mode thus changes from 0 to 1. Similarly, an excited state can fall back to the ground state, emitting a photon. These two transitions, if allowed through the selection rule, give the fundamental frequencies in a Raman spectrum that conform to Stokes and anti-Stokes scattering, respectively. In addition to fundamental bands, overtone and combination bands may appear that involve multiple photons and higher vibrational states. These bands occur due to mechanical and electrical anharmonicity. Overtones and combinations are weaker than the fundamental bands and may in turn interact with those fundamental vibrations to give even higher order vibrational motions.

An overtone band arises from a vibrational transition in which the scattering molecule acquires two (or more) energy quanta in the same vibrational mode, *e.g.* v changes from 0 to 2. The emitted scattering is double (or a multiple of) the frequency of the fundamental for a harmonic vibration, which feature a parabolic energy potential. In practice, overtones are observed at frequencies that deviate from the exact multiple due to anharmonicity. An overtone may arise from a non-degenerate fundamental as well as from a single state of a degenerate fundamental vibration or a combination of degenerate states.

Combination bands involve frequency sums and differences. A sum tone arises upon

the simultaneous gain of two (or more) energy quanta in different vibrational modes. The molecule then oscillates at the combined frequency. A difference tone arise from the absorption of an energy quantum in one vibrational state and the loss from another. It requires the scatterer to be in an excited state and therefore occurs less frequently than the sum tone of the same states. The difference band is observed at the frequency of the absorbed photon minus the frequency of the emitted photon.

Simple harmonic oscillatory motion of the vibrational normal coordinate (equation 2.22) has been assumed so far. If this does not accurately describe the vibrational motion, additional frequency terms are needed, giving rise to mechanical anharmonicity. This leads to overtones in the vibrational normal coordinate Q_{v} that lead to scattering-induced dipoles of frequencies $(2\omega_{\mathsf{v}} \pm \omega_{\mathsf{in}})$, $(3\omega_{\mathsf{v}} \pm \omega_{\mathsf{in}})$ and so forth. It will also lead to combination tones with another mode w that can give rise to various frequencies $(\omega_{\mathsf{v}} \pm \omega_{\mathsf{w}} \pm \omega_{\mathsf{in}})$ in the Raman spectrum.

Electrical anharmonicity arises when higher order terms in $\boldsymbol{\alpha}$ become relevant. Only the first two terms of equation 2.18 have been considered so far, with Rayleigh scattering being the first and Raman scattering the second order effect. If electrical harmonicity does not apply, the Raman tensor includes a third term $\boldsymbol{\alpha'}_{\mathsf{vw}}$ that involves two vibrational normal modes v and w (which may be the same to describe overtones as in equation 2.18)

$$\boldsymbol{\alpha'}_{\mathsf{vw}} = \frac{1}{2}\left(\frac{\partial^2 \alpha_{kl}}{\partial Q_{\mathsf{v}} \partial Q_{\mathsf{w}}}\right)_0 Q_{\mathsf{v}} Q_{\mathsf{w}} \tag{2.171}$$

and possibly additional higher order terms that give rise to scattering irrespective of the other terms of the polarisability tensor.

Not all overtones and combinations are Raman active. As with the fundamental transitions, symmetry determines which bands can appear in the spectrum. The same general selection rule applies: a vibrational mode is Raman active if its symmetry species includes one of the Raman tensor elements. A consequence of electrical anharmonicity is that overtones ($\mathsf{w} = \mathsf{v}$) and combinations involving a fundamental vibration can be Raman active, even if the fundamental itself is not. The symmetry species of overtones and combinations is derived as follows.

The representation Γ_{over} of an overtone of a non-degenerate level is obtained through the direct product of the representation of the fundamental Γ_{fund} with itself

$$\Gamma_{\mathsf{over}} = \Gamma_{\mathsf{fund}} \times \Gamma_{\mathsf{fund}} \times \ldots = (\Gamma_{\mathsf{fund}})^n \tag{2.172}$$

where n is the level of the overtone ($n = 1$ is the fundamental vibration, $n = 2$ is the first overtone *et cetera*). This is computed by taking the characters of the irreducible representation of the fundamental to the power n and reducing this representation into its constituent symmetry species with equation 2.166. The computation is more complicated for overtones of degenerate modes (such as those belonging to the E and F symmetry species), as these may involve overtones of a single degenerate state as well as overtones

arising from single excitations in multiple degenerate states. For an E mode of two-fold degeneracy, the first overtone therefore has threefold degeneracy. The character $\chi_{P^n}(R)$ of the $(n-1)$ overtone is computed through

$$\chi_{P^n}(R) = \frac{1}{2}\left(\chi_P(R)\chi_{P^{n-1}}(R) + \chi_P(R^n)\right) \tag{2.173}$$

which requires $\chi_P(R)$, the character of the fundamental as listed in its character table for symmetry species P, as well as $\chi_{P^{n-1}}(R)$ that of the tone below the overtone and $\chi_P(R^n)$ that of performing symmetry operation R for n times. Examples of its application are given in appendix A. The resulting set of characters defines Γ_{over}, which can be reduced as usual to find the included symmetry species.

The representation of combination tones Γ_{comb} is derived through the direct product of the symmetry species of each vibrational mode involved

$$\Gamma_{\mathsf{comb}} = \Gamma_{\mathsf{v}} \times \Gamma_{\mathsf{w}} \tag{2.174}$$

where v and w represent any vibrational mode of the molecule. This holds for both sum and difference tones. The combination may involve two fundamentals, an overtone and a fundamental, a fundamental and a combination, or even two combinations. In each case, the representation of the two components is worked out individually before taking their direct product. Γ_{comb} is then reduced to find its constituent symmetry species and assess whether the combination is Raman active or not.

The symmetry species of the overtone or combination determines the non-zero elements of the Raman tensor that can be looked up in character tables, just as for the fundamentals. The representation of the vibrational mode thus has to include the symmetry species of one of the tensor elements to be Raman active. Only those belonging to the totally symmetric species result in polarised Raman bands, all other give rise to depolarised bands.

Fermi resonance

Wavefunctions of vibrational modes interact if

1. the modes are localised in the same part of the molecule,
2. their frequencies are close together and
3. their representations include the same symmetry species.

These conditions are met in degenerate modes and result in degenerate overtones. However, some vibrational modes are accidentally degenerate whilst including the same symmetry species in their representation. This is often observed to occur between a fundamental and an overtone or a combination band and is termed Fermi resonance. It leads to the mixing of the wavefunctions of each vibrational state and thus a perturbation of the energy levels. The better the frequency match, the larger the mixing of their wavefunctions. The

fundamental mode that gives rise to the overtone or combination band which is engaged in Fermi resonance, is not distorted by the coupling.

The result of this mixing is that the higher energy level of the two is displaced upwards, while the lower is decreased in energy. In the spectrum, this results in an increase and decrease of the frequencies, respectively, from the values obtained without Fermi resonance. Moreover, the intensity of the two resonating bands is now shared and the overtone or combination gains intensity at the cost of the fundamental. The effect shows up in the Raman spectrum as overtones or combination bands of unexpectedly high intensity. These appear as a doublet with the resonant fundamental.

The separation Δ_{res} between the two resonant peaks of a Fermi doublet depends on the unperturbed separation Δ_{unp} between the same modes in the non-interacting approximation and the coupling strength W as [75]

$$\Delta_{\mathsf{res}} = \sqrt{{\Delta_{\mathsf{unp}}}^2 + 4W^2} \tag{2.175}$$

with all quantities in cm^{-1}. W is the matrix element of the perturbation function $\hat{W}$ from the overlap integral between the two uncoupled wavefunctions Ψ_1^0 and Ψ_2^0

$$W = < \Psi_1^0 | \hat{W} | \Psi_2^0 > \tag{2.176}$$

and can be seen as interaction energy of the Fermi resonance. The two wavefunctions Ψ_1 and Ψ_2 that arise from the resonance are linear combinations of the non-interacting wavefunctions Ψ_1^0 and Ψ_2^0 (reference [76], page 217)

$$\begin{aligned} \Psi_1 &= a\Psi_1^0 - b\Psi_2^0 \\ \Psi_2 &= b\Psi_1^0 + a\Psi_2^0 \end{aligned} \tag{2.177}$$

where the weighing factors a and b are given by

$$\begin{aligned} a &= \sqrt{\frac{\Delta_{\mathsf{res}} + \Delta_{\mathsf{unp}}}{2\Delta_{\mathsf{res}}}}\ , \\ b &= \sqrt{\frac{\Delta_{\mathsf{res}} - \Delta_{\mathsf{unp}}}{2\Delta_{\mathsf{res}}}}\ . \end{aligned} \tag{2.178}$$

If $\Delta_{\mathsf{unp}} = 0$, there is perfect resonance and the wavefunctions are mixed equally. If Δ_{unp} is very large, Ψ_1 and Ψ_2 are identical to the unperturbed wavefunctions. The values of a and b can be computed by combining Δ_{res} from experimental and Δ_{unp} from computational data.

An alternative approximate formula is presented in the Encyclopedia of Spectroscopy (reference [77], page 184). Working from an experimental spectrum, the wavenumber $\bar{\nu}_{\mathsf{unp}}$ of the overlapping unperturbed vibrations can be calculated from the wavenumbers $\bar{\nu}_1$, $\bar{\nu}_2$

and intensities I_1, I_2 of the observed Fermi doublet through

$$\bar{\nu}_{\mathsf{unp}} = \frac{\bar{\nu}_1 + \bar{\nu}_2}{2} + \frac{\bar{\nu}_1 - \bar{\nu}_2}{2} \cdot \frac{I_1 - I_2}{I_1 + I_2} \,. \tag{2.179}$$

Equations 2.175 and 2.179 are related through the definition $\Delta_{\mathsf{res}} \equiv |\bar{\nu}_1 - \bar{\nu}_2|$, which results in [75]

$$\frac{I_1}{I_2} = \frac{\Delta_{\mathsf{res}} + \sqrt{\Delta_{\mathsf{res}}^2 - 4W^2}}{\Delta_{\mathsf{res}} - \sqrt{\Delta_{\mathsf{res}}^2 - 4W^2}} \,. \tag{2.180}$$

The coupling strength W may then be approximated from experimental data, rather than from advanced *ab-initio* computation, if the doublet is resolved.

Molecular structure through vibrational spectroscopy

As we have seen, analysis of molecular symmetry provides insight into the number of vibrational normal modes, their symmetry species and whether these are Raman active or not (though group theory can not predict how strong the bands are). Conversely, given the Raman bands and their degrees of depolarisation from an experimental spectrum, the Raman tensor invariants, the symmetry species of the vibrational modes and hence the structure of the scattering molecule may be determined. This is one of the triumphs of spectroscopy and has been used to great effect in deducing molecular and crystal structure for decades (see, for instance [62, 63, 70, 72, 78]).

Limitations are set by the experimental sensitivity in detecting weak bands and depolarisation levels close to the fully polarised limit. Infrared absorption spectroscopy often provides additional information by probing the same vibrations through a different set of selection rules (namely through the basis vectors x, y and z rather than their binary combinations). Fundamental transitions are usually the most intense spectral features, which give rise to weaker overtones and combination bands. Frequencies overlap in some cases, reducing the number of expected bands and causing Fermi resonances if they belong to the same symmetry species.

2.6 Summary

Raman scattering arises from the interaction of light with the electric transition polarisability moment of molecular quantum-mechanical states. It is intrinsically incoherent for an ensemble of molecules. The electromagnetic field incident on a scattering molecule is absorbed and emitted at a frequency shifted by the energy taken up or released in the molecular transition. This work is concerned with the vibrational modes of a molecule.

The scattering molecule is regarded as an oscillating electric dipole, radiating a polarised and directional electromagnetic field. In the far-field, it obeys the description of a plane wave in all radial directions except along the dipole axis, where no radiation is emitted. The intensity of the radiated dipole field scales with its frequency to the forth

power.

The relation between the induced dipole and the incident electric field (both vectors) is described by a tensor of second rank, the polarisability tensor. All three quantities have to be given in the same frame of reference, which can be ensured by coordinate transformations. The Raman tensor is the second term in a Taylor series expansion of the polarisability with respect to vibrational normal coordinates. It is a symmetric tensor that can be decomposed into a sum of tensors in various ways to account for the symmetry properties of the molecule and the vibrational motion.

A vibrational transition is only Raman active if the first derivative of the polarisability tensor with respect to the vibrational normal coordinate is non-zero. Symmetry arguments are used to develop selection rules for Raman activity. Vibrational transitions are Raman active if the transition moment has the symmetry properties of the totally symmetric species of the molecular point group. For fundamental transitions from the ground state to the first vibrational excited state, this implies that the symmetry species of at least one of the six unique Raman tensor elements (or a linear combination thereof) has to match the symmetry species of the vibrational excited state or the transition will not show up in the spectrum of the molecule. It does not predict the absolute intensity, which may be below the detection limit of an experiment.

The tensorial nature of the Raman effect and the orthogonality of vibrational modes result in a spacial Raman scattering intensity distribution that depends on molecular orientation. This can be probed by varying the incident electric field as well as changing the collection of scattered light. Predicting the radiation pattern through modelling can couple the experimentally accessible radiation pattern for various Raman bands to the orientation of the scattering molecules.

Chapter 3

Experimental

This chapter addresses experimental aspects of the project in three sections. The first details the two setups used for polarised Raman spectroscopy, their optical components and variables. The second section lists employed materials with relevant properties. The third describes procedures for the preparation of samples and for the optical alignment of the Raman setup. As well as providing the particulars of the experiments discussed in this work, this chapter also includes more general experimental considerations to facilitate further research.

3.1 Polarised interfacial Raman spectroscopy

Two Raman systems have been used for this work: the adapted Renishaw setup of our group at Durham University and Dr Eric Tyrode's system at Kungliga Tekniska Högskolan (KTH) in Stockholm, Sweden. The latter is a further development of the former, sharing its general design. A polarised laser beam is delivered into the interface under study through a transparent, solid hemisphere that forms the top surface of the interface. The scattered light is collected in a microscope, filtered and delivered to a spectrometer to record the Raman spectrum.

In both Raman systems, the electromagnetic far-field approximation holds for both the incident laser light as well as the Raman scattering. The dimension of the scatterer d, the relevant wavelength in the medium λ and the distance of observation r relate as

$$d << \lambda << r \tag{3.1}$$

These are on the order of 1 nm, 600 nm and 1 cm, respectively. It is therefore the far-field Raman spectrum that is recorded in our experiments.

The sampled interface can be designed separately from the delivery and collection optics. The medium making up the second half of the interface can be a gas, liquid or solid, each requiring a different sample cell. Additional versatility is achieved by surface modification of the hemisphere (see, for instance, reference [79]). The hemisphere joins

the spectroscopic and interfacial aspects of the experiment. The resulting versatility is one of the appealing features of TIR Raman spectroscopy.

3.1.1 Sampled interfaces

The interface under investigation is formed by the flat bottom surface of the hemispherical prism through which the laser beam reaches the interface. The hemispherical shape of the incident prism was chosen to minimise optical aberrations for the incident laser beam. (Previously, trepezoid-shaped prisms were used [80].) The hemisphere is mounted in a sample holder that incorporates the lower medium. This can be a gas, a liquid (flowing or stationary) or a solid. These form the macroscopic interface that determines most of the optical properties, such as the critical angle. TIR can only occur when the light impinges from a medium of higher refractive index onto a medium of lower refractive index. The two bulk materials are therefore chosen with the refractive indices in mind. In addition to the macroscopic elements of the interface, it may contain interfacial species such as absorbed material, surfactants, surface grafts, a thin film or a combination of these. These systems can be prepared in solid-gas, solid-liquid as well as solid-solid macroscopic interfaces.

The hemisphere may be suspended in air, contained in a gas cell, mounted onto a glass flow cell for liquids, pressed against a solid or be part of a tribometric rig for friction experiments. Though the hemisphere is of a standardized size, each of these experiments places different demands on the sample environment. The sample holders and sample cells described below were constructed by the glass-blowing and mechanical workshops of Durham University's Department of Chemistry.

Solid-gas interface

In this work, only air was used as a gas-phase medium. The hemisphere is suspended in air, supported around the perimeter of its base. A rotating hemisphere clamp of own design was constructed to allow for rotation about the laboratory Y-axis, orthogonal to the plane of incidence. Figure 3.1 provides schematic top and side views of the design. A stainless steel beam carries the hemisphere, which is held in a circular recess by two polytetrafluoroethylene (PTFE) slabs. One side of the recess is cut out of the beam to allow optical access to hemisphere from the side. The beam is mounted on a dual axis micropositioner (MDE258, Elliott Scientific Ltd., Harpenden, UK), which in turn is bolted onto a precision rotation stage (MDE 282, Elliott Scientific Ltd., Harpenden, UK). The translation stage is used to position the hemisphere centrally on the rotation axis. The whole is mounted on the XYZ-microtranslation stage to bring the sample into the microscope focus.

An enclosed gas-cell has to be used for gasses other than air at ambient conditions. Such a cell was designed by Dr Laura Bingham and Dr Simon Beaumont of Durham University for *in-situ* study of heterogeneous catalysis.

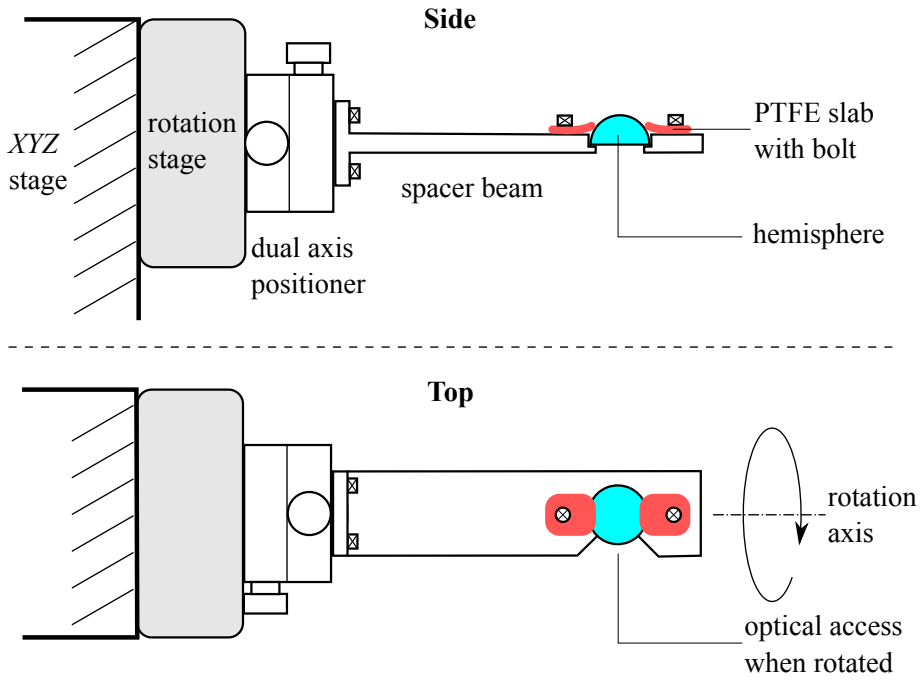

Figure 3.1: Schematic side and top views of the hemisphere rotation clamp (not to scale).

Solid-liquid interface

A solid-liquid interface is produced by mounting the hemisphere on a glass flow cell designed by Dr Eric Tyrode. For our purposes, it serves merely to confine a stationary fluid. The glass inlet tube passes through the outer wall and ends about 2 mm below the hemiphere bottom surface. The hemisphere sits on a viton O-ring under a PTFE clamp that bolts onto a support holding the glass cell. Following assembly and alignment in the setup, the cell is filled through PTFE tubing with a glass syringe. The cell is then closed at the outlet before closing the inlet. The liquid can be replaced batch-wise, as in this work, or gradually by using mechanical syringes and a continuous stirrer to obtain concentration gradients.

The latest version of the cell is described by Woods [81]. A simpler and smaller design, without the temperature-control jacket, has also been used. The volume is about 6 mL in both cases.

Solid-solid interface

The solid-solid interface studied here was made by pressing a sphere against the bottom surface of the hemisphere. This results in a ball-on-flat geometry, well-known in contact mechanics. The pressure in the contact may be deduced from microscopy images of the contact area. Other geometries could be used, but may not preserve the cylindrical symmetry of the contact, misdirect the force more readily and achieve lower pressures by an increase of the contact area. The solid-solid interface is used to pressurise a surface layer or fluid phase against the hemisphere to study confinement effects these materials.

A pressure rig was constructed by Dr Kaustav Guha, described in his thesis (reference [54], page 77). It combined manual and computer-controlled micromotion stages to align hemisphere and sphere with the optics, for making contact and for exerting pressure.

3.1.2 Durham system

Several setups for Raman spectroscopy have been developed in the Bain group at Durham University. The longest-serving one is based on a Renishaw system, which has seen various improvements over the years. This system was used in my work and its layout is described here. Other recent descriptions can be found in a review of Woods and Bain [35] and the theses of Guha [54], Woods [81] and Churchwell [82].

Optical path

Figure 3.2 gives an overview of the apparatus. A solid-state continuous-wave laser produces green light at 532 nm (Opus 532 of Laser Quantum, Stockport, UK). Its beam is linearly polarised, the direction of which can be selected manually with a half-wave plate. A telescope, consisting of a -25 mm and a $+125$ mm focal distance lens, then expands the beam diameter for increased focussing by a convex gradient-index lens (focal length 120 mm) onto the sample interface. The angle of incidence is chosen above θ_c for the studied interface (usually 73° for silica-to-water). The beam spot is aligned with the axis of the microscope objective and the centre of the flat surface of the hemisphere. The latter is usually of fused silica with low fluorescence at the laser wavelength used. The reflected beam is collected in a non-reflective beam dump.

The evanescent wave generated by total internal reflection induces Rayleigh and Raman scattering. The scattered light falling within the view of the microscope objective is collected and collimated. Rayleigh scattering at 532 nm and anti-Stokes Raman scattering are removed with two long-pass edge filters. The collection polarisation is selected by a half-wave plate and a linear polariser. Stray light is removed by focussing the scattered beam through a slit (set to about 200 μm) into the spectrograph. A spectrum of the remaining Stokes Raman scattered light is produced by reflection off a prism, diffraction from a grating with 1800 lines/mm and passing through a focussing lens before being recorded on a charge-coupled device (CCD). Each pixel of the CCD represents a bandwidth of about 1.1 cm^{-1} in the C$-$H stretch region of the collected Raman spectrum. The microscope and spectrograph were originally part of a commercial Raman microscopy system (Ramascope 1000 of Renishaw, Wotton-under-Edge, UK).

Laser beam

Properties of the laser beam, according to manufacturer specification, include the following. Wavelength of 532 nm with a spectral bandwidth (45 ± 10) GHz, which corresponds to (0.042 ± 0.009) nm. Its polarisation is horizontal, with a polarisation ratio $> 100 : 1$.

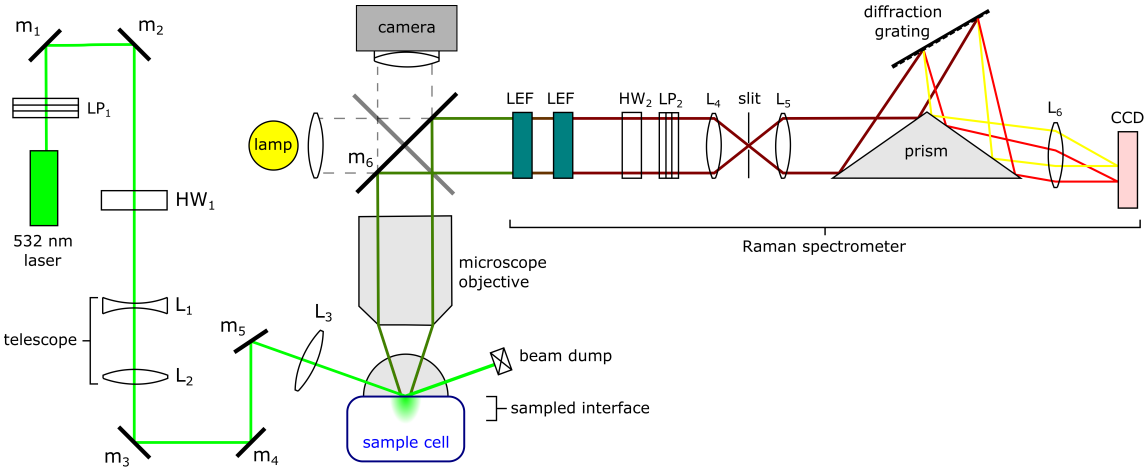

Figure 3.2: Schematic of the Raman spectroscopy experiment using total internal reflection to obtain surface selectivity. The path of the laser beam (green) and the edge of the collected scattered light are indicated. Mirror $\mathsf{m_6}$ (black) reflects the scattered light to the spectrometer and is replaced by a partly-reflective mirror (gray) when the sample is imaged with a lamp and camera. The CCD is read by dedicated software and the collected data is exported to a computer for analysis. See text for further details. [Abbreviations: CCD = charge-coupled device, HW = half-wave plate, L = lens, LEF = long-pass edge filter, LP = linear polariser, m = mirror.]

The Gaussian beam propagates in the fundamental spatial mode TEM_{00} (a single maximum centrally on the beam axis), has an ellipticity $< 1 : 1.15$, a coherence length of 7 mm and a divergence of < 0.5 mrad. The beam diameter, averaged over both elliptical axes, is (1.85 ± 0.2) mm at $e^{-2} = 0.135$ of the maximum intensity (at the beam axis) and measured at 25 cm from the laser exit port. The radial intensity distribution $I(r)$ in such a fundamental Gaussian beam is described as

$$I(r) = I_0 e^{\frac{-2r^2}{w^2}} \tag{3.2}$$

with r the radial distance from the beam axis, at which we find the maximum intensity I_0, while w is the beam radius at which the intensity falls to $e^{-2}I_0$ (or the amplitude to $e^{-1}E_0$). Using $2w$ given in the laser specification as beam diameter, figure 3.3 presents normalised radial intensity and ampitude distributions as well as the relative intensity and amplitude contained within an annulus around the beam axis. This shows that most of the laser power is carried in a ring at a radius of about 0.5 mm around the beam axis.

A telescope is used to increase the beam diameter so that it can be focussed down to a smaller spot in the sample through the gradient-index lens $\mathsf{L_3}$. The position of this lens is adjusted with a micropositioner to achieve the desired focus. Though this increases the amplitude of the field and thus the Raman scattering, it also leads to an increase in the spread of the angle of incidence. A typical spot size is about 100 $\mu\mathrm{m}^2$ with the telescope in use and 2500 $\mu\mathrm{m}^2$ without it, as recorded with the microscope camera. The working of

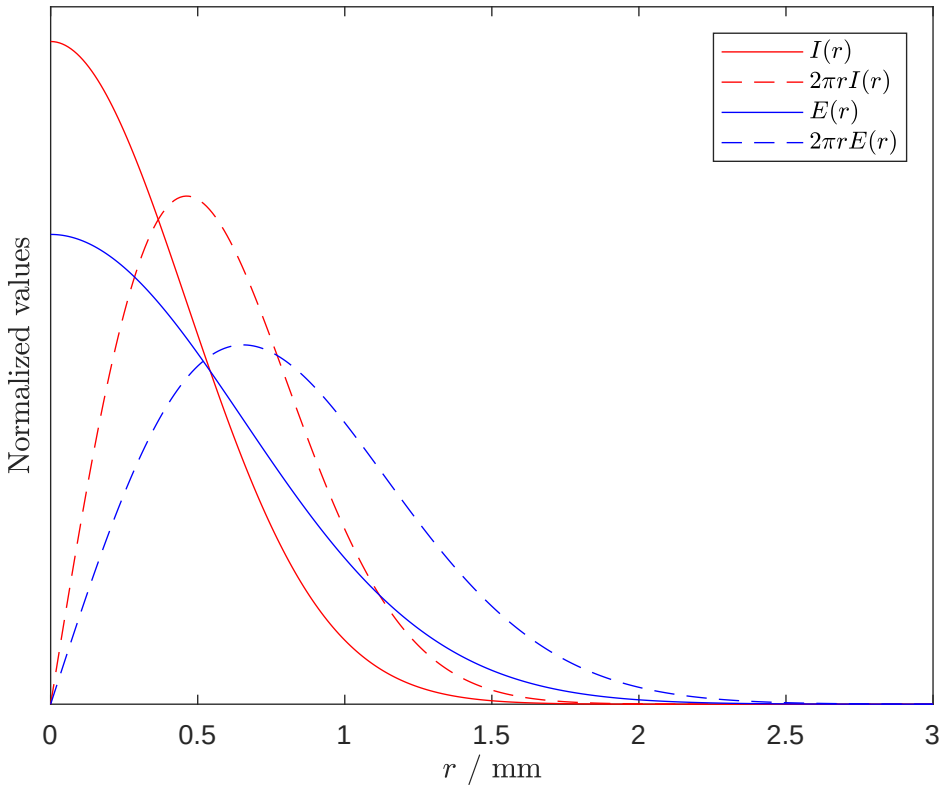

Figure 3.3: Normalised radial distribution of intensity $I(r)$ and electric field amplitude $E(r)$ in a Gaussian laser beam following equation 3.2 with $2w = 1.85$ mm. The values multiplied by $2\pi r$ reflect the relative intensity or amplitude contained within an annulus of radius r.

this telescope is explained in detail in Guha's thesis [54] from page 80 onwards.

Microscopy

A modified Leica DM-LM microscope collects the scattered light and is used with a camera to position the sample and align the laser beam. The centre of the objective focus is the origin of the laboratory frame of reference. The laser spot as well as the sample are aligned on it. The microscope image can be recorded on a digital camera. It is mounted on the microscope and images the sample using white light shining on the sample through the objective lens. A partially reflective mirror is engaged to facilitate both illumination of the sample and collection of its image. Alternatively, if a mirror is engaged in the optical path of the microscope (m_6 in figure 3.2), the collected light is reflected into the spectrometer. It is not possible in the current setup to simultaneously image and record spectra of the sample.

Two objective lenses are available with the Durham system.

- A 5x magnification N Plan objective from Leica (Wetzlar, Germany) with a numer-

ical aperture (NA) of 0.12, primarily used for positioning the sample cell, optical alignment and imaging.

- A 50x ULWD MSPlan objective from Olympus (Tokyo, Japan) with NA= 0.55 and working distance (WD) of 8 mm, primarily used to collect Raman scattering.

The parfocal distance of each lens is slightly different from the other, requiring adjustment of the alignment when switching between objectives. An important characteristic for our purposes is the numerical aperture, which determines the collected fraction of the scattered light.

Polarisations

The polarisations are set as follows. The incident polarisation (as measured at the sample position) is set manually by rotating a half-wave plate in the laser line (HW_1 in figure 3.2). The laser produces horizontally polarised light. This is turned to s-polarised light when the half-wave plate is set at the 37° position and to p at 352°. The accuracy of the polarisation is discussed in chapter 6.

The collection polarisation is set along the x-axis (parallel to the plane of incidence of the excitation laser) by engaging the linear polariser (LP_2 in figure 3.2) in the spectrometer. y-polarisation (perpendicular to the plane of incidence) is selected by adding a half-wave plate (HW_2) in front of this linear polariser. This configuration ensures that the light reaches the diffraction grating at the same linear polarisation so that its effect on the different polarisations need not be considered. If no collection polarisation is chosen, by removing both the half-wave plate and linear polariser from the optical path, the latter effect is not avoided, though it is mostly ignored in analyses.

Engaging the half-wave plate will reduce the intensity of the scattered light. Its transmission should therefore be assessed before x and y-polarised spectra can be compared quantitatively. A helium-neon laser, producing 632.8 nm light, was used to assess the transmission of the half-wave plate in the spectrometer. This wavelength corresponds to a Stokes Raman shift of 2990 cm^{-1} in our system. A Nova II Ophir power meter, set to its 30.0 mW range without averaging and using its glass cover, was used to record the laser power either with or without the half-wave plate in the laser path. The transmission proved to be $T = 0.89$. The factor T^{-1} is applied to y-polarised spectra, that require the use of this half-wave plate. The intensities are then brought to the same scale as those of the x-polarisation recorded without it.

3.1.3 Stockholm system

The Stockholm setup is constructed and maintained by Dr Eric Tyrode at KTH, Stockholm, Sweden. It has been designed as a further development of the Durham setup, with which Tyrode worked in the past. It is a home-built system, briefly described in [25], using more advanced components while following the original in its optical layout.

Optical path

A laser of the same model is used as in the Durham system, precisely controlling its polarisation with an external polariser as well as a half-wave plate. The laser beam passes through a telescope, consisting of a planar-concave and planar-convex lens, to increase its diameter and is delivered to the sample via a periscope and focussing lens. The scattered light is collected and collimated in a modified upright Axio microscope from Zeiss (Oberkochen, Germany). It passes through a RazorEdge long pass filter from Semrock (part of IDEX Health and Science, Rochester, NY, USA), an achromatic half wave plate and a polariser, before being focused on the entrance slit of a Shamrock 303i spectrometer from Andor Technology (Belfast, Ireland) where the spectrum is recorded with a CCD camera (model Newton 940 of the same supplier). Using a grating of 1800 lines/mm, a spectral range of 865 cm^{-1} is collected with a spectral resolution of 0.4 cm^{-1} in the Stokes Raman shift region around 3000 cm^{-1} (corresponding to 0.02 nm around 633 nm). A grating with 1200 lines/mm and one with 600 lines/mm are also available to collect broader yet coarser spectra.

The angle of incidence is set with a stack of two rotating cylinders that contain a Vernier scale. This facilitates accurate alignment as well as adjustment to the angle of incidence without realignment being needed. The lens that focusses the laser beam onto the sample is mounted on the outer rotor, while the mirror reflecting the light onto this lens is mounted on the inner rotor. In turn, the rotors are jointly mounted on a vertical micropositioner.

Microscopy

Two objective lenses have been used with the Stockholm system, both from the M Plan Apo range of Mitutoyo (Kawasaki, Japan). These are long-working-distance objectives for bright-field observation, all with the same parfocal distance. This latter feature ensures that the sample remains in focus when engaging another lens in the revolver of the microscope.

- A 10x objective with NA = 0.28, WD = 34.0 mm and depth of field (DOF) is ± 3.5 μm.
- A 50x objective with NA = 0.55, WD = 13.0 mm and DOF = ± 0.9 μm.

Both objectives were used to collect Raman spectra.

Polarisations

In the Stockholm setup, both polarisers are controlled digitally with microstepper motors. The collection polariser and half-wave plate are placed on the optical table, before the spectrometer. Both are engaged in all measurements. The last polariser ensures that the polarisation of the light entering the spectrograph is always vertical, while this is horizontal in the Durham system.

3.1.4 Comparison of Durham and Stockholm systems

Improvements of the Stockholm setup over the one in Durham include the following.

- The angle of incidence can be set readily with the coaxially rotating Vernier scales to high precision.
- The spread of incident polarisation is minimal with a highly selective linear polariser in the laser beam path.
- Control of the angular position of the linear polarisers is increase by use of microstepper motors. It avoids manual handling of the optics and increases precision and reproducibility.
- The Stockholm spectrometer features three gratings: at 600, 1200 and 1799 lines/mm while the Durham setup only has one at 1800 lines/mm. In the former, spectra can be acquired of wider spectral window in shorter times.
- While the CCD in Durham is limited to a time resolution of 1 s, exposure times in Stockholm can be 10 times shorter due to faster read-out.
- The half-wave plate used to set the collection polarisation is always in the optical path, avoiding a scaling factor needed in the Durham setup to compensate for its presence. All polarisations pass through the same optics, reducing experimental uncertainty when comparing spectra of various polarisations.
- A wider range of objective lenses is available in Stockholm, in particular a set with the same working distance so that repositioning is not needed between experiments with different objectives.
- The Stockholm system features more space between the optical table and the microscope in which the sample cell has to be positioned.

Having worked with both systems, my experience is that the ease of use, adaptability, precision and signal-to-noise ratio at comparable acquisition times are substantially improved in the Stockholm system.

3.1.5 Experimental variables

The experimental approach provides a range of variables and degrees of freedom that effect the recorded Raman spectra. These include geometrical and optical variables, as well as the spectral acquisition and laser power setting and any modulation of the sample environment. A number of these are interdependent.

Spectral acquisition

The range of the Raman spectrum is determined by the grating in the spectrograph. The line density of the grating determines its dispersion power: more lines means more datapoints per wavenumber but a smaller spectral range. The angular orientation of the grating determines the region of the spectral window, *i.e.* around what absolute Raman shift the spectrum is centred. The dispersed scattering is projected onto the CCD through a focussing lens. Though the centre of the spectrum is usually well-focussed, aberrations in the lens cause the outer parts of the spectrum to spread over the CCD. This is most obvious along the vertical direction, but also affects the horizontal direction, the spectral axis along which the light is dispersed.* The spectral resolution is therefore highest in the centre of the spectrum and reduces towards its perimeter. The spectral region of interest should therefore always be centred.

The control software includes various modes of data acquisition. In Durham, two modes are available through Renishaw's WiRE software package (version 2, service pack 9): static acquisition and extended range scan. In a static acquisition, the grating is positioned, the CCD exposed for a predetermined amount of time and finally read out. The exposure can be as short as 1 s. The spectral window is about 660 cm^{-1}. In long static exposures, the variation in sensitivity between CCD pixels becomes apparent. However, this does not have a significant impact on the analysis of such spectra. In an extended range scan, the spectral range is increased by smoothly tilting the motorised grating while the CCD is exposed and the spectrum is recorded from high to low Raman shift. The exposure time is 10 s for each scan and spectra ranging from 100 to 3000 cm^{-1} are readily obtained. The pixel-to-pixel variation is not relevant in this case as the process averages the contribution of each pixel. In both static and scan modes, multiple acquisitions may be summed to improve the signal-to-noise ratio of the spectrum.

The Andor spectrometer in Stockholm has a number of CCD-readout options. Because multiple gratings are available that form wide-ranging spectra, a scanning option is unnecessary. In our work, the options full vertical beam (FVB) and multi-track (MT) were used. Both are static acquisitions similar to those in the Renishaw spectrometer. Whichever setting is used on either Renishaw or Andor spectrometers, a rectangular subset of CCD pixels is selected for read-out. This determines the spectral range within the limits set by the grating and enhances the signal-to-noise by preventing unexposed pixels from adding noise to the data. In the Andor FVB setting, the whole exposed spectrum is read out, while in its MT setting, only a selected subset is processed.

Laser power

In setting the output laser power, care has to be taken to avoid damaging the sample. At the same time, a high power is desired to increase the signal strength and thus achieve

*Note that the spectrum is in fact dispersed in the vertical direction in the spectrometer but is presented horizontally in the analysis software to match the way spectra are plotted.

a better signal-to-noise ratio. A further limit is set by the CCD: saturation of its pixels in the desired acquisition time should be avoided. Neutral optical density filters can be used to reduce the laser power well below its stable operating regime. Another option to reduce the power density is to increase the laser spot size. This is achieved by defocussing the laser beam by moving the gradient index lens towards the hemisphere so that its focus lies beyond the interface.

The laser power is generally quoted as the value set with its controls. After passing through the delivery optics, about 2/3 of the original power is delivered to the hemisphere (530 mW from a 800 mW output as presented in [82]).

Geometrical variables

The positioning of the sample within the optical arrangement has a number of geometrical degrees of freedom that depend on the sample holder. Motion along various axes is required to obtain alignment of the components and allow selective, reproducible investigation of the interface. The geometry determines the illuminated part of the sample and what section of its scattering is collected by the microscope.

Traditionally, the interface is aligned perpendicular to the axis of the microscope objective. In later chapters I will show that this may not be the most favourable condition to collect scattering. Roll and pitch angles can be introduced to collect different sections of the scattering, which may be more intense. The relative orientation of the interface with respect to the objective lens is therefore treated as a variable in our analysis. The rotating hemisphere clamp was designed with this purpose in mind. Note that adjusting the sample orientation also affects the angle of incidence of the laser.

Optical variables

Once the sample is aligned, four optical experimental variables remain. Though the Durham and Stockholm Raman systems vary in their technical detail, they both incorporate these variables.

- The angle of incidence θ_i of the laser beam.
- The linear polarisation of the incident laser beam, which is traditionally set to either p or s but can take intermediate values.
- The collection polarisation, which is set either along x or y, or none at all in the Durham system. In the Stockholm setup, it is always included and can take intermediate values.
- The objective lens that collects the scattered light, in particular its NA.

Chapter 5 addressed these variables in detail. A few remarks suffice here.

The angle of incidence determines the penetration depth of the evanescent electric field and its magnitude at the interface. At the critical angle, these are maximised. When

the moiety of interest is only located at the interface and not in the bulk of the second medium, the penetration depth is less relevant than for species that partition between bulk and interface.

The p and s polarisation of the incident radiation allows for investigation of the directionality of the scattering moiety, in addition to assessing its presence near the interface.The collection polarisation further adds to this orientational selectivity. It can be set along either the x or y laboratory frame axis. Alternatively, no collection polarisation is selected and all scattering for a given laser polarisation is collected. The combination of linear incoming and collection polarisation results in four distinct spectra: px, py, sx and sy. The incident polarisation can also take an intermediate value to probe a combination of components. The same can be done with the collection polarisation in the Stockholm system, though this feature has not been explored here.

The polarisation combinations are distinct from conventional polarised and depolarised Raman scattering as introduced in section 2.5. In the conventional case, the Raman peak intensity for a mode can be deduced analytically for a given orientational distribution of the scattering moiety. It only depends on the rotational invariants of the Raman tensor.[61] However, these can not be used in our case of total internal reflection. Linearly polarised spectroscopy provides access to four experimental polarisation combinations, and thus four Raman peak intensities for a particular mode. However, these four recorded intensities are not independent, as they combine the elements of the laboratory frame Raman tensor in more intricate ways on top of the (unknown) orientation distribution. Modelling efforts are needed to disentangle the various contributions.

Environmental modulation

The sample cell may introduce further variables to test the response of a system to environmental modulations or even chemical reactions. Changing the physical and chemical environment at the interface can affect changes in the recorded spectrum. Such changes may affect the Raman spectrum in various ways. It may affect

1. the relative abundance of species in the sampled volume, thus affecting peak intensities,

2. the orientational distribution of a species, affecting the observable laboratory-frame Raman tensor,

3. the intermolecular distances, leading to constrained or relaxed vibrations giving rise to peaks at slightly shifted frequency, or it may

4. generate new moieties with Raman-active modes.

The Raman tensors of vibrational modes expressed in the frame of the scattering moiety may not be affected, but the orientation of the moiety might, which results in a different laboratory-frame Raman tensor. The effect of this can be detected as intensity changes of

particular peaks in the recorded spectra. Changing the pH, temperature or composition of the liquid medium can alter the composition or chemical state of surface species. Exerting pressure on an interfacial layer or submitting it to shear forces can alter the composition of lubricant mixtures and the orientation of molecules at the surface. Facing reagents in gas phase, heterogeneous catalysts can form transients species and products that give rise to additional Raman features in the spectrum.

3.2 Materials

3.2.1 Chemicals

Water was used from Milli-Q purification systems (Merck Millipore, Darmstadt, Germany) with a resistivity of 18.2 MΩ cm at 25°C and a total organic carbon (TOC) content of $\leq$ 5 ppb.

The following chemicals were used as supplied.

Carbon tetrachloride, CCl_4, was obtained from Sigma Aldrich (now part of Merck, Darmstadt, Germany) at $\geq$ 99.95% purity.

Chloroform, $CHCl_3$, was obtained from Fisher Scientific (Loughborough, UK) at $\geq$ 99% purity.

Ammonium sulfate[†], $(NH_4)_2SO_4$, was obtained at $\geq$ 99% purity from Sigma Aldrich.

Zinc sulfate was obtained from Sigma Aldrich at 99.999% purity in the pentahydrate form, $ZnSO_4.5H_2O$.

Arachidic acid was obtained from Aldrich Chemical Company (now Merck, Darmstadt, Germany) at $\geq$ 99% purity. It is a saturated fatty acid with twenty carbon atoms of formula $C_{20}H_{40}O_2$ and is presented as a stretched chain in figure 3.4. In a fully stretched chain, all C−C bonds are in the anti-conformation and the potential energy is minimized. Upon rotation around a C−C bond, gauche-conformations are obtained, which represent local minima of the potential energy surface. Newman projections of these two conformational isomers are presented in figure 3.5. The intermediate eclipsed state presents a barrier to the rotation. In solution, gauche butane lies 2.5 kJ mol^{-1} above its anti conformation with a rotational barrier about the central C−C bond of 14 kJ mol^{-1} in going from the anti to one of the gauche conformations.[83] In longer alkane chains, the potential energy difference between the anti and gauche conformations as well as the rotational barrier between the two is higher due to increased electron delocalisation in the anti conformation.[84, 85]

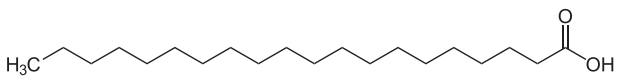

Figure 3.4: Chemical structure of arachidic acid as a stretched chain.

[†]The IUPCA-recommended spelling for sulphate is used throughout this work.

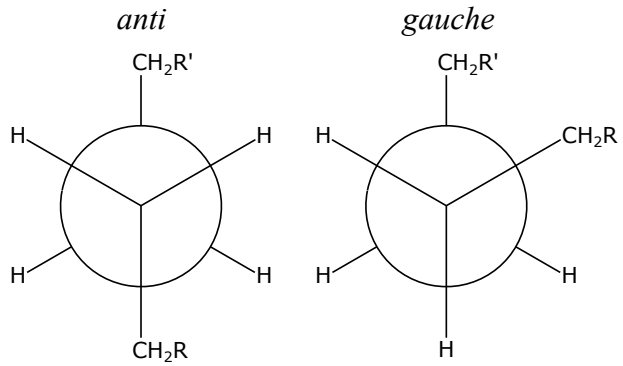

Figure 3.5: Newman projections of two conformational isomers of a C−C bond in an alkane chain.

3.2.2 Isotopologues

The isotopic composition of a molecule has two important effects in vibrational spectroscopy. First, the occurrence of isotopes affects the molecular symmetry as different isotopes of the same atom are not symmetry-equivalent. This leads to a different point group and possibly a different choice of axes. The Raman tensors are affected and may display different forms for each isotopologue.

Second, the reduced masses of vibrational modes that involve isotopes are affected, causing a frequency shift in the vibrational spectrum. This can be understood readily for simple harmonic motion, where the angular frequency ω is determined by the force constant k and mass m through

$$\omega = \sqrt{\frac{k}{m}} \tag{3.3}$$

As the force constant of the system remains unchanged (the electronic structure is not affected in isotopologues), the increased mass due to a heavy isotope will slow the oscillation down. Furthermore, heavier isotopes lower the amplitudes of the molecular vibrations in which they are involved, including the zero-point amplitude of equation 4.52. This reduces the deformation of the electron cloud through the vibrational motion and thus the polarisability derivative. The Raman effect for heavy isotopes is thus expected to be weaker.

These effects should be born in mind when analysing Raman spectra quantitatively. The relative abundance of an isotopologue in combination with the signal-to-noise ratio determine whether or not the isotopologue can be detected in a spectroscopic experiment. It is therefore prudent to assess the relative abundance of isotopologues in the materials used in our Raman scattering experiments. Appendix B includes such analysis based on the terrestrial abundance of isotopes. We build on that here to select relevant isotopologues for use in our analyses.

Toluene

In toluene, the most abundant isotopologue at 92.7% is $^{12}C_7{}^{1}H_8$. The seven forms of $^{12}C_6{}^{13}C^{1}H_8$ contribute 0.993% each, only four of which affect the symmetry of the molecule. Moreover, the reduced mass is not likely to strongly affect the vibrational mode of interest (the symmetric ring breathing mode that involves all atoms of the phenyl moiety). The mass involved in this vibration only increases by a factor of 1/77. Only the most abundant isotopologue is therefore taken into account.

Alkane

An alkane chain of arbitrary length is analysed in appendix B as a generalised model for arachidic acid. As our interest lies with the C−H vibrations, the acid group is ignored. The methyl moiety is assumed to be pure $^{12}C^{1}H_3$, as its abundance is 98.9%. In the 18 methylene moieties of arachidic acid, the occurrence of deuterium at 0.521% can be ignored. The abundance of chains with one ^{13}C is 15.9% in total; 0.884% at each of the 18 carbon positions. The total mass of the methylene moieties only changes by a factor of 1/252. Moreover, the symmetry of a stretched alkane is unaffected by carbon isotopic impurities. It remains C_s. We assume that the combined vibrational features of these isotopologues are not discernible from those of the most abundant isotopologue $^{12}C_{20}{}^{16}O_2{}^{1}H_{40}$ and only the latter is used in our analysis.

CCl_4

Carbon tetrachloride has 10 isotopologues and occurs in three point groups: 46.4% belongs to C_{3v}, 33.4% to T_d and 20.2% to C_{2v}. Contrary to the other species considered here, the most abundant isotopes do not produce the most abundant isotopologue. The three most abundant forms of carbon tetrachloride are considered: $^{12}C^{35}Cl_3{}^{37}Cl$ (41.7%, C_{3v}), $^{12}C^{35}Cl_4$ (32.7%, T_d) and $^{12}C^{35}Cl_2{}^{37}Cl_2$ (20.0%, C_{2v}).

Sulfate

The sulfate anion has 60 isotopologues, but only two have an abundance of over 1%. These are $^{32}S^{16}O_4^{2-}$ at 93.9% abundance and $^{34}S^{16}O_4^{2-}$ at 4.32%. Both species belong to the T_d point group. With the change of mass from 96 to 98 amu, spectral features are expected to change only minimally. Jointly, these isotopologues account for 98.2% of all sulfate anions. The most abundant isotopologue, with the most abundant isotopes, is therefore used in the analysis of sulfate spectra.

3.2.3 Glass substrates

In the Raman experiments under total internal reflection, samples are probed at the flat bottom surface of a solid, transparent hemisphere. Materials that have been used in our group include fused silica (amorphous SiO_2), borosilicate crown glass (trade name BK7),

dense flint glass (trade name SF10), sapphire (Al_2O_3), cubic zirconia (ZrO_2) and calcium as well as magnesium fluoride. The hemisphere is usually selected for its optical, mechanical and spectral properties. A specific material may be of interest as a solid substrate to investigate particular interactions. Alternatively, thin coatings can be used to provide the surface with the desired chemical functionality while retaining the optical properties of the hemisphere bulk material.

The following are relevant characteristics in assessing a material for use in TIR Raman spectroscopy.

Transparency. The hemisphere must be sufficiently transparent for the laser as well as the Raman scattered light. Deeper layers of the sampled interface need not meet this requirement.

Refractive index. The refractive index of the hemisphere at the laser wavelength (with that of the material facing the it) determines the critical angle. The refractive index at the wavelength of the Raman scattered light partly determines the signal strength. As explained in chapter 5, a higher refractive index of the hemisphere decreases the critical angle, increases the amplitude of the field that drives Raman scattering and increases the coupling of the Raman-scattered field through the hemisphere for detection.

Birefringence. Many crystalline materials exhibit birefringence, which complicates optical alignment even when the crystal axis in the hemisphere is known. Both the incoming laser as well as the Raman scattered light are affected, which should be included in a complete model description of the process.

Fluorescence. The sample materials should exhibit minimal fluorescence at the laser wavelength used. As fluorescence is generally much stronger than Raman scattering, the first will obscure the latter. A higher frequency laser (shorter wavelength) can avoid interference from fluorescence in many cases.

Raman spectrum. Ideally, the hemisphere has no strong Raman features in the region of interest, so that it does not obstruct observation of sample features. Spectral features of the hemisphere cannot be completely avoided as the laser passes through the bulk of its material. Background subtraction is routinely used to remove any spectral features of the hemisphere that overlap with the sample. However, as spectra may strongly depend on the optical geometry, one background spectrum should be recorded for every sampled geometry. Example spectra of fused silica, sapphire and SF10 are included in figure 3.6.

Surface roughness Hemispheres should be optically smooth in all cases. Strong undulations of the surface affect the local optical path and the angle at which molecules orientate with respect to the averaged interfacial plane. Scratched or damaged areas should not be sampled.

Hardness. In solid-solid contact experiments (such as those presented in chapter 7), material hardness affects the interfacial pressure distribution. Hard materials avoid deformation and surface damage, while flattening of asperities is desired to obtain a smooth contact area.

Reactivity. The hemisphere should be suitable for any desired surface treatment, such as Langmuir-Blodgett deposition, plasma treatment, thin-film deposition and cleaning routines. Furthermore, it should not exhibit undesired reactions (such as etching, irreversible absorption and dissolution) when exposed to other materials in the sample.

Other considerations include availability and cost of hemispheres of the desired material. This is not an issue with the materials used in this work. These are frequently used and have the added benefit of being well-characterised and of being employed in published studies that can be used for comparison. Further considerations are presented in the chapters where they are employed.

In this work, fused silica, SF10 and sapphire have been used. Fused silica hemispheres of 10 mm diameter as well as a fused silica sphere of 10 mm diameter were obtained from Global Optics (Poole, UK) with a surface scratch/dig ratio of 40/20. Both the IR and UV-grade silica are suitable for our application. The SF10 hemisphere with a diameter of 10 mm was obtained from ISP Optics Corp. (Irvington, New York, USA). Sapphire hemispheres, of 10 mm diameter and 40/20 surface finish, as well as a later batch of fused silica hemispheres of the same standard were supplied by Knight Optical (Harrietsham, UK).

In addition to meeting the material criteria listed above, fused silica is appealing as a reference surface for its ubiquitous use in various spectroscopy and interface investigations. The advantage of fused silica over quartz (the crystalline form of pure SiO_2) lies in the random nature of its surface and lack of birefringence. Fused silica is produced by pyrolysis of $SiCl_4$ or by melting powdered quartz into a continuous solid form to obtain a macroscopically amorphous and isotropic glass. Hemispheres of fused silica are used as the standard solid substrate in our research group.

3.2.4 Refractive index

In a Raman experiment, optical properties are of paramount importance. The considerations of transparency, low fluorescence and lack of Raman bands discussed above for choosing a hemisphere are equally valid for the optical components that collect the Raman scattered light. In TIR Raman, the refractive indices of the materials making up the sampled interface are further critical parameters. These are therefore considered in detail here.

(a)

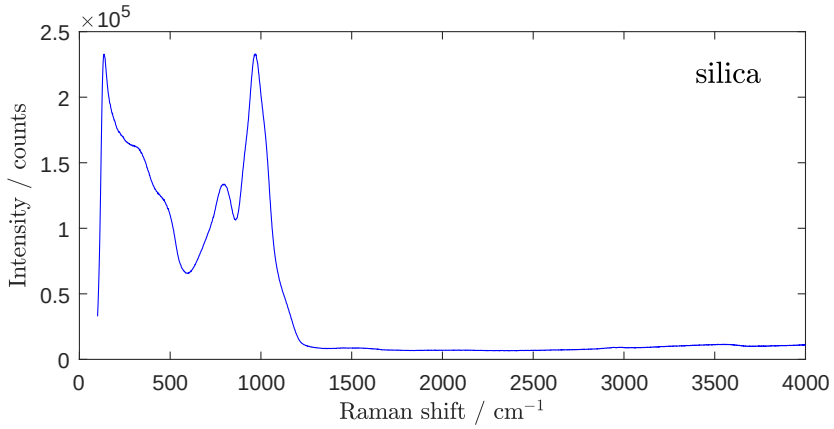

(b)

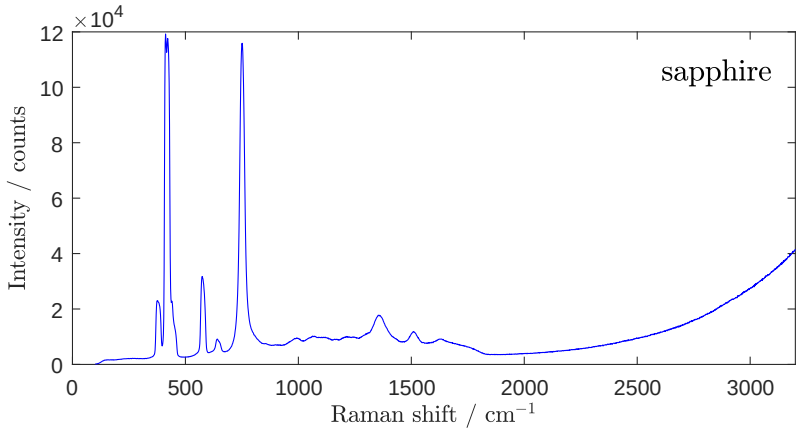

(c)

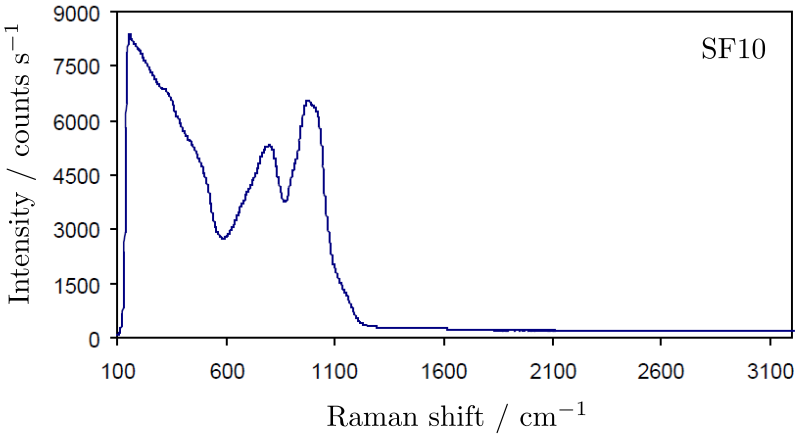

Figure 3.6: Stokes Raman spectra of hemispherical substrates collected from the solid-air interface under total internal reflection of the laser beam. Spectra were recorded as accumulated scans on the Durham system, employing S-polarised laser light without polarisation selection of the collected light, the 50× objective lens and (a) 200 mW laser output power, angle of incidence $\theta_i = 73°$, 4 accumulations of 10 s scans [data 20140114/05], (b) 200 mW, $\theta_i = 73°$, 5×10 s [data 20150326/007A], (c) 20 mW, $\theta_i = 44.2°$, 200 s [spectrum from Kaustav Guha [54]].

Sellmeier's equation

The refractive index n of a material depends on the wavelength of the light propagating through it. The Sellmeier equation describes the relationship on an empirical basis as

$$n^2(\lambda_0) = 1 + \frac{A_1 {\lambda_0}^2}{{\lambda_0}^2 - B_1} + \frac{A_2 {\lambda_0}^2}{{\lambda_0}^2 - B_2} + \frac{A_3 {\lambda_0}^2}{{\lambda_0}^2 - B_3} \tag{3.4}$$

with λ_0 the wavelength of the light in vacuum, traditionally given in μm, and up to six Sellmeier coefficients A_1 through B_3. The A parameters are dimensionless, while the B are given in μm^2 with $\sqrt{B}$ corresponding to absorption bands. Alongside the coefficients, a range of validity is always given. Here, we use data for the visible range of the electromagnetic spectrum, which covers vacuum wavelengths from 400 to 700 nm. Table 3.1 contains Sellmeier coefficients for materials used in this work. Note that sapphire is birefringent and both its ordinary and extraordinary axes are listed. Uncertainty values, where originally given in the references, have been omitted from the table. Figure 3.7 includes the refractive indices of the species included in table 3.1 as a function of vacuum wavelength in the visible using equation 3.4.

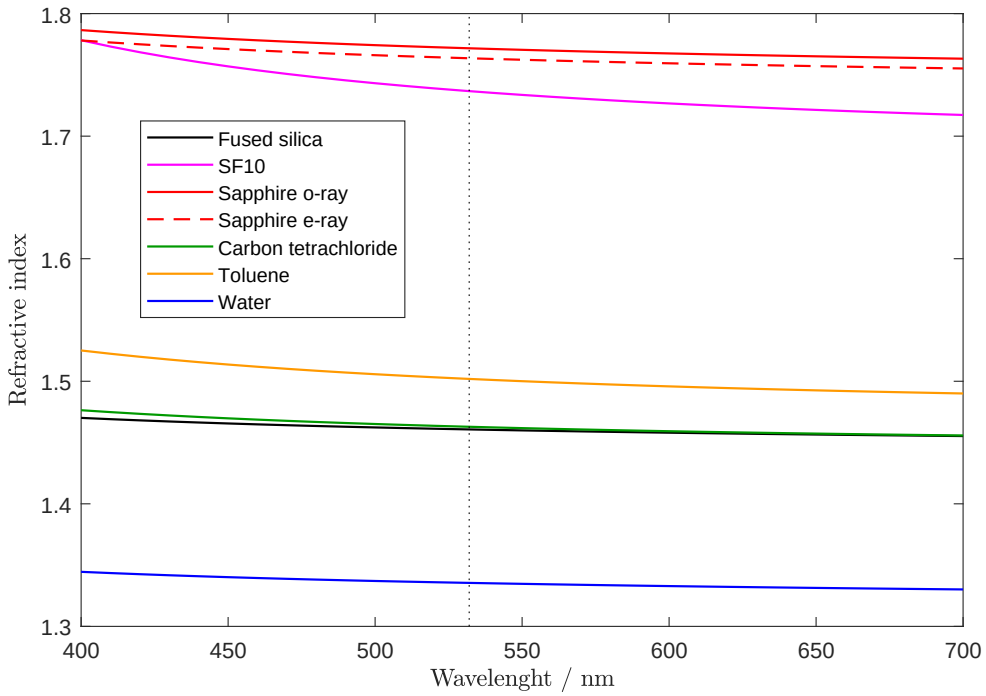

Figure 3.7: Refractive index as a function of wavelength in vacuum from equation 3.4 and the data of table 3.1. A dashed vertical line at 532 nm indicates the laser wavelength.

In sapphire, the refractive index for the *o*-ray varies no more than 0.5% from that of the *e*-ray in the wavelength range of interest. Furthermore, the exact crystal orientation of the sapphire hemisphere in our system is unknown. For these two reasons, mean values

Table 3.1: Sellmeier coefficients

	A_1	B_1/μm2	A_2	$B_2/\mu\text{m}^2$	A_3	$B_3/\mu\text{m}^2$	reference
Fused silica	0.6961663	0.004679148	0.4079426	0.01351206	0.8974794	97.93400	[86]
SF10	1.61625977	0.0127534559	0.259229334	0.0581983954	1.07762317	116.60768	[87]
Sapphire, o-ray	1.4313493	0.0726631^2	0.65054713	0.1193242^2	5.3414021	18.028251^2	[88]
Sapphire, e-ray	1.5039759	0.0740288^2	0.55069141	0.1216529^2	6.5927379	20.072248^2	[88]
Carbon tetrachloride	1.09215	0.01187					[89]
Toluene	1.17477	0.01825					[89]
Water	0.75831	0.01007	0.08495	8.91377			[89]

are used for its refractive index.

The refractive index of air varies from 1.00028276 at 400 nm to 1.00027580 at 700 nm in the visible part of the electromagnetic spectrum, a dispersion of 7 parts in 10^6 [90]. Its variation with pressure, temperature and CO_2 content is likewise deemed insignificant for our purposes. The mean of $n_{\text{air}} = 1.000279$ can therefore be used over the whole wavelength range of interest. The approximation $n_{\text{air}} = n_0 = 1$ has been used frequently in previous work of our group and is reasonable in our work as well. It is not expected to limit the accuracy of our analysis.

Sulfate solutions

Solutes affect the refractive index of liquids. This fact invites a brief assessment of its significance for the solutions of sulfate salts used in this work. Urréjola *et al.* [91] have measured the refractive indices of ammonium sulfates in water at 589.3 nm (corresponding to the sodium D-line reference wavelength). Assuming that the dispersion of these solutions is similar to pure water in the wavelength range of interest (below 0.2% from 532 to 598 nm), their values are accurate enough for our purposes. Conversely, their data permits determination of salt molal concentration using a refractometer.

In Durham, the refractive index of solutions could be determined with a RFM970 refractometer of Bellingham and Stanley Ltd. (Farnborough, UK), sampling at 20.0°C with a wavelength of 589 nm from a light emitting diode. Solutions were prepared by weight of salt measured on an analytical balance and volume of water by micropipette. A solution of 40 wt% ammonium sulfate in water showed a refractive index of 1.39339, while at 18 wt%, the refractive index was found to be 1.36098. This is an increase over that of pure water, recorded on the same refractometer as 1.33298, by 4.5 and 2.1%, respectively. For reference, the CRC Handbook [92] was consulted, providing $n_{40\text{wt}\%} = 1.3938$ and $n_{18\text{wt}\%} = 1.3616$ for the two solutions at standard temperature and pressure, confirming our measurements.

For the experiments in Stockholm, a solution of ammonium sulfate in water was prepared in a volumetric flask at a concentration of 0.2927 mol L^{-1}. This corresponds to a molality of 0.293 mol kg^{-1} (assuming that the density of the solution is that of water). Using the polynomial in [91] for ammonium sulfate solutions at 25°C, the refractive index of this solution is predicted to be 1.3386, an increase of only 0.46% from that listed for pure water (1.33248). Though our work is performed at 20°C, the expected deviation due to this lower temperature is insignificant at less than 0.07% according to data in [91].

Arachidic acid

Pure arachidic acid is a white crystalline solid at standard temperature and pressure. Its lack of transparency in the visible precludes determination of a refractive index. A comparable analogue is *n*-icosane ($C_{20}H_{42}$), which differs from arachidic acid in having a methyl group at the position of the carboxyl group. *n*-Icosane forms a colourless, waxy

solid in standard conditions and has a mean refractive index of 1.4425 at the sodium D-line [92].

The optical properties of arachidic acid monolayers on glass have, to my knowledge, not been published. However, studies on Langmuir-Blodgett films of fatty acids, alcohols and other molecules incorporating alkane chains are numerous. These may be used to gauge the refractive index of the alkane chain, which constitutes most of the molecule. The optical properties of 1-dodecanol ($C_{12}H_{24}O$) monolayers on water have previously been studied in our group by ellipsometry [10]. The relative permittivity along the two optical axes were deduced to be $\epsilon_e = 2.23 \pm 0.07$ and $\epsilon_o = 2.12 \pm 0.03$ at 20°C and 633 nm. The material forms an ordered layer that exhibits birefringence. Using approximation 2.44, the refractive indices are $n_e = 1.49$ and $n_o = 1.46$. These values differ from the refractive index of bulk 1-dodecanol, 1.4430, measured at the sodium D-line and standard temperature and pressure [92] (near its melting point of 24°C). The difference originates from dispersion, the crystalline nature of the monolayer and the film density compared to the density of the bulk material. The latter effect can be assessed through the Clausius-Mossotti relation

$$\frac{\epsilon_r - 1}{\epsilon_r + 2} = \frac{N\alpha}{3\epsilon_0} \tag{3.5}$$

with N the molecular number density in m^{-3} and α the isotropic molecular polarisability in C m^2 V^{-1}. This equation facilitates computation of the refractive index for systems of different surface densities. However, the effect of dispersion remains to be assessed before the values provided by [10] can be used. Whether or not this 2% variation significantly affects the experimental data is assessed in section 6.4.

Summary

Values used in our analyses are collected in table 3.2 for ease of reference. It lists the refractive indices at the wavelength of the incident laser as well as a number of Raman bands for each material. The dispersion is under 1% for all materials in this wavelength range. The relevance of each band is addressed in the chapters presenting the results. Conversion of a Raman shift $\bar{\nu}_R$ in units of cm^{-1}, as recorded in a spectrometer in air, to the wavelength of the Raman scattering in vacuum $\lambda_{0,R}$ in nm uses

$$\lambda_{0,R} = \frac{n_{\text{air}}}{{\lambda_{\text{laser}}}^{-1} - 10^{-7}\,\bar{\nu}_R} \tag{3.6}$$

with λ_{laser} (in nm) the wavelength in air of the laser that induces the Raman scattering. $\bar{\nu}_R$ is positive for Stokes Raman scattering, which is employed in the current work. Equation 3.6 is readily composed from equations 2.41 and 2.48.

Table 3.2: Selected refractive indices

wavelength / nm	532	546	561	562	627
Raman shift / cm^{-1}	0	460	980	1000	2870
Fused silica	1.4607		1.4594	1.4594	1.4572
SF10	1.7367				1.7236
Sapphire	1.7676	1.7667			
Air	1.0003	1.0003	1.0003	1.0003	1.0003
Carbon tetrachloride	1.4629	1.4620			
Toluene	1.5019			1.4989	
Water	1.3355				
Ammonium sulfate 40 wt%	1.3934		1.3934		
Ammonium sulfate 18 wt%	1.3610		1.3610		
Ammonium sulfate 0.3 mol L^{-1}	1.3386		1.3386		
Alkane chain	1.4425				1.4425

3.3 Procedures

This section describes procedures to prepare the Raman systems as well as the sample for experiments. The latter includes cleaning of hemispheres and other components of the flow cell and deposition of arachidic acid monolayers onto the hemisphere surface.

3.3.1 Optical

Careful positioning and alignment of the optical components is needed to record Raman spectra. Once the position of the microscopy is assured, the laser and the optics guiding the laser beam path are aligned. The spectrometer is then calibrated before the angle of incidence and the linear polarisation directions are set. Finally, the sample holder is mounted in such a way that the hemisphere is aligned correctly. Not all procedures need be executed for every experiment. In Durham, re-alignment of the microscope and full laser path as well as calibration of the polarisation directions were not attempted. Instead, existing alignment marks were used. For the Stockholm system, all of the following steps were taken.

Alignment of microscope and laser

The microscope and optical table are positioned vertically and horizontally with respect to the earth's gravitation. This is confirmed with a theodolite, which serves as an external reference for these two orthogonal directions. The focal axis of the microscope objective, parallel to the vertical, is the laboratory z axis. The point where this axis strikes the optical table is confirmed with the lamp in the microscope. The origin of the laboratory frame of reference is at the focus of the microscope objective lens.

The path of the laser beam is then aligned in the horizontal plane as the x axis, orthogonal to the position of the microscope body along the y axis. A theodolite can be used to indicate the xz or yz plane. The grating of holes in the optical table may also be

used as a guide parallel to the x and y directions. The x axis, to become part of the plane of incidence, is then marked on the optical table. The desired laser path is set parallel to the optical table by two apertures, closed to a pin hole, at the same height along the x axis. Two mirrors just after the laser source, m_1 and m_2 in figure 3.2, are used to align the laser beam to this direction.

The beam is then deflected upwards, parallel to the z axis, by mirror m_4. The new direction is confirmed by the theodolite and marked on the laboratory ceiling as a reference for easy re-alignment. Another mirror (m_5) is then put in its path to deflect the laser beam towards the sample position. This mirror is aligned by turning it so that the laser path follows the x axis set out on the optical table. These last two mirrors form a periscope that guide the laser beam onto the sample from above. When the angle of incidence is adjusted (see below), the last mirror has to rotate about the y-direction and move along the z-direction. The laser beam is made to pass through the focal point of the microscope objective.

The lenses of the telescope can now be placed in the beam path between the established apertures. The lenses are aligned centrally on the axis of the laser beam and perpendicular to it using their back-reflections.

The gradient-index lens is mounted perpendicular to the beam axis (using its back-reflections) at roughly its focal distance to the focal point of the objective lens. It is held in a micropositioner to adjust its focus within about 1 cm.

Using a strongly scattering sample (such as a silicon wafer or a mirror), the mirrors in the collection part of the systems can be set to guide the collimated scattering into the spectrometer. The lens that focusses the collimated scattering through the slit (L_4) into the spectrometer is now aligned. Raman spectra are continuously acquired to optimize the position of this lens and the width of the slit.

Angle of incidence

The angle of incidence of the laser is measured with respect to the z axis, the laboratory vertical. The laser beam is guided through the focal point of the microscope objective lens, which defines the origin of the laboratory frame of reference. This location will receive the sample from which Raman scattering is to be measured.

The Durham and Stockholm systems follow different procedures to set the angle of incidence. In Durham, the angle is determined by measuring the vertical and horizontal position of the laser beam just before and after the laboratory frame origin. A vertical ruler and graph paper are used for this purpose. The angle of incidence is computed from these coordinates. Conversely, for a desired angle of incidence, the coordinates are calculated geometrically and the beam is made to pass through these points by adjusting the height and tilt of mirror m_5. The gradient index lens is removed from the beam path until the correct angle is achieved.

In Stockholm, the angle of incidence is set with two concentric rotors, each bearing a

Vernier scale to measure the angular position. These are mounted on a vertical translation stage. The inner rotor carries the top mirror of the periscope ($\mathsf{m_5}$) while the focussing lens $\mathsf{L_3}$ is attached to the outer rotor. The position of the rotors is set to 0° and the mirror is positioned to ensure its back-reflection overlaps the incoming laser beam. The desired angle of incidence can then be set by turning the inner rotor to the $\theta_i/2$ position on the Vernier scale. The vertical position of the rotors is then adjusted to assure that the beam path crosses the laboratory origin. Finally, the focussing lens is positioned in the laser path at its focal distance from the sample.

In both Raman systems, a dish of water can provide a perfectly horizontal surface. Positioned at the height of the sample, it reflects the laser beam as would be the case for a perfectly aligned sample interface. Using the water surface, the path of the reflected laser beam can also be used to assure the angle of incidence as $\theta_i = \theta_r$. The position of the reflected beam is then marked on the vertical ruler (in Durham) or with a pin-hole aperture (in Stockholm) to aid in positioning the sample cell along the horizontal plane.

Spectrometer calibration

Once the setup is properly aligned, a calibration is performed on the 520 cm^{-1} Raman shift of a clean silicon wafer. An off-set correction is applied to the whole spectral range using the spectrometer software. Figure 3.8 presents an example of such a calibration spectrum. The calibration ensures the correct angular position of the diffraction grating in the spectrometer and couples it to the CCD pixel locations. A single-point calibration is sufficient to achieve this.

Polarisation direction

Setting the polarisation of the experiment involves two linear polarisers and two half-wave plates (LP_1, HW_1, HW_2 and LP_2 in figure 3.2). These are set centrally in the beam paths of the laser and collimated scattered light. The following procedure is used to reassure or correct the linear polarisation directions given a correctly aligned system. It sets to find the angular orientation of each component to comply with the p, s, x and y conventions. It employs polarised reflection at the Brewster angle to calibrate the incident polarisation (p and s) and polarised Raman scattering for the collection polarisation (x and y). The procedure has been executed with the Stockholm system. The Durham system does not easily allow for setting the collection polarisation as both half-wave plate HW_2 and linear polariser LP_2 are fixed within the spectrometer and cannot be rotated without disassembling the components.

The linear polariser at the laser source (LP_1) is set to match the horizontal polarisation of the laser light. This can be confirmed by measuring the transmitted power as a function of the angular orientation of the polariser.

To calibrate half-wave plate HW_1, a water sample is mounted and its surface aligned with the laboratory frame origin. The angle is incidence is set to the Brewster angle for

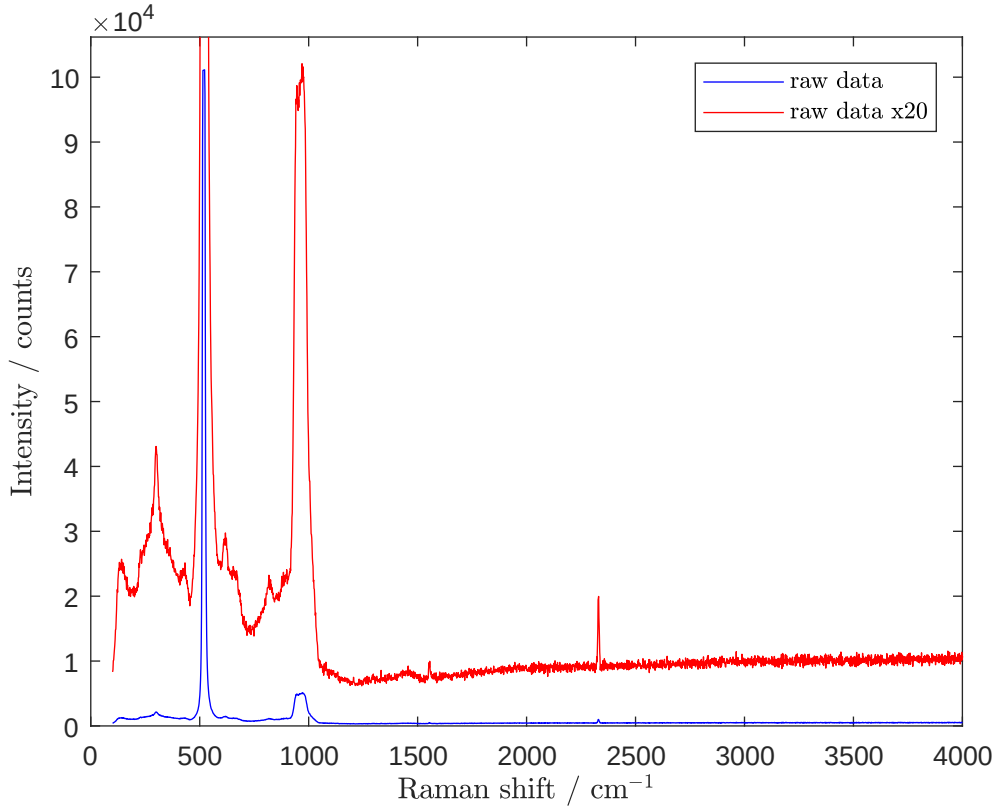

Figure 3.8: Raman spectrum of mono-crystalline silicon from the top surface of a wafer, accumulation of 5 scans with the Durham system, 100 mW laser output, *s*-polarised [data 20131112/028]. The peak at 520 cm^{-1} is used to calibrate Raman spectra. At about 2330 cm^{-1}, the Q-branch of nitrogen in observed.

the air-water interface, $\theta_B = 53.17°$. The angular position of HW_1 is then adjusted until a minimum is observed in the reflected intensity.[‡] This corresponds to *p*-polarised light. *s*-polarised light is obtain by increasing the angular setting of the half-wave plate by 45.0°.

The Brewster angle is also known as the polarisation angle. Reflected light from an unpolarised source incident under this angle is *s*-polarised. In other words, the reflection coefficient for *p*-polarised light r_p is zero at $\theta_i = \theta_B$. The reflection coefficient is the ratio of the reflected to the incident amplitude of the electric field. It depends on the linear polarisation direction of the light, its angle of incidence θ_i and the refractive indices of the meeting materials. The relations are derived in chapter 5 and presented as part of the Fresnel equations 5.28. From solving $r_p(\theta_B) = 0$ and using Snell's Law (equation 5.10), it is found that

$$\theta_B = \arctan\left(\frac{n_t}{n_i}\right) \tag{3.7}$$

where n_i is the refractive index of the incident medium and n_t that of the transmitted medium (in the present case, air and water, respectively). Figure 3.9 presents plots of

[‡]Multiple reflections may be observed if a transparent container is used for the water. Only the reflection at the top should then be considered.

the reflection coefficients and its square (which is proportional to the observed intensity), using refractive indices of table 3.2. Note that a polarisation angle is only observed for light traversing from an optically less dense medium, *i.e.* if $n_i < n_t$.

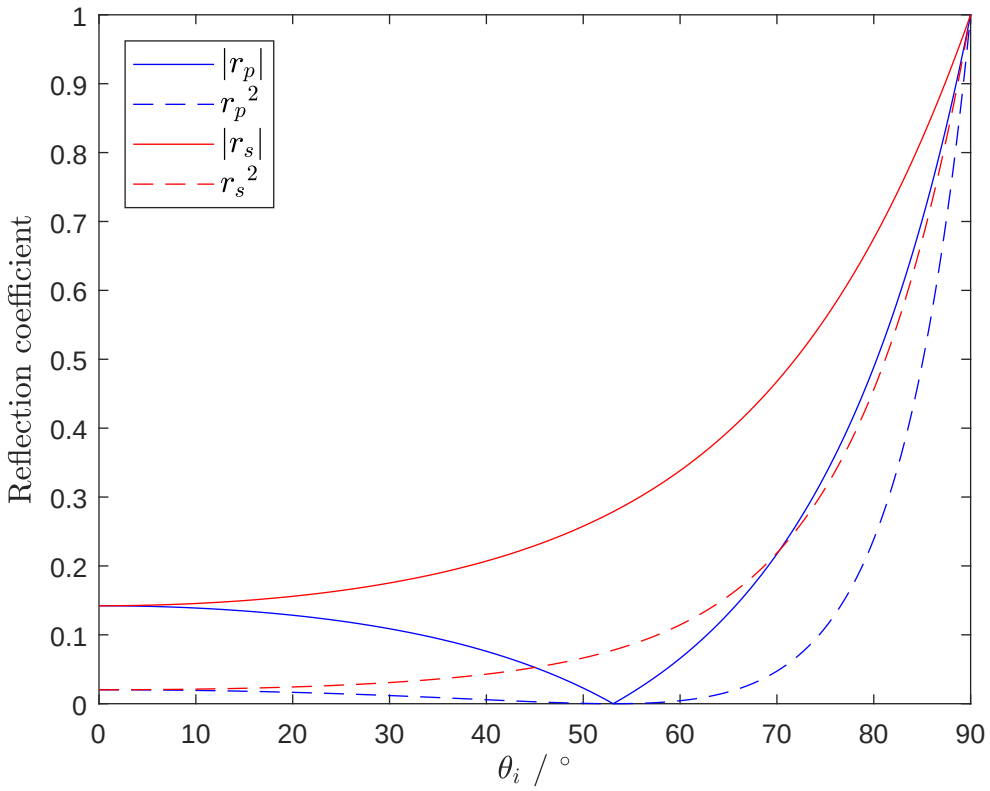

Figure 3.9: Reflection coefficient r for p and s-polarised visible light incident under angle θ_i on the air-water interface. The angle of incidence at which r_p has its minimum value is known as the Brewster angle θ_B.

The incident polarisation needs to be determined before the collection polarisation can be set. It is set to s and a toluene sample in a small glass vial is mounted with HW_2 removed from the setup. The relation between the angular position of LP_2 and the resulting linear polarisation direction is established through the intensity minima and maxima of the Raman bands observed in the spectrum. Polarised bands exhibit a maximum intensity in traditional polarised Raman spectroscopy, which is similar (but not equivalent) to the px and sy polarisation combinations in our system.

Toluene is used for its strong polarised band at about 1000 cm^{-1}, which arises from the ring breathing mode. This modes belongs to the A' symmetry species, the fully symmetric species of the C_s point group to which toluene belongs (see appendix A for details).

Setting the incident polarisation to s, LP_2 is rotated until the maximum intensity of the 1000 cm^{-1} is observed. This establishes the sy polarisation combination and thus the angular position of LP_2, which is held fixed. It should now be aligned along the slit of the spectrometer (or orthogonal to it in the Durham system).

The half-wave plate for the collection polarisation, HW_2, is now properly aligned and its rotational settings calibrated with the same toluene band. The minimum intensity is sought, giving the angular position of HW_2 conforming to the sx polarisation combination. Turning this half-wave plate by 45° selects y-polarised scattering.

With the angular positions of the linear polarisers affirmed and the half-wave plates calibrated, the four polarisation combinations can be summarized for reference. The values for the Stockholm system are

	HW_1	HW_2
px	33.5°	58.5°
py	33.5°	13.5°
sx	78.5°	58.5°
sy	78.5°	13.5°

which can be set reproducibly with the automated rotation stages.

Sample positioning

The sample is positioned once the laser beam is properly aligned in the xz-plane an its focus coincides with the focus of the microscope objective. The sample holder is positioned on the optical axis of the microscope by three orthogonal micro-translation stages, one along each of the three laboratory frame axes x, y and z. The interface at the bottom of the hemisphere is brought into focus using the translation stages while monitoring the position with the microscope camera using white light illumination through the objective. After focussing on the top of the hemisphere, the bottom is brought into focus. The dead centre is then found by superimposing the out-of-focus back-reflection of the top surface onto the in-focus image of the bottom surface.

If using the hemisphere rotation clamp, additional alignment is needed. The rotational axis is aligned with the laboratory frame y-axis when the reflected laser beam follows the xz plane at all tilt angles of the hemisphere. The centre of the hemisphere bottom surface is in turn positioned onto the rotational axis of the clamp in an iterative fashion using the microscope image as a guide. As the hemisphere is rotated, the bottom surface will come in and out of focus until it is brought on the rotation axis by the dual axis micropositioner on the clamp.

The pitch and roll angles of the interface are adjusted manually on the sample holder, using the reflection of the laser beam as a guide. A dish of water was used as a perfectly horizontal reference, spanning the laboratory xy plane, in setting the angle of incidence. The reflected beam path, for a particular angle of incidence, can now be used to align the sample interface to the xy plane.

Once the angle of incidence is set and the sample is positioned accurately, fine adjustment of the laser focus to the dead centre of the hemisphere bottom surface is achieved in the follow way. Along the x direction, positioning is achieved by z-translation of the last mirror and gradient index lens, jointly mounted on a micropositioner. Small deviations

along the y direction, perpendicular to the plane of incidence, are resolved by adjusting the penultimate mirror, at the bottom of the periscope. The angle of the beam within the plane of incidence is not changed. The laser is focussed to the desired degree by translating the gradient-index lens along the beam path.

Some iteration in positioning the sample, adjusting its tilt and fine-tuning the position and focus of the laser beam is usually needed.

3.3.2 Cleaning

Cleaning of the sample cell components serves to prevent contamination of the studied interface by materials that affect the surface deposition of monolayers or interfere with the desired Raman spectra. Established, and very similar, protocols were followed in both laboratories. These involve cleaning with purified water, ethanol (purity $\leq$ 99%) and chromic acid, abbreviated as BIC. The latter is a mixture of $Na_2Cr_2O_7$ and concentrated sulfuric acid, requiring appropriate safety precautions. Its was only used in PTFE beakers.

In Durham, cleaning of hemispheres involved 10 minute sonication in water, followed by 15 minute sonication in ethanol, three rinses with water and immersion in BIC for 1.5 hour. It was then rinsed thrice with water, sonicated in water for 15 minutes and immersed in BIC for another hour before rinsing with water four times (or until the water runs clear) and immersing the hemisphere in water, covered, until use. This procedure follows the one outlined by Kaustav Guha ([54] page 87-88) to facilitate comparison of data.

Cleaning the hemisphere suffices for solid-air interfaces. In the solid-liquid experiments, other equipment that could (indirectly) contaminate the surface was cleaned similarity to the process outlined below.

In Stockholm, the cleaning and assembly protocol of Tyrode's research group was followed. After completing the following cleaning steps, the flow cell was assembled in a laminar-flow cabinet to prevent dust getting in. Where sonication is mentioned, this was for 15 minutes in an ultrasound water bath at 35°C.

Fused silica hemispheres were sonicated separately in ethanol, rinsed with water, put in a BIC solution for 45 minutes, rinsed fifteen times with water, sonicated in water, rinsed five times with water and kept submerged in water until used.

The glass flow cell, PTFE tubing and connectors were cleaned by sonication in a solution of 5% v/v Deconex laboratory glass cleaner in water, rinsed with water fifteen times, sonicated in water, rinsed five times with water and kept submerged in water until used.

O-rings were sonicated in ethanol, rinsed fifteen times with water, sonicated in water, rinsed five times with water and kept submerged in water until used.

Tools reserved for assembly of the cell were wiped down with ethanol using lint-free laboratory wipes, rinsed with water and blown dry with filtered air.

The glass syringe, only used for water and sulfate solutions, was rinsed with ethanol

followed by rinsing with water fifteen times.

3.3.3 Monolayer production

Monolayers of zinc arachidate were formed on fused silica hemispheres through Langmuir-Blodgett (LB) deposition. A monolayer of zinc arachidate is formed by adding arachidic acid to the surface of an aqueous solution of zinc sulfate. Pulling the previously submerged hemisphere through this surface, at a constant surface pressure, ensures transfer of the floating monolayer onto the solid substrate. The procedure replicates the process described in Guha's thesis[54], using the same batch of arachidic acid though the LB trough and hemisphere holder for the deposition were different.

The Langmuir-Blodgett trough, model KN2002 of KSV NIMA (Biolin Scientific, Gothenburg, Sweden), was placed a box to prevent flow of air over the liquid surface. The balance records the surface pressure Π by means of a platinum Wilhelmy plate. Π is the change in surface tension from a clean subphase to one with surfactant. As the total surface area is decreased by two motorised barriers skimming the surface, the surface density of surfactant species increase, reducing the surface tension and increasing the surface pressure.

The trough, its barriers and the Wilhelmy plate were cleaned with ethanol and water. The balance was calibrated before use. Zinc sulfate in water at 1 10^{-4} mol L^{-1} (indicator strips gave a pH of 7) was pored in the trough and the dipper with hemisphere was submerged. The subphase surface was cleaned by aspiration of surface impurities, concentrated in the centre of the trough by closing the barriers. This process was repeated until the change in Π was less than 0.25 mN m^{-1}. After re-opening the barriers again, the balance was set to zero. A solution of 1 mg mL^{-1} arachidic acid in chloroform was then carefully spread on the surface of the subphase using a glass microsyringe (30 μL ensured sufficient coverage). The chloroform was allowed to evaporate off in 15 minutes. The surface is then compressed to $\Pi = 35$ mN m^{-1} at a constant barrier speed of 2.0 mm $minute^{-1}$ and left to equilibrate for 5 minute before raising the dipper at 2.0 mm $minute^{-1}$ from the subphase. Once emerged from the subphase, the coated hemisphere is left to dry in air.

The surface pressure is held at 35 mN m^{-1} via feedback to the barriers. Their maximum inward and outward speed were set to no more than 2.5 and 0.5 mm $minute^{-1}$, respectively, to reduce fluctuations in the surface pressure.

Compression isotherm

A compression isotherm (figure 3.10) was recorded at 20°C and a constant-speed compression of 2.0 mm $minute^{-1}$, without a hemisphere being submerged. It shows the surface pressure versus the mean molecular area, which is computed from the surface area of the subphase in the trough and the number of arachidic acid molecules brought onto it. This metric assumes that all molecules collect at the surface, whereas that amount varies between experiments. It should therefore not be taken as an absolute value and the isotherm could be shifted along the horizontal axis. However, the features of the

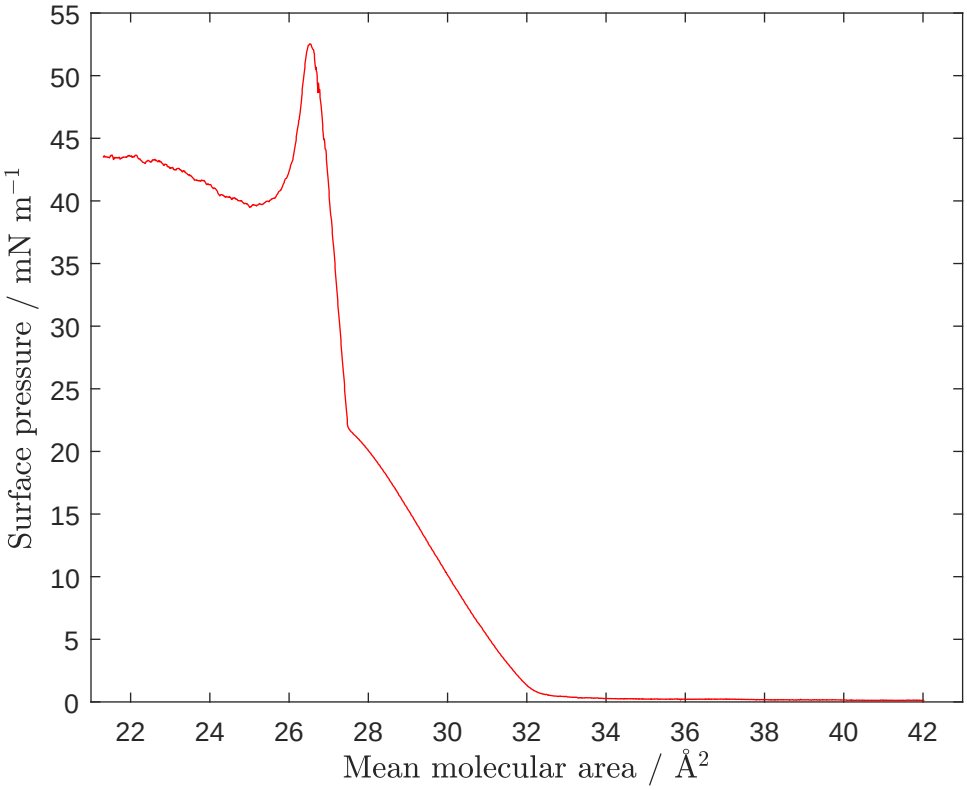

Figure 3.10: Surface compression isotherm of arachidic acid on water subphase with 10^{-4} mol L^{-1} zinc sulfate at 20°C. The mean molecular area should be taken as relative, rather than absolute. [data 20170303iso]

isotherm can be superimposed with repeat experiments. The surface pressure, rather than the mean molecular area, characterises the surface layer. While decreasing the available surface area, the surface layer displays the characteristic behaviour of three phases: a two-dimensional gas phase (Π close to zero), a liquid-expanded and liquid-condensed phase (up to $\Pi \approx 22$ mN m^{-1}) and a solid phase until the maximum surface pressure of 52.5 mN m^{-1} is achieved. Valdes-Covarrubias *et al.* [93] reported a collapse pressure of 57 mN m^{-1} at a mean molecular area of 24 Å^2 for arachidic acid on water at 24°C. At lower temperature, the collapse pressure increases while the mean molecular area decreases. Further compression of the surface area leads to collapse of the monolayer into multilayers and crystalline patches [93]. The mean molecular area is no longer an appropriate measure in this regime.

The second-order phase transition at about 22 mN m^{-1} involves the reordering of the alkane chains from tilted to an upright orientation as proven by X-ray diffraction and reflection studies [94, 95]. The all-*trans* alkane chains form a centred orthorhombic (pseudohexagonal) lattice with a uniform tilt towards their nearest neighbour with a positional correlation length of about 150 Å [94]. The tilt angle is reduced on compression from 30° at a mean molecular area of 23.0 Å^2 to 0° (fully upright) at 19.8 Å^2 but the density in the

hydrocarbon region remains constant [95].

The monolayer is deposited in the liquid-condensed phase at a constant surface pressure of 35 mN m^{-1}. The mean molecular area varied between measurements at that point but 22 $Å^2$ was observed in three out of five experiments. Guha [54] obtained a value of 19 $Å^2$ for the same material. Note that the structure of the monolayer on certain solid substrates is known to deviate from that on a water subphase [96].

Dipper

The hemisphere holder used for the deposition is of own design (figure 3.11), produced by three-dimensional extrusion from poly(methyl methacrylate) (PMMA) resin (Form 2 by Formlabs, Sommerville, MA, USA). Compared to the PTFE holders used by Guha, PMMA features a rougher surface and lower resistance to solvents, raising the risk of contamination. The extruded dippers were bathed in isopropanol for 1.5 minute to remove unpolymerised resin, dried at 50°C for an hour and left overnight to cure fully (hardening under ultraviolet light was attempted but was not successful, likely due to the low power of the lamp). An advantage of the current design over the previous dipper holder is that it exposes the hemisphere bottom surface freely along the direction of deposition. The previous model clamps the hemisphere on a circular cut-out all around. Moreover, the new dipper facilitates manipulation of (coated) hemispheres[§] and can be reproduced easily.

Transfer

The question arises whether the transferred monolayer has the same density on the solid substrate as on the liquid subphase in the trough. This is characterised by the transfer ration, which is unity if the exposed surface area of hemisphere and dipper are equal to the compression of the trough surface area during the deposition. This was tested and the transfer ratio was found to be 0.96[¶] overall, though the different materials of hemisphere and dipper may not have been coated equally.

[§]For example, a hemisphere lying on its curved face can be picked up by sliding the dipper vertically over it and slotting it in the two notches of its legs. It can then be slotted out on its flat face onto the sample cell for mounting.

[¶]The submerged surface area of the dipper was 6.50 cm^2, that of the hemisphere 2.36 cm^2 while the change in surface area of the monolayer on the subphase was 8.47 cm^2. [data 20170123]

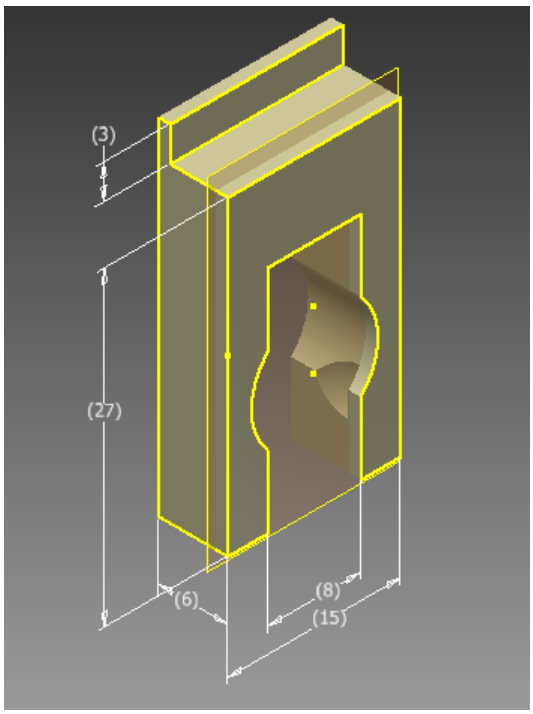

Figure 3.11: Drawing of the hemisphere holder for LB-deposition. The opening at the bottom end allows the subphase to flow freely from the hemisphere surface.

Chapter 4

Computation of Raman tensors

This chapter discusses procedures to establish the form of a Raman tensor for a given vibrational transition as well as the numerical values of its components. The Raman tensor forms the link between the molecular description and the macroscopically observed Raman scattering. Insight into the Raman tensor and how it arises from molecular vibrations is therefore fundamental to our approach.

Several strategies are available to deduce the form of the Raman tensor. With 'form' we mean the placement of zero and non-zero components in the second rank tensor and which of the non-zero components share the same numerical value and have the same or opposite sign. This information can be deduced through group theory and symmetry arguments. In another approach, the Raman tensor is constructed from the appropriate combination of individual bond polarisability derivatives. This last approach is demonstrated for fundamental phenyl, methylene and methyl stretch modes. An overview of all Raman active symmetry species for a range of point groups is given with literature references.

Numerical values of Raman tensor components can be deduced from experimental peak intensities in favourable cases. As discussed in the previous chapter, the experimental geometry has to be chosen appropriately with the expected form of the (isotropically averaged) Raman tensor in mind. Individual components can only be deduced if the experimental geometry allows for their decoupling. A computational approach is therefore presented here. Such methods are generally applied to one isolated molecule in vacuum in its equilibrium geometry. A vibrational analysis is performed and Raman tensors are deduced for all modes in the theoretical framework used, usually involving a set of approximations. The results of computations with GAUSSIAN on the sulfate anion, carbon tetrachloride and decanoic acid are presented in this chapter. These molecules are used in the experiments to validate our model description of interfacial Raman spectroscopy (chapter 6) and in its application on a boundary lubricant under static pressure (chapter 7). Additionally, results for toluene are included in appendix G.1.

4.1 Form of the Raman tensor

The form of the Raman tensor for a particular fundamental can be derived by combining bond polarisabilities following the vibrational normal coordinate of that mode. Having gained insight through some examples, a generalisation is presented for a range of point groups. The use of an unambiguous definition of axes is emphasised.

4.1.1 The bond-polarisability model

An explicit formulation of the Raman tensor follows from the combination of polarisabilities of individual bonds involved in the vibrational mode of the molecule. This is the bond-polarisability model. It rests on the assumption that the values of the bond polarisability tensor depend on the nature of the bond only, not on the molecular environment it is in. The individual bond polarisabilities are transferable and may be combined according to the vibrational motion under consideration to form a polarisability tensor for the vibrational mode as a whole.

In this section, the bond-polarisability model is applied to selected fundamental transitions of phenyl, methylene and methyl to link known vibrational motions to their Raman tensor in a chosen frame of reference. Although this approach can be used to obtain numerical values, it is only used to obtain the form of the Raman tensor here. More advanced computations are employed to deduce numerical values of Raman tensor elements in section 4.3. The aim here is to provide an insight into why particular tensor elements are zero or non-zero, from which bonds these arise and how these could therefore be affected by a loss of symmetry or a distortion in the normal mode.

The procedure employed here is as follows. An alternative, including derivation of numerical values, can be found in Appendix B of Le Ru and Etchegoin's work [41].

The polarisability tensor of a bond in the bond frame of reference b can be given as

$$\boldsymbol{\alpha}^{\mathsf{b}}_{\mathsf{bond}} = \begin{pmatrix} \alpha_1 & 0 & 0 \\ 0 & \alpha_2 & 0 \\ 0 & 0 & \alpha_3 \end{pmatrix} \tag{4.1}$$

describing a polarisability ellipsoid with its axes aligned with the axes of the frame of reference of the bond. Before the bond polarisabilities can be combined, they have to be brought in the same frame of reference such as the frame of the functional group, moiety or molecule. Following the definitions presented in section 2.2.3, a coordinate transformation is effected as

$$\boldsymbol{\alpha}^{\mathsf{g}}_{\mathsf{bond}} = \mathbf{T}_{\mathsf{b}\to\mathsf{g}} \boldsymbol{\alpha}^{\mathsf{b}}_{\mathsf{bond}} {\mathbf{T}_{\mathsf{b}\to\mathsf{g}}}^{-1} \tag{4.2}$$

where g indicates the group frame of reference.

The polarisability tensors of the bonds in the group frame are combined following the vibrational normal coordinate $Q_{\mathsf{v}}(t)$ that describes the combined motion of the bonds in

vibrational mode v as a function of time t through

$$Q_{\mathsf{v}}(t) = \sum_{\text{bonds}} q_{\mathsf{v},\text{bond}}(t) \tag{4.3}$$

where each q includes an amplitude and phase that describe the motion of one of the bonds or bond angles. Both Q and q are dimensionless quantities, independent of frame of reference. The amplitudes of q are such that the amplitude Q_{v} of $Q_{\mathsf{v}}(t)$ is normalised

$$Q_{\mathsf{v}}^2 = \sum_{\text{bonds}} q_{\mathsf{v},\text{bond}}^2 = 1 \, . \tag{4.4}$$

The polarisability tensor of the vibrational mode is then found through combining the bond polarisabilities while taking their relative phases and amplitudes into account

$$\boldsymbol{\alpha}_{\mathsf{v}}^{\mathsf{g}} = \sum_{\text{bonds}} q_{\mathsf{v},\text{bond}} \boldsymbol{\alpha}_{\text{bond}}^{\mathsf{g}} \tag{4.5}$$

which holds for any frame of reference. As the whole procedure is carried out in the equilibrium geometry of the molecule, the derivative of $\boldsymbol{\alpha}_{\mathsf{v}}^{\mathsf{g}}$ with respect to the normal coordinate

$$\boldsymbol{\alpha'}_{\mathsf{v}}^{\mathsf{g}} = \frac{\partial \boldsymbol{\alpha}_{\mathsf{v}}^{\mathsf{g}}}{\partial Q_{\mathsf{v}}} \tag{4.6}$$

results in the form of the Raman tensor for the desired vibrational mode. Another coordinate transformation may be needed to bring $\boldsymbol{\alpha'}^{\mathsf{g}}$ into the molecular frame of reference m, which is used in data interpretation and our modelling effort.

This approach is now demonstrated for selected vibrational modes of moieties used in this work. Starting from the polarisability of individual C−H bond, the breathing mode of a phenyl group (included as appended section G.1.1) as well as the stretch modes of methylene and methyl are analysed.

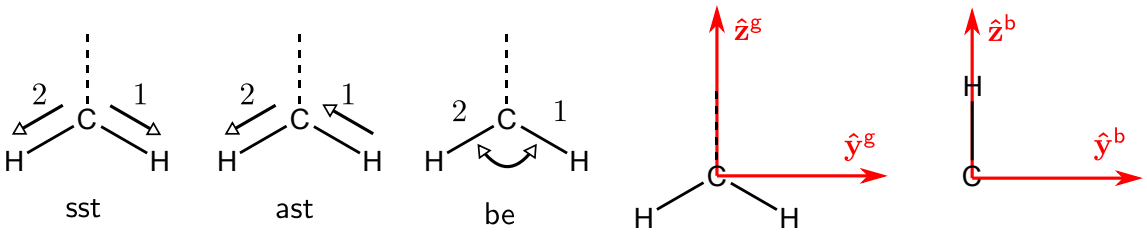

Figure 4.1: The three vibrational normal modes of an isolated methylene moiety (open arrows; sst symmetric stretch, ast antisymmetric stretch and be bend motion) and the choice of axes (red) in the functional group and bond frames of reference.

4.1.2 Methylene stretch modes

The axes of the methylene group are dictated through symmetry assignment, presented in figure 4.1. The Cartesian axes in the C−H bond frame of reference are chosen such that one elementary rotation can bring them into the group frame of reference. The transformation from the axes of the group g to the bond b follows from an elementary rotation about the x axis over angle β

$$\mathbf{T}_{\mathsf{g}\to\mathsf{b}} = \mathbf{R}_x(\beta) \tag{4.7}$$

so that the inverse transformation is given through

$$\mathbf{T}_{\mathsf{b}\to\mathsf{g}} = {\mathbf{T}_{\mathsf{g}\to\mathsf{b}}}^{-1} = \mathbf{R}_x(-\beta) = \begin{pmatrix} 1 & 0 & 0 \\ 0 & \cos\beta & -\sin\beta \\ 0 & \sin\beta & \cos\beta \end{pmatrix} \tag{4.8}$$

where β is the second Euler angle, the other two being zero. The polarisability of the bond in its own frame of reference can be given as

$$\boldsymbol{\alpha}^{\mathsf{b}}_{\mathrm{C-H}} = \begin{pmatrix} \alpha_{\perp,oop} & 0 & 0 \\ 0 & \alpha_{\perp,ip} & 0 \\ 0 & 0 & \alpha_{\parallel} \end{pmatrix} \tag{4.9}$$

which is transformed into the g frame by application of equation 4.2, here resulting in

$$\begin{aligned} \boldsymbol{\alpha}^{\mathsf{g}}_{\mathrm{C-H}} &= \mathbf{R}_x(-\beta)\boldsymbol{\alpha}^{\mathsf{b}}_{\mathrm{C-H}}\mathbf{R}_x(\beta) \\ &= \begin{pmatrix} 1 & 0 & 0 \\ 0 & \cos\beta & -\sin\beta \\ 0 & \sin\beta & \cos\beta \end{pmatrix} \begin{pmatrix} \alpha_{\perp,oop} & 0 & 0 \\ 0 & \alpha_{\perp,ip} & 0 \\ 0 & 0 & \alpha_{\parallel} \end{pmatrix} \begin{pmatrix} 1 & 0 & 0 \\ 0 & \cos\beta & \sin\beta \\ 0 & -\sin\beta & \cos\beta \end{pmatrix} \\ &= \begin{pmatrix} \alpha_{\perp,oop} & 0 & 0 \\ 0 & \alpha_{\perp,ip}\cos^2\beta + \alpha_{\parallel}\sin^2\beta & (\alpha_{\perp,ip} - \alpha_{\parallel})\sin\beta\cos\beta \\ 0 & (\alpha_{\perp,ip} - \alpha_{\parallel})\sin\beta\cos\beta & \alpha_{\perp,ip}\sin^2\beta + \alpha_{\parallel}\cos^2\beta \end{pmatrix} \end{aligned} \tag{4.10}$$

The angle β for each bond is

$$\begin{aligned} \beta_1 &= -180^\circ + \frac{1}{2}\tau \\ \beta_2 &= 180^\circ - \frac{1}{2}\tau = -\beta_1 \end{aligned} \tag{4.11}$$

where the numbers $1, 2$ refer to the C−H bond labels of figure 4.1 and τ is the angle between the two bonds. The equilibrium structure is assumed to be tetrahedral, so that τ is the tetrahedral angle

$$\tau = 2\arctan\sqrt{2} \tag{4.12}$$

which is about 109.5°. The sine and cosine terms then become

$$\begin{aligned} \sin(\beta_1) &= -\sin(\beta_2) = -\sqrt{\frac{2}{3}} \\ \cos(\beta_1) &= \cos(\beta_2) = \frac{-1}{\sqrt{3}} \end{aligned} \tag{4.13}$$

The vibrational normal coordinates of the symmetric and antisymmetric stretch modes are

$$\begin{aligned} Q_{\mathsf{sst}}(t) &= q_1(t) + q_2(t) \\ Q_{\mathsf{ast}}(t) &= q_1(t) - q_2(t) \end{aligned} \tag{4.14}$$

where the amplitudes of the individual bond coordinates are the same. This leads to the amplitude normalisation

$$q = \frac{Q}{\sqrt{2}} \,. \tag{4.15}$$

The normal coordinate for the bending motion Q_{be} belongs to the same symmetry species as Q_{sst}, namely A_1 (see appendix A). This implies that the result of the analysis for the latter can be applied to the former.

Combining the bond polarisabilities in the group frame of reference, the polarisability tensor of the symmetric stretch mode is given through

$$\begin{aligned} \boldsymbol{\alpha}^{\mathrm{g}}_{\mathsf{sst}} &= \frac{Q}{\sqrt{2}} \left(\boldsymbol{\alpha}^{\mathrm{g}}_1 + \boldsymbol{\alpha}^{\mathrm{g}}_2 \right) \\ &= \frac{2Q}{3\sqrt{2}} \begin{pmatrix} \alpha_{\perp,oop} & 0 & 0 \\ 0 & \alpha_{\perp,ip} + 2\alpha_{\parallel} & 0 \\ 0 & 0 & 2\alpha_{\perp,ip} + \alpha_{\parallel} \end{pmatrix} \end{aligned} \tag{4.16}$$

where the off-diagonal components are zero irrespective of the bond angle τ. For the antisymmetric stretch mode, which belongs to the B_2 symmetry species of the point group, we find in a similar way

$$\begin{aligned} \boldsymbol{\alpha}^{\mathrm{g}}_{\mathsf{ast}} &= \frac{Q}{\sqrt{2}} \left(\boldsymbol{\alpha}^{\mathrm{g}}_1 - \boldsymbol{\alpha}^{\mathrm{g}}_2 \right) \\ &= \frac{2Q}{3} (\alpha_{\perp,ip} - \alpha_{\parallel}) \begin{pmatrix} 0 & 0 & 0 \\ 0 & 0 & 1 \\ 0 & 1 & 0 \end{pmatrix} \end{aligned} \tag{4.17}$$

which is independent of the out-of-plane bond polarisability component $\alpha_{\perp,oop}$.

The Raman tensors for the fundamental transitions from the vibrational ground state to the first excited state in each of the three normal modes can now be given. For the

symmetric stretch, we have

$$\boldsymbol{\alpha'}^{\mathsf{g}}_{\mathsf{sst}} = \frac{2}{3\sqrt{2}} \begin{pmatrix} \alpha'_{\perp,oop} & 0 & 0 \\ 0 & \alpha'_{\perp,ip} + 2\alpha'_{\parallel} & 0 \\ 0 & 0 & 2\alpha'_{\perp,ip} + \alpha'_{\parallel} \end{pmatrix} \tag{4.18}$$

with the same form for the bend mode Raman tensor $\boldsymbol{\alpha'}^{\mathsf{g}}_{\mathsf{be}}$, while for the antisymmetric stretch we have

$$\boldsymbol{\alpha'}^{\mathsf{g}}_{\mathsf{ast}} = \frac{2}{3}(\alpha'_{\perp,ip} - \alpha'_{\parallel}) \begin{pmatrix} 0 & 0 & 0 \\ 0 & 0 & 1 \\ 0 & 1 & 0 \end{pmatrix} \tag{4.19}$$

each tensor being the derivative of the polarisability tensor with respect to the vibrational normal coordinate evaluated at the equilibrium geometry. The forms of the above Raman tensors agree with those derived from symmetry considerations of the moiety discussed below.

A further coordinate transformation is needed to express the Raman tensors in the molecular frame of reference m. The choice of axes is presented in figure 4.2. Note that this choice does not follow the symmetry prioritisation. The two-fold rotational symmetry is ignored as it does not apply in stretched alkane chains with an odd number of carbon atoms nor in molecules that include a head-group such as fatty acids. The present choice is used so that the axes are the same for all molecules that contain a stretched alkane chain.

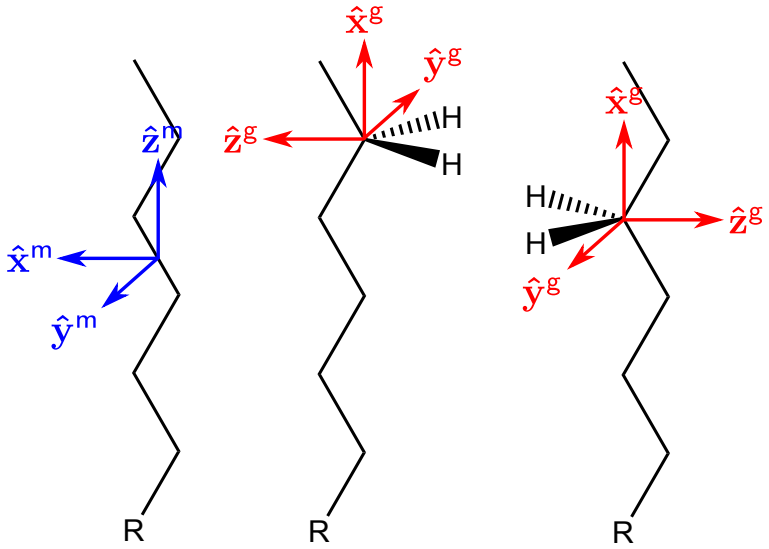

Figure 4.2: The molecule frame of reference (blue) for a stretched alkane chain and its relation to the axes of the CH_2 group (red) at two different positions. The three sets of axes are parallel. The C−C bonds lay in the $\hat{\mathbf{x}}^{\mathsf{m}}\hat{\mathbf{z}}^{\mathsf{m}}$ and the C−H bonds in the $\hat{\mathbf{x}}^{\mathsf{m}}\hat{\mathbf{y}}^{\mathsf{m}}$ plane. The positive unit vector $\hat{\mathbf{z}}^{\mathsf{m}}$ is directed towards the methyl end of the chain, with R representing an dissimilar head-group.

The coordinate transformation from the group frame of reference g to the molecule frame m only involves an exchange of axis labels. The transformation matrix is found to be

$$\mathbf{T}_{\mathsf{g}\to\mathsf{m}} = \begin{cases} \begin{pmatrix} 0 & 0 & 1 \\ 0 & -1 & 0 \\ 1 & 0 & 0 \end{pmatrix} & \text{if } \hat{\mathbf{z}}^{\mathsf{g}} = \hat{\mathbf{x}}^{\mathsf{m}} \\ \begin{pmatrix} 0 & 0 & 1 \\ 0 & 1 & 0 \\ -1 & 0 & 0 \end{pmatrix} & \text{if } \hat{\mathbf{z}}^{\mathsf{g}} = -\hat{\mathbf{x}}^{\mathsf{m}} \end{cases} \tag{4.20}$$

which depends on the location of the CH_2 group. This transformation matrix is applied as in equation 4.2. This results in

$$\boldsymbol{\alpha'}^{\mathsf{m}}_{\mathsf{sst,be}} = \frac{2}{3\sqrt{2}} \begin{pmatrix} 2\alpha'_{\perp,ip} + \alpha'_{\parallel} & 0 & 0 \\ 0 & \alpha'_{\perp,ip} + 2\alpha'_{\parallel} & 0 \\ 0 & 0 & \alpha'_{\perp,oop} \end{pmatrix} \tag{4.21}$$

for both forms of $\mathbf{T}_{\mathsf{g}\to\mathsf{m}}$, so irrespective of the side of the chain on which the CH_2 group is located. This is not the case for the antisymmetric stretch Raman tensor

$$\boldsymbol{\alpha'}^{\mathsf{m}}_{\mathsf{ast}} = \pm\frac{2}{3}(\alpha'_{\perp,ip} - \alpha'_{\parallel}) \begin{pmatrix} 0 & 1 & 0 \\ 1 & 0 & 0 \\ 0 & 0 & 0 \end{pmatrix} \tag{4.22}$$

which is positive if $\hat{\mathbf{z}}^{\mathsf{g}} = \hat{\mathbf{x}}^{\mathsf{m}}$ and negative if $\hat{\mathbf{z}}^{\mathsf{g}} = -\hat{\mathbf{x}}^{\mathsf{m}}$.

The Raman tensor for all CH_2 groups in an alkyl chain may be predicted by combining the group Raman tensors taking their relative phases into account. This in effect further extends the bond-polarisability model.

The combined Raman activity of the symmetric stretch as well as bend modes adds up from group to group if these vibrate in phase. However, adding the antisymmetric stretch Raman tensors in that way leads to a minimum in Raman activity. A phase difference of half a cycle between neighbouring groups results in a strong Raman effect for this mode. This effectively changes the sign of the Raman tensor alternately along the chain so that the overall Raman tensor adds up to a non-zero tensor. The Raman activity of the combined methylene groups is then described by a Raman tensor of the same form as that of an individual methylene group.

In a stretched alkane chain, like vibrations of individual methylene groups are known to couple and the resulting modes span one-dimensional irreducible representations that correspond one-to-one to those of the point group [97] (C_{2v} or C_{2h} for an odd or even number of carbon atoms). Each vibrational mode of the chain features a distinct phase relation between the atomic motion of neighbouring CH_2 groups. For an infinite methylene

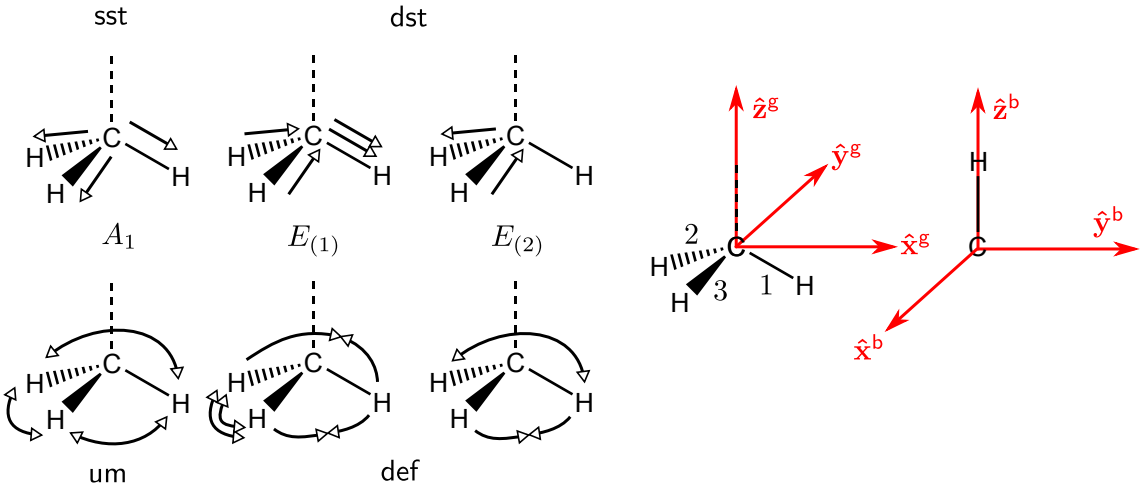

Figure 4.3: The vibrational normal modes of an isolated methyl group (atomic motion indicated with open arrows) and the choice of axes (red) in the group g and bond b frames of reference. The point group symmetry species are indicated and the modes are labelled sst for symmetric stretch, dst for degenerate stretch, um for umbrella and def for degenerate deformation.

chain, only the in-phase mode is Raman active, while only the fully out-of-phased mode (a phase shift of π radians between each methylene group) is infrared active with all other modes neither Raman nor IR active. Since the IR and Raman-active modes are at opposite extremes of the Brillouin Zone, the frequencies can be markedly different [98]. In finite chains, multiple Raman-active modes arise with non-zero phase relations between adjacent methylene groups, occurring at different frequencies and with varying spectral intensities. However, all these are each expected to have a Raman tensor of the same form as that of the elemental vibration of the constituent methylene groups. We will encounter examples of this in section D.5.

4.1.3 Methyl stretch modes

The polarisability of an individual C−H methyl bond in its own Cartesian frame of reference (see figure 4.3) is given as

$$\boldsymbol{\alpha}^{\mathsf{b}}_{\mathrm{C-H}} = \begin{pmatrix} \alpha_{\perp,v} & 0 & 0 \\ 0 & \alpha_{\perp,h} & 0 \\ 0 & 0 & \alpha_{\parallel} \end{pmatrix} \tag{4.23}$$

where the subscript $\perp, v$ stands for the component perpendicular to the bond axis which is in the vertical plane spanned by the bond (along $\hat{\mathbf{z}}^{\mathsf{b}}$) and the $\hat{\mathbf{z}}^{\mathsf{g}}$ axis of the methyl group. The horizontal component $\perp, h$ is parallel to the $\hat{\mathbf{x}}^{\mathsf{g}}\hat{\mathbf{y}}^{\mathsf{g}}$ plane. The axes of the bond frame are chosen to simply the analysis.

The transformation from bond frame b to group frame g is given by two subsequent

elemental rotations

$$\begin{aligned}\mathbf{T}_{\mathsf{b}\to\mathsf{g}} &= \mathbf{R}_z(-\phi)\mathbf{R}_y(-\theta)\\ &= \begin{pmatrix}\cos\phi & \sin\phi & 0\\ -\sin\phi & \cos\phi & 0\\ 0 & 0 & 1\end{pmatrix}\begin{pmatrix}\cos\theta & 0 & -\sin\theta\\ 0 & 1 & 0\\ \sin\theta & 0 & \cos\theta\end{pmatrix}\\ &= \begin{pmatrix}\cos\phi\cos\theta & \sin\phi & -\cos\phi\sin\theta\\ -\sin\phi\cos\theta & \cos\phi & \sin\phi\sin\theta\\ \sin\theta & 0 & \cos\theta\end{pmatrix}\end{aligned} \tag{4.24}$$

where rotation matrices are given through equation 2.12. The negative angles effect an anticlockwise active rotation of the tensor to which it is applied. These angles do not conform to the Euler angles. Using the latter requires three rotations rather than the two presented here.

The bond polarisability in the group frame of reference g can now be given through

$$\begin{aligned}\boldsymbol{\alpha}^{\mathsf{g}}_{\mathrm{C-H}} &= \mathbf{T}_{\mathsf{b}\to\mathsf{g}}\boldsymbol{\alpha}^{\mathsf{b}}_{\mathrm{C-H}}{\mathbf{T}_{\mathsf{b}\to\mathsf{g}}}^{-1}\\ &= \begin{pmatrix}\cos\phi\cos\theta & \sin\phi & -\cos\phi\sin\theta\\ -\sin\phi\cos\theta & \cos\phi & \sin\phi\sin\theta\\ \sin\theta & 0 & \cos\theta\end{pmatrix}\begin{pmatrix}\alpha_{\perp,v} & 0 & 0\\ 0 & \alpha_{\perp,h} & 0\\ 0 & 0 & \alpha_{\parallel}\end{pmatrix}\begin{pmatrix}\cos\phi\cos\theta & -\sin\phi\cos\theta & \sin\theta\\ \sin\phi & \cos\phi & 0\\ -\cos\phi\sin\theta & \sin\phi\sin\theta & \cos\theta\end{pmatrix}\\ &= \begin{pmatrix}\alpha_{\perp,v}c^2\phi c^2\theta + \alpha_{\perp,h}s^2\phi + \alpha_{\parallel}c^2\phi s^2\theta & s\phi c\phi\left(\alpha_{\perp,h} - \alpha_{\perp,v}c^2\theta - \alpha_{\parallel}s^2\theta\right) & c\phi s\theta c\theta\left(\alpha_{\perp,v} - \alpha_{\parallel}\right)\\ s\phi c\phi\left(\alpha_{\perp,h} - \alpha_{\perp,v}c^2\theta - \alpha_{\parallel}s^2\theta\right) & \alpha_{\perp,v}s^2\phi c^2\theta + \alpha_{\perp,h}c^2\phi + \alpha_{\parallel}s^2\phi s^2\theta & -s\phi s\theta c\theta\left(\alpha_{\perp,v} - \alpha_{\parallel}\right)\\ c\phi s\theta c\theta\left(\alpha_{\perp,v} - \alpha_{\parallel}\right) & -s\phi s\theta c\theta\left(\alpha_{\perp,v} - \alpha_{\parallel}\right) & \alpha_{\perp,v}s^2\theta + \alpha_{\parallel}c^2\theta\end{pmatrix}\end{aligned} \tag{4.25}$$

where s and c stand for sin and cos, respectively. The tensor is symmetric, as expected.

The equilibrium structure of the methylene group is assumed tetrahedral. The angle θ is identical for all C−H bonds in the methyl group

$$\theta_1 = \theta_2 = \theta_3 = \tau \tag{4.26}$$

with the bond labels $1, 2, 3$ following figure 4.3 and τ the tetrahedral angle (defined in equation 4.12). The sine and cosine terms of θ then become

$$\begin{aligned}\sin\tau &= \frac{2\sqrt{2}}{3}\\ \cos\tau &= \frac{-1}{3}\end{aligned} \tag{4.27}$$

The angle ϕ is given in the equilibrium configuration as $\phi_1 = 0°$, $\phi_2 = 120°$ and $\phi_3 = 240°$. The polarisability tensors of the three bonds in the group frame of reference can now be

given as

$$\boldsymbol{\alpha}_1^{\mathsf{g}} = \begin{pmatrix} \frac{1}{9}\alpha_{\perp,v} + \frac{8}{9}\alpha_{\parallel} & 0 & \frac{-2\sqrt{2}}{9}(\alpha_{\perp,v} - \alpha_{\parallel}) \\ 0 & \alpha_{\perp,h} & 0 \\ \frac{-2\sqrt{2}}{9}(\alpha_{\perp,v} - \alpha_{\parallel}) & 0 & \frac{8}{9}\alpha_{\perp,v} + \frac{1}{9}\alpha_{\parallel} \end{pmatrix}$$

$$\boldsymbol{\alpha}_2^{\mathsf{g}} = \begin{pmatrix} \frac{1}{36}\alpha_{\perp,v} + \frac{3}{4}\alpha_{\perp,h} + \frac{2}{9}\alpha_{\parallel} & \frac{1}{12\sqrt{3}}\alpha_{\perp,v} - \frac{\sqrt{3}}{4}\alpha_{\perp,h} + \frac{2}{3\sqrt{3}}\alpha_{\parallel} & \frac{\sqrt{2}}{9}(\alpha_{\perp,v} - \alpha_{\parallel}) \\ \frac{1}{12\sqrt{3}}\alpha_{\perp,v} - \frac{\sqrt{3}}{4}\alpha_{\perp,h} + \frac{2}{3\sqrt{3}}\alpha_{\parallel} & \frac{1}{12}\alpha_{\perp,v} + \frac{1}{4}\alpha_{\perp,h} + \frac{2}{3}\alpha_{\parallel} & \frac{\sqrt{2}}{3\sqrt{3}}(\alpha_{\perp,v} - \alpha_{\parallel}) \\ \frac{\sqrt{2}}{9}(\alpha_{\perp,v} - \alpha_{\parallel}) & \frac{\sqrt{2}}{3\sqrt{3}}(\alpha_{\perp,v} - \alpha_{\parallel}) & \frac{8}{9}\alpha_{\perp,v} + \frac{1}{9}\alpha_{\parallel} \end{pmatrix}$$

$$\boldsymbol{\alpha}_3^{\mathsf{g}} = \begin{pmatrix} \frac{1}{36}\alpha_{\perp,v} + \frac{3}{4}\alpha_{\perp,h} + \frac{2}{9}\alpha_{\parallel} & \frac{-1}{12\sqrt{3}}\alpha_{\perp,v} + \frac{\sqrt{3}}{4}\alpha_{\perp,h} - \frac{2}{3\sqrt{3}}\alpha_{\parallel} & \frac{\sqrt{2}}{9}(\alpha_{\perp,v} - \alpha_{\parallel}) \\ \frac{-1}{12\sqrt{3}}\alpha_{\perp,v} + \frac{\sqrt{3}}{4}\alpha_{\perp,h} - \frac{2}{3\sqrt{3}}\alpha_{\parallel} & \frac{1}{12}\alpha_{\perp,v} + \frac{1}{4}\alpha_{\perp,h} + \frac{2}{3}\alpha_{\parallel} & \frac{-\sqrt{2}}{3\sqrt{3}}(\alpha_{\perp,v} - \alpha_{\parallel}) \\ \frac{\sqrt{2}}{9}(\alpha_{\perp,v} - \alpha_{\parallel}) & \frac{-\sqrt{2}}{3\sqrt{3}}(\alpha_{\perp,v} - \alpha_{\parallel}) & \frac{8}{9}\alpha_{\perp,v} + \frac{1}{9}\alpha_{\parallel} \end{pmatrix} \tag{4.28}$$

The polarisability tensors of the vibrational modes are found by combining the bond polarisabilities for the six vibrational normal modes listed in appendix A. These belong to two symmetry species: A_1 and E, both occurring as a stretch and a deformation mode. Our choice follows [78] and is illustrated in figure 4.3. The internal coordinate Q for the totally symmetric species A_1 is

$$Q_{A_1} = \frac{1}{\sqrt{3}}(q_1 + q_2 + q_3) \tag{4.29}$$

while appropriate bases for the degenerate mode E are

$$Q_E = \begin{cases} \frac{1}{\sqrt{6}}(2q_1 - q_2 - q_3) \\ \frac{1}{\sqrt{2}}(q_2 - q_3) \end{cases} \tag{4.30}$$

where q stands for a stretch of one of the three C−H bonds or an angular coordinate related to that bond. Other degenerate bases can be chosen. This form is appropriate even when the methyl group is attached to an alkyl chain, which reduces its point group symmetry. We derive the form of the Raman tensor using the stretch modes, knowing that the result applies equally to the deformation modes of the same symmetry species.

The symmetric C−H stretch sst belongs to the A_1 symmetry species. Its normal coordinate is

$$Q_{\mathsf{sst}}(t) = q_1(t) + q_2(t) + q_3(t) \tag{4.31}$$

with amplitude normalised so that

$$q_1 = q_2 = q_3 = \frac{Q_{\mathsf{sst}}}{\sqrt{3}} \tag{4.32}$$

as all bonds oscillate in phase. The polarisability tensor for this mode is

$$\begin{aligned}\boldsymbol{\alpha}^{\mathsf{g}}_{\mathsf{sst}} &= \frac{Q_{\mathsf{sst}}}{\sqrt{3}}\left(\boldsymbol{\alpha}^{\mathsf{m}}_1 + \boldsymbol{\alpha}^{\mathsf{m}}_2 + \boldsymbol{\alpha}^{\mathsf{m}}_3\right) \\ &= \frac{Q_{\mathsf{sst}}}{\sqrt{3}}\begin{pmatrix} \frac{1}{6}\alpha_{\perp,v} + \frac{3}{2}\alpha_{\perp,h} + \frac{4}{3}\alpha_{\parallel} & 0 & 0 \\ 0 & \frac{1}{6}\alpha_{\perp,v} + \frac{3}{2}\alpha_{\perp,h} + \frac{4}{3}\alpha_{\parallel} & 0 \\ 0 & 0 & \frac{8}{3}\alpha_{\perp,v} + \frac{1}{3}\alpha_{\parallel} \end{pmatrix}\end{aligned} \tag{4.33}$$

which has two non-zero unique components and is a tensor of cylindrical symmetry. This form applies equally to the umbrella motion um, also belonging to the A_1 symmetry species. The Raman tensor for these modes are thus

$$\boldsymbol{\alpha'}^{\mathsf{g}}_{A_1} = \begin{pmatrix} a & 0 & 0 \\ 0 & a & 0 \\ 0 & 0 & b \end{pmatrix} \tag{4.34}$$

with the components

$$\begin{aligned} a &= \frac{1}{6\sqrt{3}}\alpha'_{\perp,v} + \frac{\sqrt{3}}{2}\alpha'_{\perp,h} + \frac{4}{3\sqrt{3}}\alpha'_{\parallel} \\ b &= \frac{8}{3\sqrt{3}}\alpha'_{\perp,v} + \frac{1}{3\sqrt{3}}\alpha'_{\parallel} \end{aligned} \tag{4.35}$$

for the symmetric stretch mode. This conforms to the basis vectors $xx + yy$ and zz that belong to the A_1 symmetry species for the C_{3v} point group as listed in its character table in appendix A.

The two degenerate asymmetric stretch modes dst as well as the two degenerate deformation or scissoring modes def belong to the E symmetry species. To distinguish the two, these are labelled (1) and (2), using brackets to avoid confusion with Mulliken symbols. The polarisability tensors for these modes are found to be

$$\begin{aligned}\boldsymbol{\alpha}^{\mathsf{g}}_{E_{(1)}} &= \frac{Q}{\sqrt{6}}\left(2\boldsymbol{\alpha}^{\mathsf{m}}_1 - \boldsymbol{\alpha}^{\mathsf{m}}_2 - \boldsymbol{\alpha}^{\mathsf{m}}_3\right) \\ &= \frac{Q}{\sqrt{6}}\begin{pmatrix} \frac{1}{6}\alpha_{\perp,v} - \frac{3}{2}\alpha_{\perp,h} + \frac{4}{3}\alpha_{\parallel} & 0 & -\frac{2\sqrt{2}}{3}(\alpha_{\perp,v} - \alpha_{\parallel}) \\ 0 & -\frac{1}{6}\alpha_{\perp,v} + \frac{3}{2}\alpha_{\perp,h} - \frac{4}{3}\alpha_{\parallel} & 0 \\ -\frac{2\sqrt{2}}{3}(\alpha_{\perp,v} - \alpha_{\parallel}) & 0 & 0 \end{pmatrix}\end{aligned} \tag{4.36}$$

and

$$\begin{aligned}\boldsymbol{\alpha}^{\mathsf{g}}_{E_{(2)}} &= \frac{Q}{\sqrt{2}}\left(\boldsymbol{\alpha}^{\mathsf{m}}_2 - \boldsymbol{\alpha}^{\mathsf{m}}_3\right) \\ &= \frac{Q}{\sqrt{2}}\begin{pmatrix} 0 & \frac{1}{6\sqrt{3}}\alpha_{\perp,v} - \frac{\sqrt{3}}{2}\alpha_{\perp,h} + \frac{4}{3\sqrt{3}}\alpha_{\parallel} & 0 \\ \frac{1}{6\sqrt{3}}\alpha_{\perp,v} - \frac{\sqrt{3}}{2}\alpha_{\perp,h} + \frac{4}{3\sqrt{3}}\alpha_{\parallel} & 0 & -\frac{2\sqrt{2}}{3\sqrt{3}}(\alpha_{\parallel} - \alpha_{\perp,v}) \\ 0 & -\frac{2\sqrt{2}}{3\sqrt{3}}(\alpha_{\parallel} - \alpha_{\perp,v}) & 0 \end{pmatrix}\end{aligned} \tag{4.37}$$

The form of Raman tensor for the degenerate E mode of the C_{3v} point group can therefore be written as

$$\boldsymbol{\alpha'}^{\mathsf{g}}_{E} = \begin{cases} \begin{pmatrix} c & 0 & -d \\ 0 & -c & 0 \\ -d & 0 & 0 \end{pmatrix} & (1) \\ \begin{pmatrix} 0 & c & 0 \\ c & 0 & d \\ 0 & d & 0 \end{pmatrix} & (2) \end{cases} \tag{4.38}$$

where each Raman tensor of this degenerate mode has four non-zero components of which two are unique. Its elements c and d are given as

$$\begin{aligned} c &= \frac{1}{6\sqrt{6}}\alpha'_{\perp,v} - \frac{3}{2\sqrt{6}}\alpha'_{\perp,h} + \frac{4}{3\sqrt{6}}\alpha'_{\parallel} \\ d &= \frac{2}{3\sqrt{3}}(\alpha'_{\perp,v} - \alpha'_{\parallel}) \end{aligned} \tag{4.39}$$

based on the polarisability derivatives of the individual C−H bonds involved.

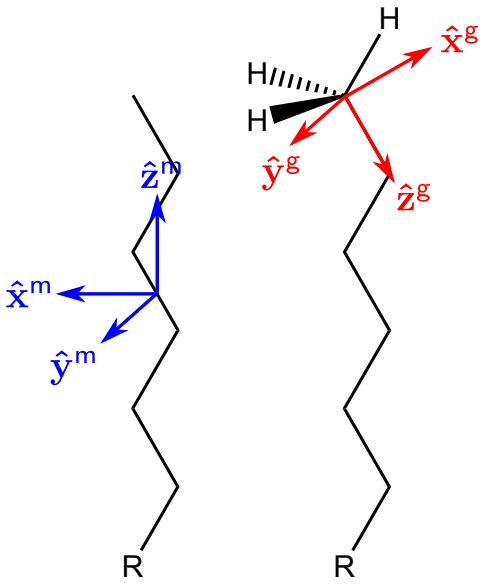

Figure 4.4: The molecule frame of reference (m, blue) for a stretched alkane chain and its relation to the axes of the CH_3 group (g, red). The unit vector $\hat{\mathbf{y}}^{\mathsf{g}} \parallel \hat{\mathbf{y}}^{\mathsf{m}}$.

Molecular frame of reference

These Raman tensors are now expressed in the molecule frame of reference m, which is defined in figure 4.2 and is again shown in figure 4.4 to relate it to the methyl group frame of reference g. The methyl group is located at one end of a stretched alkane chain in an orientated determined by the equilibrium geometry of the molecule. The appropriate

coordinate transformation involves one elemental rotation only

$$\mathbf{T}_{\mathsf{g}\to\mathsf{m}} = \mathbf{R}_y(-\theta) = \begin{pmatrix} \cos\theta & 0 & -\sin\theta \\ 0 & 1 & 0 \\ \sin\theta & 0 & \cos\theta \end{pmatrix} \tag{4.40}$$

where θ is the angle from $\hat{\mathbf{z}}^{\mathsf{g}}$ to $\hat{\mathbf{z}}^{\mathsf{m}}$ about the $\hat{\mathbf{y}}^{\mathsf{g}} = \hat{\mathbf{z}}^{\mathsf{m}}$ axis. Assuming a tetrahedral geometry around each carbon atom, geometrical reasoning readily results in

$$\theta = 90^\circ + \frac{1}{2}\tau \tag{4.41}$$

where τ is the tetrahedral angle of equation 4.12. The numerical values of the sine and cosine of θ are

$$\begin{aligned} \cos(90^\circ + \frac{1}{2}\tau) &= \frac{-1}{2}\sqrt{6} \\ \sin(90^\circ + \frac{1}{2}\tau) &= \frac{1}{3}\sqrt{3} \end{aligned} \tag{4.42}$$

The Raman tensor of the A_1 methyl modes in the molecule frame of reference can now be given by combining equations 4.34, 4.40 and 4.42 as

$$\begin{aligned} \boldsymbol{\alpha'}^{\mathsf{m}}_{A_1} &= \mathbf{T}_{\mathsf{g}\to\mathsf{m}} \boldsymbol{\alpha'}^{\mathsf{g}}_{A_1} {\mathbf{T}_{\mathsf{g}\to\mathsf{m}}}^{-1} \\ &= \begin{pmatrix} \cos\theta & 0 & -\sin\theta \\ 0 & 1 & 0 \\ \sin\theta & 0 & \cos\theta \end{pmatrix} \begin{pmatrix} a & 0 & 0 \\ 0 & a & 0 \\ 0 & 0 & b \end{pmatrix} \begin{pmatrix} \cos\theta & 0 & \sin\theta \\ 0 & 1 & 0 \\ -\sin\theta & 0 & \cos\theta \end{pmatrix} \\ &= \frac{1}{3} \begin{pmatrix} 2a+b & 0 & \sqrt{2}(b-a) \\ 0 & a & 0 \\ \sqrt{2}(b-a) & 0 & a+2b \end{pmatrix} \end{aligned} \tag{4.43}$$

which is a symmetric tensor with four non-zero, unequal but dependent, components. The form of the Raman tensors of two-fold degenerate E modes are derived in a similar way, using equations 4.38 to yield

$$\boldsymbol{\alpha'}^{\mathsf{m}}_{E} = \begin{cases} \frac{1}{3} \begin{pmatrix} 2c - 2\sqrt{2}d & 0 & -\sqrt{2}c - d \\ 0 & -c & 0 \\ -\sqrt{2}c - d & 0 & -c + 2\sqrt{2}d \end{pmatrix} & (1) \\ \frac{-\sqrt{3}}{3} \begin{pmatrix} 0 & \sqrt{2}c + d & 0 \\ \sqrt{2}c + d & 0 & \sqrt{2}d - c \\ 0 & \sqrt{2}d - c & 0 \end{pmatrix} & (2) \end{cases} \tag{4.44}$$

in the molecule frame of reference as used in our modelling effort.

In addition to having different symmetry axes, the molecule of which the methyl group

is a part may have a lower symmetry. In the case of an alkane chain, the C_{3v} point group symmetry of an isolated methyl group is reduced to C_{2v} for an even number and C_{2h} for an odd number of carbon atoms or to C_s for a differing group at the opposite end of the chain. This lifts the degeneracy of the E modes analysed here and transforms rotational motion of the methyl group into vibrations. All vibrational modes of these molecules belong to one-dimensional symmetry species. Section 4.3 derives the Raman tensors from an analysis of the whole molecule.

Choice of symmetry axes

There is ambiguity in the choice of Cartesian axes for the methyl group frame of reference. The assignment follows the symmetry operators of the C_{3v} point group: the z-axis along the C_3 axis with the x and y axis forming a right-handed system. Here, we choose $\hat{\mathbf{z}}^{\mathrm{g}}$ to point from the carbon atom to the vacant tetrahedral corner at which the methyl group is connected to the rest of the molecule and $\hat{\mathbf{x}}^{\mathrm{g}}$ is along one of the C−H bonds with the positive direction towards the hydrogen atom (figure 4.3). Many authors do not fully specify their choice of axes nor the prioritisation that gives rise to it (for example [78], [73] and the references that follow below). Our method of assigning the axes is specified in appendix A.

Given that the z-axis is along the C_3 axis, eight Cartesian axis systems remain possible that satisfy the C_{3v} point group symmetry. $\hat{\mathbf{z}}^{\mathrm{g}}$ may be chosen 'up' or 'down' while the x-axis can be parallel or perpendicular to one of the mirror planes, with $\hat{\mathbf{x}}^{\mathrm{g}}$ pointing in two possible directions in each case. These axes can be transformed into one another by symmetry operations: mirroring in the xy-plane, C_4 rotation about the z-axis and inversion. However, none of these operations are part of the C_{3v} point group so the different sets of axes are not equivalent. This means that the choice of axis will affect the form of the Raman tensor for various modes.

The Raman tensor for the fully symmetric mode $\boldsymbol{\alpha}^{\mathrm{g}}_{A_1}$ is the same in all systems. However, the forms of the Raman tensors for the degenerate modes $\boldsymbol{\alpha}^{\mathrm{g}}_{E}$ is affected by the choice of axes. Their forms have been derived following the process of the previous section using appropriate angles θ and ϕ for the three C−H bonds in each of the eight different sets of axes labelled (I) through (VIII). The results are presented in table 4.1. The values of c and d are the same in each and are given in equations 4.39 above. Axes set (I) conforms to our choice.

The axes (II) and (VI) give rise to an identical pair of Raman tensors for the degenerate E mode, while all other axes result in a different pair of tensors. However, this does not mean that these tensors can be distinguished in an experiment. The radiation due to the Raman-induced dipole $\mathbf{p}$ is the same as from a dipole $-\mathbf{p}$ that is oriented antiparallel to the original. This implies that the Raman tensor may be multiplied by -1 without consequence, as this only inverts the induced dipole while still giving rise to the same time-averaged dipole radiation field. In addition, the definitions of c and d may be changed

Table 4.1: Choice of axes determines the form of the Raman tensor for the degenerate vibrational modes of the C_{3v} point group.

Choice of axes in g frame	$\boldsymbol{\alpha'}^{\mathsf{g}}_{E_{(1)}}$	$\boldsymbol{\alpha'}^{\mathsf{g}}_{E_{(2)}}$
(I) 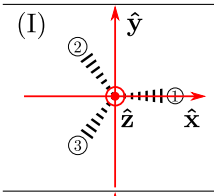	$\begin{pmatrix} c & 0 & -d \\ 0 & -c & 0 \\ -d & 0 & 0 \end{pmatrix}$	$\begin{pmatrix} 0 & c & 0 \\ c & 0 & d \\ 0 & d & 0 \end{pmatrix}$
(II) 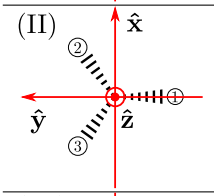	$\begin{pmatrix} -c & 0 & 0 \\ 0 & c & -d \\ 0 & -d & 0 \end{pmatrix}$	$\begin{pmatrix} 0 & -c & -d \\ -c & 0 & 0 \\ -d & 0 & 0 \end{pmatrix}$
(III) 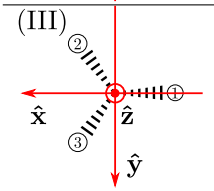	$\begin{pmatrix} c & 0 & d \\ 0 & -c & 0 \\ d & 0 & 0 \end{pmatrix}$	$\begin{pmatrix} 0 & -c & 0 \\ -c & 0 & -d \\ 0 & -d & 0 \end{pmatrix}$
(IV) 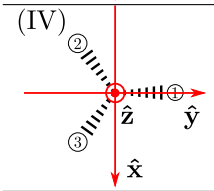	$\begin{pmatrix} -c & 0 & 0 \\ 0 & c & d \\ 0 & d & 0 \end{pmatrix}$	$\begin{pmatrix} 0 & -c & d \\ -c & 0 & 0 \\ d & 0 & 0 \end{pmatrix}$
(V) 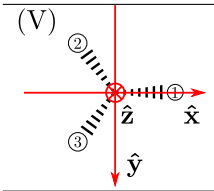	$\begin{pmatrix} c & 0 & d \\ 0 & -c & 0 \\ d & 0 & 0 \end{pmatrix}$	$\begin{pmatrix} 0 & c & 0 \\ c & 0 & -d \\ 0 & -d & 0 \end{pmatrix}$
(VI) 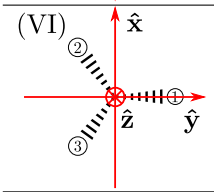	$\begin{pmatrix} -c & 0 & 0 \\ 0 & c & -d \\ 0 & -d & 0 \end{pmatrix}$	$\begin{pmatrix} 0 & -c & -d \\ -c & 0 & 0 \\ -d & 0 & 0 \end{pmatrix}$
(VII) 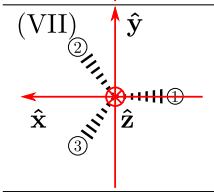	$\begin{pmatrix} c & 0 & -d \\ 0 & -c & 0 \\ -d & 0 & 0 \end{pmatrix}$	$\begin{pmatrix} 0 & -c & 0 \\ -c & 0 & -d \\ 0 & -d & 0 \end{pmatrix}$
(VIII) 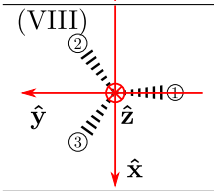	$\begin{pmatrix} -c & 0 & 0 \\ 0 & c & d \\ 0 & d & 0 \end{pmatrix}$	$\begin{pmatrix} 0 & c & -d \\ c & 0 & 0 \\ -d & 0 & 0 \end{pmatrix}$

to $-c$ and/or $-d$, as long as this is done on both sides of the equations that define these variables (such as equations 4.39 in the case of methyl). We can therefore conclude that only the relative signs of the Raman tensor components matter. Setting the signs aside, there are only two more fundamental forms of $\boldsymbol{\alpha}'^{\mathtt{g}}_E$: on the one hand those resulting from axes (I), (III), (V) and (VII) in which $\hat{\mathbf{x}}^{\mathtt{g}}$ passes through a mirror plane, and on the other (II), (IV), (VI) and (VIII) in which $\hat{\mathbf{y}}^{\mathtt{g}}$ passes through one of the mirror planes.

4.1.4 Symmetry arguments

The forms of the Raman tensors for all point groups can be deduced from symmetry considerations once a coherent procedure is established to set the Cartesian axes. A limited number of authors have taken the effort to do this, though none provide their axis choice explicitly. The variation in the forms of Raman tensors presented by various authors can be fully explained by different choices of basis vectors. This section briefly reviews their work, starting from the various tensor forms derived for the C_{3v} point group.

The forms of the Raman tensors deduced for the methyl vibrations conform to various literature sources, revealing the hidden choice of axes that their authors made. Our choice conforms to the set of axes and directions presented as (I) in table 4.1. This agrees with the result presented by Cardona [99], apart from the inclusion of antisymmetric components by that author to account for resonant effects. The overview presented there is taken from a book by Hayes and Loudon [100] which is rather difficult to obtain. Their work deviates from an earlier publication by Loudon [101], which presents Raman tensors that conform to those obtained by axes set (VIII) with $-c$ substituted for c. The choice of axes in this reference in turn is based on Nye's book on crystals [102], which was consulted and confirmed our conclusion that Loudon took the y-axis in the C_{3v} mirror plane.

The Raman tensors in the Bilbao Crystallographic Server [103] (BCS, accessible through `http://www.cryst.ehu.es/`) conform to our results obtained for axes (IV) with c changed to $-c$. This is the same as multiplying the pair of Raman tensors from either (II) or (VI) by -1. None of these operations affect the radiated dipole field.

Mortensen [104] gives the symmetry species of the intermediate states, which is relevant in resonant Raman scattering, but gives the same forms as those in the BCS though it is unclear on which source the latter is based. The choice of axes also remains unspecified.

The discrepancy between the various literature sources emphasized here for the C_{3v} point group is observed in a limited number of other point groups as well. If a symmetry operation of the point group can produce different but equally valid choices of axes, the axes choice will not affect the form of the Raman tensor. This is the case with most point groups, such as those including a C_4 axis. Comparing the crystallographic sources discussed above, we find that the point groups D_3, C_{3v}, D_{3d}, T and T_h give rise to discrepancies.

A further source of variation is the ambiguous prioritisation of the x, y and z axes in the some low-symmetry point groups. For the C_1 point group, any orientation of axes will

produce the same form of Raman tensor, though the numerical values will change upon rotation of the axes. In the C_s point group, either the y or z axis is taken as unique. This implies that the plane of symmetry is either xz or xy, with most character tables following the latter. The choice affects the form of the Raman tensor: the α'_{xy} and α'_{yz} components are interchanged with the α'_{xz} and α'_{zx}.

Loudon [101] used the results of symmetry analysis to determine the form of the Raman tensors. This approach comes down to inspecting the appropriate character table and taking the binary products listed with the symmetry species of the vibration under consideration as the only non-zero Raman tensor components, ensuring that the tensor is symmetric. In most cases, the correct form of the Raman tensor for fundamental transitions is readily constructed in this way. However, one can only read off the form of the Raman tensor from the character tables if (1) the choice of axes used to construct these tables followed an unambiguous assignment based on the molecular point group symmetry, and (2) that the researcher wishing to use the character tables follows the identical set of axes. This is complicated by a lack of standardization. Though the International Tables for Crystallography [105] provide some guidance, they leave ambiguity in the assignment of axes in a number of point groups. In other cases, one might wish to use a set of axes that coincides with a physical meaning rather than symmetry.

Most character tables list the Raman tensor components separated by commas or parenthesis. Though text books do not appear to explain it, the meaning of these is to be understood as follows. Components grouped in brackets indicate that these are basis vectors which can be transformed into one-another using the symmetry operations of the point group. Such bases are equivalent. Commas indicate basis vectors that belong to the same symmetry species but cannot be transformed into each other using the symmetry operations of the point group. The matrix elements separated by commas are taken as independent variables and those grouped in parentheses are interchangeable. The latter only occur in degenerate modes (E and F symmetry species) and because of their equivalence have the same numerical value. Normalisation of the matrix elements has to be taken into account for these modes as each basis vector is normalised.

Loudon apparently changed his choice of axes for a later publication with Hayes [100], which has been used by Cardona [99] and differs from the original version as illustrated for the E species of the C_{3v} point group in the previous section. Though Loudon's first overview includes some errors (notably in the form of the degenerate modes of the tetrahedral point groups) it has been reproduced relatively recently in [106] without further comment.

Mortensen [104] used commutation relations of symmetry operators to deduce the symmetry species of intermediate quantum states in resonant Raman scattering. Their analysis resulted in identification of the non-zero Raman tensor elements for Raman-active transitions, appropriate normalisation factors as well as whether the tensor components are of equal value. The intermediate state is relevant in resonance Raman scattering, whereas it remains virtual in normal Raman scattering considered in this work. However, the

form of the Raman tensor deduced for resonance scattering also applies to non-resonance scattering if the antisymmetric terms are ignored. The results of Mortensen are also included in Long's book [61] from page 255 onwards.

By critical comparison of our results and the cited literature, the form of the Raman tensor for each Raman active symmetry species can be derived. We have undertaken such analysis for a number of point groups using our particular choice of axes. The results are included as appendix C.

In concluding, let me stress that it is paramount to specify the choice of axes and work with it consistently before orientational analysis can be done in a meaningful way. This has not been an important issue for most researchers to date due to the nature of the experiments. On the one hand, a focus by chemists on normal Raman scattering of gases and liquids only requires dealing with isotropic averages, while on the other hand a focus by physicists on resonant Raman scattering by phonons in solids is limited to only one well-defined orientation of a particular crystal face. In our work, Raman tensors have to be specified in an unambiguous molecular frame of reference so that the orientation of this frame with respect to the laboratory-fixed environment can be analysed.

4.2 Numerical values through computation

Predicting Raman spectra through computation is a specialised field within quantum chemistry. This section provides a summary of the basic concepts behind such calculations. It serves as introduction and theoretical background to the next section, in which the GAUSSIAN software package is applied to molecules studied in this work at currently acceptable levels of theory. Literature is presented to establish what that level involves.

4.2.1 Calculation of Raman spectra

Computations of the Raman effect focus on obtaining a Raman spectrum that matches experimentally obtained spectra. This requires the calculation of all vibrational modes of the molecule and the polarisability derivatives with respect to the atomic motions in these modes as an intermediate step. The Raman tensors of the modes are thus intrinsically part of the calculation. However, the computational output may not show the tensors in a convenient way as this has not traditionally been its focus.

A Raman calculation is performed on an optimized molecular geometry. Depending on the capabilities of the computational package employed, computations may be performed on an isolated molecule to mimic the gas phase, a molecule in an effective solvent field or with explicit inclusion of surrounding molecules. The optimized geometry includes the positions of the nuclei and the wave-functions of all electrons in the molecule. It is found in a minimization process of the total potential energy. At standard temperature and pressure, this is usually the electronic and vibrational ground state of the molecule. Physical properties can be computed directly from the ground state or as a perturbation

to it.

For the Raman effect, polarisability derivatives need to be computed in an applied electric field. If the frequency is taken as zero, the static polarisability derivatives are found. These are a valid approximation in normal Raman scattering. The frequency of the field has to be specified in resonant conditions, which provides the dynamic polarisability derivatives. In both cases, these tensor components are third order derivatives of the potential energy.

The potential energy of a molecular system is found by solving the Schrödinger equation

$$\hat{H}\Psi(\mathbf{r}) = \epsilon\Psi(\mathbf{r}) \tag{4.45}$$

where $\hat{H}$ is the Hamiltonian, $\Psi(\mathbf{r})$ is the wave-function of the system at each point $\mathbf{r}$ in space and ϵ is its (quantized) energy. The Hamiltonian includes internal energy terms and the interaction with the applied electric field. The latter describes light scattering and includes the electric dipole, magnetic dipole and electric quadrupole operators for the lower and higher order effects summarised classically by equation 2.17. For Rayleigh and Raman scattering, the interaction between the molecule and the applied electric field only involves the electric dipole operator as introduced in equation 2.29. The interaction energy is then found through

$$\epsilon = -\mathbf{p} \cdot \mathbf{E} \tag{4.46}$$

which is the energy of the electric dipole moment $\mathbf{p}_e$ of the scattering molecule in the applied electric field $\mathbf{E}$. The components of the dipole moment may thus be computed as a derivative of the potential energy with respect to the applied field

$$p_j \propto \frac{\partial \epsilon}{\partial E_j} \tag{4.47}$$

while the polarisability tensor is the derivative of the dipole moment with respect to the applied electric field

$$\alpha_{ij} \propto \frac{\partial}{\partial E_i}\frac{\partial \epsilon}{\partial E_j} \tag{4.48}$$

Finally, the Raman tensor of vibrational mode v is proportional to the polarisability derivative with respect to the normal coordinate Q_v at the equilibrium geometry so that

$$\alpha_{\mathsf{v}ij} \propto \left(\frac{\partial}{\partial Q_\mathsf{v}}\frac{\partial}{\partial E_i}\frac{\partial \epsilon}{\partial E_j}\right)_0 \tag{4.49}$$

Thus, the components of the Raman tensor are a third derivative of the potential energy of the molecule at its equilibrium geometry. Only methods that include solutions to these derivatives can be used for Raman calculations.

4.2.2 Density-functional theory

A particular elegant way to solve the Schrödinger equation 4.45 is via density-functional theory (DFT) [107]. This method is more efficient in computing the electronic structure of larger molecules or clusters then conventional *ab-initio* computations such as the Hartree-Fock method. DFT is a first-principles method but not strictly speaking fully *ab intitio*. Though it fundamentally solves the Schrödinger equation for a system of coupled electrons, some parts of the problem are addressed through semi-empirical parametrization of the interactions in terms of the electronic density.

The DFT approach to solving the Schrödinger equation and finding the ground state of a molecule consists in expressing it in terms of an electronic density functional. This modified form is the Kohn-Sham equation

$$\left(\frac{-\hbar^2}{2m}\nabla^2 + V_{\mathsf{KS}}(n(\mathbf{r}),\mathbf{r})\right)\Psi(\mathbf{r}) = E\Psi(\mathbf{r}) \tag{4.50}$$

which includes the Kohn-Sham potential $V_{\mathsf{KS}}(n(\mathbf{r}),\mathbf{r})$ that depends on the electronic density $n(\mathbf{r})$. The latter, in turn, depends on the wave-function at each position

$$n(\mathbf{r}) = |\Psi(\mathbf{r})|^2 \tag{4.51}$$

so that the potential function depends on the electronic density which in turn is a function of position. Hence the name density functional.

All electronic interactions are included in the Kohn-Sham potential as a function of $\mathbf{r}$ and $n(\mathbf{r})$: the Coulomb interaction of the electrons with the nuclei (which only depends on $\mathbf{r}$), the Coulomb repulsion among electrons and the exchange potential. DFT essentially replaces the many-body problem of solving the Schrödinger equation for all electrons (a completely *ab-initio* approach) by the problem of finding a one-electron solution in a non-linear potential that depends on the electronic density.

Implementation of a DFT calculation follows an iterative approach for each set of nuclear coordinates. At the start, the wave-function $\Psi(\mathbf{r})$ is expressed as a linear combination of basis functions $\psi_i(\mathbf{r})$ that make up the basis set. From an initial guess of the ground state, the electron density $n(\mathbf{r})$ is computed from which the Kohn-Sham potential follows. Using this fixed potential, equation 4.50 is solved and the ground state $\Psi(\mathbf{r})$ is found as a new linear combination of the basis set. At the end of one iteration, $n(\mathbf{r})$ is again computed and compared to the one at the start of the iteration. The process is repeated with the new electron density. If convergence has been achieved (*i.e.* an energy minimum is found), a self-consistent solution has been found and the problem is solved. Another point in the potential energy surface is then computed by varying the nuclear coordinates. Once a global minimum is found, calculations of the desired physical properties may follow.

Crucial specifications in DFT are the method and the basis set. The method specifies the exact form of the Kohn-Sham potential and thus how it depends on $n(\mathbf{r})$. The basis set specifies the type and nature of the wave-functions used in the calculation of the

self-consistent electronic field. Any computations on an optimized geometry have to be performed with the same method and basis set that was used in the optimization.

4.2.3 Computational approaches

Several computational packages are available that can predict Raman spectra. A selection is presented here to highlight theoretical features, limitations and some applications.

The general approach for a Raman calculation is to first compute an equilibrium structure by finding a potential energy minimum for the molecular geometry. Once this electronic structure is known, the force constants between the atom are computed and the normal modes obtained. The linear polarisability tensor is computed from the electronic structure in an applied field. The polarisability derivatives are computed from deformed structures that each follow one of the vibrational patterns. A recent review including a more detailed discussion can be found in reference [108].

The geometry optimization and the Raman analysis are distinct steps and each involves specialised computational solutions that not all packages can perform. General computational packages include GAUSSIAN of Gaussian Inc. (Wallingford CT, USA) and GAMESS of Professor Mark Gordon at Iowa State University. Both are updated and expanded regularly. Some authors develop their own software with a particular application in mind and to decrease the computational resources needed for increasingly larger molecules such as buckminsterfullerene [109]. The Raman problem can be reduced by limiting the computation to selected vibrational modes (so-called procedure for investigating categories of vibrations, see [110]), treating modes as localised to a subset of atoms in the molecule [111] or by partitioning the electronic density [112]. Some of these methods can be generalised to molecular and periodic systems. In most cases, these require numerical rather than analytical derivatives, as in the case of buckminsterfullerene [109].

The predicted Raman frequencies and intensities depend on the level of detail in the theory. All frequencies should be positive and real for an optimized structure. If some are negative, the structure is unstable, if imaginary, it is at a saddle point in the potential energy surface (*i.e.* a transition state) [41]. Vibrational frequencies are usually overestimated in a computation. This is corrected by an empirical scaling factor derived from a set of experimental reference spectra. The factors vary between molecules as well as between vibrational modes of an individual molecule. A large collection of scaling factors is included in the Computational Chemistry Comparison and Benchmark Database of the United States National Institute of Technology (NIST) [113].

The predicted Raman intensity is an averaged property over all orientations of the molecule. The total scattering cross section is usually given in addition to the depolarisation ratio. These can only be compared to conventional Raman spectroscopy on bulk liquids or gasses. In ordered materials, we have to work with Raman tensors which should therefore be included in the computational output.

The intensity further depends on the amplitude of the vibrational normal mode $Q_{\mathsf{v}0}$,

which in turn depends on the frequency of the mode and whether the scattering is Stokes or anti-Stokes [41]. Computations at zero Kelvin return the zero-point amplitude of the vibrational motion. For Stokes Raman scattering from the ground state to the first vibrationally excited state (relevant to the present work) we have

$$Q_{\mathsf{v}0} = \sqrt{\frac{\hbar}{2\mu_{\mathsf{v}}\omega_{\mathsf{v}}}} = \sqrt{\frac{h}{8\pi^2 c\mu_{\mathsf{v}}\bar{\nu}_{\mathsf{v}}}} \tag{4.52}$$

for a harmonic oscillation at angular frequency ω_{v} or wavenumber $\bar{\nu}_{\mathsf{v}}$ and reduced mass μ_{v}. In an ensemble, the temperature affects the relative intensities of all Raman active transition through the population of the vibrational state. This effect can be ignored at standard temperature.

Any surrounding molecules in condensed phases may further affect the predicted frequencies and intensities through coupling of the vibrational motion or constraining its amplitude. However, such computations are stretching the current capabilities of theoretical chemistry which tend to be aimed at one of constituent challenges such as improving the anharmonic description of gas-phase molecules or at efficiently computing selected vibrations of molecular systems.

Harmonicity of the vibrational potential and electrical harmonicity (neglecting higher order terms in the expansion of the polarisability) may or may not be assumed in the computation. The double harmonic approximation is the default approach though anharmonicity has been addressed for decades and methods are continuously being developed (see, for instance, [114, 115]). A comprehensive approach with generalised second-order vibrational perturbation theory including both mechanical and electric/magnetic anharmonicity has so far been performed on gas-phase molecules of about 10 atoms [116]. Analytical solutions are proven for nitromethane [117].

Raman computations are performed at a specific frequency of the incident electric field. In a static approach, this frequency is taken to be zero to mimic the situation of a field that is constant over the extent of the molecule. Static polarisability derivates are then obtained which may be used in non-resonant (*i.e.* normal) Raman scattering [41]. In a dynamic analysis, the frequency is specified and a more involved computation is needed [118]. Such analysis is needed to find agreement with resonant and near-resonant Raman spectra [119].

The ideal computation would give a full anharmonic analysis of the dynamic polarisability tensor and its derivatives for a collection of more than 20 atoms. However, this appears to be beyond the current frontier of theoretical chemistry (see *e.g.* [118]).

4.2.4 Method and basis set

Finally, I would like to stress the importance of selecting an appropriate method and basis set. The computational method should allow analytical derivatives of the potential energy surface (3rd-order in the harmonic approximation and 5th-order if anharmonicity is taken

into account) or numerical solutions if the former are not available [117].

At present, the B3LYP functional is widely used within the theoretical chemistry community for analyses, for example in references [114, 117–119]. This method is also used in our computations. B3LYP stands for Becke's three-parameter hybrid functional with Lee-Yang-Parr non-local electron correlation [120, 121]. This specifies the exchange functional as a mixture of Hartree-Fock and DFT exchange correlation functionals.

A basis set is chosen with the purpose of the computation in mind. For organic molecules, Gaussian-like orbitals are commonly used. The number of functions and their complexity depends on the properties of interest and the computational power at hand. Computed vibrational Raman spectra depend strongly on the choice of basis set for the computation [122]. For accurate Raman spectra, the basis set should include large basis sets with diffuse and polarisation functions [114]. Examples in the literature cited here include aug-cc-pVTZ [114, 122], SNSD [115, 116] and 6-311++G(d,p) [119]. Cheeseman and Frisch [122] suggest that although Raman tensor computations require basis sets with diffuse functions, geometry optimizations and force field calculations do not, so that a two-step approach can be more efficient than using the extended basis set for all calculations.

The basis set chosen for our computations is 6-311++G(d,p). This is the 6-311G basis set of Gaussian functions augmented with diffuse functions (indicated by ++) and polarisations functions, in this case one set of d-type functions on atoms from helium onwards and one set of p-type functions on hydrogen atoms. These latter functions take account of distortions to the atomic orbitals that arise from nearby nuclei.

The 6-311G basis is a so-called split-valence triple-zeta basis set due to John Pople and makes a distinction between core and valence electrons. It employs six Gaussian-type primitive orbitals to describe each atomic core orbital basis function. Each valence orbital is composed of three basis functions, the first one formed by linear combination of three primitive Gaussian-type orbitals, the other two are a single Gaussian-type orbital. Combining the Gaussian-type orbitals in this way, rather than using these directly, increases the accuracy of the modelled anisotropic electron distribution in molecules.

Diffuse functions correct for the electronic density at large distance from the nuclei, which is underestimated in primitive Gaussians. A higher electronic density far away from the nuclei affects the dipole moment operator (given through equation 2.29) and thus the computed polarisability and its derivatives. The diffuse functions added to the basis set are s-functions for hydrogen and p-functions for helium onwards.

The level of theory chosen is thus summarised as B3LYP/6-311++G(d,p). This follows, amongst many others, the suggestion in [41] and the recent use by Fischer *et al.* [119] in their detailed IR and Raman study of dimethyl sulfoxide.

4.3 Computations in Gaussian

In this work, the computational package GAUSSIAN 09 (revision A.02) [123] is used to derive Raman tensors. Although other computational packaged are available, its ease

of use, universality, continuous improvements and the availability of technical expertise prevail for our purposes.

An accesible introduction to the implementation of DFT calculations within GAUSSIAN for Raman spectroscopy can be found in appendix A of Le Ru and Etchegoin's book on SERS (reference [41]). This was the only source that I could find to outline the computational process. Though their method was originally followed, it proved problematic for the following reasons. In the Raman computation, it includes the keyword `NoSymm` to ensures that no rotations of the frame of reference are performed. Though this may seem advantageous, it has two important drawbacks. First, avoiding symmetry considerations prevents GAUSSIAN from assigning symmetry species to the vibrational modes. Second, it creates false non-degenerate modes that should be degenerate on the basis of symmetry. A further problem in their method is the construction of Raman tensors from the printed output using atomic linear polarisability derivatives and atomic motions in each vibrational mode. The inaccuracy of the latter, given in two decimal places only, introduces significant rounding errors in the resulting Raman tensors. Components that should cancel on the basis of symmetry were not zero, but were found to be up to a tenth of the numerical value of the components that were correctly computed as finite values. Finally, Le Ru and Etchegoin's instruction includes an error where it explains the frames of reference used in GAUSSIAN. The atomic linear polarisability derivatives are given with respect to the original input coordinates used to specify the atomic positions (the so-called Z-matrix) and the normalized atomic displacement of the vibrational modes are given in the computational orientation set by GAUSSIAN, termed the standard orientation. The authors mixed this up.

Le Ru and Etchegoin's method was therefore only used as a starting point in the development of a consistent method. The documentation supplied by GAUSSIAN was another important source of information, though on its own does not provide adequate instruction to obtain Raman tensors. For instance, the internal options I came to use are not listed in its documentation. Instead, these were found on personal webpages of theoretical chemists.

The computation is divided into two steps. A geometry optimization is performed first. The Raman calculation is then performed on the optimized geometry. Both steps using the same method and basis set. The B3LYP method is used, for which third order derivatives are implemented in GAUSSIAN. The basis set is 6-311++G(d,p). The default temperature and pressure of 298.15 K and 1 atm are used. Appendix D includes relevant sections of the computational output files and MATLAB scripts to process the results.

4.3.1 Geometry optimization

The input file for a GAUSSIAN computation, the so-called Gaussian Job File (GJF), follows a strict format. Full details can be found in the online documentation of the program at `www.gaussian.com`. The GJF for a geometry optimization includes the following in its

route section

```
#T B3LYP/6-311++G(d,p) Opt
```

which lists the method, basis set and keyword `Opt` for the geometry optimization. The route section is initiated by the `#`-symbol, with `#T` indicating that output is reduced to essential information and results. The charge of the molecule and its spin multiplicity follow between white lines. The atoms are then listed, using their chemical symbols, with tentative positions in units of Å within a Cartesian coordinate system at an arbitrary origin. This list of coordinates is known as the Z-matrix.* A blank line completes the GJF.

The output of the computation, called a log file, repeats the information provided in the GJF and lists iterations of the computation in a fixed format. In each iteration, the program attempts to identify the point group of the molecule. Once found, the molecule is translated and rotated to a different coordinate system, called the standard orientation, on which the calculation is performed. The origin of the standard orientation is placed at the centre of charge of the molecule† and the axes are chosen to match its symmetry properties. Use of these symmetry-adapted Cartesian coordinates accelerates the computation. In many cases, the standard orientation conforms to the Cartesian axes assigned on the basis of molecular symmetry. As discussed above, this may involve ambiguities. The directions of axes are arbitrary and the assignment of the x and y axes vary by author. Furthermore, changing the input orientation may change the standard orientation that GAUSSIAN finds.

The atomic positions are varied until a minimum in the potential energy of the molecule is found. Each iteration is presented in the log file. Once convergence is achieved, the final values are computed and printed after the line

```
 -- Stationary point found.
```

The optimized molecular geometry is printed in the coordinate system of the standard orientation. The Raman computation is now performed on this structure.

4.3.2 Raman calculation

The atomic positions obtained through geometry optimization are taken from the optimization log file and formatted to a new GJF for the Raman calculation. The route section of this GJF is

```
#T B3LYP/6-311++G(d,p) Freq=Raman IOp(2/33=1) IOp(7/33=3)
```

where the keyword `Freq=Raman` requests a vibrational analysis of the molecule as well as computation of linear polarisability derivatives at each atom. Relevant isotopologues of

*The relative atomic positions may also be specified as distances and angles or through interdependent symbolic variables.

†This is the default, set by the `COC` option. The centre of mass can be set as the origin of the standard orientation with the option `COM`, though it has not been used here because the exact location of the origin was deemed unimportant.

a molecule are computed from a single geometry optimization. Though isotopes do not effect the electronic structure of a compound, they can change the molecular symmetry and distort vibrational motion (see section 3.2.2 for details). The most abundant isotopes are used as default. Other isotopes can be specified as `Cl(Iso=37)` in the Z-matrix of atomic coordinates. In deriving the standard orientation, GAUSSIAN does not take isotopes into account as it is based on the charge rather than the mass distribution within the molecule.

The optimized molecular geometry is specified in the standard orientation as input for the Raman computation to avoid any further coordinate transformations. If the molecule is not specified in the standard orientation, GAUSSIAN performs rotations and translation to obtain it in that orientation, complicating the analysis. The internal option `IOp(2/33=1)` provides the translation vector and rotation matrix that specify the transformation from the input orientation to the standard orientation. If these are the zero vector and identity matrix, respectively, no transformation is executed in the program.

The log of the Raman computation contains an overview of the vibrational normal modes in the following format (taken from the sulfate computation).

```
Harmonic frequencies (cm**-1), IR intensities (KM/Mole), Raman scattering
activities (A**4/AMU), depolarization ratios for plane and unpolarized
incident light, reduced masses (AMU), force constants (mDyne/A),
and normal coordinates:
                      1                      2                      3
                      E                      E                     T2
Frequencies --    398.5956               398.5956               561.5002
Red. masses --     15.9949                15.9949                17.5820
Frc consts  --      1.4973                 1.4973                 3.2660
IR Inten    --      0.0000                 0.0000                23.3316
Raman Activ --      2.2422                 2.2422                 2.3038
Depolar (P) --      0.7500                 0.7500                 0.7500
Depolar (U) --      0.8571                 0.8571                 0.8571
 Atom  AN      X      Y      Z        X      Y      Z        X      Y      Z
    1  16     0.00   0.00   0.00     0.00   0.00   0.00     0.00   0.23  -0.22
    2   8    -0.15  -0.26   0.40    -0.38   0.32   0.06     0.01  -0.33   0.34
    3   8     0.15   0.26   0.40     0.38  -0.32   0.06     0.45   0.10  -0.12
    4   8     0.15  -0.26  -0.40     0.38   0.32  -0.06    -0.45   0.11  -0.12
    5   8    -0.15   0.26  -0.40    -0.38  -0.32  -0.06    -0.01  -0.33   0.34
```

Amongst other quantities, it lists the frequency (in cm^{-1}), reduced mass (in amu) and Raman activity (in Å^4 amu^{-1}) as well as the normalised displacements of each atom along the Cartesian axes `XYZ` of the standard orientation for each vibrational mode. The Raman scattering activity S (also simply Raman activity or scattering factor) depends on the invariants of the polarisability derivative tensor and is computed through [109]

$$S = 45\bar{\alpha}'^2 + 7\gamma'^2 \tag{4.53}$$

where $\bar{\alpha}'$ and γ' are the mean of the diagonal and the anisotropy defined analogous to equations 2.127 and 2.128. The Raman activity is one of the factors that determine the intensity of a Raman band in the spectrum. Experimental factors such as the incident wavelength and the geometry of illumination and observation also play a role. Notwithstanding these limitations, the scattering factor is used to assess what vibrational modes are Raman active and to plot computational Raman spectra.

Spectra are produced by taking the Raman activity as the peak intensity and the computed frequency as the location of a Raman band. Convolution with a broadening-function produces a coarse reference spectrum that can aid in identifying bands in the experimental spectra. However, the computed frequencies are known to deviate from experimental observation. Reasons for this include a lack of anharmonic effects in the computation and its limitation to the gas phase whereas the experimental sample is a liquid. A scaling factor is usually applied that is derived from a set of experimental reference spectra [113, 124]. These factors depend on the basis set used for the computation. Andersson and Uvdal [125] found that an average factor of 0.9679 would apply for vibrational frequencies computed at our level of theory with 1.0100 for low-frequency vibrations and 0.9877 for zero-point vibrational energies. These values were computed from a set of small molecules within which there is significant variation (compare, for instance, CCl_4 with hexane in the NIST database [113]). The principal result of our computations are the Raman tensors whereas the computational spectra serve to aid in peak assignment through qualitative comparison. Though differences with experimental frequencies are noted, no scaling factor is employed in our analysis.

The internal option `IOp(7/33=3)` is used to obtain the linear polarisability derivatives with respect to the vibrational modes in tensor format. These can be computed manually from the atomic polarisability derivatives and the atomic motions in each vibrational mode. The former are listed at the end of the log file after `PolarDeriv` and have been rotated back to the original input orientation. Their format is explained in appendix D. However, this process results in significant rounding errors. The option `IOp(7/33=3)` ensures that the desired calculation is performed as part of the computation. The results are printed in the format

```
 Polarizability derivatives wrt mode          1
                  1             2             3
      1  -0.136329D+00  0.000000D+00  0.000000D+00
      2   0.000000D+00 -0.236520D+00  0.000000D+00
      3   0.000000D+00  0.000000D+00  0.372849D+00
```

where `D` indicates a power of base 10. The components are given in units of Å^2 $\text{amu}^{-1/2}$, with `1`, `2` and `3` designating the three Cartesian axes of the standard orientation. The option also provides the normalised atomic motion in each vibrational mode with respect to these axes to five decimal places. The default output of the vibrational analysis of `Freq=Raman`, limited to two decimal places, is retained.

The polarisability derivative tensor $\mathbf{P}^{\mathtt{s}}_{\mathtt{v}}$ for a particular vibrational mode `v` in the computational frame of reference `s` (the standard orientation) is constructed from linear polar-

isability derivatives with respect to the real atomic displacements $\frac{\partial \boldsymbol{\alpha}}{\partial x_n}$, $\frac{\partial \boldsymbol{\alpha}}{\partial y_n}$ and $\frac{\partial \boldsymbol{\alpha}}{\partial z_n}$ for each atom n. The displacements are given in the standard orientation in units of B, the Bohr radius. For each vibrational mode, these derivatives are multiplied by their normalised atomic displacement along each of the three Cartesian axes $\frac{\partial x_n}{\partial q_{\mathsf{v}n}}$, $\frac{\partial y_n}{\partial q_{\mathsf{v}n}}$ and $\frac{\partial z_n}{\partial q_{\mathsf{v}n}}$. The sum of the resulting three derivative tensors results in the polarisability derivative $\frac{\partial \boldsymbol{\alpha}_n}{\partial q_{\mathsf{v}n}}$ with respect to the motion of atom n as part of vibrational normal motion v. All N atomic contributions are then summed to obtain the polarisability derivative $\frac{\partial \boldsymbol{\alpha}}{\partial Q_{\mathsf{v}}}$ with respect to the vibrational mode, which is the familiar tensor $\boldsymbol{\alpha'}_{\mathsf{v}}$ proportional to the Raman tensor. GAUSSIAN multiplies this tensor by the inverse square root of the reduced mass of the vibrational mode μ_{v} to account for (part of) the zero-point amplitude $Q_{\mathsf{v}0}$ as well as for the Bohr radius in Å. In summary,

$$\mathbf{P}^{\mathsf{s}}_{\mathsf{v}} = \frac{0.529^2}{\sqrt{\mu_{\mathsf{v}}}} \sum_{n=1}^{N} \left(\frac{\partial x_n}{\partial q_{\mathsf{v}n}} \frac{\partial \boldsymbol{\alpha}}{\partial x_n} + \frac{\partial y_n}{\partial q_{\mathsf{v}n}} \frac{\partial \boldsymbol{\alpha}}{\partial y_n} + \frac{\partial z_n}{\partial q_{\mathsf{v}n}} \frac{\partial \boldsymbol{\alpha}}{\partial z_n} \right) \tag{4.54}$$

given in units of Å^2 $\text{amu}^{-1/2}$ through the factor 0.529 Å B^{-1} and μ in amu.

The process used in GAUSSIAN to obtain $\boldsymbol{\alpha'}_{\mathsf{v}}$ appears similar to the bond-polarisability model. It sums atomic contributions according to their displacement in the vibrational motion. However, it takes the whole electron distribution of the molecule into account rather than individual bonds. For Raman inactive modes, the Raman scattering activity given in the log file is zero and the resulting tensor is found to be zero through cancellation of the atomic contributions.

4.3.3 Obtaining the Raman tensor

The Raman computation has returned vibrational normal modes with their frequencies as well as polarisability derivatives with respect to these modes in tensor format. The Raman tensors $\boldsymbol{\alpha}^{\mathsf{m}}_{\mathsf{v}}$ in the desired molecular frame of reference m are computed from the linear polarisability derivative tensors $\mathbf{P}^{\mathsf{s}}_{\mathsf{v}}$. Correction for the units is needed as well as inclusion of the zero-point amplitude $Q_{\mathsf{v}0}$ for Stokes Raman scattering as given in equation 4.52, of which only the reduced mass has been taken into account so far. Working from the definition of the Raman tensor in equation 2.27, we have

$$\begin{aligned}
\boldsymbol{\alpha}^{\mathsf{m}}_{\mathsf{v}} &= Q_{\mathsf{v}0} \boldsymbol{\alpha'}^{\mathsf{m}}_{\mathsf{v}} \\
&= \sqrt{\frac{h}{8\pi^2 c \mu_{\mathsf{v}} \bar{\nu}_{\mathsf{v}}}} \boldsymbol{\alpha'}^{\mathsf{m}}_{\mathsf{v}} \\
&= \sqrt{\frac{h}{8\pi^2 c \bar{\nu}_{\mathsf{v}}}} \frac{4\pi\epsilon_0 \cdot 10^{-20}}{\sqrt{1.660539 \cdot 10^{-27}}} \mathbf{T}_{\mathsf{s}\to\mathsf{m}} \mathbf{P}^{\mathsf{s}}_{\mathsf{v}} {\mathbf{T}_{\mathsf{s}\to\mathsf{m}}}^{\mathrm{T}} \\
&= 4.5683 \cdot 10^{-40} \sqrt{\frac{1}{\bar{\nu}_{\mathsf{v}}}} \mathbf{T}_{\mathsf{s}\to\mathsf{m}} \mathbf{P}^{\mathsf{s}}_{\mathsf{v}} {\mathbf{T}_{\mathsf{s}\to\mathsf{m}}}^{\mathrm{T}}
\end{aligned} \tag{4.55}$$

where correction factors have been introduced to ensure that the Raman tensor is expressed in units of C V^{-1} m^2. This includes $1.660539 \cdot 10^{-27}$ kg amu^{-1} for the mass unit and the speed of light c given in cm s^{-1} with the wavenumber $\bar{\nu}$ of the vibrational mode v given cm^{-1}. The coordinate transformation $\mathbf{T}_{\mathsf{s}\to\mathsf{m}}$ rotates the frame of reference of the standard orientation used by the GAUSSIAN computation to the desired molecular frame of reference.

4.4 Results and discussion

Geometry optimizations and Raman computations were performed on the sulfate anion, three isotopologues of carbon tetrachloride, toluene and decanoic acid. The latter stands as a model for arachidic acid, which could not be computed at the desired level of theory with the available resources. I would like to acknowledge and thank Dr Mark Fox for performing the computations on the Hamilton cluster of Durham University.

Results presented here include computational Raman spectra and Raman tensors for selected fundamentals. Relevant sections of the GAUSSIAN log files are included in appendix D. The quantities are extracted manually for ordering into matrices and processed in MATLAB using three scripts: (1) to produce a three-dimensional plot of the molecule in GAUSSIAN's standard orientation to deduce the Euler angles needed for any transformation to the molecular frame of reference, (2) to plot Raman spectra and (3) to compute the Raman tensors. These scripts can also be found in appendix D.

The results obtained with GAUSSIAN are compared to the forms of the Raman tensors derived with the bond-polarisability model and to those found through symmetry considerations, tabulated in appendix C.1. See appendix A for more details on the symmetry and vibrations of relevant moieties. Our results are also compared to published literature.

Raman spectra are produced by placing a Lorentzian distribution at each of the computed wavenumbers with a representative full width at half maximum (fwhm) of 10 cm^{-1}. The Lorentzian function is used to model the collision broadening observed in liquids. The integrated intensity I_{v} of the peak from vibrational normal mode v is scaled to its Raman activity S_{v} and to its frequency ν_{v} as

$$I_{\mathsf{v}} \propto S_{\mathsf{v}} {\nu_{\mathsf{v}}}^3 \tag{4.56}$$

so that the relative intensities in the spectrum account for both the magnitude of the Raman tensor components (through S_{v}) as well as the photon count at the Raman frequency (through ν_{v}) as developed in equation 2.118. Note that the frequency is the absolute frequency in Hz of the scattered radiation, not the value presented in the log file, which is labelled as frequency though it is in fact a wavenumber. The frequency of the scattering depends on the wavelength of the laser that caused it. With a laser of 532 nm, the intensity scales according to

$$I_{\mathsf{v}} \propto S_{\mathsf{v}} \left(\frac{1}{532 \text{ nm}} - 10^{-7} \, \bar{\nu}_{\mathsf{v}} \right)^3 \tag{4.57}$$

while all geometrical affects are ignored for now. Though known to deviate from experimental observations, the computed wavenumbers of the modes are used without correction. Intensities are computed on the same scale of arbitrary units. These are therefore comparable between the computed spectra as long as these are convoluted with the same function. The spectra are drawn with a data point at every 0.1 cm^{-1}. The computed spectrum represents a Raman spectrum obtain from the isotropic fluid without the use of polarisation in the incident nor scattered light paths as described in section 2.5.2.

Values are generally rounded to 3 significant figures in the results presented below. In the Raman tensors, components of low values are rounded to the last decimal place of the larger three-digit significant figures for clarity. Occasionally, this leads to rounding to 0. In further calculations, the original, unrounded values are used.

4.4.1 Sulfate

The computational Raman spectrum of sulfate, given in figure 4.5, includes four bands. The symmetric stretch mode is predicted at 865 cm^{-1} as the strongest peak in the spectrum and the only one of A_1 symmetry. It is a polarised Raman line. The remaining lines are depolarised: one twofold degenerate E mode and two threefold degenerate F_2 modes. Assignment of the modes follows reference [126], though the computed wavenumbers are lower than their experimental values. The v_1 mode is the symmetric stretch of S−O bonds while v_2 is the pair-wise bending of O−S−O which is two-fold degenerate. v_3 and v_4 are triply degenerate modes, the first a set of stretching modes involving umbrella-like motions and the second a set of deformations in which the central sulfur atom moves relative to the surrounding oxygen atoms. See section A.5 for a mathematical expression of these modes.

Early Raman studies on sulfate solutions by Hester *et al.* [127] revealed that the sulfate anion is dissolved freely with a range of cations except for indium. Rull and Ohtaki [128] later showed that the position and width of the ν_1 band of sulfate is only marginally affected by the choice of alkali cation, speculating that this variation arised from hydration fluctuations. Matsumoto and co-workers [129] demonstrated that the cation only becomes relevant at 350°C and 25 MPa. A more recent study by Mabrouk *et al.* [126] confirmed the dependence of $\nu_1(SO_4^{2-})$ on the hydration state. In aqueous solution, this band could be fitted with a Voigt profile and they demonstrated linearity of its integrated intensity with the salt concentration independent of the common Na^+, K^+ or NH_4^+ cations.

The Raman tensors found for the four modes are tabulated in table 4.2. The form of the computed tensors is now compared to those derived by symmetry considerations (as summarised in table C.1). For the fully symmetric mode v_1, we have

$$\begin{pmatrix} a & 0 & 0 \\ 0 & a & 0 \\ 0 & 0 & a \end{pmatrix} = \begin{pmatrix} -16.1 & 0 & 0 \\ 0 & -16.1 & 0 \\ 0 & 0 & -16.1 \end{pmatrix} \tag{4.58}$$

Table 4.2: Vibrational modes of the sulfate anion and Raman tensors in its molecular frame of reference at B3LYP/6-311++G(d,p) theory level.

Mode	Species	$\bar{\nu}$ / cm^{-1}	S / $\mathrm{Å}^4\ \mathrm{amu}^{-1}$	$\boldsymbol{\alpha}_{\mathrm{v}}^{\mathrm{m}}$ / 10^{-42} C V^{-1} m^2
v_2	E	399	2.24	$\left\{\begin{pmatrix} -3.12 & 0 & 0 \\ 0 & -5.41 & 0 \\ 0 & 0 & 8.53 \end{pmatrix}, \begin{pmatrix} -8.05 & 0 & 0 \\ 0 & 6.73 & 0 \\ 0 & 0 & 1.32 \end{pmatrix}\right\}$
v_4	F_2	562	2.30	$\left\{\begin{pmatrix} 0 & -4.43 & 4.60 \\ -4.43 & 0 & -0.02 \\ 4.60 & -0.02 & 0 \end{pmatrix}, \begin{pmatrix} 0 & 4.30 & 4.13 \\ 4.30 & 0 & -2.28 \\ 4.13 & -2.28 & 0 \end{pmatrix}, \begin{pmatrix} 0 & 1.63 & 1.60 \\ 1.63 & 0 & 5.96 \\ 1.60 & 5.96 & 0 \end{pmatrix}\right\}$
v_1	A_1	865	48.6	$\begin{pmatrix} -16.1 & 0 & 0 \\ 0 & -16.1 & 0 \\ 0 & 0 & -16.1 \end{pmatrix}$
v_3	F_2	995	13.7	$\left\{\begin{pmatrix} 0 & -7.39 & -7.35 \\ -7.39 & 0 & -5.27 \\ -7.35 & -5.27 & 0 \end{pmatrix}, \begin{pmatrix} 0 & 6.81 & -9.00 \\ 6.81 & 0 & 3.01 \\ -9.00 & 3.01 & 0 \end{pmatrix}, \begin{pmatrix} 0 & 5.96 & 1.17 \\ 5.96 & 0 & -9.98 \\ 1.17 & -9.98 & 0 \end{pmatrix}\right\}$

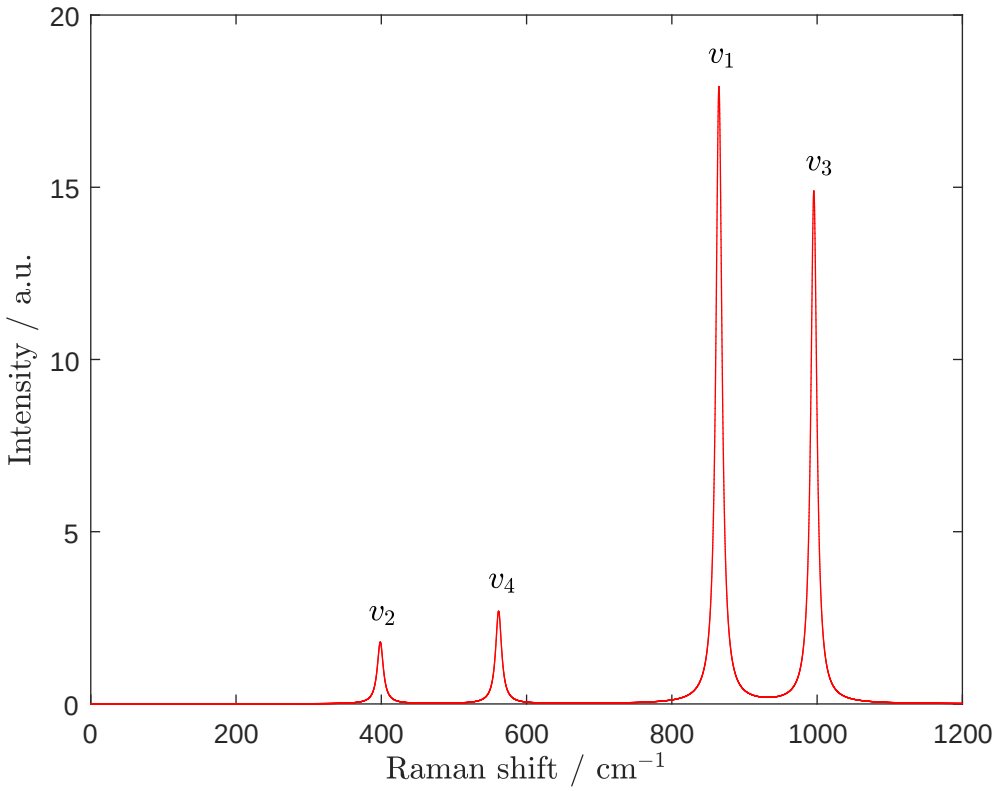

Figure 4.5: Computed Raman spectrum of sulfate in the gas phase at B3LYP/6-311++G(d,p) theory and convoluted with a Lorentzian of 10 cm^{-1} full width at half maximum.

where $a = -16.1 \cdot 10^{-42}$ C V^{-1} m^2 is read from the identity. The computed Raman tensor obeys the expected form. The remaining modes, all degenerate E and F_2 modes, do not appear to match our expectations. However, these Raman tensors are linear combinations of the orthogonal tensors of table C.1. We will now prove this for the v_2 mode of E-symmetry, and for the v_3 mode of F_2 symmetry. The Raman tensors of the v_4 mode can be decomposed in a similar fashion.

The squared sum of the symmetry-derived symbolic Raman tensors for the E mode of the T_d point group is equated to the squared sum of the computed, numerical tensors of the v_2 mode

$$\begin{pmatrix} b & 0 & 0 \\ 0 & b & 0 \\ 0 & 0 & -2b \end{pmatrix}^2 + 3 \begin{pmatrix} -b & 0 & 0 \\ 0 & b & 0 \\ 0 & 0 & 0 \end{pmatrix}^2 = \begin{pmatrix} -3.12 & 0 & 0 \\ 0 & -5.41 & 0 \\ 0 & 0 & 8.53 \end{pmatrix}^2 + \begin{pmatrix} -8.05 & 0 & 0 \\ 0 & 6.73 & 0 \\ 0 & 0 & 1.32 \end{pmatrix}^2 \tag{4.59}$$

which is given in 10^{-42} C V^{-1} m^2 and results in

$$\begin{pmatrix} 4b^2 & 0 & 0 \\ 0 & 4b^2 & 0 \\ 0 & 0 & 4b^2 \end{pmatrix} = \begin{pmatrix} 74.5 & 0 & 0 \\ 0 & 74.5 & 0 \\ 0 & 0 & 74.5 \end{pmatrix} \tag{4.60}$$

in units of 10^{-84} C^2 V^{-2} m^4. We solve for b to find

$$b = \pm 4.32 \cdot 10^{-42} \text{ C V}^{-1} \text{ m}^2 \tag{4.61}$$

where both the positive and negative solution are acceptable. This is a manifestation of multiplying the whole tensor by -1, which is of no consequence to the time-averaged Raman-scattered field. The first Raman tensor of the v_2 mode, $\boldsymbol{\alpha}^{\mathrm{m}}_{v_2(1)}$, can be reconstructed from the orthogonal basis by a weighted sum

$$w_1 \begin{pmatrix} b & 0 & 0 \\ 0 & b & 0 \\ 0 & 0 & -2b \end{pmatrix} + w_2\sqrt{3} \begin{pmatrix} -b & 0 & 0 \\ 0 & b & 0 \\ 0 & 0 & 0 \end{pmatrix} = \begin{pmatrix} -3.12 & 0 & 0 \\ 0 & -5.41 & 0 \\ 0 & 0 & 8.53 \end{pmatrix} \cdot 10^{-42} \text{ C V}^{-1} \text{ m}^2 \tag{4.62}$$

which represents the three dependent equations

$$\begin{aligned} bw_1 - \sqrt{3}bw_2 &= -3.12 \cdot 10^{-42} \text{ C V}^{-1} \text{ m}^2 \\ bw_1 + \sqrt{3}bw_2 &= -5.48 \cdot 10^{-42} \text{ C V}^{-1} \text{ m}^2 \\ -2bw_1 &= 8.53 \cdot 10^{-42} \text{ C V}^{-1} \text{ m}^2 \end{aligned} \tag{4.63}$$

Solving for the weighting factors w_1 and w_2 of the symmetry-adapted tensors, using the positive value for b just found, results in

$$\text{for } v_2(1) \begin{cases} w_1 = -0.988 \\ w_2 = -0.153 \end{cases} \tag{4.64}$$

For the second tensor of the E-mode, $\boldsymbol{\alpha}^{\mathrm{m}}_{v_2(2)}$, we find

$$\text{for } v_2(2) \begin{cases} w_1 = 0.153 \\ w_2 = 0.988 \end{cases} \tag{4.65}$$

which is exactly the opposite of the previous solution. The weights are normalized: ${w_1}^2 + {w_2}^2 = 1$ for each of the degenerate modes (1) and (2). Furthermore, each symmetry-adapted tensor contributes equally to the set of computed tensors, *i.e.* $w_1(1)^2 + w_1(2)^2 = w_2(1)^2 + w_2(2)^2 = 1$. This demonstrates that the computed Raman tensors for the two-fold degenerate mode are linear combinations of the two orthogonal tensors expressed in a symmetry-adapted basis.

The three-fold degenerate modes v_3 and v_4 similarly consist of linear combinations of

symmetry-adapted orthogonal solutions to the vibrational problem. Only the off-diagonal elements of the Raman tensors are non-zero. Squaring the components and summing the tensors of the v_3 band provides

$$\begin{pmatrix} 0 & c & 0 \\ c & 0 & 0 \\ 0 & 0 & 0 \end{pmatrix}^2 + \begin{pmatrix} 0 & 0 & c \\ 0 & 0 & 0 \\ c & 0 & 0 \end{pmatrix}^2 + \begin{pmatrix} 0 & 0 & 0 \\ 0 & 0 & c \\ 0 & c & 0 \end{pmatrix}^2 = \begin{pmatrix} 0 & 40.8 & 40.8 \\ 40.8 & 0 & 40.8 \\ 40.8 & 40.8 & 0 \end{pmatrix} \cdot 10^{-84}\ \mathrm{C}^2\ \mathrm{V}^{-2}\ \mathrm{m}^4 \tag{4.66}$$

from which we obtain

$$c = \pm 6.39 \cdot 10^{-42}\ \mathrm{C}\ \mathrm{V}^{-1}\ \mathrm{m}^2\ . \tag{4.67}$$

Deconstruction of the three computational Raman tensors $\boldsymbol{\alpha}^{\mathrm{m}}_{v_3(1)}$, $\boldsymbol{\alpha}^{\mathrm{m}}_{v_3(2)}$ and $\boldsymbol{\alpha}^{\mathrm{m}}_{v_3(3)}$ provides the weighting factors. These are readily found to be

$$\text{for } v_3(1) \begin{cases} w_1 = -0.6934 \\ w_2 = 0.7205 \\ w_3 = -0.0038 \end{cases} \tag{4.68}$$

$$\text{for } v_3(2) \begin{cases} w_1 = 0.6739 \\ w_2 = 0.6467 \\ w_3 = -0.3572 \end{cases} \tag{4.69}$$

$$\text{for } v_3(3) \begin{cases} w_1 = 0.2549 \\ w_2 = 0.2502 \\ w_3 = 0.9340 \end{cases} \tag{4.70}$$

which are all normalised in two ways. The weights that form one linear combination are normalised (${w_1}^2 + {w_2}^2 + {w_3}^2 = 1$) as well as the contribution of each symmetry-adapted basis tensor to the three computational linear combinations ($w_1(1)^2 + w_1(2)^2 + w_1(3)^2 = 1$). Our computational result thus carries the same information as the symmetry-derived Raman tensors whilst being expressed in a different and equally valid orthogonal basis of vibrational patterns.

4.4.2 Carbon tetrachloride

Computations were performed on the three most abundant isotopologues of carbon tetrachloride: $^{12}C^{35}Cl_4$, $^{12}C^{35}Cl_3{}^{37}Cl$ and $^{12}C^{35}Cl_2{}^{37}Cl_2$. Nine vibrational normal modes occur in each. As the point group symmetry of the isotopologues varies, so do the symmetry species of the normal modes and their Raman tensors.

The Raman spectra of the three isotopologues are presented in figure 4.6 with a combined spectrum based on the natural abundance of each isotope. Similar frequencies have recently been published by Wallington *et al.* [130] for the infrared spectrum of CCl_4 using

different basis sets though ignoring isotope effects. The $^{12}C^{35}Cl_4$ isotopologue, which has T_d point group symmetry, exhibits the same four vibrational modes as the sulfate anion. The degeneracy of its E and F_2 modes is successively lifted by the $^{12}C^{35}Cl_3{}^{37}Cl$ and $^{12}C^{35}Cl_2{}^{37}Cl_2$ isotopologues, which conform to the C_{3v} and C_{2v} point group, respectively. This can be observed in the bottom row of figure 4.6, where each peak is resolved into its constituent modes. The correlation between the modes is presented in table A.6 and discussed in section A.5.

The Raman tensors obtained for the three isotopologues are included in tables 4.3 to 4.5. The GAUSSIAN output is specified within the standard orientation it assigns to the T_d point group: the oxygen atoms at four corners of a cube which has its sides parallel to the three Cartesian axes. This orientation is retained for all isotopologues as the program considers charge rather than mass in assigning point group symmetry. However, this standard orientation is only appropriate for the T_d isotopologue. The others require a transformation of the axes through a transformation matrix as in equation 2.13. Section D.3 illustrates the geometries in the computational and molecular frames of reference. The Raman tensors of the C_{3v} isotopologue $^{12}C^{35}Cl_3{}^{37}Cl$ have been transformed to the symmetry-based molecular coordinates by three successive passive rotations over the Euler angles

$$(\alpha, \beta, \gamma) = (45^\circ, \frac{1}{2}\tau, 90^\circ) \tag{4.71}$$

with τ the tetrahedral angle defined in equation 4.12. For the C_{2v} isotopologue $^{12}C^{35}Cl_2{}^{37}Cl_2$, the transformation involves only one rotation with

$$(\alpha, \beta, \gamma) = (45^\circ, 0, 0)\ . \tag{4.72}$$

As with sulfate, the computational Raman tensors for the degenerate modes are linear combinations of the symmetry-derived Raman tensors of table C.1. The forms of the Raman tensors thus obtained are in agreement with those predicted on the grounds of symmetry.

Anharmonic modes

Experimental Raman spectra of carbon tetrachloride include anharmonic features in addition to the four peaks predicted in our harmonic computation. These include overtones, combination bands and Fermi resonances arising from the four fundamental bands. In discussing these modes below, the fundamental bands observed in Raman spectra of an isotopic mixture are labelled ν_1 to ν_4 as for the T_d species, implying all correlated modes in the various isotopologues. This assignment follows the literature consensus.

The strongest anharmonic feature is the $\nu_1 + \nu_4 \approx \nu_3$ Fermi doublet. The combination band $\nu_1 + \nu_4$ resonates with the ν_3 fundamental as both belong to the same symmetry species[‡], have the same frequency and involve the same atoms. Though the frequencies in

[‡] F_2 in the T_d point group, the A_1 or E species in the C_{3v} point group and the A_1, B_1 or B_2 species

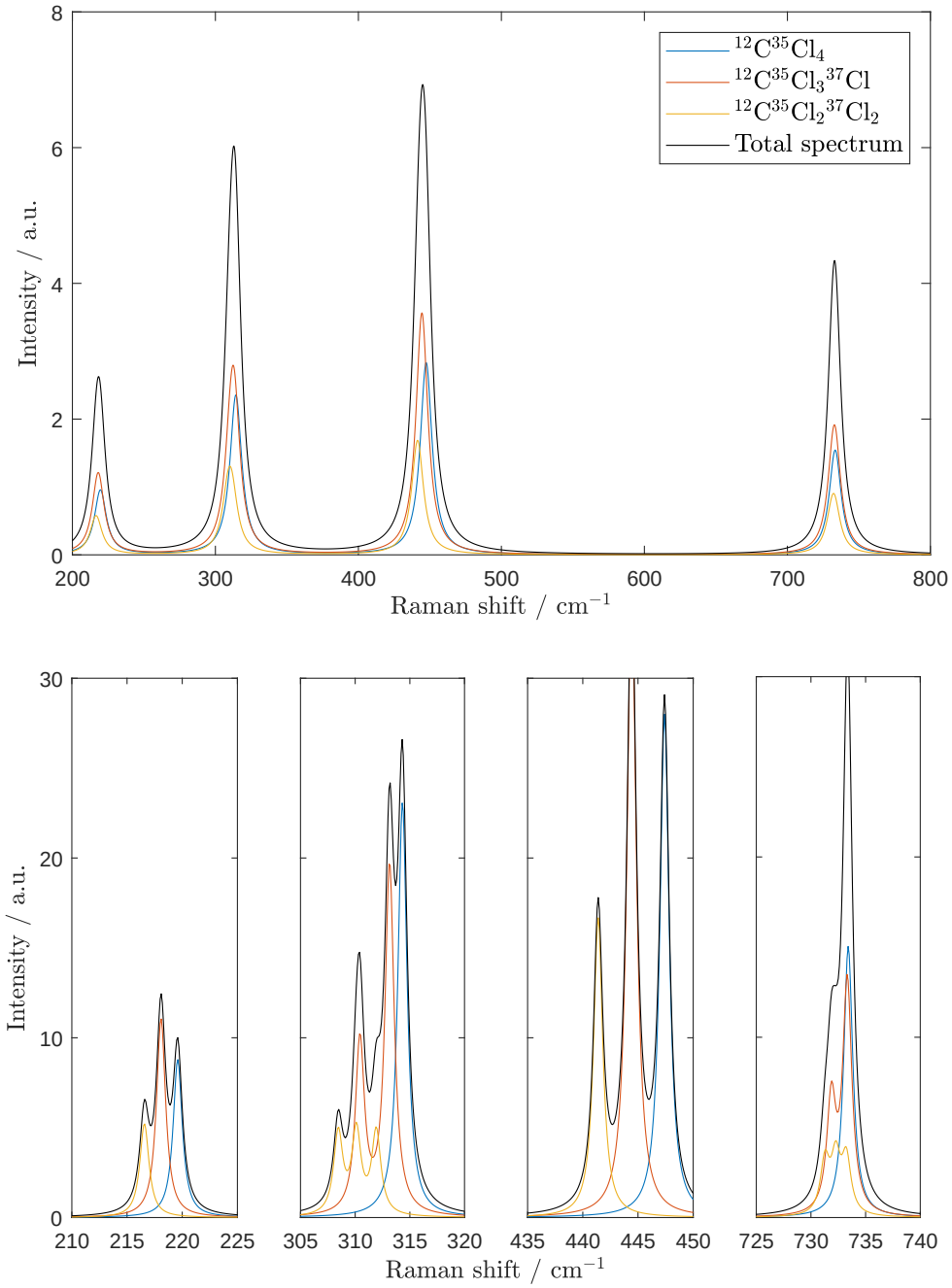

Figure 4.6: Computed Raman spectra of the three most abundant isotopologues of carbon tetrachloride in the gas phase from B3LYP/6-311++G(d,p) theory. The spectra are convoluted with a Lorentzian of 10 cm^{-1} (top) and 1 cm^{-1} (bottom) full width at half maximum. The total spectrum is the sum of the three spectra, each scaled to its natural abundance.

our computation do not match exactly, this Fermi resonance is well-known and features in many textbooks and reference works, including [63, 73, 77].

The occurrence of the Fermi doublet suggests that the two difference bands $\nu_3 - \nu_4$ and $\nu_3 - \nu_1$ might also be in resonance with the ν_1 and ν_4 fundamentals. Both are allowed by symmetry, though $\nu_3 - \nu_4 \approx \nu_1$ only in a selection of modes. The contribution of this combination band to the overall ν_1 profile was quantified by Gaynor *et al.* in [131]. He also reported on thermally populated vibrational states (so-called hot bands) that contribute to the observed ν_1 band at room temperature [132]. These appear at slightly lower wavenumber than the fundamental transitions from the ground to the first excited state of the vibrational mode.

Another Fermi resonance is expected from $2\nu_2 \approx \nu_1$, the first overtone of the ν_2 mode with the ν_1 fundamental. The overtone includes the A_1 species to which the fundamental belongs (in all three point groups of the isotopologues). In a detailed experimental study of the carbon tetrachloride spectrum by Chakraborty [133], it was not reported as a distinguishable feature. Various other first overtones, including $2\nu_4$, were observed as distinct peaks in the spectrum.

How does this anharmonicity affect the predicted Raman tensors? For an overtone, the Raman tensor is expected to be similar to the Raman tensor of its fundamental transition. In the harmonic approximation, the frequency of the vibrational motion is doubled while the motion of the atoms follows an identical path to that of the fundamental, *i.e.* the vibrational normal coordinate $Q_{\mathsf{v}}(t)$ is replaced by $Q_{\mathsf{v}}(t/2)$ for a first overtone.

In a combination band, the vibration is a linear combination of the two interacting modes. The Raman tensor of the resulting mode can thus also be described as a linear combination of the Raman tensors of the coupled fundamentals. The same holds for resonances in which three fundamentals are coupled. Our harmonic computations do not provide information on the relative contribution of each of these modes. However, the major spectral features arise from harmonic effects and anharmonic effects can be ignored in many cases. In our work, the significance of anharmonicity is assessed in the analysis of our experimental spectra and in comparing these to the computed predictions.

in the C_{2v} point group. This follows from correlation table A.6 and the multiplication rules of symmetry species.

Table 4.3: Vibrational modes of $^{12}C^{35}Cl_4$ (point group T_d) and Raman tensors in its molecular frame of reference at B3LYP/6-311++G(d,p) theory level.

Mode	Species	$\bar{\nu}$ / cm^{-1}	S / $Å^4$ amu^{-1}	$\boldsymbol{\alpha}_v^m$ / 10^{-42} C V^{-1} m^2
v_2	E	220	3.08	$\left\{\begin{pmatrix}-12.8 & 0 & 0\\ 0 & 2.3 & 0\\ 0 & 0 & 10.5\end{pmatrix}\right.$ $\left.\begin{pmatrix}-4.8 & 0 & 0\\ 0 & 13.4 & 0\\ 0 & 0 & -8.7\end{pmatrix}\right\}$
v_4	F_2	314	5.52	$\left\{\begin{pmatrix}0 & 12.8 & 0.4\\ 12.8 & 0 & 3.3\\ 0.4 & 3.3 & 0\end{pmatrix}\right.$ $\begin{pmatrix}0 & -3.3 & -0.9\\ -3.3 & 0 & 12.8\\ -0.9 & 12.8 & 0\end{pmatrix}$ $\left.\begin{pmatrix}0 & -0.6 & 13.2\\ -0.6 & 0 & 0.8\\ 3.2 & 0.8 & 0\end{pmatrix}\right\}$
v_1	A_1	447	20.5	$\begin{pmatrix}-14.6 & 0 & 0\\ 0 & -14.6 & 0\\ 0 & 0 & -14.6\end{pmatrix}$
v_3	F_2	733	3.85	$\left\{\begin{pmatrix}0 & -2.98 & -6.56\\ -2.98 & 0 & 0.52\\ -6.56 & 0.52 & 0\end{pmatrix}\right.$ $\begin{pmatrix}0 & -2.25 & 0.48\\ -2.25 & 0 & -6.85\\ 0.48 & -6.85 & 0\end{pmatrix}$ $\left.\begin{pmatrix}0 & -6.18 & 2.98\\ -6.18 & 0 & 2.24\\ 2.98 & 2.24 & 0\end{pmatrix}\right\}$

Table 4.4: Vibrational modes of $^{12}C^{35}Cl_3{}^{37}Cl$ (point group C_{3v}) and Raman tensors in its molecular frame of reference at B3LYP/6-311++G(d,p) theory level.

Mode	Species	$\bar{\nu}$ / cm^{-1}	S / $Å^4$ amu^{-1}	$\boldsymbol{\alpha}_v^m$ / 10^{-42} C V^{-1} m^2
v_6	E	218	3.04	$\begin{pmatrix} 5.18 & 4.20 & 7.53 \\ 4.20 & -5.18 & -6.11 \\ 7.53 & -6.11 & 0 \end{pmatrix}$ $\begin{pmatrix} -4.20 & 5.18 & -6.11 \\ 5.18 & 4.20 & -7.53 \\ -6.11 & -7.53 & 0 \end{pmatrix}$
v_3	A_1	310	5.41	$\begin{pmatrix} -7.3 & 0 & 0 \\ 0 & -7.3 & 0 \\ 0 & 0 & 15.5 \end{pmatrix}$
v_5	E	313	5.48	$\begin{pmatrix} -9.50 & -5.31 & 6.51 \\ -5.31 & 9.50 & -3.64 \\ 6.51 & -3.64 & 0 \end{pmatrix}$ $\begin{pmatrix} -5.31 & 9.50 & 3.64 \\ 9.50 & 5.31 & 6.51 \\ 3.64 & 6.51 & 0 \end{pmatrix}$
v_2	A_1	444	20.2	$\begin{pmatrix} -14.7 & 0 & 0 \\ 0 & -14.7 & 0 \\ 0 & 0 & -14.1 \end{pmatrix}$
v_1	A_1	732	3.72	$\begin{pmatrix} 4.24 & 0 & 0 \\ 0 & 4.24 & 0 \\ 0 & 0 & -8.07 \end{pmatrix}$
v_4	E	733	3.86	$\begin{pmatrix} 0.23 & 5.90 & -0.16 \\ 5.90 & -0.23 & 4.18 \\ -0.16 & 4.18 & 0 \end{pmatrix}$ $\begin{pmatrix} -5.90 & 0.23 & 4.18 \\ 0.23 & 5.90 & 0.16 \\ 4.18 & 0.16 & 0 \end{pmatrix}$

Table 4.5: Vibrational modes of $^{12}C^{35}Cl_2{}^{37}Cl_2$ (point group C_{2v}) and Raman tensors in its molecular frame of reference at B3LYP/6-311++G(d,p) theory level.

Mode	Species	$\bar{\nu}$ / cm^{-1}	S / $Å^4$ amu^{-1}	$\boldsymbol{\alpha}_v^m$ / 10^{-42} C V^{-1} m^2
v_4	A_1	217	3.00	$\begin{pmatrix} -6.5 & 0 & 0 \\ 0 & -7.0 & 0 \\ 0 & 0 & 13.5 \end{pmatrix}$
v_5	A_2	217	3.00	$\begin{pmatrix} 0 & -11.7 & 0 \\ -11.7 & 0 & 0 \\ 0 & 0 & 0 \end{pmatrix}$
v_9	B_2	308	5.34	$\begin{pmatrix} 0 & 0 & 0 \\ 0 & 0 & 13.1 \\ 0 & 13.1 & 0 \end{pmatrix}$
v_3	A_1	310	5.39	$\begin{pmatrix} -13.0 & 0 & 0 \\ 0 & 13.3 & 0 \\ 0 & 0 & 0.7 \end{pmatrix}$
v_7	B_1	312	5.43	$\begin{pmatrix} 0 & 0 & 13.2 \\ 0 & 0 & 0 \\ 13.2 & 0 & 0 \end{pmatrix}$
v_2	A_1	441	20.0	$\begin{pmatrix} -14.9 & 0 & 0 \\ 0 & -14.1 & 0 \\ 0 & 0 & -14.5 \end{pmatrix}$
v_8	B_2	731	3.69	$\begin{pmatrix} 0 & 0 & 0 \\ 0 & 0 & -7.08 \\ 0 & -7.08 & 0 \end{pmatrix}$
v_1	A_1	732	3.79	$\begin{pmatrix} 7.31 & 0 & 0 \\ 0 & -7.02 & 0 \\ 0 & 0 & 0.18 \end{pmatrix}$
v_6	B_1	733	3.89	$\begin{pmatrix} 0 & 0 & 7.25 \\ 0 & 0 & 0 \\ 7.25 & 0 & 0 \end{pmatrix}$

4.4.3 Decanoic acid

Decanoic acid serves as a model for arachidic acid and more generally as a model for a material with a stretched alkane chain. The computational Raman spectrum is given in figure 4.7 with a selection of modes and their Raman tensors listed in table 4.7. Our focus is on the C−H stretching region, which is the strongest part of the spectrum.

The computational results are included in section D.5 with the atomic positions presented in both the standard orientation s and molecular frame m. The transformation from the computational to the molecular frame of reference is effected by two successive rotations over Euler angles

$$(\alpha, \beta, \gamma) = (-48.39^\circ, 90^\circ, 0) \; . \tag{4.73}$$

The first rotation brings the chain of carbon atoms along the positive y axis. A further rotation about the x-axis is needed to bring the chain of carbon atoms parallel to $\hat{\mathbf{z}}^{\mathsf{m}}$ and in the $x^{\mathsf{m}}z^{\mathsf{m}}$ plane. The first Euler angle is found through the inner product (see equation 5.102) of a vector giving the direction of the carbon chain and $\hat{\mathbf{y}}^{\mathsf{s}}$, both in the original computational frame of reference. The first vector is obtained by a linear fit through the carbon positions.

Decanoic acid has 90 vibrational normal modes, all of which are Raman active. Its Raman spectrum, appropriately broadened as in figure 4.7, only shows 11 bands. Overlapping Raman bands are grouped in distinct frequency ranges due to the repetitive structure of the molecule. These are described collectively and include the following vibrational modes:

- $\omega(\mathrm{CH_2})$, wagging of $\mathrm{CH_2}$ groups around 1060 $\mathrm{cm^{-1}}$,
- $\tau(\mathrm{CH_2})$, twisting of $\mathrm{CH_2}$ groups near 1320 $\mathrm{cm^{-1}}$,
- $\delta(\mathrm{CH_2})$, scissoring or bending of the H−C−H bond angles around 1490 $\mathrm{cm^{-1}}$,
- ν(C=O) and ν(OH), distinct bond stretching modes of the carboxylic acid group at 1812 and 3759 $\mathrm{cm^{-1}}$, respectively, and
- ν(CH), the C−H stretch region of the spectrum ranging from 2991 to 3082 $\mathrm{cm^{-1}}$.

These computed frequencies are an overestimate of what has been observed experimentally in molecules with an alkane chain (amongst many others [98, 134, 135] and this work). In our experiments, the fatty acid is bound to the hemisphere surface through its COOH group. This affects the ν(C=O) and ν(OH) modes and their Raman tensors. These modes are therefore not considered in our analysis. Our focus is on the ν(CH) region which has the advantage of strong Raman scattering. It accounts for 80% of the Raman scattering activity computed for decanoic acid and is expected to be even higher for molecules with longer alkane chains. The five strongest modes in this region, numbered 73, 76, 80, 81 and 89, account for 60% of the computed total Raman scattering. These form 75% of the activity of the C−H stretch region.

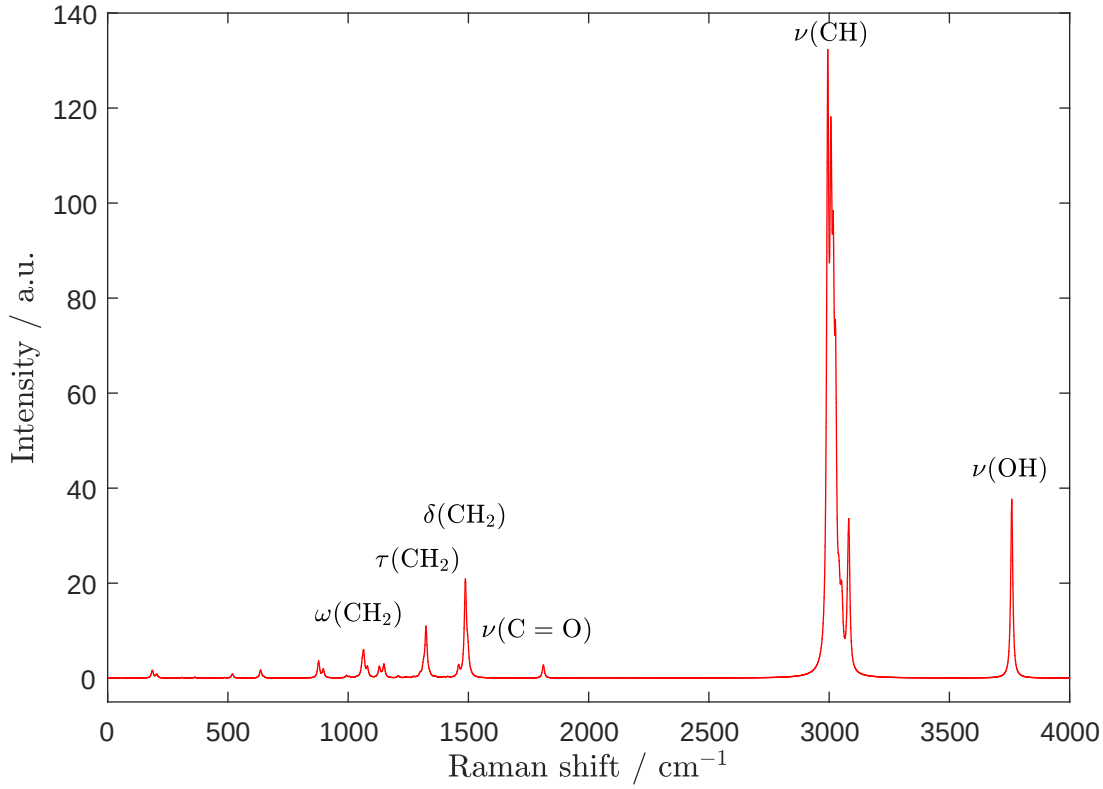

Figure 4.7: Computed Raman spectra of decanoic acid in the gas phase from B3LYP/6-311++G(d,p) theory, convoluted with a Lorentzian of 10 cm^{-1} full width at half maximum.

The C−H stretch region

Table 4.7 presents selected Raman tensors of decanoic acid, including all modes of the ν(CH) band along with the strongest bending mode $\delta(CH_2)$. The computed ν(CH) Raman band is presented in figure 4.8. The overall Raman scattering activity in the ν(CH) band is split between 70.6% A' and 29.4% A'' modes. The methylene modes give rise to 78.8% of the ν(CH) band (of which 51.4% in A' and 27.4% in A'' modes), while modes localised to the single methyl group represent 21.2% (of which 19.2% in A' and 2.1% in A'' modes) of the scattering activity.

The Raman scattering activity is clearly not proportional to the number of hydrogen or carbon atoms involved in each mode. This is consistent with *ab-initio* computations of Kathleen M. Gough and colleagues reported in a series of publications briefly reviewed in [114]. Their work focussed on the polarisability of hydrocarbons and its change upon stretching an individual bond in the molecule. They concluded that there is no single tensor for the polarisability nor its derivative that describes the C−H bond in general. It has to be considered as part of the molecule. Only the CH_2 and CH_3 group polarisabilities were found to be transferable [136, 137]. The polarisability derivatives are not.

Most of their work was limited to the computation of the trace of the polarisability

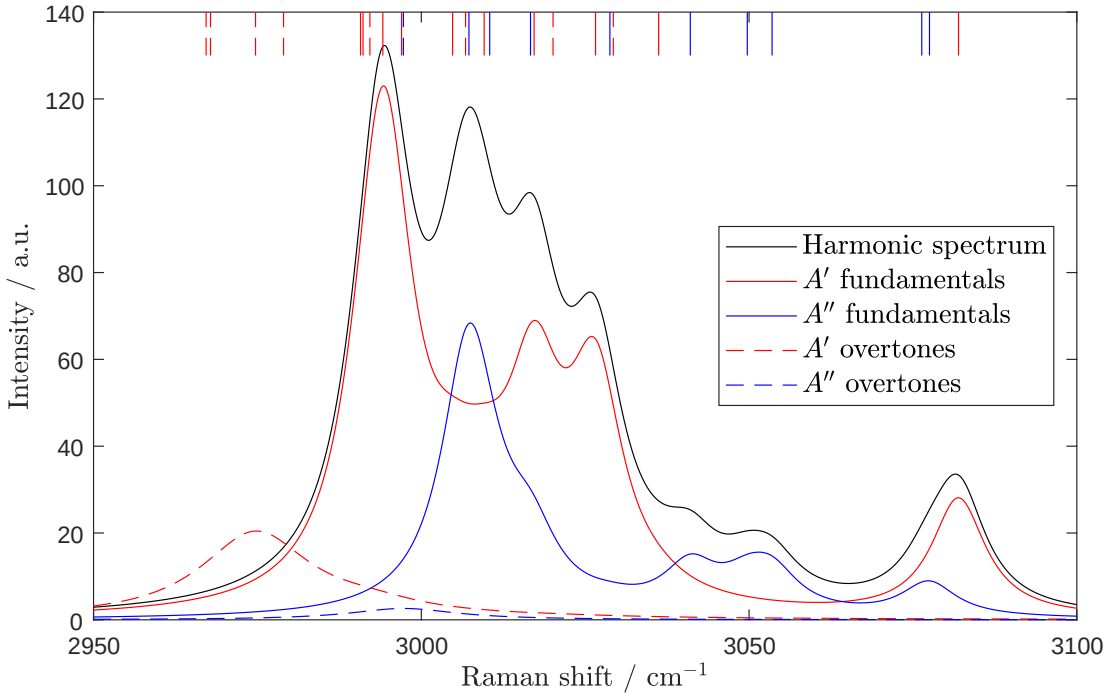

Figure 4.8: Computed harmonic Raman spectrum of the C−H stretch region of decanoic acid in the gas phase from B3LYP/6-311++G(d,p) theory, convoluted with a Lorentzian of 10 cm^{-1} full width at half maximum. The spectrum is split into modes belonging to the A' and A'' symmetry species. The first overtone bands are predicted by doubling the frequency of the harmonic fundamental modes, which also doubles their bandwidth. Central frequencies of individual modes are indicated at the top of the spectrum.

tensor (α_{xx}, α_{yy} and α_{zz}) and the mean polarisability derivative with respect to bond elongation $\partial\bar{\alpha}/\partial r$. Their choice of axes was such that the polarisability is ellipsoidal (*i.e.* the tensor has no off-diagonal components), though this is not necessarily the case for the polarisability derivatives. However, off-diagonal elements of the polarisability derivative tensor were not computed by Gough's team. Their results therefore only apply to Raman scattering from fully symmetric CH stretch modes (what they term trace Raman scattering).

Table 4.6 summarises the polarisability derivative tensors as published by Gough in [136] for short alkane chains. This is her only publication in which she includes the diagonal components $\partial\alpha_{xx}/\partial r$, $\partial\alpha_{yy}/\partial r$ and $\partial\alpha_{zz}/\partial r$ of the polarisability derivative in addition the their mean value. These were estimated numerically by displacing the hydrogen atoms from their equilibrium geometry and computing the polarisability of the molecule in GAUSSIAN86 using HF/D95** theory. The omission of electron correlation in the near-Hartree-Fock method appeared to be cancelled by the static nature of the calculation (as opposed to a dynamic calculation in which the laser frequency is included). The choice of axis by Gough requires a rotation $\mathbf{R}_z(90°)$ to agree with our definition for

Table 4.6: Polarisability derivatives of alkanes with respect to stretching of individual C−H bonds from K.M. Gough's computations [136] given in our molecular frame of reference.

Molecule	C−H bond location	$\boldsymbol{\alpha}'^{\mathrm{m}}_{\mathrm{C-H}}$ / 10^{-30} C V^{-1} m
methane		$\begin{pmatrix} 1.057 & 0 & 0 \\ 0 & 1.057 & 0 \\ 0 & 0 & 1.057 \end{pmatrix}$
ethane		$\begin{pmatrix} 1.258 & 0 & 0 \\ 0 & 1.258 & 0 \\ 0 & 0 & 0.799 \end{pmatrix}$
propane	methylene	$\begin{pmatrix} 1.448 & 0 & 0 \\ 0 & 1.639 & 0 \\ 0 & 0 & 0.314 \end{pmatrix}$
propane	methyl, in plane	$\begin{pmatrix} 0.797 & 0 & 0 \\ 0 & 0.240 & 0 \\ 0 & 0 & 2.485 \end{pmatrix}$
propane	methyl, out of plane	$\begin{pmatrix} 1.141 & 0 & 0 \\ 0 & 1.655 & 0 \\ 0 & 0 & 0.362 \end{pmatrix}$
trans-butane	methylene	$\begin{pmatrix} 1.272 & 0 & 0 \\ 0 & 1.508 & 0 \\ 0 & 0 & 0.407 \end{pmatrix}$
trans-butane	methyl, in plane	$\begin{pmatrix} 1.194 & 0 & 0 \\ 0 & 0.251 & 0 \\ 0 & 0 & 2.176 \end{pmatrix}$
trans-butane	methyl, out of plane	$\begin{pmatrix} 0.993 & 0 & 0 \\ 0 & 1.608 & 0 \\ 0 & 0 & 0.519 \end{pmatrix}$
trans-pentane	methyl, in plane	$\begin{pmatrix} 0.770 & 0 & 0 \\ 0 & 0.256 & 0 \\ 0 & 0 & 2.773 \end{pmatrix}$

the alkane chain. This comes down to swapping the xx and yy components of each tensor.

A number of observations can be made from Gough's work on C−H bonds in stretched alkane chains.

1. All polarisability derivatives are positive: longer bonds increase the polarisability of the molecule [136, 138, 139].

2. The highest polarisabilities, as well as polarisability derivatives, were found for C−H bonds oriented along the direction of the carbon skeleton of the chain [136].

3. The polarisability derivative increases non-linearly towards the ends of the chain [136].

4. The length of the C−H bond does not affect its polarisability derivative [138].

5. For the in-plane C−H bond in the methyl group, the mean polarisability derivative $\partial\bar{\alpha}/\partial r$ increases steadily with increasing chain length before plateauing from about dodecane [136, 138].

6. For the C−H bonds in the methylene groups, $\partial\bar{\alpha}/\partial r$ reduces with increased chain length and stabilises at nonane [138].

An atoms-in-molecules analysis by Gough *et al.* [140] showed that the polarisability derivative arises from charge transfer across the molecule and changes in the atomic dipoles involved in the stretched bond. Both effects are greater towards the ends of the chain and for bonds in the plane of the carbon atoms. Stretching the in-plane methyl C−H bond therefore produces the greatest change in molecular polarisability. All other distinct C−H bonds are oriented out of the carbon plane and stretching these results in lower polarisability derivatives. This explains why the methyl modes in our analysis of decanoic acid are disproportionately strong.

We now wish to compare Gough's results to our own. As all of her results only apply to symmetric stretch modes, we must compare them with a Raman tensor of such a mode. Using her values for the polarisability derivative of the central C−H bonds in *trans*-butane [136] (table 4.6) we come to a normalised polarisability derivative tensor for the methylene C−H stretch

$$\boldsymbol{\alpha'}^{\mathsf{m}}_{\mathrm{C-H}} = \begin{pmatrix} 0.631 & 0 & 0 \\ 0 & 0.749 & 0 \\ 0 & 0 & 0.202 \end{pmatrix}$$

which is not that different from the normalized Raman tensor of the in-phase symmetric CH_2 stretch (mode 73) in our computation of decanoic acid

$$\boldsymbol{\alpha}^{\mathsf{m}}_{73} = \begin{pmatrix} 0.624 & 0 & 0.001 \\ 0 & 0.714 & 0 \\ 0.001 & 0 & 0.316 \end{pmatrix} .$$

The zz components of the latter is larger, mainly at the cost of the yy component. As shown in Gough's work, this is due to the longer chain. Other vibrational modes cannot be compared as easily, since the polarisability derivatives with respect to stretching of individual C−H bonds cannot be combined to find the polarisability derivative of a vibrational pattern.

Let us now return to discussing the features of the computed spectrum (figure 4.8) and the computed Raman tensors (table 4.7) in more detail. The vibrational modes in the ν(CH) band arise from collective as well as localised motion of the C−H bonds in the methyl and methylene groups. The symmetry of the isolated groups is reduced to C_s when these form part of a stretched, linear alkane and transforms rotational motion into molecular vibrations. It also lifts the degeneracy of the E modes in methyl. The Raman tensors are unaffected if the molecular vibrational motion closely resembles that of the

isolated moiety. Vibrations that involve collective motion of groups in the molecule give rise to Raman tensors of lower symmetry forms.

Modes 80, 88 and 89 mainly arise from the methyl group at the end of the molecule. A limited number of methylene groups is weakly involved in these vibrations. Mode 80 is the strongest mode arising from the CH_3 group. It is the symmetric methyl stretch, $\nu_s(CH_3)$, of A' symmetry at 3017 cm^{-1}. Modes 88 and 89 arise from the splitting of the degenerate asymmetric E mode of an isolated methyl group belonging to the C_{3v} point group. Mode 88, at 3078 cm^{-1} and of A'' symmetry, is the antisymmetric stretching of the two C−H bonds that are out of the molecular plane. It is therefore labelled $\nu_a(CH_3)$, though it is similar to a methylene antisymmetric stretch and the normal mode weakly involves such motion throughout the chain. Mode 89, at 3082 cm^{-1} and of A' symmetry, is another methyl symmetric stretch $\nu_s(CH_3)$ and mainly involves its in-plane C−H bond. As shown by Gough, stretching of this bond results in a relatively large change in the polarisability derivative and thus a large scattering factor. In concluding our discussion of the methyl modes, we compare equation 4.44 to table 4.7 and note that the Raman tensors of the methyl modes have the same form in the molecular frame of reference, irrespective of the point group symmetry. This is due to our choice of axes and a matching definition of the degenerate normal mode.

The methylene modes fall into two categories: symmetric stretches, $\nu_s(CH_2)$, belonging to the A' symmetry species, and antisymmetric stretches, $\nu_a(CH_2)$, of the A'' species. The Raman tensors obtained through computation in GAUSSIAN (table 4.7) agree with the forms expected for the C_s point group (table C.1). The Raman tensors for isolated methylene were derived with the bond-polarisability model in section 4.1.2. The computational A'-mode tensors have small, but non-zero xz and zx components while these are zero for an isolated methylene group in the bond-polarisability model, given in equation 4.21. For the A'' modes, this is the case with the yz and zy components, which are zero in the Raman tensor for the antisymmetric stretch mode of methylene given in equation 4.22. Though the vibrational modes and their Raman tensors follow the molecular point group symmetry, they retain the features of isolated methylene moieties.

The atomic motion in the $\nu_s(CH_2)$ modes displays particular phase relations between the CH_2 groups. Modes 73 and 81 are in-phase symmetric stretches and produce strong Raman scattering. The first involves motion of the methylene groups in the centre of the chain while the latter is localised near the carboxylic acid end of the molecule.

Mode 73, at 2994 cm^{-1}, is predicted to be the strongest mode in the whole spectrum. It is the equivalent of the only Raman active mode in an infinite methylene chain: the in-phase stretch of all C−H bonds. In the finite chain, the amplitude of the atomic motion dampens towards the ends of the chain. The other modes involve a limited number of localised CH_2 groups, oscillating with a distinct phase relation. In longer chains, the in-phase symmetric mode (73 in our case) increases in strength whereas the localised modes only increase in number.

Mode 81 can be seen as complementary to mode 80, each being localised at opposite

ends of the chain. Though the scattering activity is similar, their Raman tensors differ. This is mainly due to the participation of an in-plane C−H bond in the methyl mode which contributes strongly to the zz component of $\boldsymbol{\alpha}^{\mathsf{m}}_{80}$. The atoms of the carboxylic acid group do not participate in the C−H stretch modes at all. Various out-of-phase symmetric stretch modes, including 71, 72, 74, 75 and 77, give rise to weaker scattering, though most of these are still stronger than modes in any other region of the spectrum.

The antisymmetric stretch modes, $\nu_a(\mathrm{CH_2})$, similarly display phase relations and localisation of the atomic motion in its vibrational normal modes of the ν(CH) band. Mode 76 is the strongest antisymmetric stretch mode, localised in the centre of the chain and appears at 3007 cm^{-1}. Mode 79, at 3017 cm^{-1}, involves the methylene groups of the whole chain, but is weaker. The five remaining $\nu_a(\mathrm{CH_2})$ modes have various phase relations and are localised in different parts of the chain (*i.e.* the phase as well as amplitude of the atomic motion varies over the length of the chain). These modes are even weaker and appear at higher Raman shift.

The Raman tensors of decanoic acid are compared in figure 4.9. The zero-valued components are omitted from the plots. The non-zero, unique components of each tensor are normalised (*i.e.* divided by the square root of the summed squared components) and brought on a positive scale by multiplication by -1 if the sum of the components is negative. This facilitates comparison of the relative values of the Raman tensor components. The A' and A'' modes are readily discriminated. Further divisions into sets of modes can be made, based in this plot only. Five sets can be identified in the ν(CH) band, which agree with the following assignments:

- modes 71 to 75 and 81, all $\nu_s(\mathrm{CH_2})$ modes of the A' species,
- modes 76, 78, 79, 82, 84, 85 and 86, all $\nu_a(\mathrm{CH_2})$ modes of A'' symmetry,
- mode 80, a $\nu_s(\mathrm{CH_3})$ mode of the A' species,
- modes 87 and 88, a $\nu_a(\mathrm{CH_2})$ and $\nu_a(\mathrm{CH_3})$ mode of A'' symmetry, and finally
- mode 89, another $\nu_s(\mathrm{CH_3})$ mode belonging to the A' species.

The Raman tensors group according to their vibrational mode. These are similar, irrespective or their scattering activity. This suggests that a representative Raman tensor could be used for a set of modes in a modelling approach, rather then computing every mode individually.

Fermi resonance of A' modes

Experimental spectra of hydrocarbons are more complicated then the computational spectrum in the harmonic approximation presented here. The C−H stretch band is of continued interest to researchers as it provides information on the structure of alkane chains and their environment. This band is a convolution of fundamental modes and resonances that cannot readily be distinguished at room temperature.

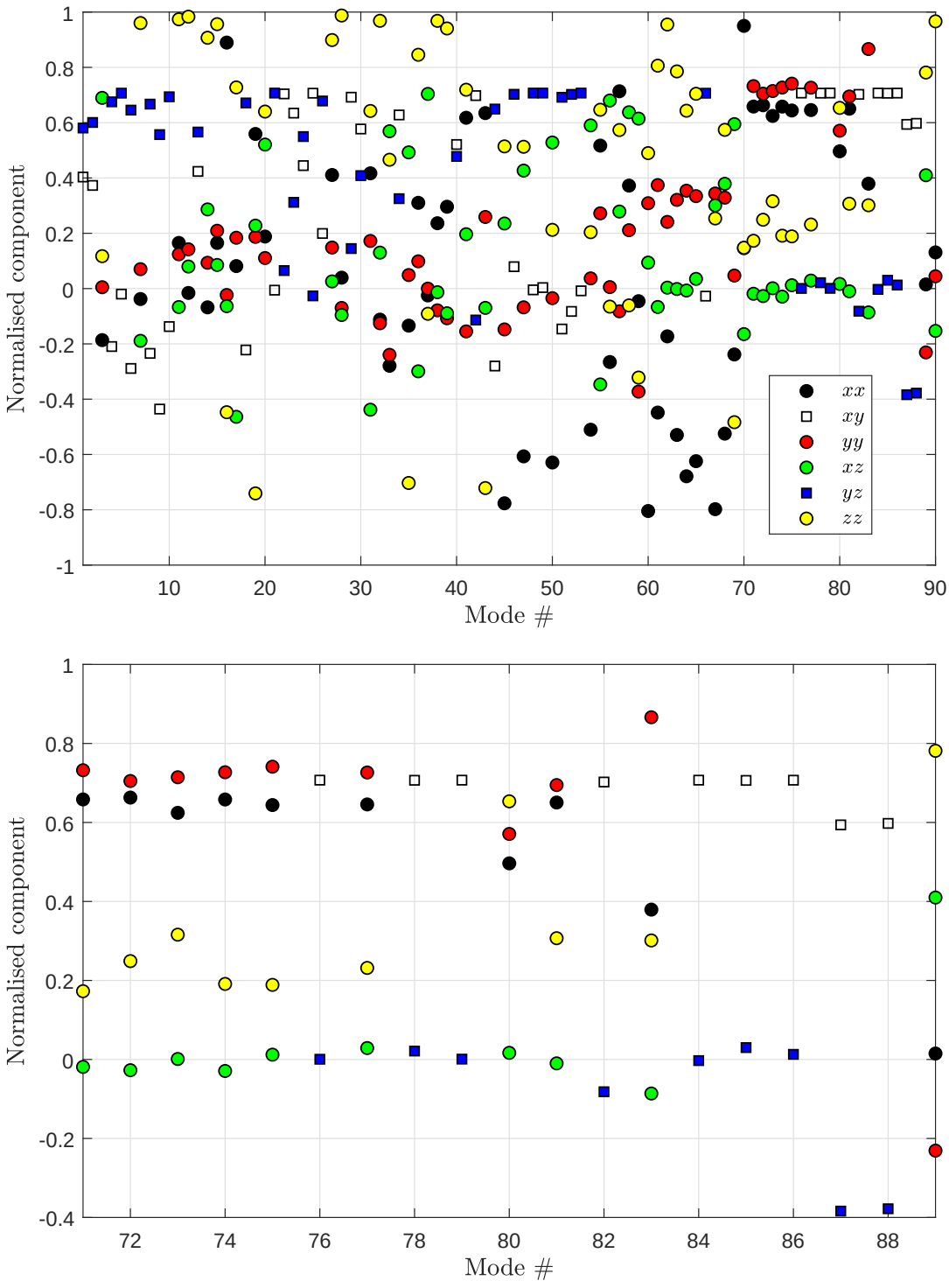

Figure 4.9: Normalised Raman tensor components of decanoic acid modes (top) and of its ν(CH) band separately (bottom). Round symbols indicate A' and square A'' modes. Some tensors have been multiplied by -1 to bring their components on a primarily positive scale.

The methylene bending modes, $\delta(CH_2)$, form multiple Raman active transitions that belong to the A' species, the strongest of which is mode 63 at 1487 cm^{-1}. The first overtone of this band comes into the $\nu(CH)$ region and couples to the $\nu_s(CH_2)$ modes, which are also of A' symmetry.[§] This gives rise to Fermi resonance: the $2\delta(CH_2)$ overtone is intensified at the cost of $\nu_s(CH_2)$ fundamentals and the frequencies are shifted away from each other. None of this is incorporated in our GAUSSIAN computation. The first harmonic overtone of the bending region $2\delta(CH_2)$ is plotted with the C−H stretch fundamentals in figure 4.8 to illustrate the overlap of the vibrational wavenumbers.

Fermi resonance occurs in a single CH_2 group and was first observed and described by Lavalley and Sheppard [141] by deuterium-isolation of the methylene in propane (*i.e.* by recording the infrared spectrum of gas-phase $CD_3CH_2CD_3$). The resonance between $\nu(CH_2)$ and $2\delta(CH_2)$ gives rise to a Fermi doublet of approximately equal intensity at 2942 and 2876 cm^1 in the infrared spectrum. More recently, Jordanov *et al.* [134] explained another overlapping band at about 2900 cm^1 as the result of the splitting of two Fermi doublets of neighbouring methylene groups. These would give rise to four infrared lines at about 2855, 2900, 2930 and 2955 cm^1.

Robert G. Snyder *et al.* systematically investigated the Raman spectrum of saturated hydrocarbon chains by experimental and theoretical approaches. They concluded that the complex band structure of the C−H stretch region is primarily a result of a redistribution of the symmetric stretch fundamental over a sharp band at about 2850 cm^{-1} and a broad band around 2898 cm^{-1} via Fermi resonance interaction in which "a continuum of bending mode binary combinations is involved" [98, 142]. The dispersion of the bending modes arises from intermolecular coupling of the bending vibrations as well as intramolecular coupling, which is sensitive to the crystallinity of the material [142]. Raman spectra of longer chains therefore show an increased spreading of the symmetric stretch mode intensity to higher wavenumbers. The intensity decreases from its maximum near 2885 cm^{-1} towards higher wavenumbers as both the density of states of the bending modes decreases and the coupling reduces from the increasing frequency mismatch. The dispersion of the $\nu_s(CH_2)$ fundamental on its own is much smaller. The dispersion of $\delta(CH_2)$ modes is further increased by interaction with CH_2 rocking overtones and through lateral interaction in crystalline phases, the details of which depends on the crystal structure. These broaden and shift the overtones of the bending modes which in turn asymmetrically broaden the $\nu_s(CH_2)$ band at 2885 cm^{-1} towards higher wavenumbers through resonance [142, 143].

As the bending overtone and symmetric stretch modes couple into Fermi resonance, the Raman tensor of the resonant mode will be of an intermediate form. The normalised Raman tensor for the strongest scattering bending vibration of decanoic acid in our com-

[§]Section A.3 discusses the symmetry species of the methylene vibrations in more detail.

putation (mode 63 at 1487 cm^{-1}) is

$$\boldsymbol{\alpha}_{63} = \begin{pmatrix} -0.529 & 0 & -0.002 \\ 0 & 0.321 & 0 \\ -0.002 & 0 & 0.785 \end{pmatrix}$$

which differs from the Raman tensor of the in-phase symmetric CH_2 stretch that gives rise to the strongest ν_s(CH) band (mode 73 predicted at 2994 cm^{-1} with its normalised tensor given in equation 4.4.3). Their xx components are of opposing signs while the relative magnitudes of their yy and zz elements are interchanged.

As discussed in section 2.5.4, the coupling strength can be deduced by combining *ab initio* computation and experimental data. Snyder and Scherer [98] obtained $W = 29\ \mathrm{cm}^{-1}$ for an isolated methylene group and an unperturbed frequency of 2879 cm^{-1} by comparing a zero-order calculation of the Fermi resonance interaction to polyethylene Raman spectra. Using equation 2.175 with $\Delta_{\mathsf{unp}} = \nu_{73} - 2\nu_{63} = 20\ \mathrm{cm}^{-1}$ from our Gaussian computation, we find $\Delta_{\mathsf{res}} = 35\ \mathrm{cm}^{-1}$. The contributions of the wavefunctions to the resonant mode (weighing factors in equation 2.177) are $a = 0.89$ and $b = 0.46$ for the symmetric stretch fundamental and the bending overtone, respectively.

Fitting the ν(CH) band

From counting the main features in figure 4.8, it appears that nine functions are needed to fit the ν(CH) band. This has been confirmed by polarised Raman scattering experiments of Harrand [144, 145] in the 1980's. Previous work by Guha in our group [54] suggests that six components suffice for an acceptable fit (in which he followed [146]). In both cases, however, the number of fitted peaks is lower than the actual number of vibrational modes in the band (19 for decanoic acid in the harmonic approximation). Some of the modes and resonances have similar frequencies and can be taken together for a phenomenological fit. However, the contribution of the underlying vibrations may vary between polarised Raman spectra as these depend on their Raman tensors, which may have components of varying magnitude or be of different forms altogether. In such cases, the intensities obtained through fitting do not relate directly to the Raman intensities for the individual vibrational modes. Where the frequencies as well as the Raman tensors are alike, one function could be used to fit these modes to obtain a physical meaningful intensity. This is further complicated by the Fermi resonances between the A' modes. In section 6.4, we further address the issue of extracting meaningful Raman intensities from the C−H stretch region of alkanes.

Table 4.7: Selected Raman fundamentals of decanoic acid and their Raman tensors in the molecular frame of reference at B3LYP/6-311++G(d,p) theory level. The modes are numbered from low to high wavenumber following the GAUSSIAN log.

Mode #	Species	Assignment	$\bar{\nu}$ / cm^{-1}	S / $Å^4$ amu^{-1}	$\boldsymbol{\alpha}_{\mathrm{v}}^{\mathrm{m}}$ / 10^{-42} C V^{-1} m^2
63	A'	$\delta(CH_2)$	1487	57.1	$\begin{pmatrix} -14.29 & 0 & -0.04 \\ 0 & 8.66 & 0 \\ -0.04 & 0 & 21.20 \end{pmatrix}$
71	A'	$\nu_s(CH_2)$	2991	21.3	$\begin{pmatrix} 6.67 & 0 & -0.19 \\ 0 & 7.50 & 0 \\ -0.19 & 0 & 1.77 \end{pmatrix}$
72	A'	$\nu_s(CH_2)$	2991	14.9	$\begin{pmatrix} 5.64 & 0 & -0.23 \\ 0 & 5.99 & 0 \\ -0.23 & 0 & 2.12 \end{pmatrix}$
73	A'	$\nu_s(CH_2)$	2994	407	$\begin{pmatrix} 27.5 & 0 & 0.05 \\ 0 & 31.5 & 0 \\ 0.05 & 0 & 13.9 \end{pmatrix}$
74	A'	$\nu_s(CH_2)$	2997	37.9	$\begin{pmatrix} -8.96 & 0 & 0.40 \\ 0 & -9.90 & 0 \\ 0.40 & 0 & -2.60 \end{pmatrix}$
75	A'	$\nu_s(CH_2)$	3005	52.9	$\begin{pmatrix} -10.4 & 0 & -0.2 \\ 0 & -11.9 & 0 \\ -0.2 & 0 & -3.0 \end{pmatrix}$
76	A''	$\nu_a(CH_2)$	3007	246	$\begin{pmatrix} 0 & -28.5 & 0 \\ -28.5 & 0 & -0.02 \\ 0 & -0.02 & 0 \end{pmatrix}$
77	A'	$\nu_s(CH_2)$	3010	53.2	$\begin{pmatrix} -10.3 & 0 & -0.5 \\ 0 & -11.6 & 0 \\ -0.5 & 0 & -3.7 \end{pmatrix}$
78	A''	$\nu_a(CH_2)$	3010	16.3	$\begin{pmatrix} 0 & -7.32 & 0 \\ -7.32 & 0 & -0.22 \\ 0 & -0.22 & 0 \end{pmatrix}$
79	A''	$\nu_a(CH_2)$	3017	55.6	$\begin{pmatrix} 0 & 13.5 & 0 \\ 13.5 & 0 & 0.02 \\ 0 & 0.02 & 0 \end{pmatrix}$

(continued on next page)

Table 4.7 (continued)

Mode #	Species	Assignment	$\bar{\nu}$ / cm^{-1}	S / $\mathrm{Å}^4\ \mathrm{amu}^{-1}$	$\boldsymbol{\alpha}_{\mathrm{v}}^{\mathrm{m}}$ / $10^{-42}\ \mathrm{C\ V^{-1}\ m^2}$
80	A'	$\nu_s(\mathrm{CH_3})$	3017	185	$\begin{pmatrix} 14.5 & 0 & 0.5 \\ 0 & 16.7 & 0 \\ 0.5 & 0 & 19.1 \end{pmatrix}$
81	A'	$\nu_s(\mathrm{CH_2})$	3027	197	$\begin{pmatrix} 19.9 & 0 & -0.3 \\ 0 & 21.2 & 0 \\ -0.3 & 0 & 9.4 \end{pmatrix}$
82	A''	$\nu_a(\mathrm{CH_2})$	3029	4.93	$\begin{pmatrix} 0 & -4.00 & 0 \\ -4.00 & 0 & 0.47 \\ 0 & 0.47 & 0 \end{pmatrix}$
83	A'	$\nu_s(\mathrm{CH_2})$	3036	4.75	$\begin{pmatrix} 1.83 & 0 & -0.41 \\ 0 & 4.17 & 0 \\ -0.41 & 0 & 1.45 \end{pmatrix}$
84	A''	$\nu_a(\mathrm{CH_2})$	3041	41.1	$\begin{pmatrix} 0 & 11.6 & 0 \\ 11.6 & 0 & 0.05 \\ 0 & 0.05 & 0 \end{pmatrix}$
85	A''	$\nu_a(\mathrm{CH_2})$	3050	23.4	$\begin{pmatrix} 0 & 8.73 & 0 \\ 8.72 & 0 & 0.37 \\ 0 & 0.37 & 0 \end{pmatrix}$
86	A''	$\nu_a(\mathrm{CH_2})$	3053	32.9	$\begin{pmatrix} 0 & 10.3 & 0 \\ 10.3 & 0 & 0.2 \\ 0 & 0.2 & 0 \end{pmatrix}$
87	A''	$\nu_a(\mathrm{CH_2})$	3076	2.82	$\begin{pmatrix} 0 & -2.53 & 0 \\ -2.53 & 0 & 1.64 \\ 0 & 1.64 & 0 \end{pmatrix}$
88	A''	$\nu_a(\mathrm{CH_3})$	3078	28.9	$\begin{pmatrix} 0 & 8.16 & 0 \\ 8.16 & 0 & -5.16 \\ 0 & -5.16 & 0 \end{pmatrix}$
89	A'	$\nu_s(\mathrm{CH_3})$	3082	109	$\begin{pmatrix} 0.4 & 0 & 10.6 \\ 0 & -6.0 & 0 \\ 10.6 & 0 & 20.2 \end{pmatrix}$

4.5 Summary and critique

This chapter presented three methods to derive Raman tensors for vibrational modes: (1) by combining bond-polarisabilities in a known vibrational pattern, (2) by considering the symmetry of a vibrational modes and (3) through *ab-initio* computation in Gaussian.

The bond-polarisability model provides an approximate empirical method to evaluate the polarisability derivative tensor for a known normal mode. It illustrates the microscopic link between the form of the Raman tensor and the vibrational pattern and shows how selection rules arise from symmetry. Combining the contribution of each bond reveals which ones add up or cancel out. A central assumption in this model is that the total polarisability derivative of the mode can be obtained by summing the changes in linear polarisability of the individual bonds participating in the oscillation. Furthermore, there are no local field corrections for a given bond due to the presence of others and the amplitude and phase of the electric field that drives the Raman scattering is assumed to be the same for all bonds.

The forms of Raman tensors are generalised in a symmetry-based approach. This can be seen as a generalisation of the insights gained with the bond-polarisability model. All Raman modes belonging to the same symmetry species of the molecular point group have the same form. This form is simplified by an appropriate choice of axes based on the symmetry of the molecule. Care must be taken with a consistent use of the axial directions since there is no consensus on this in the scientific literature.

Numerical values for Raman tensors were obtained through harmonic computations in Gaussian at the B3LYP/6-311++G(d,p) theory level. The procedure for the calculation had to be developed for a lack of accurate literature and was applied to the sulfate anion, three isotopologues of carbon tetrachloride, toluene (see appended section G.1.2) and decanoic acid. The Raman tensors obtained through computation can be used as input parameters in our model to aid interpretation of the experimental spectra.

Raman computations resulted in a spectrum of each compound and Raman tensors for each of their fundamental vibrational modes. Coordinate transformations were applied to bring these from the computational to the molecular frame of reference.[¶] The forms of the computed Raman tensors generally agreed with those predicted on the grounds of symmetry and those derived in the bond-polarisability model. Minor differences arose from small non-zero off-diagonal components in the computed Raman tensors for toluene and decanoic acid. This indicates the limitations of the bond-polarisability model and deviations of the vibrational patterns from the expected symmetries. The computed Raman tensors of the degenerate modes of sulfate and carbon tetrachloride were linear combinations of the symmetry-based tensors. Some vibrational patterns were found to be of higher symmetry than the molecule, giving rise to Raman tensors of a form belonging to a

[¶]Coordinate transformations are not relevant for species investigated in a liquid as these undergo orientational averaging. In such cases (as with sulfate salt solutions and carbon tetrachloride in this work), any frame of reference suffices. If orientational analysis is desired, such as for decanoic acid studied here, the Raman tensors have to be expressed in a properly defined molecular frame of reference.

species of higher symmetry. This was the case with most normal modes of decanoic acid.

Limitations of the GAUSSIAN computations include the harmonic approximation and the omission of coupling interactions between the vibrational modes, most notably the Fermi resonances. Literature was consulted to complement our results with the anharmonic features of the spectra. This was found to be particularly relevant for carbon tetrachloride and decanoic acid. The C−H stretch band of the latter was found to contain the strongest Raman modes of its spectrum. In addition to overlapping fundamentals, Fermi resonances of symmetric stretch modes with the first overtone of methylene bending modes complicates this part of the spectrum.

Comparison with Gough's results [136] confirmed our computations for the in-phase methylene symmetric stretch. Her work further explains why the methylene vibrations results in disproportionately strong Raman bands. The Raman tensor for symmetric methylene stretch modes in alkanes is expected to stabilise from dodecane, while that of the in-plane methyl mode stabilises from nonane [136, 138]. This suggests transferability of polarisability derivatives for long stretched alkanes.

In concluding, we note that the strongest Raman active vibrations involve atomic motion of hydrogen atoms. The extended electron distribution in these atoms give rise to a high polarisability. Combined with a large displacement in vibrational modes, due to their low mass, this results in a high polarisability derivative.

Chapter 5

Modelling Raman intensities

This chapter presents in detail the model constructed to calculate the detected Raman scattered intensity from a single scatterer near an interface. After defining the frames of reference used throughout the calculations, the chapter focusses on the electrodynamics of the Raman scattering process. The model is outlined in four steps:

1. Propagation of incoming laser light into the location of the scatterer,
2. Generation of an induced dipole in the scatterer by the local electric field,
3. Computation of the scattered light as the far-field radiation of the induced dipole, and
4. Collimation and detection of the scattered light within the field of view of the microscope objective,

after which a description of its implementation in MATLAB is given. The chapter concludes with a summary and critique of the model.

Step 1 and 3 centre on the excitation of a dipole near an interface and its emission in all directions. The electromagnetic description of these two apparently distinct processes are connected by reciprocity. Various authors have addressed either or both of these. Lukosz [147] first derived analytic expressions for the power distribution of light emitted by an electric or magnetic dipole near a planar dielectric interface. The emission depends on the orientation of the dipole, its distance from the interface and the ratio of refractive indices of the two materials. Reed *et al.* [148] later analysed radiation from a dipole embedded in a multilayer stack of dielectric media through a transfer matrix method. The use of Green's functions was only needed for the near-field, with the far-field derived by the notably simpler Lorentz reciprocity theorem. This theorem facilitates computation of the emitted electric field in a particular direction of observation by considering the field that would be generated at the location of the scatterer by plane waves incident from that direction. Reciprocity was also used by Crawford [149] to derive the radiation from a dipole embedded in a layered system, generalising for number of layers and layer thickness. He formulated amplitude coupling functions, derived from considering the field due to an incident plane

wave. Though he hinted at the applicability to Raman scattering, he considered emission only. Courtois, Courty and Mertz [150] discussed dipole radiation patterns for atoms near a vacuum-dielectric interface, again drawing heavily from reciprocity relations. Their approach was later unified by Mertz [151] for both incident as well as emitted radiation for a dipole near a loss-less interface. Both incoming and emitted light were also considered by Itoh and Hasegawa [152] for Raman scattering, drawing from [148] and [149] to address steps 1 to 3 of the process for scattering from a thin film on a substrate in air. Their work also aimed to obtain molecular orientation through polarised Raman scattering. It is discussed in more detail in section 6.4.

The papers cited above each employ particular definitions (including choice of axes, polarisation directions and angles measured with respect to the plane or its normal), with the dipole located under, within or above the interface and light entering or leaving from one side or the other in addition to various layered geometries. Most authors concerned themselves with intensities only, though vectorial amplitudes are the focus of our work as these carry information on the orientation of the scatterer. We therefore present our own derivation appropriate to the conventions introduced so far.

The model has been developed with our experimental lay-out in mind, but is not limited to its geometry. Without these restrictions, the model is of wider applicability and can be used for experimental design as well as data interpretation. A single run of the model computes the detected linearly-polarised intensities for a given optical geometry with the scattering molecule at a fixed orientation in space and using a specified Raman tensor. It employs a complex, vectorial description of the electric field amplitude to reach that goal.

5.1 Frames of reference

Four frames of reference are used in the model as detailed below. These have been defined to simplify the model as much as possible without losing general applicability. As all frames of reference are right handed, it suffices to specify two orthogonal unit vectors and an origin. The length of unit vectors is immaterial: the model provides relative intensities for a Raman mode of a particular moiety given the variable experimental geometry and orientation of the scatterer.

5.1.1 Laser frame

The laser frame of reference $\{\hat{\mathbf{x}}^{\text{L}}, \hat{\mathbf{y}}^{\text{L}}, \hat{\mathbf{z}}^{\text{L}}\}$ is given by the plane of incidence of the laser beam. Its origin is where the beam strikes the interface. As shown in figure 5.1, the directions of the basis vectors are chosen such that the surface normal $\hat{\mathbf{n}} \parallel \hat{\mathbf{z}}^{\text{L}}$ and that the propagation direction of the laser $\hat{\mathbf{k}}$ is in the $x^{\text{L}}z^{\text{L}}$ plane, with its x^{L} component in the positive $\hat{\mathbf{x}}^{\text{L}}$ direction for all non-zero angles of incidence θ_i. This frame is independent of the z^{L} component of $\hat{\mathbf{k}}$; it is the same whether the laser is incident from above or below

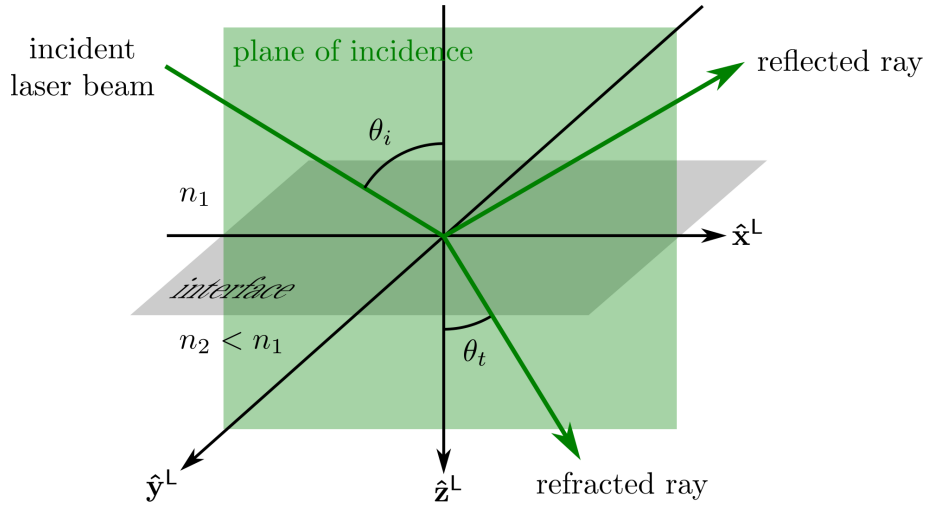

Figure 5.1: The laser frame of reference $\{\hat{\mathbf{x}}^{\mathsf{L}}, \hat{\mathbf{y}}^{\mathsf{L}}, \hat{\mathbf{z}}^{\mathsf{L}}\}$ with the plane of incidence as the $x^{\mathsf{L}}z^{\mathsf{L}}$ plane (shaded in green) and the interface between two media as the $x^{\mathsf{L}}y^{\mathsf{L}}$ plane (shaded in grey). $\hat{\mathbf{z}}^{\mathsf{L}}$ is directed from the first into the second medium, specified by refractive indices n_1 and n_2, respectively, with $n_2 < n_1$. In our experiments, the first medium is the hemisphere in which total internal reflection can occur. Here, reflection and refraction of the incident laser beam at a single interface are shown with $\theta_i < \theta_c$. For layered systems, the plane $z^{\mathsf{L}} = 0$ remains at the surface of the first medium.

the interface. A further specification is needed for $\theta_i = 0$, when $\hat{\mathbf{x}}^{\mathsf{L}}$ and $\hat{\mathbf{y}}^{\mathsf{L}}$ are chosen to be consistent with non-zero angles of incidence.

In the L-frame, the wave vector $\mathbf{k}$ is expressed in the Cartesian basis. Its specification in the spherical coordinates ρ_k, θ_k and ϕ_k is more convenient in our model as it relates the polar angle θ_k to the angles of incidence, reflection and refraction. Using equation 2.10 we obtain

$$\mathbf{k}^{\mathsf{L}} = \begin{pmatrix} k_x \\ k_y \\ k_z \end{pmatrix} = \begin{pmatrix} \rho_k \sin\theta_k \cos\phi_k \\ \rho_k \sin\theta_k \sin\phi_k \\ \rho_k \cos\theta_k \end{pmatrix} = \frac{2\pi n}{\lambda_0} \begin{pmatrix} \sin\theta_k \\ 0 \\ \cos\theta_k \end{pmatrix} \tag{5.1}$$

where the azimuthal component $\phi_k = 0$ follows from our definition of the L-frame, which spans the plane of incidence. The length of the vector $||\mathbf{k}|| = k$ (equal to ρ_k at the origin of the L-frame) is given by equation 2.49 with n the refractive index of the medium in which the wave propagates. Figure 5.2 presents how θ_k is defined and includes the linear polarisation directions p (or transverse magnetic, TM), which is parallel to the plane of incidence, and s (or transverse electric, TE), which is perpendicular to the plane of incidence. The definition of the L-frame given above specifies that $s \parallel \hat{\mathbf{y}}^{\mathsf{L}}$. Note that θ_k can be understood as the propagation direction of the light relative to the orientation of the I-frame. It is not necessarily restricted to the range of the polar spherical coordinate 0° to 180°.

The complex vectorial amplitudes $\mathbf{E}$ and $\mathbf{B}$ in the L-frame both depend on θ_k. The electric field is expressed in equation 2.57 as a plane wave in the $\{\hat{\boldsymbol{p}}, \hat{\boldsymbol{s}}, \hat{\boldsymbol{k}}\}$ basis. It is

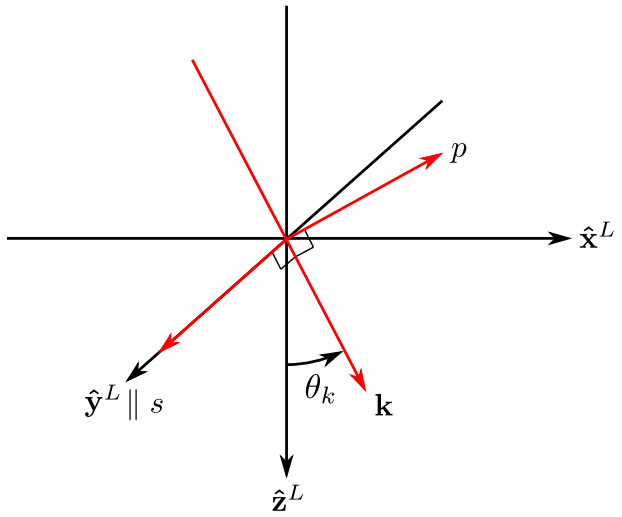

Figure 5.2: The direction of wave vector $\mathbf{k}$ is specified in the L-frame of reference by angle θ_k, the spherical polar coordinate from $\hat{\mathbf{z}}^{\mathsf{L}}$ to $\mathbf{k}$ about $\hat{\mathbf{y}}^{\mathsf{L}}$. The orthogonal polarisation directions p and s are perpendicular to $\mathbf{k}$ for a transverse wave. The directions are chosen such that the two sets of axes are parallel at $\theta_k = 0$.

transformed to basis $\{\hat{\mathbf{x}}^{\mathsf{L}}, \hat{\mathbf{y}}^{\mathsf{L}}, \hat{\mathbf{z}}^{\mathsf{L}}\}$ by applying the rotation $\mathbf{R}_y(-\theta_k)$ (a passive rotation about y as given in equations 2.12) to obtain

$$\mathbf{E}^{\mathsf{L}}(\mathbf{r}) = \begin{pmatrix} E_x \\ E_y \\ E_z \end{pmatrix} = {\mathbf{R}_y}^{\mathrm{T}}(\theta_k) \begin{pmatrix} E_p \\ E_s \\ 0 \end{pmatrix} = \begin{pmatrix} E_p \cos\theta_k \\ E_s \\ -E_p \sin\theta_k \end{pmatrix} \mathrm{e}^{\mathrm{j}\mathbf{k}\cdot\mathbf{r}} \tag{5.2}$$

where $\mathrm{j}^2 = -1$ with j the imaginary unit. The time-dependence of the field has been dropped as we are concerned with time-averaged quantities only which are proportional to the field at $t = 0$. The magnetic field is derived from equation 2.59 in a similar way and found to be

$$\mathbf{B}^{\mathsf{L}}(\mathbf{r}) = \begin{pmatrix} -E_s \cos\theta_k \\ E_p \\ E_s \sin\theta_k \end{pmatrix} \frac{n}{c} \mathrm{e}^{\mathrm{j}\mathbf{k}\cdot\mathbf{r}} \tag{5.3}$$

where equation 2.40 was used to substitute $v = c/n$. Any plane wave in the L-frame is expressed with equations 5.2 and 5.3.

5.1.2 Molecular frame

The axes $\{\hat{\mathbf{x}}^{\mathsf{m}}, \hat{\mathbf{y}}^{\mathsf{m}}, \hat{\mathbf{z}}^{\mathsf{m}}\}$ of the molecular frame of reference m are chosen along physically relevant axes of the scattering molecule. In many cases, these will align with the symmetry axes of the molecule. The scatterer is treated as infinitesimal and is located at the origin of its own frame. Its distance from the interface is specified as a position z along z^{L}. This does not affect any coordinate transformations, which have to do with axial directions only. Figure 5.3 presents an example of the m-frame as used in this work: a stretched

alkane chain with its long axis oriented along $\hat{\mathbf{z}}^{\mathsf{m}}$ and its carbon atoms in the $x^{\mathsf{m}}z^{\mathsf{m}}$ plane.

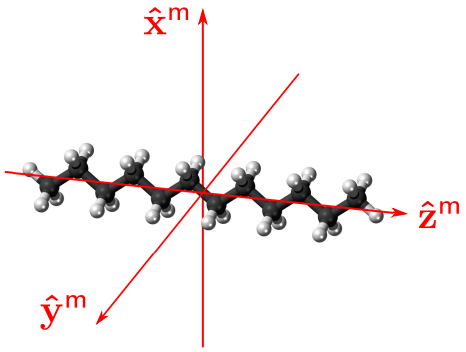

Figure 5.3: The molecular frame of reference $\{\hat{\mathbf{x}}^{\mathsf{m}}, \hat{\mathbf{y}}^{\mathsf{m}}, \hat{\mathbf{z}}^{\mathsf{m}}\}$ in red with a dodecane ball-and-stick model illustrating a possible orientation of the frame with respect to the scattering moiety (black is carbon, white is hydrogen). The choice of axes is based on the symmetry of the fully stretched chain: its long axis along $\hat{\mathbf{z}}^{\mathsf{m}}$, with all carbon atoms in the $x^{\mathsf{m}}z^{\mathsf{m}}$ plane and all CH_2 groups parallel to the $x^{\mathsf{m}}y^{\mathsf{m}}$ plane.

5.1.3 Observation frame

The observation frame of reference O with basis $\{\hat{\mathbf{x}}^{\mathsf{O}}, \hat{\mathbf{y}}^{\mathsf{O}}, \hat{\mathbf{z}}^{\mathsf{O}}\}$ is determined by the optical axis of the microscope objective and the orientation of the linear polariser in the spectrometer (LP_2 in figure 3.2). As specified in figure 5.4, $\hat{\mathbf{z}}^{\mathsf{O}}$ is directed from the origin into the microscope objective. Its entrance is positioned at $z^{\mathsf{O}} = \mathrm{WD}$. The origin of the O-frame is located at the objective focus and coincides with the L-frame origin. The directionality of $\hat{\mathbf{x}}^{\mathsf{O}}$ and $\hat{\mathbf{y}}^{\mathsf{O}}$ is unimportant as long as it conforms to the definitions of the linear collection polarisation with the Raman system in use (sections 3.1.2 and 3.1.3).

Coordinates given in the O-frame are expressed in the L-frame through transformation

$$\mathbf{T}_{\mathsf{L}\to\mathsf{O}} = \mathbf{R}_z(\gamma_{\mathsf{O}})\,\mathbf{R}_x(\beta_{\mathsf{O}})\,\mathbf{R}_z(\alpha_{\mathsf{O}}) \tag{5.4}$$

where the Euler angles $(\alpha_{\mathsf{O}}, \beta_{\mathsf{O}}, \gamma_{\mathsf{O}})$ specify the orientation of objective axes relative to the laser frame axes in the experimental geometry. Standard practice in our research group has the objective positioned on the hemisphere side of the interface and normal to the interface with the plane of incidence perpendicular to the collection polarisation. This ensures that $\hat{\mathbf{x}}^{\mathsf{O}} = \hat{\mathbf{x}}^{\mathsf{L}}$, $\hat{\mathbf{y}}^{\mathsf{O}} = -\hat{\mathbf{y}}^{\mathsf{L}}$ and $\hat{\mathbf{z}}^{\mathsf{O}} = -\hat{\mathbf{z}}^{\mathsf{L}}$ so that the Euler angles for the transformation are $(\alpha_{\mathsf{O}}, \beta_{\mathsf{O}}, \gamma_{\mathsf{O}}) = (0°, 180°, 0°)$.

5.1.4 Frame of point Q

A variable frame of reference $\mathsf{Q} = \{\hat{\mathbf{x}}^{\mathsf{Q}}, \hat{\mathbf{y}}^{\mathsf{Q}}, \hat{\mathbf{z}}^{\mathsf{Q}}\}$ is used to compute the far-field complex amplitude of Raman scattering at a point Q on a plane at the microscope objective entrance. This point is initially specified as part of a grid of points in the O-frame, before being transformed into the L-frame in both Cartesian and spherical coordinates. A plane

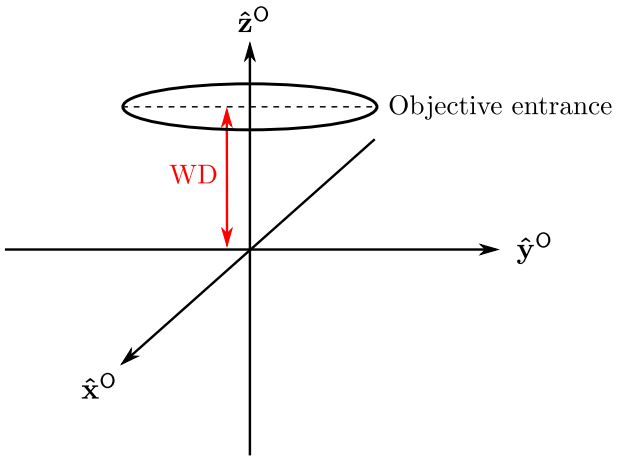

Figure 5.4: The observation frame of reference $\{\hat{\mathbf{x}}^{\mathsf{O}}, \hat{\mathbf{y}}^{\mathsf{O}}, \hat{\mathbf{z}}^{\mathsf{O}}\}$ is specified with the optical axis of the microscope objective along $\hat{\mathbf{z}}^{\mathsf{O}}$, directed from the sample side into the objective. The entrance to the objective is positioned at $z^{\mathsf{O}} = \mathrm{WD}$, its working distance. The origin thus represents the focus of the objective, which coincides with the origin of the L-frame. $\hat{\mathbf{y}}^{\mathsf{O}}$ is set parallel to the transmission axis of the linear polariser in the spectrometer, represented by the dashed line.

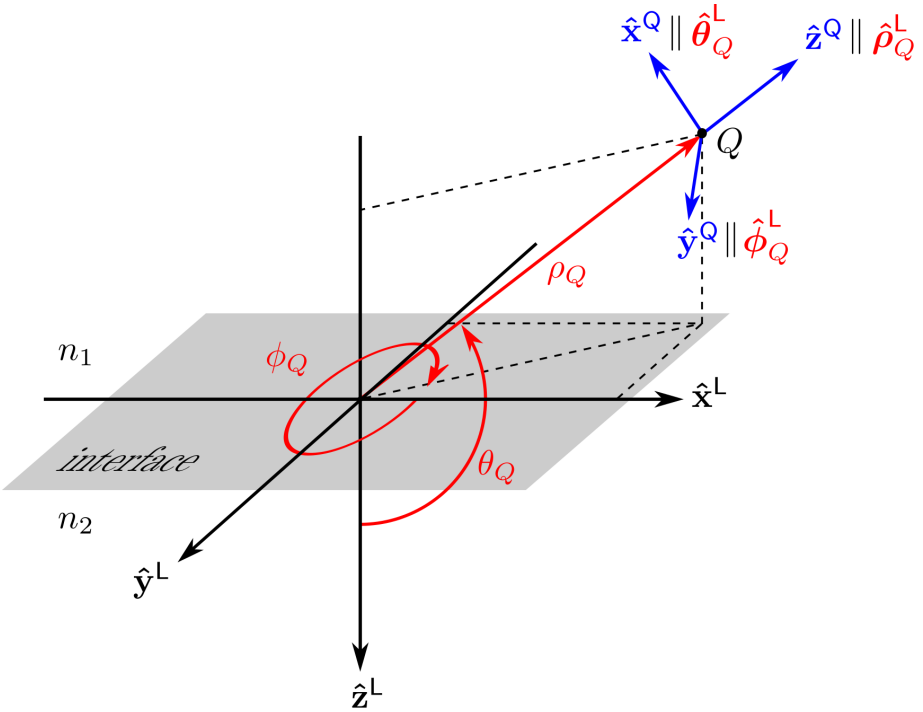

Figure 5.5: The Q-frame of reference $\{\hat{\mathbf{x}}^{\mathsf{Q}}, \hat{\mathbf{y}}^{\mathsf{Q}}, \hat{\mathbf{z}}^{\mathsf{Q}}\}$ (blue) is defined through the spherical coordinates of point $Q = [\rho_Q, \theta_Q, \phi_Q]$ in the L-frame (red). Its origin is at Q. The L-frame is presented in the same orientation as in figure 5.1 for consistency.

of incidence is defined that includes $\hat{\mathbf{z}}^L$ and Q as the $x^{\mathsf{Q}}z^{\mathsf{Q}}$ plane. This plane is used in the application of the Lorentz reciprocity theorem to deduce the p and s components of the dipole far-field at Q.

The point Q itself is the origin of its own frame. The directions of the Cartesian Q-frame unit vectors follow from the directions of the spherical basis vectors of Q in the L-frame with

$$\begin{cases} \hat{\mathbf{x}}^{\mathsf{Q}} \parallel \hat{\boldsymbol{\theta}}_Q^{\mathsf{L}} \\ \hat{\mathbf{y}}^{\mathsf{Q}} \parallel \hat{\boldsymbol{\phi}}_Q^{\mathsf{L}} \\ \hat{\mathbf{z}}^{\mathsf{Q}} \parallel \hat{\boldsymbol{\rho}}_Q^{\mathsf{L}} \end{cases} \tag{5.5}$$

as illustrated in figure 5.5. Note that the directions (relative to the L-frame) change with the location of Q. The transformations from the Q-frame also depend on Q and are specified in section 5.4.

5.2 Incident light

In this section, we derive expressions for the applied macroscopic electric field $\mathbf{E}_{\mathsf{app}}$ at the location of a scattering molecule in the L-frame. It is obtained by propagating the laser beam onto and through the interface with Maxwell's equations. The applied field is expressed as a linear function of the known incident field as

$$\mathbf{E}_{\mathsf{app}}{}^{\mathsf{L}} = \mathbf{F}\ \mathbf{E}_{\mathbf{i}} = \begin{pmatrix} F_x & 0 \\ 0 & F_y \\ F_z & 0 \end{pmatrix} \begin{pmatrix} E_{i,p} \\ E_{i,s} \end{pmatrix} = \begin{pmatrix} F_x E_{i,p} \\ F_y E_{i,s} \\ F_z E_{i,p} \end{pmatrix} \tag{5.6}$$

with coupling matrix $\mathbf{F}$ that contains a factor for each of the Cartesian axes of the L-frame. The complex polarised amplitude $E_{i,p}$ has $\hat{\mathbf{x}}^{\mathsf{L}}$ and $\hat{\mathbf{z}}^{\mathsf{L}}$ components and $E_{i,s}$ is along $\hat{\mathbf{y}}^{\mathsf{L}}$. The coupling factors depend on the layer structure of the material and the illumination geometry. In this section, the electric field near and at a planar dielectric interface is analysed as well as the field in a thin film between two dielectrics. In each case, the laser beam may be directed onto the interface from either side and under any angle.

Propagative fields are described as plane electromagnetic waves as introduced in section 2.4. Though the laser beam as a whole is better described by a Gaussian wave front (see section 3.1.2), it can be treated as a plane wave when considering an individual ray within the beam. The divergence of the beam when focussed on the sample location in air has a half-angle of $< 0.5°$ (equivalent to NA < 0.009) and $< 2°$ (NA < 0.035) when the telescope is used. Use of a plane-wave description implies that the divergence is assumed to be negligible. This is not ignoring the spread in the angle of incidence, the effect of which can still be assessed using a range of values in the model calculations (see 6).

5.2.1 Reflection and refraction

Incident plane wave

Raman scattering experiments are performed with the collimated monochromatic beam of a laser. Its electric field is described as a plane wave of vacuum-wavelength λ_0 that propagates in direction $\hat{\mathbf{k}}_i$. In the L-frame, the incident field is given as

$$\mathbf{E}_i{}^{\mathsf{L}}(\mathbf{r}) = \begin{pmatrix} E_{i,p}\cos\theta_{k,i} \\ E_{i,s} \\ -E_{i,p}\sin\theta_{k,i} \end{pmatrix} \mathrm{e}^{\mathrm{j}\mathbf{k}_i\cdot\mathbf{r}} \tag{5.7}$$

which is merely adding subscripts to equation 5.2. The complex amplitudes $E_{i,p}$ and $E_{i,s}$ are given in section 2.4 for elliptically polarised light. Here, the field is linearly polarised, so that the phase factor $\delta_p = \delta_s$. These are chosen to be zero. The polarisation angle ψ is used to specify the direction of the polarisation plane. This angle ranges from $\psi = 0°$ for a p-polarised wave to $\psi = 90°$ for s polarisation as illustrated in figure 5.6. $E_{i,p}$ and $E_{i,s}$ of equation 5.7 are then specified by ψ as

$$\begin{aligned} E_{i,p} &= A_i\cos\psi \\ E_{i,s} &= A_i\sin\psi \end{aligned} \tag{5.8}$$

where A_i is the real amplitude of the wave. It works through as a scaling factor in all modelling results and is therefore set at $A_i = 1$ for convenience.

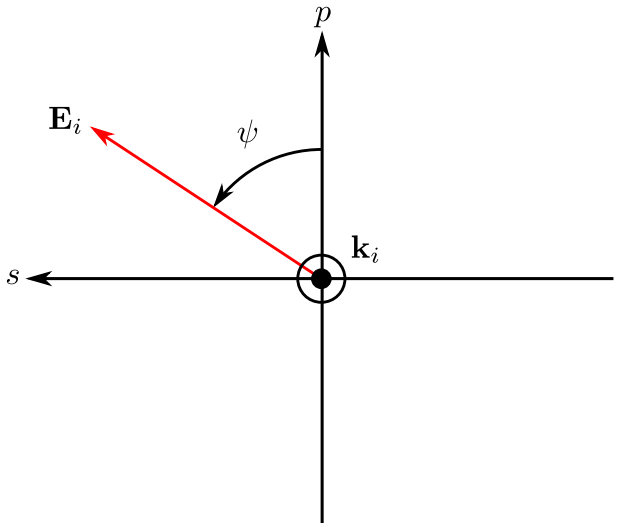

Figure 5.6: The angle of linear polarisation ψ of the incident field amplitude $\mathbf{E}_i$.

The vectorial magnetic field amplitude $\mathbf{B}_i{}^{\mathsf{L}}$ of the incident plane wave at location $\mathbf{r}$ is given as

$$\mathbf{B}_i{}^{\mathsf{L}}(\mathbf{r}) = \frac{n_i}{c}\begin{pmatrix} -E_{i,s}\cos\theta_{k,i} \\ E_{i,p} \\ E_{i,s}\sin\theta_{k,i} \end{pmatrix} \mathrm{e}^{\mathrm{j}\mathbf{k}_i\cdot\mathbf{r}} \tag{5.9}$$

where n_i is the refractive index of the incident medium. This expression is readily obtained from equation 5.3.

The incident laser beam is fully specified in the model by two quantities: the direction of propagation $\theta_{k,i}$ (*i.e.* the polar angle of $\mathbf{k}_i$) and the linear polarisation angle ψ. The laser wavelength is taken into account implicitly by using refractive indices at this wavelength. This suffices to describe the applied field in an infinite dielectric medium. The effect of an interface between two dielectric half-spaces is analysed next.

Snell's law and total internal reflection

A plane electromagnetic wave propagating through a medium with index of refraction n_i is incident on a medium with index of refraction n_t. The angle of incidence θ_i is the smaller arc between the path of the ray and the interface normal. For specular reflection, the reflected ray propagates from the interface under the same angle in the plane of incidence: $\theta_i = \theta_r$. If the second medium is transparent for the wavelength in question, the ray can be transmitted into the second medium and refraction takes place (figure 5.7). The angle of refraction θ_t at which the beam is transmitted through the second medium is given by Snell's law of refraction

$$n_i \sin\theta_i = n_t \sin\theta_t \ . \tag{5.10}$$

This relation is plotted in figure 5.8 for the silica-air and silica-water interfaces for the incident ray coming from either side of the interface.

If $n_i > n_t$, the angle of refraction θ_t is a complex number rather than a real angle for values that exceed $\theta_t = 90°$ at which the transmitted ray propagates parallel to the interface. The particular angle of incidence at which this change occurs is termed the critical angle θ_c, which follows from equation 5.10 by substituting $\theta_t = 90°$ as

$$\theta_c = \arcsin\left(\frac{n_t}{n_i}\right) \qquad \text{for } n_i > n_t \tag{5.11}$$

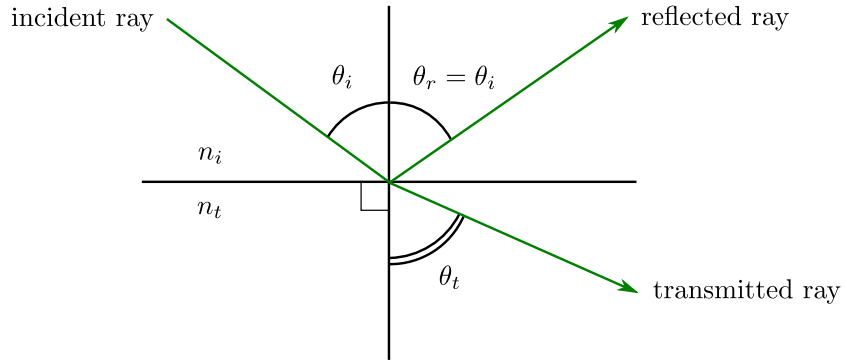

Figure 5.7: The angles of incidence θ_i, reflection θ_r and transmission θ_t are defined in the plane of incidence, which includes all rays and the interface normal. The interface is normal to the plane of the page (compare figure 5.1). In this sketch, $\theta_t > \theta_i$ which is the case if $n_i < n_t$.

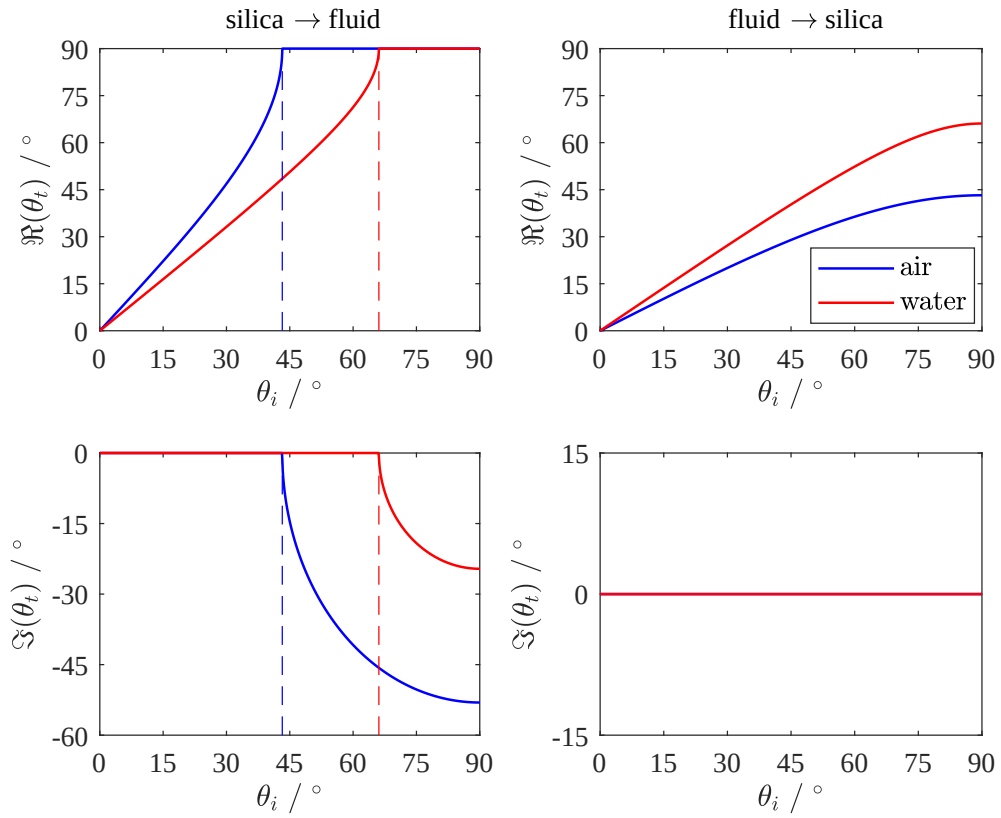

Figure 5.8: The real (top plots) and imaginary (bottom plots) parts of the angle of refraction θ_t as a function of the angle of incidence θ_i for a silica-air and silica-water interface (refractive indices at $\lambda = 532$ nm from table 3.2). With the light incident from the silica side (left plots), total internal reflection occurs if $\theta_i \geq \theta_c$ and θ_t becomes complex. This indicates an amplitude phase shift of the field. The critical angle θ_c is shown by dashed lines (43.22° and 66.10° for the silica-air and silica-water interface, respectively). A ray passing from water or air to silica (right plots) only undergoes real refraction.

If $\theta_i \geq \theta_c$, there is no transmitted ray propagating into the second medium and this is termed total internal reflection (TIR). The larger the difference in optical density between the two materials, the lower θ_c. Note that if the second medium is optically denser than the first ($n_i \leq n_t$), no total internal reflection can occur.

Radiation zones

Three zones are defined in $\theta_{k,i}$ within the range of $0° \leq \theta_{k,i} \leq 180°$ as illustrated in figure 5.9.

Zone I spans $0° \leq \theta_{k,i} < \theta_c$ where the laser is incident through the hemisphere at an angle lower than the critical angle. The transmitted angle is real.

Zone II spans $\theta_c \leq \theta_{k,i} \leq 90°$ where the laser is incident through the hemisphere at or above the critical angle. The transmitted angle is complex.

Zone III spans $90° < \theta_{k,i} \leq 180°$ where the laser is incident on the interface from the lower medium. The transmitted light enters the hemisphere under a real angle.

These zones were suggested by Lukosz [147] and used by Mertz [150, 151] as refraction is distinct in each zone. However, our numbering does *not* follow theirs. Table 5.1 summarises our definitions. It also includes the propagation angles $\theta_{k,r}$ and $\theta_{k,t}$ of the reflected and transmitted fields (following figure 5.2) as well as their relation to the angle of reflection θ_r and the angle of transmission θ_t through equation 5.10. These values are continuous over the zone boundaries. For computational purposes, the borders $\theta_{k,i} = \theta_c$ and $\theta_{k,i} = 90°$ are assigned to zone II.

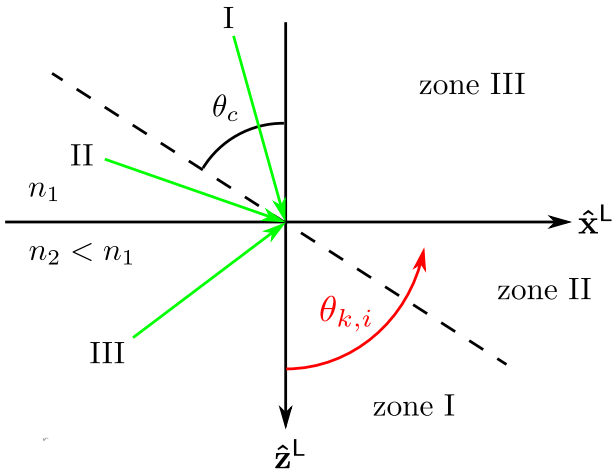

Figure 5.9: The three zones of $\theta_{k,i}$, which specifies the propagation angle of the incident plane wave in the L-frame, in the range $0° \leq \theta_{k,i} \leq 180°$. This angle is defined from the $\hat{\mathbf{z}}^{\mathsf{L}}$ to the $\hat{\mathbf{z}}^{\mathsf{L}}$ axis. Three incident rays (green arrows) are illustrated, each being incident under an angle falling within one of the three zones I, II or III. This definition of the propagation angle $\theta_{k,i}$ thus implies a propagation direction of the incident beam.

Table 5.1: Propagation angles in the L-frame and refraction angles with the radiation zones for incident light in the range $0° \leq \theta_{k,i} \leq 180°$.

Zone I	Zone II	Zone III
$0° \leq \theta_{k,i} < \theta_c$	$\theta_c \leq \theta_{k,i} \leq 90°$	$90° < \theta_{k,i} \leq 180°$
$n_i = n_1$		$n_i = n_2$
$n_t = n_2$		$n_t = n_1$
$\theta_{k,i} = \theta_i$		$\theta_{k,i} = 180° - \theta_i$
$\theta_{k,r} = 180° - \theta_r = 180° - \theta_{k,i}$		$\theta_{k,r} = \theta_r = 180° - \theta_{k,i}$
$\theta_{k,t} = \theta_t = \arcsin\left(\frac{n_1}{n_2}\sin\theta_{k,i}\right)$		$\theta_{k,t} = 180° - \theta_t = 180° - \arcsin\left(\frac{n_2}{n_1}\sin\theta_{k,i}\right)$

5.2.2 Fresnel amplitude coefficients

The propagation directions of incident, reflected and transmitted fields were derived in the previous section. We now deduce the field amplitudes at the interface by solving the electromagnetic boundary conditions.

Boundary conditions

The field amplitudes of the reflected and transmitted fields can be found through the four boundary conditions

$$\begin{cases} \epsilon_1 E_1^{\perp} = \epsilon_2 E_2^{\perp} & \text{(i)} \\ B_1^{\perp} = B_2^{\perp} & \text{(ii)} \\ \mathbf{E}_1^{\parallel} = \mathbf{E}_2^{\parallel} & \text{(iii)} \\ \frac{1}{\mu_1}\mathbf{B}_1^{\parallel} = \frac{1}{\mu_2}\mathbf{B}_2^{\parallel} & \text{(iv)} \end{cases} \tag{5.12}$$

where subscripts $1, 2$ denote the half spaces at each side of the interface. These conditions apply to the total fields in each medium at $z = 0$. If the light is incident through medium 1, the field $\mathbf{E}_1$ consists of both the incident and reflected fields while $\mathbf{E}_2$ is the transmitted field only. In our definition of axes in the L-frame, equations 5.13 become

$$\begin{cases} \epsilon_i \left(E_{i,z} + E_{r,z}\right) = \epsilon_t E_{t,z} & \text{(i)} \\ B_{i,z} + B_{r,z} = B_{t,z} & \text{(ii)} \\ E_{i,(x,y)} + E_{r,(x,y)} = E_{t,(x,y)} & \text{(iii)} \\ \frac{1}{\mu_i}\left(B_{i,(x,y)} + B_{r,(x,y)}\right) = \frac{1}{\mu_t} B_{t,(x,y)} & \text{(iv)} \end{cases} \tag{5.13}$$

where subscripts i, r, t stand for incident, reflected and transmitted as before. Though conditions (iii) and (iv) each include a pair of equations, only one component is relevant in the polarised analysis that follows. The reflected and transmitted fields will be deduced given the incident field as an s or p-polarised wave. Any polarisation can then be found by taking a combination of the two with an appropriate phase relation.

The solution to the boundary conditions depends on the choice of axes and assumed directionalities of the vectorial amplitudes [67, 68]. We therefore include a derivation

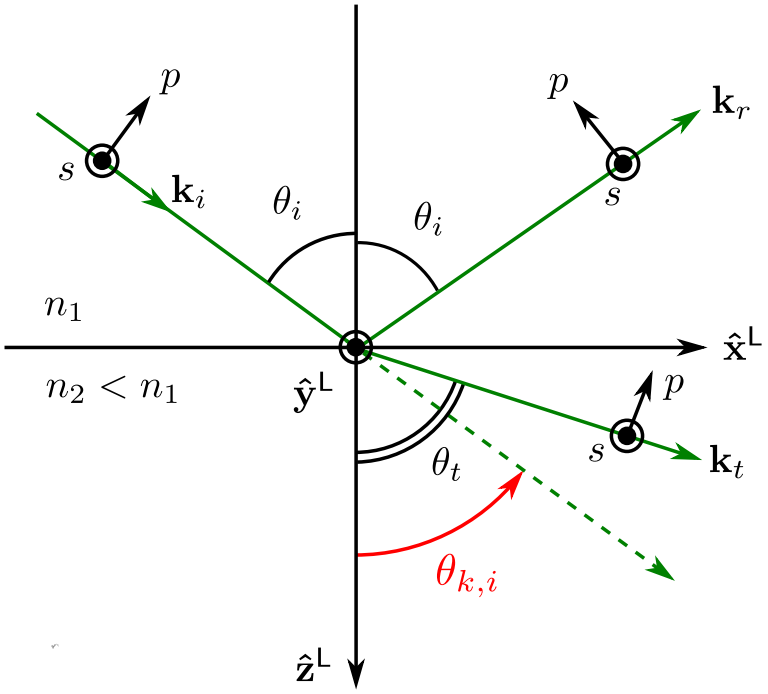

Figure 5.10: Definition of linear polarisation directions p and s for incident, reflected and transmitted waves in the L-frame. The propagation direction of the incident wave is given through its polar coordinate $\theta_{k,i}$.

of the solution strictly valid for the present set of definitions. The L-frame is used as defined above with figure 5.10 providing all directions explicitly. Note that angle k_θ is always taken from the positive $\hat{\mathbf{z}}^{\mathsf{L}}$ direction and describes the propagation direction $\mathbf{k}$ for incident, reflected and transmitted plane waves.

Once $k_{i,\theta}$ has been chosen for the incident wave, the values of $k_{r,\theta}$, $k_{t,\theta}$, θ_i, θ_r, θ_t follow from the equations in table 5.1 using the appropriate refractive indices. The vectorial amplitudes of the three fields at the interface are then expressed with equations 5.2 and 5.3. These are substituted in the boundary conditions to find the relation between the three fields.

Solving the boundary conditions

Having specified the vectorial amplitudes at the interface, their relationships are derived by meeting the boundary conditions of equations 5.13 for each polarisation.

For a p-polarised incident wave, condition (i) provides

$$\begin{aligned} -\epsilon_i E_{i,p} \sin\theta_i - \epsilon_i E_{r,p} \sin\theta_i &= -\epsilon_t E_{t,p} \sin\theta_t \\ E_{i,p} + E_{r,p} &= E_{t,p} \frac{\epsilon_t \sin\theta_t}{\epsilon_i \sin\theta_i} \end{aligned} \tag{5.14}$$

where we have used that $\theta_i = \theta_r$, while condition (ii) and the y-components in condition

(iii) result in $0 = 0$. The x-components in the latter condition provide the relation

$$\begin{aligned} E_{i,p}\cos\theta_i - E_{r,p}\cos\theta_i &= E_{t,p}\cos\theta_t \\ E_{i,p} - E_{r,p} &= \frac{\cos\theta_t}{\cos\theta_i}E_{t,p} \end{aligned} \tag{5.15}$$

where the minus sign comes from our choice of directions as follows. For $n_i = n_1$, $\theta_{k,i} = \theta_i$ while $\theta_{k,r} = 180° - \theta_i$ and *vice versa* if $n_i = n_2$. This leads to the minus sign through $\cos(180° - \theta_i) = -\cos\theta_i$, whereas $\sin(180° - \theta_i) = \sin\theta_i$. Condition (iv) provides

$$\begin{aligned} \frac{E_{i,p}}{\mu_i v_i} + \frac{E_{r,p}}{\mu_i v_i} &= \frac{E_{t,p}}{\mu_t v_t} \\ E_{i,p} + E_{r,p} &= \frac{\mu_i v_i}{\mu_t v_t}E_{t,p} \end{aligned} \tag{5.16}$$

which turns out to be the same as the expression obtained from boundary condition (i), given in equation 5.14. The fractions on the right-hand side of the two equations are identical:

$$\begin{aligned} \frac{\epsilon_t \sin\theta_t}{\epsilon_i \sin\theta_i} = \frac{\epsilon_t n_i}{\epsilon_i n_t} = \frac{\epsilon_t\sqrt{\mu_i\epsilon_i}}{\epsilon_i\sqrt{\mu_t\epsilon_t}} = \frac{\sqrt{\mu_i\epsilon_t}}{\sqrt{\mu_t\epsilon_i}} \\ \frac{\mu_i v_i}{\mu_t v_t} = \frac{\mu_i n_t}{\mu_t n_i} = \frac{\mu_i\sqrt{\mu_t\epsilon_t}}{\mu_t\sqrt{\mu_i\epsilon_i}} = \frac{\sqrt{\mu_i\epsilon_t}}{\sqrt{\mu_t\epsilon_i}} \end{aligned} \tag{5.17}$$

which is derived with Snell's law (equation 5.10) as well as equations 2.42 and 2.40.*

The boundary conditions for p-polarised waves thus reduce to

$$\begin{cases} E_{i,p} + E_{r,p} = AE_{t,p} \\ E_{i,p} - E_{r,p} = BE_{t,p} \end{cases} \tag{5.18}$$

where we have substituted

$$\begin{aligned} A &= \frac{\sqrt{\mu_i\epsilon_t}}{\sqrt{\mu_t\epsilon_i}} \\ B &= \frac{\cos\theta_t}{\cos\theta_i} \end{aligned} \tag{5.19}$$

for clarity. Solving for $E_{r,p}$ and $E_{t,p}$ results in

$$E_{r,p} = \frac{A - B}{A + B}E_{i,p} \tag{5.20}$$

and

$$E_{t,p} = \frac{2}{A + B}E_{i,p}\,. \tag{5.21}$$

In the case of an s-polarised incident wave, boundary conditions (i), the x component

*The equality can be demonstrated in many different ways. This form holds for real values of θ_t and real refractive indices, *i.e.* refraction below the critical angle with negligible absorption.

in (iii) and the y component in (iv) all result in $0 = 0$. Condition (ii) provides

$$\begin{aligned} \frac{E_{i,s}}{v_i}\sin\theta_i + \frac{E_{r,s}}{v_i}\sin\theta_i &= \frac{E_{t,s}}{v_t}\sin\theta_t \\ E_{i,s} + E_{r,s} &= E_{t,s}\frac{v_i\sin\theta_t}{v_t\sin\theta_i} \\ E_{i,s} + E_{r,s} &= E_{t,s} \end{aligned} \tag{5.22}$$

which is simplified using equations 5.10 and 2.40 that prove $v_i \sin\theta_t = v_t \sin\theta_i$. Condition (iii) immediately results in the same expression. Condition (iv) is met if

$$\begin{aligned} \frac{-E_{i,s}\cos\theta_i}{\mu_i v_i} + \frac{E_{r,s}\cos\theta_i}{\mu_i v_i} &= \frac{-E_{t,s}\cos\theta_t}{\mu_t v_t} \\ E_{i,s} - E_{r,s} &= E_{t,s}\frac{\mu_i v_i}{\mu_t v_t}\frac{\cos\theta_t}{\cos\theta_i} \end{aligned} \tag{5.23}$$

where the minus sign accounts for the choice of direction. Thus, the boundary conditions for s-polarised waves are summarised to be

$$\begin{cases} E_{i,s} + E_{r,s} &= E_{t,s} \\ E_{i,s} - E_{r,s} &= ABE_{t,s} \end{cases} \tag{5.24}$$

with the substitutions of equations 5.19. Solving for $E_{r,s}$ and $E_{t,s}$ results in

$$E_{r,s} = \frac{1 - AB}{1 + AB}E_{i,s} \tag{5.25}$$

and

$$E_{t,s} = \frac{2}{1 + AB}E_{i,s}\ . \tag{5.26}$$

The solutions found for $\mathbf{E}_r(z = 0)$ and $\mathbf{E}_t(z = 0)$ hold for an interface between any two linear, isotropic, homogeneous media. Substituting A and B from equations 5.19 back in equations 5.20, 5.21, 5.25 and 5.26 leads to

$$\begin{aligned} E_{r,p} &= \frac{\sqrt{\mu_i\epsilon_t}\cos\theta_i - \sqrt{\mu_t\epsilon_i}\cos\theta_t}{\sqrt{\mu_i\epsilon_t}\cos\theta_i + \sqrt{\mu_t\epsilon_i}\cos\theta_t}E_{i,p} \\ E_{r,s} &= \frac{\sqrt{\mu_t\epsilon_i}\cos\theta_i - \sqrt{\mu_i\epsilon_t}\cos\theta_t}{\sqrt{\mu_t\epsilon_i}\cos\theta_i + \sqrt{\mu_i\epsilon_t}\cos\theta_t}E_{i,s} \\ E_{t,p} &= \frac{2\sqrt{\mu_t\epsilon_i}\cos\theta_i}{\sqrt{\mu_i\epsilon_t}\cos\theta_i + \sqrt{\mu_t\epsilon_i}\cos\theta_t}E_{i,p} \\ E_{t,s} &= \frac{2\sqrt{\mu_t\epsilon_i}\cos\theta_i}{\sqrt{\mu_t\epsilon_i}\cos\theta_i + \sqrt{\mu_i\epsilon_t}\cos\theta_t}E_{i,s} \end{aligned} \tag{5.27}$$

following some rearrangement. In dielectrics at optical frequencies, $\mu_i \approx \mu_t \approx \mu_0$ so that the refractive index can be used to replace the square root of the relative permittivity (approximation 2.44), the absolute vacuum permittivity dropping out of the ratio. Equations 5.27 then reduce to the four Fresnel equations that define the Fresnel amplitude

coefficients

$$\begin{aligned} r_p &\equiv \frac{E_{r,p}}{E_{i,p}} = \frac{n_t \cos\theta_i - n_i \cos\theta_t}{n_t \cos\theta_i + n_i \cos\theta_t} \\ r_s &\equiv \frac{E_{r,s}}{E_{i,s}} = \frac{n_i \cos\theta_i - n_t \cos\theta_t}{n_i \cos\theta_i + n_t \cos\theta_t} \\ t_p &\equiv \frac{E_{t,p}}{E_{i,p}} = \frac{2n_i \cos\theta_i}{n_t \cos\theta_i + n_i \cos\theta_t} \\ t_s &\equiv \frac{E_{t,s}}{E_{i,s}} = \frac{2n_i \cos\theta_i}{n_i \cos\theta_i + n_t \cos\theta_t} \end{aligned} \tag{5.28}$$

which are particular to the choice of axes and directions used in this work. The above coefficients are also known as Fresnel factors and should not be confused with reflectance and transmittance which relate to intensities rather than amplitudes. Equations 5.28 are valid for all angles $0° \leq \theta_{k,i} \leq 360°$ that specify the directionality of the incident wave as long as the expressions of the electromagnetic fields strictly follow equations 5.2 and 5.3. The incident wave may come from either side of the interface under any angle.

The amplitude coefficients for a neat silica-water interface are given in figure 5.11 as a function of the angle of incidence from either side of the interface. The real maximum values lie at the critical angle, with $r_p(\theta_c) = r_s(\theta_c) = 1$, $t_p(\theta_c) = 2$ and $t_s(\theta_c) = \frac{n_i}{n_t}$. Above the critical angle, the amplitude coefficients are complex numbers as θ_t becomes complex in that range.

5.2.3 Applied field near a neat interface

We deduce the field applied to a scatterer located away from the interface in medium 2 at $\mathbf{r}^{\mathsf{L}} = (0, 0, z)$. Only locations within the focal depth of the objective lens are relevant to our analysis. The value of z should therefore be limited in computations according to the objective being modelled. The retardation exponent in the expression for the electric field (equation 5.2) is

$$\mathrm{e}^{\mathrm{j}\mathbf{k}\cdot\mathbf{r}} = \mathrm{e}^{\mathrm{j}\frac{2\pi n_2}{\lambda_0} z \cos\theta_k} = \mathrm{e}^{\mathrm{j}k_2 z \cos\theta_k} \tag{5.29}$$

where θ_k (as given in equation 5.1) depends on the wave under consideration and where the wavenumber k_2 is

$$k_2 = \frac{2\pi n_2}{\lambda_0} \tag{5.30}$$

for medium 2 in which the scattering molecule is located.

Zones I and II

We can now express the amplitude of the macroscopic electric field $\mathbf{E}_{\mathsf{app}}(z)$ at the location of the scatterer as a function of the incident plane wave $\mathbf{E}_i$ in the laser frame of reference. Throughout our model, the scatterer is located at $z \geq 0$, in the medium of refractive index $n_2 < n_1$. For light incident through the hemisphere, zones I and II with $n_i = n_1$, the applied field $\mathbf{E}_{\mathsf{app}}(z, n_i = n_1)$ is the transmitted electric field $\mathbf{E}_t(z, n_i = n_1)$. This last

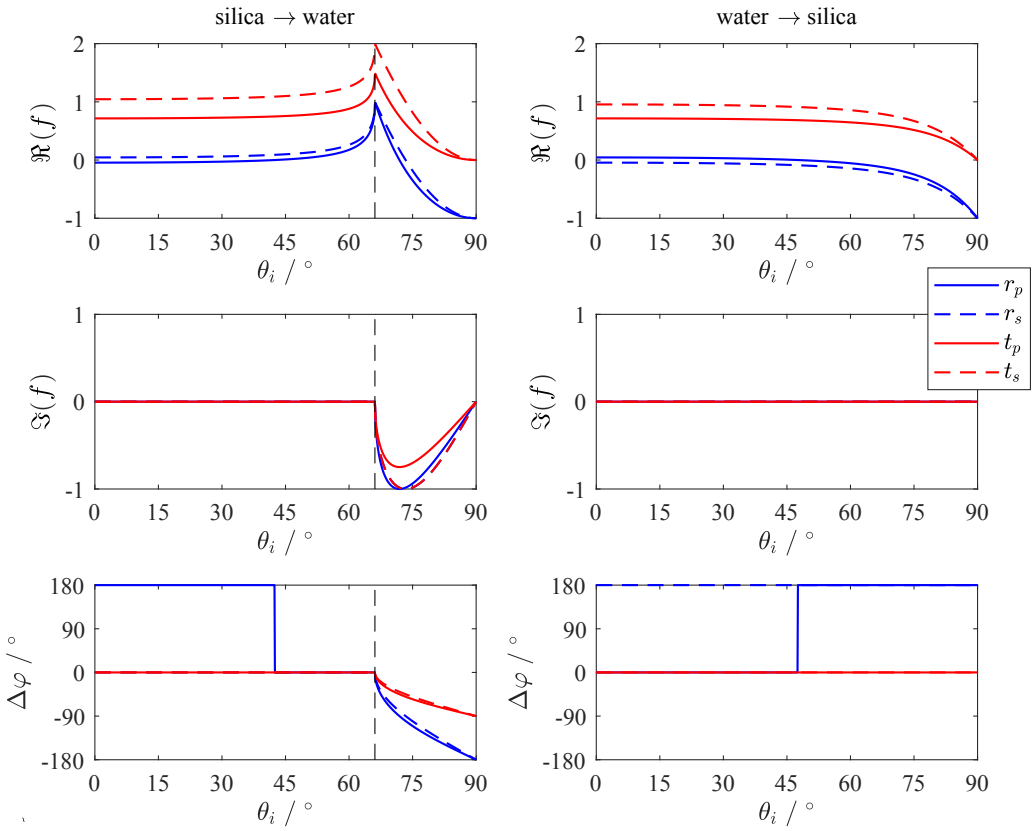

Figure 5.11: Fresnel amplitude coefficients $f = r_p, r_s, t_p, t_s$ for the silica-water interface ($n_{\text{silica}} = 1.4607$ and $n_{\text{water}} = 1.3355$ at 532 nm) as a function of the angle of incidence θ_i. The real and imaginary parts of the coefficients as well as their phase shift $\Delta\varphi$ are shown. With the light incident from the silica side (left plots), total internal reflection occurs if $\theta_i \geq \theta_c = 66.10°$ (dashed vertical line). This indicates a phase shift of the reflected and transmitted fields relative to the incident field. The reflected fields also undergo a phase shift at other angles of incidence, which relate to the sign of r_p and r_s that gives their directionality. In r_p, a further phase change is observed at Brewster angles $\theta_B = 44.4°$ and $47.6°$. A ray passing from water to silica (right plots) only undergoes real refraction (compare figure 5.8).

field is first expressed in the L-frame through equation 5.2. The angle $\theta_{k,t} = \theta_t$ as well as the amplitudes $E_{t,p} = t_p E_{i,p}$ and $E_{t,s} = t_s E_{i,s}$ are then substituted to obtain

$$\mathbf{E}_{\mathsf{app}}{}^{\mathsf{L}}(z, n_i = n_1) = \mathbf{E}_t{}^{\mathsf{L}}(z, n_i = n_1) = \begin{pmatrix} t_p E_{i,p} \cos\theta_t \\ t_s E_{i,s} \\ -t_p E_{i,p} \sin\theta_t \end{pmatrix} \mathrm{e}^{\mathrm{j}k_2 z \cos\theta_t} \tag{5.31}$$

which implicitly depends on $\theta_{k,i}$ through the amplitude coefficients and θ_t as given in the equations of table 5.1.

Zone III

The applied field at the scatterer for incident light from zone III, $n_i = n_2$, is derived as follows. The scatterer is located in the incident medium so that both the incident field and the reflected field contribute to the applied field at its location. This gives rise to interference as a function of the angle of incidence and of the depth position z. Both $\mathbf{E}_i$ and $\mathbf{E}_r$ are first expressed through equation 5.2, their propagation angles substituted according to table 5.1 and the reflected amplitudes replaced with the Fresnel coefficients of equations 5.28. The result is

$$\begin{aligned} \mathbf{E}_{\mathsf{app}}{}^{\mathsf{L}}(z, n_i = n_2) &= \mathbf{E}_i{}^{\mathsf{L}}(z, n_i = n_2) + \mathbf{E}_r{}^{\mathsf{L}}(z, n_i = n_2) \\ &= \begin{pmatrix} \left(-\mathrm{e}^{-\mathrm{j}k_2 z \cos\theta_i} + r_p \, \mathrm{e}^{\mathrm{j}k_2 z \cos\theta_i}\right) E_{i,p} \cos\theta_i \\ \left(\mathrm{e}^{-\mathrm{j}k_2 z \cos\theta_i} + r_s \, \mathrm{e}^{\mathrm{j}k_2 z \cos\theta_i}\right) E_{i,s} \\ \left(-\mathrm{e}^{-\mathrm{j}k_2 z \cos\theta_i} - r_p \, \mathrm{e}^{\mathrm{j}k_2 z \cos\theta_i}\right) E_{i,p} \sin\theta_i \end{pmatrix} \end{aligned} \tag{5.32}$$

For arbitrary linear polarisations of the incident field, the relation between the three Cartesian components of the applied field is determined by the polarisation angle ψ through equations 5.8. The sine and cosine terms in equation 5.31 and 5.32 introduce a constant phase shift of $\pi/2$ between the x and z components, making them orthogonal in phase. Additional phase shifts in each of the components of the incident and reflected fields arise from retardation. As $\mathbf{E}_{\mathsf{app}}$ undergoes further manipulation, its three spatial components are projected onto different axes. Their phase-relations then become important, hence the use of complex amplitudes throughout the model. Only the limiting cases of pure p or s polarisation prevent interaction between the three components as all are orthogonal in phase. At intermediate polarisations, the amplitude components interact to an extent determined by their phase differences.

Coupling factors

The results of this section can now be summarised in the form of the coupling factors (defined through equation 5.6) as

$$\mathbf{F}_{1\to2}(z) = \begin{cases} F_x = t_p \cos\theta_t \, \mathrm{e}^{\mathrm{j}k_2 z \cos\theta_t} \\ F_y = t_s \, \mathrm{e}^{\mathrm{j}k_2 z \cos\theta_t} \\ F_z = -t_p \sin\theta_t \, \mathrm{e}^{\mathrm{j}k_2 z \cos\theta_t} \end{cases} \tag{5.33}$$

$$\mathbf{F}_{2\to1}(z) = \begin{cases} F_x = \left(-\mathrm{e}^{-\mathrm{j}k_2 z \cos\theta_i} + r_p \, \mathrm{e}^{\mathrm{j}k_2 z \cos\theta_i}\right) \cos\theta_i \\ F_y = \mathrm{e}^{-\mathrm{j}k_2 z \cos\theta_i} + r_s \, \mathrm{e}^{\mathrm{j}k_2 z \cos\theta_i} \\ F_z = \left(-\mathrm{e}^{-\mathrm{j}k_2 z \cos\theta_i} - r_p \, \mathrm{e}^{\mathrm{j}k_2 z \cos\theta_i}\right) \sin\theta_i \end{cases} \tag{5.34}$$

In computing these coupling factors, care should be taken to use the correct values for n_i, n_t, θ_i and θ_t according to the propagation direction of the incident field (as given in table 5.1).

Figure 5.12 presents the coupling factors as a function of the relative distance z/λ_0 from the interface for a wave incident on the silica-water interface from both sides. The three radiation zones are clearly distinguishable. In zone I, the propagative incident field produces a propagative transmitted field that does not depend on z. In zone II, a short-ranging evanescent field is generated in medium 2 that falls off with increasing z. For fields incident from zone III, interference with the reflected field produces undulations at shallow angles of incidence. The coupling factors F_y and F_z show a maximum at the critical angle, on the boundary between zones I and II. This arises from the maximum in the Fresnel factors at that angle (compare figure 5.11). The applied field may thus be higher than the incident field, a fact that can be exploited in an experiment to enhance the Raman signal. However, F_x is zero for light incident at θ_c as $\cos\theta_t = 0$ in that case. The maximum in F_x is observed at normal incidence, where it is equal to F_y.

Evanescent field

The evanescent field generated with the incident field in zone II drops off with z through the exponential factor of $\mathbf{F}_{1\to2}(z)$ as

$$\mathrm{e}^{\mathrm{j}k_2 z \cos\theta_t} = \mathrm{e}^{-z/d_p} \tag{5.35}$$

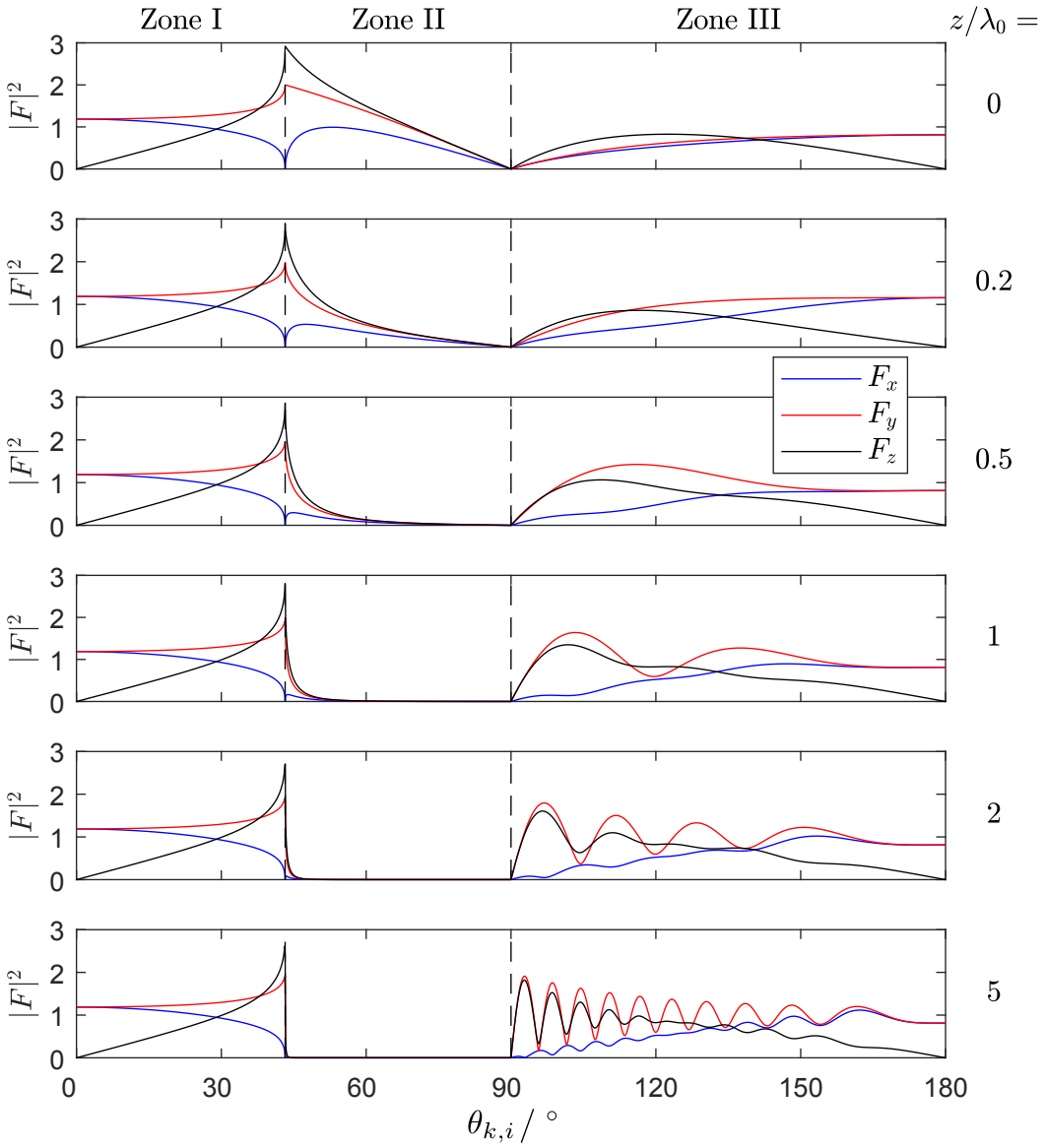

Figure 5.12: Complex modulus of the coupling factors F_x, F_y and F_z for the silica-air interface (refractive indices of table 3.2 at 532 nm) for $0° \leq \theta_{k,i} \leq 180°$ and as a function of z/λ_0 following equations 5.33 and 5.34.

where d_p is the penetration depth of the transmitted field. We can express d_p as a function of the angle of incidence, as this angle is set by the experimentalist, in the following way

$$\begin{aligned}\frac{1}{d_p} &= -\mathrm{j}\frac{2\pi n_2}{\lambda_0}\cos\theta_t \\ &= \sqrt{-1}\,\frac{2\pi n_2}{\lambda_0}\,\sqrt{1-\sin^2\theta_t} \\ &= \frac{2\pi n_2}{\lambda_0}\sqrt{\left(\frac{n_1}{n_2}\right)^2\sin^2\theta_i - 1} \\ &= \frac{2\pi n_1}{\lambda_0}\sqrt{\sin^2\theta_i - \left(\frac{n_2}{n_1}\right)^2}\end{aligned} \tag{5.36}$$

where we used the equality $\sin^2\theta_t + \cos^2\theta_t = 1$ and Snell's law (equation 5.10). The signs are chosen such that d_p is positive.

The last expression of equation 5.36 is the conventional form given for the penetration depth of the evanescent field. For $\theta_i \leq \theta_c$, we obtain $1/d_p = 0$ and the transmitted field is propagative. For $\theta_i > \theta_c$, θ_t is complex and d_p has a finite positive value. The amplitude of the transmitted field drops off exponentially with increasing distance from the interface to a minimum value at $\theta_i = 90°$ that depends on the refractive indices of the media and the wavelength used. The surface sensitivity of TIR Raman spectroscopy arises from the limited penetration depth associated with angles of incidence above the critical angle. A large difference in indices and a low wavelength reduce the penetration depth. Figure 5.13 presents d_p for the silica-air and silica-water interfaces for a 532-nm laser incident under TIR. For these interfaces, minimum penetration depth is 79.5 and 143 nm, respectively.

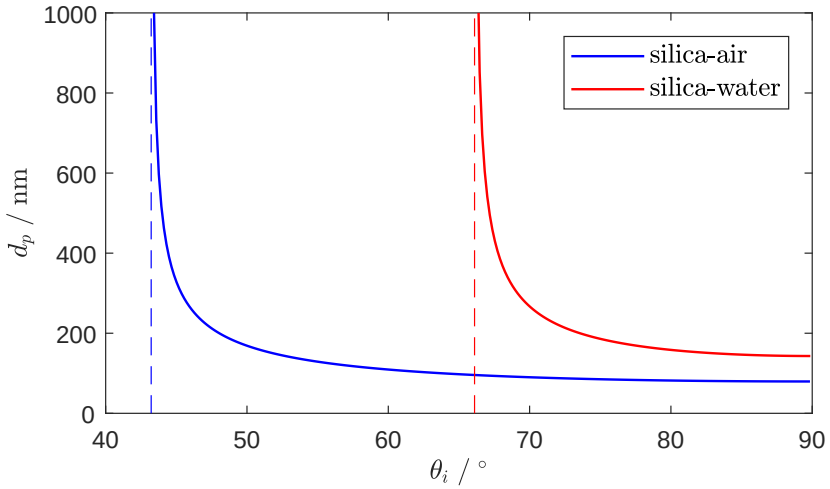

Figure 5.13: The penetration depth of the evanescent wave into air and water from a fused silica medium for incident light of 532 nm as a function of the angle of incidence $\theta_i \geq \theta_c$ (refractive indices of table 3.2). The critical angle is indicated with a dashed vertical line for each interface.

Although there is no transmitted ray propagating across the interface upon TIR, an evanescent wave arises near the interface which meets the electromagnetic boundary conditions. This evanescent wave penetrates the second medium but its amplitude decays exponentially from the interface. No energy is transferred over the interface, unless absorption or scattering takes place in the second medium. In such cases, the evanescent field is perturbed. This can be detected through the attenuation of the reflected field and through the detection of scattered light. There is, however, a non-zero net energy flux in the evanescent field along the x-direction [69]. For s-polarised incident light, the evanescent field is a transverse wave, linearly polarised along y. A p-polarised incident field generates x and z components of different complex amplitudes, rotating through the plane of incidence. Intermediate polarisations give rise to an evanescent wave of partly transverse and partly longitudinal character.

5.2.4 Applied field at the interface

For a scatterer located at the interface in medium 2, $z = 0$ and the coupling factors derived above (equations 5.33 and 5.34) simplify to

$$\mathbf{F}_{1\to2}(0) = \begin{cases} F_x = t_p \cos\theta_t \\ F_y = t_s \\ F_z = -t_p \sin\theta_t \end{cases} \tag{5.37}$$

$$\mathbf{F}_{2\to1}(0) = \begin{cases} F_x = (-1 + r_p)\cos\theta_i \\ F_y = 1 + r_s \\ F_z = -(1 + r_p)\sin\theta_i \end{cases} \tag{5.38}$$

These expressions differ in the sign of a number of components from those presented previously by our research group where the amplitude directions of the fields were left ambiguous (including references [35, 36, 54]). Strict adherence to the chosen definitions is needed to obtain meaningful modelling results.

5.2.5 Applied field in a thin film

In a thin film between two dielectric media with a layer thickness much smaller than the wavelength of the incident light as well as of the Raman scattering, the electric field is constant over the layer at any moment in time. The boundary conditions for this situation become

$$\begin{cases} \epsilon_1 E_1^{\perp} = \epsilon_2 E_2^{\perp} = \epsilon_3 E_3^{\perp} & \text{(i)} \\ B_1^{\perp} = B_2^{\perp} = B_3^{\perp} & \text{(ii)} \\ \mathbf{E}_1^{\parallel} = \mathbf{E}_2^{\parallel} = \mathbf{E}_3^{\parallel} & \text{(iii)} \\ \frac{1}{\mu_1}\mathbf{B}_1^{\parallel} = \frac{1}{\mu_2}\mathbf{B}_2^{\parallel} = \frac{1}{\mu_3}\mathbf{B}_3^{\parallel} & \text{(iv)} \end{cases} \tag{5.39}$$

where 1, 2 and 3 denote the fields in the hemisphere, thin film and lower medium, respectively. Conditions (i) and (iv) provide

$$E_{2,z} = \frac{\epsilon_3}{\epsilon_2} E_{3,z} \tag{5.40}$$

whereas the remaining conditions state that the x and y components of the field in the thin film are equal to those in medium 3 at the interface. The amplitude transmission coefficient $t_{p,1\to2}$ for light passing from the first to the second medium can then be given as

$$t_{p,1\to2} \equiv \frac{E_{2,z}}{E_{1,z}} = \frac{\frac{\epsilon_3}{\epsilon_2}E_{3,z}}{E_{1,z}} = \frac{\epsilon_3}{\epsilon_2} t_{p,1\to3} = \left(\frac{n_3}{n_2}\right)^2 t_{p,1\to3} \tag{5.41}$$

where $t_{p,1\to3}$ is the result of a single dielectric interface given in equation 5.28 with $n_i = n_1$ and $n_t = n_3$ and the angle of incidence and transmission in these media. The remaining boundary conditions for this situation result in the Fresnel coefficients for the bare dielectric interface at $z = 0$. The interface is too thin to affect the macroscopic reflection and refraction properties of the bounding dielectrics. Only the z-component of the macroscopic field within the film is affected by the refractive index of the film. The coupling factors can thus be given as

$$\mathbf{F}_{2,1\to3} = \begin{cases} F_x = t_p \cos\theta_t \\ F_y = t_s \\ F_z = -\left(\frac{n_3}{n_2}\right)^2 t_p \sin\theta_t \end{cases} \tag{5.42}$$

$$\mathbf{F}_{2,3\to1} = \begin{cases} F_x = (-1 + r_p)\cos\theta_i \\ F_y = 1 + r_s \\ F_z = -\left(\frac{n_3}{n_2}\right)^2 (1 + r_p)\sin\theta_i \end{cases} \tag{5.43}$$

where the Fresnel factors and angles are computed for a clean interface between media 1 and 3.

5.3 Induced dipole

Calculation of the Raman-induced dipole $\mathbf{p}$ starts with the applied field as developed in the previous section. Four variables are given as input: the orientation of the molecule relative to the laser frame L, the Raman tensor of the vibrational mode of interest in the molecular frame m, the polarisability and the semi-axes of the molecular ellipsoid. The last two are used for the local field correction. The applied field is first projected onto the molecular axes. This field also acts on the medium and gives rise to a macroscopic polarisation that affects the field experienced by the scattering molecule. The applied field is modified by local field correction factors to take this effect into account. These also effect the induced dipole, that produces a field in the medium acting back on itself. Finally, the resulting effective induced dipole is rotated back to the L-frame.

5.3.1 Orientation of the scattering molecule

The Raman tensor $\boldsymbol{\alpha}_{\mathsf{v}}{}^{\mathsf{m}}$ is specified in the molecular frame of reference m as detailed in chapter 4. The orientation of the molecule relative to the L-frame is fully given through the three Euler angles $(\alpha_{\mathsf{m}}, \beta_{\mathsf{m}}, \gamma_{\mathsf{m}})$ as defined in figure 2.2. To span the entire range of orientations uniquely, the angles are limited to the following ranges: $0^\circ \leq \alpha_{\mathsf{m}}, \gamma_{\mathsf{m}} < 360^\circ$ and $0^\circ \leq \beta_{\mathsf{m}} \leq 180^\circ$. These angles are physically relevant when the molecular axes have been chosen appropriately.

α_{m} gives the azimuthal orientation of the scatterer with respect to $\hat{\boldsymbol{x}}^{\mathsf{L}}$ about $\hat{\boldsymbol{z}}^{\mathsf{L}}$, *i.e.* it gives the orientation of the scatterer relative to the plane of incidence. At $\alpha_{\mathsf{m}} = 0^\circ$ or 180°, the scatterer is oriented parallel to this plane.

β_{m} gives the tilt of the scatterer with respect to $\hat{\boldsymbol{z}}^{\mathsf{L}}$. At $\beta_{\mathsf{m}} = 0^\circ$ or 180°, the scatterer is perpendicular to the interface, while it is parallel to it at $\beta_{\mathsf{m}} = 90^\circ$.

γ_{m} specifies the twist of the scatterer about its own primary axis $\hat{\boldsymbol{z}}^{\mathsf{m}}$. For tilt angles $\beta_{\mathsf{m}} = 0^\circ$ and 180°, both the azimuthal angle α_{m} and the twist angle γ_{m} describe the same orientation.

The specified angles define the transformation matrix

$$\mathbf{T}_{\mathsf{L}\to\mathsf{m}} = \mathbf{R}_z(\gamma_{\mathsf{m}})\, \mathbf{R}_x(\beta_{\mathsf{m}})\, \mathbf{R}_z(\alpha_{\mathsf{m}}) \tag{5.44}$$

and its transform $\mathbf{T}_{\mathsf{L}\to\mathsf{m}}{}^{\mathrm{T}} = \mathbf{T}_{\mathsf{m}\to\mathsf{L}}$ according to equations 2.13 and 2.15. Though the Raman tensor can be expressed in the L-frame as

$$\boldsymbol{\alpha}_{\mathsf{v}}{}^{\mathsf{L}} = \mathbf{T}_{\mathsf{L}\to\mathsf{m}}{}^{\mathrm{T}}\, \boldsymbol{\alpha}_{\mathsf{v}}{}^{\mathsf{m}}\, \mathbf{T}_{\mathsf{L}\to\mathsf{m}} \tag{5.45}$$

we choose to transform the electric field in our model rather than the Raman tensor. The model can thus calculate the effect of any particular scatterer orientation by specifying a unique set of angles as input.

5.3.2 Local field correction

The Raman polarisability tensor of the molecule $\boldsymbol{\alpha}_{\mathsf{v}}{}^{\mathsf{m}}$ is computed for an isolated molecule in an external electric field. If the scattering molecule is embedded in a dielectric medium, the effect of its surroundings on the local field at the location of the molecule should be taken into account. This has been theorised by Lorentz, Onsager, Böttcher and Scholte, amongst others [153]. From the various models, the Onsager-Scholte model of the local field was proven to be most appropriate to account for experimental Rayleigh scattering intensities [153].

Light scattering is understood as absorption followed by emission, so that a local field correction has to be applied in both processes. In Rayleigh scattering, these corrections

are identical as the frequency of the light is not altered. In Raman scattering, the mathematical description is identical but the frequency changes. This decouples the absorption from the emission process. Wortmann and Bishop [154] described the application of this model to nonlinear optical experiments in condensed media, from which we formulate a local-field correction for our situation.

Note that with this attempt at incorporating (an)isotropic local field corrections in a quantitative way, we accept that a hybrid model, which involves both a molecular and a continuum approach, captures the essential features of our systems correctly. Moreover, we assume that the interface between these two perspectives is taken into account adequately. We will see in the below analysis that there is room for both theoretical elaboration, especially when it comes to anisotropic properties, as well as for practical evidence related to the correctness of the local field correction in various experimental situations. However, it is our present aim to build a consistent model for interpretation of Raman intensities rather than advancing general solutions to the local field problem. Notwithstanding this limited ambition, references to more advanced treatments are included.

Onsager-Scholte model of the local field

In Onsager's reaction field model, a solute molecule is considered within a hypothetical cavity in a homogeneous solvent. The electric properties of the molecule are described through its polarisability $\boldsymbol{\alpha}$ and the solvent through its electric permittivity ϵ (or its refractive index $n = \sqrt{\epsilon_r}$, in a non-magnetic substance). In a pure liquid, where the molecule in the cavity is the same as the solvent, the polarisability and refractive index are related through equation 3.5, the Clausius-Mossotti relation. Scholte extended Onsager's model by a generalisation of the cavity from a spherical to an ellipsoidal shape and considering polarisation anisotropy in the molecule [153]. The local field is treated as the superposition of a cavity field and a reaction field[†]

$$\mathbf{E}_{\mathsf{local}} = \mathbf{E}_{\mathsf{cavity}} + \mathbf{E}_{\mathsf{reaction}} \tag{5.46}$$

which holds for all Fourier components of the field (*i.e.* for each frequency).

The cavity field is the electric field generated by the surrounding material at the centre of the ellipsoidal void. It arises from the applied field, modified by the macroscopic polarisation of the medium, as

$$\mathbf{E}_{\mathsf{cavity}} = \mathbf{C}\,\mathbf{E}_{\mathsf{app}} \tag{5.47}$$

with $\mathbf{C}$ a tensor of factors that depend on the shape of the cavity and the relative permittivity of the surrounding medium.

The reaction field originates from the dipole moment of the molecule in the cavity. This dipole induces polarisation in the surrounding medium, which in turn gives rise to

[†]Note that nomenclature differs in various treatments of the local field correction.

an electric field. This is the reaction field

$$\mathbf{E}_{\mathsf{reaction}} = \mathbf{R}\,\mathbf{p}_{\mathsf{ind}} = \mathbf{R}\,\boldsymbol{\alpha}\,\mathbf{E}_{\mathsf{local}} \tag{5.48}$$

which acts back on the molecule through reaction field tensor $\mathbf{R}$ in units of reciprocal polarisability, V C^{-1} m^{-2}. This field is produced by the molecular dipole, which generally consists of the permanent dipole moment plus all terms of equation 2.17. At optical frequencies in the linear approximation used here, only the induced dipole moment at the frequency of the incident light contributes. Thus, $\mathbf{p}_{\mathsf{ind}}$ arises from the local field acting on the molecule and the linear polarisability $\boldsymbol{\alpha}$ of the molecule.

Substitution of equations 5.47 and 5.48 into 5.46 gives an expression for the local field as a function of the applied field

$$\mathbf{E}_{\mathsf{local}} = \frac{\mathbf{C}}{\mathbf{I} - \mathbf{R}\,\boldsymbol{\alpha}}\mathbf{E}_{\mathsf{app}} \tag{5.49}$$

where $\mathbf{I}$ is a 3×3 identity matrix. The proportionality between the local and applied field is the local field correction $\mathbf{L}$ of dimensionless numbers. It is generally tensorial in nature. If the axes of the cavity align with the polarisability axes of the molecule, $\mathbf{C}$ and $\mathbf{R}$ are diagonal tensors in the same frame of reference. Expressing the electric fields in this frame ensures that the cross-terms in $\mathbf{L}$ disappear. The diagonal elements of $\mathbf{L}$ then contain the three local field correction factors

$$L_{ii} = \frac{E_{\mathsf{local},i}}{E_{\mathsf{app},i}} \tag{5.50}$$

with $i = x, y, z$.

Cavity and reaction field tensors

We now express the components of the cavity and reaction field tensors in the molecular frame of reference. In our analysis, we assume that the m-frame is aligned along the major axes of the polarisability and that these coincide with the ellipsoid axes that capture the overall shape of the molecule. This is a reasonable assumption as polarisability arises from electron density which depends on the geometry of the molecule. Anisotropy of molecular shape thus correlates with its anisotropy in polarisability. The tensors $\mathbf{C}$ and $\mathbf{R}$ are then given in the molecular frame as

$$\mathbf{C}^{\mathsf{m}} = \begin{pmatrix} C_{xx} & 0 & 0 \\ 0 & C_{yy} & 0 \\ 0 & 0 & C_{zz} \end{pmatrix} \tag{5.51}$$

and

$$\mathbf{R}^{\mathsf{m}} = \begin{pmatrix} R_{xx} & 0 & 0 \\ 0 & R_{yy} & 0 \\ 0 & 0 & R_{zz} \end{pmatrix} \tag{5.52}$$

These tensors are applied to $\mathbf{E}_{\mathsf{app}}$ expressed in molecular frame of reference to obtain ${\mathbf{E}_{\mathsf{local}}}^{\mathsf{m}}$. If the m-frame is not parallel to the axes of the polarisability or the molecular ellipsoid, additional rotations are required.

In the Onsager-Scholte model of the local field, the diagonal components of $\mathbf{C}$ and $\mathbf{R}$ are given through [154]

$$C_{ii} = \frac{\epsilon_r}{\epsilon_r - S_i(\epsilon_r - 1)} \tag{5.53}$$

and

$$R_{ii} = \frac{3S_i(1 - S_i)(\epsilon_r - 1)}{4\pi\epsilon_0 r_x r_y r_z \left(\epsilon_r - S_i(\epsilon_r - 1)\right)} \tag{5.54}$$

with $i = x, y, z$ and $\epsilon_r = n^2$ of the medium surrounding the cavity. The semi-axes of the ellipsoidal cavity are r_x, r_y and r_z specified in the m-frame. The reaction field depends on the size as well as the shape of the cavity, whereas the cavity field only depends on its shape. The numerical factor S_i is the shape parameter that depends on the ellipsoid radii as explained in the next paragraph. The local field correction factor has the form

$$L_{ii} = \frac{C_{ii}}{1 - R_{ii}\,\alpha_{ii}} = \frac{1}{1 - \frac{\epsilon_r - 1}{\epsilon_r} S_i \left(1 + 3(1 - S_i)\right) \frac{\alpha_{ii}}{4\pi\epsilon_0 r_x r_y r_z}} \tag{5.55}$$

with all quantities in the m-frame of reference. It depends on two molecular properties: its ellipsoidal shape and the diagonal polarisability α_{ii}.

Before we continue to address the effect of each parameter, note that the Onsager-Scholte description of the local field breaks down when

$$\frac{\alpha_{ii}}{4\pi\epsilon_0 r_x r_y r_z} = \frac{\epsilon_r}{(\epsilon_r - 1) S_i \left(1 + 3(1 - S_i)\right)} \tag{5.56}$$

as $L_{ii} \to \infty$. Higher order correction terms have been suggested to correct for the occurence of this resonance through correlations between dipoles in the liquid [155] and through taking microscopic fluctuations of the local field into account [156], using a first layer of discrete molecules around the cavity and a continuum description of the dielectric beyond that layer.

Shape parameter

The form of the cavity is an ellipsoid with semi-axes r_x, r_y and r_z in the molecular frame of reference. The Van der Waals radius of the molecule is most appropriate to describe its shape along each dimension [153]. The volume of the molecular ellipsoid is

$$V = \frac{4}{3}\pi r_x r_y r_z \tag{5.57}$$

which is related to the number density N used in the Clausius-Mossotti relation (equation 3.5) as

$$N = \frac{1}{V} \tag{5.58}$$

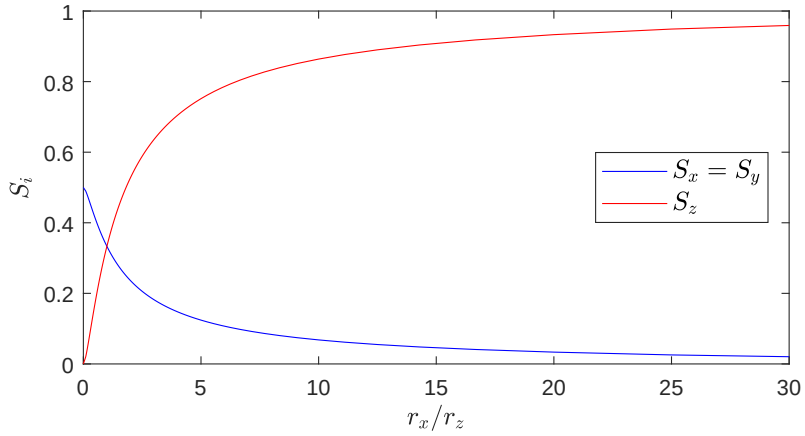

Figure 5.14: Shape parameters for a spheroid.

when considering a pure liquid, *i.e.* a cavity molecule surrounded by a medium consisting of the same molecules with equal polarisability volumes.

The shape parameter S_i along axis i (also known as the demagnetisation factor and depolarisation factor) is computed through [153]

$$S_i = \int_0^\infty \frac{r_x r_y r_z \mathrm{d}u}{2(u + {r_i}^2)\sqrt{(u + {r_x}^2)(u + {r_y}^2)(u + {r_z}^2)}} \tag{5.59}$$

with $i = x, y, z$. It is a dimensionless number ranging from 0 to 1 and the sum of the three components satisfies

$$S_x + S_y + S_z = 1 \ . \tag{5.60}$$

For larger r_i, the shape factor S_i reduces as the sum of the three remains constant. Shape parameters can be computed from the cavity semi-axes specified as either absolute or relative values. The computation has been implemented numerically in the MATLAB function `shapefactor` (included as appendix E.1).

The shape factors for a spheroid (an ellipsoid of revolution along z where $r_x = r_y$) are presented in figure 5.14. As the relative value of r_z increases, five cases are noted:

$r_x/r_z = 0$ is a long, thin needle-shaped cavity with $S_x = S_y = \frac{1}{2}$ and $S_z = 0$,

$0 < r_x/r_z < 1$ is a prolate spheroid, elongated along z, with $S_x = S_y > S_z$,

$r_x/r_z = 1$ denotes a sphere with $S_x = S_y = S_z = \frac{1}{3}$,

$r_x/r_z > 1$ forms an oblate spheroid, flattened along its z-axis with $S_x = S_y < S_z$,

$r_x/r_z \to \infty$ is the limit of a thin disk in the xy plane with $S_x = S_y = 0$ and $S_z = 1$.

To assess the effect of the shape parameter on the local field correction, we assume a molecule with an isotropic polarisability $\alpha_{xx} = \alpha_{yy} = \alpha_{zz} = \alpha$ in a cavity surrounded by a medium of the same material. Its polarisability and electric permittivity are then

related through the Clausius-Mossotti relation, which is used with equations 5.57 and 5.58 to substitute

$$\frac{\alpha}{4\pi\epsilon_0 r_x r_y r_z} = \frac{\epsilon_r - 1}{\epsilon_r + 2} \tag{5.61}$$

in the local field factor of equation 5.55. We then obtain

$$L_{ii} = \frac{1}{1 - \frac{(\epsilon_r - 1)^2}{\epsilon_r(\epsilon_r + 2)} S_i \left(1 + 3(1 - S_i)\right)} \tag{5.62}$$

which only depends on the anisotropy of the molecular ellipsoid. Equation 5.62 is plotted against S_i in figure 5.15 for a number of refractive indices $n = \sqrt{\epsilon_r}$. In vacuum, the local field is equal to the applied field in all directions, $L_{ii} = 1$, as expected. As n increases, the local field is amplified depending on the shape of the cavity. The maximum in L_{ii} occurs at shape parameter $S_i = 2/3$. The same value for L_{ii} is obtained with both $S_i = 1/3$ and $S_i = 1$, implying that the local field along a particular axis is the same for a sphere as for a disk perpendicular to this axis.

The effect of shape anisotropy of the molecular ellipsoid is to amplify the local field along the smaller axes of the ellipsoid. If, for instance, $r_x < r_y < r_z$, the shape parameters are $S_x > S_y > S_z$ (assumed that each $S_i \leq 2/3$). The local field is increased along all directions, but more along the small axis. The applied field is thus rotated towards the smaller axis of the ellipsoid. This decreases the observed anisotropy of the molecule.

Polarisability of the scattering molecule

The effect of polarisability on the local field correction is assessed by assuming a spherical cavity, $r_x = r_y = r_z = r$ resulting in $S_i = 1/3$. The local field factor of equation 5.55 is then given by

$$L_{ii} = \frac{1}{1 - \frac{\epsilon_r - 1}{\epsilon_r} \frac{\alpha_{ii}}{4\pi\epsilon_0 r^3}} \tag{5.63}$$

which only depends on the anisotropy of the polarisability. This relation is presented in figure 5.16 as a function of the ratio $\frac{\alpha_{ii}}{4\pi\epsilon_0 r^3}$ for a range of refractive indices $n = \sqrt{\epsilon_r}$. As $L_{ii} > 1$, the local field is stronger than the applied field. The higher the polarisability, the stronger the local field along this axis. The local field correction thus disproportionately amplifies the anisotropy of the polarisability of the molecules.

For a spherical molecule with an isotropic polarisability, we have $\alpha_{xx} = \alpha_{yy} = \alpha_{zz}$ so that the local field correction factors along each axis are equal: $L_{xx} = L_{yy} = L_{zz}$. In this case, the vectorial amplitude of the local field is strictly proportional to the applied field without rotation. The local field factor of a spherical molecule of isotropic polarisablity in a pure liquid further simplifies to

$$L_{\mathsf{iso}} = \frac{1}{1 - \frac{(\epsilon_r - 1)^2}{\epsilon_r(\epsilon_r + 2)}} = \frac{{\epsilon_r}^2 + 2\epsilon_r}{4\epsilon_r + 1} \tag{5.64}$$

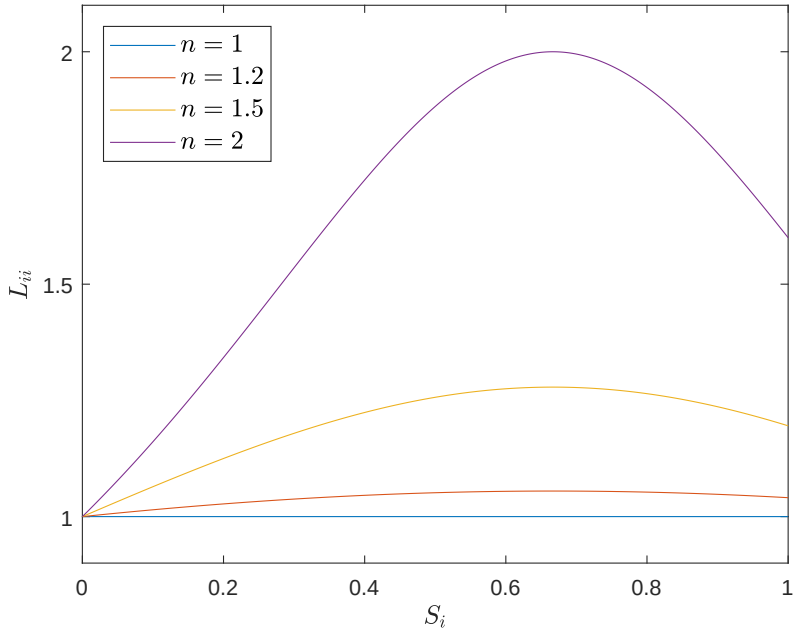

Figure 5.15: Local field factor L_{ii} for an isotropically polarisable molecule in its own pure liquid of refractive index $n = \sqrt{\epsilon_r}$ (equation 5.62) as a function of the shape parameter S_i.

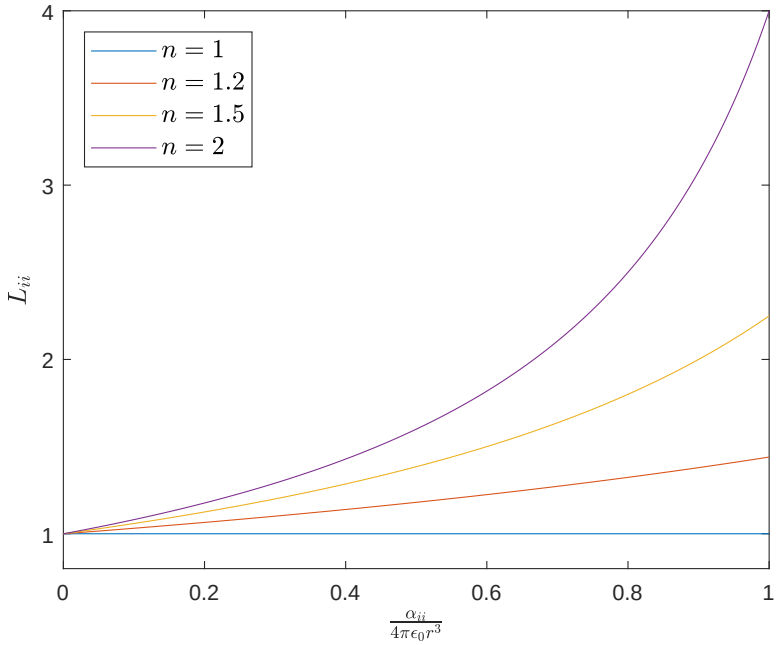

Figure 5.16: Local field factor L_{ii} for a spherical cavity (equation 5.63) in a medium of refractive index $n = \sqrt{\epsilon_r}$ as a function of the relative polarisability of the molecule at the centre of the cavity.

which applies along any axis of the system and only depends on the refractive index of the medium. This expression results from equations 5.63 and 5.61.

The fully isotropic local field factor simply scales the applied field and does not alter its directionality. This correction is only of consequence in our model when comparing materials of different refractive indices. In all other cases, it is merely a scaling factor. For ellipsoidal cavities and anisotropic polarisabilities, the local field correction has an unequal effect on the amplitude components of the applied electric field. It thus affects the computed intensities through the orientation of the scattering molecule.

Remarks

In the above treatment of the local field correction, the surrounding medium was assumed to fully enclose the cavity of the scattering molecule. This is not strictly the case for molecules at an interface or in a monolayer.

In their computations of the Lorentz local field, Lekner and Castle found that the local field deviates at most a few percent at the surface of a crystalline solid from the value in its bulk [157]. Further computations at a liquid-vapour interface with an inhomogeneous non-polar fluid give rise to similar results [158]. In a more advanced version of our current model, these effects could be taken into account though the molecular systems of this work are more complex than those assessed by Lekner and Castle.

Here, the dimensions of the cavity are taken to be the molecular Van der Waals radii. The cavity is thus the size of the molecule. Since only the effects from the surrounding medium are taken into account, effects from other parts of the molecule would be ignored. These should therefore be included with the polarisability and Raman polarisability tensors employed with the local field correction. This is the case for the computationally-derived tensors from GAUSSIAN used in this work (see section 4.3).

5.3.3 The effective Raman dipole

The local electric field $\mathbf{E}_{\mathsf{local}}$ at the molecule drives Raman scattering. This field oscillates at the laser frequency ω_l and induces a dipole $\mathbf{p}_{\mathsf{ind}}$, which oscillates at a shifted Raman frequency ω_R, through the Raman polarisability tensor $\boldsymbol{\alpha}_{\mathsf{v}}{}^{\mathsf{m}}$ of vibrational mode v with vectorial dipole moment

$$\mathbf{p}_{\mathsf{ind}}{}^{\mathsf{m}}(\omega_R) = \boldsymbol{\alpha}_{\mathsf{v}}{}^{\mathsf{m}}\ \mathbf{E}_{\mathsf{local}}{}^{\mathsf{m}}(\omega_l) \tag{5.65}$$

that in turn produces an electric field oscillating at ω_R and polarising the surrounding medium at this frequency. The polarisation of the surrounding medium results in a reaction field (introduced in equation 5.48) at the location of the originally induced Raman dipole given by

$$\mathbf{E}_{\mathsf{reaction}}{}^{\mathsf{m}}(\omega_R) = \mathbf{R}^{\mathsf{m}}(\omega_R)\ \mathbf{p}_{\mathsf{ind}}{}^{\mathsf{m}}(\omega_R) \tag{5.66}$$

with the reaction field tensor $\mathbf{R}^{\mathsf{m}}$ as defined in equations 5.52 and 5.54 with $\epsilon_r = n^2$ of the medium at the Raman-shifted wavelength. The reaction field can be seen as originating

from a reaction dipole $\mathbf{p}_{\mathsf{reaction}}$ at the centre of the cavity that modifies the originally induced dipole $\mathbf{p}_{\mathsf{ind}}$. An effective Raman dipole $\mathbf{p}_{\mathsf{eff}}$ generated in the molecule can thus be given as

$$\begin{aligned} {\mathbf{p}_{\mathsf{eff}}}^{\mathsf{m}} &= {\mathbf{p}_{\mathsf{ind}}}^{\mathsf{m}} + {\mathbf{p}_{\mathsf{reaction}}}^{\mathsf{m}} \\ &= {\mathbf{p}_{\mathsf{ind}}}^{\mathsf{m}} + \boldsymbol{\alpha}^{\mathsf{m}}\ {\mathbf{E}_{\mathsf{reaction}}}^{\mathsf{m}} \\ &= {\mathbf{p}_{\mathsf{ind}}}^{\mathsf{m}} + \boldsymbol{\alpha}^{\mathsf{m}}\ \mathbf{R}^{\mathsf{m}}\ {\mathbf{p}_{\mathsf{ind}}}^{\mathsf{m}} \\ &= (\mathbf{I} + \boldsymbol{\alpha}^{\mathsf{m}}\ \mathbf{R}^{\mathsf{m}})\ {\mathbf{p}_{\mathsf{ind}}}^{\mathsf{m}} \end{aligned} \tag{5.67}$$

where all quantities are implicitly taken at the Raman frequency ω_R.

Note that this treatment is similar to the local field correction presented above. However, there is no cavity field with the effective Raman dipole as there is no externally applied field at the Raman frequency. The local field for the dipole emission process is thus equal to the reaction field only. A cavity field does come into play for the emission process when considering the far-field of the effective Raman dipole through reciprocity (section 5.4.2).

We will term $\mathbf{D}$ the dipole reaction tensor and define it as

$$\mathbf{D}^{\mathsf{m}} = \mathbf{I} + \boldsymbol{\alpha}^{\mathsf{m}}\ \mathbf{R}^{\mathsf{m}} \tag{5.68}$$

which is specified in the molecular frame of reference. For a diagonal polarisability tensor, $\mathbf{D}$ is diagonal as all constituent tensors are diagonal in the Onsager-Scholte formalism. Using equation 5.54 to substitute R_{ii}, we then have

$$D_{ii} = 1 + \frac{\alpha_{ii}}{4\pi\epsilon_0 r_x r_y r_z} \frac{3S_i(1-S_i)(\epsilon_r - 1)}{\epsilon_r - S_i(\epsilon_r - 1)} \tag{5.69}$$

which is even further simplified if $\boldsymbol{\alpha}^{\mathsf{m}}$ is isotropic.

The relation between D_{ii} and ϵ_r as well as S_i is presented in figure 5.17 for $\alpha_{ii} = 4\pi\epsilon_0 r_x r_y r_z$. We observe that the effect of the shape parameter on the dipole reaction factor is similar to its effect on the local field factor (figure 5.15) but the maximum of D_{ii} does not occur at a fixed value of S_i. The higher the refractive index of the medium, the stronger the effect of the anisotropy of the molecular cavity. The dipole moment along the short axis of the molecule (high shape parameter) is affected more strongly by the reaction field than its moment along the longer axes. The dipole reaction tensor (through the reaction field) thus rotates the induced dipole moment towards the smaller axis of the molecule.

Summarising the results of the current and previous sections through subsequent substitution of our intermediate results, we may express the effective induced dipole in the

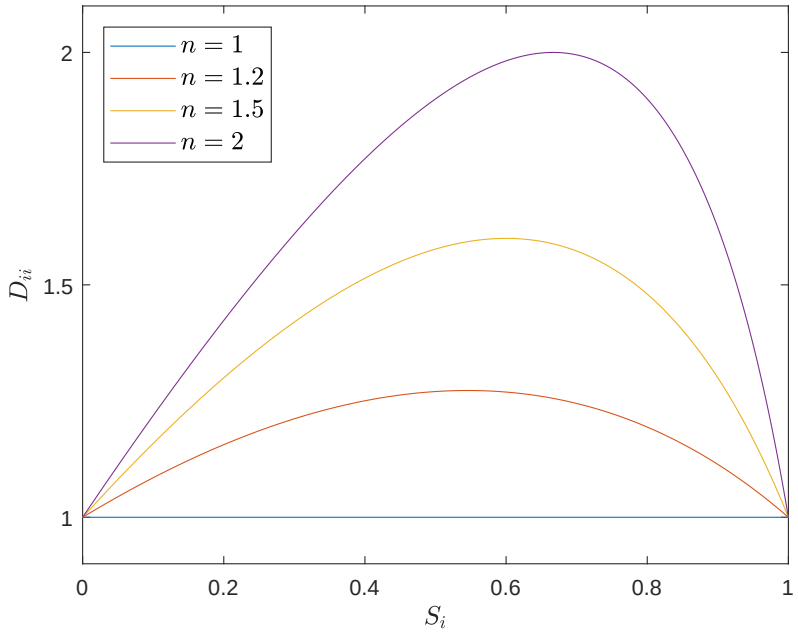

Figure 5.17: Dipole reaction factor D_{ii} (equation 5.69) as a function of shape parameter S_i and refractive index $n = \sqrt{\epsilon_r}$ of the medium for $\alpha_{ii} = 4\pi\epsilon_0 r_x r_y r_z$.

L-frame as

$$\begin{aligned}
\mathbf{p}_{\mathsf{eff}}{}^{\mathsf{L}}(\omega_R) &= \mathbf{T}_{\mathsf{L}\to\mathsf{m}}{}^{\mathrm{T}}\ \mathbf{p}^{\mathsf{m}}_{\mathsf{eff}}(\omega_R) \\
&= \mathbf{T}_{\mathsf{L}\to\mathsf{m}}{}^{\mathrm{T}}\ (\mathbf{I} + \boldsymbol{\alpha}^{\mathsf{m}}\ \mathbf{R}^{\mathsf{m}}(\omega_R))\ \mathbf{p}_{\mathsf{ind}}{}^{\mathsf{m}}(\omega_R) \\
&= \mathbf{T}_{\mathsf{L}\to\mathsf{m}}{}^{\mathrm{T}}\ (\mathbf{I} + \boldsymbol{\alpha}^{\mathsf{m}}\ \mathbf{R}^{\mathsf{m}}(\omega_R))\ \boldsymbol{\alpha}_{\mathsf{v}}{}^{\mathsf{m}}\ \mathbf{E}_{\mathsf{local}}{}^{\mathsf{m}}(\omega_l) \\
&= \mathbf{T}_{\mathsf{L}\to\mathsf{m}}{}^{\mathrm{T}}\ (\mathbf{I} + \boldsymbol{\alpha}^{\mathsf{m}}\ \mathbf{R}^{\mathsf{m}}(\omega_R))\ \boldsymbol{\alpha}_{\mathsf{v}}{}^{\mathsf{m}}\ \frac{\mathbf{C}^{\mathsf{m}}(\omega_l)}{\mathbf{I} - \mathbf{R}^{\mathsf{m}}(\omega_l)\ \boldsymbol{\alpha}^{\mathsf{m}}}\ \mathbf{E}_{\mathsf{app}}{}^{\mathsf{m}}(\omega_l) \\
&= \mathbf{T}_{\mathsf{L}\to\mathsf{m}}{}^{\mathrm{T}}\ (\mathbf{I} + \boldsymbol{\alpha}^{\mathsf{m}}\ \mathbf{R}^{\mathsf{m}}(\omega_R))\ \boldsymbol{\alpha}_{\mathsf{v}}{}^{\mathsf{m}}\ \frac{\mathbf{C}^{\mathsf{m}}(\omega_l)}{\mathbf{I} - \mathbf{R}^{\mathsf{m}}(\omega_l)\ \boldsymbol{\alpha}^{\mathsf{m}}}\ \mathbf{T}_{\mathsf{L}\to\mathsf{m}}\ \mathbf{E}_{\mathsf{app}}{}^{\mathsf{L}}(\omega_l)
\end{aligned} \tag{5.70}$$

where the frequencies of Raman scattering ω_R and incident laser ω_l are included to emphasise the distinct absorption and emission processes. This also accounts for any optical dispersion in the $\mathbf{C}$ and $\mathbf{R}$ tensors (through ϵ_r) while the molecular polarisability $\boldsymbol{\alpha}$ is assumed to be equal at both frequencies. From the above expression, an effective Raman polarisability tensor may be defined in the molecular frame of reference as

$$\boldsymbol{\alpha}_{\mathsf{v,eff}}{}^{\mathsf{m}} = (\mathbf{I} + \boldsymbol{\alpha}^{\mathsf{m}}\ \mathbf{R}^{\mathsf{m}}(\omega_R))\ \boldsymbol{\alpha}_{\mathsf{v}}{}^{\mathsf{m}}\ \frac{\mathbf{C}^{\mathsf{m}}(\omega_l)}{\mathbf{I} - \mathbf{R}^{\mathsf{m}}(\omega_l)\ \boldsymbol{\alpha}^{\mathsf{m}}} \tag{5.71}$$

which depends on molecular properties and the relative permittivity ϵ_r of the embedding medium.

5.4 Dipole radiation field

The effective dipole $\mathbf{p}_{\mathsf{eff}}{}^{\mathsf{L}}$ induced by the local field generates a radiation field propagating outward in all directions. The vectorial amplitude of this field depends on its propagation direction relative to the orientation of the dipole and is modulated by the vicinity of the interface. This section develops the computation of the field $\mathbf{E}_{\mathsf{dip}}{}^{\mathsf{L}}(Q)$ due to the dipole in the L-frame at a point Q (figure 5.5) at the entrance to the microscope objective. This far-field is derived through Lorentz reciprocity.

5.4.1 Field of view

The microscope objective collects a cone of the scattered light. The portion falling within view of the objective depends on its numerical aperture (NA) and is modelled as a square grid of discrete points Q.

Microscope objective

In the O-frame of reference, the collected portion of the scattering forms a cone of light around the z^{O}-axis. The size of this cone is given through the numerical aperture (NA) of the objective lens, which is given as input to the model. The numerical aperture of a lens is given by

$$\mathrm{NA} = n \sin \theta_{\mathsf{obj}} \tag{5.72}$$

with n the refractive index of the immersion material, which is air in the present case, and θ_{obj} half the angle of the maximum cone of light that can enter the objective.

The objective can further be specified with a working distance (WD) measured from the outer lens of the objective to the interface (disregarding any effects of the hemisphere), and a radius R_{obj}. These are geometrically linked through

$$\tan \theta_{\mathsf{obj}} = \frac{R_{\mathsf{obj}}}{\mathrm{WD}} \tag{5.73}$$

as can be seen in figure 5.18. The objective is axially aligned with the laboratory frame z^{O}-axis (in fact, it defines this axis) and the front of its first lens is positioned at $z^{\mathsf{O}} = WD$, parallel to the $x^{\mathsf{O}}y^{\mathsf{O}}$-plane. The radius of the objective entrance is than given through

$$R_{\mathsf{obj}} = \mathrm{WD}\ \tan\left(\arcsin \frac{\mathrm{NA}}{n_{\mathsf{air}}}\right) \tag{5.74}$$

To simplify the analysis, the length of the unit vector is scaled to WD so that WD = 1 in the O-frame. Only the NA of the objective is then needed to specify the size of the collection cone in the model.

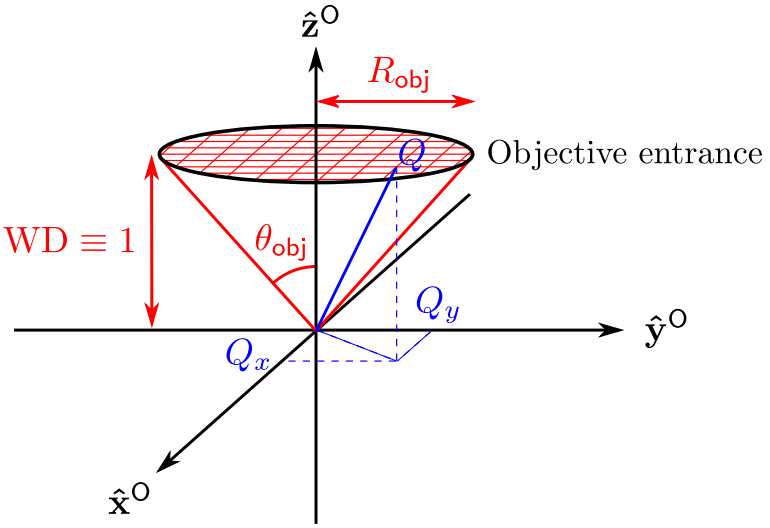

Figure 5.18: The cone of light collected by the microscope objective is characterised with working distance WD (chosen as the unit length in the O-frame of reference) and radius R_{obj}, which are linked through the maximum half-angle of the cone θ_{obj} that is specified through the numerical aperture of the lens.

Grid of rays

A square grid models the part of the scattered light that is collected by the microscope objective. It is defined parallel to the $x^{\mathsf{O}}y^{\mathsf{O}}$-plane and represents the aperture of the objective as illustrated in figure 5.18. Each node of this grid is a point Q at which the vectorial amplitude of a light ray that originates from the induced dipole is computed. As long as enough points are sampled, a square grid accurately represents the circular aperture of the objective field of view.

The position of the modelling grid along the z^{O}-axis is arbitrary. The actual working distance need not be taken as only relative amplitudes and intensities are modelled. The profile of the electric field over the grid remains the same, whatever its numerical vertical position. This can be shown as follows. The far-field of a dipole drops off with distance r as $1/r$ (equation 2.120) so that the ratio of the electric field at the centre of the grid to the field at the edge can be expressed as

$$\frac{E_{\mathsf{dip}}(\text{edge})}{E_{\mathsf{dip}}(\text{centre})} \propto \frac{1/r_{\mathsf{edge}}}{1/r_{\mathsf{centre}}} = \frac{\frac{1}{\mathrm{WD}/\cos\theta_{\mathsf{obj}}}}{\frac{1}{\mathrm{WD}}} = \cos\theta_{\mathsf{obj}} \tag{5.75}$$

which depends on θ_{obj} only for any given orientation of the dipole. The same holds for all grid nodes between the centre and the edge of the grid. Specification of θ_{obj} through the NA is therefore sufficient to model the collected cone of the scattered radiation.

For simplicity, the grid is positioned at $z^{\mathsf{O}} = 1$ with the WD as unit of measurement. This unit of length holds in all frames of reference. The diameter of the laser spot is much smaller than WD in our experiments (several μm compared to about 1 cm). Combined with the assumption that the objective faithfully images all scatterers in the focal plane,

this permits the simplification that the scatterer is in the exact origin of the laboratory frame, even when calculating multiple scatterers subsequently.

All grid nodes $Q^{\mathsf{O}} = (Q_x^{\mathsf{O}}, Q_y^{\mathsf{O}}, 1)$ fall in a circle in the $Q_z^{\mathsf{O}} = 1$ plane. The grid can be defined with any arbitrary inter-nodal distance, as long as it includes the variation of $\mathbf{E}_{\mathsf{dip}}$ within the field of view. The grid size g if specified as the number of nodes along each of the axes. The inter-nodal distance along one axis (for example the x-axis) is then given by

$$Q_x^{\mathsf{O}}(k) - Q_x^{\mathsf{O}}(k+1) = \frac{2R_{\mathsf{obj}}}{g-1} \tag{5.76}$$

for $g > 1$ where R_{obj} is the radius of the grid disc given by equation 5.74. The grid coordinates $Q_x^{\mathsf{O}}(k)$ and $Q_y^{\mathsf{O}}(l)$ of grid node $k, l = 1, 2, 3, ..., g$ are then given through

$$\begin{aligned} Q_x^{\mathsf{O}}(k) &= -R_{\mathsf{obj}} + \frac{2R_{\mathsf{obj}}}{g-1}(k-1) = R_{\mathsf{obj}}\left(\frac{2(k-1)}{g-1} - 1\right) \\ Q_y^{\mathsf{O}}(l) &= -R_{\mathsf{obj}} + \frac{2R_{\mathsf{obj}}}{g-1}(l-1) = R_{\mathsf{obj}}\left(\frac{2(l-1)}{g-1} - 1\right) \\ Q_z^{\mathsf{O}} &= 1 \end{aligned} \tag{5.77}$$

where both Q_x^{O} and Q_y^{O} range from $-R_{\mathsf{obj}}$ to $+R_{\mathsf{obj}}$. Only those nodes that satisfy

$$(Q_x^{\mathsf{O}})^2 + (Q_y^{\mathsf{O}})^2 \leq {R_{\mathsf{obj}}}^2 \tag{5.78}$$

are used, the others fall outside the view of the objective. If $g = 1$, there is only one point and $Q^{\mathsf{O}} = (0, 0, 1)$.

Coordinate transformations

The grid nodes Q are specified as Cartesian coordinates in the O-frame. Its L-frame coordinates are obtained by transformation

$$\begin{pmatrix} Q_x^{\mathsf{L}} \\ Q_y^{\mathsf{L}} \\ Q_z^{\mathsf{L}} \end{pmatrix} = \mathbf{T}_{\mathsf{O}\to\mathsf{L}} \begin{pmatrix} Q_x^{\mathsf{O}} \\ Q_y^{\mathsf{O}} \\ Q_z^{\mathsf{O}} \end{pmatrix} \tag{5.79}$$

where $\mathbf{T}_{\mathsf{O}\to\mathsf{L}} = {\mathbf{T}_{\mathsf{L}\to\mathsf{O}}}^{\mathrm{T}}$ is given by equation 5.4 through the orientation of the objective relative to the laser frame of reference. This is given as input to the model in the form of three Euler angles $(\alpha^{\mathsf{O}}, \beta^{\mathsf{O}}, \gamma^{\mathsf{O}})$. The coordinates of $Q^{\mathsf{L}} = (\rho_Q^{\mathsf{L}}, \theta_Q^{\mathsf{L}}, \phi_Q^{\mathsf{L}})$ in the spherical basis are obtained with equations 2.9.

The transformations from Q to L frame and *vice versa* depend on the location of Q. It is given through its azimuthal and polar coordinates in the L-frame. These angles specify the orientation of the Q-frame relative to the L-frame so that the transformation is given by

$$\mathbf{T}_{\mathsf{L}\to\mathsf{Q}} = \mathbf{R}_y(\theta_Q^{\mathsf{L}})\, \mathbf{R}_z(\phi_Q^{\mathsf{L}}) \tag{5.80}$$

and the inverse transformation is

$$\mathbf{T}_{\mathsf{Q}\to\mathsf{L}} = \mathbf{R}_z(-\phi_Q^{\mathsf{L}})\mathbf{R}_y(-\theta_Q^{\mathsf{L}}) \tag{5.81}$$

where the rotation matrices of equations 2.12 are used.

5.4.2 Dipole far-field through reciprocity

It now remains to find an expression for the electric field $\mathbf{E}_{\mathsf{dip}}{}^{\mathsf{L}}(Q)$ due to the dipole at each grid node Q falling within view of the microscope objective and express this in L-frame coordinates. The total of these vectors constitute the collected Raman scattering in the model.

With the location of Q specified in the L-frame of reference, the field amplitude $\mathbf{E}_{\mathsf{dip}}{}^{\mathsf{L}}(Q)$ at this point due to the dipole is given as

$$\mathbf{E}_{\mathsf{dip}}{}^{\mathsf{L}}(Q) = \mathbf{T}_{\mathsf{Q}\to\mathsf{L}}\ \mathbf{E}_{\mathsf{dip}}{}^{\mathsf{Q}}(Q) \tag{5.82}$$

with the field in the Q-frame

$$\mathbf{E}_{\mathsf{dip}}{}^{\mathsf{Q}}(Q) = \begin{pmatrix} E_x^Q \\ E_y^Q \\ E_z^Q \end{pmatrix} = \begin{pmatrix} E_p^Q \\ E_s^Q \\ 0 \end{pmatrix} \tag{5.83}$$

where the component along the $\hat{\mathbf{x}}^{\mathsf{Q}}$ direction is the p-component relative to the plane of incidence $x^{\mathsf{Q}}z^{\mathsf{Q}}$ and the $\hat{\mathbf{y}}^{\mathsf{Q}}$-component is its s-polarised component. The p and s polarisations are parallel to the spherical basis vectors $\hat{\boldsymbol{\theta}}_Q^{\mathsf{L}}$ and $\hat{\boldsymbol{\phi}}_Q^{\mathsf{L}}$, respectively, that specify the position of Q in spherical coordinates of the L-frame (figure 5.5). We now derive expressions for E_p^Q and E_s^Q using reciprocity.

Reciprocity of dipole fields

Lorentz reciprocity is a general theorem in electrodynamics that states that the volume integral over two current sources $\mathbf{J}$ and their electric fields $\mathbf{E}$ obey [148]

$$\int_V \left(\mathbf{J}_1(\mathbf{r},\omega)\cdot\mathbf{E}_2(\mathbf{r},\omega) - \mathbf{J}_2(\mathbf{r},\omega)\cdot\mathbf{E}_1(\mathbf{r},\omega)\right)\mathrm{d}^3r = 0 \tag{5.84}$$

which is valid if the magnetic permeability and electric permittivity tensors are symmetric, though these may vary in space. Equation 5.84 holds for a particular frequency ω. Discussions of this theorem and its application to dipole radiation near interfaces are presented in [148–152] in various forms. In our case, the current sources reduce to point dipoles and the integral involves two points only. Lorentz reciprocity then takes the form

$$\mathbf{p}_1{}^{\mathrm{T}}(\omega)\cdot\mathbf{E}_2(\mathbf{r}_1,\omega) - \mathbf{p}_2{}^{\mathrm{T}}(\omega)\cdot\mathbf{E}_1(\mathbf{r}_2,\omega) = 0 \tag{5.85}$$

where $\mathbf{E}_1(\mathbf{r}_2)$ is the field due to dipole $\mathbf{p}_1$ at the location $\mathbf{r}_2$ of dipole $\mathbf{p}_2$ and *vice versa* for $\mathbf{E}_2(\mathbf{r}_1)$. Both the fields and the dipole moments are column vectors. The transpose of the dipole moments is taken to effect the inner product on a row and a column vector. In the following treatment, the frequency ω is left out and implicitly assumed throughout.

In our system, we desire to know the radiation field $\mathbf{E}_{\mathsf{dip}}$ at location Q arising from the effective induced dipole $\mathbf{p}_{\mathsf{eff}}$ located at $(0, 0, z)$ in the L-frame. This field is derived by considering a test dipole $\mathbf{p}_{\mathsf{test}}$ at location Q and its field $\mathbf{E}_{\mathsf{test}}$ at the location of $\mathbf{p}_{\mathsf{eff}}$. Formulating equation 5.85 with these quantities, we obtain

$$\mathbf{p}_{\mathsf{test}}{}^{\mathrm{T}} \cdot \mathbf{E}_{\mathsf{dip}}(Q) = \mathbf{p}_{\mathsf{eff}}{}^{\mathrm{T}} \cdot \mathbf{E}_{\mathsf{test}}(0, 0, z) \tag{5.86}$$

where the dipoles and fields are understood to oscillate at the Raman-shifted frequency ω_R and all quantities are expressed in the same frame of reference.

Equation 5.86 is solved for $\mathbf{E}_{\mathsf{dip}}(Q)$ in the q-frame (figure 5.19), which is obtained by rotating the L-frame by angle ϕ_Q about the z^{L} axis as

$$\mathbf{T}_{\mathsf{L}\to\mathsf{q}} = \mathbf{R}_z(\phi_Q^{\mathsf{L}}) \, . \tag{5.87}$$

The q-frame is intermediate between the L and Q frames, involving only half the transformation $\mathbf{T}_{\mathsf{L}\to\mathsf{Q}}$ of equation 5.80. The $\hat{\mathbf{x}}^{\mathsf{q}}$ and $\hat{\mathbf{z}}^{\mathsf{q}}$ axes span a plane of incidence for light coming into the origin from point Q. The radiation field $\mathbf{E}_{\mathsf{dip}}(Q)$ due to $\mathbf{p}_{\mathsf{test}}$ is also expressed in this plane and its p and s components are parallel to $\hat{\mathbf{x}}^{\mathsf{Q}}$ and $\hat{\mathbf{y}}^{\mathsf{Q}}$, respectively, propagating outward. Note that the direction of p depends on the propagation angle of the field, consistent with figure 5.2, whereas s is along $\hat{\mathbf{y}}^{\mathsf{q}}$ in all cases.

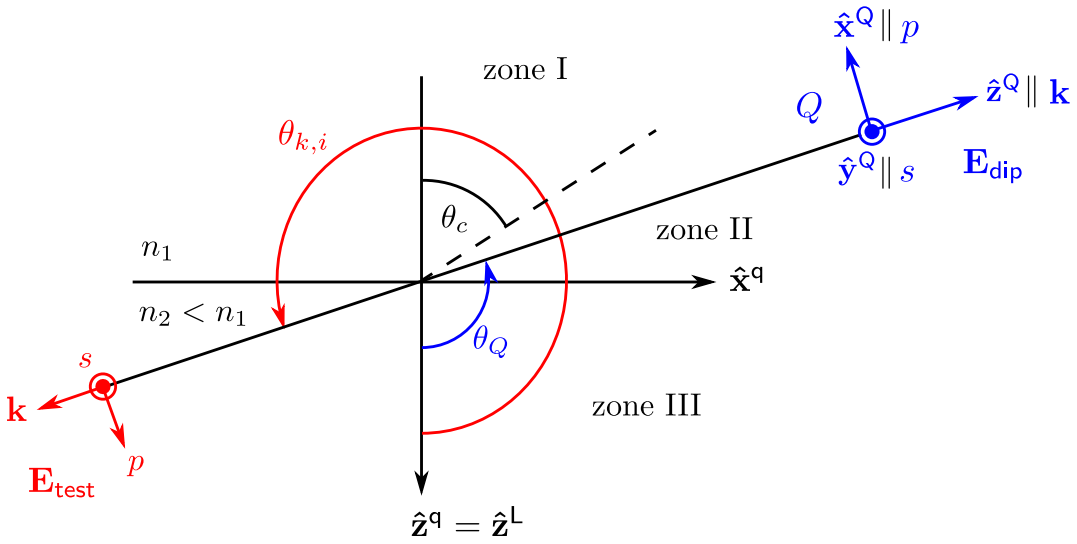

Figure 5.19: The q-frame of reference in which the reciprocity problem is solved.

The reciprocity problem is expressed in the q-frame as

$$\begin{pmatrix} p_{\mathsf{test},p} & p_{\mathsf{test},s} \end{pmatrix} \cdot \begin{pmatrix} E_p^Q \\ E_s^Q \end{pmatrix} = (\mathbf{p}_{\mathsf{eff}}{}^{\mathsf{q}})^{\mathrm{T}} \cdot \mathbf{E}_{\mathsf{test}}{}^{\mathsf{q}}(0,0,z) \tag{5.88}$$

where $\mathbf{p}_{\mathsf{eff}}{}^{\mathsf{q}}$ is the projection of $\mathbf{p}_{\mathsf{eff}}{}^{\mathsf{L}}$ onto q-frame given through

$$\mathbf{p}_{\mathsf{eff}}^{\mathsf{q}} = \mathbf{R}_z(\phi_Q^{\mathsf{L}})\ \mathbf{p}_{\mathsf{eff}}{}^{\mathsf{L}} \tag{5.89}$$

in Cartesian coordinates. $\mathbf{E}_{\mathsf{test}}{}^{\mathsf{q}}$ is equally expressed along the three Cartesian axes. However, the left-hand side of equation 5.88 has two components only: along the p and s-directions at Q.

The field $\mathbf{E}_{\mathsf{test}}{}^{\mathsf{q}}(0,0,z)$ is the far-field radiating from $\mathbf{p}_{\mathsf{test}}$, propagating to the location $(0,0,z)$ and generating a local field there in the empty molecular cavity. It is an incident field approximated as a plane wave propagating from Q to the location of the scattering molecule. This is in fact the problem addressed in section 5.2. Furthermore, the local field correction has also been addressed (section 5.3.2). Here, the applied field $\mathbf{E}_{\mathsf{app}}$ due only to $\mathbf{p}_{\mathsf{test}}$ gives rise to a cavity field. No reaction field should be considered for the local field caused by the test dipole because there is no dipole located within the cavity for the purpose of deducing the test field. Similarly, the field due to the Raman dipole is considered in absence of the test dipole. We have already accounted for the reaction field due to the Raman dipole by taking this to be the effective dipole $\mathbf{p}_{\mathsf{eff}}$ rather than the induced dipole $\mathbf{p}_{\mathsf{ind}}$ in section 5.3.3.[‡]

The test field $\mathbf{E}_{\mathsf{test}}$ at $(0,0,z)$, the location of $\mathbf{p}_{\mathsf{eff}}$, can thus readily be given in the q-frame as

$$\begin{aligned} \mathbf{E}_{\mathsf{test}}{}^{\mathsf{q}}(0,0,z) = \mathbf{C}^{\mathsf{q}}(\omega_R)\ \mathbf{E}_{\mathsf{app}}{}^{\mathsf{q}}(0,0,z) &= \mathbf{C}^{\mathsf{q}}(\omega_R)\ \mathbf{F}^{\mathsf{q}}\ \mathbf{E}_{\mathsf{test}}{}^{\mathsf{q}}(0,0,0) \\ &= \mathbf{C}^{\mathsf{q}}(\omega_R) \begin{pmatrix} F_x & 0 \\ 0 & F_y \\ F_z & 0 \end{pmatrix} \begin{pmatrix} E_{\mathsf{test},p} \\ E_{\mathsf{test},s} \end{pmatrix} \end{aligned} \tag{5.90}$$

with the coupling factors yet to be derived. The cavity tensor $\mathbf{C}$ is computed at the Raman-shifted frequency ω_R conform equations 5.51 and 5.53. This tensor is required in the q-frame though it is specified in the molecular m-frame, necessitating the following coordinate transformations

$$\begin{aligned} \mathbf{C}^{\mathsf{q}}(\omega_R) &= \mathbf{T}_{\mathsf{L}\to\mathsf{q}}\ \mathbf{T}_{\mathsf{m}\to\mathsf{L}}\ \mathbf{C}^{\mathsf{m}}(\omega_R)\ \mathbf{T}_{\mathsf{L}\to\mathsf{m}}\ \mathbf{T}_{\mathsf{q}\to\mathsf{L}} \\ &= \mathbf{R}_z(\phi_Q^{\mathsf{L}})\ \mathbf{T}_{\mathsf{L}\to\mathsf{m}}{}^{\mathsf{T}}\ \mathbf{C}^{\mathsf{m}}(\omega_R)\ \mathbf{T}_{\mathsf{L}\to\mathsf{m}}\ \mathbf{R}_z(-\phi_Q^{\mathsf{L}}) \end{aligned} \tag{5.91}$$

where transformation between the q and m frames is effected via the L-frame with $\mathbf{T}_{\mathsf{L}\to\mathsf{q}}$ specified in equation 5.87 and $\mathbf{T}_{\mathsf{L}\to\mathsf{m}} = \mathbf{T}_{\mathsf{m}\to\mathsf{L}}{}^{\mathrm{T}}$ given by equation 5.44 through specifica-

[‡]The same result is obtained if the reaction field is taken into account in deducing the reciprocity relation at this stage rather than in deriving the effective dipole before considering reciprocity.

tion of the molecular orientation as input to the model. These coordinate transformations results in mixing of molecular-frame components of the cavity tensor as the orientation of the molecule and thus its cavity may not align with the axes of the q-frame. For spherical cavities, this mixing is of no consequence.

The incident test field $\mathbf{E}_{\mathsf{test}}{}^{\mathsf{q}}(0,0,0)$ is further specified by expressing $E_{\mathsf{test},p}$ and $E_{\mathsf{test},s}$ as the amplitudes of a polarised dipole far-field with equation 2.120. It is obtained from that equation using the fact that the propagation direction of the test field is orthogonal to the test dipole moment for both p and s polarisations (so that $\sin\theta = 1$) and by substituting $k = \omega c/n$ as well as $r = \rho_Q$. The result is

$$\mathbf{E}_{\mathsf{test}}{}^{\mathsf{q}}(0,0,0) = \begin{pmatrix} E_{\mathsf{test},p} \\ E_{\mathsf{test},s} \end{pmatrix} = \frac{1}{4\pi\epsilon_0} \left(\frac{\omega_R}{c}\right)^2 \frac{1}{\rho_Q} \begin{pmatrix} -p_{\mathsf{test},p} \\ p_{\mathsf{test},s} \end{pmatrix} \tag{5.92}$$

in which the components are parallel to the dipole moment at Q. For $\mathbf{p}_{\mathsf{test}}$ along p at Q, the field $E_{\mathsf{test},p}$ is antiparallel to the dipole moment as the p-direction at the origin is opposite from that at Q. In contrast, all s-directions are parallel (figure 5.19).

The desired amplitudes E_p^Q and E_s^Q along the p and s directions of the q-frame at point Q can now be derived. We start by substituting equation 5.92 into equation 5.90 and substituting the result in equation 5.88 to obtain

$$\begin{aligned} p_{\mathsf{test},p}\, E_p^Q + p_{\mathsf{test},s}\, E_s^Q = {} & \frac{1}{4\pi\epsilon_0\rho_Q} \left(\frac{\omega_R}{c}\right)^2 \\ & \begin{pmatrix} p_{\mathsf{eff},x} & p_{\mathsf{eff},y} & p_{\mathsf{eff},z} \end{pmatrix} \cdot \left[\begin{pmatrix} C_{xx} & C_{xy} & C_{xz} \\ C_{yx} & C_{yy} & C_{yz} \\ C_{zx} & C_{zy} & C_{zz} \end{pmatrix} \begin{pmatrix} F_x & 0 \\ 0 & F_y \\ F_z & 0 \end{pmatrix} \begin{pmatrix} -p_{\mathsf{test},p} \\ p_{\mathsf{test},s} \end{pmatrix} \right] \end{aligned} \tag{5.93}$$

where all elements are specified in the q-frame. Writing out all terms, separating variables and noting that the dipole moments $p_{\mathsf{test},p}$ and $p_{\mathsf{test},s}$ drop out of the above equations, we obtain E_p^Q and E_s^Q in the q-frame of reference.

$$\begin{aligned} E_p^Q = {} & \frac{-1}{4\pi\epsilon_0\rho_Q} \left(\frac{\omega_R}{c}\right)^2 \\ & [(F_x C_{xx} + F_z C_{xz}) p_{\mathsf{eff},x} + (F_x C_{yx} + F_z C_{yz}) p_{\mathsf{eff},y} + (F_x C_{zx} + F_z C_{zz}) p_{\mathsf{eff},z}] \end{aligned} \tag{5.94}$$

$$E_s^Q = \frac{1}{4\pi\epsilon_0\rho_Q} \left(\frac{\omega_R}{c}\right)^2 [F_x C_{xy} p_{\mathsf{eff},x} + F_y C_{yy} p_{\mathsf{eff},y} + F_y C_{zy} p_{\mathsf{eff},z}] \tag{5.95}$$

These may be rewritten in matrix notation as

$$\begin{pmatrix} E_p^Q \\ E_s^Q \end{pmatrix} = \frac{1}{4\pi\epsilon_0\rho_Q} \left(\frac{\omega_R}{c}\right)^2 \begin{pmatrix} -F_x & 0 & -F_z \\ 0 & F_y & 0 \end{pmatrix} \mathbf{C}^{\mathsf{q}\mathsf{T}}\, \mathbf{p}_{\mathsf{eff}}{}^{\mathsf{q}} \tag{5.96}$$

where the inner product has been rearranged so that our expression confirms to the form presented in [151, 152]. However, our expression differs from these publications by in-

cluding a the (transform of the) cavity tensor for the local field correction. Furthermore, it additionally has a minus sign with the p-polarised component due to the antiparallel nature of the direction of this component at the origin relative to point Q. These two effects appear not to have been considered in the consulted literature.

Finally, the field $\mathbf{E}_{\mathsf{dip}}{}^{\mathsf{L}}(Q)$ due to $\mathbf{p}_{\mathsf{eff}}{}^{\mathsf{L}}$ at Q is expressed in the L-frame by substitution of equation 5.89 in equation 5.96 and subsequent application of equations 5.83 and 5.82 with 5.81 to express the effective Raman dipole and its far-field in the appropriate frames of reference.

The frequency of the Raman scattering ω_R is computed from the Raman shift $\bar{\nu}_R$ in cm^{-1} and the laser wavelength λ_{laser} given as input to the model. From $\bar{\nu}_R$, the vacuum wavelength of the Raman scattering $\lambda_{0,R}$ is computed with equation 3.6 and ω_R follows from equation 2.39. $\lambda_{0,R}$ is also needed for the depth-dependence of the coupling factors if the scattering molecule is located at a distance $z > 0$ from the interface.

Coupling factors

The coupling matrix $\mathbf{F}$ of equation 5.90 is obtained through the same process as outlined in section 5.2. Their form depends on the layer structure of the interface and the propagation direction of the incident field. The numerical values of F_x, F_y and F_z are computed with the Fresnel coefficients and angles specified for an incident ray coming from Q onto the dipole. The polar coordinate θ_Q^{L} specifies the propagation direction of the incident field with $\theta_{k,i} = 180° + \theta_Q^{\mathsf{L}}$ so that $180° \leq \theta_{k,i} \leq 360°$ in the present case. This range differs from that of the incident laser beam as the propagation direction is reversed in the reciprocity problem: the field is incident *from* a particular polar direction rather than propagating *towards* that direction.

Table 5.2: Propagation angles in the L-frame and refraction angles with the radiation zones of Q.

Zone I	Zone II	Zone III
$90° + \theta_c < \theta_Q^{\mathsf{L}} \leq 180°$	$90° \leq \theta_Q^{\mathsf{L}} \leq 90° + \theta_c$	$0° \leq \theta_Q^{\mathsf{L}} < 90°$
$270° \leq \theta_{k,i} \leq 360°$		$180° \leq \theta_{k,i} < 270°$
$n_i = n_1$		$n_i = n_2$
$n_t = n_2$		$n_t = n_1$
$\theta_{k,i} = 360° - \theta_i$		$\theta_{k,i} = 180° + \theta_i$
$\theta_{k,t} = 360° - \theta_t$		$\theta_{k,r} = 360° - \theta_i$

The angle of incidence θ_i for each grid node Q is therefore given as

$$\theta_i = \begin{cases} 180° - \theta_Q^{\mathsf{L}} & \text{for zones I and II,} \quad 90° \leq \theta_Q^{\mathsf{L}} \leq 180° \\ \theta_Q^{\mathsf{L}} & \text{for zone III,} \quad 0° \leq \theta_Q^{\mathsf{L}} < 90° \end{cases} \tag{5.97}$$

with the zones defined as above in figures 5.9 and 5.19. That is: radiation incident from zones I and II arrives through medium 1 and is transmitted through the interface to

reach the molecule; zone III involves radiation incident on the molecule directly and after reflection from the interface. As the field directions strictly follow our definitions outlined in the previous sections, the Fresnel amplitude coefficients of equation 5.28 apply with the appropriate refractive indices n_i, n_t and angles θ_i, θ_t as presented in table 5.2. Following the procedure of section 5.2 for this situation results in the following coupling factors.

$$\mathbf{F}_{1\to 2}(z) = \begin{cases} F_x = t_p \cos\theta_t \, \mathrm{e}^{\mathrm{j}k_2 z \cos\theta_t} \\ F_y = t_s \, \mathrm{e}^{\mathrm{j}k_2 z \cos\theta_t} \\ F_z = t_p \sin\theta_t \, \mathrm{e}^{\mathrm{j}k_2 z \cos\theta_t} \end{cases} \tag{5.98}$$

$$\mathbf{F}_{2\to 1}(z) = \begin{cases} F_x = \left(-\mathrm{e}^{-\mathrm{j}k_2 z \cos\theta_i} + r_p \, \mathrm{e}^{\mathrm{j}k_2 z \cos\theta_i}\right) \cos\theta_i \\ F_y = \mathrm{e}^{-\mathrm{j}k_2 z \cos\theta_i} + r_s \, \mathrm{e}^{\mathrm{j}k_2 z \cos\theta_i} \\ F_z = \left(\mathrm{e}^{-\mathrm{j}k_2 z \cos\theta_i} + r_p \, \mathrm{e}^{\mathrm{j}k_2 z \cos\theta_i}\right) \sin\theta_i \end{cases} \tag{5.99}$$

These differ from those derived for the incident laser beam (equations 5.33 and 5.34) by the minus sign for the F_z components as the propagation angle $\theta_{k,i}$ spans a different range here. Note that the field obtained through reciprocity reduces to the far-field of a dipole in a homogeneous dielectric (equation 2.120) in the absence of an interface, *i.e.* when the refractive indices are all the same.

5.5 Detected intensities

In this section, we compute $\mathbf{E}_{\mathsf{col}}{}^{\mathsf{O}}(Q)$, the collimated field due to the induced dipole at each point Q on the objective. Collimation by the objective involves the rotation of the propagation direction of each ray to align with $\hat{\mathbf{z}}^{\mathsf{O}}$ so that the amplitude components are given as

$$\mathbf{E}_{\mathsf{col}}{}^{\mathsf{O}}(Q) = \begin{pmatrix} E_x^{\mathsf{O}} \\ E_y^{\mathsf{O}} \\ 0 \end{pmatrix} \tag{5.100}$$

where x^{O} and y^{O} conform to the collection polarisation axes set in the experiment. The modelled total intensity is then given by the sum of the squared amplitudes at each grid node Q along each of the orthogonal polarisation directions.

5.5.1 Collimation

The lens function of the objective is to collimate the cone of light, which is assumed to work perfectly. Furthermore, the objective transmission function is assumed to be constant over R_{obj}. Collimation of the cone of scattered light is obtained by rotating the propagation direction of the individual rays of the modelling grid into the $\hat{\mathbf{z}}^{\mathsf{O}}$ direction. The vectorial amplitude of the electric field then lies in the $x^{\mathsf{O}}y^{\mathsf{O}}$-plane.

The dipole radiation field is first expressed in the observation frame of reference through

$$\mathbf{E}_{\mathsf{dip}}{}^{\mathsf{O}}(Q^{\mathsf{O}}) = \mathbf{T}_{\mathsf{L}\to\mathsf{O}}\, \mathbf{E}_{\mathsf{dip}}{}^{\mathsf{L}}(Q) \tag{5.101}$$

where the positions Q^{O} are the original specified coordinates of the grid nodes defined through equations 5.77 and the transformation $\mathbf{T}_{\mathsf{L}\to\mathsf{O}} = \mathbf{T}_{\mathsf{O}\to\mathsf{L}}{}^{\mathrm{T}}$ given by equation 5.4.

Collimation is implemented in the model as a rotation of $\mathbf{E}_{\mathsf{dip}}{}^{\mathsf{O}}(Q)$ over collimation angle θ_{col} about axis $\mathbf{a}_{\mathsf{col}}$, both of which depend on the location of Q. The inner product and cross product[§] are used to obtain this angle and axis from $\hat{\mathbf{z}}^{\mathsf{O}}$ and $\mathbf{Q}^{\mathsf{O}}$, the Cartesian unit vector along the z-axis and the vector from the origin to point Q both expressed in the Cartesian coordinates of the O-frame. These are given as the normalised vectors

$$\hat{\mathbf{z}}^{\mathsf{O}} = \begin{pmatrix} 0 \\ 0 \\ 1 \end{pmatrix} \tag{5.104}$$

and

$$\hat{\mathbf{Q}}^{\mathsf{O}} = \frac{1}{\sqrt{Q_x^{\mathsf{O}2} + Q_y^{\mathsf{O}2} + Q_z^{\mathsf{O}2}}} \begin{pmatrix} Q_x^{\mathsf{O}} \\ Q_y^{\mathsf{O}} \\ Q_z^{\mathsf{O}} \end{pmatrix} \tag{5.105}$$

that span a plane in which $\hat{\mathbf{Q}}^{\mathsf{O}}$ has to be rotated to $\hat{\mathbf{z}}^{\mathsf{O}}$ to effect collimation. As $\hat{\mathbf{Q}}^{\mathsf{O}}$ varies for each grid node, the procedure is completed by considering each point separately.

The angle $0° \leq \theta_{\mathsf{col}} \leq 180°$ is the collimation angle by which the field direction and thus its vectorial amplitude are rotated. It is computed through their inner product between $\hat{\mathbf{z}}_{\mathsf{O}}$ and $\hat{\mathbf{Q}}^{\mathsf{O}}$ as

$$\theta_{\mathsf{col}} = \arccos\left(\hat{\mathbf{z}}^{\mathsf{O}} \cdot \hat{\mathbf{Q}}^{\mathsf{O}}\right) \tag{5.106}$$

where normalisation is not needed as both are unit vectors. The axis $\mathbf{a}_{\mathsf{col}}$ is found through the cross product

$$\mathbf{a}_{\mathsf{col}} = \frac{\hat{\mathbf{Q}}^{\mathsf{O}} \times \hat{\mathbf{z}}^{\mathsf{O}}}{\sin\theta_{\mathsf{col}}} \tag{5.107}$$

where the order is important to obtain the correct sense of the rotation. Rodrigues' formula is now used to implement the rotation to obtain the collimated dipole field at each grid node through

$$\mathbf{E}_{\mathsf{col}}{}^{\mathsf{O}} = \mathbf{E}_{\mathsf{dip}}{}^{\mathsf{O}} \cos\theta_{\mathsf{col}} + \left(\mathbf{a}_{\mathsf{col}} \times \mathbf{E}_{\mathsf{dip}}{}^{\mathsf{O}}\right) \sin\theta_{\mathsf{col}} + \mathbf{a}_{\mathsf{col}} \left(\mathbf{a}_{\mathsf{col}} \cdot \mathbf{E}_{\mathsf{dip}}{}^{\mathsf{L}}\right) (1 - \cos\theta_{\mathsf{col}}) \tag{5.108}$$

[§] The smallest angle φ between two three-dimensional vectors $\mathbf{a}$ and $\mathbf{b}$ in the plane defined by these vectors is given through the inner product

$$\mathbf{a} \cdot \mathbf{b} = \|\mathbf{a}\|\, \|\mathbf{b}\| \cos\varphi \tag{5.102}$$

while the cross product of these vectors provides a third, orthogonal vector $\mathbf{n}$ as

$$\mathbf{a} \times \mathbf{b} = \mathbf{n}\, \|\mathbf{a}\|\, \|\mathbf{b}\| \sin\varphi \tag{5.103}$$

where the angle φ is taken from $\mathbf{a}$ to $\mathbf{b}$ about $\mathbf{n}$.

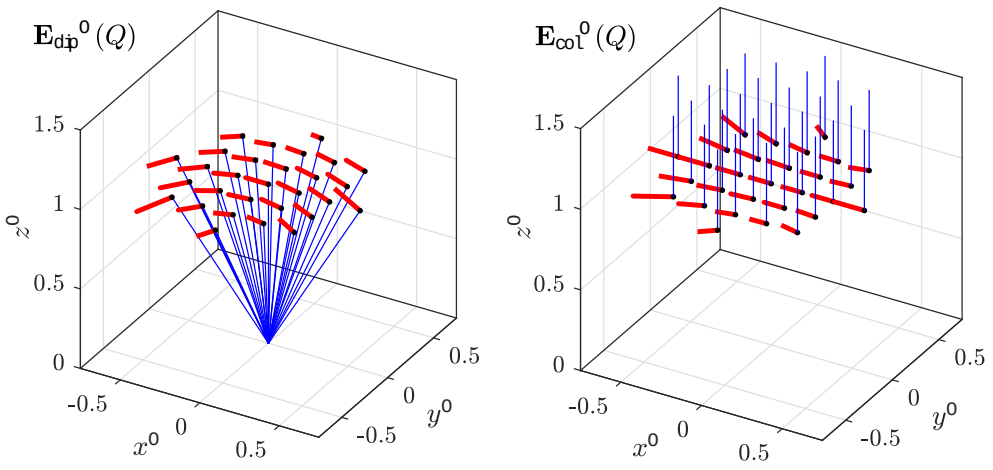

Figure 5.20: Collimation of the dipole field is effected in the model for each grid node Q (black dots) by a rotation that brings the propagation directions (blue) of the dipole field $\mathbf{E}_{\mathsf{dip}}{}^{\mathsf{Q}}(Q)$ parallel to $\hat{\mathbf{z}}^{\mathsf{O}}$. The vectorial absolute amplitudes (red) of the collimated field $\mathbf{E}_{\mathsf{col}}{}^{\mathsf{Q}}(Q)$ are parallel to the $x^{\mathsf{O}}y^{\mathsf{O}}$-plane.

where the dependence on Q of each quantity in this equation is implicit. Figure 5.20 presents an example of the collimation as implemented in our model.

5.5.2 Total linearly-polarised intensities

In an experiment, the collimated beam is passed through a linear polariser, set along either the x or y direction of the O-frame of reference. Both are computed simultaneously in our model. The polarising effect is assumed to work perfectly: the selected component of the electric field is transmitted without loss while the orthogonal component is blocked completely.

The collimated field at each grid node Q is of the form

$$\mathbf{E}_{\mathsf{col}}{}^{\mathsf{O}}(Q) = \begin{pmatrix} E_x^{\mathsf{O}} \\ E_y^{\mathsf{O}} \\ 0 \end{pmatrix} \tag{5.109}$$

which contributes to the total intensity along both x and y polarisation directions of the dipole field sent to the detector. The polarised irradiance at each grid node is given through equation 2.77 as

$$\begin{aligned} I_x(Q) &= \frac{n_{\mathsf{air}}\,\epsilon_0\,c}{2}\left(E_x{}^{\mathsf{O}}(Q)\right)^2 \\ I_y(Q) &= \frac{n_{\mathsf{air}}\,\epsilon_0\,c}{2}\left(E_y{}^{\mathsf{O}}(Q)\right)^2 \end{aligned} \tag{5.110}$$

where the square denotes the complex modulus for complex amplitude components. These

form an intensity map over the field of view of the objective, looking down its $\hat{\mathbf{z}}^{\mathsf{O}}$ axis (figure 5.21 includes an example). The total linearly-polarised intensities are the sum over all grid nodes Q

$$\begin{aligned} I_x &= \frac{1}{N_Q} \sum_{1}^{N_Q} I_x(Q) \\ I_y &= \frac{1}{N_Q} \sum_{1}^{N_Q} I_y(Q) \end{aligned} \tag{5.111}$$

which are scaled to the number of grid nodes N_Q on the objective to facilitate comparison between runs of the model with different grid sizes. The summation runs over all rays in the modelled beam, assuming that all rays end up at the detector. The total scattering intensity is simply the sum of the orthogonal components

$$S = I_x + I_y \; . \tag{5.112}$$

Note that all the above are irradiance values and not radiant intensities as no integration over a surface area is performed. The spatial variation in the field of view, modelled by the grid of rays, is lost in the spectrograph: the rays are focussed onto the detector according to their wavelength. No amplitude is lost and all of the modelled radiation thus contributes to the total detected intensity. Figure 5.21 presents the modelled intensities for the collimated field of figure 5.20.

The summation in equation 5.111 is appropriate as Raman scattering is incoherent, for an individual as well as an ensemble of molecules. Considering a single molecule, subsequent scattering events are spaced in time and individual photons are detected. In molecular ensembles, there is no phase relation between the vibrational modes of the individual molecules. This is not the case in all optical techniques. In sum-frequency generation, for example, the radiation from each scatterer is coherent. In modelling, this would mean that the amplitudes of the generated electric fields have to be summed before

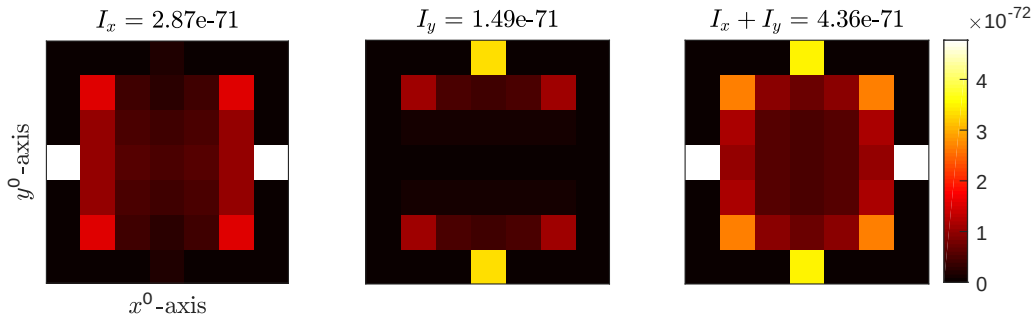

Figure 5.21: Linearly-polarised intensity maps for the modelled collimated field of figure 5.20 showing the total intensities I_x, I_y and their sum at each grid node Q in the field of view.

being squared to obtain the appropriate intensity (*i.e.* these interfere). Here, we square before summing.

5.6 Implementation in Matlab

The model outlined is this chapter is implemented in MATLAB as a function with the name `pirs`, which stands for 'polarised interfacial Raman scattering'. The code is given in appendix E.2. It is rather heavily annotated to be self-explanatory with the derivations and other details described in this text and employs the same or similar variable labels as used here.

5.6.1 Output and input

The output of the `pirs` function consists of the following for the Raman-active feature of interest:

1. the total intensity I_x polarised along x^{O} in the field of view divided with the number of grid nodes N_Q,

2. the total intensity I_y polarised along y^{O} in the field of view scaled with the number of grid nodes N_Q,

3. the x^{O}-polarised irradiance $I_x(Q)$ at each node Q on the square modelling grid,

4. the y^{O}-polarised irradiance $I_y(Q)$ at each node Q on the square modelling grid,

5. optionally, a figure with the polarised irradiance distributions $I_x(Q)$, $I_y(Q)$ and their sum presented as an intensity map in the field of view.

The intensities are relative values in an arbitrary unit as these are obtained by a sum over discrete points rather than through an integral over an analytical solution. Moreover, a number of input parameters may be given as relative rather than absolute values in SI units. An overview of all input variables is given in table 5.3 in the same order as required by the MATLAB function. All input parameters need specification in the specified array format for the code to run. The refractive indices of the three materials n_1, n_2, n_3 are for the hemisphere, thin surface layer and the rarer medium below the hemisphere, respectively. Values may be included at both the incident laser wavelength and the Raman-shifted wavelength to account for dispersion effects. Variables that may be entered as relative values are listed with the designation a.u. (arbitrary unit) and those without unit are ratios or other dimensionless quantities. Note that all angles are defined within a limited range only, as specified in this chapter.

Table 5.3: Input variables of MATLAB function `pirs`.

variable(s) / unit	symbol and format
refractive indices	$\begin{pmatrix} n_1(\lambda_{0,\mathsf{laser}}) & n_1(\lambda_{0,R}) \\ n_2(\lambda_{0,\mathsf{laser}}) & n_2(\lambda_{0,R}) \\ n_3(\lambda_{0,\mathsf{laser}}) & n_3(\lambda_{0,R}) \end{pmatrix}$
laser propagation angle / °	$\theta_{k,i}$
laser linear polarisation angle / °	ψ
laser vacuum wavelength / nm	$\lambda_{0,\mathsf{laser}}$
depth of molecule / nm	z
molecular orientation in L-frame / °	$\begin{pmatrix} \alpha_{\mathsf{m}} & \beta_{\mathsf{m}} & \gamma_{\mathsf{m}} \end{pmatrix}$
Stokes Raman shift / cm^{-1}	$\bar{\nu}_R$
Raman tensor in m-frame / a.u.	$\boldsymbol{\alpha}_{\mathsf{v}}{}^{\mathsf{m}} = \begin{pmatrix} \alpha_{\mathsf{v},xx} & \alpha_{\mathsf{v},xx} & \alpha_{\mathsf{v},xx} \\ \alpha_{\mathsf{v},xx} & \alpha_{\mathsf{v},xx} & \alpha_{\mathsf{v},xx} \\ \alpha_{\mathsf{v},xx} & \alpha_{\mathsf{v},xx} & \alpha_{\mathsf{v},xx} \end{pmatrix}$
semi-axes of molecular ellipsoid in m-frame / nm	$\begin{pmatrix} r_x^{\mathsf{m}} & r_y^{\mathsf{m}} & r_z^{\mathsf{m}} \end{pmatrix}$
polarisability tensor in m-frame / a.u.	$\boldsymbol{\alpha}^{\mathsf{m}} = \begin{pmatrix} \alpha_{xx} & \alpha_{xy} & \alpha_{xz} \\ \alpha_{yx} & \alpha_{yy} & \alpha_{yz} \\ \alpha_{zx} & \alpha_{zy} & \alpha_{zz} \end{pmatrix}$
numerical aperture	NA
objective orientation in L-frame / °	$\begin{pmatrix} \alpha_{\mathsf{O}} & \beta_{\mathsf{O}} & \gamma_{\mathsf{O}} \end{pmatrix}$
grid nodes along x^{O} and y^{O} axes	g
to produce output figure	1

5.6.2 Method of calculation

The calculations within the `pirs` function follow the order presented in this chapter. The steps are implemented with matrices that obey the conventions outlined in section 2.2. The model is compatible with the use of complex numbers. A complex vectorial amplitude in MATLAB thus consists of a 3×1 array (rows $\times$ columns) with a complex number at each entry that carries amplitude as well as phase information.

The thin-film approximation as well as the depth-dependence for a single interface are coded in the function. These cases do not apply simultaneously but may be combined to form hybrid coupling factors from equations 5.33, 5.34, 5.42 and 5.43 of the form

$$\mathbf{F}_{1\to3}(z) = \begin{cases} F_x = t_p \cos\theta_t \, \mathrm{e}^{\mathrm{j}k_3 z \cos\theta_t} \\ F_y = t_s \, \mathrm{e}^{\mathrm{j}k_3 z \cos\theta_t} \\ F_z = -\left(\frac{n_3}{n_2}\right)^2 t_p \sin\theta_t \, \mathrm{e}^{\mathrm{j}k_3 z \cos\theta_t} \end{cases} \tag{5.113}$$

$$\mathbf{F}_{3\to1}(z) = \begin{cases} F_x = \left(-\mathrm{e}^{-\mathrm{j}k_3 z \cos\theta_i} + r_p \, \mathrm{e}^{\mathrm{j}k_3 z \cos\theta_i}\right) \cos\theta_i \\ F_y = \mathrm{e}^{-\mathrm{j}k_3 z \cos\theta_i} + r_s \, \mathrm{e}^{\mathrm{j}k_3 z \cos\theta_i} \\ F_z = -\left(\frac{n_3}{n_2}\right)^2 \left(\mathrm{e}^{-\mathrm{j}k_3 z \cos\theta_i} + r_p \, \mathrm{e}^{\mathrm{j}k_3 z \cos\theta_i}\right) \sin\theta_i \end{cases} \tag{5.114}$$

which can be used with the appropriate combination of input variables. As long as $z = 0$ (the scattering molecule is located at the interface), any combination of refractive indices n_1, n_2 and n_3 can be used and the hybrid coupling factors reduce to these of the thin-film approximation. However, for $z > 0$, we must have $n_2 = n_3$ so that the factor n_3/n_2 disappears and the hybrid coupling factors reduce to those of a single interface.

Using this hybrid form facilitates computation of both cases with the same code, though care must be taken to specify the input correctly. Error messages are presented if this is not the case. Other input variables that could give rise to invalid results are equally checked before the computation starts.

A numerical loop over the grid nodes Q is used to compute the dipole field at each node. The coupling factors for the outgoing radiation towards Q are again the hybrid factors of equations 5.113 and 5.114 but with F_z multiplied by -1. Once the radiated field is known in the O-frame of reference, another loop over Q is executed to effect collimation at each grid node. The components along x^{O} and y^{O} of the collimated field are then squared. For complex values, the complex modulus is taken. This result is stored in an intensity map, that is presented as if looking down the objective towards the scatterer. The sum over these intensity maps provides the linearly-polarised intensities I_x and I_y of the modelled Raman band, scaling for the number of grid nodes as in equations 5.111.

The total intensity is affected by the spacing of the grid nodes, especially for a strongly fluctuating field. This is the case around the critical angle, the boundary between zones I and II. For intensities radiated purely into one of the zones, stable intensity values are reached more readily. In most cases presented in this thesis, stability has been observed

from about $g = 15$, resulting in 176 modelling grid nodes.

The modelled intensity distribution reduces to the dipole far-field in a homogeneous dielectric in the absence of an interface, *i.e.* when $n_1 = n_2 = n_3$, the field deduced through reciprocity is that of equation 2.120. Figure 5.22 presents the result of such a computation in our model with induced dipoles along the x^{O}, y^{O} or z^{O} axis. The first results from incident light along $\hat{\mathbf{z}}^{\mathsf{L}}$ ($\theta_{k,i} = 0°$) with p-polarisation as this field has a non-zero component along the $\hat{\mathbf{x}}^{\mathsf{L}}$-axis only. The second arises from s-polarised light incident under any angle $\theta_{k,i}$, as the amplitude of the incident field as purely along $\hat{\mathbf{y}}^{\mathsf{L}}$. The induced dipole along $\hat{\mathbf{z}}^{\mathsf{L}}$ arises from p-polarised light incident at $\theta_{k,i} = 90°$. The intensity maps of figure 5.22 represent a wide-angled observation (NA = 0.8) of a radiating dipole from three orthogonal directions through a linear polariser. The total intensities $I_x + I_y$ are cross-sections of the far-field dipole irradiance of figure 2.5.

5.6.3 Molecular ensembles

A single run of the `pirs` function provides Raman intensities for a very specific set of input variables. Many samples require modelling as ensembles, involving a distribution of orientations and multiple Raman modes. Moreover, experimental variables, such as the laser angle of incidence, may contain an inherent spread. These systems are modelled with a computational algorithm (or script) that repeatedly executes the function `pirs` in a loop and sums the resulting intensities, possibly weighted for non-uniform distributions of the input variables. As Raman scattering is an incoherent process, (weighted) summation of the computed intensities is appropriate.

Another important use of these scripts is to probe a range of input variables so that a match between modelled intensities and experimental observation can be found. This involves an additional fitting routine to interpret the spectra. The `pirs` model thus serves both to predict intensities for experimental optimisation as well as to interpret Raman spectra and assign molecular orientations or other properties to the scattering molecules.

5.7 Summary and critique

The purpose of the model outlined in this chapter is to predict polarised Raman scattering intensities arising from molecules near a planar dielectric interface. It employs a complex vectorial description of the electric field amplitudes to capture the macroscopic electrodynamics of the process. In its development, several assumptions and approximations have been made. The model can be used to aid in the design of experiments, for example by testing a range of experimental geometries for a particular system of interest, or to interpret observed Raman scattering intensities given the experimental geometry in terms of the molecular properties, including its orientation.

This chapter is concluded by a summary of the electrodynamics of the model, a list of its limitations, assumptions and approximations as well as a brief review of how our

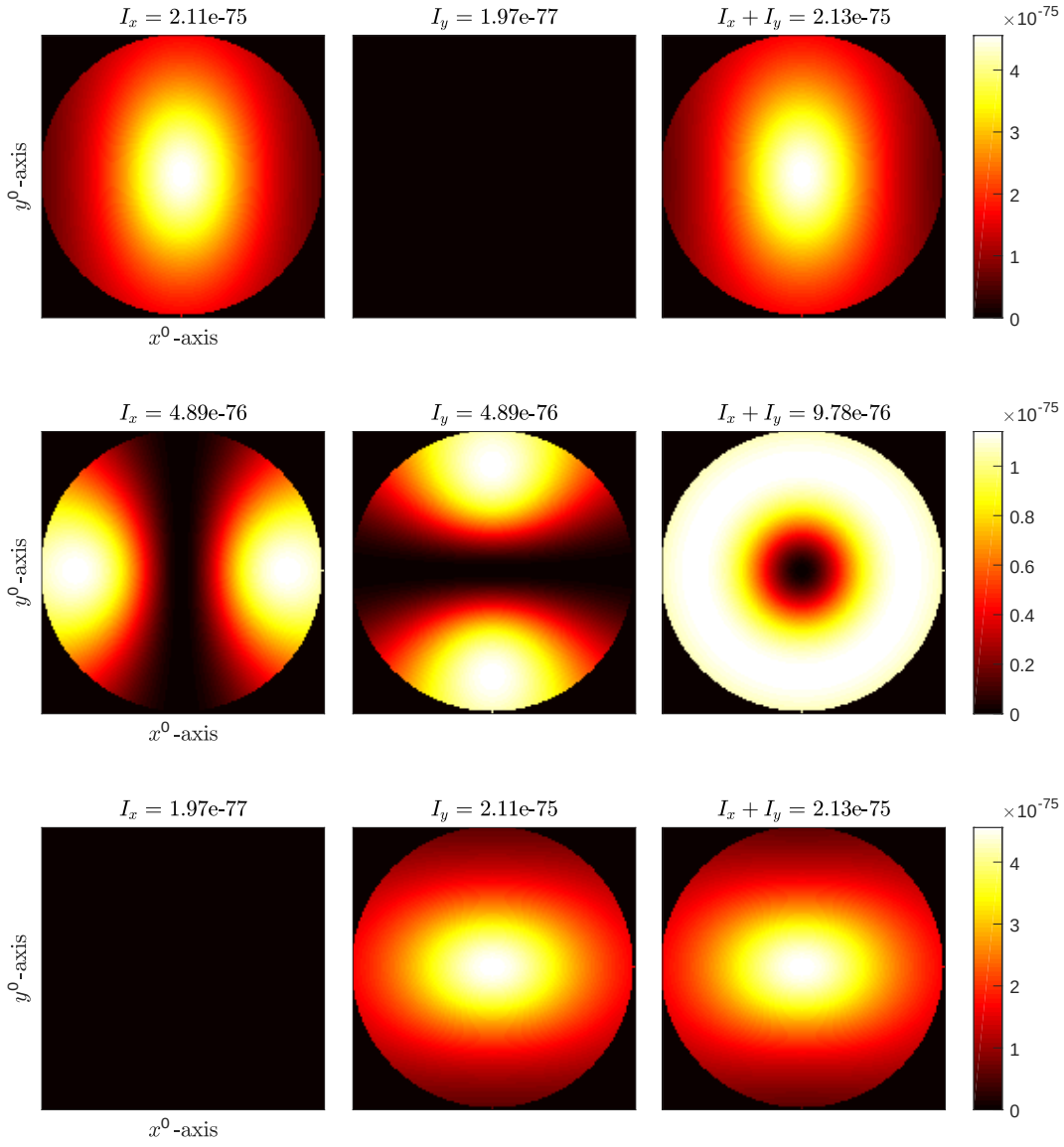

Figure 5.22: In the absence of an interface, the `pirs` function returns the field of a dipole in a homogeneous medium. In these computations, NA = 0.8 and the objective is aligned with the L-frame, *i.e.* looking down the z-axis from its positive side towards the origin. For p-polarised incident light at $\theta_{k,i} = 0°$ (top), a dipole is induced along the x^{O}-axis, while it is along z^{O} if $\theta_{k,i} = 90°$ (centre). With s-polarised incident light (bottom), the dipole is along y^{O} irrespective of $\theta_{k,i}$. The intensity values result from an electric field incident amplitude of 1 (with $g = 151$, $\boldsymbol{\alpha}_{\mathsf{v}}{}^{\mathsf{m}} = \mathbf{I} \cdot 10^{-42}$, $\boldsymbol{\alpha}^{\mathsf{m}} = \mathbf{I} \cdot 10^{-40}$, $\lambda = 532$ nm and $n_1 = n_2 = n_3 = 1.4607$) and are taken from the model output without further scaling.

approach goes beyond previously published efforts.

5.7.1 Electrodynamic description

The amplitude of the electric field is treated as a relative, time-averaged quantity. No vectors are scaled to actual physically relevant units, but numerical values are used throughout. This is appropriate when fitting the modelling result to experimental spectra and when optimising experimental design. Absolute intensities cannot be reproduced. Many factors are still included in the model to conform to the equations in this text.

The model starts with a specification of the incoming radiation as a plane wave through its propagation angle $\theta_{k,i}$ and linear polarisation angle ψ, both given in the L-frame of reference. The angle $\theta_{k,i}$ determines the incident medium and thus the coupling factors F_x, F_y, F_z that relate the incident field to the field at the location of the scattering molecule in medium 3. This relation depends on the refractive indices n_1, n_2, n_3 of the media and the thin film in between (with $n_2 = n_3$ if the molecule is located away from the interface, *i.e.* $z > 0$). The applied electric field is then computed and projected onto the molecular axes using the specified molecular azimuthal, tilt and twist angles $(\alpha_{\mathsf{m}}, \beta_{\mathsf{m}}, \gamma_{\mathsf{m}})$.

If the laser is incident from zone I, the field at the molecule is the propagative transmitted field of the laser. If incident from zone II, the laser undergoes total internal reflection and an evanescent wave is present at the location of the scattering molecule. Each of the three components of this evanescent field has a distinct phase. For zone III, the laser is incident through medium 3 and reaches the molecule directly and through a reflected field that interferes with the incident field. For zones II and III, the applied field depends strongly on the position of the molecule along z.

The field experienced by the molecule, and that thus induces the Raman dipole, is the local field. The Onsager-Scholte model is applied here and approximates a solute molecule as a polarisable point dipole located in an ellipsoidal cavity of its own shape in a solvent that is treated as an isotropic homogeneous dielectric continuum. The local field then consists of the cavity field (the field inside the empty cavity due to the applied field and the polarisation of the surrounding medium) and the reaction field (due to the macroscopic polarisation of the surrounding medium induced by the dipole moment in the cavity). These fields are expressed in terms of the applied field, the ellipsoidal shape of the molecule, its polarisability and the refractive index of the surrounding medium. The local field disproportionately amplifies the anisotropy arising from the molecular polarisability. However, it decreases the observed anisotropy arising from the molecular shape as the field along short axes is enhanced more than along long axes of the molecule.

The induced Raman-dipole is computed by applying the Raman tensor of the mode of interest to the local field. Again, a local field correction applies to the emitted field now oscillating at the Raman-shifted frequency. The Raman-induced dipole polarises the surrounding medium which acts back on the emitting molecule and enhances the induced dipole. It acts back on the induced dipole more strongly along the small molecular axis

then along the long axis. The reaction field is in incorporated in the model as an effective dipole $\mathbf{p}_{\mathsf{eff}}$ in the molecular frame of reference.

The radiation emitted by $\mathbf{p}_{\mathsf{eff}}$, expressed in the laser frame of reference, is now calculated on each point Q on a grid at the entrance to the microscope objective. Lorentz reciprocity is used the obtain the p and s-polarised components of the dipole far-field $\mathbf{E}_{\mathsf{dip}}$ at each point Q. The reciprocity relation includes a further local field correction in the form of the cavity tensor which modifies the field due to the test dipole at the location of the Raman scattering molecule inside the cavity. Similar coupling factors apply to the incident field due to the test dipole in the reciprocity relation as to the analysis of the incident laser field.

The dipole far-field is then transformed into the objective frame of reference and collimated by rotating $\mathbf{E}_{\mathsf{dip}}$ so that its propagation direction aligns with the objective axis.

Finally, the linearly-polarised intensities $I_x(Q)$ and $I_y(Q)$ at each grid node Q are obtained by taking the complex modulus of the x and y components of the collimated dipole field $\mathbf{E}_{\mathsf{col}}$. $I_x(Q)$ and $I_y(Q)$ can be used to produce intensity maps of the field of view. The total linearly-polarised intensities I_x and I_y are then obtained by summing over all points in these maps, dividing the result by the number of grid nodes in the field of view to facilitate comparison between modelling runs of different grid sizes. These intensity values constitute the core output of the model.

5.7.2 Applicability

The applicability of the model is limited by some of its hard-coded elements in addition to approximations and assumptions of the electrodynamic description. These include the items listed below. Most of these do not restrict the validity of our approach applied to Raman scattering at optical frequencies, for which the model is intended. Suggestions are presented to extend the applicability beyond the current capabilities.

1. The dipole polarisability is linear and its decay mechanism is radiative only. Furthermore, no interference arises between the incident and output fields. This is the case with Raman scattering.

2. Frequency shifts of the dipole field due to the proximity of a dielectric interface are neglected. The internal energy levels of a molecule near an interface are displaced from those in vacuum [150]. However, the shift has been predicted to be practically undetectable [159].

3. All media are non-magnetic. For most media at optical frequencies, $\mu_r = 1$ so that $n \approx \sqrt{\epsilon_r}$ is an appropriate assumption.

4. Chemical interactions between the scattering molecule and the surrounding material are ignored. This is central to our use of the gas-phase polarisability and Raman tensors. If interactions occur, these should be included in the *ab-initio* computation so that it is reflected in the molecular properties used as input to the model.

5. The computed intensities are relative and therefore only comparable between computations with the same molecule and Raman tensor. These could be made absolute by considering the differential cross-section (equation 2.135) arising from the laser intensity, the number of illuminated molecules and the solid arc at each grid node.

6. Only linear incident polarisations are used. A generalised phase relation between the two components would allow for elliptically-polarised light, which requires a reformulation of the Raman scattering problem [61]. Using circularly polarised light (known as Raman optical activity [160]) probes the structure of chiral molecules and conformational dynamics not accessible through linear polarisations.

7. The far-field approximation is used the calculate the radiation of the Raman-induced dipole through reciprocity. This is appropriate at the dimensions of our experiment as the $(kr)^{-1}$ term in the expression of the dipole field (equation 2.103) dominates for $\rho_Q >> \lambda_{0,R}$.

8. The scattered light is only collected through linear polarisation along the observation frame x or y directions. The option of selecting an arbitrary orientation is available in the Stockholm system, though it is fixed in Durham. This can be included in the model by adjusting the azimuthal angle α_{O} of the O-frame relative to the L-frame. The x^{O} component of $\mathbf{E}_{\mathsf{col}}{}^{\mathsf{O}}$ is then along the selected axis.

9. The Onsager-Scholte model of the local field correction is assumed to be valid in our system. This implies that the applied field is assumed to be constant over the extent of the molecule (which is reasonable) and that the surrounding medium is homogeneous and isotropic (*i.e.* a single dielectric constant suffices to capture its electric properties). This assumption is actually used for all media (see the next item), notwithstanding the use of an anisotropic polarisability tensor for the scattering molecule in the application of the local field correction.[¶]

10. The media are taken to be isotropic, modelled with one refractive index for all propagation directions of the light. Optical anisotropy affects the Maxwell fields as well as the local field correction. The refractive index is then expressed as a tensor $\mathbf{n}$ of rank two, which is diagonal in the medium frame of reference (*i.e.* along the axes of birefringence). This tensor is projected onto the L-frame to compute the Maxwell field, so the optical orientation of the medium must be known. The effect of anisotropy of the medium on the local field is addressed in [161] and [162].

[¶]At first sight, this might not seem consistent. However, refractive indices have so far been treated as scalars while (Raman) polarisabilities were taken as tensors. The same approach is used here with the local field correction. Consistent incorporation of optical anisotropy would require adapting both the Maxwellian description of the model as well as the local field correction. For thin films, an intermediate solution could involve the use of in-plane and out-of-plane permittivity values for two directions within the thin film, *e.g.* one value for F_z and another for F_x and F_y that might also be used in computing diagonal elements of cavity and/or reaction field tensors. An ellipsometric method of measuring such permittivities was given by Casson and Bain [10].

11. The interface consist of either a thin-film at a dielectric interface or a clean dielectric interface. This limitation is readily overcome by using coupling factors appropriate to the layered system under consideration. With the refractive index and thickness of each layer specified, the coupling factors can be formulated to depend on the same variables as in the current model. These are given for a generalised layered system by Crawford [149], including an explicit formulation for a three-layered system. The latter is also addressed in [152] with a transfer-matrix formalism.

12. The location of the scatterer in the model is along the $\hat{\mathbf{z}}^{\mathsf{L}}$ axis. It is therefore assumed that molecules at off-axis locations produce the same scattering field at the microscope objective as those located at $(0, 0, z)$. This is appropriate as the displacement along x^{L} and y^{L} is on the order of micrometers, much smaller than WD and R_{obj} of the objective lens that collects nearly identical cones of scattered light for all molecular positions in its focal volume.

13. The laterial displacement of the beam is neglected. When a linearly polarised beam of limited extent is reflected totally, the incident and reflected beam interfere with each other. This results in a lateral displacement of the beam [163] known as the Goos-Hänchen shift. Following the definitions of our coordinate system, this shift is in the $\hat{\mathbf{x}}^{\mathsf{L}}$-direction. (A transverse shift occurs for a circularly polarised beam.) Several methods exist to calculate this displacement. Using the argument of energy conservation, the shift is directly proportional to the intensity of the evanescent field [69]. It thus varies with the angle of incidence and the polarisation of the incoming beam. Experiments to measure the Goos-Hänchen shift involved multiple total internal reflections to increase the displacement to make it easily measurable [164]. The effect for a single reflection is smaller than the wavelength used [165] and is therefore ignored here.

14. The optical components of the system are assumed to work perfectly, in particular the microscope objective lens. This includes that no losses are incurred due to birefringence or partial transmission, that the objective collimates perfectly, that linear polarisers completely transmit the selected component only and that there is no sensitivity to polarisation. Any known imperfections of components could be taken into account by using transmission functions that may vary over the modelling grid and with the polarisation of the field at each point. Furthermore, all Raman scattering falling in the view of our microscope objective is collected and adds to the total detected intensity. If the beam path is truncated anywhere in the system (by design or otherwise), the relevant fraction of grid nodes can be removed readily from the modelled intensity map.

15. For comparison to experimental data, we assume perfect optical alignment of the optical components. If deviations are known, these can be included in the model as

long as it concerns the orientation of the objective to the laser frame of reference $(\alpha_{\mathsf{O}}, \beta_{\mathsf{O}}, \gamma_{\mathsf{O}})$ or the laser propagation angle $\theta_{k,i}$.

The model is not limited to our experimental method. A generalisation to other experimental geometries is included through the relative position of objective and interface and the laser incident from either side of the interface under any angle. The mathematical description may also be employed for other processes. In addition to Raman spectroscopy, the model is readily applicable to Rayleigh scattering, in which case the polarisability tensor replaces the Raman tensor throughout. With more significant alterations of the code, fluorescence intensities could be modelled. It shares the principle of absorption followed by emission. The absorption cross-section is then used for the absorption step and the emitting dipole is strictly linked to the molecular orientation. Infrared absorption could also be modelled when the emission process is omitted altogether. The static dipole moment derivative with respect to the vibrational normal coordinate is then used. It is a vector in the molecular frame of reference and Lorentz reciprocity can be employed to obtain the coupling factors into all directions to describe the absorption of an incident field. This lead to an effective absorption cross-section tensor that depends on molecular orientation as well as incident angle and polarisation of the applied field.

5.7.3 Improvement on existing models

Several authors have published work touching on the aims of our model to predict and interpret (linearly-polarised) intensities. Some of this work has already been discussed and cited above in the elementary components of our model. In roughly chronological order, additional papers are discussed now that relate directly to modelling linearly- polarised intensities from molecules near an interface in either fluorescence or Raman scattering. The model outlined in this chapter goes beyond publish work on predicting these intensities by incorporating a more complete and versatile description of the electrodynamic problem.

Luan *et al.* studied the radiation pattern of fluorescent molecules embedded in a spin-coated polymethylmethacrylate (PMMA) film on glass [166] and on a thin silver film [167]. Using a spin-coated resin to encapsulate the dye molecules ensured that these were fixed in a uniform orientation distribution. Excitation of the dye was at normal incidence and the emission was detected in photo-multiplier tube with a collection half-angle of 0.15°. This resulted in an accurate radiation profile over nearly the full range of the polar angle $0° \leq \theta \leq 180°$. The intensity profile $I(\theta)$ was accurately described by the far-field intensity distribution of an emitting dipole in a three-layer system obtained through Lorentz reciprocity, integrating over the depth of the PMMA/dye film. The fluorescent emission into the glass side of the interface was clearly enhanced over that of the air side, especially around the critical angle.

In another paper, a selection of the same authors computed the dipole near- and far-fields [168] from which they obtained a ratio of the total intensity emitted into each medium for each polarisation (though it appears that they only involved the polar angle as in their

previous study). To obtain the strongest intensities, one should collect the emitted light through the optically denser side of the interface and the refractive index difference should be as large as possible. However, as the emitting dipole is located further away from the interface, this advantage reduces. The evanescent part of the dipole near-field (zone II in our framework) no longer couples into the high-index material at larger distances. Though the authors discuss these factors in obtaining high-intensity emission, they did not apply their conclusions to the excitation light, keeping the laser beam at normal incidence from the air-side of their system [167].

Pristinski *et al.* [42] use the evanescent field to enhance both the applied field and the emitted dipole field of a surface-enhanced Raman scattering (SERS) probe in water on glass. The Raman signal at about 2105 cm^{-1} arose from SCN^- absorbed on silver nanoparticle clusters placed at the interface between a borosilicate glass prism and water. The Raman scattering was induced by a polarised laser incident through the prism above the critical angle. Scattered light was collected in a collimating lens with an effective θ_{obj} ranging from 0.4° to 1.1° in the prism at polar angles ranging from 62° to 81° in the direction of the reflected laser beam. In this geometry, the authors recorded the evanescent field of the induced dipoles, emitting into zone II.

The dependence of the SERS signal on collection angle and polarisation was modelled by taking both the incident and emission radiation into account. The authors derived the field for each scattering direction through reciprocity, scaling the detected intensity with the solid angle collected at that position. As θ_{obj} was small in their experiments, this did not limit the accuracy of their interpretation.[‖] The relatively simple model of Pristinski and co-workers could explain most of the observed variation of the Raman peak intensity with the scattering angle, assuming that the scattering hot-spots were randomly oriented in space and located at the interface. The variation of the signal with orientation of the hot-spots was not investigated. The authors recognised the potential for enhancement and increased surface sensitivity of the Raman signal by exciting the Raman dipoles with an evanescent field and collecting the evanescent part of the induced dipole field by illuminating and collecting through zone II. Moreover, they showed a successful application of the reciprocity principle to Raman scattering.

The limited modelling efforts to date on interfacial Raman intensities were also recognised by Itoh and Hasagawa [152]. They stated that "the analytical theory does not catch up with the technical improvements and it does not meet the demands of experimental spectroscopists" and presented a model to account for incident and emitted light, using transfer matrices and Lorentz reciprocity. They applied this model in the thin-film limit to the analysis of Raman spectra of cadmium stearate Langmuir-Blodgett films on a glass microscope slide. From the four polarised spectra of the CH-stretch band they collected,

[‖] Note that in our experiments, in the absence of SERS enhancement, objective lenses with larger NA are used to ensure sufficient signal. This requires integration of the intensity over the field of view. As the field can vary strongly with angular position, recalculation of the field at various points on the objective entrance is needed.

they only used the intensity ratio I_{sp}/I_{ps} of the antisymmetric CH_2 stretch mode to assign a molecular tilt angle to their system. The Raman tensor was averaged over all azimuthal and twist angles so that the absolute value of its non-zero elements dropped out of the ratio. Their experimental geometry did not take advantage of the suggestions of other authors to increase the signal, but was limited to a laser incident onto the sample through air with collection at 90° in the plane of incidence. The lens that collected the scattered light was not mentioned nor included in their computation. Unfortunately, their model remains strictly limited to the chosen experimental geometry.

Another relevant publication is of Chen *et al.* [40], in which the far-field radiation profile of a Raman dipole near or in a four-layer waveguide structure is theorised. Their calculations predict highly directional radiation depending on the layer thickness, the vicinity of the dipole to the interface and its orientation along either x, y or z. With the appropriate structure, the coupling of the dipole field into the waveguide, *i.e.* the detection depth of a potential Raman sensor, could be limited to a quarter of the evanescent field penetration depth. The authors suggested the use of such structure to analyse molecular orientation at an interface, harnessing the additional enhancement from the waveguide-coupled modes. However, their model considered the three orthogonal directions only and employed absolute values of coupling factors, appropriate for intensity values but not for field amplitudes. Moreover, their study did not consider how the scattering was induced or how it was detected, both of which affect the linearly-polarised intensities obtained at a particular molecular orientation.

The models discussed so far omit the direct use of molecular properties, choosing to assume averages in stead. Including these requires appropriate transformations between molecular and experimental frames of reference. This last point was recognised by Roy *et al.* [71], who emphasised accurate rotational operations and a consistent framework of coordinate systems when using computed molecular properties in the interpretation of vibrational spectra. Their definitions, however, differ from ours.

In summary, we note that most papers are limited to a description of dipole emission patterns. A combination of excitation and emission effects was included in [42] and [152], though the angular spread was at most rudimentary incorporated in their models. Assessing the available literature, we conclude that our electrodynamic model of Raman scattering at interfaces goes beyond the published literature. It incorporates multiple factors that modify the relative values of linearly-polarised intensities, most of which have not been addressed before in this context, let alone combined in a coherent description. These include the following.

1. The incident laser beam, under any angle with respect to the interface and any linear polarisation direction.

2. The far-field emitted by the induced dipole fields into any direction, derived through Lorentz reciprocity.

3. Position of the scattering molecule at or near the interface and in either of the bounding media.**

4. A local field correction for the incident field as well as for the induced dipole moment at the Raman-shifted frequency and for the emitted field derived by reciprocity.††

5. The integration of the linearly-polarised intensities over the field of view collected of the objective lens, taking field directions at each point into account through appropriate transformations.

6. Free positioning of the objective in space and with it the collection polarisation directions.

7. Specific molecular orientations and molecular properties, including Raman tensors, specified in the molecular axes with appropriate transformations of this frame to other frames of reference in the model.

Only the elements numbered 1 to 3 have been included in models before, while the other aspects are introduced with this work. Though the model presented in this chapter is more advanced than what has been available so far, its accuracy has to be established with experimental data. This is the focus of the next chapter.

**The depth $z \geq 0$ is specified into medium 3. By interchanging the values assigned to n_1 and n_3 in the model and adjusting the propagation direction of the incident beam $k_{i,\theta}$, the molecule can be placed on either side of the interface.

††If it is desired to omit the local field correction from the computation, the input variables may be specified with $r_x^{\mathsf{m}} = r_y^{\mathsf{m}} = r_z^{\mathsf{m}}$ and $\boldsymbol{\alpha}^{\mathsf{m}} = \mathbf{0}$. The local field correction then results in a mere scaling of the computational result (through the cavity field tensor) rather than affecting relative intensities between the various polarisation combinations.

Chapter 6

Validation of the model

This chapter presents experimental and modelling results to assess the accuracy of the model description developed in the previous chapter. Systems of increasing complexity were studied on the Raman systems of Durham and Stockholm in order to assess validity of (components of) the model. The chapter starts with an outline of the methodology developed to test our model with selected interfaces. Presented next are the experimental and modelling results for each of the three studied interfaces. The model calculations are extended beyond the experimental scope to advance our insight into the dependence of the Raman intensities on experimental variables. The chapter concludes with a summary.

6.1 Methodology

Polarised Raman scattering experiments provide highly multivariate data. Our model likewise includes many input variables (listed in table 5.3), each of which affects the modelled scattering intensities to a particular extend. Using a limited number of selected molecular systems, the effect of various input variables may be separated so that these can be studied and validated individually. Furthermore, limiting or simplifying cases may be explored.

6.1.1 Interfaces of increasing complexity

The simplest interface involves an isotropic Raman scattering mode of an isotropic molecule in a homogeneous medium, with all materials being optically isotropic. A number of spherically symmetric molecules exist, belonging to the T_d point group, that include vibrational modes of its A_1 species of which the Raman tensors are isotropic (compare table C.1). A number of such molecules exist, though some exhibit resonances between the Raman-active modes.

This leads us to the second level of complexity, which involves anisotropic Raman tensor in an isotropic molecule with an isotropic orientation distribution.

A third level of complexity is obtained with a molecular layer at the sampled interface of a known orientation.

The following molecules were selected for each level of complexity.

1. Sulfate anion, from ammonium sulfate salt dissolved in water, representing a fully isotropic molecular system with an isotropic v_1 mode against an optically isotropic fused silica hemisphere.

2. Carbon tetrachloride as a pure liquid, being randomly oriented and including isotropic as well as anisotropic Raman tensors in its various isotopologues and involving Fermi resonances. A sapphire hemisphere is chosen to increase the optical mismatch between the two materials.

3. A monolayer of zinc arachidate on fused silica, being an oriented system of which the molecular orientation is (roughly) known. The lower medium is air.

Preparation of these samples as well as the Raman systems was detailed in chapter 3.

The aqueous sulfate solution at the silica surface represents the most isotropic system in that it comprises isotropic optical media, the scattering molecule features a fully symmetric mode with an isotropic Raman tensor as well as an isotropic polarisability tensor and isotropic molecular shape, *i.e.* the molecule is essentially spherical. The effective Raman tensor for the v_1 mode of the sulfate anion isotropic and the induced dipole is along the applied electric field in the L-frame. With this system, the material and molecular properties are isotropic. Any variation between the measured and modelled Raman intensities for the various polarisation combinations should thus relate purely to the macroscopic optical properties of the interface. These experiments thus test the validity of the optical description in the model and sampling parameters such as g, z and spread in the angle of laser incidence.

Sulfate spectra were recorded on both the Durham and Stockholm Raman systems. Allowing a comparison between the two.

Carbon tetrachloride incorporates anisotropic Raman tensors, though still in a random (*i.e.* isotropic) distribution of molecular orientations. This molecule further includes degenerate modes, isotopologues and Fermi resonances in some of its modes. The sapphire hemisphere used with this material also introduces a small degree of birefringence. This sample allows testing of orientational averaging with anisotropic Raman tensors in the model and how many angular positions require sampling before convergence is achieved. Furthermore, it may be used to assess its sensitivity to the local field correction. Isotopological abundances and Fermi resonances are also considered.

The zinc arachidate monolayer on fused silica provides a sample with anisotropic Raman modes in an molecule at a roughly known orientation. Monolayers of fatty acids and their salts are well-studied samples of scientific and applied interest [96]. The CH-stretch region of the molecule has our primary focus. This region includes overlapping modes of various symmetries and Fermi resonances. The monolayer may be modelled in the thin-film limit.

In short, these samples provide Raman tensors of various forms, testing of experimental variables and optimisation of model sampling parameters. A modelling script is employed for each calculation. This modelling script (which calls the `pirs.m` function) depends on the specific system and variables being modelled. An example of such scripts is included as appendix E.3 (sulfate v_1 band intensity as a function of collection polarisation and incident polarisation angle ψ).

6.1.2 Fitting experimental spectra

Raman intensities have to be extracted from experimental spectra in order to compare these with the model predictions. For each of the sampled systems, a method of extracting relevant peak intensities from the experimental spectra is presented. Various methods are used, including baseline subtraction, background subtraction and fitting of individual bands. These have been kept as straightforward as possible to aid in the physical interpretation of the Raman spectra. A black-box fitting algorithm for a whole spectrum may be advantageous once it is validated with our model.

Baseline subtraction involves removing a linear or curved intensity profile from (part of) a spectrum. This baseline is adjusted to the spectrum itself without requiring an external reference. Here, we fit a polynomial through regions of the spectrum from which Raman features are absent to obtain neat peak intensities for the remaining parts of the spectrum.

Background subtraction involves recording a background spectrum, preferably at very similar conditions to the sample spectrum from which it is to be subtraction to obtain neat peak intensities.

Fitting individual bands or overlapping spectral features is generally performed with Gaussian and/or Lorentzian profiles. These profiles find a physical basis in line-broadening mechanisms. Broadening of (Raman) peaks results from a number of factors, including the following.

- The lifetime of the quantum state involved (through the uncertainty principle).
- Intermolecular coupling of modes (such as in resonances) and phase relations between modes of the same molecule.
- Coupling with other molecules (*i.e.* intramolecular coupling), which may be inhomogeneous, in that the coupling involves different average environments, or homogeneous, in that the coupling results from fluctuations in the same average environment (such as dephasing of vibrations over the lifetime of the state and frequency changes due to variations in the quantum state).
- Collision broadening, involving perturbations of outer electrons due to molecular collisions and thus changes in the vibrational/rotational energy levels.

- Doppler broadening, arising from random motion of molecules which includes various relative velocities causes broadening of the Raman band.

Various software packages are available to perform fitting of spectra. Here, MATLAB and FYTIK [169] are used.

Once the experimental intensities are known, modelled intensities may be fitted to these as a function of model input parameters. Generally, least-squares algorithms are followed. Sample-specific methods may also be developed. For example, principal component analysis (PCA) has been used to study interfacial water with TIR Raman [51]. In our group, target-factor analysis (TFA) has been used for samples that include at least two different types of molecules for which a pure spectrum is known. TFA may be applied to deduce surface excess of competing absorption by multiple surfactants [81]. In both of these examples, a relatively high number of spectra may be analysed in an automated, statistical manner.

6.1.3 Cavity shape and polarisability tensors

Application of the local field correction in our model requires a polarisability tensor $\boldsymbol{\alpha}$ and a cavity shape (r_x, r_y, r_z) as input, both specified in the m-frame.

Burnham *et al.* [153] studied various local field theories with Rayleigh scattering. For the Onsager-Scholte model of the local field correction, they found that the experimental intensities were best described when the van der Waals radii of the molecules were used for the dimensions of the cavity. As the electromagnetic description of Rayleigh scattering is equivalent to that of Raman scattering, we also choose to employ molecular van der Waals radii to specify the cavity shape.

For both molecular polarisability and molecular ellipsoid, we employ the computational results from GAUSSIAN presented in chapter 4 which should be consistent with the Raman tensors. The polarisability tensor and semi-axes of the molecule may need rotation into the m-frame just like the Raman tensors. The polarisability tensor is computed in GAUSSIAN for an electric field of zero frequency, the so-called static polarisability of the molecule. It is included in the final section of the log file after `\Polar=` as six tensor elements α_{xx}, α_{xy}, α_{yy}, α_{xz}, α_{yz} and α_{zz} in units of B^3, which can be converted to the appropriate SI unit $C\,V^{-1}\,m^2$ by multiplication with $1.649 \cdot 10^{-41}$.

The atomic coordinates in the m-fame are used to find outer dimensions of the molecular shape. The van der Waals radius of relevant outer atoms are added to these coordinates to obtain the molecular dimension. This provides a molecular ellipsoid diameter along each axis, which are halved to obtain radii. The resulting parameters are given in table 6.1 with all relevant GAUSSIAN output included in appendix D. The atomic radii are taken from a recent study by Alvarez [170]. The van der Waals radii given by this author correspond to the most frequent intermolecular non-bonded contact distance found in vast collections of crystallographic databases. The values include 1.20 Å for hydrogen, 1.50 Å for oxygen and 1.82 Å for chlorine.

Table 6.1: Molecular polarisabilities and molecular ellipsoid radii

molecule	$\boldsymbol{\alpha}^{\mathsf{m}}$ / 10^{-40}C V^{-1} m^2	$r_x{}^{\mathsf{m}}$ / Å	$r_y{}^{\mathsf{m}}$ / Å	$r_z{}^{\mathsf{m}}$ / Å
SO_4^{2-}	$8.01 \cdot \mathbf{I}$	3.03	3.03	3.03
CCl_4	$10.2 \cdot \mathbf{I}$	3.61	3.61	3.61
Decanoic acid	$\begin{pmatrix} 20.1 & 0 & -0.28 \\ 0 & 17.1 & 0 \\ -0.28 & 0 & 27.7 \end{pmatrix}$	2.54	2.08	8.34
Arachidate	$\begin{pmatrix} 35.6 & 0 & 0 \\ 0 & 31.9 & 0 \\ 0 & 0 & 48.2 \end{pmatrix}$	2.54	2.08	14.5

The polarisability of decanoic acid includes an off-diagonal element (xy and yx in the standard axes) which results in small residual polarisabilities for the xz and zx elements in the m-frame tensor. This is a consequence of the coordinate transformation, which is based on atomic positions, not centre of charge or mass. For decanoic acid, $r_x > r_y$ because the $x^{\mathsf{m}}z^{\mathsf{m}}$ plane contains the chain of carbon atoms. Its shape parameters (equation 5.59) are $S_x = 0.409$, $S_y = 0.506$ and $S_z = 0.0850$.

The parameters for arachidate are estimated as follows. As explained in chapter 4, no computations could be performed to obtain these directly.

The molecular radii of arachidate are only expected to differ from those of decanoic acid along its long axis. A value for r_z is estimated from decanoic acid by discounting the hydrogen atom from its acid group, adding twice the length of its C3-C8 carbon atoms and adding both the oxygen and hydrogen van der Waals radius. The resulting shape parameters are $S_x = 0.431$, $S_y = 0.530$ and $S_z = 0.0395$.

The mean molecular polarisability of n-alkanes is known to increase linearly with chain length (see, for example, [171], [172] and the cited studies by Gough *et al.*). We therefore estimate a polarisability tensor for eicosane by linear extrapolation of those computed by Gough [136]. This provides α_{xx}, α_{yy} and α_{zz} values. To these diagonal tensor elements, we add the effect of the carboxylic acid group, estimated from the difference between the polarisability computed with GAUSSIAN for decanoic acid and that extrapolated for decane from Gough's data. This approach is supported by the empirical fact that group polarisabilities are transferable (section 4.4.3). Figure 6.1 shows the diagonal polarisability tensor elements and linear fits. Off-diagonal elements are assumed to be negligible throughout this process.*

*The mean molecular polarisability of arachidic acid $\bar{\alpha}$ is thus estimated to be $38.6 \cdot 10^{-40}$ C V^{-1} m^2. This value leads to underestimation of the molecular volume with the Clausius-Mossotti equation (equation 3.5 with refractive index of table 3.2) by a factor of up to 585, depending on molecular packing, compared to the molecular volume given by its molecular ellipsoid. For decanoic acid, however, the discrepancy in molecular volume from both calculations is a factor 600 and thus to be expected.

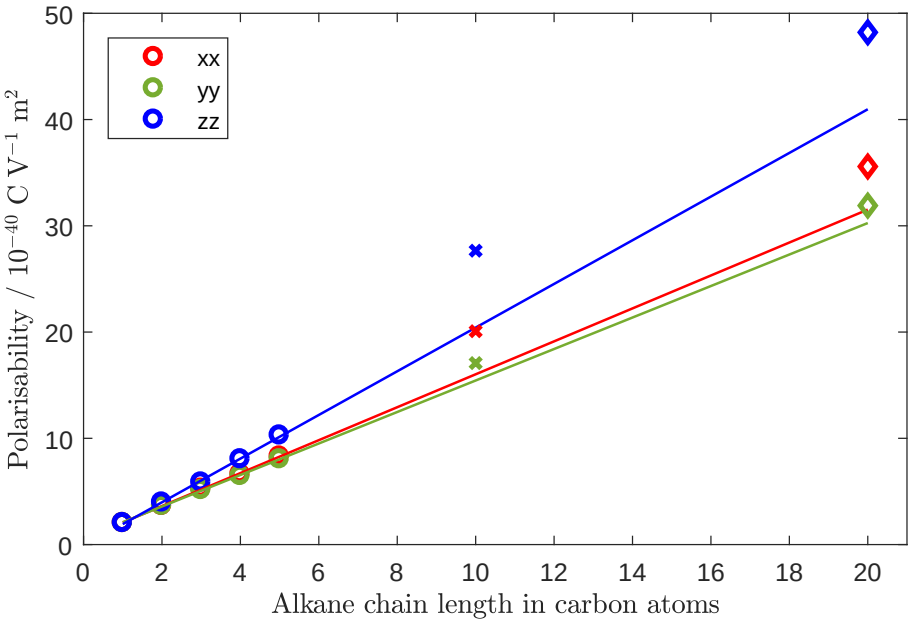

Figure 6.1: The diagonal polarisability tensor elements for stretched n-alkanes computed by Gough [136] (circles) are linearly extrapolated (lines) up to 20 carbon atoms. The computed values for decanoic acid (crosses) and an estimate for arachidic acid (diamonds) are also indicated. The latter values are obtained from the linear extrapolation plus the difference between the polarisabilities of decanoic acid and the extrapolation at 10 carbon atoms.

6.2 Ammonium sulfate solutions on silica

The goal of our studies on sulfate salt solutions were to establish the validity of the optical description of the scattering process in our model. The molecule and its Raman-active mode were chosen for this particular purpose. The sulfate v_1 Raman band is the symmetric stretch mode associated with the transition from the ground state to the first vibrationally excited state of the sulfate anion and belongs to the fully symmetric species of its T_d point group. The Raman tensor of this mode is therefore diagonal and results in a polarised peak in the spectrum. It appears at about 980 cm^{-1} in solution [126], a higher shift than predicted by our *ab-initio* computation (chapter 4). As its Raman tensor is isotropic, the molecular orientation has no effect on the orientation of the Raman-induced dipole and the observed intensities are identical. Furthermore, the local field correction is isotropic due to the spherical shape of the molecule and its isotropic polarisability. Comparing modelled to experimental scattering intensities thus only involves the applied and scattered fields as modulated by the macroscopic optical components in the chosen experimental geometry.

Ammonium sulfate was chosen from the numerous sulfate salts for its high solubility in water (74.4 g per 100 mL at 20.0°C [92]) and immediate availability at high purity. Experiments were conducted on the interface formed by fused silica and a solution of ammonium sulfate. The v_1 band proved distinguishable from the strong and broad silica

Raman signal in that range. As is shown below, the background could readily be fitted and removed to obtain intensities due to sulfate only.

Experiments were conducted in Durham as well as Stockholm. Raman spectra were collected for a selection of linear polarisation angles of the laser, laser incident angles, sulfate salt concentrations (which affect the refractive index of the solution), objective lenses and collection polarisations. More extensive modelling results are presented to show how these parameters affect the polarised Raman intensities of the sulfate v_1 band. The observed linearly-polarised intensities are compared to the model predictions. In turn, components of the experimental systems can be evaluated once the effect of each is known through an accurate model description.

6.2.1 Experimental results from Stockholm

Thirty polarised Raman spectra of the interface between a fused silica hemisphere and an ammonium sulfate solution are presented here. These were acquired on the Stockholm system using a flow cell to hold the sample. The spectra were recorded with the grating of 1200 lines mm^{-1} set to centre the spectrum around 560 nm on the CCD, recording in multi-track mode. The position of the objective remained in its standard position, *i.e.* observing through the hemisphere with its axes (anti)parallel to the plane of laser incidence.

Five experimental variables were explored:

1. the collection polarisation, set to either x or y,
2. the linear incident polarisation, set in the range $0° \leq \psi \leq 90°$,
3. the numerical aperture of the objective, either NA = 0.28 or NA = 0.55,
4. the laser propagation angle $\theta_{k,i}$, under which the laser is incident on the interface, set to 70°, 73° or 75°.

The range of incident angles was restricted by the device holding the hemisphere towards the upper end and by the objective towards the lower end of the range. The two objectives have the same parfocal distance, so that these can be exchanged without having to reposition the sample or incident laser beam.

The diameter of the laser beam was estimated to be 9 mm before focussing it over a distance of 80 mm onto the sample, giving an approximate spread of ±3.2° about the central angle of incidence. The critical angle of the silica-solution interface is 66.4° at the laser wavelength and 66.5° at a Stokes Raman shift of 980 cm^{-1}.

Spectra were acquired with 15 accumulations of 8 s exposures with the small-NA objective and with 12 accumulations of 5 s exposures with the large-NA objective. The number of accumulations was set to ensure a smooth spectrum and the exposure time was chosen to reach about three-quarters of the detector saturation, all to obtain a satisfactory signal-to-noise ratio in the shortest time.

Our analysis is limited to the v_1 band of the sulfate anion, observed at about 980 cm^{-1}. The other sulfate bands can not be distinguished from the strong silica-water background signal in the recorded spectra.

Linear polarisation angle

A set of spectra were recorded with NA = 0.55, $\theta_{k,i} = 75°$ and ψ varying from 0° to 90° in steps of 15° with the collection polarisation set to x or y. The linear polarisation angle ψ was defined in figure 5.6 with $\psi = 0°$ conforming to p and $\psi = 90°$ to s-polarised incident light. The spectral region around the sulfate v_1 Raman band is presented in figure 6.2 for all polarisation combinations.

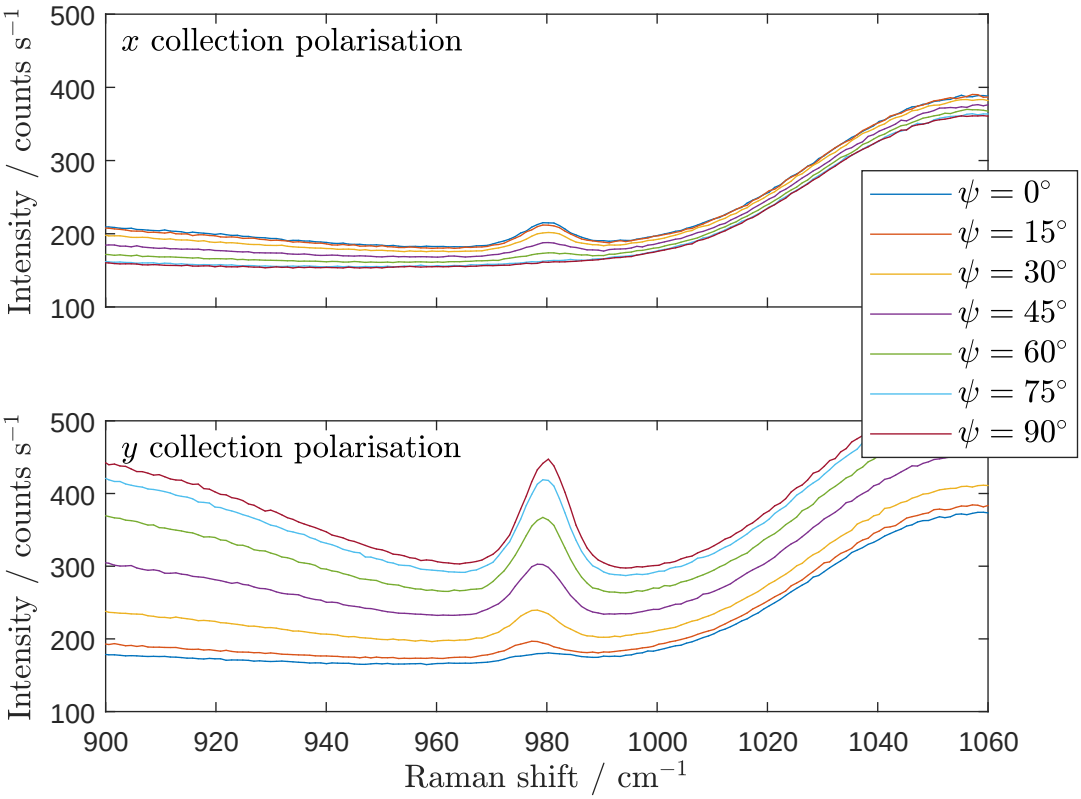

Figure 6.2: Raman spectra of ammonium sulfate solution at the fused silica interface for linear incident polarisations ranging from p-polarisation ($\psi = 0°$) to s-polarisation ($\psi = 90°$) at $\theta_{k,i} = 75°$ and NA = 0.55. A limited spectral region is shown. The band at 980 cm^{-1} is the v_1 mode of the sulfate anion, silica and water contribute to the smooth baseline. [data: 20170324/022-035]

The silica-water background signal is fitted with a seventh-order polynomial and subtracted from the recorded intensity to obtain the intensity due to the sulfate v_1 band (examples of this are given in figure 6.3). The use of a polynomial to fit the background profile, rather then subtracting a separately collected silica-water background spectrum, is appropriate as the v_1 band can be distinguished from its smoothly varying baseline.

The spectral ranges 920–960 cm^{-1} and 1000–1040 cm^{-1} are used to fit the background. The v_1 intensity is the sum of the background-subtracted intensities at each data point between 960 and 1000 cm^{-1}, divided by the exposure time of the detector. Figure 6.4 presents the obtained values for each combination of incident and collection polarisation. For x-polarised collection of the scattered light, the intensity reduces with ψ, while it increases for collection of y-polarised scattering. At $\psi \approx 20°$, the intensities are equal. The outer values of the data range relate to the standard px, py, sx and sy polarisation combinations as indicated in figure 6.4. Their intensities are in the order $sy > px > py > sx$. The Raman band is strongest in the polarised spectra, as expected for a Raman mode of this symmetry species.

Incident angle and numerical aperture

The effect of the numerical aperture as well as the angle of incidence on the polarised Raman spectra was assessed in a series of spectra recorded with the four standard polarisation combinations. The v_1 region of these spectra is presented in figure 6.5. This includes the cases $\psi = 0°$ and 90° from the dataset presented in the previous paragraph. The intensities are markedly lower with the smaller aperture, as less scattered light is collected into the objective. The intensities are increased for angles of incidence nearer the critical angle (66.4° with this interface), as expected from the Fresnel amplitude coefficients. The intensity of the sulfate v_1 band in each spectrum is obtained through the same background subtraction process as outlined above. The results are summarised in table 6.2.

6.2.2 Experimental results from Durham

Three sets of polarised spectra were recorded on the Durham Raman system with the laser (set to a 200 mW output) incident at $\theta_{k,i} = 73°$ while collecting scattered light in the NA = 0.55 objective. The diameter of the laser beam on the focus lens L_3 ($f = 120$ mm) was measured to be 4 mm, giving an estimated spread in the incident angle θ_i of 1°.

Sulfate solutions of two different concentrations were pumped in the flow-cell under a fused silica hemisphere. The concentration affects the refractive index and thus the critical angle of the interface. Spectra were recorded in the standard polarisation combinations px, py, sx and sy in the static collection mode of the CCD software, centred at a Stokes Raman shift of 800 cm^{-1} (covering a spectral range of about 380—1240 cm^{-1}).

The following sets of polarised Raman spectra were collected:

B a 40 wt% ammonium sulfate solution, acquired by accumulation of four spectra of 5 s exposure each,

C the same sample recorded a day later, allowing for crystallisation of the near-saturated solution (accumulating 8 acquisitions of 5 s exposure),

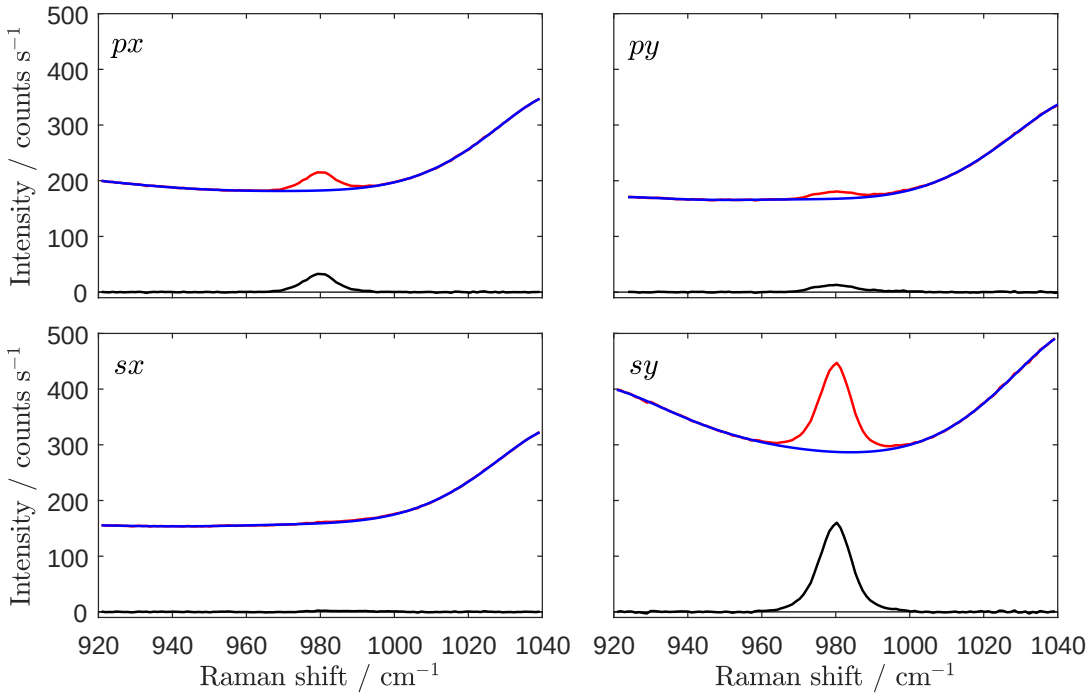

Figure 6.3: The v_1 sulfate band (black) is obtained by subtracting the silica-water background intensity, fitted by a seventh-order polynomial (blue) to the surrounding spectral region, from the recorded Raman spectrum (red). The four polarised spectra are from the dataset of figure 6.2.

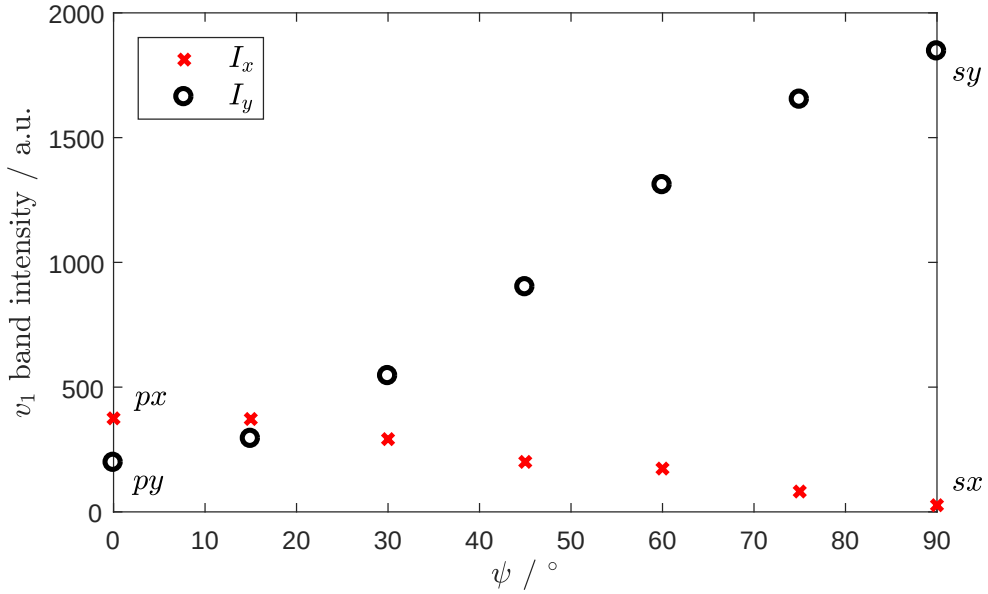

Figure 6.4: Intensity of the v_1 sulfate band as a function of the linear polarisation angle ψ of the incident laser for the x and y collection polarisations. The data points conforming to the standard polarisation combinations px, py, sx and sy are indicated.

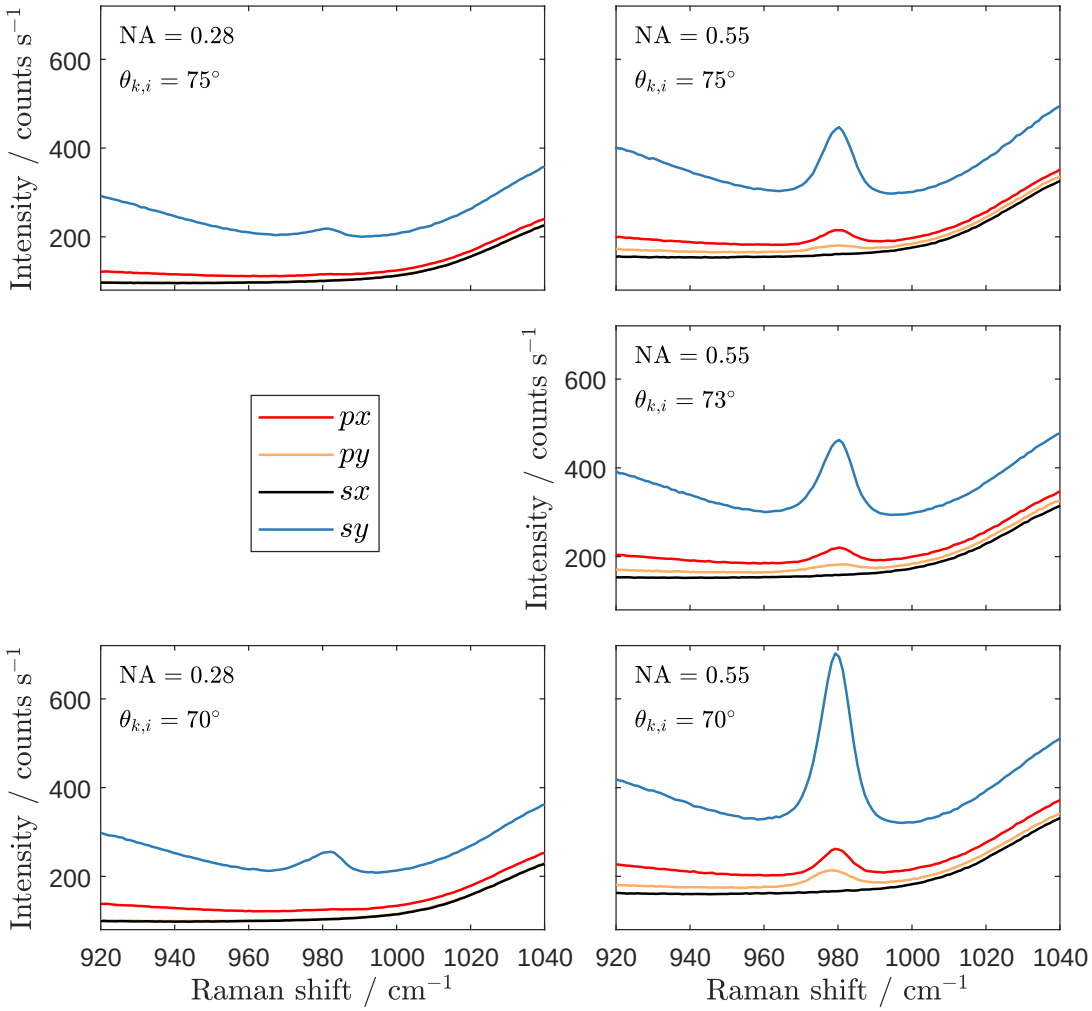

Figure 6.5: Raw Raman spectra of ammonium sulfate solution at the fused silica interface with different numerical aperture (NA) and laser propagation angle $\theta_{k,i}$ collected with the Stockholm system. A limited spectral region is shown. The band at 980 cm^{-1} is the v_1 mode of the sulfate anion, silica and water contribute to the smooth baseline. The px and sx spectra overlap in the plots on the left. [data: 20170324/022,028,029,035,042-045,047-050,053-056,067-070]

Table 6.2: Experimental intensities (in counts s^{-1} cm^{-1}) of the sulfate v_1 Raman band in the four polarisation combinations with varying numerical aperture (NA) and laser propagation angle $\theta_{k,i}$ for the data obtained with the Stockholm Raman system (figure 6.5).

NA	$\theta_{k,i}$ / °	I_{px}	I_{py}	I_{sx}	I_{sy}
0.28	70	62.30	12.33	14.25	705.0
0.28	75	58.70	0.9758	18.01	293.6
0.55	70	650.7	491.6	5.685	4359
0.55	73	419.1	226.9	7.215	2093
0.55	75	374.9	197.0	267.2	1846

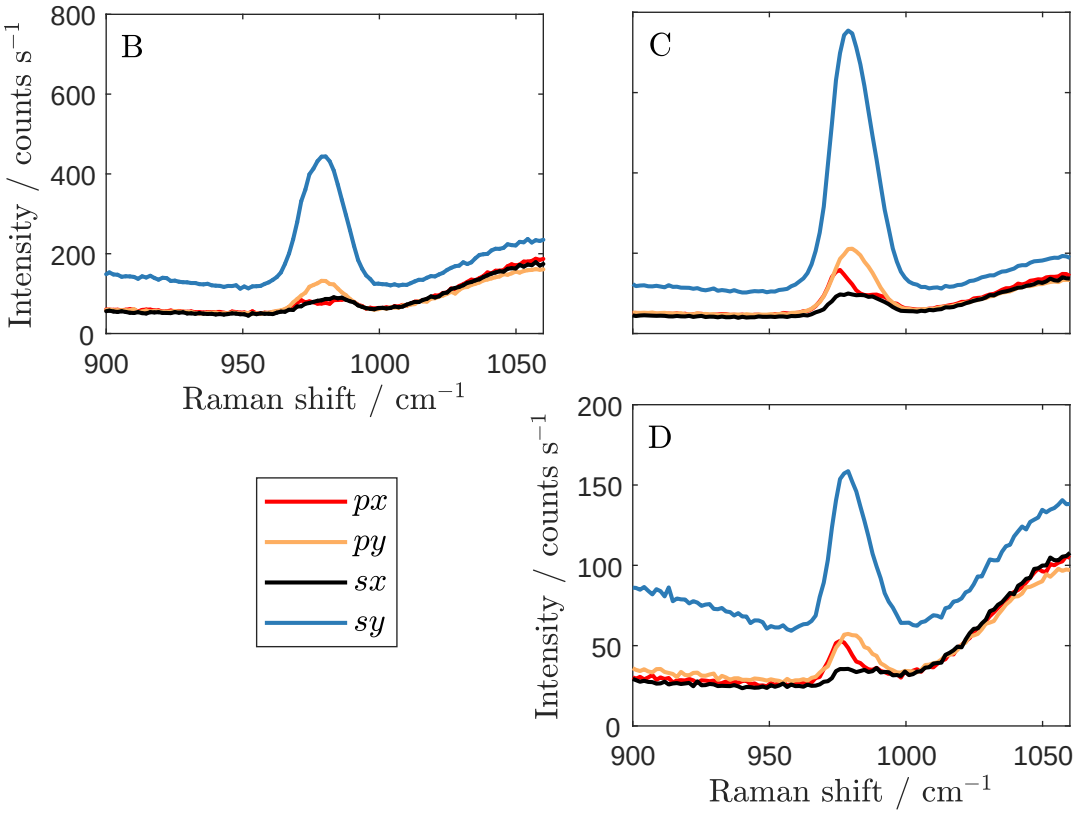

Figure 6.6: Raman spectra of ammonium sulfate solution at the fused silica interface collected with the Durham system. The spectral region around the sulfate v_1 band is shown. Silica and water contribute to a relatively smooth baseline. [data: 20150505/026-029,037-040,044-047]

Table 6.3: Experimental intensities (in counts s^{-1} cm^{-1}) of the sulfate v_1 Raman band in the four polarisation combinations recorded on the Durham system with different salt concentrations (spectra of figure 6.6).

dataset	concentration / wt%	I_{px}	I_{py}	I_{sx}	I_{sy}
B	40	542.9	1111	580.9	4729
C	40	1171	2096	786.5	8729
D	18	282.6	399.7	165.8	1364

D a 18 wt% ammonium sulfate solution, pumped into the flow cell after rinsing (accumulating 8 acquisitions of 5 s exposure).

The region of the Raman spectra around the sulfate v_1 band is presented in figure 6.6. Dataset B was recorded at high concentration, near the maximum solubility, to achieve strong Raman scattering. The increased intensities in spectra C are attributed to overnight crystallisation at the silica surface. This process increased the number or Raman scatterers in the probed volume of the sample. Crystallisation was confirmed by optical microscopy of the interface, which showed a speckle pattern not seen previously, indicating reflections of the laser beam off crystal faces. Crystallisation does not affect the relative intensities observed in zone I, as is the case here, because the Raman tensor of the v_1 mode is isotropic. The double peak, most clearly seen in the *px* spectra, contains the v_1 Raman mode of both freely solvated sulfate anions and its crystalline form at a slightly higher shift [126]. The net effect of crystallisation at the silica surface is an overall increase of the Raman intensity that does not affect our model interpretation.

The lower concentration of dataset D results in less intense sulfate bands, though these spectra still benefit from some crystals at the surface. The change in refractive index also reduced the intensities, which can be seen from the reduced silica-water baseline. This last effect is explained through the Fresnel factors. The electric field at the interface is reduced because the angle of incidence is further from the critical angle for dataset D ($\theta_c = 68.7°$) than for datasets B and C ($\theta_c = 72.5°$).

The polarised sulfate v_1 band intensities were obtained through the same process as with the Raman spectra collected in Stockholm. The fitting interval was 900–960 cm^{-1} and 1000–1060 cm^{-1} for the baseline subtraction. A wider spectral range was used to fit the background profile for the Durham data as these spectra include less data points per wavenumber and their noise level is higher. Table 6.3 includes the obtained intensities.

6.2.3 Modelled v_1-band intensities

The sulfate Raman spectra are used to test the optical description of the scattering process. We first assess the impact of the model grid size g and sampling depth z before computing intensities as a function of the laser linear polarisation angle ψ, the laser propagation angle $\theta_{k,i}$, numerical aperture (NA) and refractive index of the solution n_3. For each computation, we use the experimental settings as input variables while scanning the free variable over an appropriate range. The refractive indices of silica and the sulfate solutions were given in table 3.2 and the Raman tensor of the sulfate v_1 mode in table 4.2. The following hold for all computations presented in this section: $\lambda_{0,\mathsf{laser}} = 532$ nm, $(\alpha_\mathsf{m}, \beta_\mathsf{m}, \gamma_\mathsf{m}) = (0°, 0°, 0°)$ and $\bar{\nu}_R = 980$ cm^{-1} as well as the semi-axes of the molecular ellipsoid and the polarisability tensor of the sulfate anion (presented in section 6.1.3 from computations in GAUSSIAN). Finally, the objective orientation in the L-frame is

$(\alpha_{\mathsf{O}}, \beta_{\mathsf{O}}, \gamma_{\mathsf{O}}) = (0°, 180°, 0°)$ as with all experiments, though α_{O} and β_{O} are varied in some of the computations presented here.

Grid size

The grid size of the model should be large for an accurate representation of the Raman-scattered field yet it should be as small as possible to reduce the time required for the computation. An appropriate grid size retains all significant variation in a reasonable computation time. To find this balance, the intensities were computed as a function of grid size parameter g, using $z = 0$, $\theta_{k,i} = 75°$, NA = 0.55 and the refractive index of the 0.3 mol L^{-1} ammonium sulfate solution. The results are presented in figure 6.7 and show that the intensities converge with increasing g. The computation with $g = 1$ conforms to NA $\to 0$ and differs significantly from the intensities obtained at large g. This indicates the importance of modelling the actual spread of collection angles for the radiation field. The input $g = 2$ does not provide a relevant result in our model as it positions four grid nodes on the corners of a square around the circular field of view, all of which are thus ignored in the computation and $N_Q = 0$. For the remaining computations in this section, we choose to use $g = 15$.

The intensities in figure 6.7 are expressed as relative values, *i.e.* $I_{px} + I_{py} + I_{sx} + I_{sy} = 1$ for each value of g. The order of the modelled intensities agrees with the experimental observation (top right spectra in figure 6.5) in which $I_{sy} > I_{px} > I_{py} > I_{sx}$. Moreover, we observe quantitative agreement with the experimental relative intensities in the converged region.

Sampling of depth position

The depth-dependence of the scattered intensities is computed for the above experimental parameters, using the optimised grid parameter $g = 15$. Figure 6.8 presents both absolute and relative linearly-polarised intensities with the microscope objective positioned to collected radiation into zone I, II or III. In the experiments presented here, the objective was positioned in its standard orientation above the hemisphere, perpendicular to the interface, thus collecting radiation into zone I only as the NA is too low ($\theta_{\mathsf{obj}} < \theta_c$) to capture any other radiation.

In zone I, the modelled intensities decay exponentially with z, as expected. The incident coupling factors $\mathbf{F}_{3\to1}$ share an identical z-dependence through the exponential factor while the outgoing coupling factors $\mathbf{F}_{1\to3}$ involve a propagative wave only and thus do not depend on z. Integration of the intensity over z is not needed in this system as the relative intensities are independent of z. Moreover, it implies that the modelled intensities are not affected by the concentration profile of the Raman scatterer. If this would be the case, summation over $I(z)$ for a number of modelled points can be implemented.

The constant relative intensities in z as computed for radiation into zone I are not seen for modelled radiation into zones II and III. Scattering into zone II originates from

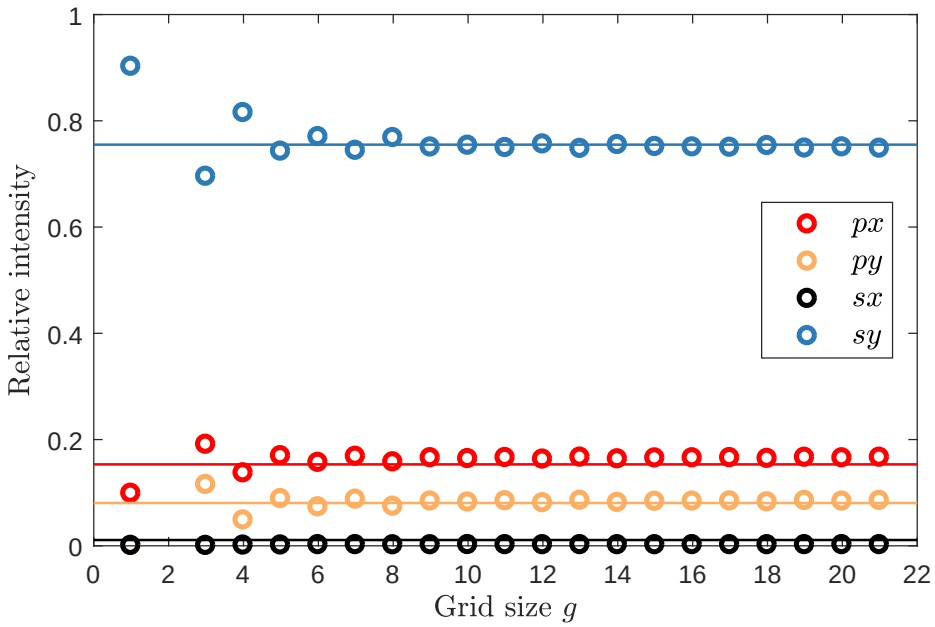

Figure 6.7: Relative modelled (markers) and experimental (lines) intensities for polarised Raman scattering of the sulfate v_1 band as a function of the modelling grid size parameter g. The experimental intensities are derived from the top-right spectra in figure 6.5 and the model input follows the experimental parameters.

the evanescent near-field of the dipole, which depends on the vectorial dipole moment and decays exponentially with z. The scattered intensities thus depend on a double exponential with different decays rates: one for the evanescent incident field and one for the evanescent dipole radiation field. The relative intensities change monotonically and stabilise from $z \approx \lambda_{0,\mathsf{scat}}$. Note that the order of intensities is $I_{py} > I_{sy} > I_{px} > I_{sx}$, different from that in zone I. The depolarised components of the dipole moment couple more strongly into the hemisphere in zone II than in zone I and therefore lead to enhanced intensities I_{py} and I_{sx}.

For scattering into zone III, *i.e.* observing the interface through medium 3, the double-exponential nature of the $I(z)$ curves is more pronounced. Interference in the $\mathbf{F}_{1\to3}$ terms gives rise to an oscillatory z-dependence of the relative intensities with a periodicity determined by both incident and scattered wavelengths. The order of the intensities for zone III is the same as for zone I: $I_{sy} > I_{px} > I_{py} > I_{sx}$. In both zones I and III, the radiation field arises from a propagative dipole field.

Incident linear polarisation angle

Figure 6.9 presents the intensities obtained by modelling the experiment with varying incident polarisation angle ψ ranging from 0° (p-polarised) to 90° (s-polarised). Relative intensities are presented, *i.e.* $I_x + I_y = 1$ at each ψ. The relative intensities derived from the Raman spectra of figure 6.2 are closely followed by the model.

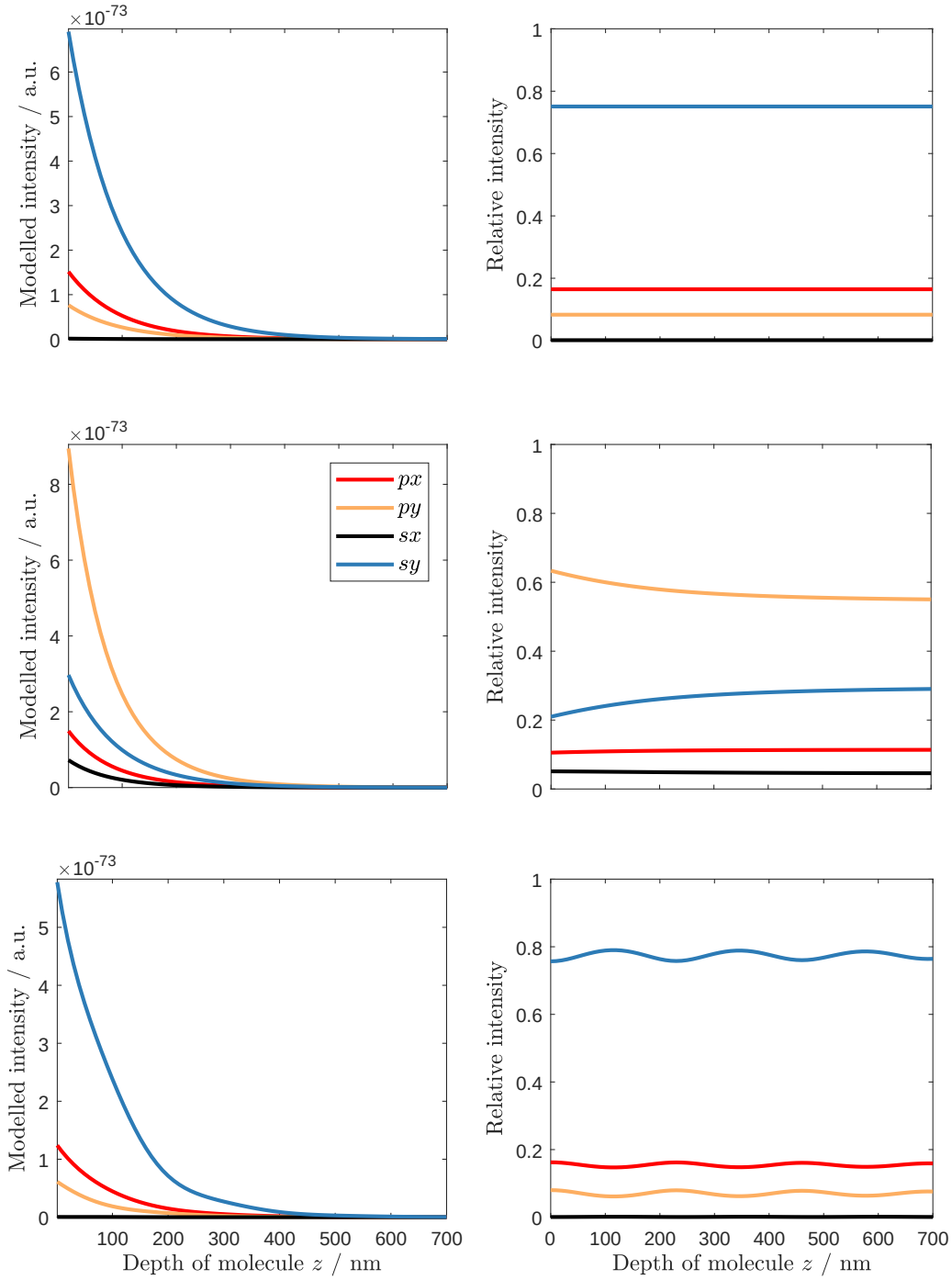

Figure 6.8: Absolute (left) and relative (right) intensities modelled for Raman scattering of the sulfate v_1 band near a fused silica surface as a function of the distance z of the scattering molecule from the interface. The objective of NA = 0.55 is tilted at $\beta_O = 180°$ (top) to collect radiation into zone I, at $\beta_O = 130°$ (centre) for zone II and at $\beta_O = 0°$ (bottom) for zone III. The laser is incident at $\theta_{k,i} = 73°$, above the critical angle.

The model predicts that $I_x = I_y$ at $\psi = 18°$. This cross-over point depends on the laser angle of incidence: it decreases from $\psi = 45°$ at $\theta_{k,i} = 0°$ and 180° to $\psi = 0°$ at $\theta_{k,i} = \theta_c$. This holds for radiation into zone I (modelled here) as well as for zone III. For scattered light into zone II, the cross-over point is at $\psi \approx 64°$ for $\theta_{k,i} = 0°, 180°$ while the condition $I_x = I_y$ is not met for any $0° \leq \psi \leq 90°$ at a range of incident angles from roughly $\theta_{k,i} = 42°$ to 133° in the system modelled here.

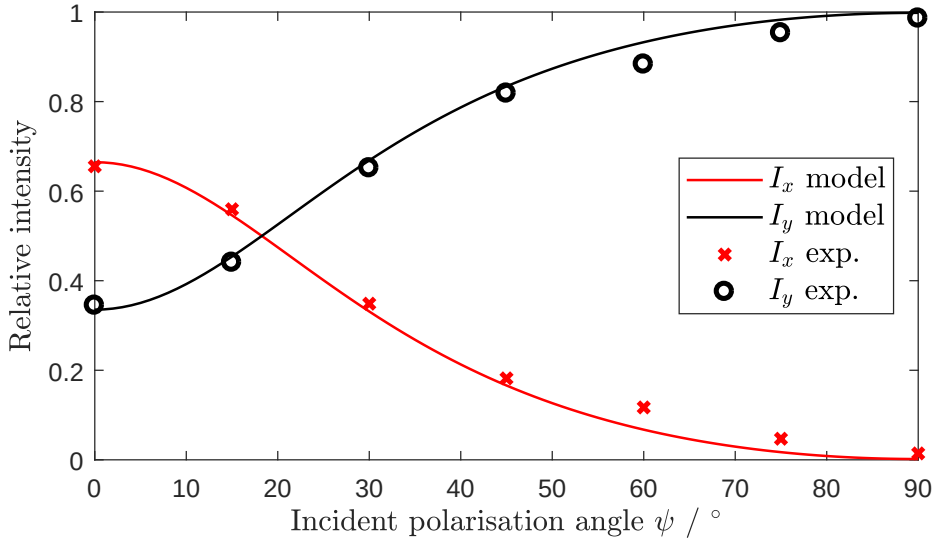

Figure 6.9: Modelled and experimental relative intensities for polarised Raman scattering of the v_1 band from a 0.3 mol L^{-1} sulfate solution at a fused silica surface as a function of ψ, the incident linear polarisation angle at $\theta_{k,i} = 75°$.

Angle of laser incidence

The experimental data collected with the Stockholm Raman system at various angles of incidence is now modelled. Using NA = 0.55, $\theta_{k,i}$ was varied in its full range from 0° to 180°. The results are presented as absolute intensities for the four polarisation combinations in figure 6.10. At $\theta_{k,i} = 0°$ and 90°, the px and sy intensities are equal. The order of the intensities is $I_{sy} > I_{px} > I_{py} > I_{sx}$ for all other values of $\theta_{k,i}$. The intensity for the sx polarisation combination is negligible over the full range in the current depolarised geometry. Practically no Raman scattering of the polarised v_1 band is collected. The py geometry is only fully depolarised at normal incidence, hence $I_{py}(0°) = I_{py}(180°) = 0$. At other angles, the $z^{\perp}$ component of the applied field induces a dipole moment along that axis. Though radiation from this component is zero along this direction (into the centre of the objective in this geometry), its radiation also reaches the perimeter of the objective field of view and contributes to the detected I_{py} intensity. As $\theta_{k,i}$ increases from 0°, p-polarised incident radiation induces an increasingly stronger dipole moment along $z^{\perp}$ at the coast of its $x^{\perp}$ component. I_{px} reduces and I_{py} increases up to the critical angle, where these are equal: $I_{px}(\theta_c) = I_{py}(\theta_c)$. With $\theta_{k,i} > 90°$, *i.e.* the laser beam is incident

through the optically rarer medium, these intensities do not equalise at all and $I_{px} > I_{py}$. The maximum intensity for the *py* and *sy* polarisation combinations is obtained at the critical angle and the range just beyond this value. All intensities reduce to zero at grazing incidence, *i.e.* at $\theta_{k,i} = 90°$.

So far, the propagation angle of the laser $\theta_{k,i}$ has been treated as an infinitely precise quantity. The modelling results so far fit the experimental data well with this assumption. In practice, the laser produces a beam with a Gaussian intensity distribution which is expanded in a telescope before being focussed onto the interface. The incident light is more accurately described as a cone of light around a central $\theta_{k,i}$ value with an angular Gaussian intensity profile. This can be implemented in our model by running the calculation for a range of $\theta_{k,i}$ and α_{O} around their respective central values and weighting the obtained intensities according to the Gaussian distribution of the incident laser intensity at the particular combination of $\theta_{k,i}$ and α_{O} used with each run of the model. Working from equation 3.2, the incident intensity distribution may be given as a weighting factor G of a two-dimensional Gaussian function scaled to unity

$$G(\Delta\theta_i, \Delta\alpha_{\mathsf{O}}) = e^{\frac{-2\tan^2\sqrt{\Delta\theta_i{}^2+\Delta\alpha_{\mathsf{O}}{}^2}}{\tan^2\theta_w}} \tag{6.1}$$

where $\Delta\theta_i$ and $\Delta\alpha_{\mathsf{O}}$ the deviation from their central values with θ_i specified through $\theta_{k,i}$ as in table 5.1. θ_w is the conical half-angle of the focussed beam computed geometrically through

$$\theta_w = \arctan\left(\frac{w}{f}\right) \tag{6.2}$$

with w the waist radius of the laser beam (measured in the experiment or taken as a modelling parameter) and f the focal distance of the lens (L_3 in figure 3.2) that focusses the laser beam onto the sample.

The variation in $\theta_{k,i}$ represents the spread of the laser beam in the plane of incidence and α_{O} the angular spread along the y^{L} direction. Considered in isolation, the effect of $\theta_{k,i}$ on the modelled intensities was presented in figure 6.10 for the four standard polarisation combinations with $\alpha_{\mathsf{O}} = 0°$. The dependence of these intensities on α_{O} is given in figure 6.11 for the same experimental geometry with $\theta_{k,i} = 75°$. As α_{O} increases from 0° to 45°, the strong polarisation combinations *px* and *sy* decrease in intensity while the weak polarisation combinations *py* and *sx* increase until $I_{px} = I_{py}$ and $I_{px} = I_{py}$ at $\alpha_{\mathsf{O}} = 45°$. Here, the dipole field at the objective projects equally onto its x^{O} and y^{O} axes. As α_{O} increases further, the intensities swap over until the y^{O} axis runs parallel to the x^{L} axis at $\alpha_{\mathsf{O}} = 90°$. The *sy* intensity now represents depolarised Raman scattering, while it refers to fully polarised scattering at $\alpha_{\mathsf{O}} = 0°$.

We now quantify the effect of the beam waist w on the relative scattering intensities for the four standard polarisation combinations, using the experimental conditions of the Stockholm data (table 6.2). The relative intensities computed with NA = 0.55 as a function of $\theta_{k,i}$ and α_{O} are presented as false-colour intensity maps in figure 6.12. A strong

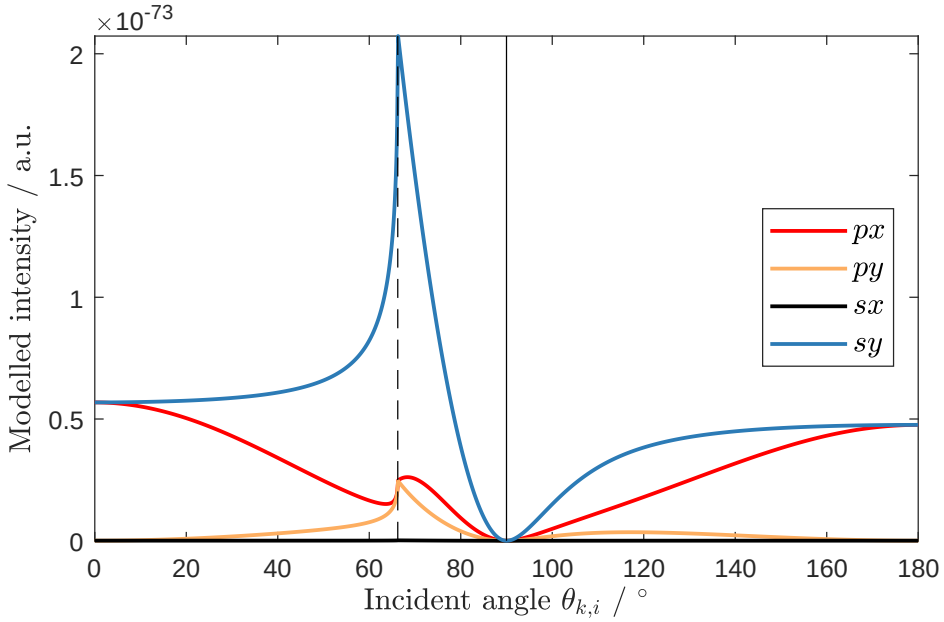

Figure 6.10: Modelled intensities for polarised Raman scattering of the v_1 band from a 0.3 mol L^{-1} sulfate solution at a fused silica surface as a function of $\theta_{k,i}$, the laser incident angle. The critical angle is indicated with a dashed and the interface with a solid vertical line. The scattered light is collected normal to the interface through the hemisphere with an objective of NA = 0.55.

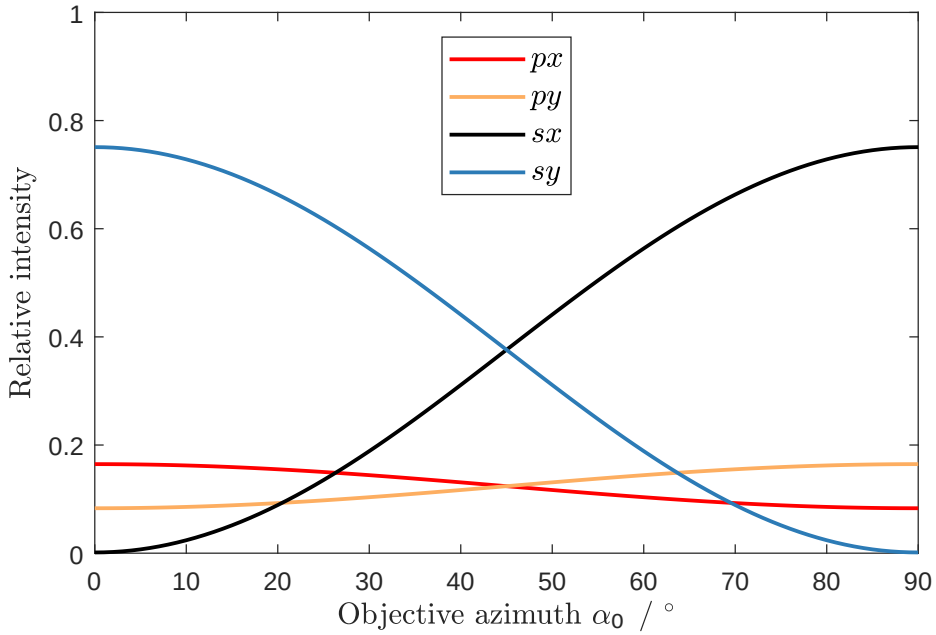

Figure 6.11: Modelled relative intensities for polarised Raman scattering of the v_1 band from a 0.3 mol L^{-1} sulfate solution at a fused silica surface as a function of α_O, the azimuthal orientation of the microscope objective, at $\theta_{k,i} = 75°$ and NA = 0.55. At $\alpha_O = 0°$, the x and y axes of the laser plane of incidence are (anti)parallel to the collection polarisation directions.

variation is seen around $\theta_{k,i} = 66.4°$, the critical angle, except in the *sx* plot. I_{sx} varies more strongly with α_{O} than with $\theta_{k,i}$, also apparent from figures 6.10 and 6.11. The intensities at each coordinate $(\theta_{k,i}, \alpha_{\mathsf{O}})$ are weighted with the two-dimensional Gaussian incident intensity distribution of equation 6.1 with the experimentally determined beam diameter $2w = 9$ mm. This distribution is plotted in figure 6.13. The Gaussian-weighted intensities $I(\theta_{k,i}, \alpha_{\mathsf{O}}) \times G(\Delta\theta_i, \Delta\alpha_{\mathsf{O}})$ are then summed and scaled to obtain relative total intensity values for each set of four polarisation combinations. These relative total intensities are presented in the left-hand plot of figure 6.14 as a deviation from the intensities as function of w from the intensity computed at $w = 0$.

On the basis of this analysis, no summation over the beam shape appears necessary for this experimental geometry as the deviation in the relative intensities at the experimental beam width from those at $w = 0$ is less than 0.5%. This is insignificant compared to the precision of the experimental variables. The assumption of no spread in the angle of incidence is appropriate for this dataset.

A comparison of modelled to experimental relative intensities is given in the left-hand plot of figure 6.15 (NA = 0.55) and shows agreement between the two within ± 0.009, the standard deviation on the relative intensity scale. The mean of the deviations between experiment and model is zero because the sum of the four intensities is set to unity at each set of experimental or modelling parameters. A deviation in one of the intensities is thus compensated by a shift in the opposite direction for the other relative intensities.

Numerical aperture

The final experiment with sulfate in Stockholm involved the exchange of the microscope objective, from NA = 0.55 to NA = 0.28, reducing the magnification from 50× to 10×. The field of view is narrowed and the working distance is increased, factors that decrease the amount of scattered radiation collected in the objective. The depth of field increases, meaning that the a thicker slab of the interface is in focus of the low-NA objective. More material contributes to the detected Raman scattering, with increased intensity levels from the bulk material located further away from the interface. A lower numerical aperture is thus expected to provide worse data for interface-selective measurements. These objections are mitigated by the fact that the laser spot only illuminates a section of the total focal volume and that the scattered radiation passes through a slit before reaching the detector. This produces a quasi-confocal arrangement. Comparing the spectra in figure 6.5, we note that the intensity from the silica-water background is less reduced than the sulfate band at NA = 0.28 compared to NA = 0.55. The v_1 band can hardly be discerned, except in the *sy* spectra. A larger NA is clearly advantageous.

Modelling results for NA = 0.28 demonstrate the following. First, the intensities vary slightly stronger with the laser beam diameter (right-hand plot of figure 6.14) than for an objective with NA = 0.55, though this remains insignificant. The stronger variation with beam waist arises from the second observation, namely that the intensities vary stronger

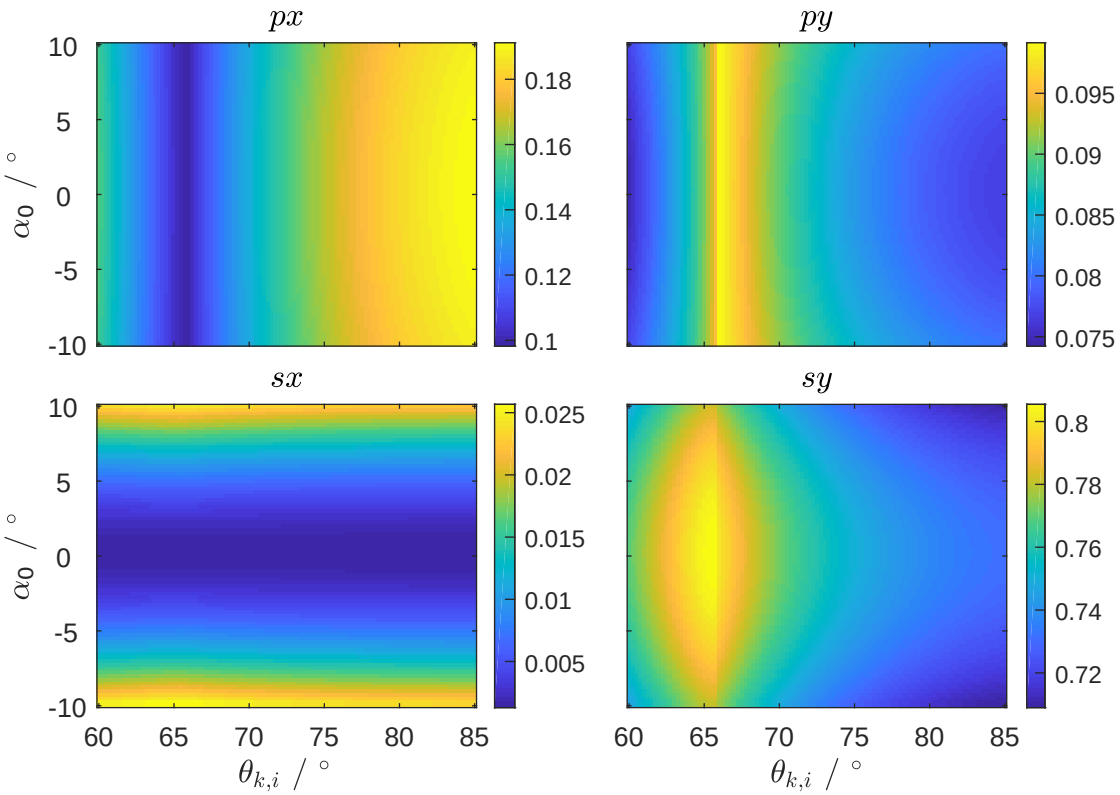

Figure 6.12: Modelled relative intensities for polarised Raman scattering of the v_1 band from a 0.3 mol L^{-1} sulfate solution at a fused silica surface as a function of α_O, the azimuthal orientation of the microscope objective, and the angle of laser incidence $\theta_{k,i}$ with NA = 0.55. The sum of the four linearly-polarised intensities at each coordinate $(\theta_{k,i}, \alpha_O)$ is scaled to 1.

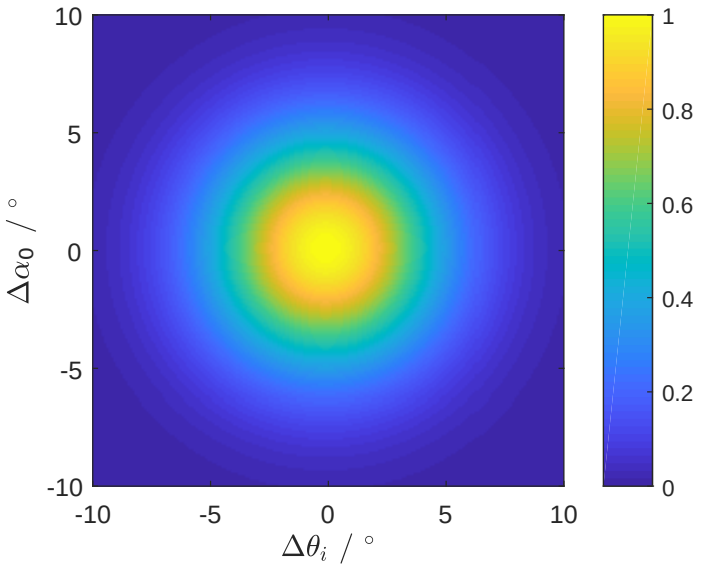

Figure 6.13: Distribution of intensity in a Gaussian beam of 9 mm diameter in the angular coordinates $(\theta_{k,i}, \alpha_O)$ that specify its incident propagation direction relative to the plane of incidence and collection polarisation direction.

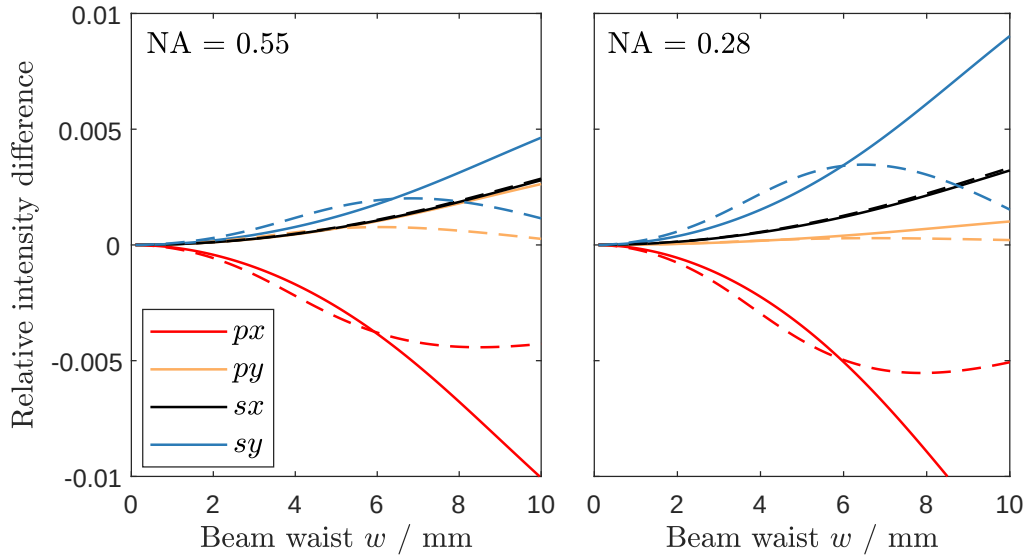

Figure 6.14: Deviation in the relative Raman intensities as a function of the waist of the incident laser beam w for $\theta_{k,i} = 75°$ (solid lines) and $\theta_{k,i} = 70°$ (dashed lines) for the two objectives employed in the Stockholm experiments. This model describes the ν_1 band of a 0.3 mol L^{-1} sulfate solution at a fused silica surface with the microscope objective at $(\alpha_O, \beta_O, \gamma_O) = (0°, 180°, 0°)$.

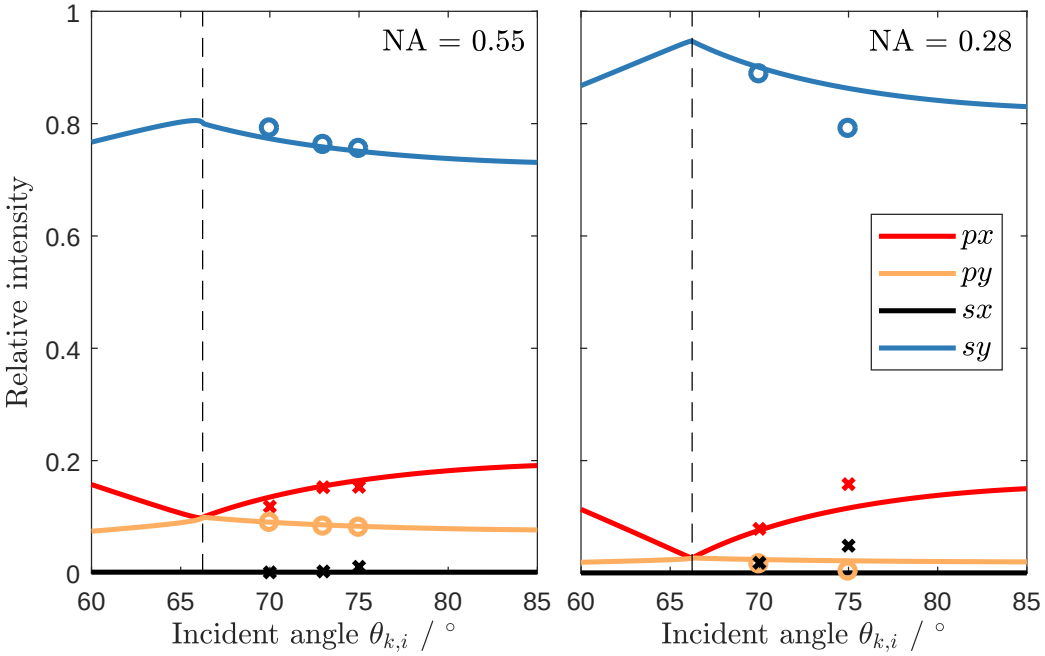

Figure 6.15: Modelled (lines) and experimental (markers) relative intensities for polarised Raman scattering of the ν_1 band from a 0.3 mol L^{-1} sulfate solution at a fused silica surface as a function of $\theta_{k,i}$, the laser incident angle, and the numerical aperture (NA) of the objective lens. The critical angle is indicated with a dashed line.

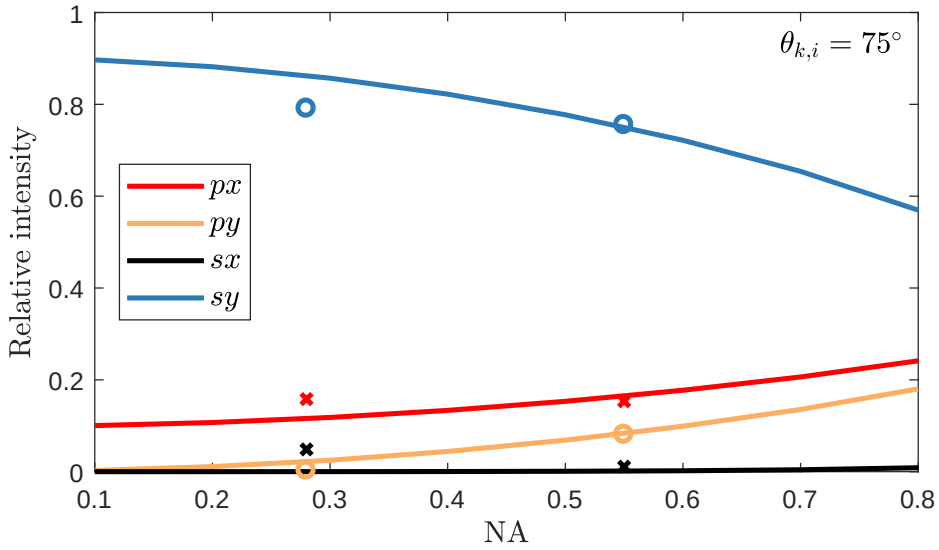

Figure 6.16: Modelled (lines) and experimental (markers) relative intensities for polarised Raman scattering of the v_1 band from a 0.3 mol L^{-1} sulfate solution at a fused silica surface as a function of the numerical aperture (NA).

with laser propagation angle $\theta_{k,i}$. The low-NA objective is more sensitive to angle of incidence. Modelling and experimental data are shown in the right-hand plot of figure 6.15. The deviation between model and experiment with the low-NA objective (NA = 0.28) is ± 0.04, larger than the deviation for the data collected with NA = 0.55, presented in the previous paragraph. Reasons for this are discussed below. Third, the relative intensities, in the present geometry, depend on the NA as given in figure 6.16. As the NA increases, more depolarised Raman scattering falls within the field of view and contributes to the detected intensities. The relative intensities of the *py* of *sx* polarisation combinations therefore increase with NA. I_{px} also increases with NA as the z^{L} component of the induced dipole contributes more near the edge of the objective field of view than at its centre. The inverse is true for I_{sy}, which decreases with angular position from the objective axis. Note that these arguments apply to the present case because the experimental geometry involves illumination under a non-zero angle and collection of Raman scattering normal to the interface.

Refractive index of the sulfate solution

Raman spectra were collected from ammonium sulfate solutions at three concentrations: 0.3 mol L^{-1} with the Stockholm system and 40 wt% as well as 18 wt% with the Durham system, all at $\theta_{k,i} = 73°$ and with an objective of NA = 0.55 positioned at $(\alpha_{\mathsf{O}}, \beta_{\mathsf{O}}, \gamma_{\mathsf{O}}) = (0°, 180°, 0°)$. This effectively changed the refractive index of the lower medium n_3 while keeping the experimental geometry constant. The data also allows for a comparison be-

tween the two Raman systems.†

The modelling results with varying n_3 are presented in figure 6.17 on an absolute and relative intensity scale. The experimental intensities are plotted with the latter. The curves are reminiscent of figure 6.10 with a clear maximum at a critical refractive index, rather than at a critical angle. The critical refractive index is the value of n_3 at which the angle of incidence is equal to the critical angle, in this case $\theta_c = \arcsin(n_3/1.4607) = 73°$. At $n_3 = 1$, $\theta_{k,i}$ is far from the critical angle for this interface and the Fresnel amplitude coefficients for the transmitted light are low. As the refractive index of the lower medium increases, $\theta_{k,i}$ approaches the critical angle. The applied field near the interface increases until the critical refractive index is reached and drops off quickly beyond this value.

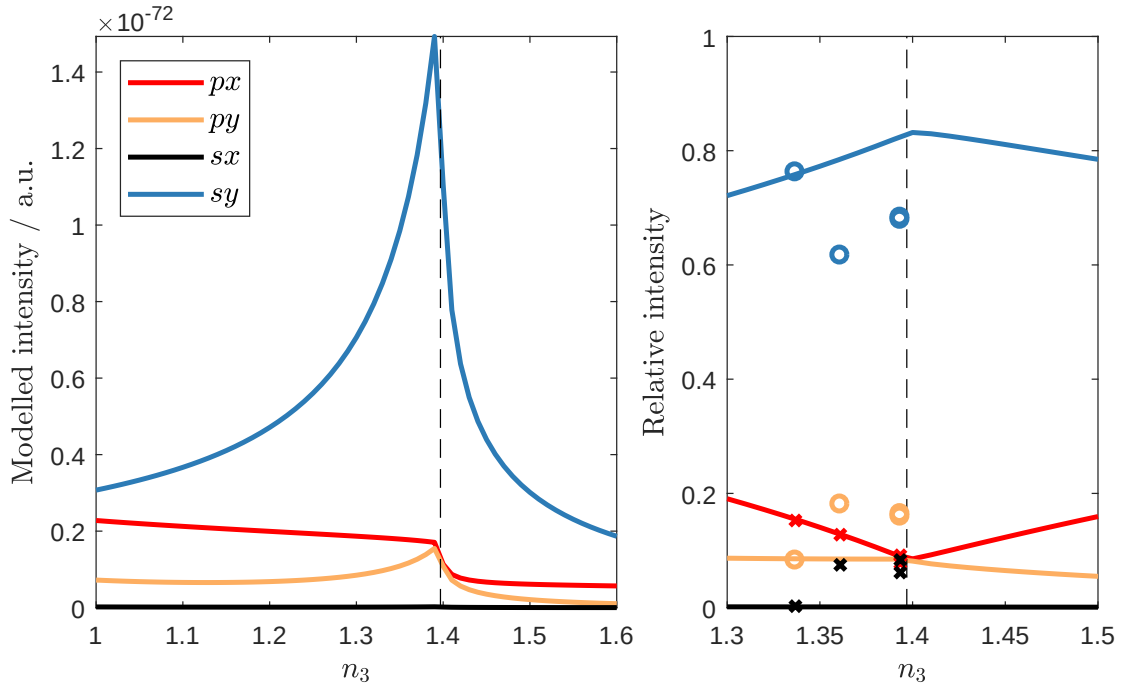

Figure 6.17: Modelled absolute (left) and relative (right) intensities for polarised Raman scattering of the v_1 band from sulfate solutions at various concentrations at a fused silica surface for $\theta_{k,i} = 73°$. The refractive index of the solution (n_3) varies with concentration. For $n_3 = 1.397$ (dashed line), $\theta_{k,i} = \theta_c$. The experimental relative intensities are indicated with markers.

The relative intensities of the spectra collected with the Stockholm system (at $n_3 = 1.3368$) are closely met by the model, whereas the Durham data (at $n_3 = 1.3610$ and $n_3 = 1.3934$) clearly differ from our modelling results. In the latter data sets, the relative intensities in the (partly) depolarised *py* and *sx* spectra are higher than the model calculation at the expense of the relative intensity of the polarised *sy* spectrum. The relative intensity in the *px* spectrum appears unaffected, probably fortuitous. Likely causes for this aberration are discussed in the next section. The relative intensities for datasets B

†A small shift of the v_1 band is known to occur as a function of concentration [128]. However, this is irrelevant in our current discussion.

and C are similar, as anticipated. Crystallisation of the sulfate salt at the silica surface merely enhances the Raman signal.

6.2.4 Discussion

Agreement between model and experiment

Our analysis of the Stockholm data collected with the NA = 0.55 objective demonstrates agreement between the relative intensities obtained from experiment and those computed with our model. This indicates that the optical description of the scattering process in our model is essentially correct. This experimental data has thus validated the `pirs` function for isotropic Raman tensors in a spherical molecular ellipsoid to an accuracy of about 1% in the relative intensity values I_{px}, I_{py}, I_{sx} and I_{sy}.

The effect of the variation of experimental parameters was predicted and proven to be correct for at least the range probed in the experiments. Collection of scattering was limited to zone I, where the relative intensities are independent of z, the distance of the scattering molecule from the interface. Illumination was limited to zone II with $\theta_{k,i} = 70°$, 73° and 75°, incident angles just above the critical angle. The relative intensities were in the order $I_{sy} > I_{px} > I_{py} > I_{sx}$ for the whole dataset. This order as well as the variation of the intensities with the experimental geometry is explained by the coupling factors for the incident and radiated fields. These in turn depend on polarisation directions, propagation angles and refractive indices. The effect of the angular spread in the incident laser beam proved insignificant, whereas the numerical aperture of the objective strongly affects the relative intensities. With the objective positioned above the hemisphere, normal to the interface, a larger NA collects increased amounts of depolarised scattering. This also depends strongly on the angle of laser incidence with a maximum at the critical angle. The order of the intensities is understood from this effect. The intensities depend on $\theta_{k,i}$ and n_3 in a very similar way because both refer to the angle of incidence relative to the critical angle for the interface. The variables ψ and α_{O} also have a similar effect on the relative intensities as both affect the relative orientation of the plane of incident polarisation with respect to the plane of collection polarisation. These observations are general for isotropic Raman tensors. The relative intensities carry no information on molecular orientation, as this is intrinsically absent with an isotropic Raman tensor.

These insights may be useful in the design of experiments to optimise the amount of Raman scattering. In general, maximum Raman scattering is observed for the *sy* polarisation combination, illumination of the sample at an angle as close as possible to the critical angle (informed by the desired sampling depth), collection of scattered light around the critical angle on the hemisphere side of the interface, using a large aperture and by adjusting the refractive indices of the media and the laser wavelength where possible. The geometrical arrangement of positioning both the laser and the objective near the critical angle has not been employed so far. It requires positioning of the objective out of the path of the reflected laser beam to prevent damage to optical components of the spectrometer.

This geometry can be achieved by rotating the sample over the x^{L} axis, for instance.

The model may also be employed to improve the assignment of intensities to Raman bands. An example is this is the fit of the experimental $I_x(\psi)$ and $I_y(\psi)$ to the modelled data in figure 6.9. The modelled intensity curves may be used as a reference to optimise the fit with the experimental intensities by adjusting the spectral windows used to fit the background and integrate the v_1 Raman band intensity. However, this process should not be driven to an extreme. The residual intensities should reflect the noise level fluctuating around zero and the Raman bands should not be distorted. Both scaled absolute intensities as well as relative intensities may be used for this, though the latter require two measurements at each ψ (as employed here). Scanning the incident polarisation and recording either the $I_x(\psi)$ or $I_y(\psi)$ Raman spectrum would then provide a sufficient dataset to assign the fully polarised Raman bands and determine their intensities. The obtained peak specifications may then be employed with the analysis of other spectra without further optimisation. This process was used here and reduces the risk of tuning the modelling or fitting parameters beyond the reasonable to obtain a satisfactory fit.

Deviations of modelled from experimental intensities

We have also presented data that does not agree well with the model calculations. These are the experimental results from Stockholm obtained with the NA = 0.28 objective and the results from the Durham system. Assuming that the model is essentially correct, we will now use it to evaluate potential sources of experimental error.

For the Stockholm data with NA = 0.28 (figure 6.15), the observed deviation is an increased I_{sx} compared to the model prediction. This appears hardly significant at $\theta_{k,i} = 70°$ but it is clearly not matching the modelled relative intensities at $\theta_{k,i} = 75°$, where I_{px} is higher while I_{py} and I_{sy} are lower than their modelled values. The intensity order is changed as $I_{py} > I_{sx}$ rather than the other way round as predicted for this geometry.

Looking at the raw spectra in figure 6.5, we note that the sulfate bands are weak on a strong background, especially at the higher angle of incidence. The py and sx spectra are practically superimposed. The variation in the obtained v_1 band intensities in these spectra is a reflection of the uncertainty in the spectra. As the intensities are lower overall, the relative noise level is higher for this dataset. The v_1 band intensity in the sy spectra is 6 and 8 times lower in the NA = 0.28 spectra compared to those collected with NA = 0.55 at the same angles of incidence. The standard deviation of the difference between modelled and experimental intensities is correspondingly higher, indicating that at least part of the discrepancy is due to the uncertainties in the background-subtracted spectrum.

The deviation might also arise from use of a different objective lens in a system aligned and calibrated for another. None of the objective lenses used in this study were manufactured specifically for use in polarised microscopy. Such objectives (marked P, PO or Pol) are produced without strain in the optical glass components that could introduce birefringence and with cement layers that transmit all radiation without altering its plane

of polarisation. The employed objectives do not strictly meet this standard. Calibration of the collection polarisation directions should therefore be performed for each objective lens separately, unless these are of the quality used in polarised microscopy. However, any defects in the NA = 0.55 objective do not significantly effect our model interpretation of the detected intensities. This is likely the same with the NA = 0.28 objective of the same supplier and standard.

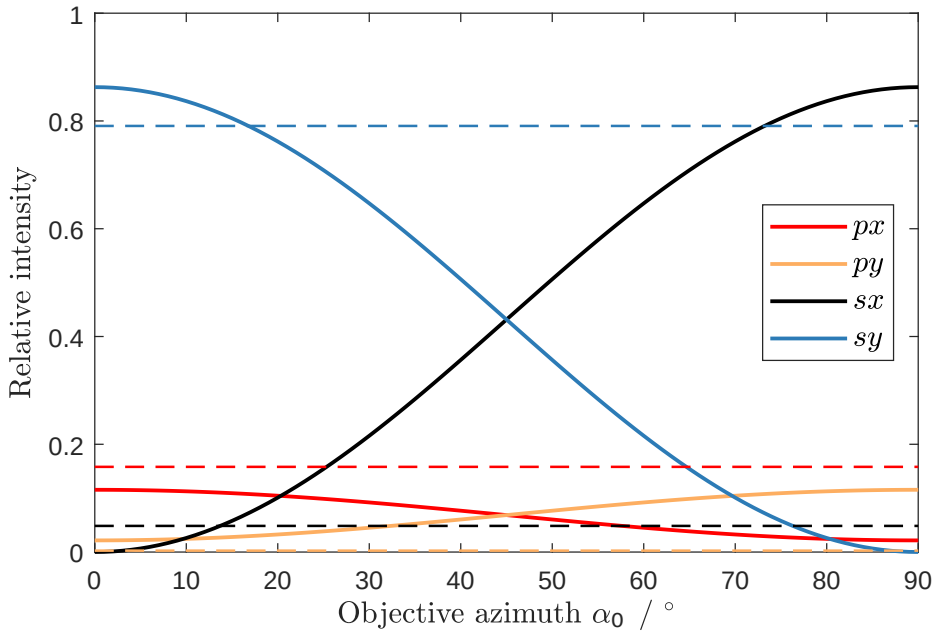

Figure 6.18: Modelled (solid line) and experimental (dashed line) relative intensities for polarised Raman scattering of the v_1 band from a 0.3 mol L^{-1} sulfate solution at a fused silica surface as a function of α_O, the azimuthal orientation of the microscope objective, at $\theta_{k,i} = 75°$ and NA = 0.28. At $\alpha_O = 0°$, the x and y axes of the laser plane of incidence are parallel to the collection polarisation directions.

We use our model to investigate this deviation further. Figure 6.18 presents relative intensities computed for the four standard polarisation combinations as a function of α_O, the off-set between L-frame and O-frame that could account for an error in the calibration of the collection polarisation. The curves are steeper than those for NA = 0.55 (figure 6.11). The order of the experimental intensities, $I_{sy} > I_{px} > I_{sx} > I_{py}$, is predicted for α_O between about 10° and 20°. However, the model does not match the experimental relative intensities at any point. We may therefore conclude that the experimental errors in the measured intensities are too large to be explained purely by an error in polarisation directions. A new calibration of the collection polarisation direction for this objective would not substantially increase the accuracy of the experiment. Errors introduced by the low signal and background subtraction appear to limit the interpretation of this data.

The experimental error could be quantified further at $\alpha_O = 45°$, collecting a number of spectra and assessing the statistical variation in the similarity of $I_{px} \approx I_{py}$ and $I_{sx} \approx I_{sy}$.

In a perfect objective, these are expected to be equal pairwise and with the same settings for the incident and collection polarisers. A bias in any of these pairs indicates an undesired polarisation sensitivity along x^{O} or y^{O} in the objective.

We now turn to the disagreement between the modelled intensities and the data collected with the Durham Raman system. The intensities were given in the right-hand plot of figure 6.17, at $n_3 = 1.3610$ and 1.3934 for the 18 and 40 wt% solution, respectively. The experimental relative intensity I_{sy} is lower than the model expectation while I_{py} and I_{sx} are higher. The latter in particular is striking, as it is expected at near-zero intensity. However, in the sx spectra collected with the Durham system (the black spectra in figure 6.6), the v_1 band appears as a rather distinct feature. The measured I_{sx} is therefore not likely to be a result of uncertainty introduced by the background subtraction.

What experimental factors could contribute to such high depolarised intensities? We can draw from our analysis so far to suggest causes. An error in the refractive index of the solution is unlikely to effect the observed difference. The order of the intensities is predicted to be $I_{sy} > I_{px} > I_{py} > I_{sx}$ with $I_{sx} \approx 0$ in the relevant range of n_3 (figure 6.17) but it is measured as $I_{sy} > I_{py} > I_{px} > I_{sx} \neq 0$. An inaccuracy in the laser propagation angle $\theta_{k,i}$ would also change the relative intensities (in a way very similar to figure 6.10), but not their order. The finite beam waist causes an angular spread of incident angles around the central propagation direction. Its effect on the relative intensities is negligible (see figure 6.19). This leaves the linear polarisation angle of the laser ψ and the angle α_{O} that specifies the collection polarisation direction $\hat{\mathbf{x}}^{\mathsf{O}}$ as an anticlockwise rotation from $\hat{\mathbf{x}}^{\mathsf{L}}$ about $\hat{\mathbf{z}}^{\mathsf{L}}$. These are determined by the half-wave plates and linear polarisers as well as any other unintentionally polarisation-sensitive components.

The effect of ψ and α_{O} on the relative intensities is now analysed. Figure 6.20 presents contour maps of $I_x/(I_x + I_y)$ as a function of ψ and α_{O} for both the 40 wt% and 18 wt% solution. The four standard polarisation combinations are related to incident polarisation angle ψ and collection polarisation direction angle α_{O} as

$$\begin{aligned} px &\rightarrow (\psi, \alpha_{\mathsf{O}}) = (0^\circ, 0^\circ) \\ py &\rightarrow (\psi, \alpha_{\mathsf{O}}) = (0^\circ, 90^\circ) \\ sx &\rightarrow (\psi, \alpha_{\mathsf{O}}) = (90^\circ, 0^\circ) \\ sy &\rightarrow (\psi, \alpha_{\mathsf{O}}) = (90^\circ, 90^\circ) \end{aligned} \tag{6.3}$$

which specify the four corners of the contour maps in figure 6.20. These maps are symmetric around the ψ and α_{O} axes and periodic in each so that these only require specification in the range $0^\circ \leq \psi, \alpha_{\mathsf{O}} \leq 90^\circ$. Its horizontal cross-section gives $I_x(\alpha_{\mathsf{O}})$, which is similar to the relative intensity curves in figure 6.18, while the vertical cross-section is $I_x(\psi)$ which behaves as in figure 6.9. The refractive index is higher in the present case with $\theta_{k,i}$ nearer the critical angle so that I_x at low ψ is near 0.5. This implies that $I_{px} \approx I_{py}$. The minimum of I_x is at $(\psi, \alpha_{\mathsf{O}}) = (90^\circ, 0^\circ)$ and its maximum at $(\psi, \alpha_{\mathsf{O}}) = (90^\circ, 90^\circ)$. These conform to the sx and sy polarisation combinations, respectively.

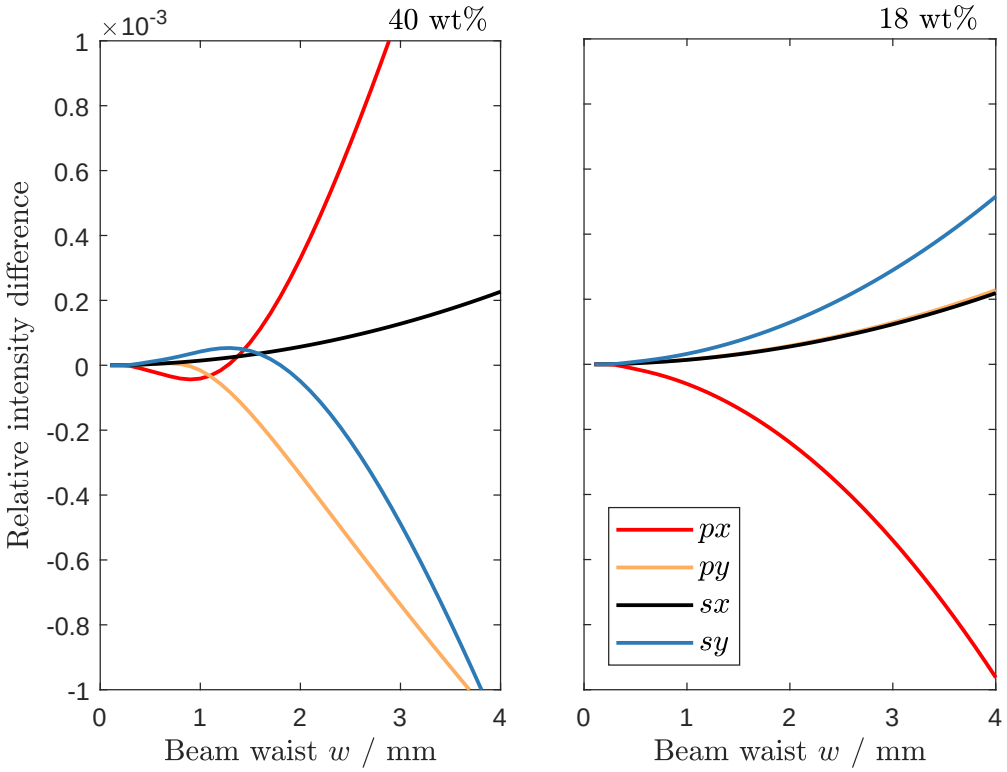

Figure 6.19: Deviation in the relative Raman intensities as a function of the waist of the incident laser beam w for $\theta_{k,i} = 73°$ for the two sulfate concentrations employed in the Durham experiments at a fused silica surface. The model describes the sulfate v_1 band intensity with the objective at $(\alpha_O, \beta_O, \gamma_O) = (0°, 180°, 0°)$.

Looking at the contour lines in figure 6.20, we note that the derivative with respect to the angles (ψ, α_O) is lowest at the four corners of the map. The impact of an experimental error in the calibration of the polarisation angles is thus minimal when using either of the four standard polarisation combinations. The standard polarisation combinations are the best choice following this argument. However, the uncertainty introduced with near-zero intensities reduces this advantage as seen with the Stockholm data discussed above. We further observe that the derivative of I_x with respect to ψ is zero at $\alpha_O = 45°$, but as $I_x = I_y$ in this case, any information on the orientation of the scattering molecule is lost.

The difference between the model prediction and the experimental relative intensities in this case centres on two discrepancies: $I_{sx} \neq 0$ and $I_{px} \neq I_{py}$. If the collection polarisation is not exactly along x^L, the high-intensity sy spectrum contributes to the low-intensity sx. These spectra may be said to mix. The px and py intensities also mix if α_O is off-set and are increasingly different for larger ψ. The cause of the discrepancy may thus lay in an off-set of the polarisation angles, which we will now derive.

The relative intensity from the px Raman spectra $I_{px}/(I_{px} + I_{py})$ is computed and plotted as a yellow contour line in the intensity maps of figure 6.20. On these lines, the relative modelled intensities match those obtained from the Raman spectra. The fit is

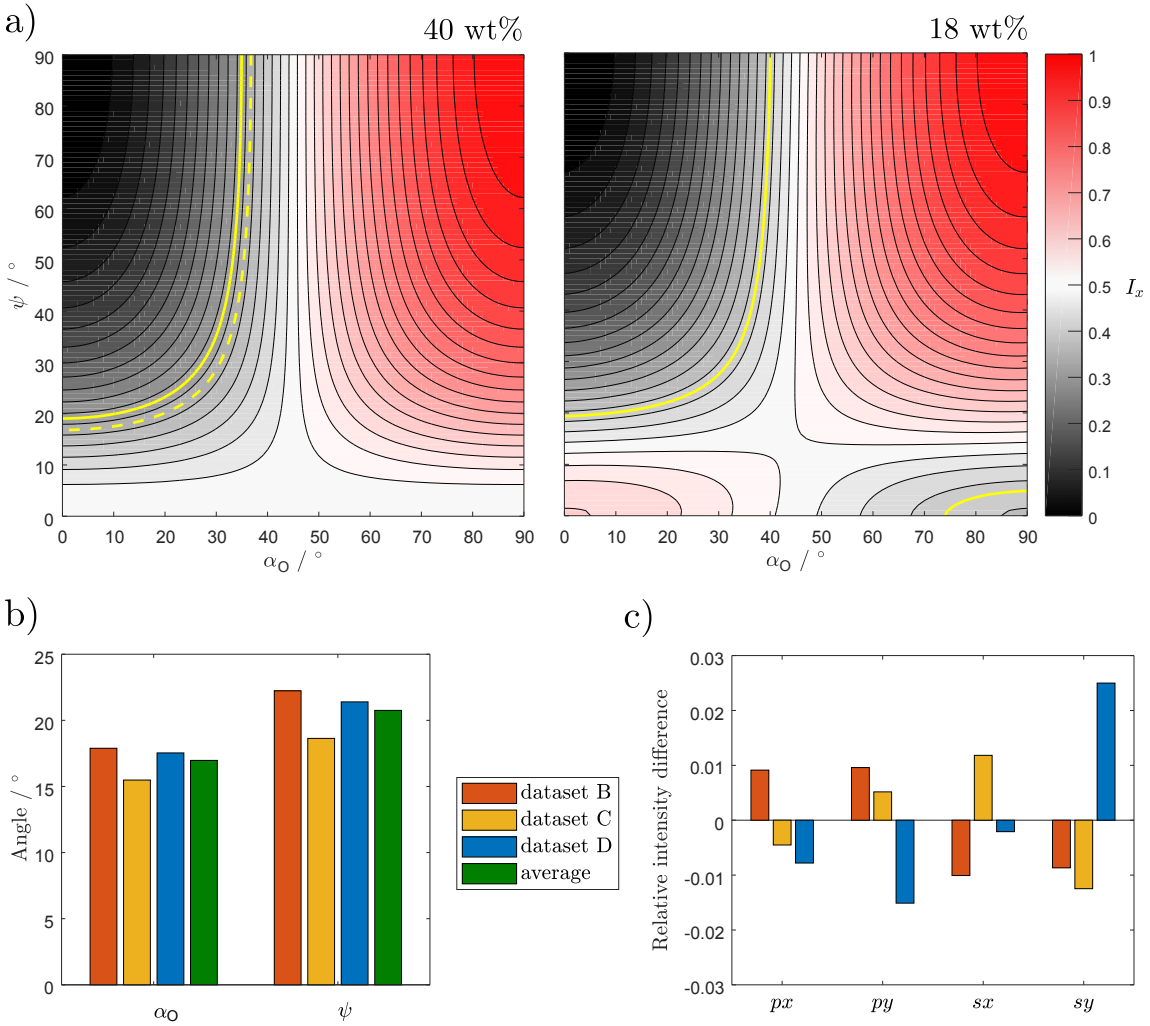

Figure 6.20: Analysis of polarisation off-set in the Durham Raman system analysed with scattering from the sulfate v_1 band. (a) Contour plots of the modelled relative I_x intensities for polarised Raman scattering as a function of α_O, the azimuthal orientation of the microscope objective, and ψ, the incident linear polarisation angle. The left-hand plot contains the experimental relative I_{px} for dataset B (solid yellow line) and dataset C (dashed yellow line), with dataset D in the right-hand plot. Diagram (b) presents angles (α_O, ψ) that fall on the yellow contour lines and provide the best fit with the relative experimental intensities. The obtained angles are similar and their averages are used to recompute scattering intensities, given in (c) as the difference between relative modelling and experimental intensities.

further optimised by computing $I_{sx}/(I_{sx} + I_{sy})$ for each $(\psi, \alpha_{\mathsf{O}})$ on the contour line. The best fit is found by equating the relative intensities from the experiment to the model I_x value. The deduced polarisation angles fall within a range of 3.6° (diagram (b) in figure 6.20), indicating that a systematic off-set is likely. Their average values are $\psi = 21°$ and $\alpha_{\mathsf{O}} = 17°$. The experimental intensities are best described by modelled intensities computed with these polarisation angles.

The average fitted values $(\psi, \alpha_{\mathsf{O}}) = (21°, 17°)$ are now used to recompute the relative intensities I_{px}, I_{py}, I_{sx} and I_{sy}. These are then compared to the experimental relative intensities. Their difference (modelled minus experimental) is shown in diagram (c) of figure 6.20. We find that the relative intensities differ less than 0.025 with a standard deviation of 0.012 (on the relative intensity scale from 0 to 1). The mismatch between model and experiment can thus be explained by an effective rotation of the polarisation plane. The remaining uncertainty of about 1% reflects that found for the Stockholm data with the NA = 0.55 objective and calibrated polarisation angles.

We may conclude from this analysis that though the experiment is not as perfect as the model assumes, it may still be modelled as such by adjusting input parameters that capture the same net effect. In this case, the off-set can be taken as an error in the angular position of the half-wave plates, for which the positioning is half the off-set in ψ or α_{O}, giving HW_1 at 10° and HW_2 at 8.5°, respectively. The rotation may also be caused by polarisation upon reflection from the mirrors in the optical system or polarisation sensitivity in the objective. Whatever the exact origin of the deviation, from a modelling point of view, these effects appear best incorporated as an off-set in the angular orientation of the polarisation planes.

The foregoing illustrates the use of the model to assess experimental imperfections. It may be used to analyse what factors could contribute to experimentally observed intensity variations. Working from a known molecular system and having validated the model for this system with a calibrated experimental setup, as is the case here, a correction may be applied to experimental results from another (less-well calibrated) experiment by adjusting model input parameters to account for the experimentally-induced intensity variation. However, care must be taken to avoid adjusting the model input to such extend that it results in fitting towards an experimental result without physical basis.

6.2.5 Conclusion

The isotropic Raman tensor of the sulfate v_1 mode was used to validate the optical description of our model. This mode is particularly useful because it comprises a fully symmetric Raman mode in a spherical molecule. Thus, averaging over molecular orientations and local field correction are irrelevant. Furthermore, it favourably lacks anharmonicities. Finally, the depth position of the sulfate molecule with respect to a silica surface is not expected to affect the relative intensities.

The model provides relative intensities for the four standard polarisation combinations

that agree with those obtained with the Stockholm Raman system, as long as the polarisation directions are calibrated for the specific objective being used. The agreement is characterised by a standard deviation of 0.01 on a scale from 0 to 1. A square grid of 15 nodes along each direction ensured convergence of the modelling result.

However, data collected by the Durham system differed. The difference can be explained by imperfections in the (settings of the) optical components. These are best modelled as an off-set in the polarisation directions. The effect of such an off-set can be seen as causing mixing of polarised with depolarised spectra, notably giving rise to clear non-zero intensities with the *sx* polarisation combination though this was predicted to be zero. This explanation illustrates use of the model to test experimental components or explain deviations that these might cause. Errors in background subtraction also contributed to the observed differences.

The dependence on incident polarisation direction closely followed the experimentally determined relative intensities. The same was the case for the incident angle, though a significant deviation again occurred with the objective for which the polarisation directions were not calibrated. According to model calculations, the spread in the angle of incidence does not significantly affect the Raman intensities.

Increasing the concentration of the sulfate anion in its aqueous solution results in an increased refractive index. This alters the critical angle of the studied interface. The effect on the scattering intensities is similar to that of a change in the angle of incidence.

A smaller numerical aperture enlarges the variation between the intensities, reducing especially those collected with *px* and *py* polarisation combinations. This presents an example of using the model to increase contrast between polarisation combinations or peaks in a spectrum.

The experiments and modelling of the v_1 Raman band of the sulfate anion presented in this section thus lead us to conclude that the optical description of our model is essentially correct. We now proceed to apply the model to increasingly complex systems to explore its limits.

6.3 Carbon tetrachloride on sapphire

The sapphire-CCl_4 interface was produced by mounting a sapphire hemisphere on the flow cell and filling it with liquid carbon tetrachloride. It was studied in the Durham Raman system. Sapphire was used with carbon tetrachloride as it has sharper peaks than fused silica in the low-shift spectral range where the CCl_4 bands appear. Moreover, the refractive index of CCl_4 is similar to that of fused silica but differs substantially from that of sapphire (see figure 3.7). This contrast has two advantages. First, the sapphire-CCl_4 interface is more readily observed in the microscope and can thus be positioned more accurately than the silica-CCl_4 interface. Second, the critical angle is lower so that the field near the interface is stronger for sapphire-CCl_4 than for silica-CCl_4 at the same angle of incidence, thus enhancing the Raman signal. However, sapphire is birefringent, which

may introduce errors in our analysis.

6.3.1 Experimental results

Raman spectra were recorded with the four standard polarisation combinations of the Durham system: px, py, sx and sy with the laser polarisation p or s set through HW_1 and the collection polarisation x or y set by introducing HW_2 into the beam path. Polarised spectra were recorded for both the sapphire-air interface background as well as the sapphire-CCl_4 interface signal. Subtracting the former from the latter provides the interfacial CCl_4 spectrum.

The laser was set to an output power of 200 mW and was incident through zone II at $\theta_{k,i} = 73°$. The critical angle is 34.5° for the sapphire-air interface and 55.9° for sapphire-CCl_4 at the laser wavelength and throughout the spectral range of interest. Scattering was collected in the NA = 0.55 objective positioned in its standard orientation orthogonal to the interface above the sapphire hemisphere with polarisation directions parallel to the plane of laser incidence. Spectra were acquired by accumulation of five spectra of 5 s each, centred at a Raman shift of 460 cm^{-1}.

Raman spectra

The recorded Raman spectra (figure 6.21) show partially overlapping features in the range 200-800 cm^{-1}. Five features can be attributed to sapphire. Due to its crystalline form, these bands are narrow and sensitive to polarisation. The CCl_4 modes arise from the various isotopologues of the molecule and are labelled according to the T_d point group symmetry (see section 4.4.2). The locations of these four CCl_4 bands are indicated in the sapphire-CCl_4 spectra. The sapphire band around 750 cm^{-1} obscures the v_3 mode of CCl_4 in all four polarisation combinations. The symmetric v_1 mode of CCl_4 appears as a shoulder to the sapphire band around 430 cm^{-1} while the v_4 and v_2 bands are fully resolved.

Peak intensities

Four polarised CCl_4 Raman spectra are obtained by subtracting each polarised sapphire-air spectrum from its sapphire-CCl_4 complement (see figure 6.22). A single background spectrum for all polarisation combinations is inappropriate here as the sapphire spectrum changes qualitatively with the employed polarisations. Furthermore, a match between background and signal is not expected because of variation in the critical angle and slight realignment after filling the flow cell with the toxic sample in a fume hood away from the Raman system. The background spectra can thus not be matched to the signal. Parts of the spectrum without any features are therefore used to scale the background relative to the signal, if needed.

The sapphire-air background intensities were multiplied by 0.75 for the py and sy spectra before subtraction to ensure that the residual baseline flattens out at zero intensity

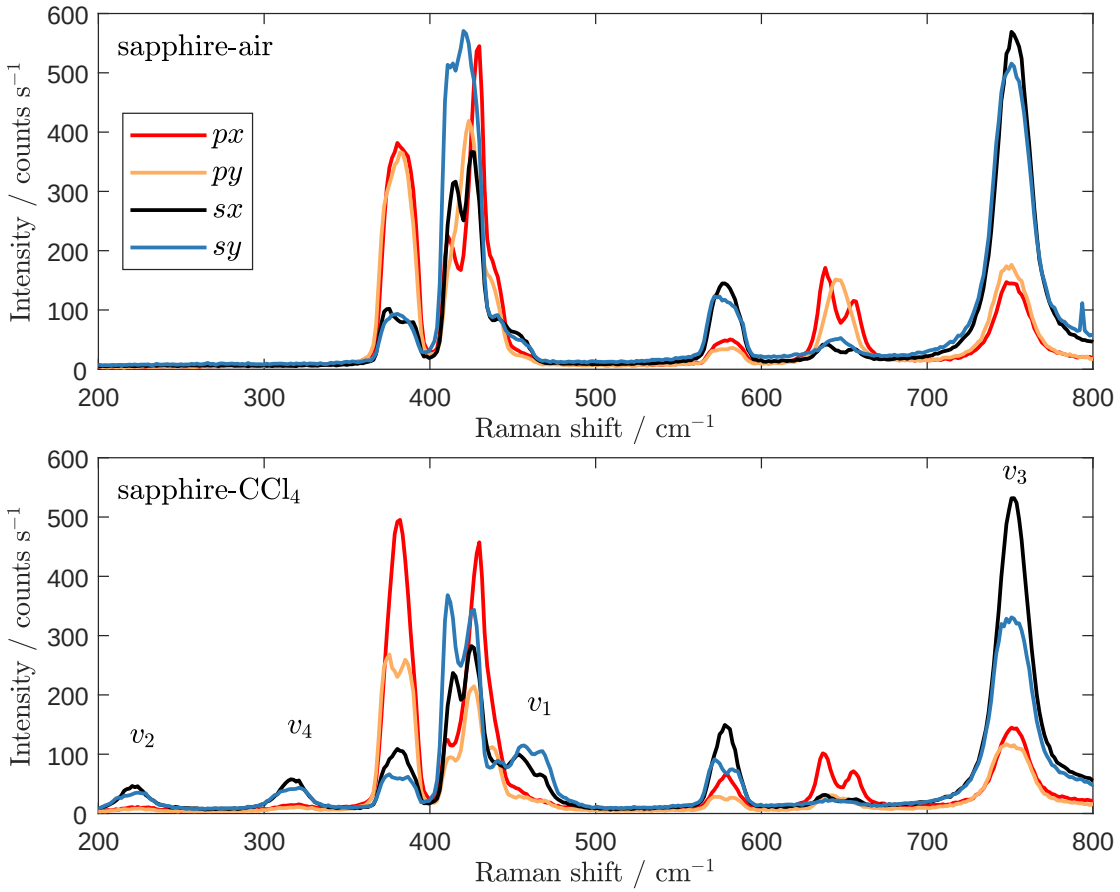

Figure 6.21: Raw Raman spectra of the sapphire-air and sapphire-CCl_4 interfaces for the four polarisation combinations collected with the Durham system. [data: 20150326/009,010,018,019]

near the CCl_4 features. For the *px* and *sx* spectra, no multiplication was needed. The intensities of the v_2, v_4 and v_1 modes of CCl_4 can then be obtained by numerical integration over each peak, *i.e.* summing the background-subtracted intensities over a specified spectral range. The integrated intensities obtained from the Raman spectra with *y* collection polarisation have been divided by 0.89 to correct for the transmittance of HW_2, which was added to the beam path for the *py* and *sy* spectra but absent with the *px* and *sx* spectra. Table 6.4 lists the spectral range and intensity obtained for each band. Though the integrated intensities are strictly in units of counts s^{-1} cm^{-1}, their relative values only are required for interpretation with our model.

6.3.2 Modelled band intensities

The carbon tetrachloride Raman spectra are used to evaluate the model description with computational Raman tensors in the harmonic approximation. The Raman tensors found for CCl_4 are not isotropic (see section 4.4.2) contrary to the v_1 mode of the sulfate anion treated in section 6.2. There, we concluded that the grid size parameter $g = 15$ ensures

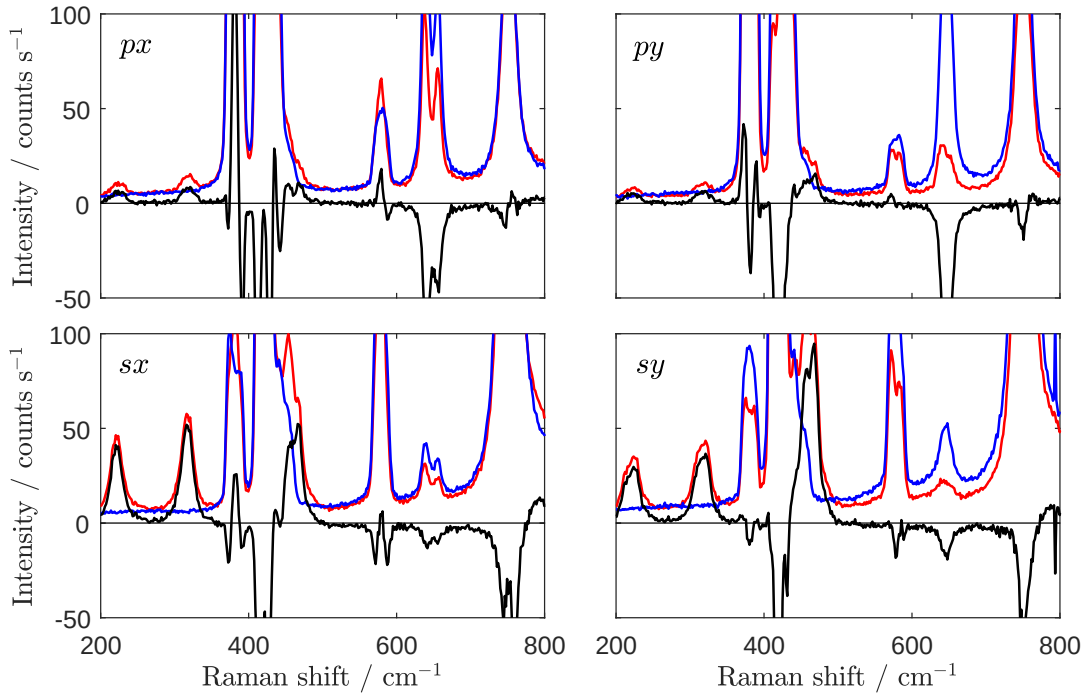

Figure 6.22: Each polarised CCl_4 spectrum (black) is obtained by subtracting the background sapphire-air spectrum (blue) from the sapphire-CCl_4 spectrum (red). For the *py* and *sy* polarisation combinations, the background is multiplied by 0.75 before subtraction to ensure a flat baseline around zero intensity.

Table 6.4: Experimental Raman intensities (in counts s^{-1} cm^{-1}) of the CCl_4 bands in the four polarisation combinations. Relative intensities are listed in red below corresponding absolute values. The v_3 band is obscured by the sapphire signal.

band	range / cm^{-1}	I_{px}	I_{py}	I_{sx}	I_{sy}
v_2	190—286	103.7	102.0	594.7	595.3
		0.0743	0.0730	0.4261	0.4266
v_4	286—346	123.6	111.2	719.9	691.4
		0.0751	0.0676	0.4373	0.4200
v_1	445—500	150.4	261.5	773.5	1685
		0.0524	0.0911	0.2695	0.5870

convergence of the modelling result, which was confirmed to be the case for the carbon tetrachloride intensities as well.

The scattered light is collected in zone I so that the relative intensities are expected to be independent of the distance z of the scatterer from the interface. We therefore set $z = 0$ to model the full depth of the probed layer of liquid carbon tetrachloride. Further, $\bar{\nu}_R =$ 248, 316 and 473 cm^{-1} for the v_2, v_4 and v_1 modes, respectively, and $\lambda_{0,\mathsf{laser}} = 532$ nm.[‡] The refractive indices of the sapphire hemisphere and the carbon tetrachloride liquid were given in table 3.2 and the Raman tensors of the three CCl_4 isotopologues in tables 4.3 to 4.5. The radius of the molecular sphere and the polarisability tensor of the carbon tetrachloride molecule were presented in section 6.1.3 from computations in GAUSSIAN. These last quantities are independent of the isotopic composition of the molecule.

We further ignore the spread of the laser incident angle as it is of negligible consequence to the relative intensities. This was found to be the case with the ammonium sulfate solutions as well. Birefringence of the sapphire hemisphere as well as dispersion in the materials are also ignored. The change in relative intensities is insignificant, especially when illuminating the sample far from the critical angle, as is the case here.

The objective orientation in the L-frame is $(\alpha_\mathsf{O}, \beta_\mathsf{O}, \gamma_\mathsf{O}) = (0°, 180°, 0°)$ in all calculations. The off-set in the polarisation directions as determined for the Durham Raman system with the sulfate solution in section 6.2.4 is not included here.

For each computation, we use the experimental settings as input parameters while summing the intensities over all molecular orientations $(\alpha_\mathsf{m}, \beta_\mathsf{m}, \gamma_\mathsf{m})$ for each of the four standard polarisation combinations. To do this efficiently, we first investigate what angular interval is sufficient to sample the azimuthal, tilt and twist angles. We then investigate the sensitivity of the relative intensities on the local field correction through the molecular radius and the molecular polarisability. Finally, the relative intensities are computed for the three most abundant isotopologues in the isotropic orientational average. This last modelling result is compared to the experimental intensities.

Sampling of molecular orientations

Carbon tetrachloride exhibits random molecular orientations in its liquid state. For an individual molecule, every three-dimensional orientation is equally likely, *i.e.* the distribution of orientations is uniform. The Raman intensity arising from this ensemble is due to its isotropic average. In our modelling approach, we have to pick discrete orientations and ensure the full range of Euler angles $(\alpha_\mathsf{m}, \beta_\mathsf{m}, \gamma_\mathsf{m})$ is sampled. The isotropic average is then given by the sum of the intensities computed for each orientation. This sum approaches the isotropic average as more angles are sampled, though at a computational cost.

In computing the Raman intensity for the isotropic average, the intensity for each particular orientation $I(\alpha_\mathsf{m}, \beta_\mathsf{m}, \gamma_\mathsf{m})$ is multiplied by the factor $\sin\beta_\mathsf{m}$. This ensures equal

[‡]The Raman shifts are taken from the experimental spectra. Note however, that Raman shifts are irrelevant for relative intensity values obtained by the model when $z = 0$. The laser wavelength is likewise of no consequence here, though its value has to be non-zero to prevent computational errors.

sampling of all directions as (the polar regions of the sphere describing the molecular orientations are oversampled compared to its equatorial regions as the three angles are sampled with equal intervals). The β_{m}-weighted intensities are then summed to obtain the isotropic average.

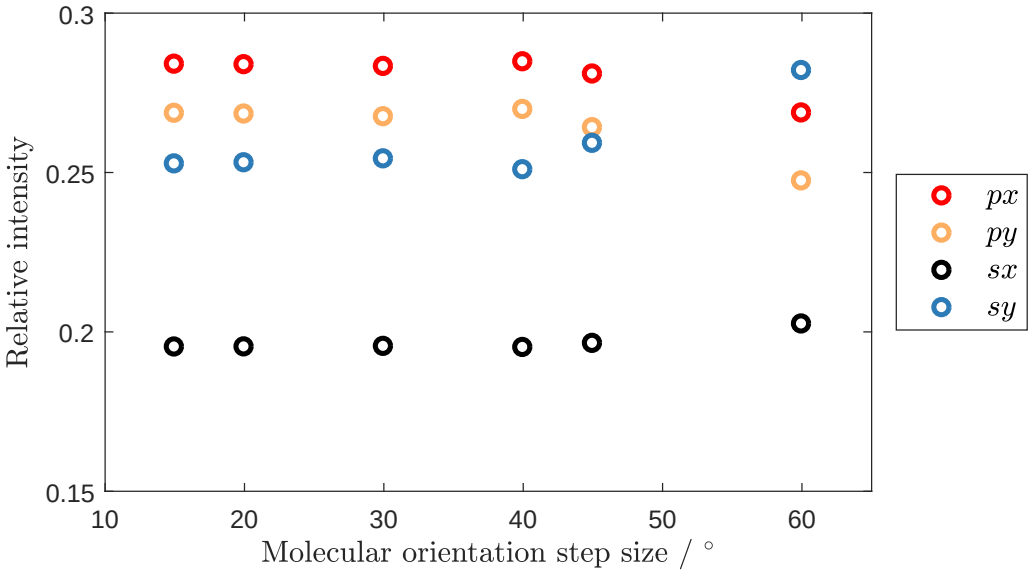

Figure 6.23: Modelled relative intensities for the isotropic average of the $v_2(1)$ mode of $^{12}C^{35}Cl_4$ obtained by a summation of intensities computed for specific molecular orientations, sampled with a varying interval in orientation angles. Below an interval of about 30°, the relative intensities stabilise to the values for the isotropic average.

How coarse can we sample the orientations in our model? Figure 6.23 presents the relative intensities in the four standard polarisation combinations obtained by modelling scattering from the $v_2(1)$ mode of $^{12}C^{35}Cl_4$ (the first of its degenerate E modes given in table 4.3). As the interval, or step size, in α_{m}, β_{m} and γ_{m} is reduced from 60° to 15°, the relative intensities settle on a stable value, conforming to the isotropic average.

The remaining modelling of this section employs an angular interval of 20°. As $\beta = 0°$ results in zero intensity due to the $\sin\beta_{\mathsf{m}}$ weighting factor, the angular range is taken from half the angular step size and ranges up to the upper limit minus half this interval. That is, the computation starts at 10° for each Euler angle, taking steps of 20° towards a final value of 350° for α_{m} and γ_{m} and of 170° for β_{m}. All combinations of these angles are sampled. The isotropic average thus comprises 2916 molecular orientations.

Individual Raman tensor elements

The individual diagonal and paired off-diagonal Raman tensor elements contribute to the intensity of the isotropic average in possibly different ways. Figure 6.24 presented relative intensities for the isotropic average due to these tensor elements. This modelling result is obtained by setting one of the diagonal elements or one symmetric pair of off-diagonal

elements to 1 with the remaining elements at zero. It is specific to the experimental geometry investigated here.

From figure 6.24 we conclude that the relative intensities for the isotropic average of the three diagonal elements xx, yy and zz are practically identical. This is also the case for the pairs of off-diagonal elements xy, xz and yz (where the symmetric complements are implied). However, the relative intensities arising from diagonal and off-diagonal elements differ in that the diagonal elements produce stronger relative intensities in the sy polarisation combination while the off-diagonal elements contribute more to py, sx and px spectra though at a reduced extend for the latter. The order of the intensities is $I_{sy} > I_{px} > I_{py} > I_{sx}$ for the diagonal Raman tensor elements while this is $I_{px} > I_{py} > I_{sy} > I_{sx}$ for the off-diagonal elements.

The observed differences in relative intensities can be understood from the depolarising effect of the off-diagonal elements while the diagonal elements mainly result in polarised Raman scattering. In the present experimental geometry, polarised and depolarised scattering are mixed so that off-diagonal elements also contribute substantially to polarised (px and sy) and diagonal elements to depolarised scattering (py and sx). In experimental geometries such as this, polarised and depolarised terminology no longer applies in its strict sense though these represent illustrative limiting cases within the currently available experimental options.

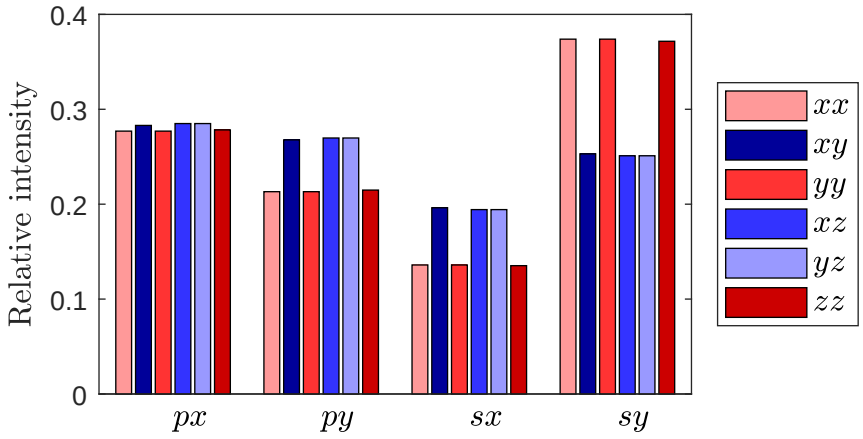

Figure 6.24: Modelled relative intensities arising from each of the six Raman tensor elements computed for an isotropic orientation distribution of the scattering molecule in the experimental geometry employed with the CCl_4 spectra. For off-diagonal elements (blue), the Raman tensor is symmetrised (*i.e.* elements xy and yx are equal).

In the fully isotropic orientation distribution, the Raman tensor is rotated onto all possible molecular axes. The result is an isotropic averaging of the Raman tensor, usually expressed in the laboratory frame of reference. The Raman-scattering intensity may be computed in one step using such an isotropically averaged Raman tensor. This approach can be used in traditional Raman experiments on liquids as described in section 2.5.2. (Ref-

erences to isotropic averages of the Raman tensor for illumination-observation geometries along the laboratory frame axes are included there.) However, there is no straight-forward approach to compute the isotropic average of the Raman tensor in the laboratory frame of reference for our geometry, taking into account the angular spread of the incident and scattered light cones. Our discrete modelling approach offers an alternative way to compute the effect of the orientation distribution on the Raman scattering intensities, with the additional benefit that any distribution and any experimental geometry can be modelled.

Local field correction

To what extend does the local field correction affect the intensities for a spherical molecule with non-isotropic Raman tensors? We answer this question by modelling the intensities for the four standard polarisation combinations while varying the local field parameters by ±20%. These parameters are the radius of the spherical molecule and the isotropic polarisability. The modelling is performed on the isotropic orientation distribution with the experimental parameters described above. Two CCl_4 Raman tensors are used:

- mode v_3 of $^{12}C^{35}Cl_3{}^{37}Cl$, a diagonal Raman tensor given in table 4.4, with modelling results presented in figure 6.25,
- mode $v_4(1)$ of $^{12}C^{35}Cl_4$, a Raman tensor given in table 4.3 with off-diagonal elements only, modelling results presented in figure 6.26.

These modes represent equivalent modes in two different isotopologues of carbon tetrachloride both appearing in the v_4 band around 316 cm^{-1}. The computational results may therefore be compared directly.

In figure 6.25, we note that the absolute intensities decrease with increasing molecular radius while these increase (roughly linearly) with the polarisability of the molecule. Similar behaviour is observed with the off-diagonal Raman tensor in figure 6.26. The similarity is to be expected because both modes are essentially the same vibration expressed in two different molecular frames, each dictated by the symmetry of the isotopologue. Their differences average out in the isotropic orientation distribution mimicked here. The absolute scattering intensities arising from the off-diagonal Raman tensor (figure 6.26) are at most 2% higher than those from the diagonal Raman tensor (figure 6.25). However, the relative intensities differ no more than 0.002 while the strength of the Raman polarisability in both modes, assessed through the Euclidean norm of the respective Raman tensors, only differs by about 0.3%. This slight difference is thus amplified through the scattering process.

The relative intensities are practically constant for each tensor, whatever the molecular radius or polarisability. Smaller molecular radius enhances the local field and thus results in increased Raman intensities. The cavity field tensor is unaffected as the shape factor stays the same. However, the diagonal elements of the reaction field tensor $\mathbf{R}$ decrease conform equation 5.54 as the molecular radius $r = r_x = r_y = r_z$ increases. The local field is thus enhanced through the reduced denominator in equation 5.49 but the effective Raman

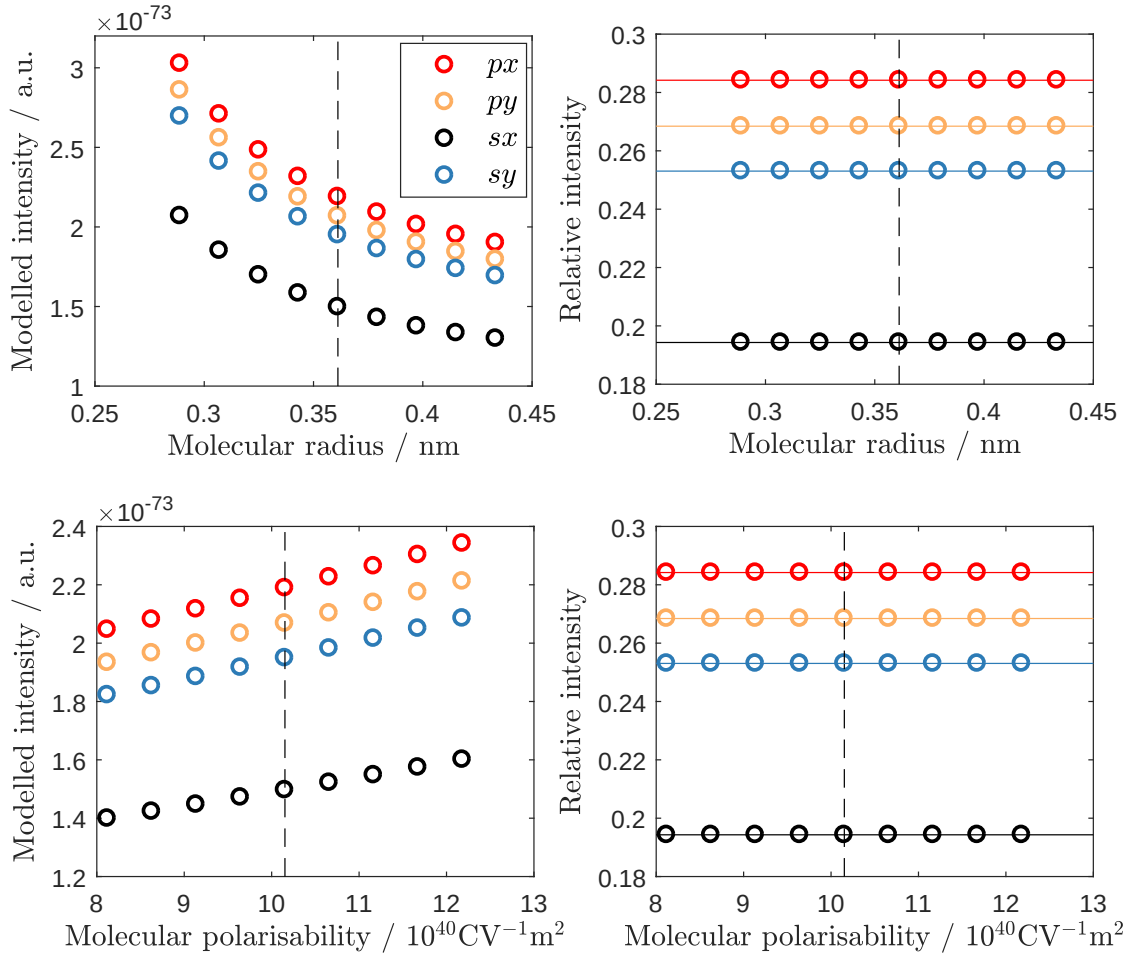

Figure 6.25: Modelled absolute (left) and relative (right) Raman intensities for the v_3 mode of $^{12}C^{35}Cl_3{}^{37}Cl$ as a function of the radius of the molecular ellipsoid (top) and the molecular polarisability (bottom). The values computed in GAUSSIAN for CCl_4 are indicated with dashed vertical lines. The solid horizontal lines in the right-hand plot indicated the relative intensities computed without local field correction.

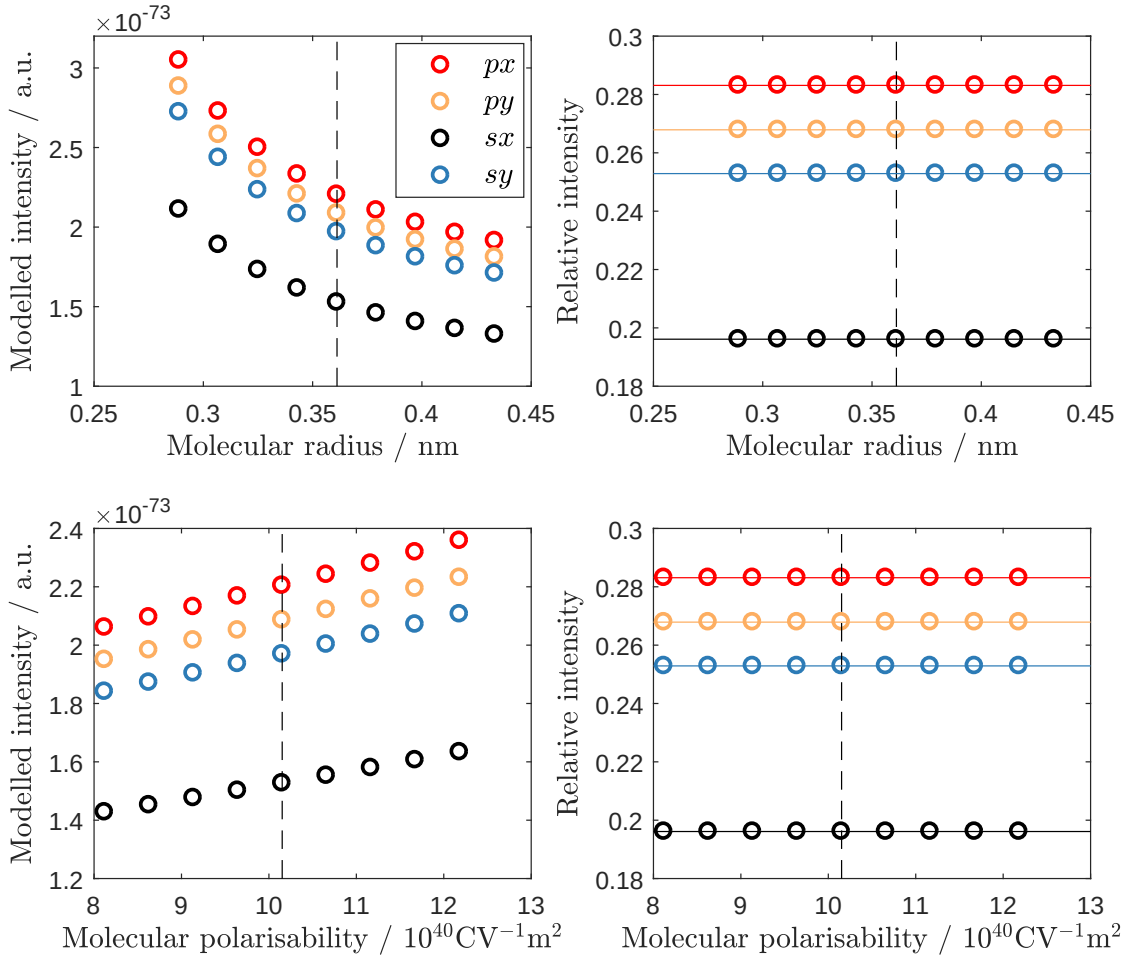

Figure 6.26: Modelled absolute (left) and relative (right) Raman intensities for the $v_4(1)$ mode of $^{12}C^{35}Cl_4$ as a function of the radius of the molecular ellipsoid (top) and the molecular polarisability (bottom). The values computed in GAUSSIAN for CCl_4 are indicated with dashed vertical lines. The solid horizontal lines in the right-hand plot indicated the relative intensities computed without local field correction.

dipole is increased through the dipole reaction factor of equation 5.67. Both expressions are summarised in equation 5.70. On the basis of the same equations, a higher isotropic molecular polarisability $\boldsymbol{\alpha}$ is expected to result in a lower local field as well as in an enhanced Raman dipole, thus lowering and increasing scattering intensities. In this case, the effective Raman polarisability tensor (equation 5.71) may be expressed as

$$\boldsymbol{\alpha}_{v_4,\mathsf{eff}}{}^{\mathsf{m}} = \frac{1+\alpha R}{3(1-\alpha R)}\boldsymbol{\alpha}_{v_4}{}^{\mathsf{m}} \tag{6.4}$$

because $\mathbf{C}$, $\mathbf{R}$ and $\boldsymbol{\alpha}$ are diagonal, with $C_{ii} = 1/3$ due to the spherical cavity, and optical anisotropy is negligible. Within the presently modelled range, the scattered intensity thus increases with $R \propto 1/r^3$ and with α.

In the absence of the local field correction, identical relative intensities are computed. The local field correction is removed from the model by deleting part IV from the `pirs.m` code, except the definition of ϵ_0, and replacing this part with the line

```
p_eff_L = T_L_to_m'*RAMANTENSOR_m*E_app_m;
```

Furthermore, in step (4) of part VI of the code, `C_scat_m` as well as `C_scat_q` are removed. The thus obtained absolute intensities are indicated by the horizontal lines in figures 6.25 and 6.26. However, the absolute intensities are reduced to 0.7 10^{-73} C V^{-1} m^2 with px and to 0.5 10^{-73} C V^{-1} m^2 with sx when the local field correction is not applied. This does not correspond to a simple extrapolation of the modelled intensities to zero polarisability and infinite molecular radius. The local field correction in the model leads to a threefold enhancement of the predicted Raman scattering intensity, which may be seen as an effective increase of the Raman polarisability.

We conclude that the isotropic average for a spherical molecule with isotropic polarisability provides identical relative intensities whatever the Onsager-Scholte local field correction factors, at least in this experimental geometry. The experiments are thus not sensitive to the molecular ellipsoids or polarisability tensors from our GAUSSIAN computations. This may be advantageous, as it reduces the number of unknowns, but it equally does not provide us with a test of the local field correction or its parameters.

Harmonic band intensities

We now model the intensities of the v_2, v_4 and v_1 Raman bands arising from the vibrational modes of the three most abundant CCl_4 isotopologues. Relative intensities are obtained from a combination of absolute intensities computed for each of the degenerate modes with the terrestrial abundance of each isotopologue. The modelling results are included in figure 6.27 along with the experimental relative intensities. Along with the results for the v_1 mode, relative intensities arising from an isotropic Raman tensor are shown for comparison.

For the v_2 band, we observe that the modelled relative intensities range from 0.20 to 0.28 in the order $I_{px} > I_{py} > I_{sy} > I_{sx}$. All six Raman tensors used to model this

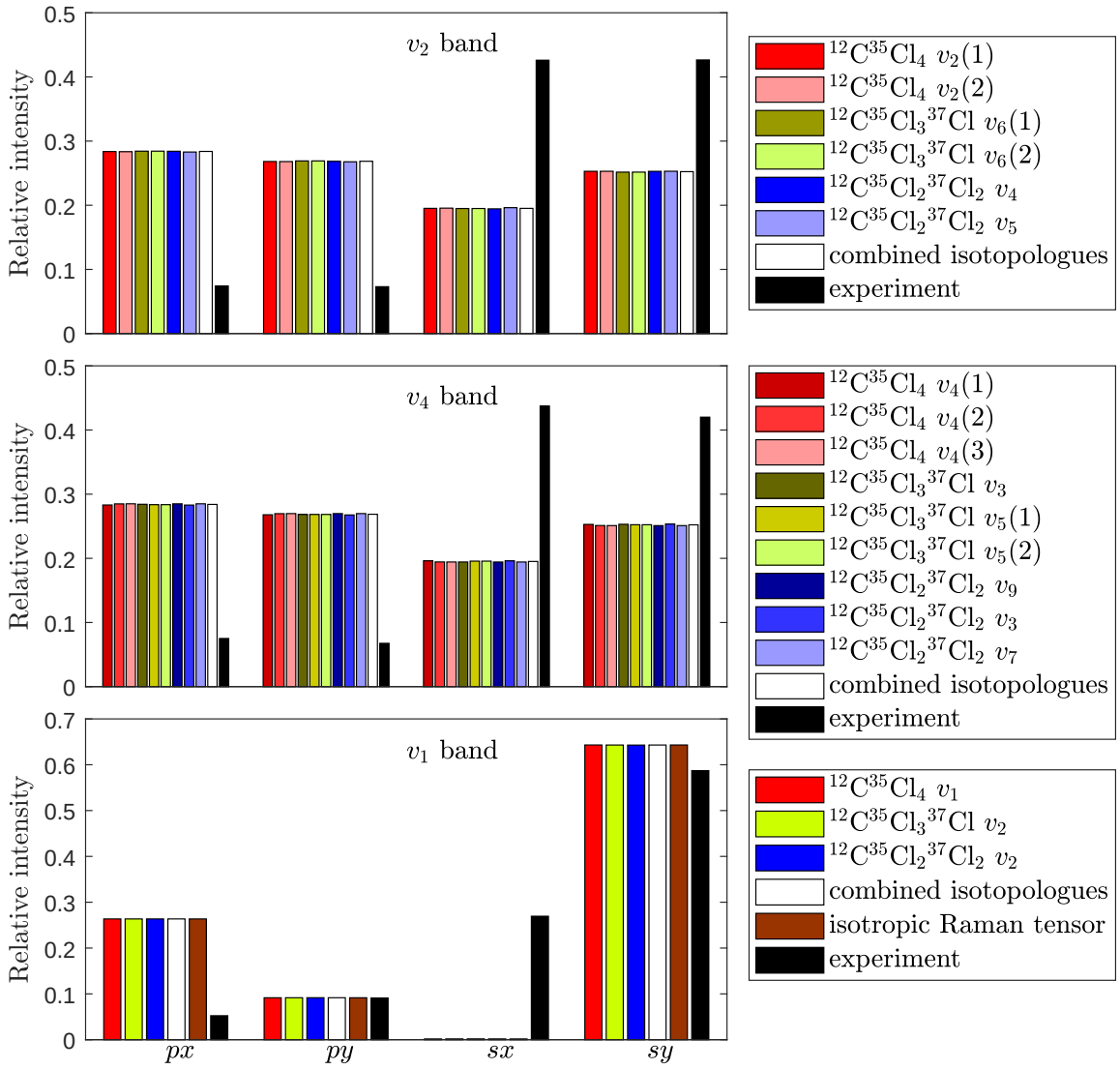

Figure 6.27: Experimental and modelled relative intensities for the v_2, v_4 and v_1 Raman bands of CCl_4. The three most abundant isotopologues are modelled separately and their combined intensity is obtained according to their natural abundance. For the v_1 band, the relative intensities modelled for the three isotopological modes conform to those arising from an isotropic Raman tensor and are all just below 0.002 in the sx polarisation combination.

band result in the same relative intensities which are thus also seen with the combined isotopologues. The *px* and *py* polarisation combinations result in roughly similar intensities, while *sx* and *sy* clearly deviate. This contrast the experimental data, for which the relative intensities are in the order $I_{sx} \approx I_{sy} > I_{px} \approx I_{py}$.

The modelled intensities of the v_4 band (middle plot in figure 6.27) are practically identical to those of the v_2 band. Again, the modelled vibrational modes (nine in this case) provide very similar relative intensities for each of the four polarisation combinations due to the orientational averaging. The experimental relative intensities are somewhat different from those of the v_2 band, though differing no more than about 0.01 on that scale, and share the same order. The modelled relative intensities thus again differ substantially from relative intensities derived from the experimental Raman spectra. Potential causes for this mismatch are discussed below.

Finally, the modelling results for the v_1 band are in the order $I_{sy} > I_{px} > I_{py} > I_{sx}$, different from the previous two bands. This order conforms to that of the v_1 mode of the sulfate anion (as given in figure 6.15, for example). The modes contributing to this band in carbon tetrachloride are non-degenerate in each isotopologue and have diagonal Raman tensors. Their relative intensities are identical to those obtained by an isotropic Raman tensor (bottom plot in figure 6.27): isotropic averaging of the molecular orientation turns the v_1 band diagonal Raman tensors into apparently isotropic ones.[§] The model suggests predominant polarised Raman scattering with the *sy* polarisation combination and to a lesser extend with *px* in contrast to low depolarised intensities at just over 9% with *py* and hardly any with *sx*. However, the relative intensities of the v_1 band derived from the experimental Raman spectra are in the order $I_{sy} > I_{sx} > I_{py} > I_{px}$, which differs from that of the modelled relative intensities in that the *px* and *sx* are interchanged.

The modelled relative intensities deviate from the experimentally determined values in all three bands. This deviation appears to more than a matter of statistical error or uncertainty. The order of the relative intensity differs to such an extend, that the relative intensities are qualitatively different. This mismatch may arise from experimental factors as well as oversimplifications in the model or combinations of these. This is now discussed.

6.3.3 Discussion

The modelled relative intensities presented in figure 6.27 do not compare favourably to those derived from the experimental CCl_4 spectra. What experimental and modelling errors could have contributed to this mismatch?

[§]In contrast, the v_2 band includes modes with diagonal Raman tensors that have substantially differing tensor elements (see tables 4.3-4.5). The discriminating factor is that all elements of the v_1-band Raman tensors have the same sign.

Background subtraction

The experimental intensities were derived after subtracting sapphire-air background spectra. Background subtraction appears to be a major cause for error in the experimental intensities of the v_1 band (figure 6.22). Analysis of this band was nevertheless attempted and shown to explore how far our current methodology could take us. This band is partly obscured by sapphire features that are polarisation sensitive and that differ between background and signal measurements.

The v_2 and v_4 bands appear less prone to error from background subtraction. As with the sulfate spectra, a fitted background could have been employed though without substantial improvement to the analysis.

Optical effects

The raw data of figure 6.21 strongly suggest that background subtraction is problematic for the sapphire-CCl_4 interface as the Raman intensities deviate both quantitatively and qualitatively from the sapphire-air interface. Due to the difference in refractive index between air and carbon tetrachloride, the laboratory-fixed angle of incidence results in substantially different refraction at the interface. The Fresnel factors thus differ for each and give rise to different fields at and near the interface that, combined with the birefringence of sapphire, cause polarisation effects in the sapphire Raman spectra. Birefringence of the sapphire hemisphere also affects the optical path of the scattered Raman light, altering polarisation sensitivity. No birefringence is included in the model. Incorporation of it would require knowledge of the orientation of the optical axes of sapphire with respect to the laser frame of reference.

The incident laser beam may split in e and o-rays upon passing through the sapphire hemisphere. These rays may interfere at the laser focus, *i.e.* the location from which Raman scattering is collected. As the beam is incident perpendicular to the outer, curved hemisphere surface, no refraction takes place. The phase shift $\Delta\phi$ between the two rays depends on the refractive indices n_e, n_o along the optical axes of the sapphire crystal, the vacuum wavelength λ_0 of the light in question and the path length d (here, the 5 mm radius of the hemisphere) as

$$\Delta\phi = \left(\frac{2\pi d}{\lambda_0}|n_o - n_e|\right) \bmod 2\pi \tag{6.5}$$

which is defined as a positive quantity in all cases. The modulus is taken to ensure $\Delta\phi$ ranges from 0 to 2π.

No birefringence occurs when the laser is incident along the optical axis of sapphire. In all other cases, some degree of interference will occur depending on the polarisation angle, which determines the amplitudes along e and o-rays, and the phase shift between the two. For the incident laser beam, $\Delta\phi = 68°$.

Interference only arises if the laser beam is substantially coherent over its optical path

through the hemisphere. The coherence length of the laser is 7 mm in air and reduces to 4 mm in sapphire, below the 5 mm radius of its hemisphere. It is thus realistic to assume that birefringence takes place and that this affects the vectorial electric field amplitude at the location of the Raman scatterer to some extend. The manufacturing tolerance of the hemisphere and inaccuracies in alignment of the laser are ignored here.

Interference between e and o-rays may also arise in the Raman-scattered light. Each individual scatterer emits a coherent wave-packet of Raman scattering, propagating along both e and o axes of sapphire to interfere once these reach air. For the Raman-wavelengths of 539, 541 and 545 nm for the v_2, v_4 and v_1 bands, respectively, we find $\Delta\phi = 76°$, 337° and 142°. This phase shifts comes on top of any phase differences between the Cartesian components of the electric field amplitude tensors derived by the coupling factors. The resultant fields may destructively interfere to suppress certain components of the field while enhancing others. It is thus plausible that birefringence affects the observed Raman intensities though this is not quantified with the current model.

The phase shift of the light effectuates a rotation of its plane of polarisation. This process may correspond to the observation of higher relative py and sx intensities (that is, depolarised Raman scattering) than the model anticipates. The strengthening of depolarised scattering is especially pronounced in the v_1 band. This observation may be congruent with the estimated phase shift which would lead to destructive interference.

Another optical factor that could erroneously affect the modelled relative intensities is an off-set in the polarisation directions. This argument was considered for the sulfate data collected with the Durham system (see section 6.2.4). An off-set of $(\psi, \alpha_{\mathsf{O}}) = (21°, 17°)$ was deduced there. Applying this off-set to the current CCl_4 calculations results in the following relative intensities.

- With the v_1 band: 0.2336, 0.1588, 0.0719 and 0.5358 for the px, py, sx and sy polarisation combinations, respectively. The depolarised intensities are increased at the cost of the polarised intensities, mainly I_{sy}. However, this result is qualitative similar to the previous.

- With the v_2 band: 0.2727, 0.2659, 0.2098 and 0.2516 for the px, py, sx and sy polarisation combinations, respectively. Including the off-set in polarisation angles results in a slight shift of the relative intensities towards a common 0.25 value. Again, this does not offer basis for a qualitatively different interpretation.

A final optical factor is the local field correction. Recomputing relative intensities without the local field correction in our model leads to practically identical results. The local field correction cannot explain the observed experimental intensities.

Raman tensors

The Raman tensors computed with GAUSSIAN are harmonic. As discussed in section 4.4.2, several combination bands, overtones and Fermi resonances are known to arise in the CCl_4

spectrum. Such anharmonicities are enhanced in the liquid phase compared to the gas phase due to increased intermolecular coupling interactions.[¶] To what extend would these alter our model predictions?

In our Raman spectra, the following anharmonic features may be relevant (labelling modes according to the T_d point group and implying corresponding modes in the other point groups).

(1) The difference $v_3 - v_1$ may be in resonance with the v_4 fundamental. However, no distinct spectral feature is observed that could embody this Fermi resonance.

(2) The overtone $2v_2$ may be in resonance with the v_1 fundamental, leading to a tentative doublet observed in the experimental spectra.

(3) The difference $v_3 - v_4$ may be in resonance with the v_1 fundamental, again potentially contributing to the tentative v_1 doublet.

Feature (1) is concluded to be insignificant because the relative intensities of the v_4 band are practically identical to those of the fundamental v_2 band which is not affected by any combinations or resonances. Furthermore, feature (1) does not significantly affect the appearance of the v_4 band, as it is similar to that of the v_2 band. Even if a resonance were contributing significantly to the observed intensity, it may not be separable from the overall band intensity.

Features (2) and (3) relate to the v_1 band, which is perceived as a doublet in some of the experimental spectra. This doublet may arise from strengthening of the weaker overtone $2v_2$ and/or difference band $v_3 - v_4$ at the expense of the stronger v_1 fundamental. These resonances occur only between modes of one isotopologue that meet the resonance conditions (see section 2.5.4).

We now estimate the contribution of the $2v_1$ overtone to the v_1 band intensity. A reasonable maximum estimate of the effect of the interaction in the Raman spectrum is computed by taking an equally-weighted average of the modelled absolute intensities. Alternatively, we combine the Raman tensors of the interacting fundamentals to predict relative intensities. Note that both procedures only provide estimates, as the Raman tensor should normally be computed from the anharmonic vibrational motion of the atoms which is currently unavailable to us.

The modelled absolute intensities for the v_1 fundamental are of the same magnitude as those for the v_2. We estimate the relative intensities for the $2v_2 \approx v_1$ doublet by taking the direct sum for each polarisation combination and normalising this estimate to find relative intensities of 0.2703, 0.1516, 0.0677 and 0.5104 for the px, py, sx and sy polarisation combinations, respectively. This result is practically identical for all modes of the isotopologues in the v_2 band.

[¶]This implies that even if fully anharmonic computations were performed in GAUSSIAN on a single molecule, the computational results would not be directly applicable to the liquid phase because the interaction strengths between the various modes would differ.

As an alternative to the above averaging, we now combine the Raman tensors of the constituent mode. The Raman tensor for this particular resonance may be approximated as a linear combination of v_2 and v_1 band Raman tensors. A number of combinations is possible with the various isotopologues. Taking $^{12}C^{35}Cl_4$ as example, we opt for its $v_2(1)$ and v_1 Raman tensors in a linear combination with the same weight factors for each. This provides

$$\boldsymbol{\alpha}_{2v_2(1)\approx v_1}(^{12}C^{35}Cl_4) = \frac{1}{\sqrt{2}}\boldsymbol{\alpha}_{v_2(1)} + \frac{1}{\sqrt{2}}\boldsymbol{\alpha}_{v_1} = \frac{1}{\sqrt{2}}\begin{pmatrix} -27.4 & 0 & 0 \\ 0 & -12.3 & 0 \\ 0 & 0 & -4.1 \end{pmatrix} \tag{6.6}$$

in units of 10^{-42} C V^{-1} m^2. Using this Raman tensor as input to the model (while all other parameters conform to the previous computation), we obtain the relative intensities 0.2699, 0.1491, 0.0653 and 0.5157 for the *px*, *py*, *sx* and *sy* polarisation combinations, respectively.

Repeating the computation for the three isotopologues and two Raman modes in each provides means and standard deviations of 0.2702±0.0003, 0.1497±0.0005, 0.0655±0.0003 and 0.515±0.001. Surprisingly, this result is highly similar to the previously derived result that was based on a coarse sum of intensities. A likely cause for this similarity is the isotropic averaging.

In the v_1 band intensities of CCl_4, I_{px} and I_{py} are interchanged in the intensity order compared to the experimental order. The same was observed with the sulfate v_1 band intensities measured in Durham. The CCl_4 data furthermore show an increase of I_{sx} to a level well above both *p*-polarised intensities. Combinations of Raman tensors can not fully account for this observation.

Feature (3) arises from resonances between the $v_3 - v_4 \approx v_1$ bands. With the $^{12}C^{35}Cl_2{}^{37}Cl_2$ isotopologue, this resonance may involve the modes $v_1 - v_3 \approx v_2$, which is symmetry-allowed as all involved modes belong to the A_1 species of its C_{2v} point group. The Raman tensor for the difference tone is estimated as

$$\boldsymbol{\alpha}_{v_1-v_3}(^{12}C^{35}Cl_2{}^{37}Cl_2) = \frac{1}{\sqrt{2}}\boldsymbol{\alpha}_{v_1} - \frac{1}{\sqrt{2}}\boldsymbol{\alpha}_{v_3} = \frac{1}{\sqrt{2}}\begin{pmatrix} 20.3 & 0 & 0 \\ 0 & -20.3 & 0 \\ 0 & 0 & -0.55 \end{pmatrix} \tag{6.7}$$

in units of 10^{-42} C V^{-1} m^2. This Raman tensor results in relative intensities of 0.2830, 0.2677, 0.1962 and 0.2531 for the *px*, *py*, *sx* and *sy* polarisation combinations, respectively. These are nearly identical to those for the v_2 and v_4 fundamental bands. The fundamental v_3 band, not separately modelled here, may thus be expected to feature the same relative intensities as well.

The above difference tone mixes with a v_1 band fundamental through Fermi resonance as their frequencies are similar. We may estimate the resulting Raman tensor for the C_{2v}

isotopologues as

$$\boldsymbol{\alpha}_{v_1-v_3\approx v_2}(^{12}\mathrm{C}^{35}\mathrm{Cl}_2{}^{37}\mathrm{Cl}_2) = \frac{1}{\sqrt{3}}\boldsymbol{\alpha}_{v_1} - \frac{1}{\sqrt{3}}\boldsymbol{\alpha}_{v_3} + \frac{1}{\sqrt{3}}\boldsymbol{\alpha}_{v_2} = \frac{1}{\sqrt{3}}\begin{pmatrix} 5.04 & 0 & 0 \\ 0 & -34.4 & 0 \\ 0 & 0 & -15.0 \end{pmatrix} \tag{6.8}$$

in units of 10^{-42} C V^{-1} m^2. By application of the model, this tensor results in relative intensities of 0.2748, 0.1935, 0.1143 and 0.4174 for the *px*, *py*, *sx* and *sy* polarisation combinations, respectively. These values are somewhat reminiscent of the relative intensities estimated for the $2v_2 \approx v_1$ resonance. However, the relative *sy* intensity is significantly lower while the remainder are increased. We must thus again conclude that the experimental intensities are not fully explained by the Fermi resonance as estimated by combinations of Raman tensors. Using particular weight factors for each tensor would not alter this conclusion because a qualitative difference in the order of the Raman scattering intensities as a function of the polarisation combination remains in all cases.

6.3.4 Conclusion

Polarised Raman spectra from the CCl_4-sapphire interface comprise features from all isotopologues involved, their (degenerate) vibrational modes and anharmonicities as well as birefringence in the sapphire hemisphere. The v_2, v_4 and v_1 bands could be observed, though the latter is distorted by the sapphire signal. An error due to background subtraction is therefore expected for its (relative) intensity.

The v_1 band is composed of fundamentals from each isotopologue, as well as $v_3 - v_4$ combination bands and thermally populated vibrational states. The overtone $2v_1$ also comes into its range. The v_2 and v_4 bands appear undistorted by background subtraction and not engaged in significant anharmonic effects.

The relative intensities of the v_2 and v_4 bands are substantially identical while differing from those of the v_1 band in both experimental spectra and the modelled intensities. This likely arises from a qualitative difference between the highly isotropic Raman tensors involved in the v_1 band compared to the symmetries of those in the v_2 and v_4 bands. Considering the similarity between the observed v_2 and v_4 bands, it is likely that the v_4 is not significantly affected by anharmonic effects.

Our modelled relative intensities are qualitatively different from those derived from experiment. The model overestimates the relative *px* and *py* intensities and/or underestimates those of *sx* and *sy*. The experimental intensities of the v_2 and v_4 band show no difference between polarised and depolarised scattering, though these are predicted by our model. Furthermore, the *s*-polarisations are strongly favoured. In the v_1 band of CCl_4, a trend similar to that observed in sulfate is observed, wherein depolarised scattering is much higher than anticipated by our model and the *sx* intensity even surpasses the *p*-polarised intensities. Potential causes for these differences were investigated.

Our model only involves Raman tensors of harmonic vibrations and uses a single

refractive index for sapphire, ignoring its birefringence. These approximations contribute to the difference of the relative intensities derived with our model to those of experimental spectra. Furthermore, any experimental errors with the Durham Raman system may contribute. One such error was assessed for the sulfate spectra in section 6.2 and a similar error may also apply to the CCl_4 data. However, none of these contributing factors taken on its own could account for the observed difference. An aggregate effect is therefore to be expected.

To take such aggregate effect into account would require incorporating birefringence of the hemisphere into the model description, obtain anharmonic Raman tensors by anharmonic vibrational computations for each isotopologue and calibration of the polarisation directions as suggested in our analysis of the sulfate data.

Modelling of CCl_4 scattering intensities further leads us to conclude that the isotropic average of molecular orientations ensures that the local field correction does not affect relative intensities, though absolute intensities are affected by the molecular radius as well as the molecular polarisability. The spherical shape of the molecule probably also supports this effect. Sufficient precision was obtained with steps of 20° in the molecular orientation angles, at which interval the modelled intensities were fully converged.

The orientational average also ensures that degenerate modes result in the same intensities, which may be understood from the contribution of individual Raman tensor element in the isotropic average. This is also the case for corresponding modes in the three most abundant isotopologues, which all provide practically the same relative intensities for each mode within a band. Differences between tensors are thus smeared out by the local field correction until these are no longer distinguishable. This effect likely also causes the strong similarity between the relative intensities obtained from summing intensities due to individual Raman tensors and the relative intensities obtained from combined Raman tensors.

From the above analysis, it is not obvious what Raman tensor would give rise to the experimental intensities in the isotropic average. It is plausible that these intensities are affected by all factors investigated, including their cooperative effects. This may be assessed further by investigating the v_2 mode to avoid anharmonicity as much as possible. No background spectrum is needed for this mode as its peak sits on a smooth line unobstructed by sapphire features. Further experiments should include calibration of the polarisation directions with the objective to be used and assessment of the birefringence of sapphire, possibly establishing its optical axis. This would allow investigation of the effect of birefringence alone on the scattering intensities. Currently, this can not be modelled. The sapphire-CCl_4 interface appears to involve too many unknowns for unambiguous interpretation with our model.

6.4 Zinc arachidate monolayer on silica in air

A monolayer of zinc arachidate was arranged on the flat side of a fused silica hemisphere by Langmuir-Blodgett deposition according to section 3.3.3 and suspended in air in the Stockholm Raman system. Raman scattering was recorded in the four polarisation combinations centred on the C−H stretch region around a Raman shift of 2900 cm^{-1}, corresponding to a wavelength in air of about 625 nm.

In the arachidate molecule, both shape anisotropy as well as polarisability anisotropy play a role. These affect the local field correction, for which this molecular system presents a test case. The molecular tilt angle is roughly known from other techniques, with which our outcomes are compared.

It should be noted that the presence of a monolayer is assumed based on the established procedure that was followed. Zinc cations are expected to bridge the negatively charged silica surface and the acid group of arachidate, with the alkyl chain branching away from the surface. Confirmation by, for example, atomic force microscopy can be performed to check that the deposit was in fact a monolayer. Although blobs appeared locally under optical microscopy (see figure 6.28), spectra were collected from smooth surface areas. Blobs may arise from disordered zinc arachidate patches that have been caused by too high a surface pressure during Langmuir-Blodgett deposition and/or contamination-induced aggregation.

6.4.1 Experimental results

Spectra were collected with the Stockholm Raman system after full calibration of the polarisation directions, using the NA = 0.55 microscope objective lens. The laser beam was incident under $\theta_{k,i} = 75°$ (above the critical angle) and set to 150 mW output power while also employing an OD1 filter to avoid any sample damage during the data acquisition series. Grating 2 of 1200 lines mm^{-1} was used to disperse the Raman spectrum onto the CCD detector, collecting five acquisitions of 60 s each in the MT mode with the slit of the spectrometer at 100 μm. A spectrum was recorded for each of the four standard polarisation combinations.

Figure 6.29 presents the four spectra as raw data and after subtracting a linear baseline, fitted through the data in the ranges 2760-2800 and 3050-3150 cm^{-1} where no features of arachidate can be distinguished. The resulting baseline-subtracted spectra are shown superimposed in figure 6.30 for comparison.

Comparing the experimental spectra to the computational spectrum of the C−H stretch region obtained by GAUSSIAN for gas-phase decanoic acid (figure 4.8), we note that the frequencies of the experimental spectrum are lower than the computational frequencies by about 140 cm^{-1} at the low-frequency end of the band. Symmetric methylene stretch modes are observed as a peak at about 2845 cm^{-1}, while anti-symmetric methylene stretch occurs around 2881 cm^{-1}. The methyl modes, distinctly predicted for decanoic acid at the high-frequency end of this spectral region, are not resolved in the experimen-

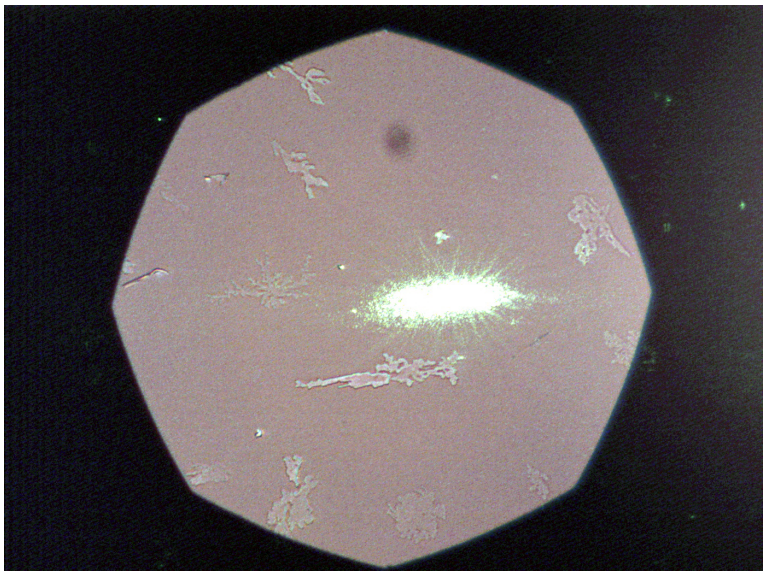

Figure 6.28: Microscopy image (10× objective) of the zinc arachidate layer on fused silica, showing patches on an otherwise optically smooth surface. The green laser spot causes Raman scattering. [data: 20170321/30]

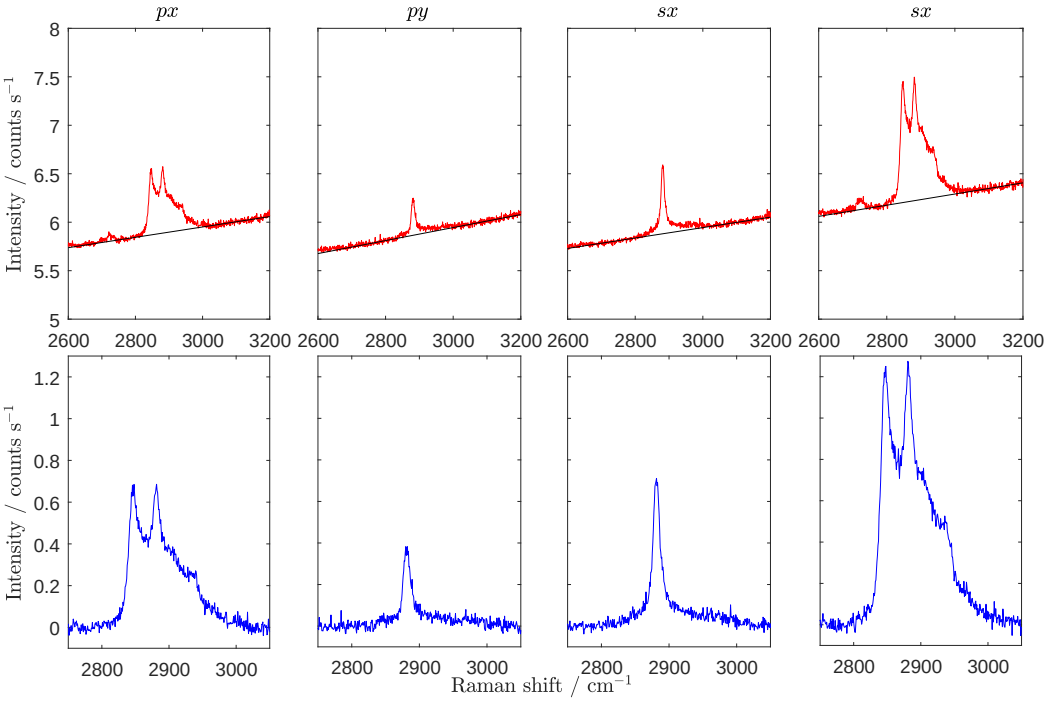

Figure 6.29: Raman spectra of a Langmuir-Blodgett monolayer of zinc arachidate on fused silica in the C−H stretch region, collected with the Stockholm Raman system in the four standard polarisation combinations. Raw data (red) is subtracted by a linear baseline (black) to obtain net intensities (blue). Note the smaller horizontal axis in the bottom plots. [data: 20170321/30-33]

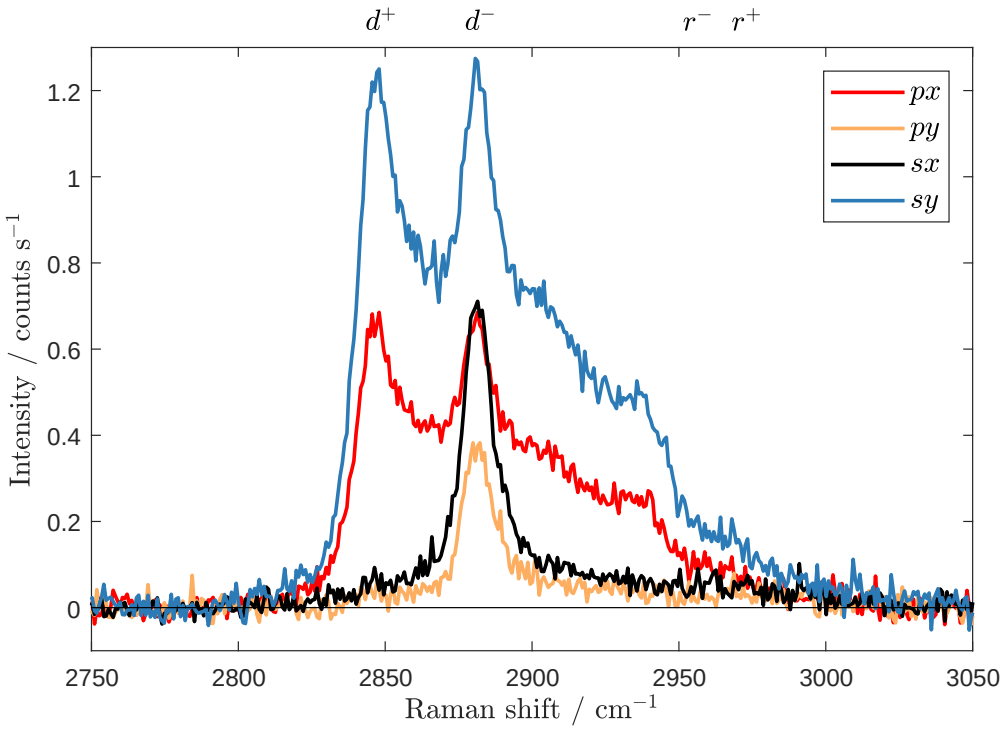

Figure 6.30: Combined plot of the baseline-subtacted spectra of figure 6.29. The d^+ peak occurs around 2845 cm^{-1} and the d^- peak around 2880 cm^{-1}. The broad shoulder between 2900-2950 cm^{-1} comprises both Fermi resonant A' as well as fundamental A'' modes of the alkane chain. The methyl r^+ and r^- peaks lie at the high frequency end of the C−H stretch band.

tal spectra of arachidate. Further comparing the four polarisations to our computational spectrum, we may assume at this stage that the px and sy spectra primarily arise from A' modes of arachidate while the sx and py spectra arise from its A'' modes. The range from about 2900 to 2950 cm^{-1} is expected to primarily include further A' modes. As the arachidate alkane chain is longer than the computed decanoic acid, it is likely that an increased number of CH_2 stretching modes fills this part of the C−H stretch region.

The main symmetric CH_2 stretch band at about 2845 cm^1 is generally termed the d^+ band with the main antisymmetric methylene stretch feature at about 2880 cm^1 being the d^- band. The primary methyl features (tentatively assigned at about 2970 cm^{-1}) are likewise conventionally labelled as r^+ and r^-. Note that the d^+, d^-, r^+ and d^- peaks are empirical features of the spectrum, arising from multiple Raman-active modes. The intensities of these peaks therefore -in principle- do not directly correspond to a particular vibrational mode of a finite alkane chain.

Qualitative interpretation of the C-H stretch region

For a better understanding of the collected zinc arachidate spectra, we briefly review literature on experimental Raman spectra of alkane chains before extracting peak intensities

from our experimental spectra. A recent summary of C−H stretch band features is also given by Ahmed *et al.* [135] in their Raman study of curvature effects on lipid bilayers supported on nanoparticles, some of which is paraphrased here.

Section 4.4.3 introduced the Fermi resonances between CH_2 bending overtones and the symmetric CH_2 stretch modes. In the crystalline phase, as studied here, lateral interaction between the alkane chains of neighbouring molecules broadens the overtones of the bending modes observed between 2900—2940 cm^{-1} [98, 142, 173]. This strengthens its Fermi resonance with the $\nu_s(CH_2)$ modes. In an isotopically isolated all-trans chain, these Fermi resonances result in a strong 2845 cm^{-1} band and two broader bands at 2890 cm^{-1} (underlying the antisymmetric CH_2 stretch fundamental) and a less intense band at about 2930 cm^1. Most of the intensity of the symmetric stretch is in these broad bands [142]. The intensities of these three bands is affected by the order within the material. In going from a crystal to a liquid, the frequency separation between the symmetric methylene peaks at 2930 and 2845 cm^{-1} decreases and the first gains intensity over the latter [143]. In our *px* and *sy* spectra, a shoulder is observed at about 2936 cm^{-1}, indicating one of the Fermi resonant $\nu_s(CH_2)$ modes.

The width of the antisymmetric fundamental decreases with chain length and increases with temperature [143]. A higher temperature leads to an increase of *gauche* conformers at the slightly shifted frequency of 2920 cm^{-1} with the *trans* form remaining at 2890 cm^{-1} [174]. The bandwidth of the *trans* conformer is sensitive to chain mobility. Temperature-dependent broadening of the d^- peak arises from rotational broadening [175], which is less of an issue in our case as the molecules are surface-bound. The antisymmetric modes are less sensitive to environmental changes of the extended alkane chain than the symmetric modes. In all of our four spectra, the $\nu_a(CH_2)$ fundamental is distinctly observed at about 2880 cm^{-1}.

The methyl modes are not resolved in our spectra and thus underly the Fermi resonant symmetric methylene as well as the antisymmetric methylene modes. In highly oriented polyethylene with few methyl groups or in CD_3 terminated alkanes, the Fermi resonances were found to occur near 2850, 2900, and 2925 cm^{-1} and at similar frequencies in the melt, though with different intensity ratios [143]. We may conclude that the broad shoulder around 2935 cm^{-1} has contributions from Fermi resonances of a symmetric methylene stretch near 2922 cm^{-1}, which is affected by chain conformation [176], and from the methyl stretch near 2938 cm^{-1} which remains unaffacted [143, 176].

The appearance of the C−H stretch band thus depends on the structure of the alkane and its environment. The A' methylene modes are affected by Fermi resonance, the interactions of which are increased with molecular order. This gives rise to an apparent filling of the spectral range from the d^+ peak towards the methyl modes. The A'' methylene modes as well as the methyl modes reside on top of these resonances.

Conventionally, the C−H stretch band of alkanes is interpreted using the recorded peak intensities, possibly with curve fitting, attributed to the d^+, d^-, r^+ and r^- features (such as in [31, 54, 173]). In most Raman experiments, only the d^+ and d^- peaks are resolved.

The peak intensities $I(d^+)$ and $I(d^-)$ may thus be obtained from the baseline subtracted spectrum at each polarisation combination. The ratio between the two, particularly in conventional polarised scattering, provides a measure of the degree of order within the material [177, 178] (other order/disorder metrics of alkyl chains are reviewed in [179]). As $I_{sy}(d^-)/I_{sy}(d^+)$ increases for an alkane-chain comprising monolayer, its molecular order increases. That is, the chains are more in their all-*trans* conformation, closely packed and well-aligned, particularly for $I_{sy}(d^-)/I_{sy}(d^+) > 1$. This arises in part because of increased Fermi resonances that underlie the d^- feature and thus increase its height. Intensities for our experiments are given in table 6.5. In our spectra, we find $I_{sy}(d^-)/I_{sy}(d^+) = 1.01$ when taking the peak maxima at 2881 and 2848 cm^{-1}, indicating a partly ordered liquid-like layer. Integrated intensities of the whole ν(CH) region are also obtained.

Table 6.5: Experimental Raman intensities from the zinc arachidate C−H stretch band in the four polarisation combinations. Relative intensities are listed in red below corresponding absolute intensities, given in counts s^{-1} for a single wavenumber or in counts s^{-1} cm^{-1} for intensities obtained by integration over a spectral range.

feature	spectral range / cm^{-1}	I_{px}	I_{py}	I_{sx}	I_{sy}
d^+ peak	2848	0.685	0.044	0.041	1.250
		0.339	0.022	0.020	0.619
d^- peak	2881	0.686	0.375	0.711	1.268
		0.226	0.123	0.234	0.417
ν(CH) band	2800–3000	0.317	0.068	0.126	0.605
		0.284	0.061	0.113	0.542
$\nu_s(\mathrm{CH_2})$ mode	2830–2846	0.424	0.021	0.046	0.753
		0.341	0.017	0.037	0.605
$\nu_a(\mathrm{CH_2})$ mode	2870–2892	0.178	0.200	0.370	0.334
		0.164	0.185	0.342	0.309

Mode intensities

Intensities of individual modes can not be obviously derived from our experimental Raman spectra. We thus opt for a metric that is proportional to one of the stronger modes in the spectrum, allowing extraction of a physically relevant parameter that can be modelled.

For the A' methylene modes, we note that most of the C−H stretch band is complicated by Fermi resonances, which may not be deconvoluted unambiguously. However, these resonances occur primarily at frequencies above the d^+ peak. The low-frequency side of this peak is only minimally distorted. It therefore appears a reasonable approximation to assume that the integrated intensity of the low-shift half of the d^+ peak is proportional the Raman scattering intensity arising from the strongest $\nu_s(\mathrm{CH_2})$ fundamental. (In our decanoic acid computations, this is mode 71.)

The A'' methylene modes can be said to reside on top of a Fermi resonant A' background. In our spectra, the major d^- peak is distinctly observed. A clean intensity metric

may thus be obtained by subtracting the A' background (possibly after fitting with a polynomial) from the recorded spectrum to obtain a residual intensity that is proportional to the scattered intensity from the $\nu_a(CH_2)$ fundamental (mode 76 in our decanoic acid computations).

The above metrics are now applied to our experimental spectra. Intensities for the $\nu_s(CH_2)$ mode are obtained by summing the intensities of the baseline-subtracted spectra in the range of 2830–2846 cm^1. For the $\nu_a(CH_2)$ mode, intensities are obtained by fitting a third-order polynomial through the 2850–2870 and 2892–2912 cm^1 ranges of the baseline-subtracted spectra. This polynomial is then subtracted from the interval 2870–2892 cm^1, which comprises scattering from the $\nu_a(CH_2)$ mode, and the obtained intensities are summed and divided by the spectral range. Table 6.5 provides the obtained intensities as absolute as well as relative values. The relative intensities are scaled to the sum $I_{px} + I_{py} + I_{sx} + I_{sy}$ for each mode.

Errors in the experimental intensities arise from noise in the spectrum (roughly within 0.05 counts s^{-1}) and the accuracy of the background subtraction routine. Peak heights (especially when near-zero) are particularly affected by these uncertainties. The integrated intensities are less affected. Other errors arise in assigning experimental intensities to particular Raman bands, especially where these can not be fully deconvoluted. For example, the $\nu_a(CH_2)$ feature may include scattering from symmetric stretch modes. However, the current method is relatively insensitive to changes of ± 10 cm^{-1} in the selected spectral ranges, which suggests that optimisation of the routine will not significantly affect the results.

A fitting routine to obtain mode-specific Raman intensities was also attempted, but proved problematic with near-zero intensities, such as the d^+ peak in the px and sy spectra, and for distinguishing A' from A'' intensities.

The d^+ peak and $\nu_s(CH_2)$ mode intensities are near-zero in the py and sx spectra while the sy intensity is nearly twice that of the px spectrum. The d^- peak intensity is about equal in the px and sx spectra, though the $\nu_a(CH_2)$ intensities are nearly equal pairwise. The pair of px and py $\nu_a(CH_2)$ intensities are similar, as are the sx and sy pair, though the latter are just under twice the intensity of the former. We now investigate whether our model also predicts this behaviour.

6.4.2 Modelling Raman intensities

In order to further analyse the arachidate spectra, we first compare these to computational Raman spectra for decanoic acid, using the GAUSSIAN results combined with our model description of the scattering process. From these, we try to establish what Raman modes predominantly contribute (in the harmonic approximation) to the d^+ and d^- features in the experimental geometry employed at Stockholm. For these $\nu_s(CH_2)$ and $\nu_a(CH_2)$ modes, sensitivity of the modelled intensities with respect to variation of model input parameters is assessed. In the next section, intensities for arachidate are estimated and

compared to the experimental results to assess orientation of its alkane chain.

Computational spectrum of decanoic acid

Figure 6.31 presents computed Raman spectra of an upright decanoic acid molecule at the silica-air interface for the four standard polarisation combinations. The molecular orientation is $\beta_{\mathsf{m}} = 0°$ while the intensities are summed over the full range of the azimuthal angle α_{m} in steps of 20°. The molecular twist angle γ_{m} is redundant in this case. The intensity with each polarisation combination is modelled for the Raman modes 71–89, using the Raman tensors as computed with GAUSSIAN (table 4.7) and the parameters of the zinc arachidate experiment. All Raman lines in this computational spectrum are convoluted with a Lorentzian (fwhm of 10 cm^{-1}) to obtain spectra that may be qualitatively compared to the experimental ones.

A likewise computation is performed for a flat orientation of decanoic acid, *i.e.* with $\beta_{\mathsf{m}} = 90°$. The alkane chain is thus oriented along the silica-air interface. Figure 6.32 presented the modelled intensities for this case, in which the azimuthal as well as twist angles are sampled at an interval of 20° (as determined to result in converged intensities with the carbon tetrachloride calculations of section 6.3.2).

These two sets of modelled spectra may be compared to that of figure 4.8, which was obtained only from the GAUSSIAN computation without considering experimental geometry. The intensities presented there arise from the scattering activity S, which can be seen as an isotropically averaged intensity in a conventional unpolarised Raman experiment. Such a spectrum has the features of a combination of all presently modelled spectra. In a random distribution of molecular orientations, the $\sin\beta_{\mathsf{m}}$ weighting factor ensures that orientations around $\beta_{\mathsf{m}} = 90°$ are more prevalent. The d^+ peak is thus stronger than the d^- peak in such unpolarised spectrum.

An upright alkane chain (figure 6.31), modelled by decanoic acid in the present experimental geometry, is thus predicted to give rise to A' features exclusively in the px and sy spectra while A'' features appear in all four polarisation combinations. Furthermore, intensities arising from modes belonging to the A'' species have $I_{px} \approx I_{py}$ and $I_{sx} \approx I_{sy}$ while the symmetric modes (of the A' species) are clearly stronger in the sy than in the px spectrum.

For alkane chains parallel to the interface (figure 6.32), the A' modes contribute to the spectra in all four polarisation combinations in the order $I_{sy} > I_{px} > I_{sx} > I_{py}$. The A'' modes are no longer pairwise equal, but are manifested as $I_{sy} > I_{px} > I_{py} > I_{sx}$. Furthermore, the methyl modes appear clearly in all four spectra, while these are distinctly weaker for an upright chain.

We now compare the above modelled spectra to the baseline-subtracted experimental spectra of figure 6.30 and readily conclude that the experimental spectra are most similar to the upright chain. However, the d^+ and d^- peaks reach a similar intensity, which is not observed in the modelled spectra at either tilt angle. This may be explained from the

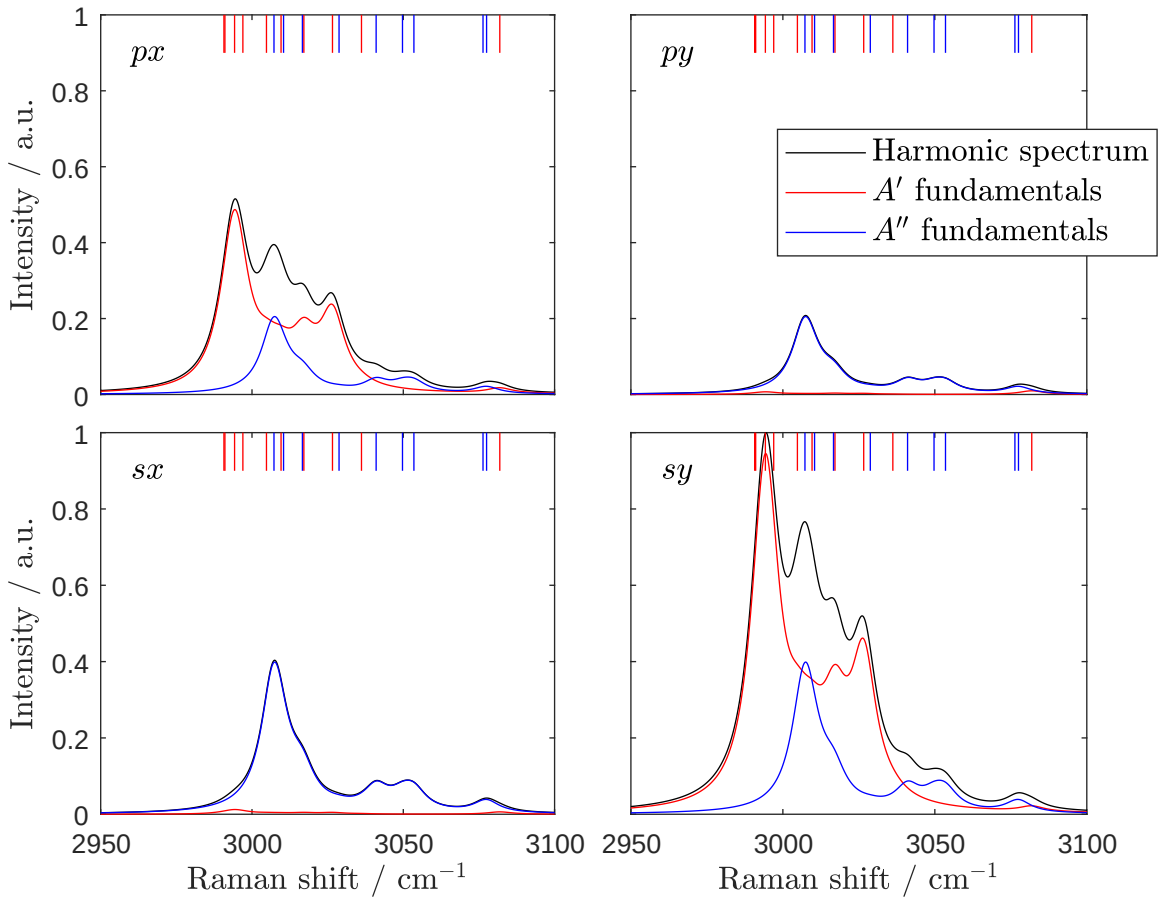

Figure 6.31: Modelled Raman scattering intensities for upright decanoic acid ($\beta_{\mathsf{m}} = 0°$) at the interface between fused silica and air. The Raman modes result from GAUSSIAN computations at the B3LYP/6-311++G(d,p) theory level while our model is used to compute the scattering intensities with input variables according to the experiments presented in figure 6.30.

increased number of CH_2 stretch modes in the longer arachidate chain compared to those in decanoic acid and from the occurrence of Fermi resonances, which are not included in the harmonic modelled spectra. Both would increase the scattering intensity around the wavelengths of the d^- peak (around 2880 cm^{-1} in the experimental and at 3007 cm^{-1} in the modelled spectra). Notwithstanding this simplification, the modelled spectra provide at least a qualitatively useful comparison.

A more precise tilt angle for the zinc arachidate monolayer is yet to be derived, preferably based on individual modes. A fit of the experimental C−H stretch band intensities using modelled spectra for this band is inappropriate since the modelled spectra lack C−H stretch modes and Fermi resonances which account for a significant part of the observed features. Moreover, computing all possible orientations at a sufficiently narrow interval to allow fitting is computationally expensive. If a limited number of harmonic fundamental

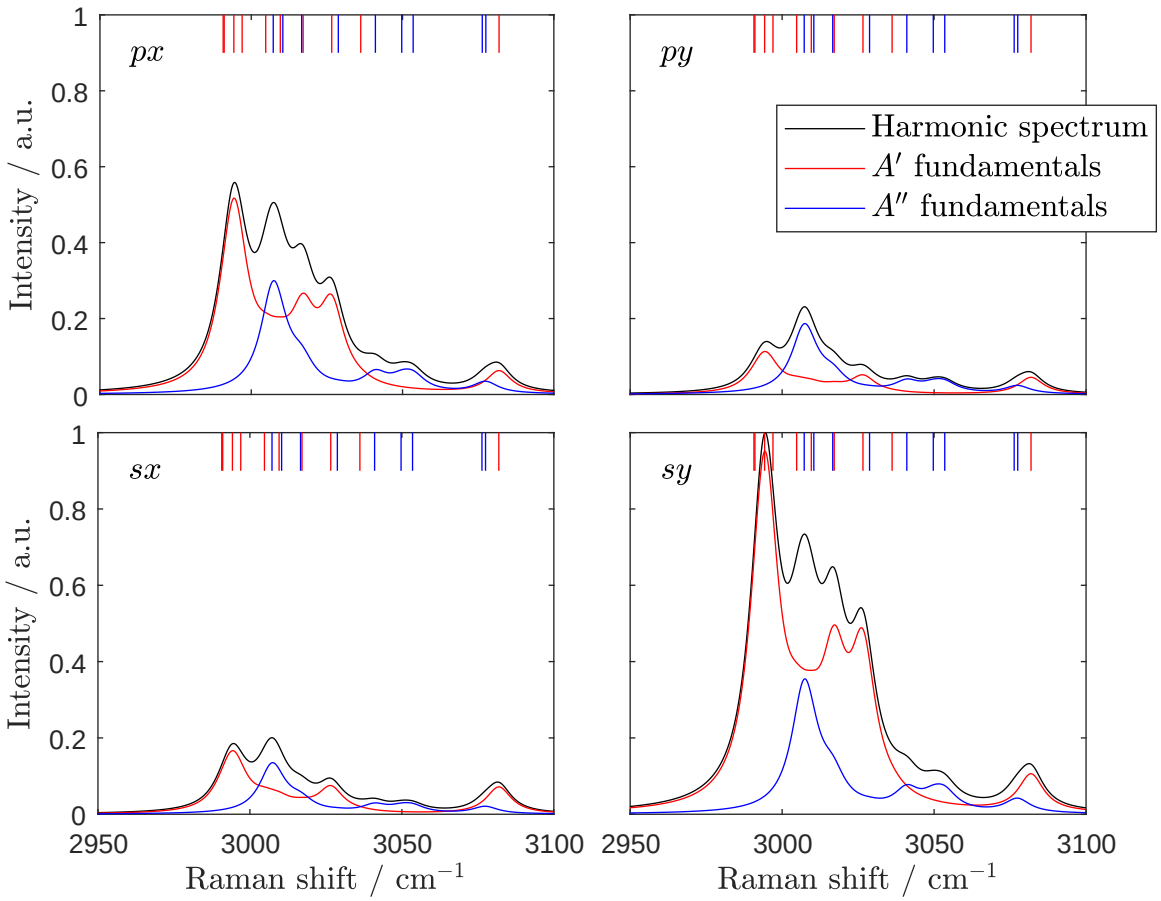

Figure 6.32: As figure 6.31 but with decanoic acid at $\beta_{\mathsf{m}} = 90°$, *i.e.* parallel to the interface. Both azimuthal (α_{m}) and twist (γ_{m}) angles of the molecular orientation are isotropically averaged.

modes could be used in our model to capture the essential behaviour of (features of) the ν(CH) band, this would greatly simplify our current analysis. This is therefore further investigated.

Starting with the A'' fundamentals, we note that the ratio of intensities arising from these modes is constant, irrespective of the polarisation combination. This is suggested by the band shapes in the modelled spectra and confirmed by computing intensities relative to the strongest mode. This constant-ratio relationship was found to hold for all methylene modes at both tilt angles (though not for the methyl mode at $\beta_{\mathsf{m}} = 90°$). This implies that it is sufficient to use one of the $\nu_a(\mathrm{CH_2})$ mode to represent the intensity arising all $\mathrm{CH_2}$ antisymmetric stretch modes in our modelling efforts. This is further supported by the fact that these modes (belonging to the A'' species) are not affected by Fermi resonances. We opt for mode 76 of decanoic acid, its strongest $\nu_a(\mathrm{CH_2})$ mode. As the form of this tensor remains unaffected by chain length and it only sports one pair of off-diagonal elements that is substantially non-zero (namely the xy, yx elements), we assume that this mode is

also representative of like vibrations in arachidate.

The A' fundamentals do not show as strong a fixed intensity relation between themselves. However, the variation between the modes comprised by the d^+ peak (modes 71-75 and 77) is below 5% of the strongest $\nu_s(CH_2)$ mode (mode 73). The modes surrounding mode 73 are at most 18% of the intensity due to mode 73 so that the variation of the intensity contribution to the d^+ peak is no more than 1% for each mode in this experimental geometry. On the low-frequency side, this is even further reduced to below 0.2%. In the harmonic approximation, mode 73 may thus be employed to represent the $\nu_s(CH_2)$ modes as well as the d^+ peak in our modelling. Fermi resonances mainly occur at the high-frequency side of this peak, so that their impact is minimised by using its low-frequency side. Furthermore, it is reasonable to assume that the Raman tensor of a Fermi-resonant mode in the orientational average over the azimuthal angles (as modelled here), results in Raman intensities that are proportional to those observed for the fundamental affected by that resonance.

Proportionality between mode 73 and the $\nu_s(CH_2)$ modes and d^+ peak intensities as well as between mode 76 and $\nu_s(CH_2)$ mode intensity in decanoic acid is thus assumed and by extension also applied for our modelling of arachidate. As this proportionality holds to an approximation within 0.2% (for Lorentzian peaks with a fwhm of 10 cm^{-1}) at both extremes of the tilt angle, it should apply to the full range of β_{m} from upright to flat.

Sensitivity analysis

We now model Raman scattering intensities as a function of various model input variables. This analysis is used to assess the sensitivity of the model outcome with respect to these variables, thus providing an estimate of its uncertainty, and to explore variations or improvements to the experiment. The test case is an upright alkane chain at the silica-air interface and its primary symmetric and antisymmetric CH_2 stretch modes, determined to be modes 73 and 76 in our decanoic acid computation.

To assess the effects of the local field correction, we vary the molecular polarisability and the molecular shape.

Variation of element α_{zz} of the molecular polarisability tensor $\boldsymbol{\alpha}^{\mathsf{m}}$ in the range from 0 to 80 C V^{-1} m^2 has no effect on the modelled intensities. These remain constant at the previously modelled level.

Scaling of the molecular polarisability tensor as a whole by a multiplication factor ranging from 0.1 to 1000* results in the intensities of figure 6.33. Note the logarithmic axes to accommodate the wide range. A broad asymptotic resonance is observed around a multiplication factor of 5.5 while a narrower resonance occurs at about 14. Such resonances were anticipated in section 5.3.2, arising from a division by near-zero values in the reaction field correction, which depends on the molecular polarisability. Though these

*Such high factors are taken to check whether a gross underestimation of α would affect the modelling results. An underestimated value may be feared from applying the Clausius-Mossotti equation with the optical refractive index (section 6.1.3).

asymptotes affect the modelled intensities by several orders of magnitude, the relative intensities are affected in a much narrower range of multiplication factors. This suggests that the precision of the absolute values of the polarisability tensor are less critical when considering those relative intensities, as long as the values are sufficiently far removed from any of the asymptotes.

Next, the molecular cavity shape is varied by adjusting r_z, its ellipsoidal radius along the alkane chain of the molecule. Sensitivity with respect to chain length is especially relevant as we aim to employ properties computed for decanoic acid for interpretation of arachidate data.

In figure 6.34, the modelled Raman scattering intensities reduce as r_z increases before reaching a steady value from about $r_z \approx 4$ nm. However, the relative intensities already stabilise before a value of $r_z = 0.4$ nm is reached, which amounts to an alkane chain of about five carbon atoms. We may thus conclude that the difference in chain length between decanoic acid and arachidate does not affect the modelled relative intensities significantly.

The local field correction thus affects the modelled intensities but results in the same relative intensities around the computational values used as input to our model. This suggests that, at least for an upright alkane chain in the present experimental geometry, the relative intensities of its Raman scattering are unaffected by the local field correction.

The insignificance of the local field correction may (in part) arise from averaging over the azimuthal molecular orientation employed here. However, as the absolute intensities are clearly affected, the cavity and reaction field tensors give rise to an effective Raman tensor which significantly differs from that of the uncorrected Raman tensor. It is therefore not obvious that the local field correction should not be applied with molecular tilt angles other than $\beta_{\mathsf{m}} = 0°$. For specific cases, such as the present conformation, it may be argued that the local field correction can be omitted.

Next, the angle of laser incidence $\theta_{k,i}$ is varied from 0° to 180°. Modelling results for mode 73 and 76 are presented in figure 6.35 and 6.36, respectively. The intensity profiles presented here share their overall features with those modelled for the sulfate v_1 band (figure 6.10). In the symmetric CH_2 stretch mode 73, polarisation combinations py and sx lead to low levels of Raman intensities at all angles of incidence. In the antisymmetric CH_2 stretch mode 76, px and py result in identical intensities, as do sx and sy. When $\theta_{k,i} = \theta_c = 43.2°$, the critical angle for the silica-air interface at the laser frequency, scattering is strongest in the sy polarisation combination for both modes. Illumination from the air side of the interface, that is with $\theta_{k,i} > 90°$, results in lower levels of scattering being collected by the microscope objective.

In the experiment, $\theta_{k,i} = 75°$ was employed. This angle was chosen to ensure that appreciable levels of I_{px} would be detected within an experimentally accessible range. However, this angle can be seen to result in sub-optimal levels of scattering. The present modelling indicates that for $\theta_{k,i} = 53°$, a maximum arises in I_{px} while I_{sy} is also elevated. In the antisymmetric modes, this also leads to increased py and sx intensities. Appropriate modelling may thus ensure optimisation of the experimental geometry to improve signal

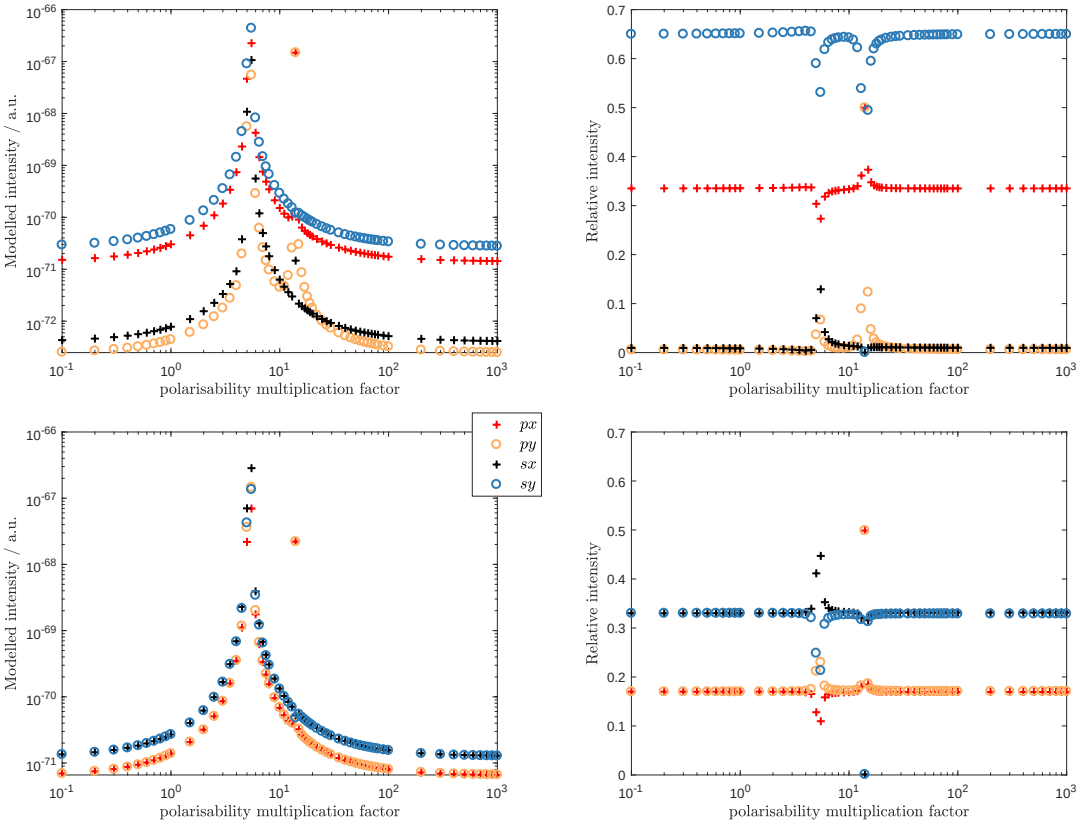

Figure 6.33: Modelled absolute and relative intensities for modes 73 ($\nu_s(CH_2)$, top plots) and 76 ($\nu_a(CH_2)$, bottom plots) of decanoic acid at the silica-air interface as a function of multiples of the molecular polarisability tensor, $\boldsymbol{\alpha}^{\mathsf{m}}$, which affects the local field correction. The other model input parameters conform to the Stockholm arachidate experiments. Around a factor of 1, the relative intensities are constant. Two asymptotes are observed at multiplication factors of about 5.5 and 14.

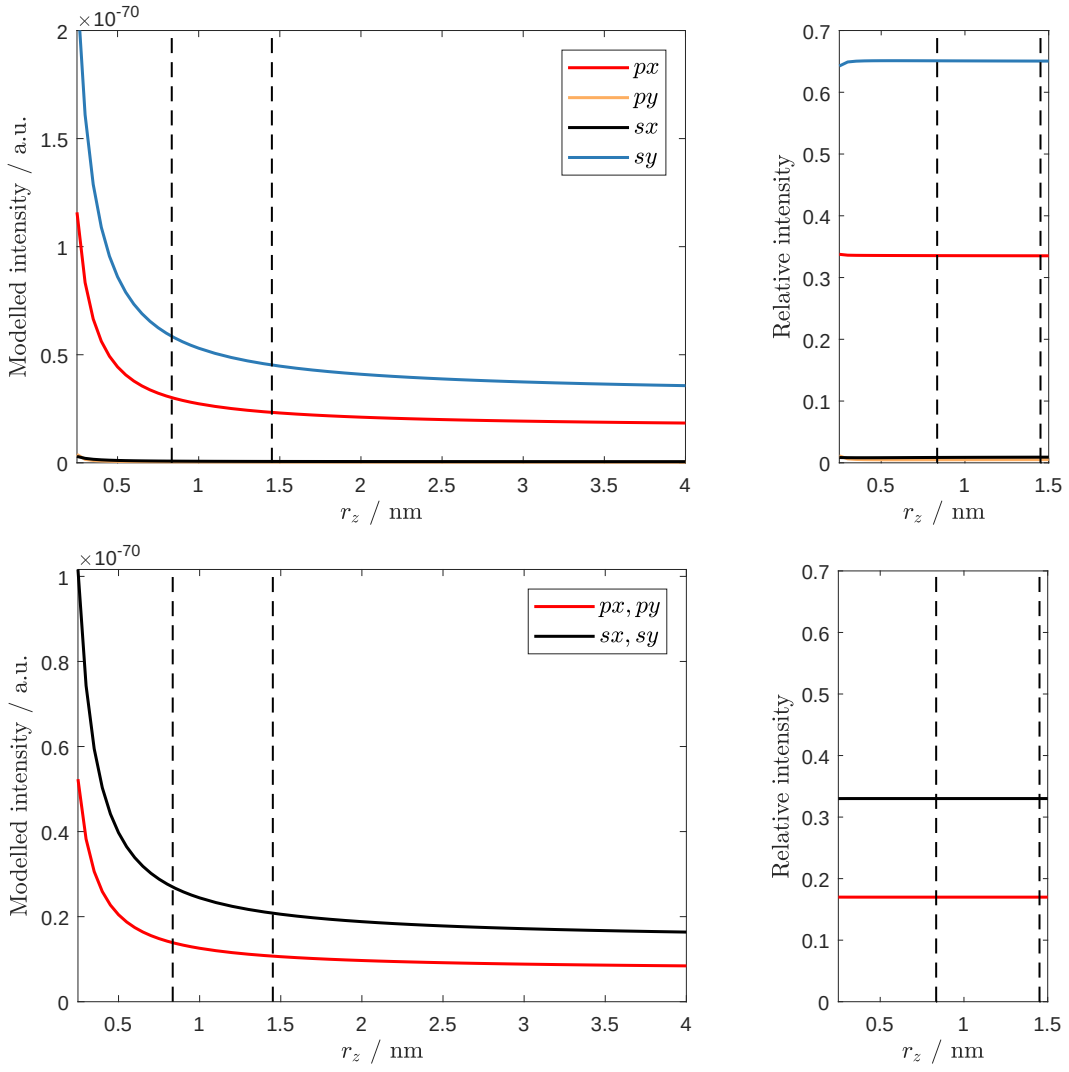

Figure 6.34: Modelled absolute and relative intensities for modes 73 (symmetric CH_2 stretch, top plots) and 76 (antisymmetric CH_2 stretch, bottom plots) of decanoic acid at the silica-air interface as a function of r_z, the molecular ellipsoidal radius along the length of the alkane chain. The other model input parameters conform to the Stockholm arachidate experiments. The r_z values used for decanoic acid and arachidate are indicate with dashed vertical lines. The relative intensities are constant in this range. In the bottom plots, the sx and sy curves overlap as well as those of the px and py polarisation combinations.

strength over noise in the collected Raman spectra.

We further vary the position of the microscope objective lens relative to the interface by sampling β_{O} in the range from 0° to 180° (figures 6.37 and 6.38). These angles conform to observation of the interface in the plane of laser incidence $x^{\mathsf{L}}z^{\mathsf{L}}$.[†] At $\beta_{\mathsf{O}} = 0°$, the objective collects Raman scattering from the air side of the interface, perpendicular to said interface. This geometry provides low Raman intensities. At $\beta_{\mathsf{O}} = 180°$, the geometry employed in the arachidate experiments, Raman scattering is collected through the fused silica hemisphere, which results in enhanced intensities. At about $\beta_{\mathsf{O}} = 140°$, maxima are observed. These arise from collection around the critical angle, at which Raman scattering couples strongly into the hemisphere. Undulations in this region arise from the discrete nature of positioning grid nodes at which local scattering intensity is computed.

Figure 6.39 presents modelled (relative) intensities for a pinhole aperture, that is as NA $\to 0$. This is readily implemented in the model by setting $g = 1$ to ensure that Raman scattering is computed at only one point at the centre of the objective lens, irrespective of specified NA. The maximum Raman scattering intensity is predicted for $\beta_{\mathsf{m}} = 136°$, which is near the critical angle $\theta_c = 44°$ on the hemisphere side of the interface.[‡] It is not identical to the critical angle because the refractive index of the interfacial layer (n_2 different from n_1 and n_3) modifies coupling of the Raman scattering into the hemisphere. This slightly increases the angle at which the maximum is predicted.

At the lower NA limit, the symmetric mode does not produce appreciable py and sx intensities at any angular position of the objective within the laser plane of incidence. At the larger NA of 0.55, significant intensities are observed for such depolarised scattering since this larger objective also collects Raman scattering away from the plane of laser incidence where the x and y directions of each point Q project differently onto the O-frame axes. For the symmetric mode, the intensities at larger NA (figure 6.38) appear to be more of a convolution over the intensities obtained at NA $\to 0$ (bottom plots of figure 6.39).

For upright alkanes, we may gather that the highest intensities for a single polarisation combination are obtained with $\beta_{\mathsf{O}} = 180°$ while collecting I_{sy} only. Alternatively, if various polarisation combinations are to be collect, each with substantially non-zero intensities, a collection angle of 120° is opportune. This value holds for an objective with NA = 0.55. With smaller NAs, this optimum lies closer to $\beta_{\mathsf{O}} = 136° \approx \theta_c + 90°$. Such experimental geometries may be achieved by tilting the sample under a fixed microscope, for instance by means of the rotation clamp described in section 3.1.1.

We now assess the effect of the thin-film refractive index n_2 on the modelled intensities.

[†]Note that the direct laser reflection off the interface is not included in the model, though it limits the feasibility of corresponding experiments.

[‡]Similar directional radiation was observed and modelled by Luan *et al.* [166] for isotropically averaged, fluorescent rhodamine B molecules embedded in a thin film of polymethyl-methacrylate on an SF11 substrate using a pinhole aperture. However, their study did not include the geometry of excitation. Furthermore, pinhole apertures generally reduce intensities to below detection thresholds in Raman scattering experiments.

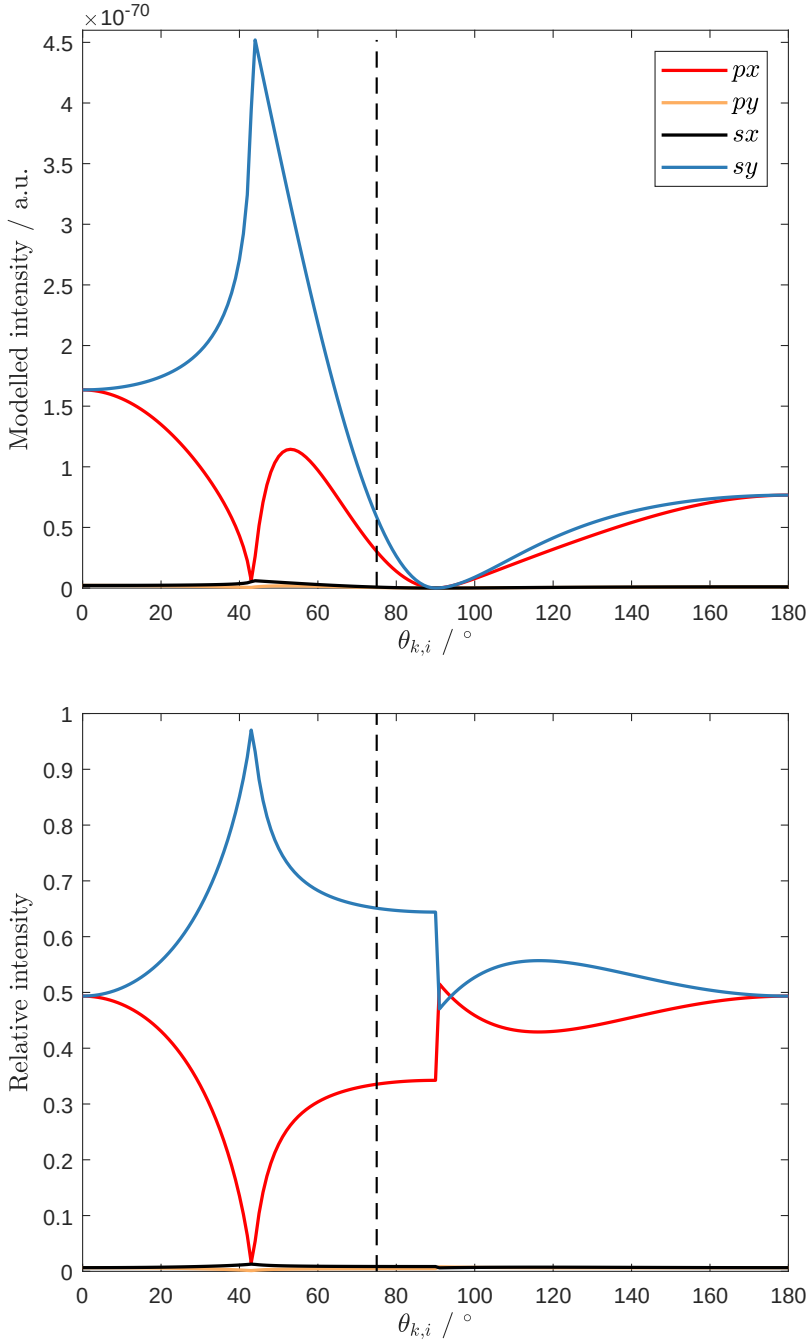

Figure 6.35: Modelled absolute and relative intensities for mode 73 of decanoic acid, its strongest CH_2 symmetric stretch, as a function of laser incidence angle $\theta_{k,i}$. The other model input parameters conform to the Stockholm arachidate experiments. The experimental value of $\theta_{k,i} = 75°$ is indicated with a dashed vertical line.

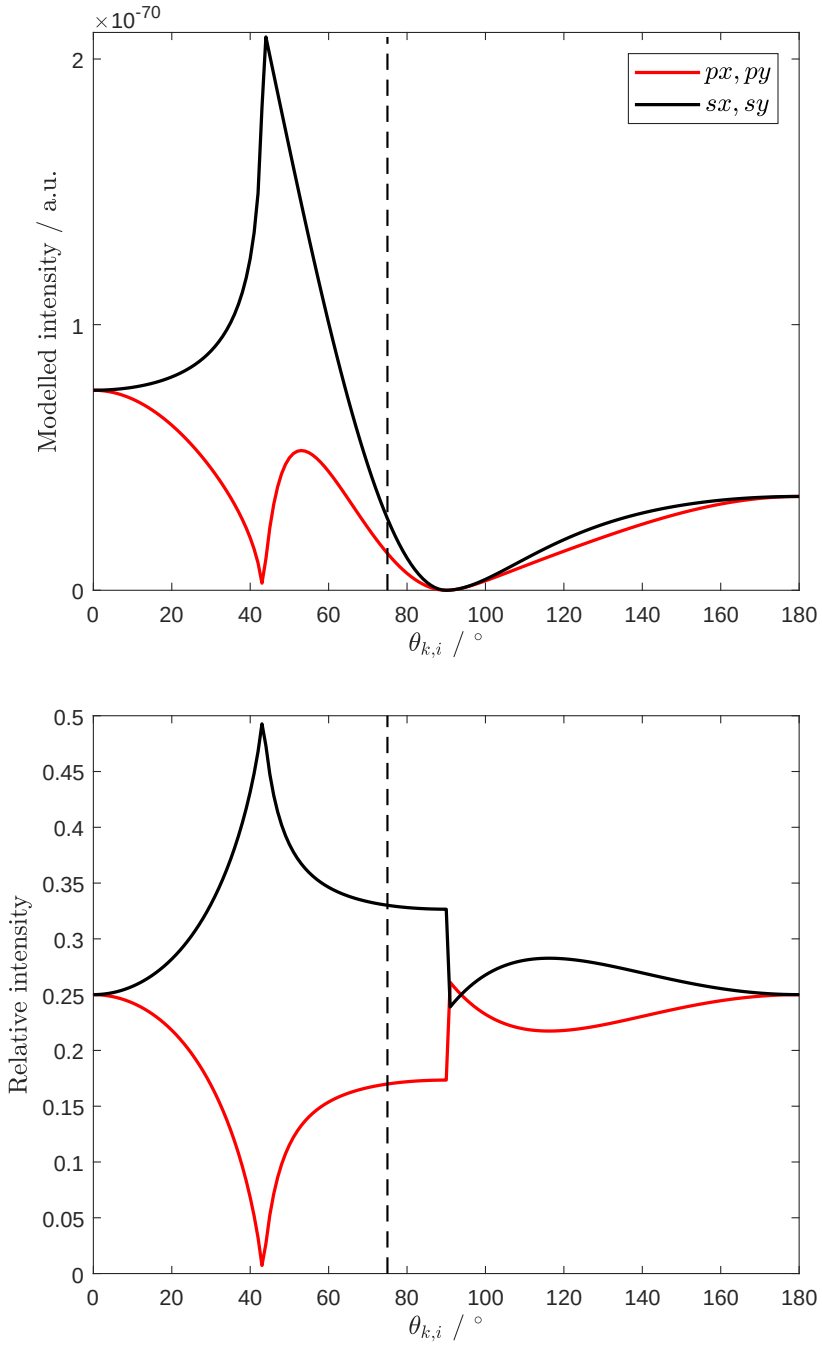

Figure 6.36: As figure 6.35 but with mode 76 of decanoic acid, its strongest CH_2 antisymmetric stretch.

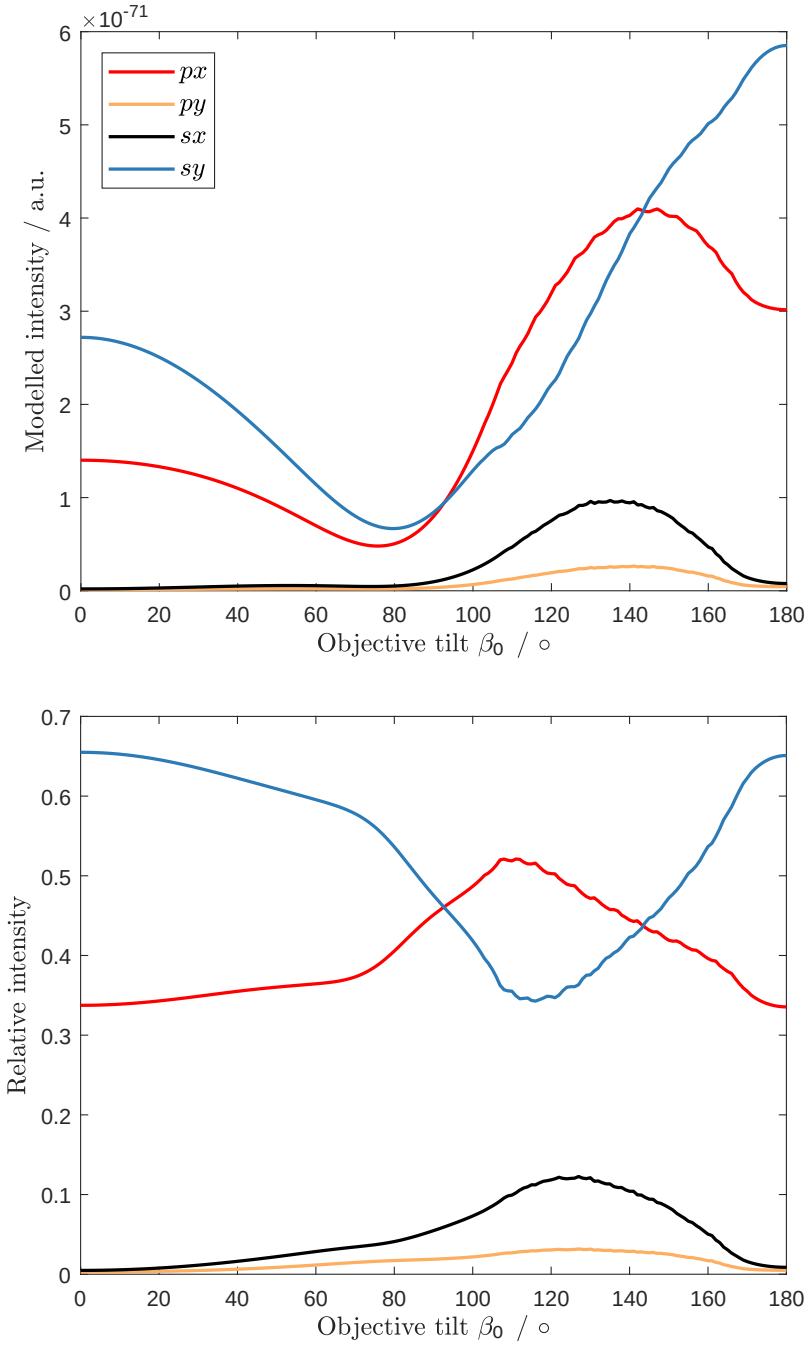

Figure 6.37: Modelled absolute and relative intensities for mode 73 of decanoic acid, its strongest CH_2 symmetric stretch, as a function of microscope objective tilt angle β_O. The other model input parameters conform to the Stockholm arachidate experiment.

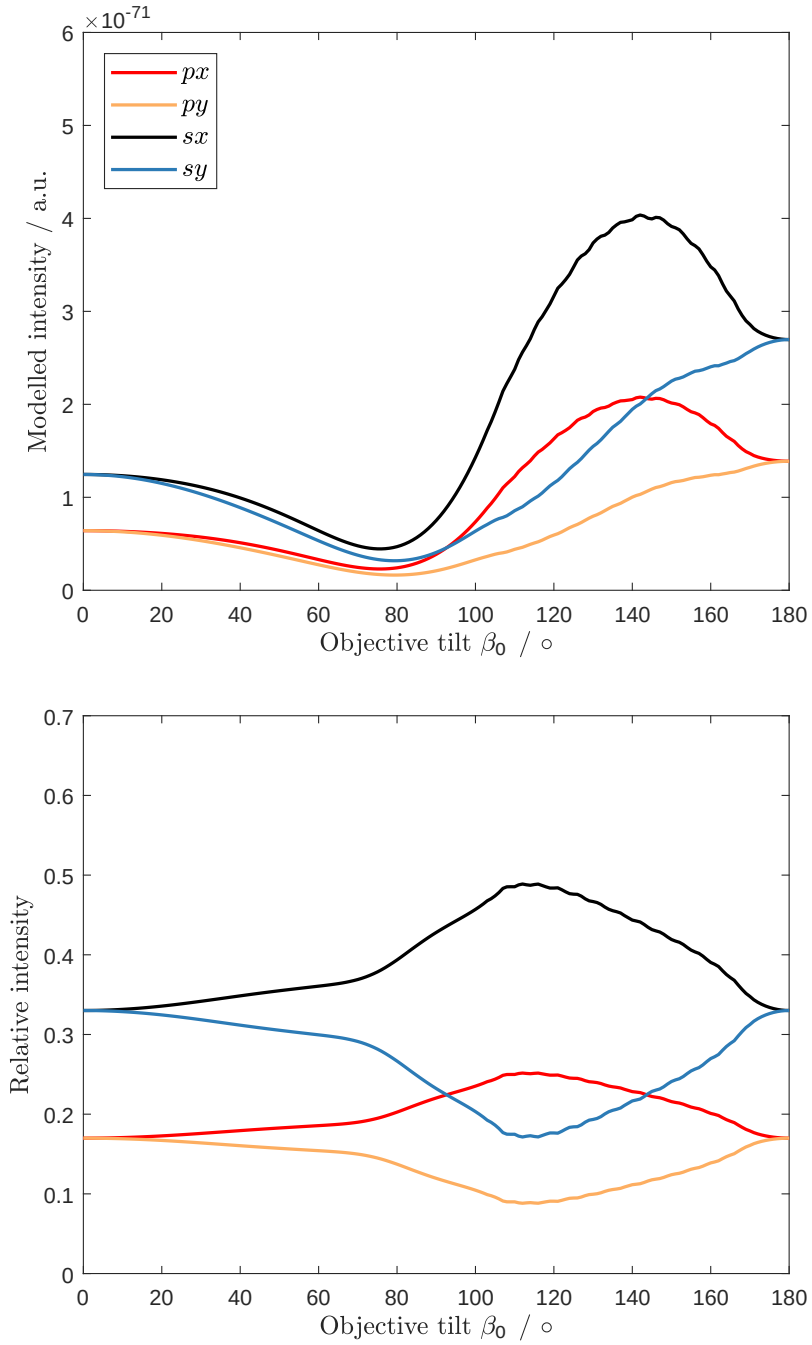

Figure 6.38: As figure 6.37 but with mode 76 of decanoic acid, its strongest CH_2 antisymmetric stretch.

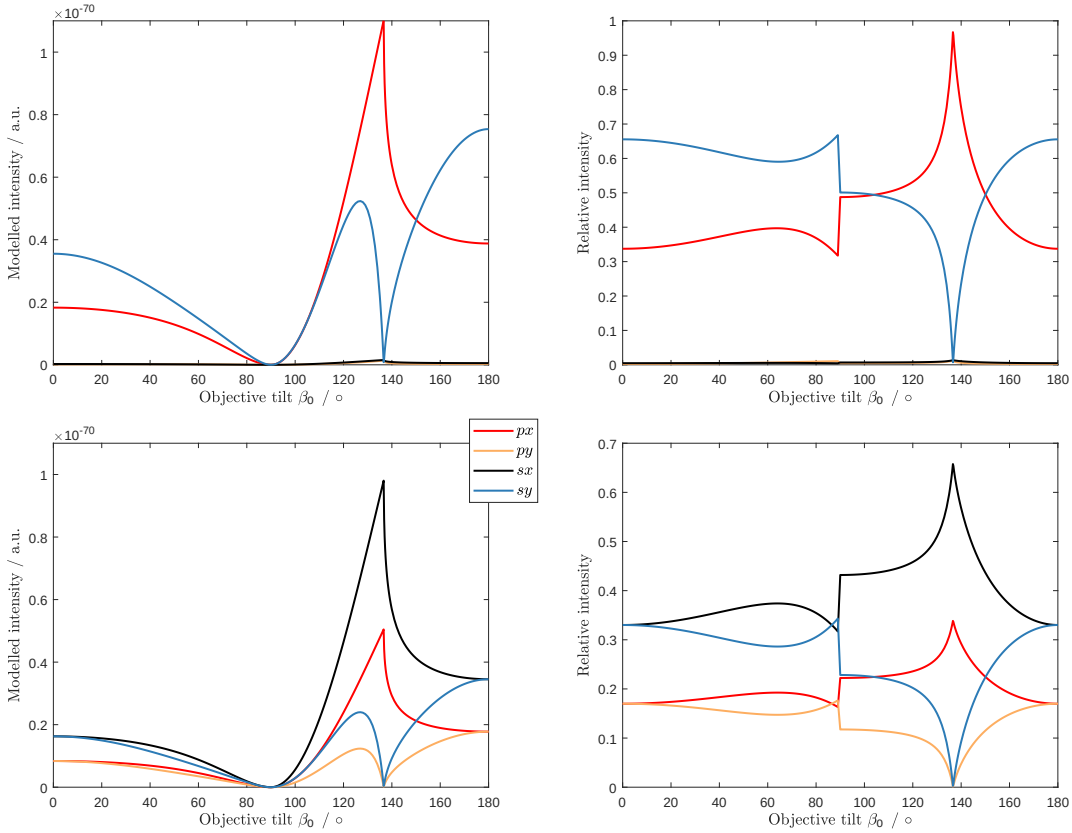

Figure 6.39: Modelled absolute and relative intensities for mode 73 (top) and 76 (bottom) of decanoic acid as a function of microscope objective tilt angle β_O as NA $\rightarrow$ 0. The other model input parameters conform to the Stockholm arachidate experiments.

The accuracy of refractive indices was discussed in section 3.2.4 and it is here checked whether this might significantly alter our interpretation of the arachidate data in the thin-film limit.

The modelled intensities from both the symmetric and antisymmetric CH_2 stretch modes increases with increasing n_2. However, the relative intensities are constant for the antisymmetric stretch (not shown) and plateau for the symmetric stretch (figure 6.40). The relative intensities of the latter converge at about $n_2 = 1.2$. This value is lower than any refractive index considered for the alkane interfacial layer. It is thus not required to specify this refractive index with great precision for upright alkanes in this experimental geometry as it does not affect the modelling outcome.

Finally, we assess the impact on the modelled intensities of variations within the Raman tensor. In $\nu_s(CH_2)$ mode 73, the zz component $\alpha^{\mathsf{m}}_{73,zz}$ is varied in the range of 0–$2 \cdot 10^{-40}$ C V^{-1} m^2 (figure 6.41). Its xx and yy components mix due to orientational averaging over α_{m} at $\beta_{\mathsf{m}} = 0°$, so that additional variation of these two components would lead to redundant results. The modelled px and py intensities increase with increasing $\alpha^{\mathsf{m}}_{73,zz}$. This increase becomes noticeable when its value exceeds that of the $\alpha^{\mathsf{m}}_{73,xx}$ and $\alpha^{\mathsf{m}}_{73,yy}$ components (from roughly $40 \cdot 10^{-42}$ C V^{-1} m^2), leading to an increase in the relative py intensity at the expense of the relative sy intensity. However, even if the zz component of the Raman tensor for arachidate were to be twofold that of decanoic acid (relative to its xx and yy components), this would only affect the modelled intensities within 0.004 on their relative scale. This is deemed to be insignificant with respect to other errors in our analysis.

For antisymmetric CH_2 stretch mode 76, as similar analysis is performed on the yz component, which is equal to its symmetric counterpart zy. Modelling results are presented in figure 6.42 for the range from -0.3 to $0.3 \cdot 10^{-42}$ C V^{-1} m^2. A positive as well as negative range of $\alpha^{\mathsf{m}}_{76,yz}$ is sampled because its remaining non-zero element at xy, yx was computed to be negative (table 4.7). However, the sign turns out to be irrelevant here, as the plots are symmetric around $\alpha^{\mathsf{m}}_{76,yz} = 0$. As the yz component increases, the scattering intensities increase, though $I_{px} = I_{py}$ increase more than $I_{sx} = I_{sy}$. The relative intensities of the latter thus decrease with increasing $\alpha^{\mathsf{m}}_{76,yz}$.

The computed value for $\alpha^{\mathsf{m}}_{76,yz}$ is near zero and variation around this value does not provide significant changes in absolute nor relative intensities. Scattering is here dominated by the $xy = yx$ component of the Raman tensor. This only changes when the additional $yz = zy$ component is of a significant magnitude relative to the $xy = yx$ component. Similar behaviour is expected for the Raman tensors of the other $\nu_a(CH_2)$ modes, all of which have a relatively small component in addition to a clearly dominant component. The only exception is mode 87, which is the weakest Raman scattering mode in the C−H stretch band. The same considerations are expected to hold for the antisymmetric CH_2 stretch modes of longer alkane chains. In an infinite chain, the A'' modes are not Raman active as all polarisability changes in the vibrational normal mode then cancel each other.

From this sensitivity analysis, we may conclude that reasonable variation in the model

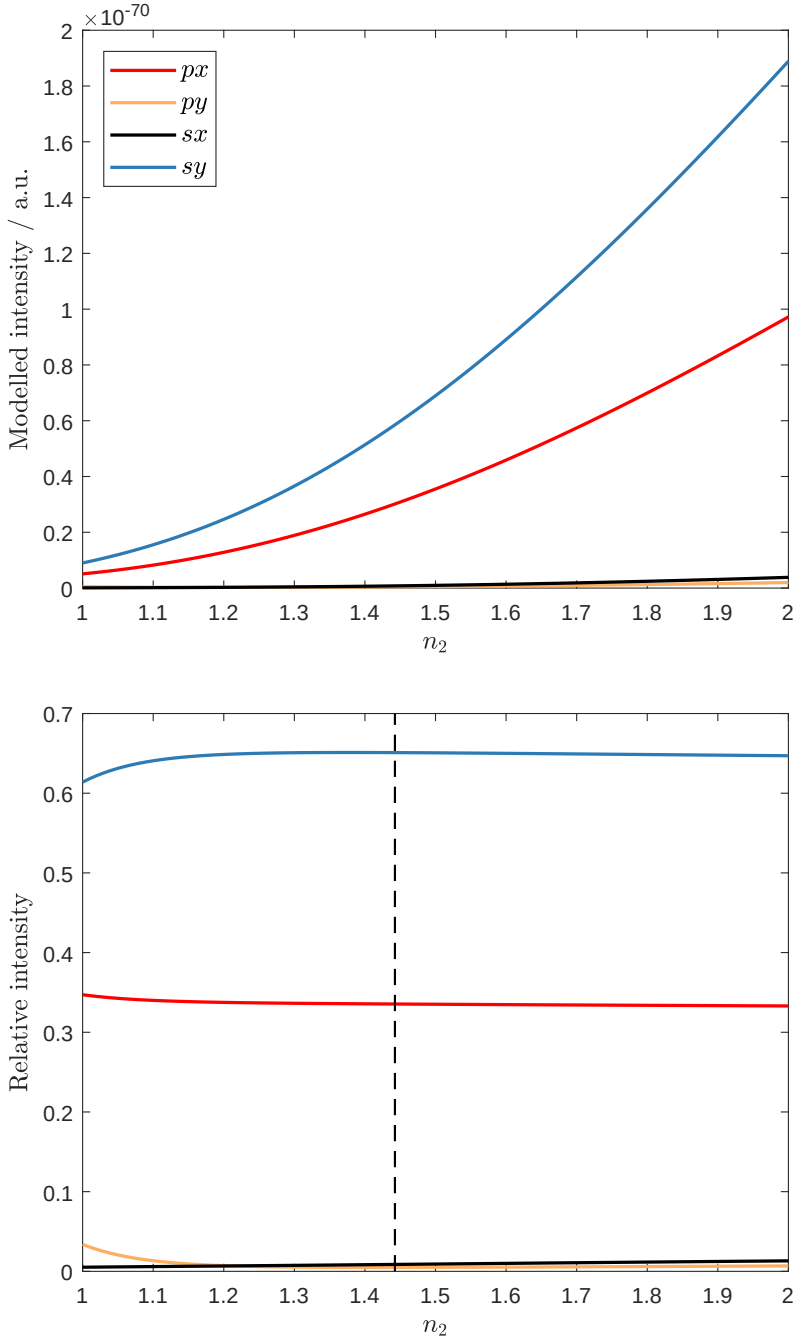

Figure 6.40: Modelled absolute and relative intensities arising from mode 73 of decanoic acid (the dominant $\nu_s(CH_2)$ mode) at the silica-air interface as a function of n_2, the refractive index of the interfacial alkane layer. The estimated value used in other calculations is indicated with a dashed line. Other model input parameters conform to the Stockholm arachidate experiments.

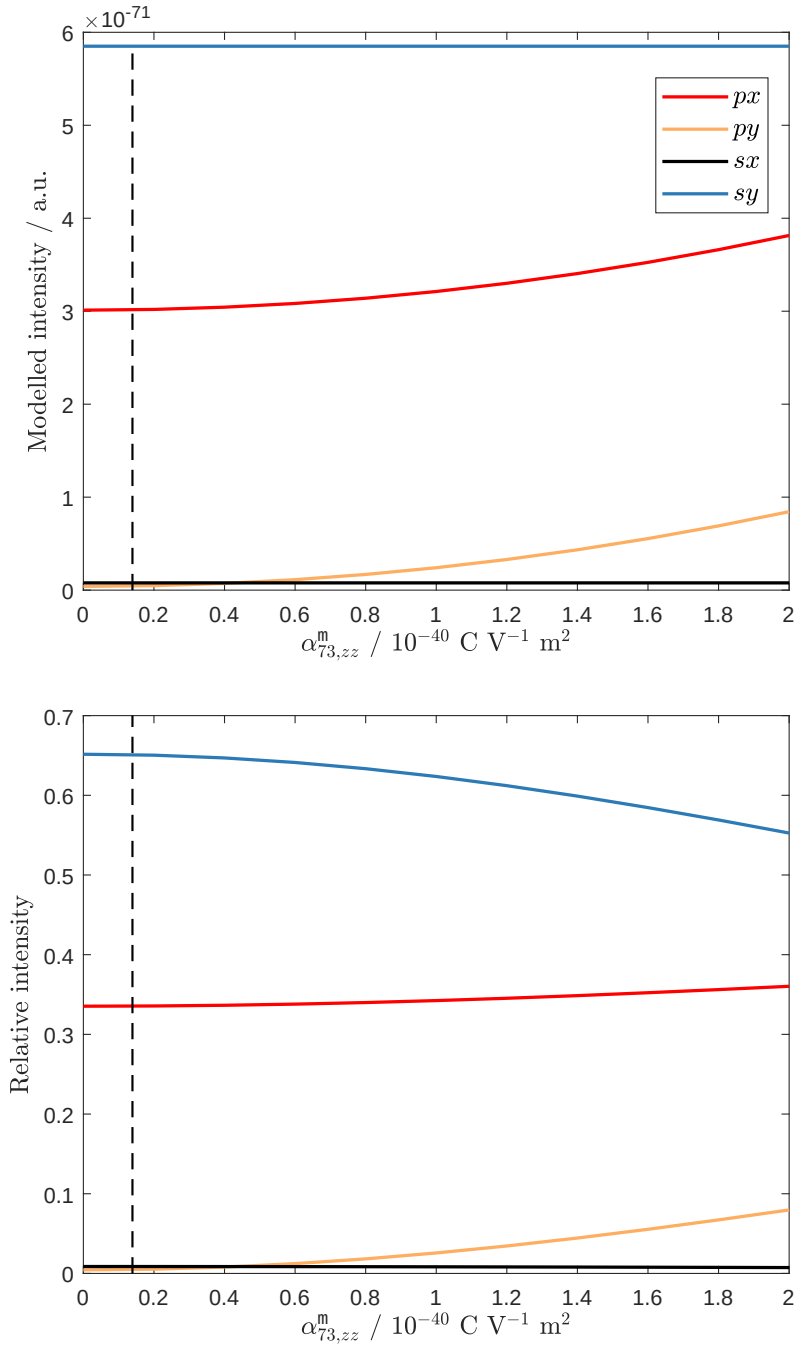

Figure 6.41: Modelled absolute and relative intensities for the dominant $\nu_s(CH_2)$ (mode 73) of decanoic acid at the silica-air interface as a function of $\alpha^{\mathtt{m}}_{73,zz}$. The estimated value used in other calculations is indicated with a dashed line. Other model input parameters conform to the Stockholm arachidate experiments.

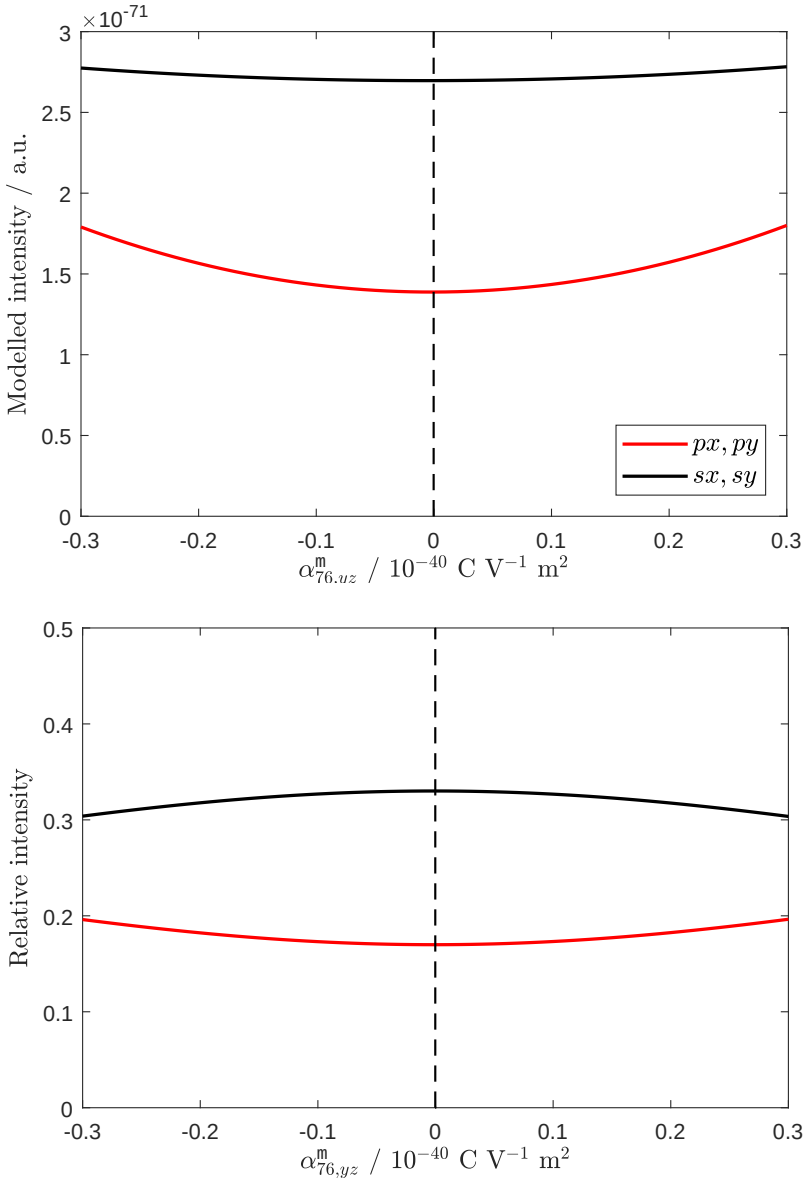

Figure 6.42: Modelled absolute and relative intensities for the dominant $\nu_a(CH_2)$ (mode 76) of decanoic acid at the silica-air interface as a function of $\alpha^{\mathtt{m}}_{76,yz} = \alpha^{\mathtt{m}}_{76,zy}$. The estimated value used in other calculations is indicated with a dashed line. Other model input parameters conform to the Stockholm arachidate experiments.

input parameters does not significantly affect the resulting relative intensities around the parameters of the arachidate Raman experiment. The modelling results further show that there is room for experimental optimisation, in particular by lowering the angle of laser incidence towards the critical angle and/or by collecting Raman scattering around this angle.

Table 6.6: Modelled relative intensities arising from $\nu_s(CH_2)$ mode 73 and $\nu_a(CH_2)$ mode 76 of decanoic acid, modelled in this molecule and in arachidate at a silica-air interface according to the Stockholm experiment.

β_{m}	mode	model	px	py	sx	sy
0°	$\nu_s(CH_2)$	arachidate	0.3352	0.0049	0.0091	0.6509
	$\nu_s(CH_2)$	decanoic acid	0.3355	0.0049	0.0087	0.6509
	$\nu_a(CH_2)$	arachidate	0.1699	0.1699	0.3301	0.3301
	$\nu_a(CH_2)$	decanoic acid	0.1699	0.1699	0.3301	0.3301
90°	$\nu_s(CH_2)$	arachidate	0.2860	0.0753	0.1147	0.5240
	$\nu_s(CH_2)$	decanoic acid	0.2973	0.0632	0.0923	0.5471
	$\nu_a(CH_2)$	arachidate	0.3071	0.1913	0.1383	0.3633
	$\nu_a(CH_2)$	decanoic acid	0.3071	0.1913	0.1383	0.3633

The relative intensities as modelled for decanoic acid are listed in table 6.6 for both $\beta_{\mathsf{m}} = 0°$ and 90°, using the Raman tensors computed for decanoic acid and the experimental parameters of the zinc arachidate Raman experiments. Similar computations have been performed with the estimated molecular polarisability and shape parameters of arachidate (relevant for the local field correction), keeping the other input parameters identical. The values are found to agree with those computed for decanoic acid up to at least three decimals when $\beta_{\mathsf{m}} = 0°$. This is in line with our findings that the local field correction does not significantly affect the relative intensities. Furthermore, the same values would be obtained for any stretched alkane of at least ten carbon atoms. These relative intensities approach the experimentally derived relative intensities of table 6.5, suggesting a roughly upright orientation of the alkane chains.

If the alkane chain is oriented parallel to the interface ($\beta_{\mathsf{m}} = 90°$), slightly different relatives intensities are found for arachidate compared to decanoic acid with the symmetric stretch mode. This difference remains small, with a maximum of ± 0.023 on a scale from 0 to 1. We may thus conclude that variation of the parameters for a flat chain has a larger effect on the modelled relative intensities, though still to an arguably insignificant level.

6.4.3 Molecular tilt of the arachidate monolayer

As observed from a comparison to the modelled spectra of figures 6.31 and 6.32, the experimental spectra of figure 6.30 conform better to the modelled spectra for an upright alkane chain than to those for a chain oriented parallel to the interface. We now investigate further the intensity variation as a function of β_{m}, aiming to quantify the tilt of the zinc

arachidate monolayer from the Stockholm experiments. We first compute the arachidate Raman spectrum in the ν(CH) band as a function of its molecular tilt angle. This provides us with modelled (relative) intensities for the whole band as well as d^+ and d^- peak intensities at the four standard polarisation combinations. Intensities are next computed for the dominant $\nu_s(CH_2)$ and $\nu_a(CH_2)$ modes to see whether these can be used to avoid computation of the whole band. Various methods of fitting the modelled intensities to the experimental intensities are presented.

The C-H stretch band

Modelled spectra of the C−H stretch region in the harmonic approximation are presented in figure 6.43 for each polarisation combination in the employed experimental geometry using various molecular tilt angles. These spectra arise from the Raman tensors of decanoic acid (modes 71-89) and the molecular parameters estimated for arachidate and thus resemble the spectra of figures 6.31 and 6.32. The computed intensities for each Raman line is convoluted with a Lorentzian profile of 10 cm^{-1} fwhm to generate the spectrum. β_m was sampled in steps of 2°, though shown at larger intervals in figure 6.43 for clarity.

The modelled spectra indicate that the scattering intensity detected in the *px* and *sy* polarisation combination reduces with increasing tilt of the molecule. However, when employing the *py* or *sx* polarisation combination, the d^- peak decreases while the d^+ peak increases with increasing β_m. The ν(CH) spectrum thus changes qualitatively in these cases. The methyl modes (around 3080 cm^{-1}) hardly change with molecular tilt angle and thus do not form a probe of alkane chain tilt.

We further observe that the heights of the d^+ and d^- peaks approach each other as β_m increases towards 90°. Changes in the spectra are most prominent around $\beta_m \approx 45°$ and smallest around 0° and 90°. This indicates a comparison between experimental data and modelled spectra is most sensitive to small changes in β_m in its central range (at least in this Raman scattering geometry). However, the fractional reduction of the d^- peak intensity is not the same for each polarisation combination. This suggests that relative intensities (that is, a peak intensity recorded at a particular polarisation combination relative to those recorded at other polarisation combinations) are a useful measure in analysing the spectrum. For example, the d^- intensity in the modelled *sx* spectrum is increased by a factor of about four at $\beta_m = 0°$ compared to $\beta_m = 90°$ while in the *px* spectrum, this increase is distinctly lower at a factor of about two. In this example, the ratio $I_{px}(d^-)/I_{sx}(d^-)$ might thus be an indicator for β_m.

The experimental spectra of figure 6.30 present peaks at frequencies different to those of the modelled spectrum. This arises from a known off-set between quantum-mechanical computations and actual Raman spectra (addressed in section 4.3) and from the presence of Fermi resonances in the experimental spectrum, which shifts interacting peak frequencies away from each other. These resonances also account for a significant intensity below the d^- peak in the experimental spectra, which is most prominent with the *px* and *sy*

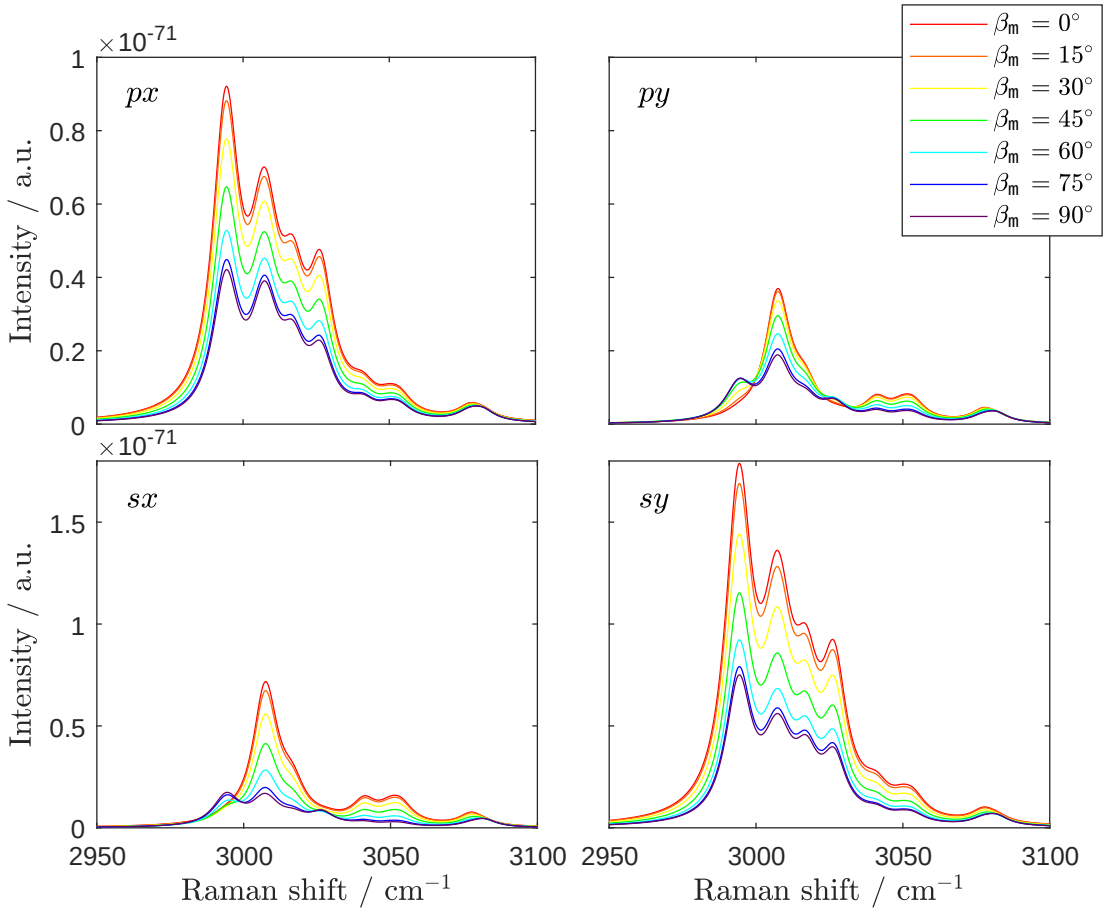

Figure 6.43: Modelled harmonic Raman spectra of the ν(CH) band for arachidate at the silica-air interface for various molecular tilt angles β_{m} with respect to the interface normal. The spectral intensities are summed over the full full range of molecular azimuthal and twist angles. Modelling parameters conform to the arachidate Raman experiment while employing computational Raman tensors of decanoic acid (modes 71-89). Each modelled Raman line is convoluted with a Lorentzian of 10 cm^{-1} fwhm to generate the spectra.

polarisation combinations. In absolute terms, the d^+ and d^- peaks are at equal intensities in the experimental spectrum. Such behaviour is only seen in the modelled harmonic spectra near $\beta_{\mathsf{m}} = 90°$ which is however based on an unrelated effect because the latter omit Fermi resonances.[§] The py and sx spectra of the experiment show hardly any d^+ intensity as well as a broadening of the d^- peak towards higher Raman shift. Both features conform to the modelled intensities, in particular to those at low molecular tilt angles.

Intensities are now derived from the modelled spectra of figure 6.43 to quantify their variation with respect to β_{m}. Figure 6.44 shows values obtained for the total intensity of the C−H stretch band $I(\nu(\mathrm{CH}))$, the peak intensities $I(d^+)$ and $I(d^-)$ for each of the four polarisation combinations while intensities attributed to the dominant $\nu_s(\mathrm{CH_2})$ and $\nu_a(\mathrm{CH_2})$ modes are shown in figure 6.45. Both absolute and relative intensities are shown and compared to the experimentally obtained relative intensities of table 6.5. Modelled intensities are obtained similarly to the experimental intensities explained above, though the frequency ranges differ as follows. The $\nu(\mathrm{CH})$ band is integrated from 2950 to 3100 $\mathrm{cm^{-1}}$, the d^+ peak is located at 2995 $\mathrm{cm^{-1}}$ and d^- at 3008 $\mathrm{cm^{-1}}$. The $\nu_a(\mathrm{CH_2})$ mode intensities are obtained by integrating the low-frequency side of the d^+ peak between 2950–2995 $\mathrm{cm^{-1}}$ while the $\nu_a(\mathrm{CH_2})$ mode intensities are obtained by integration over the range 3002–3014 $\mathrm{cm^{-1}}$ after removing a third-order polynomial baseline, fitted to spectral windows of 4 $\mathrm{cm^{-1}}$ on either side of this range.

Though the amount of Lorentzian broadening of the modelled Raman lines is arbitrary, picking a realistic value should reduce erratic effects in integrated intensities derived from the modelled spectra. Here, the choice of a fwhm of 10 $\mathrm{cm^{-1}}$ results in a half-width of the d^+ peak at its low-frequency side of about 35 $\mathrm{cm^{-1}}$ from top to baseline, which is similar to that observed in the experimental spectra. It is thus expected that the essential features due to line broadening are captured with this fwhm value.

Agreement with the experimental relative intensities is seen for the intensity metrics based on the full $\nu(\mathrm{CH})$ band, the d^+ and d^- peak heights and the $\nu_s(\mathrm{CH_2})$ intensity, assessed by integration over the low-frequency half of the d^+ peak. However, the $\nu_a(\mathrm{CH_2})$ intensities do not agree well. A difference in the order of the intensities is most striking. Whereas $I_{sx} > I_{sy} > I_{py} > I_{px}$ is obtained from the experimental spectra, the order is $I_{sy} > I_{sx} > I_{px} > I_{py}$ for the modelled spectra. A likely cause for this difference lies in the removal of the A' background, which introduces error in deriving the $\nu_a(\mathrm{CH_2})$ intensities. If the model is assumed essentially correct, based on the agreement found with the other intensity metrics, we may conclude that the A' background is overestimated in the px and sy spectra. This results in decreased $I_{px}(\nu_a(\mathrm{CH_2}))$ and $I_{sy}(\nu_a(\mathrm{CH_2}))$ values relative to $I_{py}(\nu_a(\mathrm{CH_2}))$ and $I_{sx}(\nu_a(\mathrm{CH_2}))$, which are less prone to error in the subtraction routine because the background is much weaker.

As previously observed, the modelled and experimental intensities match best at low β_{m} in our current plots as well. This is quite surprising for the d^- peak height, which

[§]The Fermi resonances could be quantified based on observed differences between the harmonic modelled spectra and the anharmonic experimental spectra.

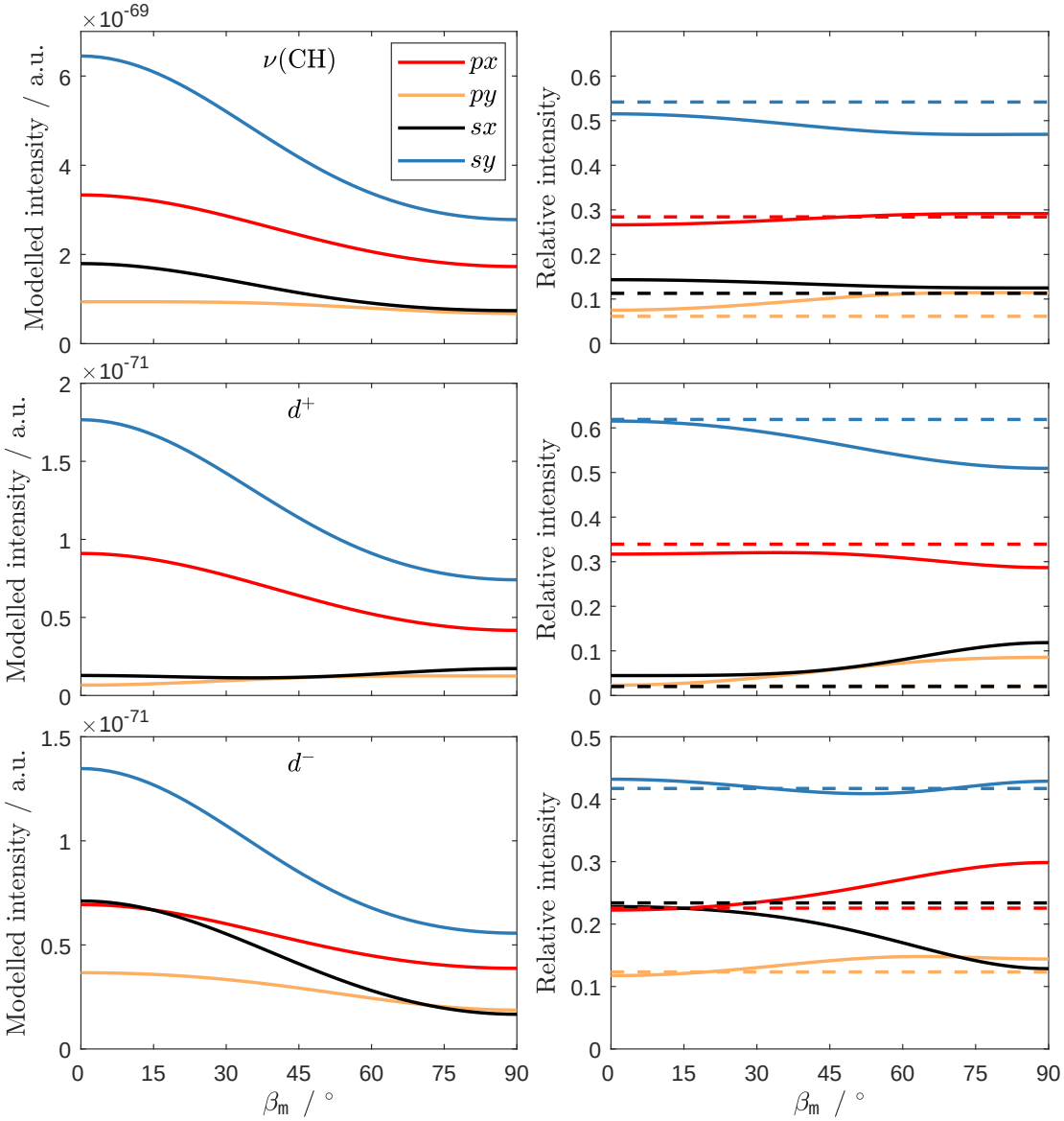

Figure 6.44: Absolute and relative harmonic intensities modelled for the ν(CH) band (top), the d^+ peak (centre) and the d^- peak (bottom) of arachidate at the silica-air interface as a function of molecular tilt angle β_{m} (derived from the modelled spectra presented in figure 6.43). Corresponding experimental relative total intensities are indicated by dashed horizontal lines.

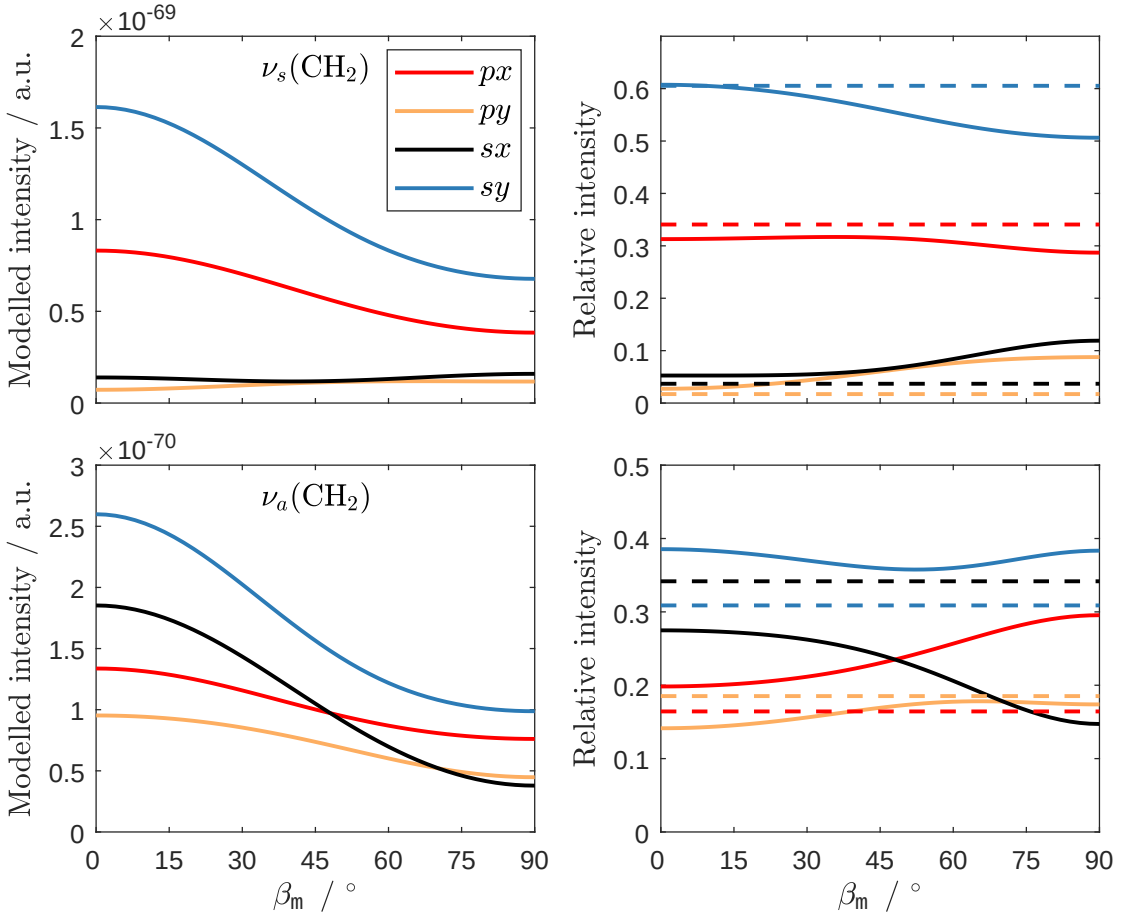

Figure 6.45: Absolute and relative $\nu_s(CH_2)$ (top) and $\nu_a(CH_2)$ (bottom) mode intensities obtained from modelled harmonic spectra of the ν(CH) band of arachidate at the silica-air interface at various molecular tilt angles β_m (derived from the modelled spectra presented in figure 6.43). Corresponding experimental relative total intensities are indicated by dashed horizontal lines.

includes Fermi resonances and additional stretch modes in the experimental but not in the modelled spectra. These effects might scale roughly proportionally with the height of the d^- peak, resulting in the fortuitous agreement between relative intensities observed here.

Best fit metrics

Where the experimental and modelled (relative) intensities match (or at least agree most closely), a 'best fit' is found for the molecular tilt angle. However, the best fit value does not result in the same value for β_m for each polarisation combination. Moreover, some of the modelled intensity curves do not cross the corresponding experimentally determined line. A metric is thus required to provide a best fit using the whole dataset or selected parts thereof. The absolute or relative intensities may be compared within a set of four values, arising from the four polarisation combinations. At a perfect fit, all modelled relative intensities match those observed in the experiment. Likewise, a ratio of absolute intensities from model and experiment should provide the same value for all four polarisation combinations when the model accurately describes the experimental observation. We may also compare multiple features in a spectrum simultaneously, enlarging the dataset.

We first determine a best fit for each of the five intensity metrics of figures 6.44 and 6.45 using all four (relative) intensities indiscriminately. This results in best-fit values ranging between $\beta_\mathsf{m} = 0°$ and 46° (table 6.7) using the three fitting metrics shown in figure 6.50. These metrics are all normalised for mutual comparison and involve the following.

- $\mathrm{var}(I_\mathsf{mod}/I_\mathsf{exp})$, the variance arising from the ratios of the modelled intensity to the experimental intensity at each polarisation combination. If the variance is low, the ratios are similar for all polarisation combinations (and all peaks, where applicable), which thus indicates that the modelling result conform to the experimental observation.

- $\mathrm{var}(I_\mathsf{mod,rel}/I_\mathsf{exp,rel})$, the variance arising from the ratios of the modelling relative intensity to the experimental relative intensity at each polarisation combination. The best fit for the molecular tilt angle β_m is here obtained from the minimum of the model-to-experiment relative intensity ratio variance.

- $\Sigma(I_\mathsf{mod,rel} - I_\mathsf{exp,rel})^2$, the sum of the squared differences between the modelled and experimental relative intensities. This metric provides a least-squares fit of the modelled to the experimental relative intensity.

The variance is calculated here as the square of the standard deviation, that is as

$$\mathrm{var}(\mathbf{f}) = \frac{1}{N-1}\sum_{i=1}^{N}(f_i - \bar{f})^2 \tag{6.9}$$

where $\mathbf{f}$ is a vector of N elements, each with a value f_i, having a mean of $\bar{f}$. Each of the above fitting metrics is computed based on four intensity values ($N = 4$), *i.e.* one for each

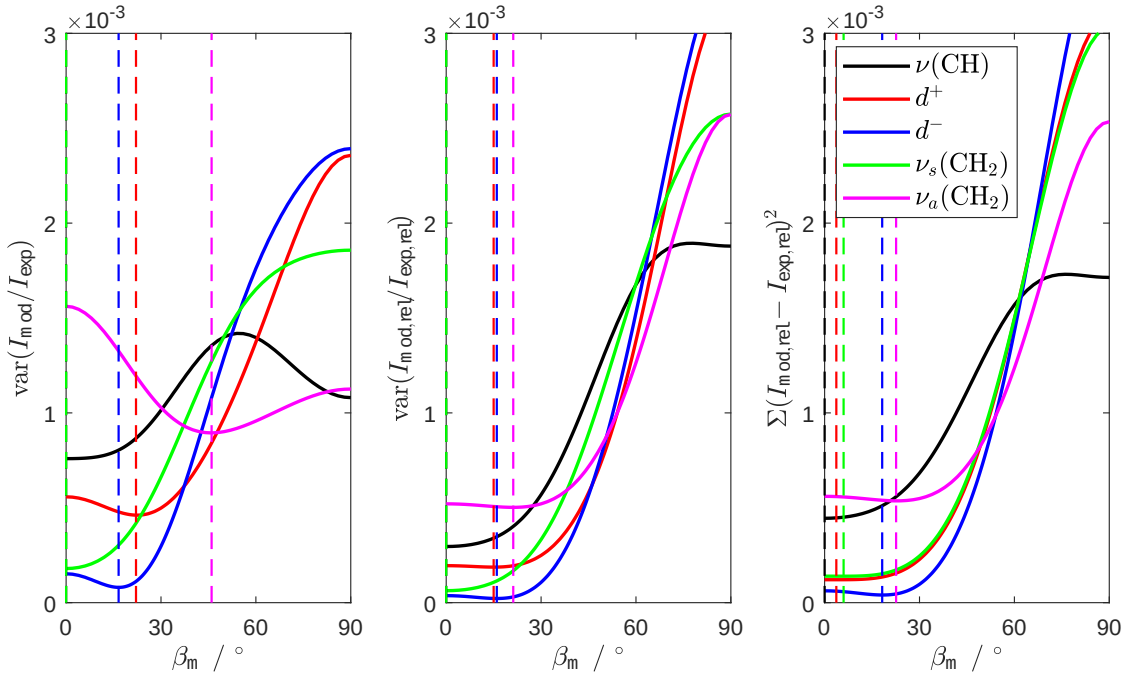

Figure 6.46: Metrics comparing modelled intensities to experimental intensities as a function of molecular tilt angle β_{m}. The intensity metrics of figures 6.44 and 6.45 are compared to corresponding experimental intensities. Each curve is normalised to bring it to the same scale. In the left-hand plot, the variance of the model-to-experiment intensity ratio is used, while in the centre plot, the variance is similarly computed with relative intensities. In the right-hand plot, the sum of the squared residuals is shown for the modelled minus experimental relative intensities. The minima represent 'best fit' values for β_{m} (table 6.7), indicated as a vertical dashed line with each curve.

Table 6.7: Best fit molecular tilt angles of arachidate at the silica-air interface for various intensities of the modelled harmonic ν(C−H) band (figures 6.44, 6.45 and 6.47).

metric	$I(\nu(\mathrm{CH}))$	$I(d^+)$	$I(d^-)$	$I(\nu_s(\mathrm{CH_2}))$	$I(\nu_a(\mathrm{CH_2}))$
$\mathrm{var}(I_{\mathsf{mod}}/I_{\mathsf{exp}})$	0.0°	22.1°	16.6°	0.0°	46.0°
$\mathrm{var}(I_{\mathsf{mod,rel}}/I_{\mathsf{exp,rel}})$	0.0°	15.0°	16.0°	0.0°	21.2°
$\Sigma(I_{\mathsf{mod,rel}} - I_{\mathsf{exp,rel}})^2$	0.0°	3.7°	18.2°	6.0°	22.6°
I_{px}/I_{sy}	-	35.4°	-	44.6°	-
I_{py}/I_{sx}	-	-	11.1°	-	17.6°

of the four polarisation combinations. As a function of β_{m}, a global minimum is observed in each of these metrics, indicating the best fit of the model to the experimental data at a particular value of β_{m}.

Figure 6.50 shows the fitting metrics as a function of β_{m}. The best fit varies between intensity metrics. For the $\nu_a(\mathrm{CH_2})$ intensity, right-hand bottom plot in figure 6.45 already showed general disagreement between modelled and experimental intensities. A minimum in best-fit metric can still be found (at the highest β_{m} value in each metric), though this is not indicative of a physical parameter that describes the monolayer. The other metrics provide a molecular tilt ranging from $0 - 22°$.

The lowest best-fit metrics are obtained with the d^- intensities with minima in the relative narrow range of $16.0 - 18.2°$. This is a consequence of the relatively close match between modelled and experimental relative intensities (bottom right-hand plot of figure 6.44). The choice of fitting metric is less relevant in this case. In contrast, the $\nu_s(\mathrm{CH_2})$ and d^+ intensities provide more disparate tilt angles.

With the $\nu(\mathrm{CH})$ intensities, the monolayer is determined to comprise fully upright chains. This is also found with the $\nu_s(\mathrm{CH_2})$ intensities with the variance-based fitting metrics. However, it contrasts with the other tilt angles which are all non-zero. This arises from an underestimate of the modelling intensities for the *px* and *sy* spectra while overestimating the *py* and *sx* relative intensities (top right-hand plot in figure 6.44). Similar behaviour is observed with the $\nu_s(\mathrm{CH_2})$ and d^+ intensities. This may be caused by absence of anharmonic effects as well as additional modes (due to the longer arachidate chain) in the modelled spectra. The *px* and *sy* experimental spectra contain these Fermi resonances and additional modes that enhance the total intensity in the C−H stretch band. The relative *px* and *sy* intensities are thus increased at the cost of those in the *py* and *sx* spectra. The limiting value of $\beta_{\mathsf{m}} = 0°$ then provides the best fit, though the modelled intensities still deviate from the experimental intensities. In these cases, comparison of all four polarisation combinations at once results in skewing the fit towards low tilt angles.

Intensity ratios

From the above considerations, we may wish to omit the more error-prone intensities from our analysis in order to improve the fit of our model to the experimental intensities. Intensity ratios may be used to this end. Note that the often employed empirical ratio $I(d^-)/I(d^+)$ should be avoided in our analysis, as the modelled spectra do not include the anharmonic effects known to significantly alter scattering intensities in this Raman band.

First, we omit the near-zero d^+ peaks in the *py* and *sx* polarisation combinations from our analysis. These near-zero intensities vary greatly due to noise and thus contribute to a large error in the extracted intensity values. The d^+ feature is then analysed based on I_{px} and I_{sy}, which resemble polarised conventional Raman scattering. As only two values are involved, these may be characterised by their ratio $I_{px}(d^+)/I_{sy}(d^+)$.

Contrarily, the *px* and *sy* spectra are omitted for the d^- analysis because these include

errors introduces by subtraction of the fitted intensity arising from modes of the A' species. The py and sx polarisation combinations are clearly less obscured and resemble depolarised conventional Raman scattering spectra. Again, a ratio may be used to characterise the d^- feature, in this case $I_{py}(d^-)/I_{sx}(d^-)$.

Both of the above ratios are plotted in figure 6.47 *versus* the molecular tilt angle. Similar ratios based on the integrated $\nu_s(\mathrm{CH_2})$ and $\nu_a(\mathrm{CH_2})$ intensities are also presented. A 'best fit' between model and experiment may be estimated from these plots by interpolating the modelled data points. We find that the modelled ratio coincides with the experimentally derived ratio at molecular tilt angles of 11.1 and 17.6° from the d^- and $\nu_a(\mathrm{CH_2})$ ratios, respectively. This is consistent with the best-fit obtained above from comparison of the $I(d^-)$ in the $\nu(\mathrm{CH})$ band.

The d^+ and $\nu_s(\mathrm{CH_2})$ intensity ratios vary less strongly with β_m and provide a best fit at $\beta_\mathsf{m} \approx 35°$ and 45°. However, these values are inconsistent with the observation that the symmetric stretch modes are hardly visible in the experimental spectra. The absence of these peaks is stronger evidence. The disparate β_m values arise from variation in experimentally derived ratios, which are higher with the $\nu_s(\mathrm{CH_2})$ and $\nu_a(\mathrm{CH_2})$ integrated intensities than with the d^+ and d^- peak heights. The modelled intensity ratios are more consistent. From the analysis so far, we tentatively conclude a molecular tilt angle in the zinc arachidate monolayer in the range $11 - 18°$.

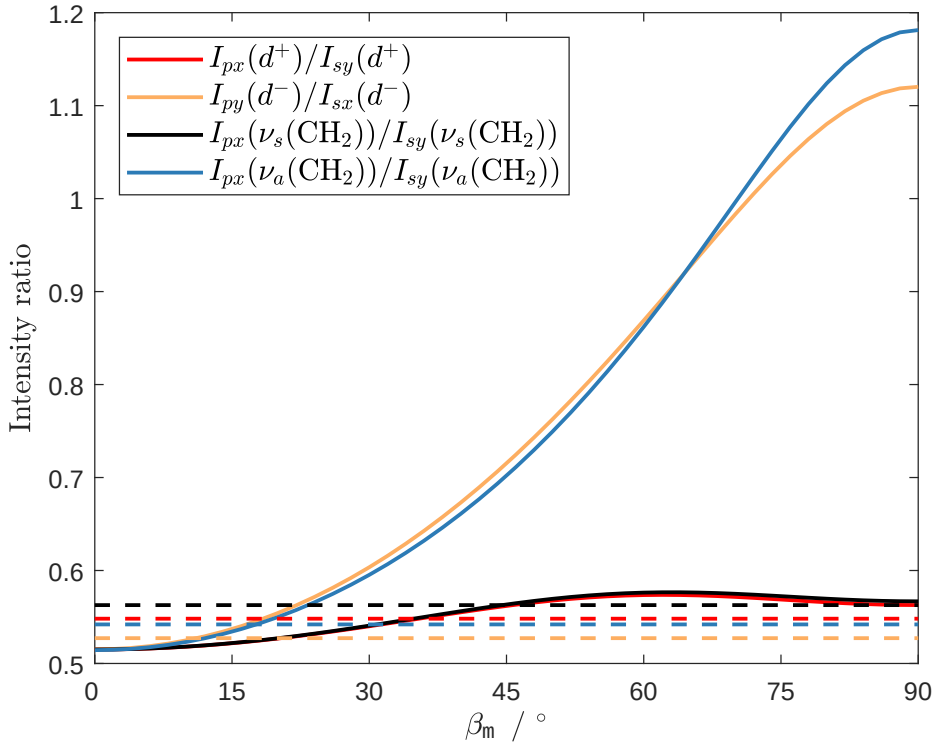

Figure 6.47: Ratios of modelled intensities at various molecular tilt angles β_m. Ratios from experimental intensities are presented as horizontal dashed lines, matching the colours of the modelled ratios.

We may quantify the combined contribution of the anharmonicities and additional symmetric stretch modes by analysing the mismatch between modelled and experimental relative intensities (the ν(CH) intensity metric of figure 6.44). This mismatch is evaluated at a tilt angle of 12°, found from the best fit of the d^- peak ratio which is least affected by the additional scattering intensity in the symmetric modes. Figure 6.48 shows the relative intensities for the whole ν(CH) band in which the modelled absolute px and py intensities have been multiplied by a factor ranging from 1 to 2. At 1.34, agreement is observed between the multiplied modelled intensities and the experimental intensities. This indicates that the modelled intensities for the px and sy polarisation combinations is underestimated. Additional symmetric modes and resonances between symmetric modes are thus expected to make up about 34% of the observed intensity. This value is an upper limit, as the py and sx spectra also contain additional intensity unaccounted for by the model. This includes both antisymmetric stretch modes as well as symmetric contributions that arise at the slightly tilted molecular orientation.

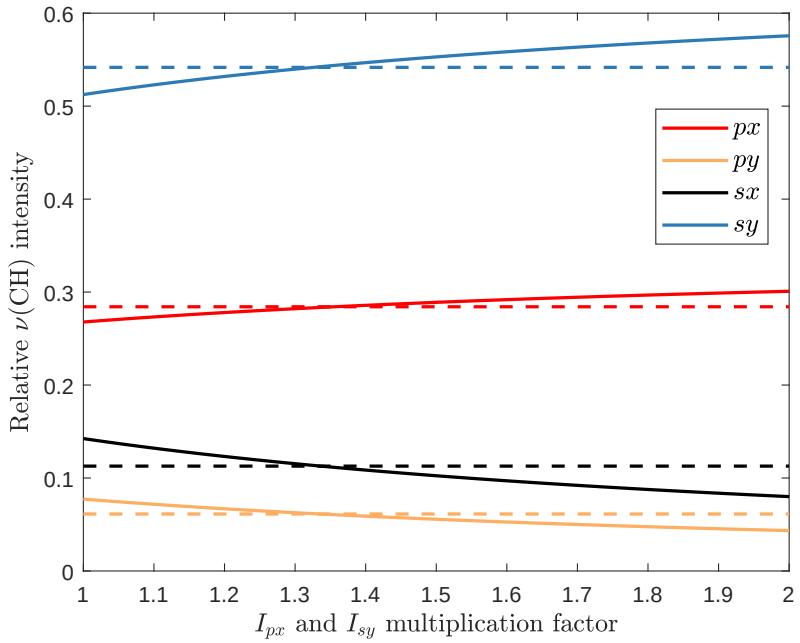

Figure 6.48: Modelled relative intensities for the ν(CH) band of arachidate at the silca-air interface at $\beta_{\mathsf{m}} = 12°$. The px and sy intensities have been multiplied by a factor from $1-2$ to assess the impact of additional symmetric stretch modes as well as resonances that are not included in the model. Corresponding intensities of the experimental spectra are indicated as dashed horizontal lines.

Individual modes

It would reduce computational expense if single modes were to capture to behaviour of relevant spectral features, at least sufficiently to assess a molecular tilt angle. We therefore

also investigate the dependence of scattering intensities on β_{m} for individual modes. The strongest symmetric and antisymmetric CH_2 stretch modes (modes 73 and 76 in decanoic acid) are employed as these were found to give rise to representative scattering intensities for all $\nu_s(CH_2)$ and $\nu_a(CH_2)$ modes, respectively, in the harmonic approximation for a stretched alkane chain. Mode 73 is the dominant $\nu_s(CH_2)$ mode, with in-phase symmetric stretch motion, and mode 76 is the dominant $\nu_a(CH_2)$ mode, having all methylene moieties vibrate with a phase shift of π relative to their nearest neighbours. Figure 6.49 shows the modelled intensities for each standard polarisation combination as a function of β_{m}. Experimentally derived relative intensities are also indicated as horizontal lines. We now further analyse these results.

For mode 73 of decanoic acid, I_{px} and I_{sy} decrease while I_{py} and I_{sx} increase when the molecular tilt increases. The intensities of this mode in the py and sx spectrum cross twice, though these are similar in intensity up to roughly $\beta_{\mathsf{m}} = 60°$, beyond which $I_{sx} > I_{py}$. However, $I_{sy} > I_{px}$ at all tilt angles. Comparing these modelling results to the experimental intensities, we note that all fall within the range obtained by modelling. Further, knowing that low tilt angles are applicable, the d^+ experimental values agree best with the modelling results for mode 73 with lower (relative) and equal intensities in the py and sx spectra.

The modelling results for mode 76 show that its Raman intensity decreases from a maximum value at $\beta_{\mathsf{m}} = 0°$, where $I_{px} = I_{py} < I_{sx} = I_{sy}$, to a minimum at $\beta_{\mathsf{m}} = 90°$, where the intensities are no longer equal but in the order $I_{sy} > I_{px} > I_{py} > I_{sx}$. As the p-polarised intensities increase less than those of s-polarisation, the relative px and py intensities increase with molecular tilt angle. The experimental $\nu_a(CH_2)$ intensities are nearest the modelled values, though fall outside the predicted range by up to 0.012 for the sx polarisation combination. The experimental d^- intensities do not match at all since these include intensity arising from additional A' modes in the arachidate chain and their Fermi resonances.

From our analysis so far, it is clear that the modelled intensities for mode 73 is best compared with the experimental d^+ peak height and those for mode 76 with the integrated $\nu_a(CH_2)$ intensity taken from the d^- peak of the experimental spectra. When all relative intensity data of figure 6.49 is used indiscriminately, we find best-fit values ranging between $\beta_{\mathsf{m}} = 15°$ and $41°$ (table 6.8) using the three metrics discussed above and shown in figure 6.50 for the current intensity metrics. Each of the fitting metrics is computed with eight intensity values ($N = 8$), *i.e.* one for each of the four polarisation combinations for each of the two peaks, as well as for each peak separately ($N = 4$). A single minimum is observed in each of these metrics.

The best-fit β_{m} varies between fitting metrics and intensity metrics. The variance and sum of squares are negatively affected by the worst fitting of the four (or eight) curves. A subset may be chosen to decrease their spread. The variance of the relative intensity ratios is particularly sensitive as an error in one of the absolute intensities will affect all relative intensities in the set of four values. For example, I_{sy} dominates in mode 73 at all

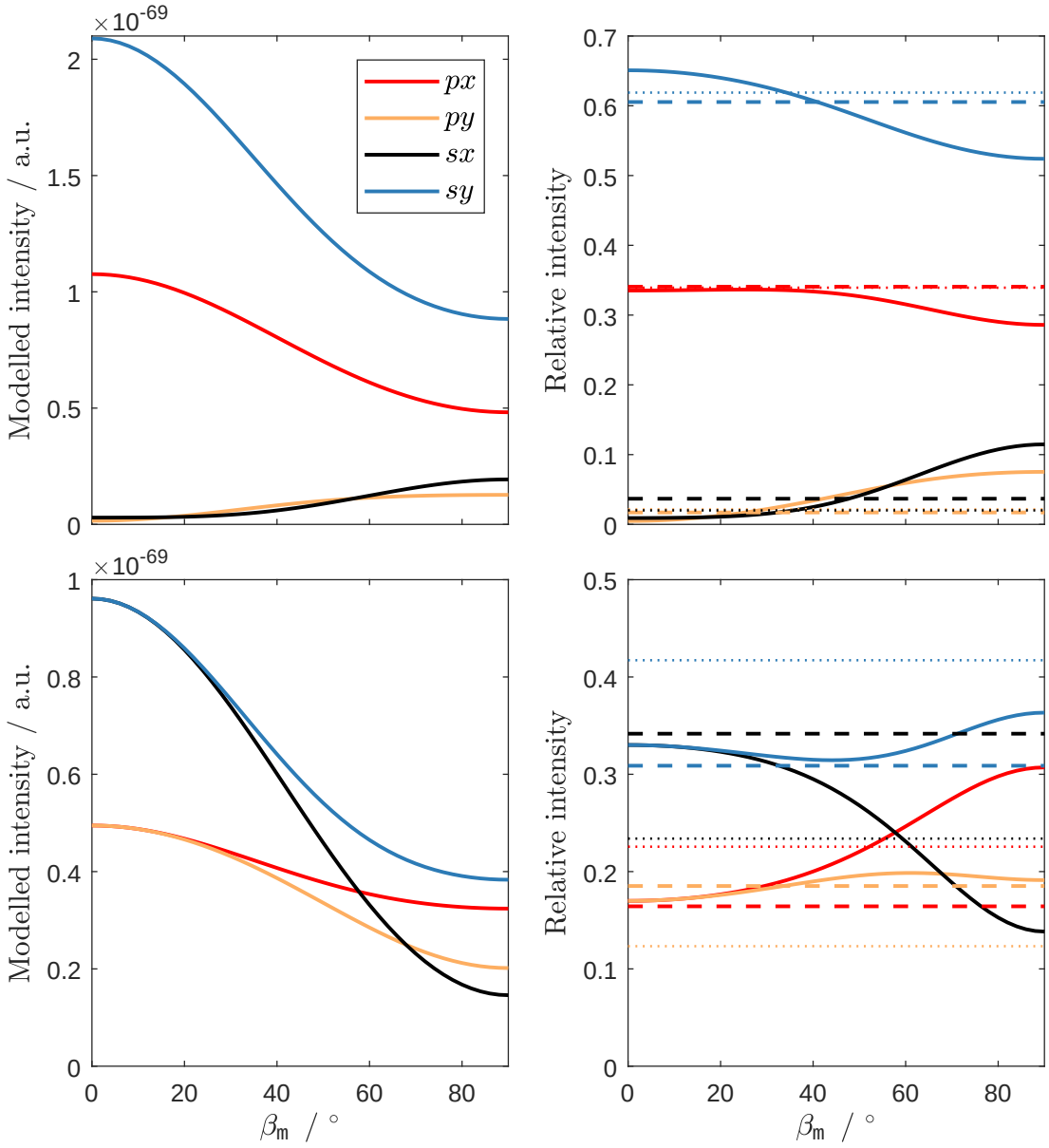

Figure 6.49: Modelled absolute and relative intensities for mode 73, the in-phase $\nu_s(CH_2)$ mode, (top) and mode 76, the π phase-shifted $\nu_a(CH_2)$ mode, (bottom) for arachidic acid at the silica-air interface as a function of molecular tilt angle β_m with respect to the surface normal. The experimentally derived relative intensities are indicated as horizontal lines for the d^+ and d^- peak heights (dotted) and for the integrated $\nu_s(CH_2)$ and $\nu_a(CH_2)$ intensities (dashed).

tilt angles (top right plot of figure 6.49) while the remaining relative intensities show a relatively flat curve, skewing the fitting result towards the best fit that would be found for the *sy* curve on its own. This makes the fitting procedure highly sensitive to what exact intensity was obtained from the experimental spectrum in the first place. For ratios of absolute intensities, there is no such 'cross-contamination' of error. The issue is also likely to arise in fitting procedures based on the sum of squared errors, though it appears less of a problem in that case as the best-fit value of the combined modes lies between those found for the individual modes.

As suggested by our analysis of the modelled ν(C−H) band, ratios of the substantially non-zero intensities may also be employed. This removes the near-zero, error-prone intensities from the analysis. Figure 6.51 presents the appropriate intensity ratios as a function of β_{m}. For mode 73, this is $I_{px}(v_{73})/I_{sy}(v_{73})$ which is compared to the ratio $I_{px}(d^+)/I_{sy}(d^+)$ of experimental peak heights. For mode 76, we have $I_{py}(v_{76})/I_{sx}(v_{76})$ for our modelling result as a function of β_{m} which is compared to $I_{py}(\nu_a(\mathrm{CH_2}))/I_{sx}(\nu_a(\mathrm{CH_2}))$ from our experimental spectra. A best fit in this case simply arises from matching ratios, arising at $\beta_{\mathsf{m}} = 38.8°$ and 18.6°, respectively (included in table 6.8). The precision of this value is given by the sampling of the curve and does not reflect the error arising from the method, which is influenced by the gradient of the modelled curve, amongst many other factors.

Though the molecular tilt angles derived from intensity ratios are higher than those obtained from the individual modes 73 and 76, the former lie within the shallow minimum observed in the best-fit metrics of the latter (figure 6.50). The shallow minimum arises from small variation in both absolute and relative intensities in the range $0° \leq \beta_{\mathsf{m}} \leq 40°$ predicted by our model.

In our previous analysis of similar ratios for intensities derived from modelling the ν(CH) band, a best fit was found at 11.1° and 17.6° for the I_{py}/I_{sx} ratios of antisymmetric stretch intensities compared to 18.6° here. Similarly, the I_{px}/I_{sy} ratio of symmetric stretch intensities produced a best fit at 35.4° and 44.6° which here lies is at 38.8°. This suggests that the analysis based on individual modes rather than the whole band leads to similar results. There is consistency between the various approaches, at least at the selected degree of line broadening involved in producing the model spectra.

6.4.4 Discussion

In this section, a summarising discussion of the employed methodology is given as well as a comparison between the molecular tilt angle of zinc arachidate monolayer at the silica-air interface deduced here to those found for similar interfaces in literature.

Methodology

Experimental Raman spectra of zinc arachidate present a convoluted C−H stretch band. Total band intensities can readily be obtain after subtraction of the silica signal, which

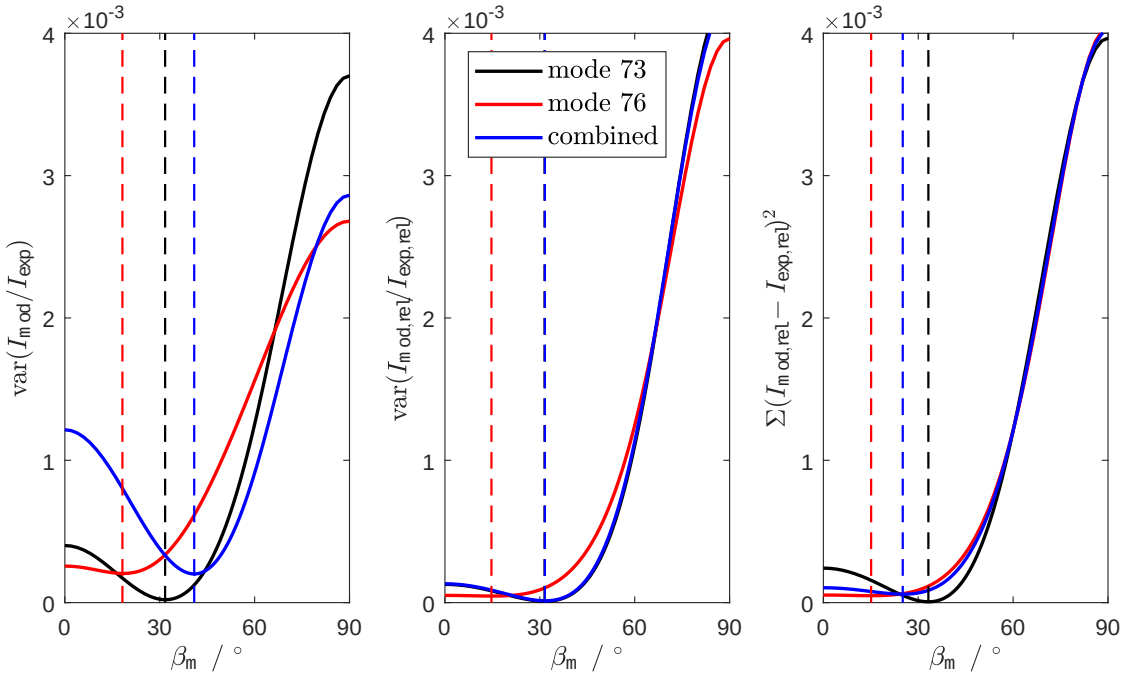

Figure 6.50: Metrics comparing modelled intensities to experimental intensities as a function of molecular tilt angle β_{m}. Intensities for mode 73 are compared to the experimental d^+ peak height and mode 76 to the integrated $\nu_a(\mathrm{CH}_2)$ intensity of the d^- peak. Each curve is normalised to bring them to the same scale. In the left-hand plot, the variance of the model-to-experiment intensity ratio is used, while in the centre plot, the variance is similarly computed but for relative intensities. In the right-hand plot, the sum of the squared residuals is shown for the modelled minus experimental relative intensities. The minima represent 'best fit' values for β_{m} (table 6.8), indicated as a vertical dashed line with each curve.

Table 6.8: Best fit molecular tilt angles of arachidate at the silica-air interface for individual modes of figure 6.50 and for intensity ratios of figure 6.51.

metric	mode 73	mode 76	combined
$\mathrm{var}(I_{\mathsf{mod}}/I_{\mathsf{exp}})$	31.7°	18.2°	40.9°
$\mathrm{var}(I_{\mathsf{mod,rel}}/I_{\mathsf{exp,rel}})$	31.5°	14.7°	31.6°
$\Sigma(I_{\mathsf{mod,rel}} - I_{\mathsf{exp,rel}})^2$	33.2°	15.1°	25.1°
I_{px}/I_{sy}	38.8°	-	-
I_{py}/I_{sx}	-	18.6°	-

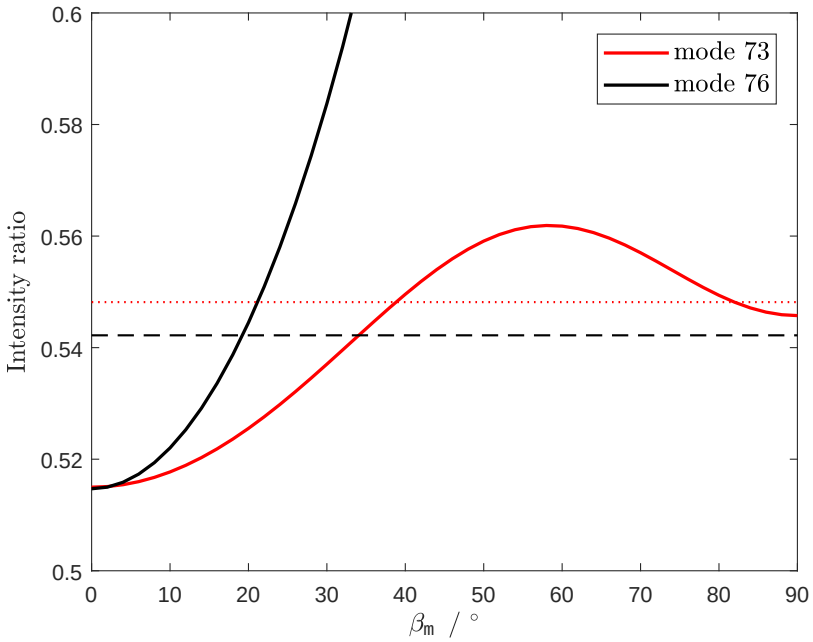

Figure 6.51: Ratio of modelled intensities for mode 73 ($I_{px}(v_{73})/I_{sy}(v_{73})$) and mode 76 ($I_{py}(v_{76})/I_{sx}(v_{76})$) as a function of molecular tilt angles β_{m}. Horizontal lines indicate corresponding experimental ratios $I_{px}(d^+)/I_{sy}(d^+)$ (dotted red) and $I_{py}(\nu_a(\mathrm{CH_2}))/I_{sx}(\nu_a(\mathrm{CH_2}))$ (dashed black). A 'best fit' for β_{m} is given in table 6.8.

may be approximated as a linear baseline in this region of the spectrum. It is more difficult to extract intensities that correspond to individual Raman modes. The d^+ and d^- peak heights are conventionally used. From our analysis, d^+ peak height is representative of intensities arising from harmonic $\nu_s(\mathrm{CH_2})$ modes while d^- peak heights do not correspond to any individual mode. The latter is a superposition of fundamental modes from both A' and A'' symmetries as well as Fermi resonances arising from interacting A' fundamentals.

Notwithstanding these complexities, fully harmonic computational spectra may be used to interpret experimental spectra and come to an estimate of the molecular tilt angle based on the presence or absence of a distinguishable d^+ feature. In the current case, absence of the d^+ peak in *py* and *sx* spectra is indicative of low β_{m}, that is, roughly upright alkyl chains.

The harmonic spectra are obtained by applying Raman tensors, found by *ab initio* computation for an isolated molecule, in our model. The model accounts for the optical geometry of the experiment while the Raman tensor (and molecular polarisability and ellipsoid radii) account for the molecular properties. Modelling for zinc arachidate was based on estimated molecular properties, using Raman tensors found for decanoic acid and extrapolating $\boldsymbol{\alpha}$ and r_z from this molecule and short alkane chains. Using these parameters was not found to provide significantly different modelled relative intensities compared to those modelled for decanoic acid.

The molecular orientation is used as an input variable to the model. As the orientations are averaged over all azimuthal (and twist) orientations, the local field correction applied by the model is only significantly affecting absolute modelled intensities, while relative values are not affected to a significant level. The local field correction may thus be omitted to accelerate computations in such a case.

The sensitivity of the modelled intensities with respect to changes in other input parameters was also assessed. Given the Raman tensor, the length of the alkane chain r_z appears irrelevant (beyond 0.4 nm). The same was found to be the case for the refractive index of the thin film and for Raman tensor elements. This implies that both parameters may be estimated without seeking to optimise their precision. This also hints at a more universal applicability of the modelling results (given the experimental geometry), as the modelled intensities vary little with chain length. Results obtained for a molecule with a particular alkyl moiety may thus be applied to Raman spectra of comparable other molecules collected in similar experimental geometries.

The model may also be used to optimise or design an experimental geometry. For example, the intensities of the zinc arachidate spectra could have been amplified by choosing a lower angle of laser incidence and/or by tilting the microscope objective with respect to the interface. In both cases, advantage is taken from the high coupling factors around the critical angle of the silica-air interface. This would also increase the intensities from symmetric modes in the *py* and *sx* spectra, which may be desired to obtain substantially non-zero scattering intensities.

Zinc arachidate tilt angle

Our model serves to account for the optical geometry, polarisation of the electric fields and the tensorial nature of the Raman effect while assuming a single molecular orientation. In determining a single molecular tilt angle for the zinc arachidate monolayer, we assume that the physical distribution of molecular orientations may be modelled by a single tilt and a uniform distribution over azimuth and twist angles.

The effect of a distribution of β_{m} values can be assessed by convoluting the absolute intensities with a β_{m}-distribution function. The $I(\beta_{\mathsf{m}})$ curves (such as in figure 6.49) would then show more linear behaviour. Such analysis would introduce another variable which may be derived but which also further complicates analysis.

The assumption that α_{m} and γ_{m} are randomly distributed is supported by experimental findings of the domain size of fatty acid chains and their salts. In condensed phases, these molecules pack in domains of $10^4 - 10^6$ Å^2 in which bond orientation is conserved [96]. These domains are much smaller than the area of the laser spot and microscope focus employed in our experiments. An abundance of domains is thus probed, all of which are independently orientated.

Tilt angles were derived from a variety of intensity metrics. First, the whole ν(CH) band was modelled as a function of β_{m}, using Raman tensors computed for decanoic acid

in the harmonic approximation with an arbitrary though realistic degree of Lorentzian line broadening. This spectrum was used to quantify molecular tilt, though the comparison to experimental spectra is hampered by lack of Fermi resonances in the A' modes and additional symmetric and antisymmetric CH_2 stretch modes in the modelled spectrum. These features mainly contribute to the central region of the C−H stretch band but also alter the d^+ peak position and height.

Various intensity metrics were derived from the experimental as well as the modelled spectra: overall intensity, d^+ and d^- peak heights and integrated $\nu_s(CH_2)$ as well as $\nu_a(CH_2)$ intensities. The last metric proved inadequate because a clean subtraction of the A' background is not presently possible. The other intensity metrics gave relative intensities that roughly agreed with the experimental ones, especially at low tilt angles. Best-fits were found in the range $0 - 22°$. The d^- in particular showed consistent best fit at $\beta_\mathsf{m} = 17.0°$.

The comparison between modelled and experimental intensities was found to be most sensitive to changes in β_m around $\beta_\mathsf{m} = 45°$. In this experimental geometry, it is hard to distinguish between tilt angles below about 30° as the intensities vary little in this range. Small variations, including errors in intensities extracted from experimental spectra, thus have a large effect on the derived molecular tilt angle. A promising metric is the variance between model-to-experiment intensity ratios. When using relative intensities, error in one of the four intensities impacts all others, thus skewing the best fit towards the most deviating relative intensity. This results in a shallower best-fit minimum.

Intensity ratios of the least error-prone features were also used. I_{px}/I_{sy} for the main symmetric stretch feature proved less sensitive to molecular tilt angle than the antisymmetric stretch ratio I_{py}/I_{sx}. Furthermore, the latter provided lower β_m values (11.1° and 17.6°) while the former came up to a value of about 45°, which disagrees with the absence of the d^+ feature in the experimental spectra. Based on the modelled C−H stretch band, this absence indicates $\beta_\mathsf{m} < 30°$.

Scattering intensities from the dominant $\nu_s(CH_2)$ modes was also modelled. It essentially captures behaviour of the d^+ peak as a function of tilt angle. However, its *sy* intensity is higher at $\beta_\mathsf{m} = 0°$ than that found for the d^+ peak as part of the C−H stretch band. This leads to a higher estimate of the molecular tilt angle.

The dominant antisymmetric mode provides relative intensities that do not match to order of the experimental relative intensities. At $\beta_\mathsf{m} = 0°$, modelling predicts $I_{sx}(v_{76}) = I_{sy}(v_{76})$, while the experimental $\nu_a(CH_2)$ integrated intensities show a difference of 0.04 on the relative intensity scale. This indicates the error with which the A' background signal is removed from the spectra, which apparently leads to an underestimation of the intensities in the *px* and *sy* spectra.

The *px* and *sy* spectra provide no clean intensities for the antisymmetric mode, so that the ratio $I_{py}(v_{76})/I_{sx}(v_{76})$ was used for comparison to the experimental intensities found for the dominant $\nu_a(CH_2)$ mode. This resulted in a matching ratios at $\beta_\mathsf{m} = 18.6°$, which compares favourably to 17.6° deduced with the same ratio for the whole C−H stretch

band. We thus conclude that the alkyl chains of the zinc arachidate monolayer are on averaged oriented at an angle of $\beta_{\mathsf{m}} = 18°$ from the surface normal.

For the following reasons, this value is deemed to be the most reliable of all best-fits presented here. First, uncertainty in the experimentally derived intensities is reduced when using a ratio, because an over- or underestimate of the absolute intensity will occur in both numerator and denominator intensities, thus at least partly cancelling out. This is not the case when comparing absolute intensities directly. Second, only substantial non-zero intensities are used. The error-prone near-zero intensities of the symmetric stretch modes in the *py* and *sx* spectra are avoided. Subtraction of the A' spectral background is performed to remove these intensities. Third, the ratio $I_{py}(v_{76})/I_{sx}(v_{76})$ varies more strongly with β_{m} than its symmetric stretch counterpart $I_{px}(73)/I_{sy}(73)$, which spans a relatively narrow range of ratios. This again reduces the effect of uncertainty in the experimental ratio on the assessed molecular tilt angle. Finally, the modelled antisymmetric stretch mode is harmonic and has a Raman tensor of well-known form with only one pair of non-zero components, the numerical value of which does not affect the intensity ratio.

Literature comparison

Fatty acids on a substrate have been studied before, including assessments of their overall alkyl chain tilt angle. A summary is provided in a review by Peng, Barnes and Gentle [96], from which table 6.9 is compiled. The tilt angle ranges from $0 - 33°$ in these studies. Only arachidate salts are included here, deposited via the Langmuir-Blodgett method. The traditionally preferred cation for this is cadmium. No studies of the tilt angle of a monolayer of zinc arachidate were found. A study by Dhanabalan *et al.* [180] using X-ray diffraction on Langmuir-Blodgett deposited zinc arachidate multilayers revealed that multilayer packing strongly varies with subphase pH. Zinc salts were found to form from pH 6.6.[¶] Three types of packing arrangements were identified, corresponding to tilt angles of 0°, 19° and 31° which coexisted in certain ranges of subphase pH. However, monolayers were not assessed and the structure of multilayers does not necessarily correspond to that of monolayers [96].

Table 6.9 presents the derived chain tilt values in chronological order to highlight its spread. The surface film need not be homogeneous and the various techniques probe different aspects of it. In Fourier-transform infra-red spectroscopy (FTIR), molecular vibrational modes are probed, as with Raman. Scattering techniques, such as near edge X-ray absorption fine structure (NEXAFS) and grazing-incidence X-ray diffraction (GIXD), probe atomic scattering length densities. Ordered regions in the surface film give rise to diffraction patterns from which crystal parameters may be derived. While vibrations arise from all molecules in the film, diffraction only arises from ordered parts of the film. The molecular tilt angle thus depends on the technique employed to derive it. The molecular tilt angles derived for our system (tables 6.7 and 6.8) generally agree with this range,

[¶]In our experiments, the monolayer was formed on a subphase of pH 7.

Table 6.9: Chain tilt angles for archidate salt monolayers on a solid substrate in air.

Cation	Substrate	Technique	$\beta_{\mathsf{m}}/^\circ$	Reference
Cd	silver	GIR-FTIR	< 8	[181]
Cd	Gold	GIR-FTIR	> 0 or disordered	[182]
Cd	silver gratings	SERS	> 0 or disordered	[183]
Ca	oxidised silicon	NEXAFS	33 ± 5	[184]
Cd	oxidised silicon	NEXAFS	< 15	[184]
Cd	glass	photoacoustic FTIR	≈ 0	[185]
Cd	silicon wafer	NEXAFS	≈ 0	[186]
Ca	silicon wafer	NEXAFS	≈ 0	[186]
Cd	silicon wafer	NEXAFS	33	[187]
Ca	Silicon	NEXAFS	29	[187]
Cd	CaF_2	FTIR-RAS	≈ 0	[188]
Pb	Silicon	in-plane GIXD	20	[189]

though some less reliable metrics result in tilt angles beyond the literature range.

More recently, Itoh and Hasegawa employed a Raman spectroscopy approach in their analysis of Langmuir-Blodgett cadmium stearate film on a glass microscope slide [152]. For a single monolayer deposited at $\Pi = 30$ mN m^{-1}, a molecular tilt angle of 29° was deduced[‖] based on the ratio $I_{sx}(d^-)/I_{py}(d^-)$ (using our definitions, the authors term it $R_{\mathrm{SP/PS}}$). They employed a 90° Raman scattering configuration, illuminating and collecting light from the air side of the interface. Based on a similar metric, we have found this to be 18° for zinc arachidate deposited at $\Pi = 35$ mN m^{-1}. This may be explained by the slightly longer chains (twenty *versus* eighteen carbon atoms), by the different cation and by the higher surface pressure, at which alkane chains are known to come to an increasingly upright orientation [96].

The model employed by Itoh and Hasegawa is specific to the intensity ratio they used and includes incident and scattering coupling factors in the thin-film approximation. For the interfacial layer of cadmium stearate, a refractive index orthogonal to the interface of 1.56 was used. This is said to account for optical anisotropy. However, just like in our model, the value of n_2 only affects the F_z coupling factors in the thin-film limit. Their model does not take into account the depth of the molecule, local field corrections nor the numerical aperture of the lens that collects the Raman scattering. The latter in particular might lead to error, as seen in the modelled intensities presented in this work. Though the authors seem to suggest a finite aperture in their publication (lens L_2 in figure 3 of [152]), its NA is not specified. To assess its relevance, we apply our model to their experimental configuration with the Raman tensor

$$\boldsymbol{\alpha}_{\mathsf{as}} = \begin{pmatrix} 0 & 1 & 0 \\ 1 & 0 & 0 \\ 0 & 0 & 0 \end{pmatrix} \tag{6.10}$$

[‖] In a previous study, Hasegawa *et al.* also investigated this system by multiple-angle infrared absorption spectroscopy [16]. There, a tilt angle of 25° was found.

which applies to the antisymmetric CH_2 stretch mode. Using our model, intensities are predicted for a pinhole aperture and for $NA = 0.55$ in the thin-film limit. Scattering is collected at $(\alpha_{\mathsf{O}}, \beta_{\mathsf{O}}, \gamma_{\mathsf{O}}) = (0°, 0°, 0°)$. Other model input parameters are likewise taken from their publication as: $n_1 = 1.52$, $n_2 = 1.56$, $n_3 = 1.00$, $\theta_{k,i} = 158.6°$, $\lambda_{0,\mathsf{laser}} = 532$ nm, $z = 0$, $\bar{\nu}_R = 2879\ \mathrm{cm}^{-1}$ with molecular ellipsoid and polarisability as estimated for arachidate. Figure 6.52 presents these modelling results as absolute and relative intensities. Intensity ratios are also shown.

Comparing the top and bottom plots of figure 6.52, a small effect due to the numerical aperture of the objective is seen. The absolute intensities are reduced for NA = 0.55 compared to NA $\to$ 0 because the intensity is scaled to the number of grid nodes in the model. At larger NA, scattering intensities nearer the edges of the objective are reduced, thus leading to an overall lower modelled intensity. Relative intensities are hardly affected by the increased NA. There is no difference at $\beta_{\mathsf{m}} = 0°$ and at $\beta_{\mathsf{m}} = 90°$, a decrease by 0.007 of the relative px and sy intensities is observed with a corresponding increase of the py and sx intensities. This results in a slightly higher $I_{sx}(d^-)/I_{py}(d^-)$ at this tilt angle. The experimental geometry of Itoh and Hasegawa has thus been chosen appropriately to ensure that a finite aperture of the objective may be disregarded.

In their experiments, Itoh and Hasegawa obtained $I_{sx}(d^-)/I_{py}(d^-) = 1.0$, which according to their interpretation meant a tilt angle of 25°. However, our modelling results of their experiments suggest $\beta_{\mathsf{m}} = 47°$. When using our estimate of the thin-film refractive index of $n_2 = 1.4425$, a tilt angle of 41° is obtained. This difference is not explained by the local field correction, which was found to have no significant effect on the relative intensities nor on the intensity ratios.

A substantial difference that remains standing after discounting the previous considerations is the way in which our model computes intensities compared to that of Itoh and Hasegawa. They use squared Raman tensor elements that are averaged over the azimuthal and twist angles of the molecular orientation in the laboratory frame of reference and combine these with squared coupling factors to compute intensities. Contrarily, our model uses a complex vectorial description of the scattering process. It computes amplitudes of Raman scattering for each molecular orientation as it arises from the complete Raman tensor, before squaring the scattered amplitude to obtain intensities and finally summing over all orientations. As the various Raman tensor elements simultaneously effect Raman scattering, it appears inappropriate to separate these elements, effectively omitting cross-terms in the amplitudes along the three Cartesian axes in which the scattering is modelled.

However, looking at the modelling outcomes, molecular tilt angles of $41 - 47°$ for a monolayer of cadmium stearate on glass are quite removed from tilt angles found by other authors. These are comparable to the values for arachidatic acid salts, in the range $0 - 30°$ [96]. This divergence is likely aggrevated by low experimental signal over a strong and noisy background (figure 5 of [152]) in Itoh and Hasegawa's Raman spectra of the monolayer. Adjusting the experimental geometry could readily improve the quality of their Raman spectra.

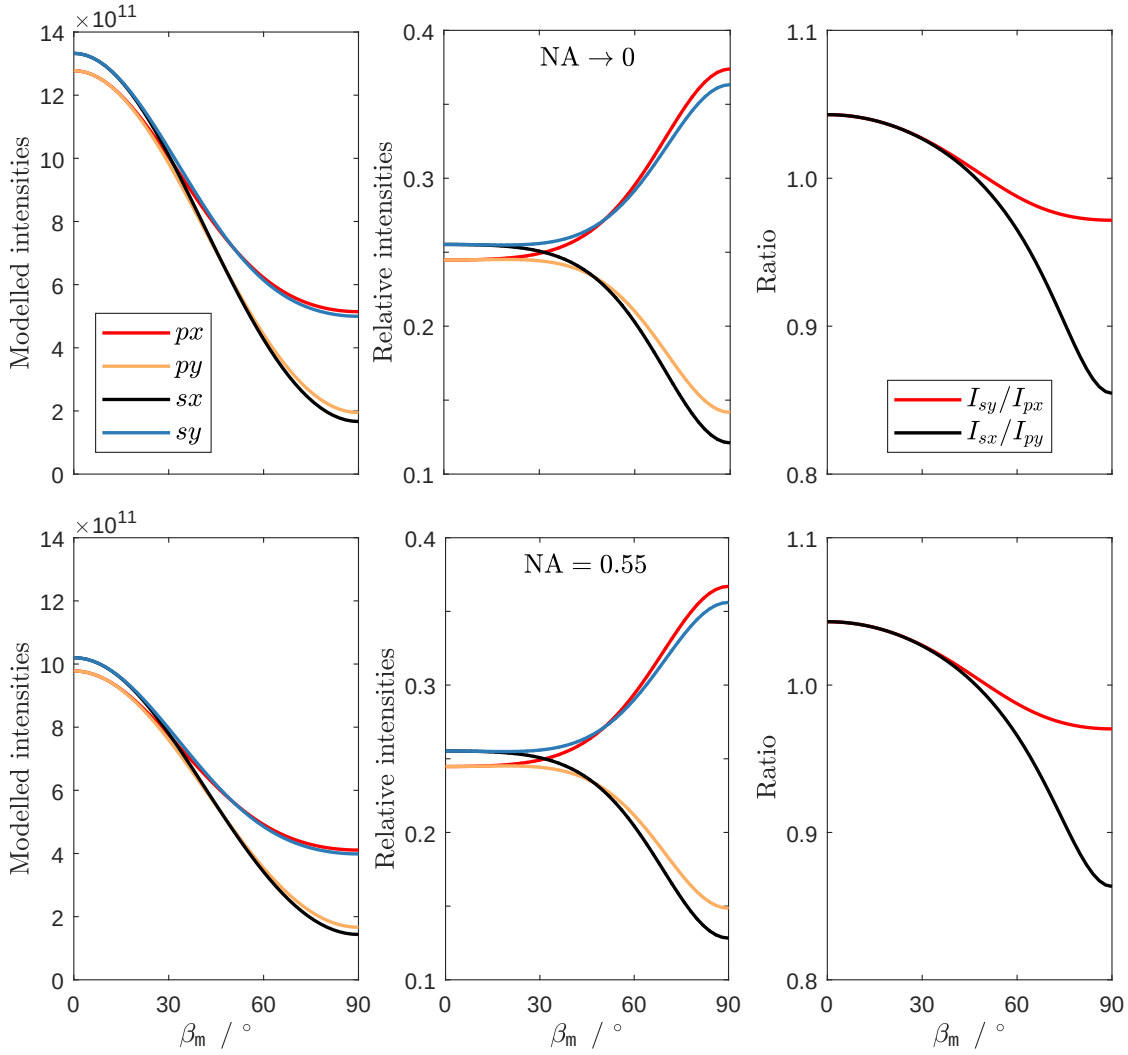

Figure 6.52: Intensities (left), relative intensities (centre) and intensity ratios (right) modelled for the antisymmetric CH_2 stretch of stearate at the air-glass interface as a function of molecular tilt angles $\beta_{\mathtt{m}}$. The experimental parameters conform to those of [152]. The top plots are computed for a pinhole aperture while NA = 0.55 for the bottom plots.

The main cause of the discrepancy between the two models is likely to be the following. As the ratio obtained by our model spans a nearly four times narrower range (from 1.043 down to 0.855) than that of Itoh and Hasegawa (compare figure 6 of [152]), our model is more sensitive to experimental errors. A molecular tilt angle of 25° would be predicted from a ratio of 1.03, rather than 1.0 as currently used. Within the significance interval of this ratio ($0.95 - 1.05$), our model predicts a tilt angle in the range $0 - 65°$ (with a maximum ratio of 1.043), whereas their model provides a range of about $22 - 35°$. A similar sensitivity was observed in the analysis of our own experimental spectra with the symmetric CH_2 stretch mode (figure 6.51). Such behaviour should be taken into account when designing experiments to ensure that appropriate metrics are in fact reasonably sensitive to molecular orientation. Our model may be employed to explore experimental variables because it includes such variables as computational input.

6.4.5 Conclusion

A monolayer of zinc arachidate at the silca-air interface provides a multi-faceted test case of our model. Its alkyl chain gives rise to a convoluted C−H stretch band that is encountered in numerous soft-matter interfaces of interest. Insight in this band is provided by modelling harmonic spectra, using *ab initio* Raman tensors and the optical description of our model. Intensities in these spectra, relative to those of all four standard polarisation combinations, do not significantly change with variation of the molecular parameters. The modelling results may thus be extended from decanoic acid to longer alkyl chains, such as contained in arachidate. However, the longer chain of the latter gives rise to additional fundamental modes which contribute to integrated band intensities.

Various intensity metrics may be employed to assess molecular tilt from experimental spectra. Absence of the d^+ feature in polarised Raman spectra (the *px* and *sy* polarisation combinations) is a strong indicator of low molecular tilt β_{m}. However, this should be established with spectra of sufficient signal-to-noise. This may be improved by experimental geometry, in particular by illuminating the sample through the high-index material near the critical angle and collecting Raman scattered light around the same angle (though avoiding the reflected laser beam).

When comparing experimental to modelled intensities, a metric must be chosen that corresponds to the situation. Errors in experimentally derived intensities may skew the fitting result. Variance within a set intensity ratios as a function of β_{m} form a suitable metric if all spectra can be used. If this is not the case, ratios may be employed. For the monolayer of zinc arachidate, deposited at a surface pressure of 35 mN m^{-1}, we find a molecular tilt angle of 18.6° based on the ratio of antisymmetric CH_2 stretch intensities recorded at the *py* and *sx* polarisation combinations. The symmetric stretch intensities prove rather indiscriminate with respect to molecular tilt in the employed experimental geometry. When using all four intensities, minimal variance in the model-to-experimental ratio is obtained at $\beta_{\mathsf{m}} = 18.2°$ for the main antisymmetric and at 31.7° for the main

symmetric stretch mode intensities. These are in line with published values for similar systems, though there is presently no literature consensus on tilt angles, which depend on the technique used for their determination.

6.5 Summary

In this chapter, our model was tested with three interfaces. A solution of ammonium sulfate on a fused silica hemisphere was used to assess the optical description of the model. As sulfate anions have an isotropic polarisability as well as shape, there is no anisotropic effect from the local field correction. Furthermore, sulfate has a fully symmetric vibrational mode (v_1) with an isotropic Raman tensor. Its Raman scattering does not depend on molecular orientation.

Sulfate Raman scattering from its v_1 mode was recorded at various polarisation combinations. The numerical aperture, incidence angle and concentration of the solution (affecting its refractive index) were varied in the experiments, conducted with both the Stockholm and Durham Raman systems. These parameters were also varied (over a wider range) in our model.

Taking the spread of the laser incidence angle into account in the model, proved insignificant to the modelled intensities. The same was found to apply to the depth z of the molecule, though undulating relative intensities were computed for Raman scattering into the hemisphere above the critical angle.

The model matched the Stockholm data well, which was judged to validate the optical description of the model. However, deviations were observed when using the objective of smaller NA because it provided Raman intensities that proved too low for accurate interpretation. The general trends predicted by the model were still seen in the spectra.

The Durham system provided noisier spectra that were less well described by the model. This could be explained by modelling intensities with an off-set in the polarisation directions, providing an example how the model could be used to assess experimental parameters and their uncertainties.

Carbon tetrachloride provides a spherical molecule with an isotropic polarisability though isotropic as well as anisotropic Raman tensors. Isotopologues are also relevant for this molecule. Liquid CCl_4 was combined with a sapphire hemisphere. Spectra showed distinct v_2 and v_4 bands, while its v_1 mode was affected by strong sapphire features. Birefringence of sapphire further complicated the spectra, including a problematic subtraction of background sapphire-air spectra which all proved polarisation sensitive to different degrees.

With non-isotropic Raman tensors, averaging of the molecular orientation becomes relevant. A step size of 20° was found to be sufficient to achieve converged modelled intensities that represent the isotropic average. In this average, diagonal and off-diagonal Raman tensor elements each contribute to the modelled intensities in the same way. In the isotropic average, the local field correction does not affect modelled relative intensities,

though the absolute intensities decrease with increasing molecular radius and increase with molecular polarisability as anticipated.

Modelled intensities for CCl_4 did not agree with its experimental spectra. Several potential sources for this difference were assessed. Birefringence of sapphire, rotations in the plane of polarisation and anharmonicities affecting the Raman tensors were tested. None of the effects could individually explain the observed intensities, leading us to conclude that combined effects are likely causing the observed intensities and that our model currently faces too many unknowns in the sapphire-CCl_4 interface, thus preventing unambiguous interpretation with our model. Additional experiments were suggested to rule out at least the polarisation uncertainties. The v_2 band of CCl_4, likely to be the least affected by anharmonicity, can then be used to assess the inaccuracies of the model arising from its omission of birefringence in the hemisphere.

A zinc arachidate monolayer at the silica-air interface proved a further interesting sample to test our model. It is known to form a hexagonally packed monolayer in orientationally ordered domains at tilt angles in the range $0 - 33°$, according to previous studies of Langmuir-Blodgett deposited arachidate salts [96]. Its convoluted C−H stretch band was investigated. This band contains symmetric methylene stretch modes that engage in Fermi resonance with a bending overtone. These features underlie antisymmetric methylene stretch modes while relatively weak methyl stretches appear near the high-frequency side of the band.

Harmonic Raman spectra were generated with our model using computational Raman tensors of decanoic acid. The azimuthal and twist angles of the molecules were isotropically averaged as these are randomly distributed in the monolayer. A qualitative comparison with the experimental spectra pointed to roughly upright chains with $\beta_{\mathsf{m}} < 30°$, indicated by the absence of symmetric stretch modes in the *py* and *sx* spectra. The spectra are most sensitive to molecular tilt around $\beta_{\mathsf{m}} = 45°$, indicating that an assessment at the expected near-upright orientation is of relatively low accuracy.

The local field correction was again found not to affect the modelled relative intensities within reasonable variation of the molecular polarisability or shape. Its influence was largest for molecular orientations parallel to the interface. At high tilt angles, or in an azimuthally oriented material, it should not be ignored.

Furthermore, the Raman tensors do not strongly affect the relative intensities. This suggests that the model provides the same results, whatever long-chain alkane is employed (at least for relatively upright chains). Generalised conclusions may thus be drawn for alkyl chains above about ten carbon atoms. Corollary, these similarities allow use of generalised 'long-chain' properties (Raman tensor, molecular polarisability, molecular ellipsoid radii) when assessing chain tilt angle with respect to the interface. This finding supports our use of decanoic acid Raman tensors in analysing arachidate spectra.

The angle of laser incidence, objective position and refractive index of the surface film were also assessed. For the silica-air interface, n_2 results in the same relative intensities over a range of $1.2 - 2.0$ in the current experimental geometry. Exceedingly accurate

assessments of n_2 can thus be avoided, including that of any anisoptropy of the thin film at the interface. The model predicts highly directional far-field Raman scattering (conforming to other derivations, such as by Luan *et al.* [168]), which may be employed to enhance Raman signals at desired polarisations.

Various intensity metrics as well as fitting metrics were tested to arrive at a consistent interpretation of the experimental spectra based on a single molecular tilt angle. Different values for β_{m} were found with metrics based on the whole ν(CH) band, parts of it or the main symmetric or antisymmetric methylene stretch modes. Overall, the most reliable metric is concluded to be the intensity ratio I_{py}/I_{sx} for the integrated $\nu_a(\mathrm{CH_2})$ intensity (obtained from modelling the harmonic ν(CH) band) and main antisymmetric stretch mode, which were judged to be least error-prone in this dataset. These provided $\beta_{\mathsf{m}} = 17.6°$ and $18.6°$, respectively, in line with other studies of fatty acid salts.

In our case, the ratio of symmetric stretch intensities proved insensitive to molecular tilt. Exceedingly small variations in the experimental intensities here resulted in large differences in the obtained tilt angle. This problem also arose in the application of our model to experiments on a cadmium stearate monolayer performed by Itoh and Hasegawa [152], who used a similar ratio. Our ratio resulted in a tilt angle somewhere between $0°$ and $65°$ based on the precision of the experimentally determined ratio. This again emphasised the importance of sufficient signal-to-noise in the collected spectra.

In all analyses presented in this chapter, proper background subtraction proved crucial. Experimental intensities should be assigned to features that are at least proportional to the actual Raman scattering mode being investigated. Errors introduced through background subtraction restricted the interpretation of spectra as well as the fit between modelled and experimental intensity metrics. Further limitations in applying the model were encountered with low-intensity spectra, where deviations from zero intensity significantly affect the relative intensities.

In addition to comparing the modelled intensities to experimental intensities, insight was gained into why and how intensities increase or decrease upon variation of model input parameters, most of which correspond to experimental choices. The model may thus be used to design experiments to achieve optimal intensities in particular desired Raman lines or increase sensitivity to a particular parameter, such as molecular tilt angle. For example, near-zero intensities may be avoided by an appropriate choice of linear polarisation directions.

The model itself is restricted to optically isotropic refractive indices, though n_2 can take the value of n_z, the refractive index of the interfacial layer perpendicular to the interface, in the thin-film limit. However, modelled intensities are not always sensitive to particular values of n_2, as observed in the arachidate analysis. Strong variation is affected by variation of the experimental geometry, including angle of laser incidence, objective position and polarisations. The effect on (relative) intensities from the form of the Raman tensor is mitigated in cases where isotropic averaging applies.

Chapter 7

Boundary lubricant under static pressure

This chapter presents an application of the approach developed so far to a system of applied relevance. Interfacial Raman spectroscopy allows access to buried interfaces, such as encountered in the field of tribology.

The experiments presented in this chapter were performed by Kaustav Guha on $8-10$ September 2008 during his doctoral studentship in our research group. The results are included in his thesis [54] with a qualitative analysis. Materials and methods are also given in chapter 3 of the present work for convenience. In brief, a static solid-solid interface was constructed from an SF10 hemisphere and a fused silica sphere, which were both coated with a zinc arachidate monolayer. Various static loads were applied to the contact and Raman spectra were collected at the four standard polarisation combinations alongside optical microscopy images of the contact area.

This experiment combines optical and Raman observation of boundary lubrication to relate macroscopic changes in pressure to changes in molecular orientation. The analysis presented here, has been performed afresh on the raw data. Mechanics of the contact, measured by optical microscopy, are first discussed, after which the experimental Raman spectra are presented. Modelling is then performed for this system before fitting modelled intensities to the experimentally derived intensities as a function of molecular tilt angle. A summary of the approach is presented in figure 7.1, including experimental geometry, polarisation directions and molecular orientation.

7.1 Contact mechanics

The static pressure exerted on the interface is deduced from its microscopy image using classical contact mechanics. The contact area between the two surfaces increases as the load increases while interference fringes appear around the edges of the contact.

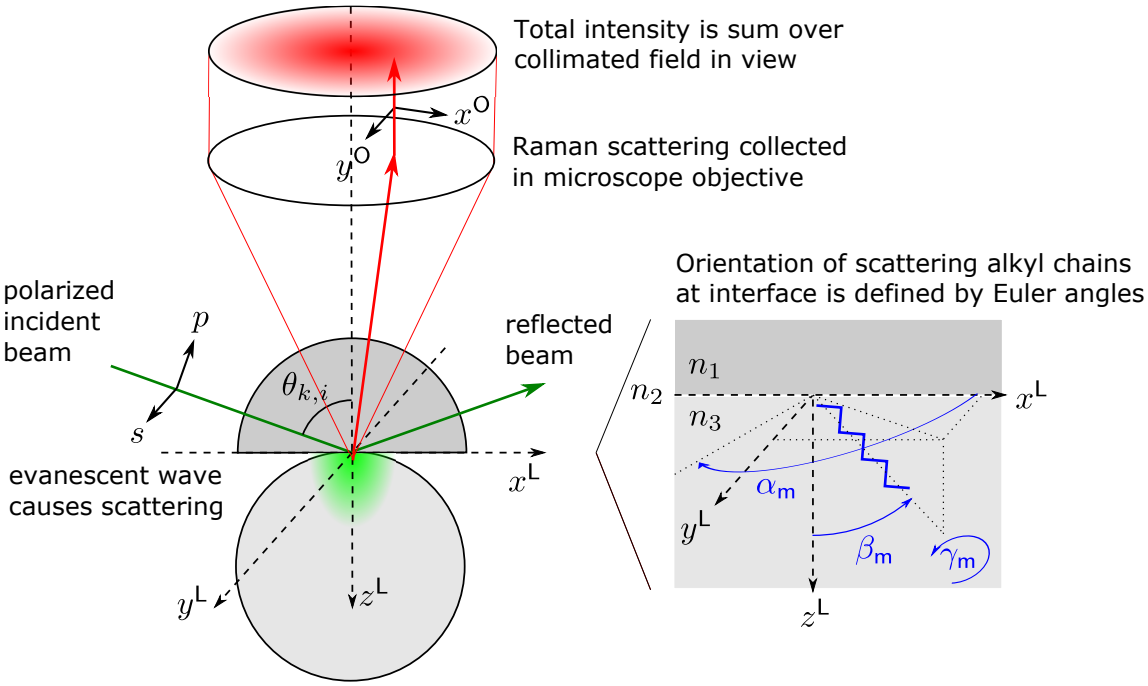

Figure 7.1: Schematic overview of experimental layout and geometry definitions. A 5 mm flint glass glass hemisphere contacts a 10 mm fused silica ball, both coated with a zinc arachidate monolayer by Langmuir-Blodgett deposition. Pressure is exerted by manual and micromotion stages holding these element. Incident laser beam is linearly polarised. The collection polarisation is set along the $y^{O} \parallel y^{L}$ or $x^{O} \parallel x^{L}$ axis. When modelling the spectra in this geometry, the thin-film approximation is used with the confined alkyl chains in a single orientation specified through Euler angles (azimuthal angle α_m, tilt angle β_m and twist angle γ_m) as defined in section 2.2.3.

7.1.1 Hertzian contact theory

Deformation and pressure in a non-adhesive, frictionless contact between two elastic solids is described by Hertzian contact mechanics. For the sphere-on-flat geometry employed here, the radius of the circular contact area a is given through [1]

$$a = \left(\frac{3FR}{4E^*}\right)^{1/3} \tag{7.1}$$

with F the normal force exerted on the contact, R the radius of the spherical surface and E^* the composite modulus defined as

$$\frac{1}{E^*} = \frac{1-{\nu_1}^2}{E_1} + \frac{1-{\nu_2}^2}{E_2} \tag{7.2}$$

where E_1, E_2 and ν_1, ν_2 are Young's modulus and the Poisson ratio of the materials in contact. The mean contact pressure P_m is then computed through

$$P_m = \frac{F}{\pi a^2} = \frac{4E^* a}{3\pi R} \tag{7.3}$$

where equation 7.1 is used to substitute F. The local normal pressure in the circular contact depends on the radial position r as

$$P(r) = P_c \sqrt{1 - \frac{r^2}{a^2}} \tag{7.4}$$

where P_c is the pressure at the centre of the contact, from which Raman spectra have been recorded. It is the maximum pressure in the contact and is given by [1]

$$P_c = \frac{3}{2} P_m = 2a \frac{E^*}{\pi R} \tag{7.5}$$

which can be computed from the diameter of the contact spot $2a$, measured by microscopy of the contact area. The properties of the mating fused silica sphere and the flat surface of the SF10 hemisphere are given in table 7.1. The mechanical properties are taken from specifications of glass manufacturer Schott AG (Mainz, Germany) [87]. These result in $E^* = 34.5$ GPa for the composite modulus.

Table 7.1: Properties of the materials in contact.

Material	E / GPa	ν	R / mm
Fused silica	72	0.17	5.0
SF10	60.8	0.235	-

7.1.2 Microscopy of the contact area

Microscopy images of the contact area through the 5× objective are presented in figure 7.2 in order of data acquisition, numbered 1 to 7. The sphere was first brought in the correct position and aligned with the microscope focus after which the hemisphere was brought down on top. Pressure was exerted by the micro-motion stages that held the mating solids. It is assumed that no shear forces arose in this process.

The pressure rig was aligned on the microscope focus before collecting Raman scattering from the centre of the contact spot. The load was increased in steps with an overnight break between measurements 3 and 4. Mechanical relaxation of the pressure rig explains the slightly reduced contact area observed in the latter.

The illuminating white light undergoes interference in the gap between the two surfaces, which gives rise to bright and dark fringes known as Newton rings. The central dark area is the contact area of the elastically-deformed sphere and planar surface. The radius of the contact area is extracted from the microscope images with a MATLAB routine. The script is included in appendix F and its working is explained there. The results of this

analysis are given in table 7.2. As the load on the contact is increased from measurement 1 to 7, the contact area enlarges and P_c scales linearly with its diameter (equation 7.5).

Table 7.2: Diameter $2a$ of the contact area and its central pressure P_c for the seven measurements.

#	$2a$ / μm	P_c / MPa
1	141	309
2	175	384
3	213	467
4	202	442
5	233	512
6	262	575
7	386	628

Surface adhesion forces are assumed to be zero in the Hertzian description of a contact. In our experiments, the exerted pressure is much larger than the adhesive surface forces, which we estimate at no more than 2 MPa based on surface forces on the order of 10 mN/m as reported by Ruths *et al.* [190] from surface-force-apparatus measurements.

The Hertzian contact pressure as a function of radial position is presented in figure 7.3, using equation 7.4 and the values of P_c and a obtained from analysis of the microscopy images. As the ellipsoidal axes of the laser beam are about $10 - 30$ μm, practically all laser light falls within the substantially flat range of the pressure curves. This ensures that Raman spectra are collected from molecules that experience a similar load.

The pressure range investigated here mimics local pressures at asperity contacts in macroscopic applications [1, 2]. Bearing surfaces are generally designed to make contact over a large surface area in order to reduce pressure and thereby prevent wear. Hydrodynamic lubrication is usually desired in which a lubricating film is dragged into the contact to keep the mating surfaces apart. However, when insufficient hydrodynamic forces are generated, molecular layers absorbed to the surfaces come into contact. This is the boundary lubrication regime. In this regime, asperities of mating surfaces experience much higher local pressures, such as those generated in the present experiments. It is then down to the boundary lubricant to prevent wear.

7.2 Experimental Raman spectra

SF10 and fused silica form a transparent and optically isotropic interface on which the laser was incident under 57.6° from the surface normal. This is just above the critical angle of 57.3° at the laser frequency, while $\theta_c = 57.7°$ at the Raman-shifted frequency of the C−H stretch band. Raman scattering was collected through the SF10 hemisphere by the NA = 0.55 microscope objective positioned perpendicular to the interface. The acquisition time for each spectrum was 600 seconds.

Figure 7.4 presents the spectra for the seven contact pressures recorded with the px,

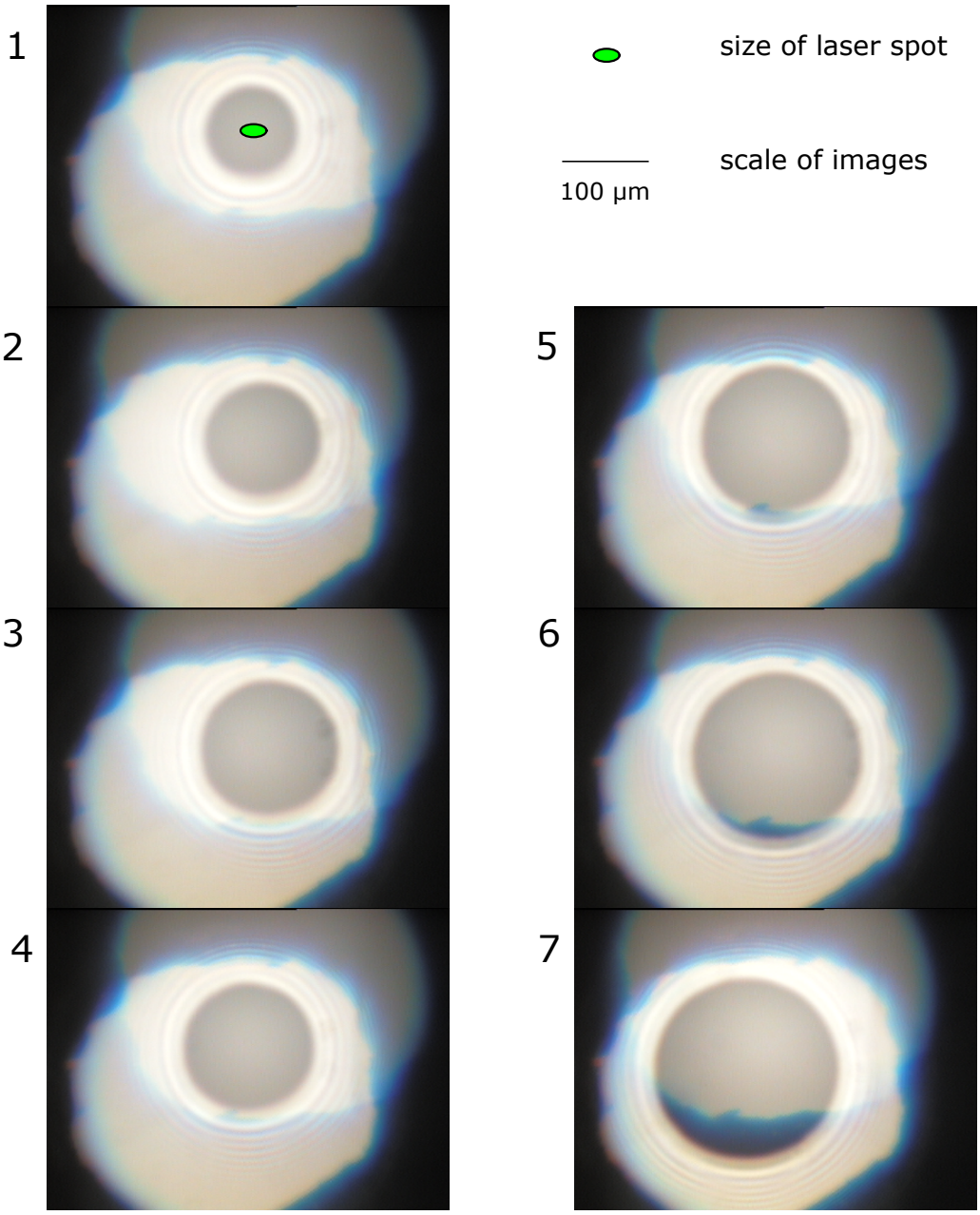

Figure 7.2: Microscope images of the contact area collected through the 5x objective lens. The approximate size of the laser spot is indicated as a green ellipsoid. The images are about 460 μm across. [data KG080908/spot1-7]

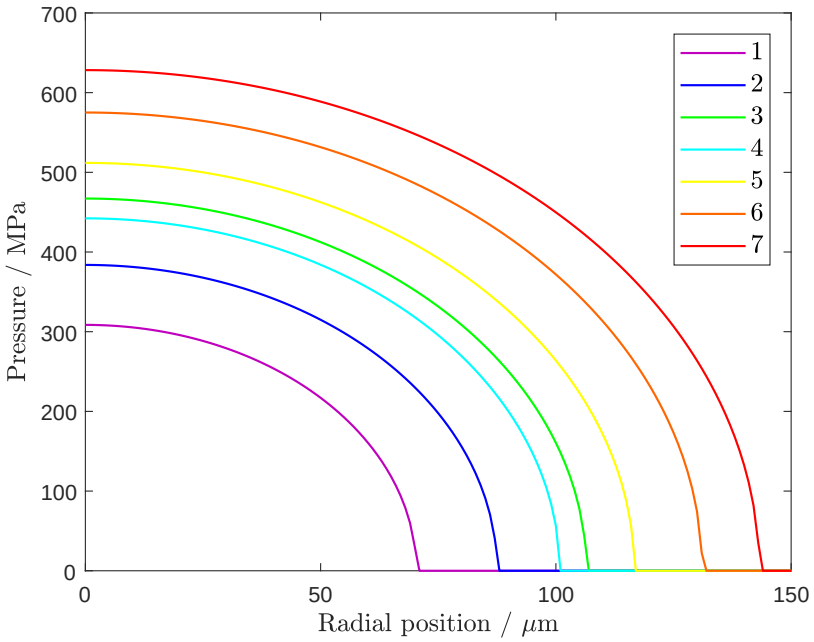

Figure 7.3: Hertzian pressure as a function of radial position in the circular contact derived from each microscopy image $1-7$ of the contact area. Note that spot 4 experienced a lower load than spot 3.

py, *sx* and *sy* polarisation combinations. A linear baseline (fitted to the spectral ranges of $2580-2620$ and $3160-3200$ cm^{-1}) has been subtracted from each spectrum.

7.2.1 Conventional interpretation

Interpretation of Raman spectra of alkyl chains traditionally focusses on three aspects of the d^+ and d^- peaks:

(1) presence and absence of peaks,

(2) shifts of peak locations and

(3) the d^-/d^+ intensity ratio.

Figure 7.5 presents peak heights extracted from the baseline-subtracted spectra. Intensities of the y collection polarisation have been divided by 0.89 to correct for the transmission of the additional half-wave plate in the path of the scattered light.

As discussed with the zinc arachidate monolayer in air (section 6.4), absence of the d^+ peak in depolarised spectra (here: *py* and *sx*) indicates uprights chains. In the current spectra, substantially non-zero intensities are observed in all polarisations, leading us to conclude that the chains are in fact tilted from the surface normal. As the contact pressure is increased, the d^+ peak grows in the p-polarised spectra but decreases in the s-polarised spectra.

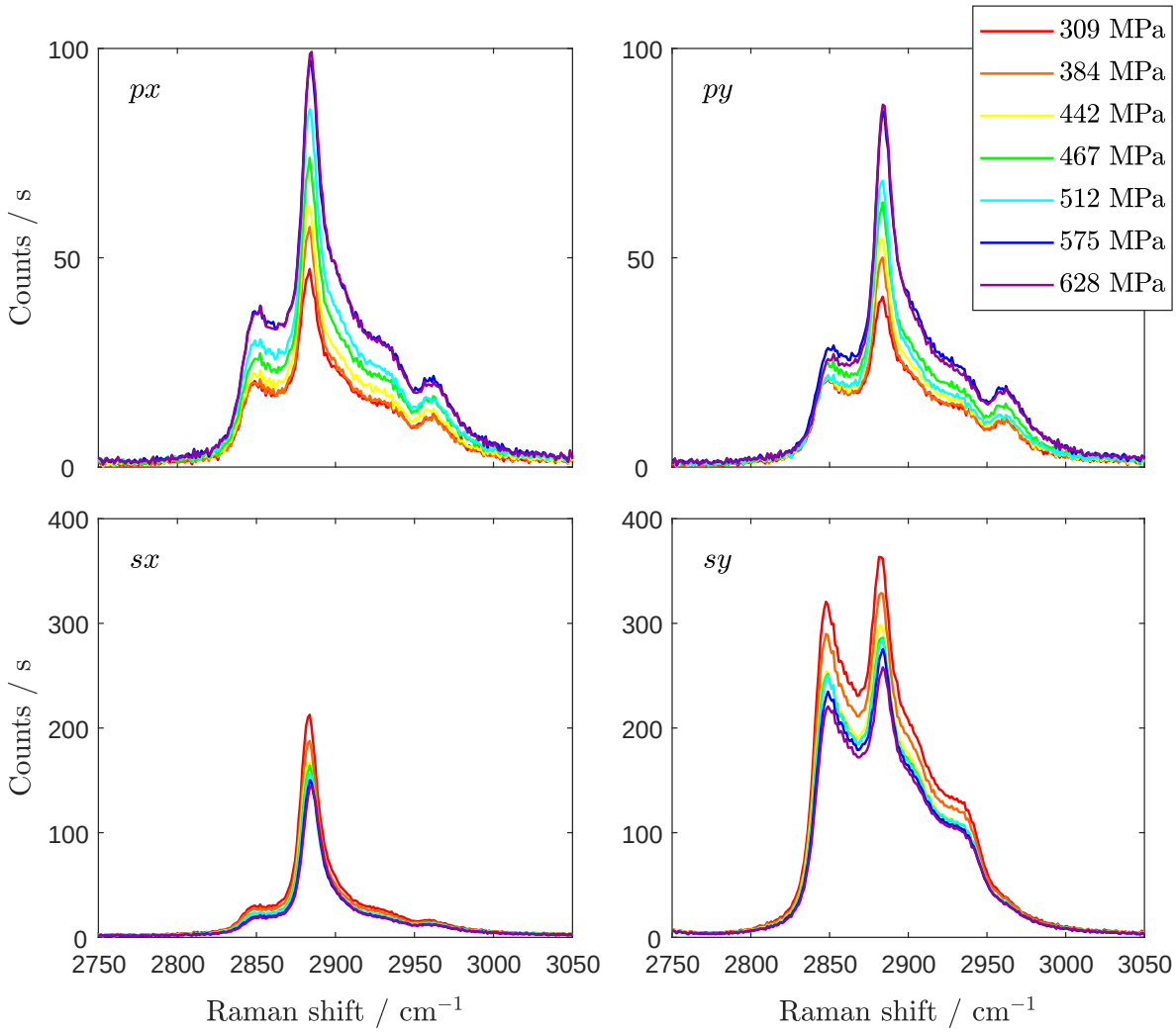

Figure 7.4: Baseline-subtracted Raman spectra of the SF10-silica ball-on-flat contact under various levels of static load with zinc arachidate monolayers on both surfaces. The laser was incident just over the critical angle. [data KG080908]

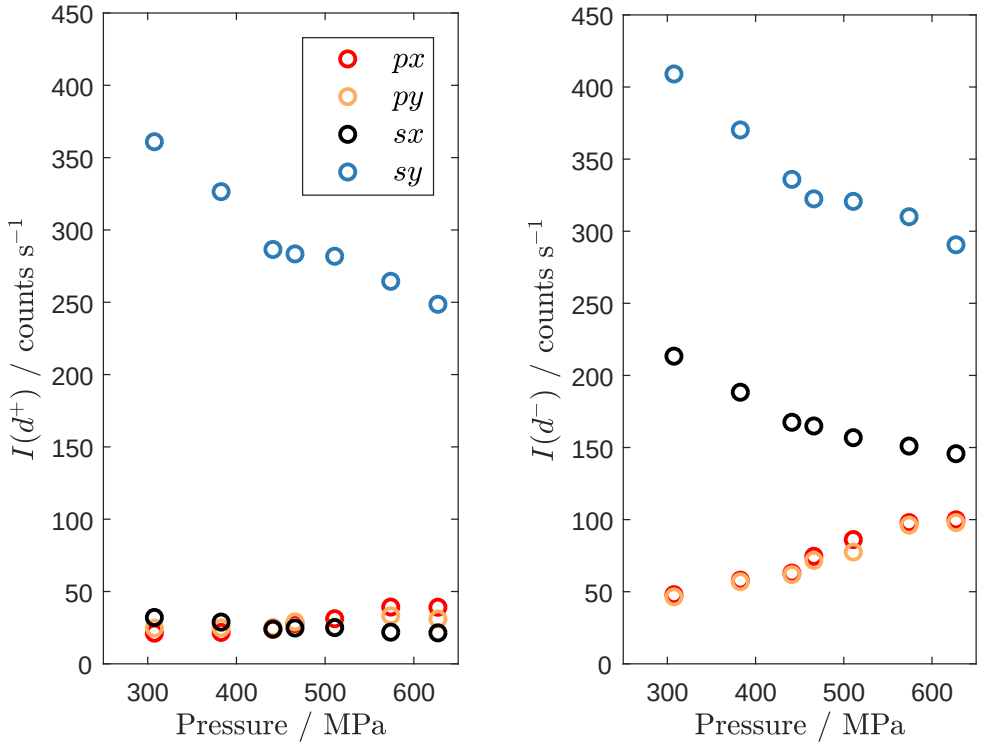

Figure 7.5: Heights of the d^+ peak (left) and d^- peak (right) at about 2849 and 2883 cm^{-1}, respectively, from the experimental spectra of figure 7.4. The *py* and *sy* intensities are corrected for the transmission of the half-wave plate used to change the collection polarisation from x to y.

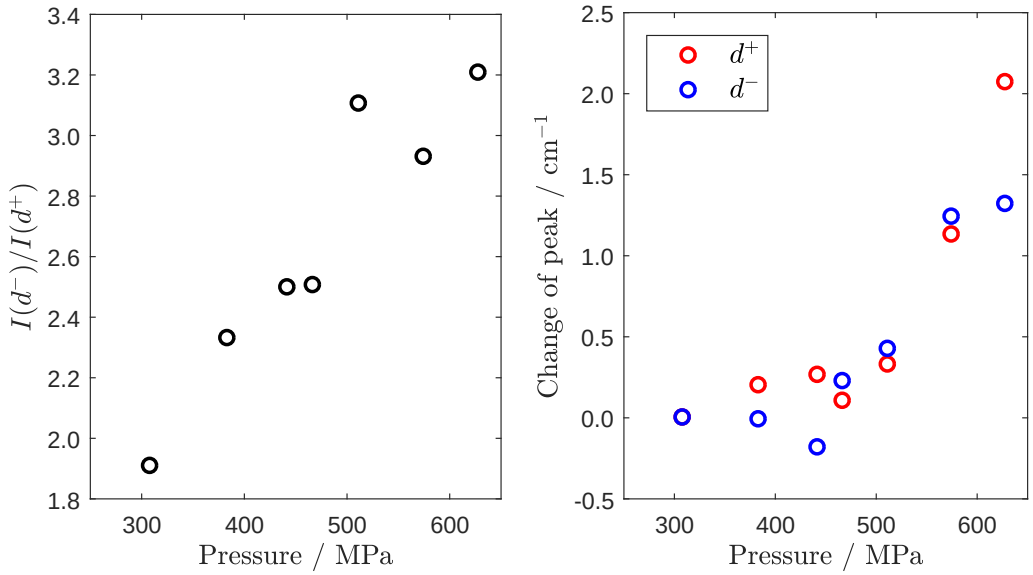

Figure 7.6: Metrics for conventional interpretation of alkyl chain Raman spectra from the *py* spectrum of figure 7.4 based on peak height ratio (left) and Raman shift change (right) relative to peak location at 300 MPa. Their increase with contact pressure indicates increased order and chain interactions at higher pressures.

Figure 7.6 shows (2) and (3) of the above metrics using peak heights and peak locations from the *py* spectra, which show a clear relationship to the contact pressure. Peak locations were deduced by a fitting routine to improve accuracy of its estimate. The d^+ peak location was found from fitting a Lorentzian to its low-frequency half (*i.e.* the tail extending to lower Raman shift from the peak maximum). The location of the d^- peak was deduced by removing background A' intensity (estimated by a spline function fitted through adjacent features) from the spectrum to obtain a neat d^- feature that was described well by a Gaussian profile.

An increase in chain order is understood to occur from the higher d^-/d^+ intensity ratios [142, 191] with increasing contact pressure. Furthermore, the d^+ and d^- peak maxima are positioned at higher Raman shift as the contact pressure increases. This is indicative of increasing interchain coupling [191]. From a conventional interpretation of the Raman spectra, we may thus conclude that the alkyl chains in the boundary lubricant film are compacting laterally while increasing in order as the load on the contact increases. The chains are tilted away from the surface normal in the whole pressure range. However, these observations do not form a basis for quantification of this tilt angle or its change with pressure.

7.2.2 Band and peak intensities

Peak heights for the d^+ and d^- features in the experimental spectra were presented in figure 7.5, varying around 2849 and 2883 cm^{-1}, respectively. The peaks are strongest in the *sy* polarisation combination and reduce with pressure in both the *sy* and *sx* spectrum. However, an increase is seen with the *p*-polarised spectra. The peak heights in the *px* and *py* spectra are about equal throughout the pressure range. This makes sense because the laser beam is incident near the critical angle, inducing a Raman dipole along z^{L} with practically no x^{L} component. This induced dipole generates a rotationally symmetric field at the microscope objective, which is transmitted equally by the x and y polarisers.* This contrasts with the spectra of the zinc arachidate monolayer at the silica-air interface (section 6.4.1), collected with the laser incident far from the critical angle.

Similar behaviour is observed for the integrated intensities of the ν(CH) band, obtained by integrating over the baseline-subtracted spectra from 2750 to 3050 cm^{-1} (figure 7.7). The *sx* intensity reduces to below that of the *px* and *py* spectra at the two highest contact pressures.

Errors in the data of figures 7.5, 7.6 and 7.7 arise from uncertainties in the deduced pressures and spectral intensities. In deducing contact pressure, applicability of Hertzian contact mechanics was assumed. Errors in the contact area and material parameters are assumed insignificant. The spectral intensities are hardly affected by spectral noise and baseline subtraction, though the peak intensity is in principle more sensitive to noise and the integrated band intensity more sensitive to choice of baseline. Near-zero intensities do

*This effect is similar to the central plots of figure 5.22 for a free dipole oriented along the z^{L} axis.

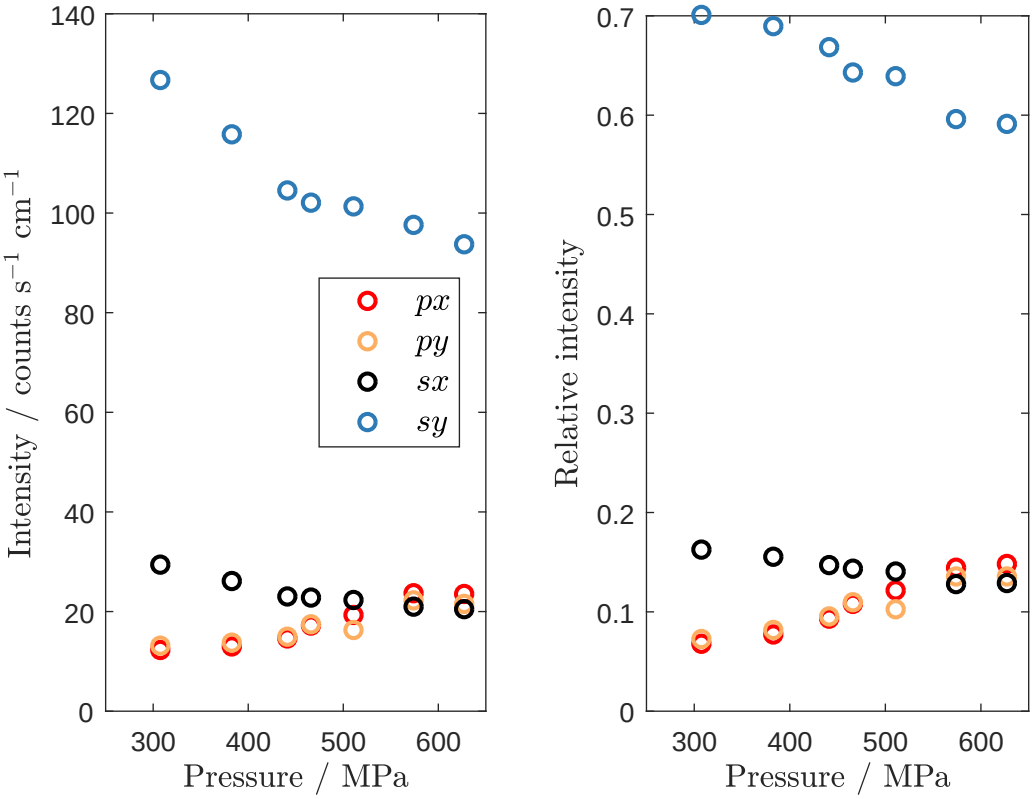

Figure 7.7: Absolute (left) and relative (right) experimental intensities for the ν(CH) band of arachidate in the SF10-silica contact *versus* the contact pressure (from the experimental spectra presented in figure 7.4 and corrected for the half-wave plate in the y collection polarisation).

not arise in this dataset. The assignment of Raman intensity to a particular mode is of importance when comparing the experimental intensities to modelled intensities. Due to the increased convolution of the spectra at all polarisation combinations, only the overall intensity ν(CH) is used here.

7.3 Modelling results

Raman intensities are modelled with parameters corresponding to the experiment and to material properties as described previously. The thin-film limit is applied and $g = 15$ is used for the modelling grid size. The whole C−H stretch band is modelled as a function of molecular tilt angle β_{m} in steps of 2°. For comparison, the main symmetric and antisymmetric stretch modes are also modelled separately.

The present sample includes two monolayers, each in contact to one of the mating surfaces via its headgroup. The molecules are thus positioned in opposite directions with respect to the surface. However, modelling the full range of β_{m} from 0° to 180° is not required. The range $0° \leq \beta_{\mathsf{m}} \leq 90°$ fully specifies the intensities; modelling over $90° <$

$\beta_{\mathsf{m}} \leq 180°$ is redundant (see appended figure G.3). This implies that the position of the headgroup or absolute orientation can not be deduced from this analysis.

7.3.1 The C-H stretch band

Figure 7.8 provides the modelled, harmonic ν(CH) band at various molecular tilt angles. The *px* and *py* spectra are identical at $\beta_{\mathsf{m}} = 90°$ and slightly differ at low tilt angle. This difference arises from the local field correction, which rotates the induced dipole towards the shorter molecular axis. For *p*-polarised incident radiation, a small *x*-component is induced which gives rise to Raman scattering polarised along this direction, thus contributing to the *px* spectrum. This scattering does not reach the detector when the collection polarisation is set along *y*. The difference between the *px* and *py* spectra is thus indicative of the effect of the local field correction applied in the model. When the local field correction is omitted from the model computation, these spectra are identical as shown in appended figure G.4. Without the local field correction, the methyl stretches are predicted to be much stronger, decreasing with molecular tilt in the *px* and *py* spectra, which is not observed in the experimental spectra.

As β_{m} increases, the intensities of the *px* and *py* spectra shown an overall increase in intensities. In contrast, the *sx* and *sy* spectra show a decrease. This conforms to the experimental observation with increasing contact pressure, thus suggesting an increase in the molecular tilt angle of the arachidate layer. However, a slight increase in the d^+ peak is predicted with increasing tilt angle for the *sx* spectra. This is prominent from $\beta_{\mathsf{m}} \approx 45°$, though this value is affected by the (somewhat arbitrary) degree of line broadening chosen in computing the spectrum. This last effect is not observed in the experimental *sx* spectra, which feature an overall decrease in intensity with increasing contact pressure. The molecular tilt angle is thus expected to remain lower than about 45° for all contact pressures.

The modelled spectra provide the integrated ν(CH) intensities as well as d^+ and d^- peaks heights of figure 7.9, which are used for quantitative comparison below.

7.3.2 The main methylene stretch modes

Scattering intensities for the main symmetric and antisymmetric methylene stretch modes (v_{73} and v_{76} of decanoic acid, respectively) are also modelled as a function of β_{m}. The results are presented in figure 7.10. For v_{73}, only the *sy* spectrum is predicted to show significant intensity at $\beta_{\mathsf{m}} = 0°$. As β_{m} increases, the symmetric stretch appears in the *px* and *py* spectra and later in the *sx* spectrum when the molecule is approaching a flat orientation. The *sy* intensity is strongest at all tilt angles.

For v_{76}, the intensity variation is stronger in that the *px* and *py* intensities increase to a level above that of *sx* and *sy* from about 45° onwards. The *sx* intensity is equal to the *sy* intensity for low tilt angles but decreases with increasing β_{m} and provides the weakest scattering intensities when $\beta_{\mathsf{m}} > 45°$.

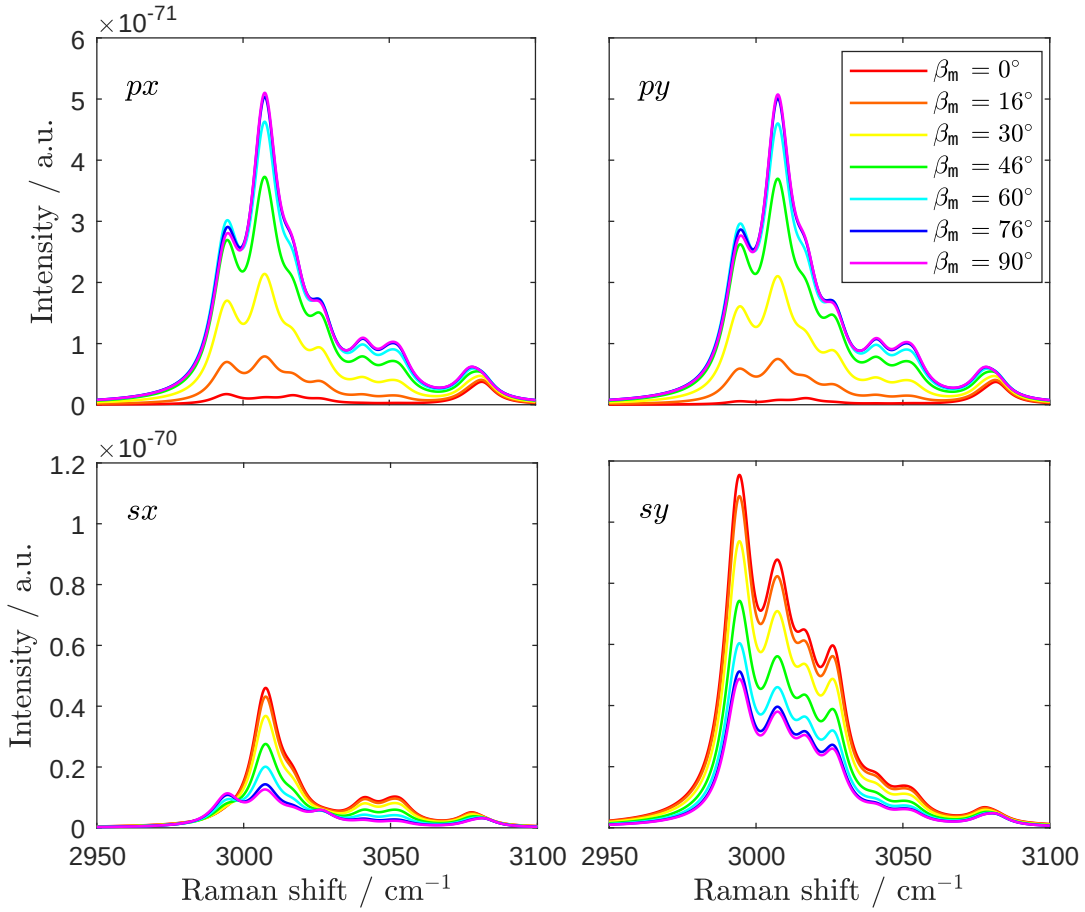

Figure 7.8: Modelled harmonic Raman spectra of the ν(CH) band for zinc arachidate in the SF10-silica contact for various molecular tilt angles β_{m} with respect to the interface normal. The spectral intensities are summed over the full full range of molecular azimuthal and twist angles. Modelling parameters conform to the contact Raman experiment while employing computational Raman tensors of decanoic acid (modes 71-89). Each modelled Raman line is convoluted with a Lorentzian of 10 cm^{-1} fwhm to generate the spectra.

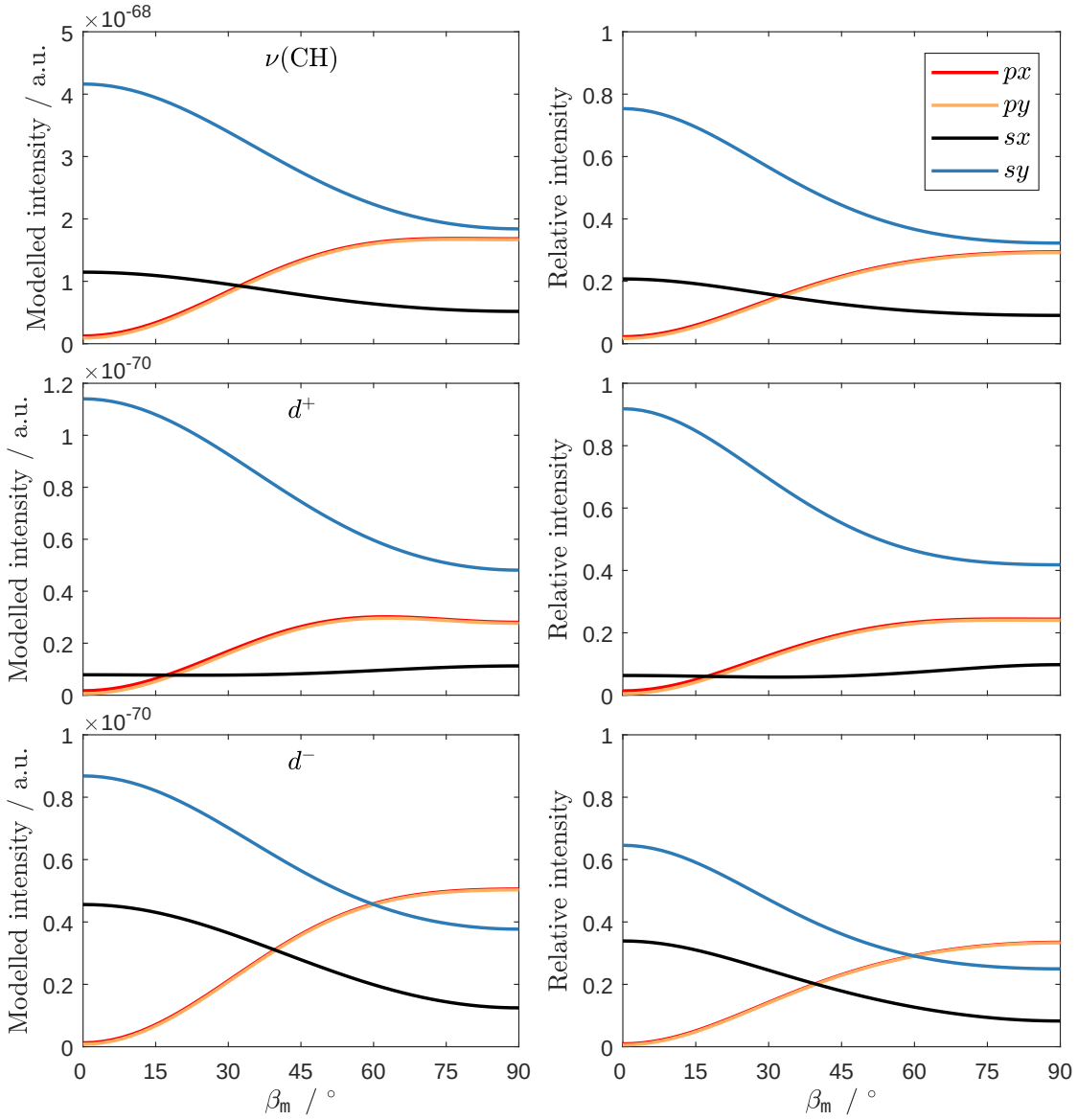

Figure 7.9: Absolute and relative intensities of the ν(CH) band (top), the d^+ peak (centre) and d^- peak (bottom) of the modelled Raman spectra (figure 7.8) of zinc arachidate in the SF10-silica contact as a function of molecular tilt angle β_{m} with respect to the surface normal.

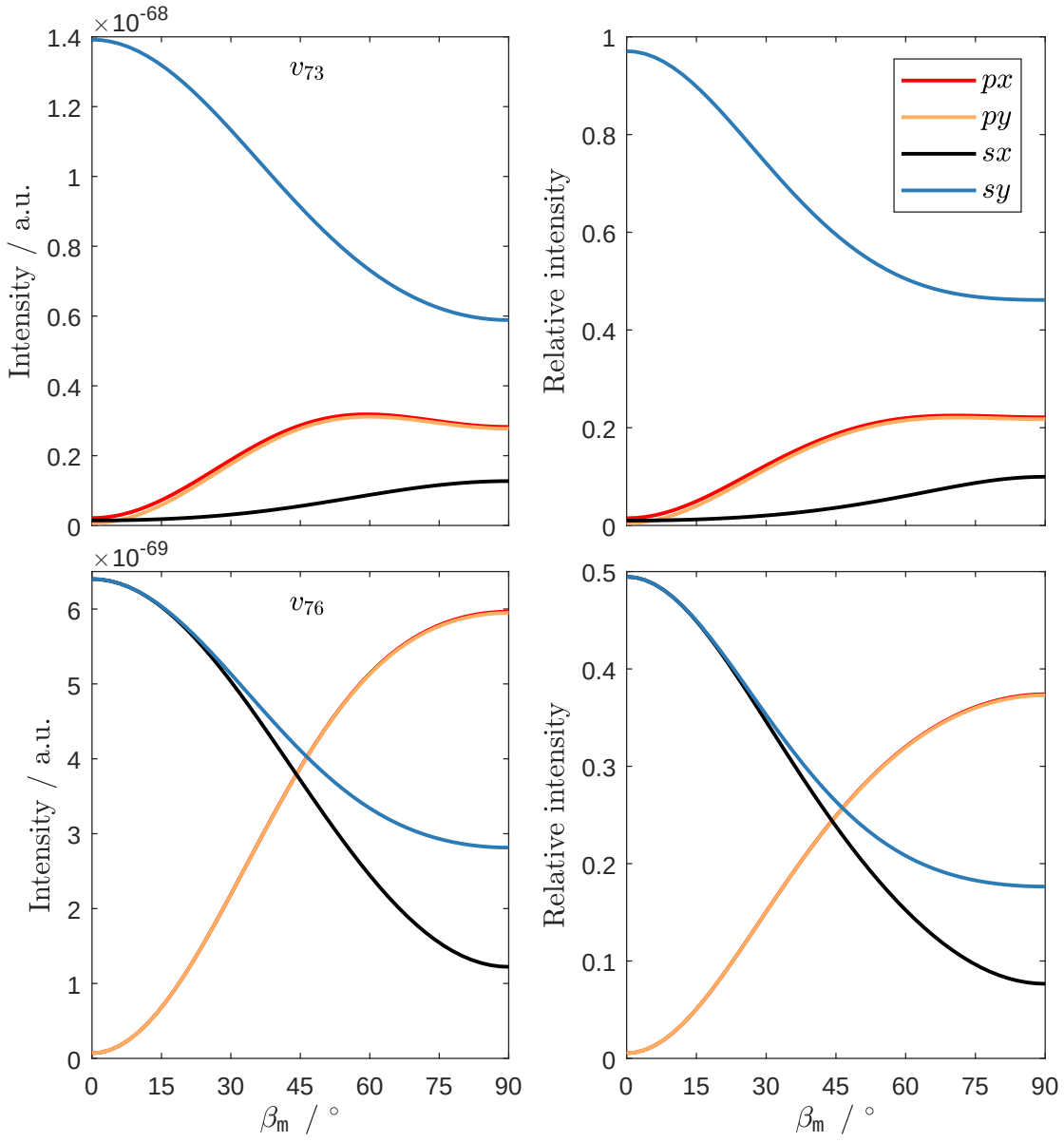

Figure 7.10: Modelled absolute and relative intensities for the symmetric CH_2 stretch (v_{73}, top) and the antisymmetric CH_2 stretch (v_{76}, bottom) of decanoic acid representing zinc arachidate in the SF10-silica contact as a function of molecular tilt angle β_m with respect to the surface normal.

For both modes, the px and py intensities are practically equal because the laser is incident under an angle very close to the critical angle for the SF10-silica interface. Only in the symmetric stretch mode with a low molecular tilt angle, is the px spectrum slightly stronger than py. This is caused by anisotropic effects of the local field correction.

The intensity curves for the individual modes differ from those of the ν(CH) band. Due to line broadening in the modelled spectra, the d^+ and d^- peak heights (figure 7.9) show behaviour that is a combination of the v_{73} and v_{76} curves with respect to β_{m}. In the modelled band, I_{sx} is therefore significantly non-zero at all molecular tilt angles and for both spectral features. This model prediction conforms to the experimental observation. The cross-over point of I_{sy} and $I_{px} = I_{py}$ also varies: from 45° with the v_{76} modes taken separately, to 40° in the d^- feature and 33° in the integrated ν(CH) intensity. The antisymmetric lines also contribute to the d^+ peak height, exemplified by the presence of similar cross-over at $\beta_{\mathsf{m}} = 18°$. This contrasts with the zinc arachidate monolayer at the silica-air interface discussed in section 6.4, where the symmetric stretch modes clearly dominated the band intensities (compare figures 6.44 and 6.45). In that case, the angle of laser incidence was far above the critical angle for the probed interface, contrasting with our present case where symmetric and antisymmetric intensities mix more profusely.

7.4 Comparison and discussion

The modelled intensities are now compared to the experimental intensities to assess molecular tilt of the zinc arachidate monolayers in the contact.

7.4.1 C-H stretch band intensities

From inspection of the ν(CH) intensity curves (figures 7.7 and 7.9, top), the trends of the intensities as a function of contact pressure conform to an increase in β_{m} predicted by the model. The cross-over points at about 550 MPa and 33°, respectively, may correspond, thus indicating a molecular tilt angle around that value.

Similar observations may be made with the d^+ and d^- peak heights (figures 7.5 and 7.9). However, the cross-over of the sx and px intensities of the d^+ peak lies at lower pressure and tilt angle of about 440 MPa and 18°, respectively. For the d^- peak, the trends in intensities conform to the previous observations, though no cross-over is seen in the experimental peak heights. Following our modelled peak heights, this indicates tilt angles below 40°.

The tilt angle is now quantified with the methodology developed in section 6.4. The variance of the model-to-experiment intensity ratios is used for each of the three intensity metrics of the ν(CH) band: its integrated intensity, its d^+ peak height and its d^- peak height. Figure 7.11 shows the normalised variance for each contact pressure and intensity metric. These provide global minima that indicate the molecular tilt angle as a function of contact pressure (figure 7.12). As the contact pressure is increased, the molecular chains

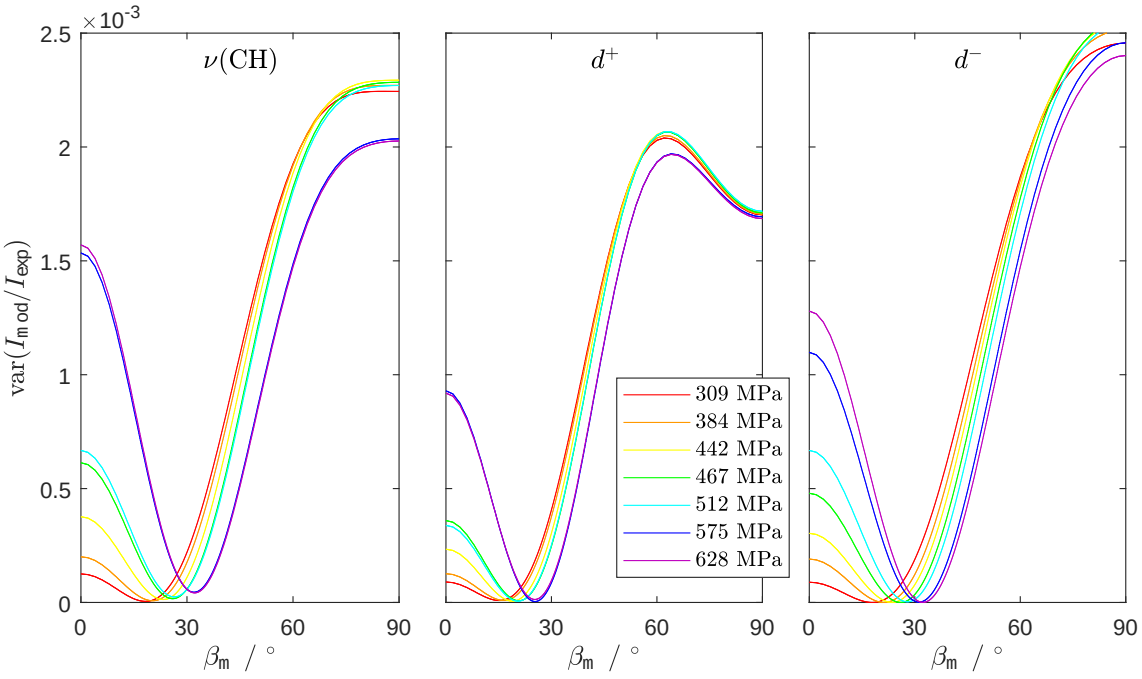

Figure 7.11: Normalised variance of modelled to experimental intensity ratios for each contact pressure. The global minimum in each variance curve provides a best fit β_{m} value.

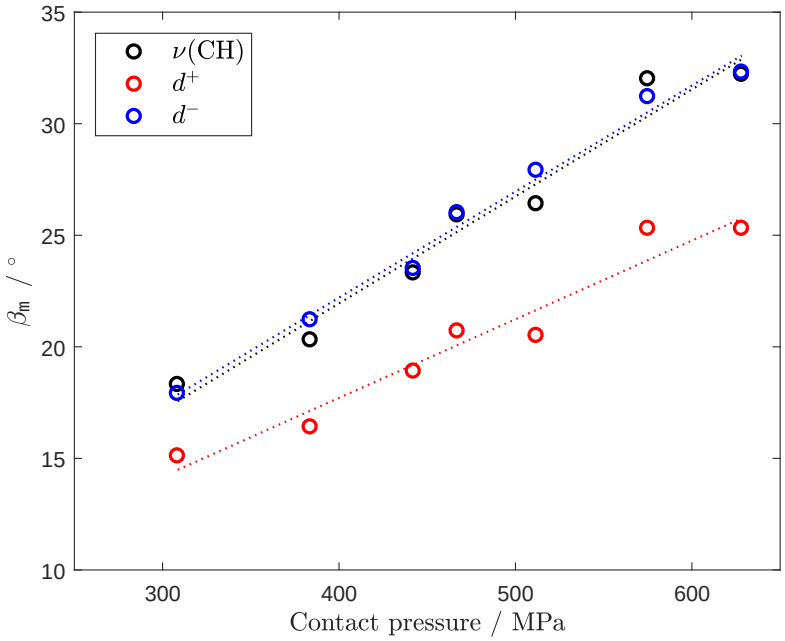

Figure 7.12: Best fit β_{m} from variance in figure 7.11 for each of the total intensity of the C−H stretch band as well as its d^+ and d^- peak heights. The dotted lines indicate linear fits (parameters given in table 7.3).

Table 7.3: Linear regression parameters for $\beta_{\mathsf{m}}(P) = a \cdot P + b$ derived from variance minimum as a function of contact pressure (figure 7.12). Regression uncertainties are included at one standard deviation.

Intensity metric	a / ° per 100 MPa	b / °	β_{m} at 500 MPa / °
integrated ν(CH)	4.8 ± 0.5	3 ± 3	27 ± 4
d^+ height	3.5 ± 0.5	4 ± 2	21 ± 3
d^- height	4.8 ± 0.3	3 ± 2	27 ± 3
the above combined	4.4 ± 0.6	3 ± 3	25 ± 4

tilt towards the surface normal. This was anticipated based on a quantitative comparison and can now be quantified by linear regression of the variance minima *versus* contact pressure. Table 7.3 provides the regression results.

The tilt angles derived from the total ν(CH) band intensity and the d^- peak height agree well. They range from 17.6° at the lowest to 33.0° at the highest contact pressure and result in linear regressions that are identical within error. The d^+ peak heights provides lower tilt angles (ranging from 14.5° to 25.8°) at a lower gradient with respect to the contact pressure.† The difference between the regression results indicates uncertainty in our methodology. By using decanoic acid in the harmonic approximation, additional methylene stretch modes as well as Fermi resonances between the A' modes are omitted. These additional modes affect the d^+ and d^- peak heights in different ways, for example by increasing the symmetric stretch intensity around the centre of the band, thus contributing to the observed difference. The effect of experimental errors, further reduced by linear regression, is assumed to be much smaller.

7.4.2 Main symmetric stretch mode

Intensities modelled for the main symmetric methylene stretch mode (v_{73} of decanoic acid) are now used to asses molecular tilt angle by comparison to the d^+ peak height in selected experimental spectra. The main antisymmetric methylene stretch mode (v_{76} of decanoic acid) is not used here, since it is strongly affected by intensities from A' modes in all spectra. For the present analysis, we employ the ratio $I_{py}(d^+)/I_{sy}(d^+)$ while omitting the px and sx spectra. The px and py spectra are the same, so one of these can be used as no additional information is comprised in the other. Furthermore, the d^+ feature in the sx spectrum is strongly affected by a dominating d^- feature. We thus only employ the py and sy spectra in an attempt to enhance precision. The modelled $I_{py}(v_{73})/I_{sy}(v_{73})$ ratio is presented in the left-hand plot of figure 7.13 as a function of β_{m} along with the experimental $I_{py}(d^+)/I_{sy}(d^+)$ ratios for each contact pressure. The intersections of these

†Extrapolated to zero pressure, the zinc arachidate monolayer could be said to have a chain tilt angle of $3° \pm 3°$. However, such extrapolation bears no physical meaning as the linearity of the tilt-pressure relation is not ascertained here. Furthermore, our analysis of the zinc arachidate monolayer at the silica-air interface provides a distinctly higher tilt angle. A stabilisation of the tilt angle is expected when the contact pressure is lowered below the range tested here. A minimum practically feasible contact pressure is expected to arise due to surfaces forces, *i.e.* when bringing the surfaces in close proximity, these snap into contact at a non-zero contact pressure even without an external force being applied.

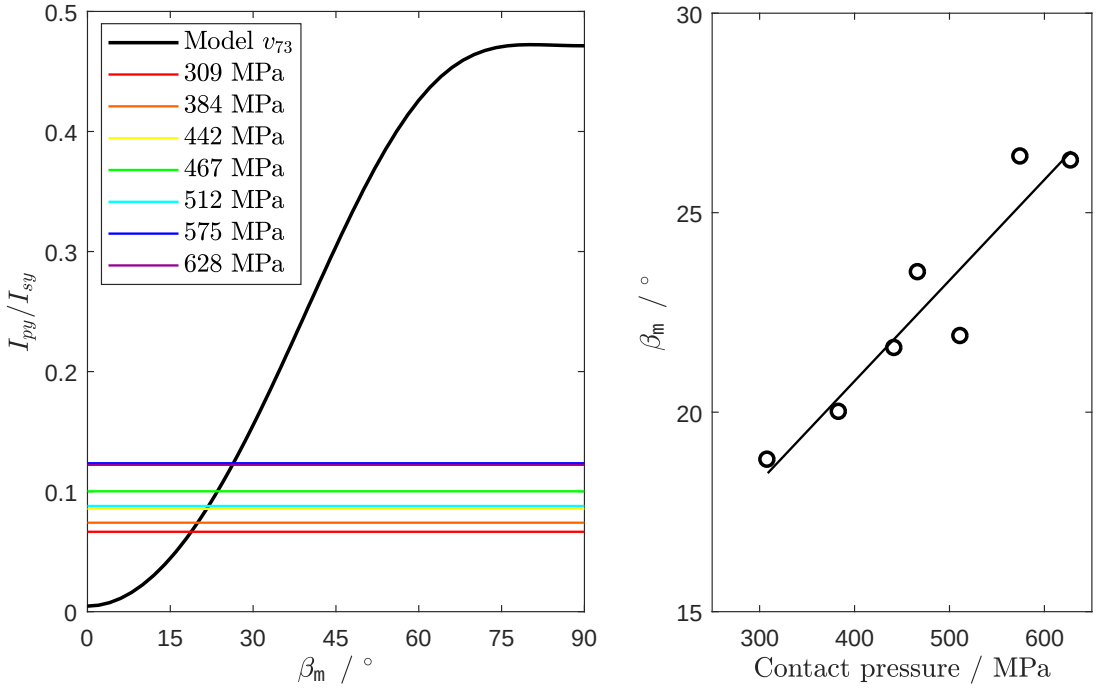

Figure 7.13: Molecular tilt angle β_{m} derived from the modelled *py*-to-*sy* symmetric stretch intensity ratio (black curve) compared to corresponding experimental d^+ peak height ratios (coloured horizontal lines). The right-hand plot shows the matching points (markers) and a regression line with a gradient of 0.025° MPa^{-1}.

lines provide the 'best-fit' molecular tilt angles, presented in the right-hand plot of said figure. Linear regression through these points provides a gradient of 2.5±0.5° per 100 MPa in this range and extrapolates to 11 ± 2° at 0 MPa. The gradient is lower than that of the previous analysis with the modelled spectrum rather than with an individual mode used here. The molecular tilt angle ranges from 18.5° to 26.5°, which is in line with our earlier analysis. The difference lies in omitting contributions of antisymmetric stretch modes to the modelled intensities in the present analysis. These increase the *py* intensity more than the *sy* intensities, thus increasing the I_{py}/I_{sy} ratio and leading to higher tilt angles. In contrast to our analysis of the zinc arachidate monolayer at the silica-air interface (section 6.4), we may conclude that individual modes do not provide a good intensity metric for the spectral features of the ν(CH) band. Symmetric and antisymmetric modes are too convoluted in the present case because the laser is incident near the critical angle.

7.4.3 Layer stiffness

The stiffness of the zinc arachidate layer in the contact can be quantified with Young's modulus, computed from

$$E = \frac{\Delta P}{\Delta d \,/\, d} \tag{7.6}$$

where d is the layer thickness in the contact and Δd is its change upon increasing the contact pressure by ΔP. The exact length of the molecule drops out of the equation, only tilt angles and pressures remain after substitution. The linear regressions of the derived molecular tilt angles for the ν(CH) and d^- intensities provide a modulus of 3.0 GPa for deformation caused by pressure applied orthogonal to the interface in the $300 - 600$ MPa range. For the d^+ peak height, a modulus of 5.0 GPa is found while the intensity ratio results in 6.4 GPa. These values allow comparison with other experimental techniques, such as the surface force apparatus or colloidal-probe atomic force microscopy, which measure forces rather than tilt angles.

7.5 Concluding summary

Zinc arachidate monolayers were confined in a solid-solid contact of SF10 and fused silica. Static load was applied to the contact from $309 - 628$ MPa, as determined by optical microscopy of the contact area and Hertzian contact theory. Raman spectra were collected at the four standard polarisation combinations at seven distinct contact pressures. This previously collected dataset formed a case study for our present model and presented an application of Raman spectroscopy to boundary lubrication by fatty acids. Qualitative analysis suggested an increase in packing order and lateral chain interaction with increasing contact pressure. A quantitative analysis proved possible with our modelling approach.

Spectra were modelled with our model description of the scattering process using Raman tensors from GAUSSIAN computations of decanoic acid in the harmonic approximation. These modelled spectra provided integrated band intensities as well as d^+ and d^- peak intensities that were compared to the corresponding experimentally observed intensities. A qualitative comparison suggested tilt angles below 40°. The variance of model-to-experiment intensity ratios showed a global minimum, from which a best-fit β_{m} value was extracted, ranging from 17.6° at the lowest to 33.0° at the highest contact pressure for the total ν(CH) band intensity and the d^- peak height. The d^+ peak height provided lower tilt angles ranging from 14.5° to 25.8°. This corresponded to a layer stiffness of 3.0 GPa and 5.0 GPa, respectively, in the tested pressure range.

Here, scattering from individual Raman-active modes does not represent the ν(CH) band well. This contrasts with our analysis of the zinc arachidate monolayer at the silica-air interface (section 6.4). A likely cause for this is the incidence angle of the laser beam, which is very near the critical angle in the present experiments, resulting in convolution of the symmetric and antisymmetric methylene modes in spectra of all four standard polarisation combinations.

Chapter 8

Concluding remarks

This chapter summarises the conclusions of the foregoing chapters and suggests routes for further development of the methodology and its application.

8.1 Summary of conclusions

Raman scattering is a tensorial effect and thus intrinsically affected by orientation of the scattering molecule with respect to the electric field that causes it. In this work, a consistent framework is developed to use this tensorial dependence to obtain knowledge of scatterer orientation, in particular at an interface. It combines experiment with theory in a consistent modelling framework.

The experimental approach uses laser Raman spectroscopy combined combined with collection of the scattered light through a microscope objective lens. The incident laser beam is preferably incident above the critical angle for the interface under study, thus causing total internal reflection, to achieve surface sensitivity and to amplify scattering from molecules near the interface. The position of the microscope objective also affects the collected amount of Raman scattering. Incident as well as collection linear polarisation directions may be adjusted. Calibration of all experimental variables is essential to obtain spectra that can be compared quantitatively to modelling results.

In addition to the experimental considerations, the material under study determines the spatial distribution of Raman scattering. Here, molecular vibrations are probed. Transitions between fundamental and first excited vibrational modes of the studied molecule give rise to Raman scattering when the transition dipole moment includes the fully symmetric species of the point group to which the molecule belongs. At least one of the six Raman tensor elements is then non-zero. The symmetry of the vibrational mode involved determines the form of the Raman tensor. Examples of its derivation are presented and the form of Raman tensors is tabulated for practically all relevant symmetry species using a consistent definition of molecular axes.

In a classical description, the strength of Raman scattering is given by the first derivative of the molecular dipole moment with respect to the vibrational normal coordinate

of the (first) excited state to which the molecule is excited by the incident light. It may be assessed by the bond-polarisability model, symmetry considerations as well as by *ab intitio* electronic structure computations. A method for computation of Raman tensors in the commercial software package GAUSSIAN is developed. Currently, the B3LYP/6-311++G(d,p) theory level is available to provide harmonic vibrational normal modes and their Raman tensors.

A model description incorporating the above experimental parameters and molecular properties is developed. Starting from an incident linearly polarised laser beam, classical electrodynamics is used to derive the field at the location of the scattering molecule. The scattering molecule is located beyond or in front of an interface or is embedded in a thin film between two dielectrics. At this location, a formulation of the local field correction is developed to account for cavity and reaction fields. An effective Raman dipole is induced by the local field via the Raman polarisability tensor. The emitted Raman scattering is computed at the entrance to the microscope objective via a grid of nodes which spans it aperture. At each node, Lorentz reciprocity is employed to derive the far-field due to the Raman-induced dipole, again involving a cavity field correction. The field is collimated and summed along x and y polarisation directions to obtain total Raman intensities. The model is implemented in MATLAB using vectorial, complex electric field amplitudes. Appropriate coordinate transformations are applied throughout.

The model presents a consistent method to compute Raman scattering intensities taking into account the experimental geometry, material properties, molecular orientation and Raman tensor. A model spectrum of a chosen polarisation combination can be generated by computing the Raman intensities for all relevant modes with the appropriate Raman tensors and broadening the obtained lines with an appropriate function. The dependence of the Raman intensity on experimental parameters as well as molecular properties may thus be assessed. This can be used in analysis or interpretation of Raman spectra as well as in designing experiments for optimised scattering intensities.

The model is tested with three systems: sulfate salt solutions at a fused silica surface, carbon tetrachloride at a sapphire surface and a Langmuir-Blodgett monolayer of zinc arachidate on fused silica in air. The v_1 mode of the sulfate anion provides a test of the optical description of the model, which proved to correctly predict the v_1 intensity as a function of linear polarisation angles, angle of laser incidence and numerical aperture. The accuracy of the match between model and experimental relative intensities is limited by calibration of the experimental components. The model may be used to assess experimental error with such known Raman scatterer.

The Raman spectra of liquid carbon tetrachloride on a sapphire hemisphere are not correctly predicted with our current model. No individual parameter explains to observed intensities, suggesting a combination of experimental error in polarisation directions and birefringence of sapphire, which is not included in the model and which affects both signal and background intensities in different ways.

For both sulfate and CCl_4, relative intensities were not affected by the local field

correction. Furthermore, averaging of the molecular orientation ensures that all diagonal Raman tensors result in the same relative intensities as do the off-diagonal Raman tensors. This implies that total scattering intensities, such as arising from various isotopologues, scale with the number of similar modes involved while their relative intensities are equal to that arising from one of the involved modes.

The monolayer of zinc arachidate on silica produces a convoluted ν(CH) stretch band, including symmetric and antisymmetric methylene stretch modes. The symmetric modes engage in Fermi resonances which alter line intensities within the band. This is compared to modelled Raman spectra using harmonic electronic structure computations of decanoic acid to represent the modes of the alkyl chain. The *py*-to-*sx* intensity ratio of the main antisymmetric methylene stretch feature is judged to be most reliable and provides a molecular tilt angle of 18°, in line with other studies of condensed monolayers of fatty acid salts. Other metrics prove relatively insensitive to molecular orientation, mainly because of the experimental geometry and the omission of anharmonic effects in modelling the spectra.

Raman scattering intensities thus depend on a combination of optical geometry, refractive indices of the materials involved, orientation (distribution) of the Raman scattering molecule and the Raman tensor of the vibrational mode of interest. These parameters can be isolated with our model to investigate their effect. This allows optimisation of Raman experiments where, for example, high intensities in a single polarisation combination or a high sensitivity with respect to molecular orientation is desired. It is also possible to compute Raman spectra by modelling multiple Raman lines and applying an appropriate line broadening function.

Finally, the approach is applied to interpret Raman spectra of a two-monolayer thick film of zinc arachidate in a SF10-silica contact under static load, increasing from roughly 300 to 600 MPa. The molecular tilt angle is found to increase with increasing load, the extend of which depends on the intensity and best-fit metrics used in analysing the spectra. For the integrated ν(CH) band intensity, the molecular tilt β_{m} can be expressed in degrees as a function of contact pressure P in units of 100 MPa as

$$\beta_{\mathsf{m}}(P) = (4.8 \pm 0.5) \cdot P + (3 \pm 3) \tag{8.1}$$

over the sampled range. This example demonstrates to application of Raman spectroscopy to the tribological investigation of a buried, lubricated interface. The molecular response is measured *in situ* as a function of macroscopic modulations of the interface with quantitative interpretation of the observed changes in the Raman spectra.

8.2 Further work

The current work forms a starting point for further research. Ideas are briefly presented for Raman theory, the developed model and Raman scattering experiments.

8.2.1 Theory

In some cases, exact knowledge of the Raman tensor is not needed. These include fully symmetric modes, such as v_1 of sulfate, or antisymmetric modes with only one non-zero off-diagonal tensor element, such as v_{76} of decanoic acid. In these cases, modelled intensities are simply scaled with the actual numerical value of the Raman tensor element. However, interpretation of Raman scattering intensities is currently limited for modes that are difficult to predict on the basis of symmetry considerations alone.

Computational Raman tensors provide the needed information. A lack of accurate Raman tensors for molecular spectra that involve significant anharmonic contributions currently limits the accuracy of interpretation of such spectra. It is further desired that *ab intitio* computations are made possible for increasingly larger molecules. Convoluted bands such as the C−H stretch band in long alkyl chains can then be interpreted more reliably by fitting the experimental spectrum as a whole with a modelled spectrum. The field of computational chemistry is continuously advancing and it is hoped that the current work encourages developments in Raman calculations.

The present methodology in principle lends itself to evaluation of Raman tensors. For a molecule of known orientation, a well-calibrated experimental system provides scattering intensities that can be linked directly to its Raman-active mode. By modelling the intensities as a function of the Raman tensor elements, a best-fit may be found just like any other unknown variable. In the current implementation, this would lead to relative values for the Raman tensor elements as no absolute scattering intensities are computed.

8.2.2 Model

The model developed in this work was tested with a limited number of samples. Other tests of the model can include calculations for a traditional Raman experimental setup, in which the laser beam is incident on a bulk liquid sample under 90° relative to the direction of observation. For a given Raman tensor, the intensity ratio is then expected to conform to the depolarisation ratio ρ, which depends on the tensor invariants. Toluene presents another interesting test case with multiple Raman modes in close proximity.

The model can be extended and improved in various ways, a number of which were addressed in section 5.7.2.

Currently, modelled intensities are relative quantities only, requiring at least two spectra for mutual comparison. If only one spectrum was needed, acquisition times would be halved and dynamic measurements would be made much more accessible. This may be achieved with materials that present two Raman peaks in the same spectral region, where these could be used as an internal calibration. For example, the symmetric v_2 feature of the CCl_4 spectra could be employed for comparison with the antisymmetric v_4 mode. Such situations are not at all universal, so that quantitative calculation of intensities would increase the applicability of the model.

At present, an incident amplitude of unity results in discrete intensities at individual

grid nodes, which are averaged for the final intensity. Identical grids should be used when comparing modelling outcomes. Proper physical constants and units are used throughout the `pirs.m` function, resulting in modelled intensities in an order of magnitude of roughly 10^{-70}. Physical units of irradiance can be obtained by taking the actual dimensions of the objective entrance into account. Quantitative intensities may be achieved by using the actual incident laser irradiance in the model and by implementing physical distance measures, including the size of the objective lens. Transmission coefficients of various optical components may also need to be included for collimated parts of the light trajectory where physical distances are less critical.

Furthermore, the model may be extended to layered materials and thick films (*i.e.* thickness on the scale of the employed wavelength or larger). Currently, the model is restricted to a single interface between two infinite half-spaces with the scatterer located at a distance from this interface and to a thin film of scatterers between such half-spaces. More complex interfaces may readily be implemented in the model by adjusting the coupling factors to those appropriate for the interface.

Coupling factors for a dipole embedded in a thick film may be found in [148] and [149], including a generalisation for a stack of layers. The transfer-matrix method can be used to derive coupling factors in other geometries, described in [192, 193] for intensities (squared amplitudes) and summarised in appendix A of [152]. More advanced treatments are developed for amplitudes [194, 195], where coherent as well as incoherent interference may play a role.

Furthermore, fields inside a layered structure including optical anisotropy can be computed in software packages, some of which are freely available, including LayerOptics [196].

The model was used in this work to explore variation of the Raman intensities with respect to various input parameters in different experimental settings. A number of other dependencies may be of interest, including the following.

- What is the effect of experimental geometry, including laser angle of incidence as well as NA and position of the objective, on the sensitivity of the orientational analysis for a given system (*i.e.* known Raman tensor and refractive indices)? This sensitivity depends on the molecular orientation. If this orientation is roughly known, the experimental geometry may be optimised to provide strongest variation in that range.

- Can intermediate incident polarisations be used to improve spectra and/or their analysis? A mix of *p*- and *s*-polarised incident laser radiation may be used to probe all Raman modes in a single spectrum.

- What if the refractive index of the hemisphere varies significantly between the incident laser radiation and the wavelength of the Raman scattering? If dispersion increases to significant levels, for any material in the sample, the incident laser and

the Raman scattering propagate differently through the interface and give rise to an additional complexity in the radiation pattern that can be exploited. For example, if the refractive index of the hemisphere is larger at the Raman-shifted frequency, the critical angle of the interface reduces, so that more of the dipole near-field couples into the hemisphere, enhancing the signal.

- To what extend can the model be applied to Raman microscopy? Both laser illumination and collection of scattered light take place through the microscope objective. The incident field thus spreads over an appreciable cone of angles and its polarisation depends on the position within said cone. How sensitive is the modelled intensity to molecular orientation in this case?

8.2.3 Experiment

For an experimental point of view, it is strongly suggested to perform a calibration of the polarisers with each of the objective lenses. The telescope may be used without hesitation to reduce the laser spot size when $\theta_{k,i}$ is sufficiently far removed from the critical angle. The spread in angle of incidence was not found to result in significantly different Raman intensities.

The angle of laser incidence may be set at the critical angle to maximise Raman scattering from interfacial molecules. At this angle, the px and py spectra are equal for isotropically averaged molecules. A difference between these spectra (for a non-symmetric mode) indicates a preferred azimuthal orientation in the plane of the interface. The model may be applied to deduce this information without requiring additional measurements at various azimuthal orientations of the sample. A tribological interface can thus be investigated as it undergoes both load and shear, possibly aligning lubricant molecules.

Above the critical angle, the evanescent field that drives the dipole has a strong z-dependence. Similarly, the dipole near-field is evanescent and couples back into the hemisphere with an equally strong dependence on the depth of the molecule. The Raman scattered intensity thus depends on z via two exponentials in an experimental geometry where $\theta_{k,i} > \theta_c$ and the objective collects Raman scattering in radiation zone II. This geometry may be employed to probe interfacial molecules with an increased selectivity and perform depth-profiling with increases sensitivity. The collection system designed by Stefan Seeger and co-workers for supercritical angle fluorescence [7, 8] could also be applied in current Raman systems. In 2017, his research group published a proof-of-principle of what they termed supercritical angle Raman microscopy [197].

The NA and position of the objective can be used effectively to enhance the Raman signal. Though a larger NA results in higher intensities, tilting the object so that it detects the intensity spike around the critical angle is more effective. This configuration can be implemented with the developed rotation clamp (section 3.1.1) and a relatively small NA would suffice in this case. Care should be taken that the laser beam reflection does not fall into the objective lens.

Using all four standard polarisation combinations is not required when seeking to derive one molecular parameter only, such as β_{m}. Polarisation combinations with highest signal-to-noise should be chosen without comprising redundant information. Duplicate spectra can thus be avoided.

The linear polarisation direction of the laser and of collection can be adjusted for optimal scattering intensities. The incident polarisation can be set to a value between p and s to excite all Raman-active modes in a single spectrum. Both polarised and depolarised Raman modes are then observed. A reduced number of spectra may then be collected to capture all relevant spectral information from the sample. This reduces acquisition time. Analysis of molecular orientation as a function of an external modification is still possible with the current model after establishing the molecular orientation once with a full dataset (*i.e.* at least two spectra of different polarisation combinations) and then collecting only spectra of one of the polarisation combinations. The relation between the intensities in the latter then directly relate to changes in molecular orientation as predicted by the model.

Alternatively, selection of polarisations may be automated in time. For example, spectra of at least two different polarisation combinations may be collected in a gated fashion continuously while, for example, adjusting an external parameter slowly in order to investigate the effect of this parameter of the molecular orientation.

8.2.4 Areas of application

The method of interpreting Raman spectra with our model is applicable to all interfacial Raman scattering. As usual, fluorescence or obscuring background Raman lines are to be avoided. Furthermore, it may be extended readily to other scattering-based phenomena.

For each application, an appropriate intensity metric and fitting metric has to be established. If whole spectra are modelled, these may be fitted to the experimental spectra with a least-squares procedure after baseline subtraction.

When multiple isotopologues are present, the total recorded intensities may be split according to their abundance. Modes may thus be isolated. Alternatively, fitting the experimental spectra may also provide isotopological abundance of a sample where this is unknown.

Our approach may also be applied to study interactions between materials. The orientation of molecules bound to a surface by adsorption from bulk, by (covalent) bonds or by polymerisation from a graft may all be established. Interactions with various materials may be assessed by variation of the surface by exchanging hemispheres or by treatment of its bottom surface.

Materials to consider include surfactants [79, 81], phospholipids [54] (bilayers of which have recently been simulated as a function of pressure [198, 199]), liquid crystals, polymers [200] and fatty acids. Raman spectroscopy of such materials has previously been demonstrated successfully in our research group. Other materials preferably include small well-characterised molecules of which Raman tensors can be computed with high accuracy.

The model may further be applied to study (model) membranes at surfaces. The distribution of molecular orientations differs in various membrane conformations. Different Raman intensities are thus expected to arise from a bilayer structure as opposed to vesicles or tubes. Furthermore, pollutants, active agents [201] or (drug) cargo molecules [200] may be investigated. These may bind to membranes with a preferred orientation, possibly illuminating their mechanism of action. Other 'doped' materials may be investigated as well, preferably with strong Raman bands for the dopant in an unobstructed part of the Raman spectrum. Deuteration can also be used to isolate otherwise obstructed spectral features.

A further extension of the approach involves mapping of the interface, recently developed in our group [200]. It involves collecting total scattering intensities for a selected spectral region and mapping this onto the spectrometer detector. A graphical representation of the integrated Raman intensity is thus obtained. When combining this with selection of linear polarisation, intensity maps can be obtained that are sensitive to molecular orientation. Our model may then be used to compute intensities integrated over the selected spectral range and deduce molecular orientation at each location on the sampled interface. This approach may be of particularly interest to lubrication and wear in a contact spot of non-uniform pressure and/or shear.

To what other techniques can the developed methodology be applied? The mathematical description of Raman scattering is similar to that of other phenomena in which absorption is followed by emission, such a Rayleigh scattering and fluorescence.

The model may be amended for application to Rayleigh scattering by substituting the molecular polarisability tensor for the Raman polarisability tensor, removing the frequency shift and adjusting various equations. Intensities of interfacial Rayleigh scattering may then be analysed quantitatively. However, chemical specificity is lost.

Fluorescence may also be modelled, though the molecular orientation may change in the time-frame between absorption and emission processes. The delay between excitation of the fluorophore and emission of the fluorescent light limits the application of the current model description to cases where there is no (appreciable) movement of the molecule on the interval between excitation and emission. A tensorial absorption cross-section should be used while the 'Raman-induced dipole' is now replaced by the fluorophore dipole moment, which is also linked to the molecular orientation.

In the above suggested applications, detection of emitted light could follow the currently developed routine of computing far-field dipole radiation at the entrance to the microscope objective.

8.3 A final word

The main impact of this research lies in providing a coherent electromagnetic description of the Raman scattering process in combination with computational Raman tensors to enhance understanding of Raman spectra of molecules at interfaces. In combining experi-

ment, theory and modelling into one consistent description, a great number of variables can be assessed quantitatively. Molecular orientation is one of these properties of appreciable historic and current interest.

The approach is complementary to other spectroscopic (infrared, sum-frequency), optical (ellipsometry) and structural techniques (X-ray or neutron scattering) that can be applied to buried interfaces. For many of these, advanced theories and models exist. With the current work, it is hoped that the field of Raman spectroscopy is further advanced with a modelling framework for quantitative interpretation of Raman spectra. The ubiquitous nature of Raman scattering, its access to direct molecular information without altering the system under observation lends itself to wildly varying applications that become increasingly realistic as technological developments in lasers and detectors progress. It would be a shame if data interpretation would be hampered by a lack of understanding how the Raman intensities arise, what factors contribute to its spectra and how measurements could be optimised.

It is hoped that this thesis provides the reader with insights as well as ideas to encourage and advance their application of Raman spectroscopy.

finis

References

[1] B. Bhushan, *Introduction to Tribology.* John Wiley & Sons, New York, NY, USA (2002).

[2] C. M. Mate, *Tribology on the Small Scale: A Bottom Up Approach to Friction, Lubrication, and Wear.* Mesoscopic Physics and Nanotechnology. Oxford University Press, Oxford, UK (2008).

[3] A. Unsworth, *Tribology of artifical hip joints*, Proceedings of the Institution of Mechanical Engineers, Part J: Journal of Engineering Tribology **220** (8), 711–718 (2006).

[4] J. N. Israelachvili, *Intermolecular and Surface Forces (Third Edition).* Academic Press, San Diego (2011).

[5] K. J. Wahl, R. R. Chromik and G. Y. Lee, *Quantitative in situ measurement of transfer film thickness by a Newton's rings method*, Wear **264** (78), 731–736 (2008).

[6] A. Esguerra Arce, C. Amaya, N. A. Sánchez, J. Muñoz-Saldaña, Y. Castro and L. Ipaz, *Wear mechanisms analysis by Scanning Electron Microscopy of bone-AISI 304ss/Ti-Al-N tribological pairs*, Microscopy: advances in scientific research and education, 936–943 (2014).

[7] J. Enderlein, T. Ruckstuhl and S. Seeger, *Highly efficient optical detection of surface-generated fluorescence*, Applied Optics **38** (4), 724–732 (1999).

[8] T. Ruckstuhl, J. Enderlein, S. Jung and S. Seeger, *Forbidden Light Detection from Single Molecules*, Analytical Chemistry **72** (9), 2117–2123 (2000).

[9] M. Ponjavic, A. Chennaoui and J. S. Wong, *Through-Thickness Velocity Profile Measurements in an Elastohydrodynamic Contact*, Tribology Letters **50** (2), 261–277 (2013).

[10] B. D. Casson and C. D. Bain, *Determination of the Optical Properties of Monolayers on Water*, Langmuir **13** (20), 5465–5469 (1997).

[11] J. Israelachvili et al., *Recent advances in the surface forces apparatus (SFA) technique*, Reports on Progress in Physics **73** (3), 036601 (2010).

[12] M. Chen, W. H. Briscoe, S. P. Armes and J. Klein, *Lubrication at Physiological Pressures by Polyzwitterionic Brushes*, Science **323** (5922), 1698–1701 (2009).

[13] A. Dedinaite, E. Thormann, G. Olanya, P. M. Claesson, B. Nystrom, A.-L. Kjoniksen and K. Zhu, *Friction in aqueous media tuned by temperature-responsive polymer layers*, Soft Matter **6** (11), 2489–2498 (2010).

[14] A. Dedinaite, T. Pettersson, B. Mohanty and P. M. Claesson, *Lubrication by organized soft matter*, Soft Matter **6** (7), 1520–1526 (2010).

[15] D. Marsh, *Quantitation of Secondary Structure in ATR Infrared Spectroscopy*, Biophysical Journal **77** (5), 2630–2637 (1999).

[16] T. Hasegawa, Y. Nakano and Y. Ishii, *Molecular Orientation Analysis of a Single-Monolayer Langmuir-Blodgett Film on a Thin Glass Plate by Infrared Multiple-Angle Incidence Resolution Spectrometry*, Analytical Chemistry **78** (6), 1739–1742 (2006).

[17] R. Mendelsohn, G. Mao and C. R. Flach, *Infrared reflectionabsorption spectroscopy: Principles and applications to lipidprotein interaction in Langmuir films*, Biochimica et Biophysica Acta - Biomembranes **1798** (4), 788–800 (2010).

[18] O. P. Khatri, C. D. Bain and S. K. Biswas, *Effects of Chain Length and Heat Treatment on the Nanotribology of Alkylsilane Monolayers Self-Assembled on a Rough Aluminum Surface*, The Journal of Physical Chemistry B **109** (49), 23405–23414 (2005).

[19] C. D. Bain, *Sum-frequency vibrational spectroscopy of the solid/liquid interface*, Journal of the Chemical Society, Faraday Transactions **91** (9), 1281–1296 (1995).

[20] J. F. D. Liljeblad and E. Tyrode, *Vibrational Sum Frequency Spectroscopy Studies at Solid/Liquid Interfaces: Influence of the Experimental Geometry in the Spectral Shape and Enhancement*, The Journal of Physical Chemistry C **116** (43), 22893–22903 (2012).

[21] G. L. Richmond, *Molecular Bonding and Interactions at Aqueous Surfaces as Probed by Vibrational Sum Frequency Spectroscopy*, Chemical Reviews **102** (8), 2693–2724 (2002).

[22] H.-F. Wang, W. Gan, R. Lu, Y. Rao and B.-H. Wu, *Quantitative spectral and orientational analysis in surface sum frequency generation vibrational spectroscopy (SFG-VS)*, International Reviews in Physical Chemistry **24** (2), 191–256 (2005).

[23] E. Tyrode and J. Hedberg, *A Comparative Study of the CD and CH Stretching Spectral Regions of Typical Surfactants Systems Using VSFS: Orientation Analysis of the Terminal CH_3 and CD_3 Groups*, The Journal of Physical Chemistry C (116), 1080–1091 (2011).

[24] P. Y. Hsu and A. Dhinojwala, *Contact of Oil with Solid Surfaces in Aqueous Media Probed Using Sum Frequency Generation Spectroscopy*, Langmuir **28** (5), 2567–2573 (2011).

[25] E. Tyrode and J. F. D. Liljeblad, *Water Structure Next to Ordered and Disordered Hydrophobic Silane Monolayers: A Vibrational Sum Frequency Spectroscopy Study*, The Journal of Physical Chemistry C **117** (4), 1780–1790 (2012).

[26] A. D. Curtis, S. R. Burt, A. R. Calchera and J. E. Patterson, *Limitations in the Analysis of Vibrational Sum-Frequency Spectra Arising from the Nonresonant Contribution*, The Journal of Physical Chemistry C **115** (23), 11550–11559 (2011).

[27] Y. Tong, Y. Zhao, N. Li, M. Osawa, P. B. Davies and S. Ye, *Interference effects in the sum frequency generation spectra of thin organic films. I. Theoretical modeling and simulation*, The Journal of Chemical Physics **133** (3), 034704 (2010).

[28] Y. Tong, Y. Zhao, N. Li, Y. Ma, M. Osawa, P. B. Davies and S. Ye, *Interference effects in the sum frequency generation spectra of thin organic films. II: Applications to different thin-film systems*, The Journal of Chemical Physics **133** (3), 034705 (2010).

[29] G. Li, A. Dhinojwala and M. S. Yeganeh, *Interference Effect from Buried Interfaces Investigated by Angular-Dependent InfraredVisible Sum Frequency Generation Technique*, The Journal of Physical Chemistry C **115** (15), 7554–7561 (2011).

[30] R. Fraenkel, G. E. Butterworth and C. D. Bain, *In Situ Vibrational Spectroscopy of an Organic Monolayer at the Sapphire-Quartz Interface*, Journal of the American Chemical Society **120** (1), 203–204 (1998).

[31] D. A. Beattie, S. Haydock and C. D. Bain, *A comparative study of confined organic monolayers by Raman scattering and sum-frequency spectroscopy*, Vibrational Spectroscopy **24** (1), 109–123 (2000).

[32] D. A. Beattie, R. Fraenkel, S. A. Winget, A. Petersen and C. D. Bain, *Sum-Frequency Spectroscopy of a Monolayer of Zinc Arachidate at the Solid-Solid Interface*, The Journal of Physical Chemistry B **110** (5), 2278–2292 (2006).

[33] A. Ghalgaoui, R. Shimizu, S. Hosseinpour, R. lvarez Asencio, C. McKee, C. M. Johnson and M. W. Rutland, *Monolayer Study by VSFS: In Situ Response to Compression and Shear in a Contact*, Langmuir **30** (11), 3075–3085 (2014).

[34] C. Meltzer, J. Paul, H. Dietrich, C. M. Jger, T. Clark, D. Zahn, B. Braunschweig and W. Peukert, *Indentation and Self-Healing Mechanisms of a Self-Assembled Monolayer – A Combined Experimental and Modeling Study*, Journal of the American Chemical Society **136** (30), 10718–10727 (2014).

[35] D. A. Woods and C. D. Bain, *Total internal reflection Raman spectroscopy*, Analyst **137** (1), 35–48 (2012).

[36] D. A. Woods and C. D. Bain, *Total internal reflection spectroscopy for studying soft matter*, Soft Matter **10** (8), 1071–1096 (2014).

[37] C. Sourisseau, *Polarization Measurements in Macro- and Micro-Raman Spectroscopies: Molecular Orientations in Thin Films and Azo-Dye Containing Polymer Systems*, Chemical Reviews **104** (9), 3851–3892 (2004).

[38] I. W. Hamley, V. Castelletto, C. M. Moulton, J. Rodríguez-Pérez, A. M. Squires, T. Eralp, G. Held, M. R. Hicks and A. Rodger, *Alignment of a Model Amyloid Peptide Fragment in Bulk and at a Solid Surface*, The Journal of Physical Chemistry B **114** (24), 8244–8254 (2010).

[39] J. C. Rodriguez-Perez, I. W. Hamley and A. M. Squires, *Determination of orientations of aromatic groups in self-assembled peptide fibrils by polarised Raman spectroscopy*, Physical Chemistry Chemical Physics **15** (33), 13940–13950 (2013).

[40] C. Chen, J.-Y. Li, L. Wang, D.-F. Lu and Z.-M. Qi, *Waveguide-coupled directional Raman radiation for surface analysis*, Physical Chemistry Chemical Physics **17** (33), 21278–21287 (2015).

[41] E. C. Le Ru and P. G. Etchegoin, *Principles of Surface-Enhanced Raman Spectroscopy and related Plasmonic Effects*. Elsevier, Amsterdam, Oxford (2009).

[42] D. Pristinski, E. C. Le Ru, S. Tan, S. Sukhishvili and H. Du, *Surface-enhanced Raman scattering at a planar dielectric interface beyond critical angle*, Optics Express **16** (24), 20117–20125 (2008).

[43] C. K. A. Nyamekye, S. C. Weibel, J. M. Bobbitt and E. A. Smith, *Combined measurement of directional Raman scattering and surface-plasmon-polariton cone from adsorbates on smooth planar gold surfaces*, Analyst **143** (2), 400–408 (2018).

[44] R. Zhang et al., *Chemical mapping of a single molecule by plasmon-enhanced Raman scattering*, Nature **498** 82 (2013).

[45] C. Chen, N. Hayazawa and S. Kawata, *A 1.7 nm resolution chemical analysis of carbon nanotubes by tip-enhanced Raman imaging in the ambient*, Nature Communications **5** 3312 (2014).

[46] A. Syed and E. A. Smith, *Raman Imaging in Cell Membranes, Lipid-Rich Organelles, and Lipid Bilayers*, Annual Review of Analytical Chemistry **10** (1), 271–291 (2017).

[47] M. D. Lesoine, J. M. Bobbitt, S. Zhu, N. Fang and E. A. Smith, *High angular-resolution automated visible-wavelength scanning angle Raman microscopy*, Analytica Chimica Acta **848** 61–66 (2014).

[48] C. A. Damin, V. H. T. Nguyen, A. S. Niyibizi and E. A. Smith, *Application of scanning angle Raman spectroscopy for determining the location of buried polymer interfaces with tens of nanometer precision*, Analyst **140** (6), 1955–1964 (2015).

[49] J. M. Bobbitt, D. Mendivelso-Pérez and E. A. Smith, *Scanning angle Raman spectroscopy: A nondestructive method for simultaneously determining mixed polymer fractional composition and film thickness*, Polymer **107** 82–88 (2016).

[50] J. M. Bobbitt and E. A. Smith, *Extracting interface locations in multilayer polymer waveguide films using scanning angle Raman spectroscopy*, Journal of Raman Spectroscopy **49** (2), 262–270 (2018).

[51] C. Ota, *Investigation of the structure of water at hydrophobic and hydrophilic interfaces by angle-resolved TIR Raman spectroscopy*, Physical Chemistry Chemical Physics **17** (39), 26435–26442 (2015).

[52] K. J. Park et al., *Raman system for sensitive and selective identification of volatile organic compounds*, Sensors and Actuators B: Chemical **220** 491–499 (2015).

[53] D. A. Beattie, S. A. Winget and C. D. Bain, *Raman Scattering from Confined Liquid Films in the Sub-Nanometre Regime*, Tribology Letters **27** (2), 159–167 (2007).

[54] K. Guha, *Molecular Tribology.* Doctoral thesis, Durham University (2011).

[55] M. Praveena, C. D. Bain, V. Jayaram and S. K. Biswas, *Total internal reflection (TIR) Raman tribometer: a new tool for in situ study of friction-induced material transfer*, RSC Advances **3** (16), 5401–5411 (2013).

[56] M. Praveena, K. Guha, A. Ravishankar, S. K. Biswas, C. D. Bain and V. Jayaram, *Total internal reflection Raman spectroscopy of poly(alpha-olefin) oils in a lubricated contact*, RSC Advances **4** (42), 22205–22213 (2014).

[57] C. V. Raman and K. S. Krishnan, *A New Type of Secondary Radiation*, Nature **121** (501), 3048 (1928).

[58] C. V. Raman, *The Molecular Scattering of Light, Nobel lecture*, 267–275. Elsevier Publishing Company, Amsterdam (1965).

[59] C. V. Raman, *A new radiation*, Indian Journal of Physics **2** 387–398 (1928).

[60] *The Nobel Prize in Physics 1930*, Nobel Media AB, Stockholm, Sweden (2014).

[61] D. A. Long, *The Raman Effect: A Unified Treatment of the Theory of Raman Scattering by Molecules.* John Wiley & Sons, Ltd, Chichester, UK (2002).

[62] J. A. Koningstein, *Introduction to the Theory of the Raman Effect.* D. Reidel Publishing Company, Dordrecht (1972).

[63] K. Nakamoto, *Infrared and Raman Spectra of Inorganic and Coordination Compounds (4th edition).* John Wiley & Sons, Inc., New York. (1982).

[64] G. Placzek, *Rayleigh-Streuung und Raman-Effekt*, Handbuch der Radiologie **6** 205–374 (1934).

[65] M. Born and E. Wolf, *Prinicples of Optics, 6th edition (with corrections).* Pergamon Press, Oxford (1989).

[66] J. A. Souza, *Alternative derivation of the electric dipole radiation fields*, American Journal of Physics **51** (1), 54–54 (1983).

[67] E. Hecht, *Optics, fourth edition.* Addison Wesley, San Francisco, 4th Ed. (2002).

[68] D. J. Griffiths, *Introduction to Electrodynamics.* Pearson Benjamin Cummings, San Francisco (2008).

[69] F. de Fornel, *Evanescent waves: from Newtonian optics to atomic optics.* Springer series in optical sciences. Springer-Verlag, Berlin, Heidelberg (2001).

[70] L. Woodward, *Introduction to the theory of molecular vibrations and vibrational spectroscopy.* Clarendon Press, Oxford (1972).

[71] S. Roy, K.-K. Hung, U. Stege and D. K. Hore, *Rotations, Projections, Direction Cosines, and Vibrational Spectra*, Applied Spectroscopy Reviews **49** (3), 233–248 (2014).

[72] E. B. Wilson Jr., J. C. Decius and P. C. Cross, *Molecular Vibrations. The Theory of Infrared and Raman Vibrational Spectra.* McGraw-Hill, New York (1955).

[73] G. Davidson, *Group Theory for Chemists.* Macmillan Physical Science Series. Macmillan Education Ltd, Basingstoke (1991).

[74] F. A. Cotton, *Chemical applications of group theory (3rd edition).* John Wiley & Sons, Inc., New York. (1990).

[75] J. M. Rodgers, R. M. Abaskharon, B. Ding, J. Chen, W. Zhang and F. Gai, *Fermi Resonance as a Means to Determine the Hydrogen-Bonding Status of Two Infrared Probes*, Physical Chemistry Chemical Physics **19** (24), 16144–16150 (2017).

[76] G. Herzberg, *Molecular Spectra and Molecular Structure. Volume II. Infrared and Raman Spectra of Polyatomic Molecules (reprinted edition with corrections).*, Krieger Publishing Company, Malabar, FL, USA (1991).

[77] H.-H. Perkamus, *Encyclopedia of spectroscopy.* VCH Verlagsgesellschaft mbH, Weinheim, Germany (1995).

[78] B. P. Straughan, A. V. Golton, S. Walker and J. K. Burdett, *Spectroscopy (volume two).* Chapman and Hall, London (1976).

[79] A. P. Dudgeon, *Surfactant Adsorption at Liquid-Solid Interfaces.* Doctoral thesis, Durham University (2017).

[80] P. R. Greene and C. D. Bain, *Total internal reflection Raman spectroscopy*, Spectroscopy Europe **16** 8–15 (2004).

[81] D. A. Woods, *Dynamics of Surfactant Adsorption at Solid-Liquid Interfaces.* Doctoral thesis, Durham University (2011).

[82] J. H. Churchwell, *TIR-Raman Spectroscopy of Model Supported Lipid Bilayers.* Doctoral thesis, Durham University (2014).

[83] M. J. Jones, *Organic Chemistry (3rd edition).* W. W. Norton & Company, New York (2005).

[84] Y. Mo, *A Critical Analysis on the Rotation Barriers in Butane*, The Journal of Organic Chemistry **75** (8), 2733–2736 (2010).

[85] M. Yirong, *Rotational barriers in alkanes*, Wiley Interdisciplinary Reviews: Computational Molecular Science **1** (2), 164–171 (2011).

[86] I. H. Malitson, *Interspecimen Comparison of the Refractive Index of Fused Silica*, Journal of the Optical Society of America **55** (10), 1205–1209 (1965).

[87] *Schott Data Sheet SF10 728284.428 (version 02/01/2014)*, SCHOTT North America, Inc. (2014).

[88] M. J. Dodge, *Refractive Index*, Handbook of Laser Science and Technology, Volume IV, Optical Materials: Part 2, p. 30. CRC Press, Boca Raton (1986).

[89] S. Kedenburg, M. Vieweg, T. Gissibl and H. Giessen, *Linear refractive index and absorption measurements of nonlinear optical liquids in the visible and near-infrared spectral region*, Optical Materials Express **2** (11), 1588–1611 (2012).

[90] P. E. Ciddor, *Refractive index of air: new equations for the visible and near infrared*, Applied Optics **35** (9), 1566–1573 (1996).

[91] S. Urréjola, A. Sánchez and M. F. Hervello, *Refractive Indices of Sodium, Potassium, and Ammonium Sulfates in Ethanol-Water Solutions*, Journal of Chemical and Engineering Data **55** (8), 2924–2929 (2010).

[92] *CRC Handbook of Chemistry and Physics (64th edition).* CRC Press, Boca Raton (1984).

[93] M. A. Valdes-Covarrubias, R. D. Cadena-Nava, E. Vásquez-Martínez, D. Valdez-Pérez and J. Ruiz-García, *Crystallite structure formation at the collapse pressure of fatty acid Langmuir films*, Journal of Physics: Condensed Matter **16** (22), S2097 (2004).

[94] K. Kjaer, J. Als-Nielsen, C. A. Helm, P. Tippman-Krayer and H. Moehwald, *Synchrotron X-ray diffraction and reflection studies of arachidic acid monolayers at the air-water interface*, The Journal of Physical Chemistry **93** (8), 3200–3206 (1989).

[95] P. Tippmann-Krayer and H. Moehwald, *Precise determination of tilt angles by X-ray diffraction and reflection with arachidic acid monolayers*, Langmuir **7** (10), 2303–2306 (1991).

[96] J. B. Peng, G. T. Barnes and I. R. Gentle, *The structures of Langmuir-Blodgett films of fatty acids and their salts*, Advances in Colloid and Interface Science **91** (2), 163–219 (2001).

[97] R. L. Flurry and S. F. Abdulnur, *Vibrations of the n-alkanes and the nonrigid molecular symmetry group*, Journal of Molecular Spectroscopy **63** (1), 33–42 (1976).

[98] R. G. Snyder and J. R. Scherer, *Band structure in the CH stretching region of the Raman spectrum of the extended polymethylene chain: Influence of Fermi resonance*, The Journal of Chemical Physics **71** (8), 3221–3228 (1979).

[99] M. Cardona, *Resonance Phenomena*, Light Scattering in Solids II, basic concepts and instrumentation, ch. 2. Topics in Applied Physics. Springer-Verlag, Berlin (1982).

[100] W. Hayes and R. Loudon, *Scattering of Light by Crystals.* Wiley, New York (1978).

[101] R. Loudon, *The Raman Effect in Crystals*, Advances in Physics **13** (52), 423–482 (1964).

[102] J. Nye, *Physical Properties of Crystals.* The Clarendon Press, Oxford (1957).

[103] M. I. Aroyo, J. M. Perez-Mato, D. Orobengoa, E. Tasci, G. De La Flor and A. Kirov, *Crystallography online: Bilbao crystallographic server*, Bulgarian Chemical Communications **43** (2), 183–197 (2011).

[104] O. S. Mortensen and S. Hassing, *Polarization and Interference Phenomena in Resonance Raman Scattering.* Heyden & Son, Ltd., London (1980).

[105] *International Tables for Crystallography, Volume A: Space-group symmetry.* International Union of Crystallography, second online edition (2016).

[106] M. S. Amer, *Raman Spectroscopy, Fullerenes and Nanotechnology.* RSC Nanoscience & Nanotechnology. Royal Society of Chemistry, London (2010).

[107] F. Nogueira, A. Castro and M. A. L. Marques, *A Tutorial on Density Functional Theory*, 218–256. Springer, Berlin, Heidelberg, Germany (2003).

[108] J. Bloino, A. Baiardi and M. Biczysko, *Aiming at an accurate prediction of vibrational and electronic spectra for medium-to-large molecules: An overview*, International Journal of Quantum Chemistry **116** (21), 1543–1574 (2016).

[109] J. Neugebauer, M. Reiher, C. Kind and B. A. Hess, *Quantum chemical calculation of vibrational spectra of large molecules–Raman and IR spectra for Buckminsterfullerene*, Journal of Computational Chemistry **23** (9), 895–910 (2002).

[110] M. V. P. dos Santos, Y. G. Proenza, A. Mahmood and R. L. Longo, *PICVib: an accurate, fast and simple procedure to investigate selected vibrational modes at high theoretical levels and evaluate Raman intensities*, Journal of Raman Spectroscopy (2016).

[111] P. T. Panek and C. R. Jacob, *Efficient Calculation of Anharmonic Vibrational Spectra of Large Molecules with Localized Modes*, ChemPhysChem **15** (15), 3365–3377 (2014).

[112] P. Partovi-Azar and T. D. Kühne, *Efficient On-the-Fly calculation of Raman Spectra from Ab-Initio molecular dynamics: Application to hydrophobic/hydrophilic solutes in bulk water*, Journal of Computational Chemistry **36** (29), 2188–2192 (2015).

[113] *NIST Computational Chemistry Comparison and Benchmark Database*, NIST Standard Reference Database Number 101, Release 19, April 2018.

[114] K. M. Gough, C. Lupinetti and R. Dawes, *Computation and interpretation of Raman scattering intensities*, Journal of Computational Methods in Sciences and Engineering **4** 597–609 (2004).

[115] V. Barone, M. Biczysko and J. Bloino, *Fully anharmonic IR and Raman spectra of medium-size molecular systems: accuracy and interpretation*, Physical Chemistry Chemical Physics **16** (5), 1759–1787 (2014).

[116] J. Bloino, M. Biczysko and V. Barone, *Anharmonic Effects on Vibrational Spectra Intensities: Infrared, Raman, Vibrational Circular Dichroism, and Raman Optical Activity*, The Journal of Physical Chemistry A **119** (49), 11862–11874 (2015).

[117] Y. Cornaton, M. Ringholm, O. Louant and K. Ruud, *Analytic calculations of anharmonic infrared and Raman vibrational spectra*, Physical Chemistry Chemical Physics **18** (5), 4201–4215 (2016).

[118] A. Baiardi, J. Bloino and V. Barone, *Accurate Simulation of Resonance-Raman Spectra of Flexible Molecules: An Internal Coordinates Approach*, Journal of Chemical Theory and Computation **11** (7), 3267–3280 (2015).

[119] S. A. Fischer, T. W. Ueltschi, P. Z. El-Khoury, A. L. Mifflin, W. P. Hess, H.-F. Wang, C. J. Cramer and N. Govind, *Infrared and Raman Spectroscopy from Ab Initio Molecular Dynamics and Static Normal Mode Analysis: The C-H Region of DMSO as a Case Study*, The Journal of Physical Chemistry B **120** (8), 1429–1436 (2016).

[120] C. Lee, W. Yang and R. G. Parr, *Development of the Colle-Salvetti correlation-energy formula into a functional of the electron density*, Physical Review B **37** (2), 785–789 (1988).

[121] A. D. Becke, *Density-functional thermochemistry. III. The role of exact exchange*, The Journal of Chemical Physics **98** (7), 5648–5652 (1993).

[122] J. R. Cheeseman and M. J. Frisch, *Basis Set Dependence of Vibrational Raman and Raman Optical Activity Intensities*, Journal of Chemical Theory and Computation **7** (10), 3323–3334 (2011).

[123] M. J. Frisch et al., *Gaussian 09, Revision A.02.* Gaussian, Inc, Wallingford CT (2009).

[124] A. P. Scott and L. Radom, *Harmonic Vibrational Frequencies: An Evaluation of Hartree-Fock, Møller-Plesset, Quadratic Configuration Interaction, Density Functional Theory, and Semi-empirical Scale Factors*, The Journal of Physical Chemistry **100** (41), 16502–16513 (1996).

[125] M. P. Andersson and P. Uvdal, *New Scale Factors for Harmonic Vibrational Frequencies Using the B3LYP Density Functional Method with the Triple-ζ Basis Set 6-311+G(d,p)*, The Journal of Physical Chemistry A **109** (12), 2937–2941 (2005).

[126] K. Ben Mabrouk, T. H. Kauffmann, H. Aroui and M. D. Fontana, *Raman study of cation effect on sulfate vibration modes in solid state and in aqueous solutions*, Journal of Raman Spectroscopy **44** (11), 1603–1608 (2013).

[127] R. E. Hester, R. A. Plane and G. E. Walrafen, *Raman Spectra of Aqueous Solutions of Indium Sulfate, Nitrate, and Perchlorate*, The Journal of Chemical Physics **38** (1), 249–250 (1963).

[128] F. Rull and H. Ohtaki, *Raman spectral studies on ionic interaction in aqueous alkali sulfate solutions*, Spectrochimica Acta Part A: Molecular and Biomolecular Spectroscopy **53** (5), 643–653 (1997).

[129] Y. Matsumoto, H. Harada, K. Yui, H. Uchida, K. Itatani and S. Koda, *Raman spectroscopic study of aqueous alkali sulfate solutions at high temperature and pressure to yield precipitation*, The Journal of Supercritical Fluids **49** (3), 303–309 (2009).

[130] T. J. Wallington, B. P. Pivesso, A. M. Lira, J. E. Anderson, C. J. Nielsen, N. H. Andersen and Ø. Hodnebrog, *CH_3Cl, CH_2Cl_2, $CHCl_3$, and CCl_4: Infrared spectra, radiative efficiencies, and global warming potentials*, Journal of Quantitative Spectroscopy and Radiative Transfer **174** 56–64 (2016).

[131] J. D. Gaynor, A. M. Wetterer, E. J. Valente and S. G. Mayer, *The $\nu_3 - \nu_4$ difference band contribution to the CCl_4 symmetric stretch (ν_1) mode*, Journal of Raman Spectroscopy **46** (1), 189–193 (2014).

[132] J. D. Gaynor, A. M. Wetterer, R. M. Cochran, E. J. Valente and S. G. Mayer, *Vibrational Spectroscopy of the CCl_4 ν_1 Mode: Effect of Thermally Populated Vibrational States*, Journal of Chemical Education **92** (11), 1949–1952 (2015).

[133] T. Chakraborty and S. N. Rai, *Comparative study of infrared and Raman spectra of CCl_4 in vapour and condensed phases: Effect of LO-TO splitting resulting from hetero-isotopic TD-TD interactions*, Spectrochimica Acta Part A: Molecular and Biomolecular Spectroscopy **65** (2), 406–413 (2006).

[134] B. Jordanov, D. Tsankov and E. H. Korte, *Peculiarities in the stretching vibrations of the methylene groups*, Journal of Molecular Structure **651653** 101–107 (2003).

[135] S. Ahmed, Z. Nikolov and S. L. Wunder, *Effect of Curvature on Nanoparticle Supported Lipid Bilayers Investigated by Raman Spectroscopy*, The Journal of Physical Chemistry B **115** (45), 13181–13190 (2011).

[136] K. M. Gough, *Theoretical analysis of molecular polarizabilities and polarizability derivatives in hydrocarbons*, The Journal of Chemical Physics **91** (4), 2424–2432 (1989).

[137] R. F. W. Bader, T. A. Keith, K. M. Gough and K. E. Laidig, *Properties of atoms in molecules: additivity and transferability of group polarizabilities*, Molecular Physics **75** (5), 1167–1189 (1992).

[138] K. M. Gough and J. R. Dwyer, *Effect of Structure and Conformation on Raman Trace Scattering Intensities in Hydrocarbons*, The Journal of Physical Chemistry A **102** (16), 2723–2731 (1998).

[139] K. M. Gough, J. R. Dwyer and R. Dawes, *Ab initio analysis of C-H and C-C stretching intensities in Raman spectra of hydrocarbons*, Canadian Journal of Chemistry **78** (7), 1035–1043 (2000).

[140] K. M. Gough, H. K. Srivastava and K. Belohorcov, *Analysis of Raman trace scattering intensities in alkanes with the theory of atoms in molecules*, The Journal of Chemical Physics **98** (12), 9669–9677 (1993).

[141] J. C. Lavalley and N. Sheppard, *Etude des spectres de vibration du propane CD_3-CH_2-CD_3, et remarque sur les fréquences de vibration de valence symétrique des groupements CH_2 et CH_3*, Spectrochimica Acta Part A: Molecular Spectroscopy **28** (5), 845–854 (1972).

[142] R. G. Snyder, S. L. Hsu and S. Krimm, *Vibrational spectra in the CH stretching region and the structure of the polymethylene chain*, Spectrochimica Acta Part A: Molecular Spectroscopy **34** (4), 395–406 (1978).

[143] R. G. Snyder, H. L. Strauss and C. A. Elliger, *Carbon-hydrogen stretching modes and the structure of n-alkyl chains. 1. Long, disordered chains*, The Journal of Physical Chemistry **86** (26), 5145–5150 (1982).

[144] M. Harrand, *Polarized Raman spectra of oriented dipalmitoylphosphatidylcholine (DPPC). I. Scattering activities of skeletal stretching and methylene vibrations of hydrocarbon chains*, The Journal of Chemical Physics **79** (11), 5639–5651 (1983).

[145] M. Harrand, *Conformational analysis of long acyl chains in solid and liquid thin films: polarization and decomposition of the v(CH) Raman band*, Journal of Molecular Structure **214** 71–91 (1989).

[146] A. Percot and M. Lafleur, *Direct Observation of Domains in Model Stratum Corneum Lipid Mixtures by Raman Microspectroscopy*, Biophysical Journal **81** (4), 2144–2153 (2001).

[147] W. Lukosz, *Light emission by magnetic and electric dipoles close to a plane dielectric interface. III. Radiation patterns of dipoles with arbitrary orientation*, Journal of the Optical Society of America **69** (11), 1495–1503 (1979).

[148] C. E. Reed, J. Giergiel, J. C. Hemminger and S. Ushioda, *Dipole radiation in a multilayer geometry*, Physical Review B **36** (9), 4990–5000 (1987).

[149] O. H. Crawford, *Radiation from oscillating dipoles embedded in a layered system*, The Journal of Chemical Physics **89** (10), 6017–6027 (1988).

[150] J. Y. Courtois, J. M. Courty and J. C. Mertz, *Internal dynamics of multilevel atoms near a vacuum-dielectric interface*, Physical Review A **53** (3), 1862–1878 (1996). PRA.

[151] J. Mertz, *Radiative absorption, fluorescence, and scattering of a classical dipole near a lossless interface: a unified description*, Journal of the Optical Society of America B **17** (11), 1906–1913 (2000).

[152] Y. Itoh and T. Hasegawa, *Polarization Dependence of Raman Scattering from a Thin Film Involving Optical Anisotropy Theorized for Molecular Orientation Analysis*, The Journal of Physical Chemistry A **116** (23), 5560–5570 (2012).

[153] A. K. Burnham, G. R. Alms and W. H. Flygare, *The local electric field. I. The effect on isotropic and anisotropic Rayleigh scattering*, The Journal of Chemical Physics **62** (8), 3289–3297 (1975).

[154] R. Wortmann and D. M. Bishop, *Effective polarizabilities and local field corrections for nonlinear optical experiments in condensed media*, The Journal of Chemical Physics **108** (3), 1001–1007 (1998).

[155] D. R. Martin and D. V. Matyushov, *Microscopic fields in liquid dielectrics*, The Journal of Chemical Physics **129** (17), 174508 (2008).

[156] R. A. L. Vallée, M. Van Der Auweraer, F. C. De Schryver, D. Beljonne and M. Orrit, *A Microscopic Model for the Fluctuations of Local Field and Spontaneous Emission of Single Molecules in Disordered Media*, ChemPhysChem **6** (1), 81–91 (2005).

[157] J. Lekner and P. Castle, *Local fields near the surface of a crystalline dielectric*, Physica **101A** 89–98 (1980).

[158] P. Castle and J. Lekner, *Variation of the local field through the liquid-vapour interface*, Physica **101A** 99–111 (1980).

[159] R. R. Chance, A. Prock and R. Silbey, *Frequency shifts of an electric-dipole transition near a partially reflecting surface*, Physical Review A **12** (4), 1448–1452 (1975). PRA.

[160] S. Ostovar pour, L. D. Barron, S. T. Mutter and E. W. Blanch, *Raman Optical Activity*, Chiral Analysis (Second Edition), 249–291. Elsevier (2018).

[161] O. Levy and E. Cherkaev, *Effective medium approximations for anisotropic composites with arbitrary component orientation*, Journal of Applied Physics **114** (16), 164102 (2013).

[162] L. A. Apresyan and D. V. Vlasov, *On depolarization factors of anisotropic ellipsoids in an anisotropic medium*, Technical Physics **59** (12), 1760–1765 (2014).

[163] F. Goos and H. Hänchen, *Ein neuer und fundamentaler Versuch zur Totalreflexion*, Annalen der Physik **436** (7-8), 333–346 (1947).

[164] A. Puri and J. L. Birman, *Goos-Hänchen beam shift at total internal reflection with application to spatially dispersive media*, Journal of the Optical Society of America A **3** (4), 543–549 (1986).

[165] F. Krayzel, R. Pollès, A. Moreau, M. Mihailovic and G. Granet, *Simulation and analysis of exotic non-specular phenomena*, Journal of the European Optical Society - Rapid Publications **5** (10025), (2010).

[166] L. Luan, P. R. Sievert, B. Watkins, W. Mu, Z. Hong and J. B. Ketterson, *Angular radiation pattern of electric dipoles embedded in a thin film in the vicinity of a dielectric half space*, Applied Physics Letters **89** (3), 031119 (2006).

[167] L. Luan, P. R. Sievert, W. Mu, Z. Hong and J. B. Ketterson, *Highly directional fluorescence emission from dye molecules embedded in a dielectric layer adjacent to a silver film*, New Journal of Physics **10** (7), 073012 (2008).

[168] L. Luan, P. R. Sievert and J. B. Ketterson, *Near-field and far-field electric dipole radiation in the vicinity of a planar dielectric half space*, New Journal of Physics **8** (11), 264 (2006).

[169] M. Wojdyr, *Fityk: a general-purpose peak fitting program*, Journal of Applied Crystallography **43** (5 Part 1), 1126–1128 (2010).

[170] S. Alvarez, *A cartography of the van der Waals territories*, Dalton Transactions **42** (24), 8617–8636 (2013).

[171] D. V. Nickel, A. J. Garza, G. E. Scuseria and D. M. Mittleman, *The isotropic molecular polarizabilities of single methyl-branched alkanes in the terahertz range*, Chemical Physics Letters **592** 292–296 (2014).

[172] C. Van Dyck, T. J. Marks and M. A. Ratner, *Chain Length Dependence of the Dielectric Constant and Polarizability in Conjugated Organic Thin Films*, ACS Nano **11** (6), 5970–5981 (2017).

[173] R. G. Snyder, J. R. Scherer and B. P. Gaber, *Effects of chain packing and chain mobility on the Raman spectra of biomembranes*, Biochimica et Biophysica Acta - Biomembranes **601** 47–53 (1980).

[174] Y. Cho, M. Kobayashi and H. Tadokoro, *Raman band profiles and mobility of polymethylene chains*, The Journal of Chemical Physics **84** (8), 4636–4642 (1986).

[175] S. L. Wunder, M. I. Bell and G. Zerbi, *Band broadening of CH_2 vibrations in the Raman spectra of polymethylene chains*, The Journal of Chemical Physics **85** (7), 3827–3839 (1986).

[176] S. Abbate, G. Zerbi and S. L. Wunder, *Fermi resonances and vibrational spectra of crystalline and amorphous polyethylene chains*, The Journal of Physical Chemistry **86** (16), 3140–3149 (1982).

[177] M. Ho and J. E. Pemberton, *Alkyl Chain Conformation of Octadecylsilane Stationary Phases by Raman Spectroscopy. 1. Temperature Dependence*, Analytical Chemistry **70** (23), 4915–4920 (1998).

[178] M. W. Ducey, C. J. Orendorff, J. E. Pemberton and L. C. Sander, *Structure-Function Relationships in High-Density Octadecylsilane Stationary Phases by Raman Spectroscopy. 1. Effects of Temperature, Surface Coverage, and Preparation Procedure*, Analytical Chemistry **74** (21), 5576–5584 (2002).

[179] L. C. Sander, K. A. Lippa and S. A. Wise, *Order and disorder in alkyl stationary phases*, Analytical and Bioanalytical Chemistry **382** (3), 646–668 (2005).

[180] A. Dhanabalan, N. Prasanth Kumar, S. Major and S. S. Talwar, *Variation of monolayer behaviour and molecular packing in zinc arachidate LB films with subphase pH*, Thin Solid Films **327-329** 787–791 (1998).

[181] D. L. Allara and J. D. Swalen, *An infrared reflection spectroscopy study of oriented cadmium arachidate monolayer films on evaporated silver*, The Journal of Physical Chemistry **86** (14), 2700–2704 (1982).

[182] T. Arndt and C. Bubeck, *Fourier transform IR spectroscopy of protonated cadmium arachidate layers in different positions of a perdeuterated multilayer*, Thin Solid Films **159** (1), 443–449 (1988).

[183] C. Duschl and W. Knoll, *Structural characterization of Langmuir-Blodgett multilayer assemblies by plasmon surface polariton field-enhanced Raman spectroscopy*, The Journal of Chemical Physics **88** (6), 4062–4069 (1988).

[184] J. P. Rabe, J. D. Swalen, D. A. Outka and J. Stöhr, *Near-edge X-ray absorption fine structure studies of oriented molecular chains in polyethylene and Langmuir-Blodgett monolayers on Si(111)*, Thin Solid Films **159** (1), 275–283 (1988).

[185] T. Nakanaga, M. Matsumoto, Y. Kawabata, H. Takeo and C. Matsumura, *Observation of FTIR-PA spectra of Langmuir-Blodgett films of cadmium arachidate on glass plates*, Chemical Physics Letters **160** (2), 129–133 (1989).

[186] G. Hähner, M. Kinzler, C. Wöll, M. Grunze, M. K. Scheller and L. S. Cederbaum, *Near edge X-ray-absorption fine-structure determination of alkyl-chain orientation: Breakdown of the "building-block" scheme*, Physical Review Letters **67** (7), 851–854 (1991). PRL.

[187] M. Kinzler, A. Schertel, G. Hähner, C. Wöll, M. Grunze, H. Albrecht, G. Holzhüter and T. Gerber, *Structure of mono- and multilayer Langmuir-Blodgett films from Cd arachidate and Ca arachidate*, The Journal of Chemical Physics **100** (10), 7722–7735 (1994).

[188] D. Blaudez, T. Buffeteau, N. Castaings, B. Desbat and J. Turlet, *Organization in pure and alternate deuterated cadmium arachidate monolayers on solid substrates and at the air/water interface studied by conventional and differential Fourier transform infrared spectroscopies*, The Journal of Chemical Physics **104** (24), 9983–9993 (1996).

[189] J. B. Peng, *Studies of the structures of Langmuir-Blodgett films of fatty acid salts.* Doctoral thesis, University of Queensland (1998).

[190] M. Ruths, S. Lundgren, K. Danerlöv and K. Persson, *Friction of Fatty Acids in Nanometer-Sized Contacts of Different Adhesive Strength*, Langmuir **24** (4), 1509–1516 (2008).

[191] C. J. Orendorff, M. W. Ducey and J. E. Pemberton, *Quantitative Correlation of Raman Spectral Indicators in Determining Conformational Order in Alkyl Chains*, The Journal of Physical Chemistry A **106** (30), 6991–6998 (2002).

[192] K. Ohta and H. Ishida, *Matrix formalism for calculation of electric field intensity of light in stratified multilayered films*, Applied Optics **29** (13), 1952–1959 (1990).

[193] K. Ohta and H. Ishida, *Matrix formalism for calculation of the light beam intensity in stratified multilayered films, and its use in the analysis of emission spectra*, Applied Optics **29** (16), 2466–2473 (1990).

[194] E. Centurioni, *Generalized matrix method for calculation of internal light energy flux in mixed coherent and incoherent multilayers*, Applied Optics **44** (35), 7532–7539 (2005).

[195] M. C. Troparevsky, A. S. Sabau, A. R. Lupini and Z. Zhang, *Transfer-matrix formalism for the calculation of optical response in multilayer systems: from coherent to incoherent interference*, Optics Express **18** (24), 24715–24721 (2010).

[196] C. Vorwerk, C. Cocchi and C. Draxl, *LayerOptics: Microscopic modeling of optical coefficients in layered materials*, Computer Physics Communications **201** 119–125 (2016).

[197] D. Serrano and S. Seeger, *Supercritical angle Raman microscopy: a surface-sensitive nanoscale technique without field enhancement*, Light: Science & Applications **6** (10), e17066–e17066 (2017).

[198] W. Ding, M. Palaiokostas, W. Wang and M. Orsi, *Effects of Lipid Composition on Bilayer Membranes Quantified by All-Atom Molecular Dynamics*, The Journal of Physical Chemistry B **119** (49), 15263–15274 (2015).

[199] W. Ding, M. Palaiokostas, G. Shahane, W. Wang and M. Orsi, *Effects of High Pressure on Phospholipid Bilayers*, The Journal of Physical Chemistry B **121** (41), 9597–9606 (2017).

[200] C. L. Mercier, *Uptake and release of cargo molecules from responsive surfaces.* Doctoral thesis, Durham University (2019).

[201] M. A. Shackleford, *Lifecycle of the Antibacterial Triclosan.* Doctoral thesis, Durham University (2016).

[202] J. Meija et al., *Isotopic compositions of the elements 2013*, IUPAC Technical Report (2016).

[203] J. Kapitan, L. Hecht and P. Bour, *Raman spectral evidence of methyl rotation in liquid toluene*, Physical Chemistry Chemical Physics **10** (7), 1003–1008 (2008).

Appendix A

Symmetry and vibrational analysis

A.1 Introduction

Schönflies nomenclature is used for all point groups and conventional symbols are used for the symmetry operators with I the identity operator (which is sometimes listed as E), C a rotation, σ a reflection, i the inversion and S a rotation-reflection operation. The irreducible representation or symmetry species A is one-dimensional, as is B, while E is two-dimensional and F is three-dimensional (the symbol T is sometimes used for the last species). Accents and subscripts have their usual meaning as part of Mulliken symbols, see *e.g.* [73, 78] for details.

The equilibrium structures of the molecules considered here are given in figure A.1. The choice of Cartesian axes is indicated and follows conventional assignment as far as this is unambiguously defined. There is no convention for the x and y axes in a number of point groups. An arbitrary choice has therefore been made. This is also the case for the positive directions of all three axes. The procedure of assigning axes follows the prioritisation as follows.

1. The z-axis is chosen
   (a) along the unique axis of highest rotational order (the principal axis), or
   (b) along the two-fold axis that passes through most atoms, or
   (c) in a mirror plane,* or
   (d) along the axis which cuts most bonds in the molecule.
2. The x-axis is subsequently assigned
   (a) for planar molecules,
      i. with the z-axis in the molecular plane, the x-axis is normal to that plane, or

*In the C_s pointgroup, this priority ensures that the xz plane is the mirror plane. This choice is not uniform. Most character tables seem to assume that the mirror plane is the xy plane.

ii. if the z-axis is normal to the molecular plane, the x-axis passes through the most atoms;

(b) for non-planar molecules, the x-axis is

i. along the C_2' axis that passes through the most atoms, or

ii. in the σ_v plane that passes through the most atoms, or

iii. chosen to pass through most atoms.

3. The y-axis and its positive direction $\hat{\mathbf{y}}$ follow from the arbitrary choice of positive directions $\hat{\mathbf{x}}$ and $\hat{\mathbf{z}}$ for the x and z axes through the right hand rule.

The origin follows from the intersection of the axes, which is usually at the centre of mass.

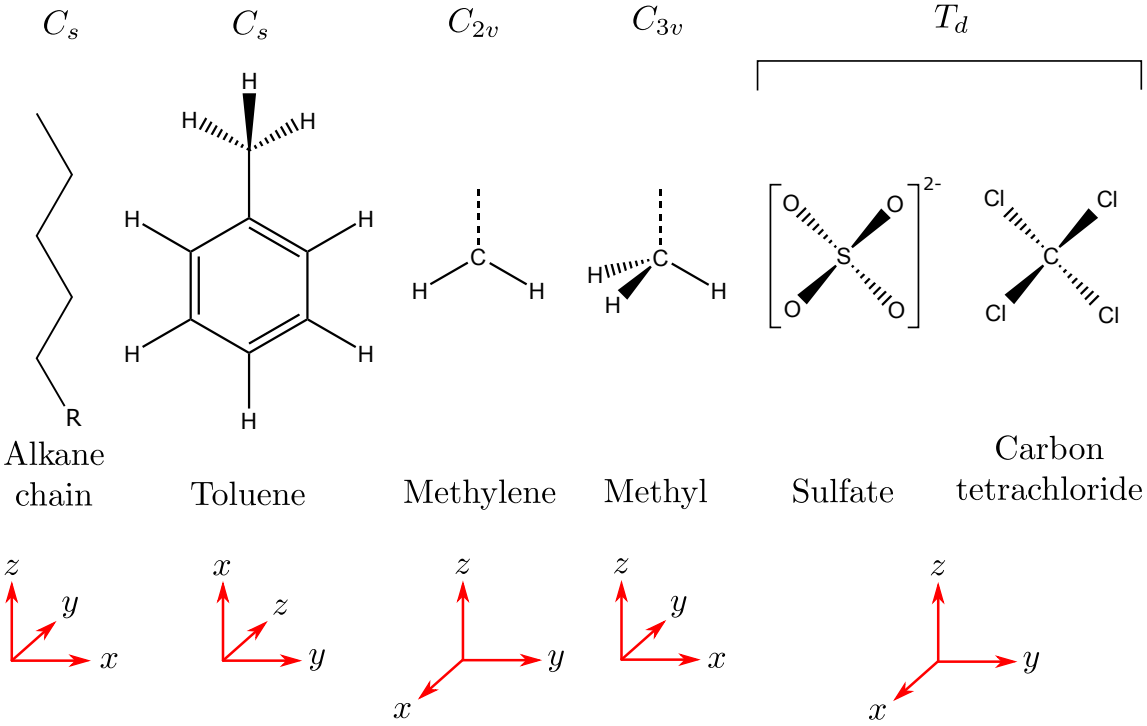

Figure A.1: Molecular equilibrium structures with choice of Cartesian axes.

A convenient overview of the symmetry species of translation, rotation and polarizability tensor elements is given in [61] from page 145 onwards for all molecular point groups. However, it lacks the symmetry operators and the characters of the irreducible representations which allow the computation of the number of vibrational fundamentals and their symmetry species. The analysis presented here builds from low to high symmetry. Only first overtones and combinations of two vibrational modes are considered as these are most relevant in spectral analysis.

Vibrational normal modes and their internal coorinates are described in several reference works, including Nakamoto [63] and Herzberg [76]. The internal coordinates Δr stands for a change in bond length and $\Delta\theta$ for a change in bond angle from their respective values in the equilibrium geometry of the molecule. A numerical subscript is used to differentiate the various bonds and angles.

Vibrational normal modes are numbered in a specific pattern. Fundamental bands are indicated with symbol v_n with $n = 1$ for the totally symmetric mode of highest frequency (highest wavenumber), then numbering the modes in descending frequency within each symmetry species. The order of the symmetry species follows the character tables.

For modes that are mainly localised, the following symbols can be used to represent the atomic motion: ν for bond stretching, δ for deformation or angle bending, τ for twisting or torsional motion, ω for wagging and ρ for rocking. The notation is used as in $\nu(CH_3)$, which stands for the bond stretching mode(s) in a methyl group.

Table A.1: Contribution to character of Γ_{3N} per unshifted atom

R	$\chi(R)$
I	$+3$
i	-3
σ	$+1$
C_2	-1
C_3^1, C_3^2	0
C_4^1, C_4^3	$+1$
C_6^1, C_6^5	$+2$
S_3^1, S_3^5	-2
S_4^1, S_4^3	-1
S_6^1, S_6^5	0

A.2 Toluene

Toluene consist of a benzene ring with one H-atom substituted by a methyl group (figure A.1). It contains 15 atoms, so that $3 \cdot 15 - 6 = 39$ vibrational normal modes are expected. The point group of its equilibrium structure is C_s, a symmetry group of order two. Its character table is presented in table A.2.

Table A.2: Character table for the C_s point group.

C_s	I	σ_h		
A'	1	1	$\mathbf{T_x}$, $\mathbf{T_y}$, $\mathbf{R_z}$	xx, yy, zz, $xy + yx$
A''	1	-1	$\mathbf{T_z}$, $\mathbf{R_x}$, $\mathbf{R_y}$	$xz + zx$, $yz + zy$

The representation Γ_{3N} incorporates the three-dimensional motion of all atoms. It is derived by counting the number of unshifted atoms when applying a typical symmetry operator R of each symmetry class on the molecular equilibrium structure. This contributes to the character $\chi(R)$ of the representation through table A.1. And results in

C_s	I	σ_h
unshifted atoms	15	13
Γ_{3N}	45	13

which is reduced into irreducible representations with the reduction formula of equation 2.166.

$$\begin{aligned}\Gamma_{3N} &= a_{A'}A' + a_{A''}A'' \\ &= \frac{1}{2}\left((1\cdot 1\cdot 45 + 1\cdot 1\cdot 13)\,A' + (1\cdot 1\cdot 45 + 1\cdot -1\cdot 13)\,A''\right) \\ &= 29A' + 16A''\end{aligned} \tag{A.1}$$

This representation is the combination of translation, rotation and vibrational representations. Table A.2 provides the symmetry species of the translations ($\mathbf{T_x}$, $\mathbf{T_y}$ and $\mathbf{T_z}$) and of the rotations ($\mathbf{R_x}$, $\mathbf{R_y}$ and $\mathbf{R_z}$), so that

$$\Gamma_{\mathsf{trans}} = 2A' + A'' \tag{A.2}$$

$$\Gamma_{\mathsf{rot}} = A' + 2A'' \tag{A.3}$$

which are removed from Γ_{3N} to obtain the representation of the vibrational fundamental modes.

$$\begin{aligned}\Gamma_{\mathsf{vib}} &= \Gamma_{3N} - \Gamma_{\mathsf{trans}} - \Gamma_{\mathsf{rot}} \\ &= 26A' + 13A''\end{aligned} \tag{A.4}$$

The vibrational representation includes 39 one-dimensional symmetry species. This agrees with the expected number of vibrational degrees of freedom.

There are 26 fully symmetrical modes, to which the binary elements xx, yy, zz and $xy+yx$ belong and thus the Raman tensor components α'_{xx}, α'_{yy}, α'_{zz} and $\alpha'_{xy} = \alpha'_{yx}$. This indicates that all A' modes are Raman active. These give rise to polarised Raman bands in the spectrum because A' is the totally symmetric symmetry species of the point group. The Raman tensors of these modes can be given in the symmetry axes in the general form

$$\boldsymbol{\alpha'}(A') = \begin{pmatrix} a & d & 0 \\ d & b & 0 \\ 0 & 0 & c \end{pmatrix} \tag{A.5}$$

consisting of at most four unique non-zero elements. Each of the 26 modes has a distinct set of numerical values for a, b, c and d. As $xz + zx$ and $yz + zy$ belong to A'', the 13 modes of this symmetry species are Raman active too but give rise to depolarised peaks in the Raman spectrum. The Raman tensor for these modes is of the general form

$$\boldsymbol{\alpha'}(A'') = \begin{pmatrix} 0 & 0 & e \\ 0 & 0 & f \\ e & f & 0 \end{pmatrix} \tag{A.6}$$

with different d and e for each of the 13 non-degenerate normal modes. In our molecular frame of reference (figure A.1), the x and z axes are interchanged from the symmetry

assignment in the point group table, altering the form of the above tensor to those listed in table C.1.

Ring breathing mode

We will not present a full analysis of all normal modes, but address the ring breathing mode only. This mode is the simultaneous stretching of the five C−H bonds in the phenyl ring. Its normal coordinate Q_{br} can be expressed as

$$Q_{\mathsf{br}}(t) = \Delta r_1(t) + \Delta r_2(t) + \Delta r_3(t) + \Delta r_4(t) + \Delta r_5(t) \tag{A.7}$$

where Δr_1 is the change length of bond 1 from its value in the equilibrium geometry. This mode belongs to A', the fully symmetric symmetry species of the point group.

The phenyl group on its own, belongs to the C_{2v} point group. It has 39 vibrational normal modes that display a higher symmetry than those of the C_s point group. The Raman tensor for the ring breathing mode will therefore have a higher symmetry. The form of equation A.12 presented in the next section will apply, rather than the one of equation A.5 derived here. This separation of vibrational modes between moieties of the same molecule arises when the force constant of the bonds differ sufficiently to give rise to non-resonant frequencies. In the case of toluene, the C−H bonds in the methyl group differ from those in the aromatic ring. This can be investigated computationally or experimentally as outlined in chapter 4.

Overtones, combinations and resonances

The symmetry species of the first overtones are found through the direct product of the symmetry species of the fundamentals with themselves, as none of the modes are degenerate

$$\Gamma_{\mathsf{over}} = \begin{cases} A'^2 = A' \times A' = A' \\ A''^2 = A'' \times A'' = A' \end{cases} \tag{A.8}$$

and for combination bands

$$\Gamma_{\mathsf{comb}} = \begin{cases} A' \times A' = A' \\ A'' \times A'' = A' \\ A' \times A'' = A'' \end{cases} \tag{A.9}$$

which are all found by multiplication of the characters and reduction of the resulting representation (or by using look-up tables that summarise the multiplication results, for example from [73]). All overtones and combinations are Raman-allowed and have Raman tensors of the same structure as presented for the fundamental modes. The first overtones have A' symmetry and could therefore interact amongst themselves as well as with the fundamental A' modes to give rise to Fermi resonance if the frequencies are sufficiently

close. Combinations belong to either the A' or A'' symmetry species and could also interact with other vibrational modes.

Isotopoloques

Toluene isotopologues with a ^{13}C at the 1, 2 or 5 position will not affect the symmetry assignment of the C_s point group as these atoms lie in the mirror plane. If at any other position, the symmetry of the molecule reduces to C_1. Considering the phenyl group in isolation, the mirror plane changes to the plane of the carbon atoms. Only its two-fold rotational symmetry is affected by isotopes. However, its point group will not reduce to lower symmetry than C_s.

Summary

In summary, toluene has 39 fundamental vibrational modes, all of which are Raman active according to symmetry. These belong to the A' (26 polarised bands, including the ring breathing mode) and A'' symmetry species and can produce overtones and combination bands without symmetry restrictions, resulting in Fermi resonances if the frequencies match.

A.3 Methylene

The methylene group ($-CH_2$), considered in isolation, is of C_{2v} symmetry (character table A.3). It has three atoms, providing $3 \cdot 3 - 6 = 3$ degrees of freedom for vibrational motion. The representation of the atomic motion Γ_{3N} is found to be

C_{2v}	I	C_2	$\sigma_v(xz)$	$\sigma'_v(yz)$
unshifted atoms	3	1	1	3
Γ_{3N}	9	-1	1	3

which is reduced into a combination of irreducible presentations with the reduction formula (equation 2.166) to yield

$$\Gamma_{3N} = 3A_1 + A_2 + 2B_1 + 3B_2 \, . \tag{A.10}$$

Removing the symmetry species of the three translations and three rotations returns the vibrational representation

$$\Gamma_{\text{vib}} = 2A_1 + B_2 \tag{A.11}$$

that has two fully symmetric modes and one antisymmetric mode. Inspection of the character table reveals that the symmetric modes involves all diagonal tensor elements

xx, yy and zz, giving rise to a diagonal Raman tensors

$$\boldsymbol{\alpha'}(A_1) = \begin{pmatrix} a & 0 & 0 \\ 0 & b & 0 \\ 0 & 0 & c \end{pmatrix} \tag{A.12}$$

while the antisymmetric mode involves the $yz + yz$ basis only and gives rise to a Raman tensor

$$\boldsymbol{\alpha'}(B_2) = \begin{pmatrix} 0 & 0 & 0 \\ 0 & 0 & d \\ 0 & d & 0 \end{pmatrix} \tag{A.13}$$

with only one unique non-zero element. Both tensors are specified with reference to the axes given in figure A.1. The basis vectors $\hat{\mathbf{x}}\hat{\mathbf{y}} + \hat{\mathbf{y}}\hat{\mathbf{x}}$ and $\hat{\mathbf{x}}\hat{\mathbf{z}} + \hat{\mathbf{z}}\hat{\mathbf{x}}$ do not form a suitable basis for any of the vibrational normal modes of methylene.

Normal modes

Wanting to deduce what molecular motion relates to which fundamental vibration, we establish a representation of the C−H bond stretch vectors $\Gamma_{\mathsf{stretch}}$. These two vectors point from C to H atom and transform as

C_{2v}	I	C_2	$\sigma_v(xz)$	$\sigma'_v(yz)$
$\Gamma_{\mathsf{stretch}}$	2	0	0	2

under the symmetry operators of the point group. This can be reduced to

$$\Gamma_{\mathsf{stretch}} = A_1 + B_2 \tag{A.14}$$

which leaves one vibrational mode of A_1 symmetry unaccounted for. Through

$$\Gamma_{\mathsf{vib}} = \Gamma_{\mathsf{stretch}} + \Gamma_{\mathsf{deform}} \tag{A.15}$$

this is assigned to a deformation of the bond angles. The only bond angle that cannot be described as a translation or a rotation of the molecule as a whole is the H−C−H angle. This vibrational motion must therefore belong to the left-over fully symmetric species A_1

$$\Gamma_{\mathsf{deform}} = \Gamma_{\mathsf{vib}} - \Gamma_{\mathsf{stretch}} = A_1 \tag{A.16}$$

Table A.3: Character table for the C_{2v} point group.

C_{2v}	I	C_2	$\sigma_v(xz)$	$\sigma'_v(yz)$		
A_1	1	1	1	1	$\mathbf{T_z}$	xx, yy, zz
A_2	1	1	-1	-1	$\mathbf{R_z}$	$xy + yx$
B_1	1	-1	1	-1	$\mathbf{T_x}$, $\mathbf{R_y}$	$xz + zx$
B_2	1	-1	-1	1	$\mathbf{T_y}$, $\mathbf{R_x}$	$yz + zy$

and gives a polarised Raman band in the spectrum of the moiety. The stretch modes result in one polarised and one depolarised Raman band.

The normal coordinates of the vibrations Q_{sst}, Q_{ast} and Q_{be} describe symmetric stretching of the two bonds, antisymmetric stretching and bending motions through

$$\begin{aligned} Q_{\mathsf{sst}}(t) &= \Delta r_1(t) + \Delta r_2(t) \\ Q_{\mathsf{ast}}(t) &= \Delta r_1(t) - \Delta r_2(t) \\ Q_{\mathsf{be}}(t) &= \Delta\theta_{12}(t) \end{aligned} \tag{A.17}$$

where Δr_1 is the change in length of bond 1, as before, and $\Delta\theta_{12}$ is the change in the H−C−H bond angle from its value in the equilibrium geometry.

Note that the three rotations of the methylene group become vibrations when the moiety is part of a molecule. In addition to the stretch and bending modes, wagging, rocking and twisting modes then arise.

Overtones, combinations and resonances

Analysing the symmetry species of any overtones and combinations gives

$$\Gamma_{\mathsf{over}} = \begin{cases} {A_1}^2 = A_1 \times A_1 = A_1 \\ {B_2}^2 = B_2 \times B_2 = A_1 \end{cases} \tag{A.18}$$

$$\Gamma_{\mathsf{comb}} = \begin{cases} A_1 \times A_1 = A_1 \\ A_1 \times B_2 = B_2 \end{cases} \tag{A.19}$$

(note that a combination of two B_2 modes can only be achieved through the second, fourth, sixth,... overtone of the B_2 fundamental, which is outside the scope of our analysis). We conclude that an overtone of the antisymmetric mode could interact with the symmetric fundamental vibrations (and their overtones or combinations) on the grounds of symmetry. The result of such an interaction necessarily belongs to the fully symmetric species A_1, is Raman active and polarised. The symmetric modes and their overtones and combinations can interact amongst themselves and the result is similarly Raman active and polarised. The strengths of this interaction depends on the frequencies of the modes involved and cannot be predicted on the grounds of symmetry considerations alone.

Isotopologues

Carbon isotopes do not affect the symmetry of an isolated methylene group. One hydrogen isotope reduces it from C_{2v} to C_s. The Raman tensor for these isotopologues have the forms deduced above for toluene.

Summary

In summary, isolated methylene has three Raman active fundamental bands: a symmetric CH_2 stretch, an antisymmetric CH_2 stretch and a symmetric H−C−H bending mode. The symmetric modes give polarised Raman peaks and can interact to give overtones and combinations as well as Fermi resonances if the vibrational frequencies are close.

A.4 Methyl

The geometry of an isolated methyl group ($-CH_3$) belongs to the C_{3v} point group (character table A.4). The four atoms give rise to $3 \cdot 4 - 6 = 6$ vibrational degrees of freedom. The representation of the atomic motion is found to be

C_{3v}	I	$2C_3$	$3\sigma_v$
unshifted atoms	4	1	2
Γ_{3N}	12	0	2

and can be reduced to

$$\Gamma_{3N} = 3A_1 + A_2 + 4E \tag{A.20}$$

showing that it consists of four one-dimensional and four two-dimensional irreducible representations. The vibrations of E symmetry represent two-fold degenerate every levels. The vibrational representation is obtained by removing the symmetry species of translations and rotations. This gives

$$\Gamma_{\mathsf{vib}} = 2A_1 + 2E \tag{A.21}$$

which shows that all fundamental modes are Raman active. The element $xx+yy$, belonging to A_1, is a linear combination of two binary elements. Its opposite is $xx - yy$ and with $xy + yx$ forms a basis for E (as it is a two-dimensional irreducible representation, it requires two basis vectors). The only undisturbed binary combination is zz. The individual elements xx and yy are not resolved in this case, indicating cylindrical symmetry in the Raman tensor for the fully symmetry modes

$$\boldsymbol{\alpha'}(A_1) = \begin{pmatrix} a & 0 & 0 \\ 0 & a & 0 \\ 0 & 0 & b \end{pmatrix} \tag{A.22}$$

Table A.4: Character table for the C_{3v} point group.

C_{3v}	I	$2C_3$	$3\sigma_v$		
A_1	1	1	1	$\mathbf{T_z}$	$xx + yy$, zz
A_2	1	1	-1	$\mathbf{R_z}$	
E	2	-1	0	($\mathbf{T_x}$, $\mathbf{T_y}$), ($\mathbf{R_x}$, $\mathbf{R_y}$)	($xx - yy$, $xy + yx$), ($xz + zx$, $yz + zy$)

while the general form of the Raman tensor for the degenerate modes is

$$\boldsymbol{\alpha'}(E) = w_1 \begin{pmatrix} c & 0 & -d \\ 0 & -c & 0 \\ -d & 0 & 0 \end{pmatrix} + w_2 \begin{pmatrix} 0 & c & 0 \\ c & 0 & d \\ 0 & d & 0 \end{pmatrix} \tag{A.23}$$

with two unique non-zero elements c and d. Two bases are appropriate for the E species so that $\boldsymbol{\alpha'}(E)$ can be written as a linear combination of two Raman tensors pertinent to each of these bases with normalised weights w_1 and w_2. In an unperturbed molecule, the frequencies of the degenerate vibrational modes are equal and any linear combination of solutions also satisfies the symmetry requirements.

Normal modes

The vibrational representation is composed of a representation of the stretch and deformation modes. Analysing the symmetry behaviour $\Gamma_{\mathsf{stretch}}$ gives

C_{3v}	I	$2C_3$	$3\sigma_v$
$\Gamma_{\mathsf{stretch}}$	3	0	1

which is reduced in symmetry species. This results in

$$\Gamma_{\mathsf{stretch}} = A_1 + E \tag{A.24}$$

$$\Gamma_{\mathsf{deform}} = A_1 + E \tag{A.25}$$

indicating that each representation is composed of a fully symmetric mode (polarised in the Raman spectrum) and a degenerate mode, also Raman active and giving depolarised bands in the spectrum. The A_1 stretch mode is the symmetrically stretching of all C−H bonds, while the A_1 deformation mode is the bending of these in unison. In the E modes, the bonds stretch or bend out of synchrony. The vibrational normal coordinates pertaining to these modes are [78]

$$\begin{aligned} Q_{\mathsf{sst}} &= \frac{1}{\sqrt{3}}\left(\Delta r_1 + \Delta r_2 + \Delta r_3\right) \\ Q_{\mathsf{dst}} &= \begin{cases} \frac{1}{\sqrt{6}}\left(2\Delta r_1 - \Delta r_2 - \Delta r_3\right) \\ \frac{1}{\sqrt{2}}\left(\Delta r_2 - \Delta r_3\right) \end{cases} \\ Q_{\mathsf{um}} &= \frac{1}{\sqrt{3}}\left(\Delta\theta_{12} + \Delta\theta_{23} + \Delta\theta_{31}\right) \\ Q_{\mathsf{def}} &= \begin{cases} \frac{1}{\sqrt{6}}\left(2\Delta\theta_{23} - \Delta\theta_{12} - \Delta\theta_{31}\right) \\ \frac{1}{\sqrt{2}}\left(\Delta\theta_{12} - \Delta\theta_{31}\right) \end{cases} \end{aligned} \tag{A.26}$$

where sst stand for symmetric stretch, dst for degenerate stretch, um for the symmetric bending umbrella motion and dbe for degenerate bend. Q_{sst} and Q_{um} belong to the A_1 symmetry species while the remainder belong to the E species. The bond angles θ relate

to the bonds in subscript, with 0 denoting the bond along the z-axis that connects the methyl group to its molecule and $1, 2, 3$ denote the three C−H bonds.

Isotopologues

As quantified in appendix B, isotope effects are negligible for methyl.

Overtones, combinations and resonances

An overtone or combination of the symmetric modes belongs to A_1 as we have seen before. For overtones of the degenerate modes, a distinction has to be made between overtones of the same degenerate state (denoted E^2) and of a single excitation in each of the two degenerate states (denoted $E \times E$, as for a combination band). The characters for each are different and found through equation 2.173 and the direct product, respectively. For the first overtone of interest here, equation 2.173 simplifies to

$$\chi_{P^2}(R) = \frac{1}{2}\left(\chi_P(R)^2 + \chi_P(R^2)\right) \tag{A.27}$$

which is given in the following overview for the E species of the C_{3v} point group.

R	I	C_3	σ_v
R^2	$I^2 = I$	$(C_3)^2 = C_3^2$	$(\sigma_v)^2 = I$
$\chi_E(R)$	2	-1	0
$\chi_E(R^2)$	2	-1	2
$\chi_{E^2}(R)$	3	0	1

The representation for the overtone E^2 is then reduced as usual. The symmetry species for the overtones of methyl can now be listed as

$$\Gamma_{\mathsf{over}} = \begin{cases} {A_1}^2 = A_1 \times A_1 = A_1 \\ E^2 = A_1 + E \\ E \times E = A_1 + A_2 + E \end{cases} \tag{A.28}$$

in which the A_2 species is not Raman active. The following combination tones, involving fundamentals and first overtones only, are possible

$$\Gamma_{\mathsf{comb}} = \begin{cases} A_1 \times A_1 = A_1 \\ A_1 \times A_2 = A_2 \\ A_1 \times E = E \\ A_2 \times E = E \\ E \times E = A_1 + A_2 + E \end{cases} \tag{A.29}$$

from which only the A_1 and E species are Raman active. Several overtones and combination bands might mix with fundamental modes to produce Fermi resonances.

Summary

The methyl group has six vibrational normal modes: two fully symmetric modes (the symmetric stretch and the umbrella mode) and two two-fold degenerate modes (asymmetric stretches and deformations). The first two belong to the fully symmetric species of the C_{3v} point group, to which all relevant isotopologues belong.

A.5 Sulfate and carbon tetrachloride

The equilibrium structure of the sulfate anion (SO_4^{2-}) and carbon tetrachloride (CCl_4) both have a tetrahedral geometry and each contain five atoms (figure A.1). The vibrational properties of its $3 \cdot 5 - 6 = 9$ fundamental modes are thus identical, as far as a symmetry analysis is concerned. Their point group is T_d, presented in table A.5.

The symmetry properties of the representation of atomic motions are

T_d	I	$8C_3$	$3C_2$	$6S_4$	$6\sigma_d$
Γ_{3N}	15	0	-1	-1	3

which is reduced to

$$\Gamma_{3N} = A_1 + E + F_1 + 3F_2 \; . \tag{A.30}$$

It includes the vibrational motions

$$\Gamma_{\mathsf{vib}} = A_1 + E + 2F_2 \tag{A.31}$$

consisting of a fully symmetric mode, a two-fold degenerate mode and two triple degenerate modes, totalling nine normal modes as predicted. All of these are Raman active, as confirmed through the character table. The basis vector $xx + yy + zz$ that belongs the A_1 species, the fully symmetric mode of this point group, is a linear combination of all diagonal elements of the Raman tensor. It represents a spherical Raman tensor with one unique non-zero element

$$\boldsymbol{\alpha'}(A_1) = \begin{pmatrix} a & 0 & 0 \\ 0 & a & 0 \\ 0 & 0 & a \end{pmatrix} \tag{A.32}$$

There are two degenerate bases for the E species that contain one unique non-zero element

Table A.5: Character table for the T_d point group.

T_d	I	$8C_3$	$3C_2$	$6S_4$	$6\sigma_d$		
A_1	1	1	1	1	1		$xx + yy + zz$
A_2	1	1	1	-1	-1		
E	2	-1	2	0	0		$(2zz - xx - yy,\, xx - yy)$
F_1	3	0	-1	1	-1	$(\mathbf{R_x}, \mathbf{R_y}, \mathbf{R_z})$	
F_2	3	0	-1	-1	1	$(\mathbf{T_x}, \mathbf{T_y}, \mathbf{T_z})$	$(xy + yx,\, xz + zx,\, yz + zy)$

on the diagonal conforming to tensors of cylindrical and planar symmetry

$$\boldsymbol{\alpha'}(E) = w_1 \begin{pmatrix} b & 0 & 0 \\ 0 & b & 0 \\ 0 & 0 & -2b \end{pmatrix} + w_2 \begin{pmatrix} -b & 0 & 0 \\ 0 & b & 0 \\ 0 & 0 & 0 \end{pmatrix} \tag{A.33}$$

though a linear combination of the two can result in a tensor of elliptical symmetry. Here, the two bases contribute to the same tensor elements, contrary to the E species in methylene discussed above. The general form of the Raman tensor for a vibrational mode of the F_2 species involves off-diagonal elements only and one non-zero unique tensor value

$$\boldsymbol{\alpha'}(F_2) = w_1 \begin{pmatrix} 0 & c & 0 \\ c & 0 & 0 \\ 0 & 0 & 0 \end{pmatrix} + w_2 \begin{pmatrix} 0 & 0 & c \\ 0 & 0 & 0 \\ c & 0 & 0 \end{pmatrix} + w_3 \begin{pmatrix} 0 & 0 & 0 \\ 0 & 0 & c \\ 0 & c & 0 \end{pmatrix} \tag{A.34}$$

involving up to three normalised weighing factors, one for each of the three degenerate modes.

Normal modes

Analysing the symmetry properties of bond stretching vectors results in

T_d	I	$8C_3$	$3C_2$	$6S_4$	$6\sigma_d$
$\Gamma_{\mathsf{stretch}}$	4	1	0	0	2

which is reduced to give the symmetry species of the fundamental bond stretching modes, while the remainder is made up of deformations, so that

$$\Gamma_{\mathsf{stretch}} = A_1 + F_2 \tag{A.35}$$

$$\Gamma_{\mathsf{deform}} = E + F_2 \tag{A.36}$$

which shows that the totally symmetric mode is a synchronous stretching of all S−O or C−Cl bonds. The triply-degenerate modes involve asynchronous stretching and bending of bonds whereas the two-fold degenerate mode is a deformation mode.

The normal coordinates Q of the vibrations are as follows, where sst stands for symmetric stretch, dst for degenerate stretch, 2dd for two-fold degenerate deformation and

3dd for three-fold degenerate deformation.

$$
\begin{aligned}
Q_{\mathsf{sst}} &= \frac{1}{\sqrt{4}}\left(\Delta r_1 + \Delta r_2 + \Delta r_3 + \Delta r_4\right) \\
Q_{\mathsf{dst}} &= \frac{1}{\sqrt{4}} \begin{cases} \Delta r_1 - \Delta r_2 + \Delta r_3 - \Delta r_4 \\ \Delta r_1 - \Delta r_2 - \Delta r_3 + \Delta r_4 \\ \Delta r_1 + \Delta r_2 - \Delta r_3 - \Delta r_4 \end{cases} \\
Q_{\mathsf{2dd}} &= \begin{cases} \frac{1}{\sqrt{12}}\left(2\Delta\theta_{14} + 2\Delta\theta_{23} - \Delta\theta_{12} - \Delta\theta_{34} - \Delta\theta_{13} - \Delta\theta_{24}\right) \\ \frac{1}{\sqrt{4}}\left(\Delta\theta_{12} + \Delta\theta_{34} - \Delta\theta_{13} - \Delta\theta_{24}\right) \end{cases} \\
Q_{\mathsf{3dd}} &= \frac{1}{\sqrt{2}} \begin{cases} \Delta\theta_{12} - \Delta\theta_{34} \\ \Delta\theta_{13} - \Delta\theta_{24} \\ \Delta\theta_{14} - \Delta\theta_{23} \end{cases}
\end{aligned}
\tag{A.37}
$$

Isotopologues

The most abundant isotopologue of carbon tetrachloride is $^{12}C^{35}Cl_3{}^{37}Cl$, which belongs to the C_{3v} point group. The analysis presented on the basis of tetrahedral symmetry only applies to 33.4% of the molecules, while 46.4% and 20.2% belong to the C_{3v} and C_{2v} point groups, respectively.

This isotope effect is less dramatic for sulfate, with 99.0% of the ions expected to be of T_d symmetry and the balance belonging to C_{3v}. Only a negligible fraction belongs to C_{2v}. The isotopes of sulfur and oxygen are less abundant than the chloride isotope, even though the former feature multiple stable isotopes that allow for a higher number of isotopological combinations.

Symmetry analysis of C_{3v} and C_{2v} moieties is presented above. The results presented there are not directly applicable to carbon tetrachloride and sulfate due to the different number of atoms in the molecule. We will briefly present the analysis for a generalised molecule XY_3Z, belonging to the C_{3v} point group (character table A.4).

Five atoms in a non-linear molecule imply that there are 9 vibrational normal modes. The reducible representation Γ_{3N} including all atomic motions is

C_{3v}	I	$2C_3$	$3\sigma_v$
unshifted atoms	5	2	3
Γ_{3N}	15	0	3

and can be reduced to

$$\Gamma_{3N} = 4A_1 + A_2 + 5E \tag{A.38}$$

which includes the rotational and translational motions. Removing these returns the vibrational representation

$$\Gamma_{\mathsf{vib}} = 3A_1 + 3E \tag{A.39}$$

which one additional A_1 and E mode compared to the methyl group analysed above. The two F_2 triply-degenerate modes in XY_4 are now reduced to an A_1 and E mode each, keeping the total number of modes constant, but reducing the number of degeneracies and thus increasing the number of spectral lines.

The vibrations can be broken down into stretch and deformation modes. The symmetry behaviour of the four bond vectors is

C_{3v}	I	$2C_3$	$3\sigma_v$
$\Gamma_{\mathsf{stretch}}$	4	1	2

which is reduced into symmetry species. The balance of the species in Γ_{vib} are the deformation modes. This results in

$$\Gamma_{\mathsf{stretch}} = 2A_1 + E \tag{A.40}$$

$$\Gamma_{\mathsf{deform}} = A_1 + 2E \tag{A.41}$$

which again differs from the methyl case as well as from the pure tetrahedral geometry of the isotopic pure species. This gradual reduction of symmetry is summarised in correlation tables (see *e.g.* [73] and [63]). In going from the T_d point group to C_{3v}, a point group of lower symmetry with all its symmetry operations part of T_d, the symmetry species of the vibrational normal modes are partly preserved. The original A_1 and E species of T_d become A_1 and E species of C_{3v} while the F_2 species of T_d become A_1 and E in the C_{3v} point group. The Raman tensors of the modes for the XY_3Z isotopes thus all have the forms of equations A.22 or A.23.

The normal coordinates adjust accordingly. The normal coordinates Q_{sst} and Q_{2dd} stay the same, noting that bond 1 now refers to the unique X−Z bond. The normal coordinates Q_{dst} and Q_{3dd}, originally describing F_2 modes, now split into a stretch of the X−Z bond, an umbrella mode of the three X−Y bonds, both belonging to the A_1 species, as well as two degenerate deformations belonging to the E species of the C_{3v} point group. The correlation table A.6 summarises the relations between the symmetry species as the symmetry of the molecule changes from T_d to C_{3v} or C_{2v}.

Table A.6: Correlation of the symmetry species of the T_d point group to the symmetry species of its subgroups C_{3v} and C_{2v} [73].

T_d	C_{3v}	C_{2v}
A_1	A_1	A_1
A_2	A_2	A_2
E	E	$A_1 + A_2$
F_1	$A_2 + E$	$A_2 + B_1 + B_2$
F_2	$A_1 + E$	$A_1 + B_1 + B_2$

Analysing the nine normal modes of the C_{2v} isotopologue XY_2Z_2, we obtain the representations Γ_{3N} for the atomic and $\Gamma_{\mathsf{stretch}}$ for the bond stretch motion as

C_{2v}	I	C_2	$\sigma_v(xz)$	$\sigma'_v(yz)$
unshifted atoms	5	1	3	3
Γ_{3N}	15	-1	3	3
$\Gamma_{\mathsf{stretch}}$	4	0	2	2

which are reduced to

$$\begin{aligned}
\Gamma_{3N} &= 5A_1 + 2A_2 + 4B_1 + 4B_2 \\
\Gamma_{\mathsf{rot}} &= A_1 + B_1 + B_2 \\
\Gamma_{\mathsf{trans}} &= A_2 + B_1 + B_2 \\
\Gamma_{\mathsf{vib}} &= 4A_1 + 2A_2 + 4B_1 + 4B_2 \\
\Gamma_{\mathsf{stretch}} &= 2A_1 + B_1 + B_2 \\
\Gamma_{\mathsf{deform}} &= 2A_1 + A_2 + B_1 + B_2
\end{aligned} \tag{A.42}$$

where Γ_{rot} and Γ_{trans} are read off the character table A.3 to deduce the symmetry species of the vibrational modes Γ_{vib} and the deformation motions Γ_{deform}. All normal modes of the C_{2v} isotopologues are Raman active. Table A.6 presents the correlation between these symmetry species to those of the higher symmetry T_d isotopologues. The Raman tensors for the C_{2v} modes have the forms presented in table C.1. A description of all vibrational motions in the isotopologues of reduced symmetry can be found in [63].

Overtones, combinations and resonances

The T_d symmetry species of overtones of degenerate modes is derived following the overview below, obtained through equation A.27, and using the reduction formula (equation 2.166).

R	I	C_3	C_2	S_4	σ_d
R^2	$I^2 = I$	$(C_3)^2 = C_3^2$	$(C_2)^2 = I$	$(S_4)^2 = C_2$	$(\sigma_d)^2 = I$
$\chi_E(R)$	2	-1	2	0	0
$\chi_E(R^2)$	2	-1	2	2	2
$\chi_{E^2}(R)$	3	0	3	1	1
$\chi_{F_2}(R)$	3	0	-1	-1	1
$\chi_{F_2}(R^2)$	3	0	3	-1	3
$\chi_{{F_2}^2}(R)$	6	0	2	0	2

The symmetry properties of the various overtones are

$$\Gamma_{\mathsf{over}} = \begin{cases}
{A_1}^2 = A_1 \times A_1 = A_1 \\
E^2 = A_1 + E \\
E \times E = A_1 + A_2 + E \\
{F_2}^2 = A_1 + E \\
F_2 \times F_2 = A_1 + E + F_1 + F_2
\end{cases} \tag{A.43}$$

in which the modes of A_2 and F_1 symmetry are not Raman active. The remainder may interact with the fundamental vibrational modes of the same symmetry. In particular, overtones of the degenerate E mode can interact with the A_1 fundamental and its overtones.

The possible combinations of two fundamentals and of a fundamental with a first overtone include all symmetry species of the point group

$$\Gamma_{\mathsf{comb}} = \begin{cases} A_1 \times A_2 = A_2 \\ A_1 \times E = E \\ A_1 \times F_1 = F_1 \\ A_1 \times F_2 = F_2 \\ A_2 \times E = E \\ A_2 \times F_1 = F_2 \\ A_2 \times F_2 = F_1 \\ E \times E = A_1 + A_2 \\ E \times F_1 = F_1 + F_2 \\ E \times F_2 = F_1 + F_2 \\ F_1 \times F_2 = A_2 + E + F_1 + F_2 \end{cases} \tag{A.44}$$

some of which are Raman active and may interact with other modes. In contrast to the overtones, most combinations cannot mix with the fully symmetric stretch mode on the basis of symmetry. The degenerate modes can give rise to Fermi resonances in multiple ways if there is sufficient frequency overlap between their vibrations.

The most abundant isotopologue of carbon tetrachloride belongs to the C_{3v} point group. Analysis of its overtones, combinations and resonances follows the same procedure as for the methyl group described above.

The overtones of C_{2v} fundamentals all belong to its A_1 symmetry species. The combination mode of an overtone with one of the fundamentals thus belongs to the symmetry species of the fundamental. None of the six combinations of fundamentals belongs to the fully symmetric species.

$$\Gamma_{\mathsf{comb}} = \begin{cases} A_1 \times A_2 = A_2 \\ A_1 \times B_1 = B_1 \\ A_1 \times B_2 = B_2 \\ A_2 \times B_1 = B_2 \\ A_2 \times B_2 = B_1 \\ B_1 \times B_2 = A_2 \end{cases} \tag{A.45}$$

On the grounds of symmetry alone, Fermi resonances are therefore possible between any first overtones with an A_1 fundamental mode or between a combination and a fundamental

where there is no involvement of an A_1 mode.

Summary

Tetrahedral molecules containing five atoms possess 9 vibrational modes: a symmetric stretch, a three-fold degenerate asymmetric stretch and a two-fold as well as three-fold degenerate deformation. Isotopologues of carbon tetrachloride are abundant and reduce the molecular symmetry from T_d to C_{3v} or C_{2v} and affect the form of the Raman tensor. This is not the case with sulfate as it is naturally of a higher isotopic purity.

Appendix B

Isotopologues

Vibrational analysis is generally performed on a molecule containing the most abundant isotopes only. The symmetry of such a molecule is reduced when isotopes are considered. Table B.1 lists the abundance of relevant isotopes, based on the latest values of the Commission on Isotopic Abundances and Atomic Weights of IUPAC [202]. Presented are the mean values of the uncertainty intervals given for representative isotopic abundance of terrestrial samples.

A combinatorial analysis can be used to predict the abundance of isotopologues from the isotopic abundance. However, the isotopic abundance in laboratory materials may differ from the average terrestrial distribution quoted by IUPAC. Mass spectroscopy can be employed to verify the isotope and isotopologue abundance in individual samples.

Table B.1: Stable isotopes of selected elements and their average abundance from the latest representative values of the IUPAC [202].

Atomic number	Element	Isotopic weight	Isotopic abundance
1	H	1	0.999855
		2	0.000145
6	C	12	0.9894
		13	0.0106
8	O	16	0.99757
		17	0.0003835
		18	0.002045
16	S	32	0.9485
		33	0.00763
		34	0.04365
		36	0.000158
17	Cl	35	0.758
		37	0.242

B.1 Toluene

The most abundant isotopologue of toluene is $^{12}C_7{}^{1}H_8$ at 92.7%, followed by $^{12}C_6{}^{13}C^{1}H_8$ at 6.95% which occurs in seven forms. If the methyl group is freely rotating, as argued in [203], toluene sports C_{2v} symmetry. Assignment to this point group is retained in forms of $^{12}C_6{}^{13}C^{1}H_8$ that contain the ^{13}C isotope in the methyl group or at the 1 or 3 position of the phenyl ring. For the four remaining positions, symmetry is reduced to C_s.

In this work, the relevant spectral features of toluene arise from its phenyl ring only. The phenyl ring, C_6H_5, has 2048 isotopologues, as each carbon and hydrogen atom can be one of two stable isotopes. However, a number of these are symmetrically equivalent. Based on the terrestrial abundance of the isotopes given in table B.1, the most abundant isotopologue is expected to be $^{12}C_6{}^{1}H_5$ at 93.7%, followed by $^{12}C_5{}^{13}C^{1}H_5$ at 6.03%. The atoms of the latter can be arranged in six distinct ways, which contributes to the abundance of this isotopologue. All others occur at less than 1% mole fraction.

Considered in isolation, the phenyl group displays C_{2v} symmetry. Two of its $^{12}C_5{}^{13}C^{1}H_5$ isotopologues, having the ^{13}C atom at the 1 or 3 position, still belong to this point group. If the ^{13}C atom is at any other position in the phenyl ring, its symmetry is reduced to that of the C_s point group. The abundance of these species is 4.02%.

B.2 Alkane chains

B.2.1 Methylene

The $^{12}C^{1}H_2$ isotopologue of methylene, containing the most abundant isotopes, is the most abundant. It is expected to occur in 98.9% of the moieties, based on the terrestrial isotopic abundance (table B.1). The second most abundant isotopologue is $^{13}C^{1}H_2$ at 1.06% and equally belongs to the C_{2v} point group. If the hydrogen atoms are of different isotopes, the symmetry is reduced to that of the C_s point group. Such isotopologues can be ignored safely for spectroscopy applications, as the most abundant of these, $^{12}C^{1}H^{2}H$, only occurs in 0.0287% of the moieties.

In alkane chains, the probability of isotopic purity decreases with chain length. The abundance of the three most abundant isotopologues is presented in figure B.1, again based on the terrestrial isotopic abundances. The chance of at least one isotopic impurity in a chain is more than half when it contains more than 63 methylene groups. The presence of deuterium only raises above 1% in chains containing more than 68 hydrogen atoms, *i.e.* in a saturated alkane chain of 31 carbon atoms. Chains of such length are not considered in this work.

B.2.2 Methyl

The isotopological distribution of methyl does not deviate greatly from that of methylene as presented in figure B.1. The abundance of ^{1}H over ^{2}H reduces the effect of a third

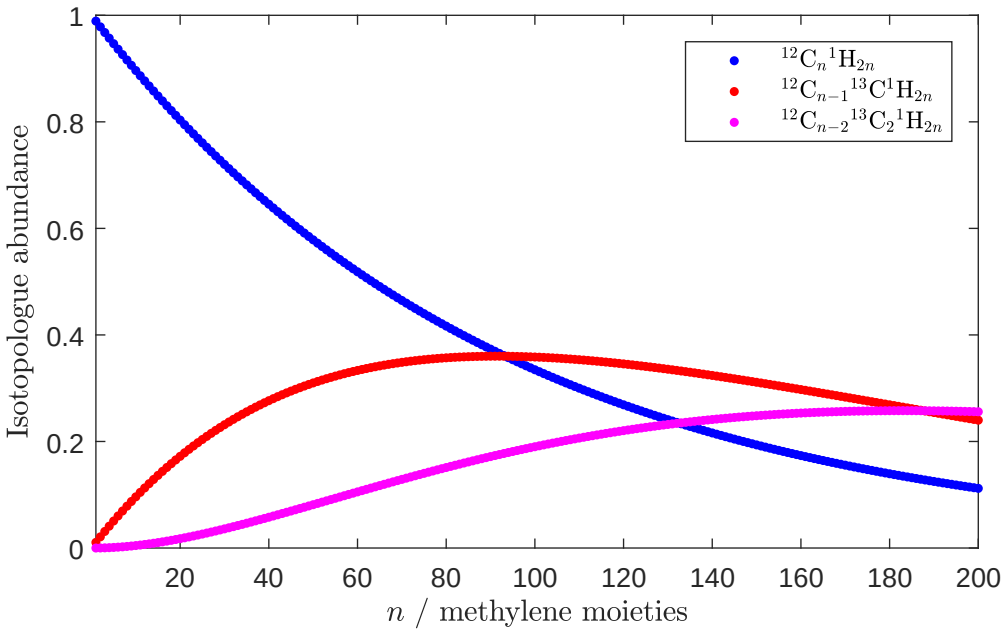

Figure B.1: Abundance of three methylene isotopologues in an alkane chain containing n methylene moieties.

hydrogen atom. The most abundant methyl isotopologue is $^{12}C^1H_3$ at 98.9%, followed by $^{13}C^1H_3$ at 1.06%, both of which belong to the C_{3v} point group. The remaining isotopologues are of negligible abundance. This also holds for unbranched alkane chains treated here, as methyl groups occur no more than twice in such molecules.

B.3 Carbon tetrachloride

The abundance of an isotopologue is predicted from the isotopic abundances presented in table B.1 and the number of combinations that are possible for each chosen set of isotopes. Table B.2 presents the results of such an analysis for CCl_4, which has ten stable distinct isotopologues with a total of 32 combinatorial conformations.

B.4 Sulfate anion

The sulfate anion has 60 distinct isotopologues, giving rise to 324 combinatorial conformations. Table B.3 lists the most abundant sulfate isotopologues and their point groups.

Table B.2: Stable isotopologues of CCl_4 and their abundance predicted from terrestrial isotopic abundances.

Isotopologue	Combinations	Abundance	Point group
$^{12}C^{35}Cl_3{}^{37}Cl$	4	0.417	C_{3v}
$^{12}C^{35}Cl_4$	1	0.327	T_d
$^{12}C^{35}Cl_2{}^{37}Cl_2$	6	0.200	C_{2v}
$^{12}C^{35}Cl^{37}Cl_3$	4	0.0424	C_{3v}
$^{13}C^{35}Cl_3{}^{37}Cl$	4	0.00447	C_{3v}
$^{13}C^{35}Cl_4$	1	0.00350	T_d
$^{12}C^{37}Cl_4$	1	0.00339	T_d
$^{13}C^{35}Cl_2{}^{37}Cl_2$	6	0.00214	C_{2v}
$^{13}C^{35}Cl^{37}Cl_3$	4	0.000456	C_{3v}
$^{13}C^{37}Cl_4$	1	0.0000364	T_d

Table B.3: The most abundant stable isotopologues of SO_4^{2-} predicted from terrestrial isotopic abundances.

Isotopologue	Combinations	Abundance	Point group
$^{32}S^{16}O_4^{2-}$	1	0.939	T_d
$^{34}S^{16}O_4^{2-}$	1	0.0432	T_d
$^{32}S^{16}O_3{}^{18}O^{2-}$	4	0.00770	C_{3v}
$^{33}S^{16}O_4^{2-}$	1	0.00756	T_d
$^{32}S^{16}O_3{}^{17}O^{2-}$	4	0.00144	C_{3v}
$^{34}S^{16}O_3{}^{18}O^{2-}$	4	0.000354	C_{3v}
$^{36}S^{16}O_4^{2-}$	1	0.000156	T_d
$^{33}S^{16}O_3{}^{18}O^{2-}$	4	0.0000620	C_{3v}
$^{34}S^{16}O_3{}^{17}O^{2-}$	4	0.0000665	C_{3v}
$^{32}S^{16}O_2{}^{18}O_2^{2-}$	6	0.0000237	C_{2v}
$^{33}S^{16}O_3{}^{17}O^{2-}$	4	0.0000116	C_{3v}

Appendix C

Forms of the Raman tensor

Table C.1 on the following two pages presents an overview of Raman tensor forms for all Raman active symmetry species in a number of point groups. The tensor forms are taken from [99] with those for the icosahedral point groups taken from [106] and additional point groups (with five-fold rotation axes and the linear groups $C_{\infty v}$ and $D_{\infty h}$) from [104] by comparison. Antisymmetric components, listed in some of the cited sources, are ignored. The tensors therefore only apply to normal (*i.e.* non-resonant) Raman scattering. Furthermore, the tensors of the C_s point group are corrected for our prioritisation of the symmetry axes (*i.e.* the plane of symmetry is xz here rather than xy). The form of the tensor follows from the choice of axes used. In the present work, the assignment of these follows from symmetry considerations as outlined in appendix A. Section 4.1.4 further discusses this topic.

Table C.1: Form of the normal vibrational Raman scattering tensor for Raman active symmetry species of various molecular point groups. The symbol $-1\times$ indicates a change of sign for one tensor of a degenerate mode.

C_1	A				
C_i	A_g				
	$\begin{pmatrix} a & d & e \\ d & b & f \\ e & f & c \end{pmatrix}$				
C_s	A'	A''			
	$\begin{pmatrix} a & 0 & d \\ 0 & b & 0 \\ d & 0 & c \end{pmatrix}$	$\begin{pmatrix} 0 & e & 0 \\ e & 0 & f \\ 0 & f & 0 \end{pmatrix}$			
C_2	A	B			
C_{2h}	A_g	B_g			
	$\begin{pmatrix} a & d & 0 \\ d & b & 0 \\ 0 & 0 & c \end{pmatrix}$	$\begin{pmatrix} 0 & 0 & e \\ 0 & 0 & f \\ e & f & 0 \end{pmatrix}$			
D_2	A	B_1	B_2	B_3	
C_{2v}	A_1	A_2	B_1	B_2	
D_{2h}	A_g	B_{1g}	B_{2g}	B_{3g}	
	$\begin{pmatrix} a & 0 & 0 \\ 0 & b & 0 \\ 0 & 0 & c \end{pmatrix}$	$\begin{pmatrix} 0 & d & 0 \\ d & 0 & 0 \\ 0 & 0 & 0 \end{pmatrix}$	$\begin{pmatrix} 0 & 0 & e \\ 0 & 0 & 0 \\ e & 0 & 0 \end{pmatrix}$	$\begin{pmatrix} 0 & 0 & 0 \\ 0 & 0 & f \\ 0 & f & 0 \end{pmatrix}$	
C_4	A	B	E		
S_4	A	B	E	$-1\times$	
C_{4h}	A_g	B_g	E_g		
	$\begin{pmatrix} a & 0 & 0 \\ 0 & a & 0 \\ 0 & 0 & b \end{pmatrix}$	$\begin{pmatrix} c & d & 0 \\ d & -c & 0 \\ 0 & 0 & 0 \end{pmatrix}$	$\begin{pmatrix} 0 & 0 & e \\ 0 & 0 & f \\ e & f & 0 \end{pmatrix}$	$\begin{pmatrix} 0 & 0 & -f \\ 0 & 0 & e \\ -f & e & 0 \end{pmatrix}$	
D_{2d}	A_1	B_1	B_2	E	
D_4	A_1	B_1	B_2	E	$-1\times$
C_{4v}	A_1	B_1	B_2	E	
D_{4h}	A_{1g}	B_{1g}	B_{2g}	E_g	$-1\times$
	$\begin{pmatrix} a & 0 & 0 \\ 0 & a & 0 \\ 0 & 0 & b \end{pmatrix}$	$\begin{pmatrix} c & 0 & 0 \\ 0 & -c & 0 \\ 0 & 0 & 0 \end{pmatrix}$	$\begin{pmatrix} 0 & d & 0 \\ d & 0 & 0 \\ 0 & 0 & 0 \end{pmatrix}$	$\begin{pmatrix} 0 & 0 & e \\ 0 & 0 & 0 \\ e & 0 & 0 \end{pmatrix}$	$\begin{pmatrix} 0 & 0 & 0 \\ 0 & 0 & e \\ 0 & e & 0 \end{pmatrix}$
C_3	A	E			
C_{3i}	A_g	E_g			
	$\begin{pmatrix} a & 0 & 0 \\ 0 & a & 0 \\ 0 & 0 & b \end{pmatrix}$	$\begin{pmatrix} c & d & e \\ d & -c & f \\ e & f & 0 \end{pmatrix}$	$\begin{pmatrix} d & -c & -f \\ -c & -d & e \\ -f & e & 0 \end{pmatrix}$		

(continued on next page)

Table C.1 (continued)

D_3	A_1	E	$-1\times$		
C_{3v}	A_1	E			
D_{3d}	A_{1g}	E_g	$-1\times$		
	$\begin{pmatrix} a & 0 & 0 \\ 0 & a & 0 \\ 0 & 0 & b \end{pmatrix}$	$\begin{pmatrix} c & 0 & -d \\ 0 & -c & 0 \\ -d & 0 & 0 \end{pmatrix}$	$\begin{pmatrix} 0 & c & 0 \\ c & 0 & d \\ 0 & d & 0 \end{pmatrix}$		
C_{3h}	A'	E''		E'	
C_5	A	E_1		E_2	
C_6	A	E_1		E_2	
C_{6h}	A_g	E_{1g}		E_{2g}	
	$\begin{pmatrix} a & 0 & 0 \\ 0 & a & 0 \\ 0 & 0 & b \end{pmatrix}$	$\begin{pmatrix} 0 & 0 & c \\ 0 & 0 & d \\ c & d & 0 \end{pmatrix}$	$\begin{pmatrix} 0 & 0 & -d \\ 0 & 0 & c \\ -d & c & 0 \end{pmatrix}$	$\begin{pmatrix} e & f & 0 \\ f & -e & 0 \\ 0 & 0 & 0 \end{pmatrix}$	$\begin{pmatrix} f & -e & 0 \\ -e & -f & 0 \\ 0 & 0 & 0 \end{pmatrix}$
D_{3h}	A'_1	E''	$-1\times$	E'	
C_{5v}	A_1	E_1		E_2	
C_{5h}	A'	E''_1		E'_2	
D_5	A_1	E_1	$-1\times$	E_2	
D_{5h}	A'_1	E''_1	$-1\times$	E'_2	
D_6	A_1	E_1	$-1\times$	E_2	
C_{6v}	A_1	E_1		E_2	
D_{6h}	A_{1g}	E_{1g}	$-1\times$	E_{2g}	
$C_{\infty v}$	$A_1 = \Sigma^+$	$E_1 = \Pi$		$E_2 = \Delta$	
$D_{\infty h}$	Σ^+_g	Π_g		Δ_g	
	$\begin{pmatrix} a & 0 & 0 \\ 0 & a & 0 \\ 0 & 0 & b \end{pmatrix}$	$\begin{pmatrix} 0 & 0 & c \\ 0 & 0 & 0 \\ c & 0 & 0 \end{pmatrix}$	$\begin{pmatrix} 0 & 0 & 0 \\ 0 & 0 & c \\ 0 & c & 0 \end{pmatrix}$	$\begin{pmatrix} d & 0 & 0 \\ 0 & -d & 0 \\ 0 & 0 & 0 \end{pmatrix}$	$\begin{pmatrix} 0 & d & 0 \\ d & 0 & 0 \\ 0 & 0 & 0 \end{pmatrix}$
T_d	A_1	E		F_2	
O_h	A_{1g}	E_g		F_{2g}	
	$\begin{pmatrix} a & 0 & 0 \\ 0 & a & 0 \\ 0 & 0 & a \end{pmatrix}$	$\begin{pmatrix} b & 0 & 0 \\ 0 & b & 0 \\ 0 & 0 & -2b \end{pmatrix}$	$\sqrt{3}\begin{pmatrix} -b & 0 & 0 \\ 0 & b & 0 \\ 0 & 0 & 0 \end{pmatrix}$	$\begin{pmatrix} 0 & c & 0 \\ c & 0 & 0 \\ 0 & 0 & 0 \end{pmatrix}$	
				$\begin{pmatrix} 0 & 0 & c \\ 0 & 0 & 0 \\ c & 0 & 0 \end{pmatrix}$	$\begin{pmatrix} 0 & 0 & 0 \\ 0 & 0 & c \\ 0 & c & 0 \end{pmatrix}$
I_h	A_g	H_g			
	$\begin{pmatrix} a & 0 & 0 \\ 0 & a & 0 \\ 0 & 0 & a \end{pmatrix}$	$\begin{pmatrix} b & 0 & 0 \\ 0 & b & 0 \\ 0 & 0 & -2b \end{pmatrix}$	$\sqrt{3}\begin{pmatrix} -b & 0 & 0 \\ 0 & b & 0 \\ 0 & 0 & 0 \end{pmatrix}$		
		$\sqrt{3}\begin{pmatrix} 0 & b & 0 \\ b & 0 & 0 \\ 0 & 0 & 0 \end{pmatrix}$	$-\sqrt{3}\begin{pmatrix} 0 & 0 & b \\ 0 & 0 & 0 \\ b & 0 & 0 \end{pmatrix}$	$\sqrt{3}\begin{pmatrix} 0 & 0 & 0 \\ 0 & 0 & b \\ 0 & b & 0 \end{pmatrix}$	

Appendix D

Computations in Gaussian

This appendix includes relevant sections of GAUSSIAN [123] Raman computation log files as well as MATLAB scripts to process these results. The following quantities are extracted from the log files:

1. atomic coordinates of the optimised molecular geometry in the computational standard orientation,
2. normalized atomic motion in the vibrational normal modes,
3. the frequency of each mode (given as wavenumbers),
4. the Raman scattering activity of each mode,
5. the tensorial polarizability derivative with respect to each vibrational mode.

The first is used to obtain the transformation, if any, required to bring the output quantities into the desired molecular frame of reference. The optimised atomic coordinates are presented in figures. The second relevant output gives insight into what atoms are involved in each mode and whether these are localised. Together with the frequencies, these aid in assigning the modes. The frequencies and Raman scattering activities are used to produce computational Raman spectra. The last quantity, the polarisability derivative tensors, are the main purpose of our Raman calculations. The deduced transformation matrix is applied to obtain the Raman tensor in the molecular frame of reference.

This appendix allows full calculation of the results presented in section 4.4. Where lines are left out from the original log files, this is indicated with `[...]`. The logs of the sulfate computations are given more fully with additional explanation while only a minimum is shown for the other molecules.

A secondary use of the computational results is to estimate local field corrections from the molecular shape and its static polarisability tensor as outlined in section 5.3. The semi-axes of the molecular ellipsoid are listed in the output as

polarisability tensor quantities can be found n addition to the results for the Raman

D.1 Processing of Gaussian output in Matlab

The purpose of the following three MATLAB functions is (1) to plot the atomic positions of a molecule in its the optimized geometry, (2) to produce a computational Raman spectrum and (3) to compute the Raman tensors of the vibrational normal modes according to equation 4.55. The input and output quantities of each function are detailed at the beginning of each script.

D.1.1 Molecular structure

```
function plotmolecule(atom,position)
%OUTPUT
%A 3D plot of the molecule with a letter at each of the atomic positions
%
%INPUT
%atom     = Nx1 character array of atomic species
%position = Nx3 array of XYZ position of each eatom
%
% Raymond Rammeloo - 27 August 2018

figure; hold on
for N = 1:length(atom)
    text(position(N,1),position(N,2),position(N,3),atom(N,:),...
        'HorizontalAlignment','center','FontWeight','bold')
end
axislength = 1.2*max(max(abs(position)));
axis([-axislength axislength -axislength axislength -axislength axislength])
hold on
plot3([0 axislength],[0 0],[0 0],'-r')
text(1.05*axislength,0,0,'$\mathbf{\hat{x}}^\mathsf{s}$','color','r',...
    'interpreter','latex','fontsize',12,'horizontalalignment','center')
plot3([0 0],[0 axislength],[0 0],'-r')
text(0,1.05*axislength,0,'$\mathbf{\hat{y}}^\mathsf{s}$','color','r',...
    'interpreter','latex','fontsize',12,'horizontalalignment','center')
plot3([0 0],[0 0],[0 axislength],'-r')
text(0,0,1.05*axislength,'$\mathbf{\hat{z}}^\mathsf{s}$','color','r',...
    'interpreter','latex','fontsize',12,'horizontalalignment','center')
view([120,45])
axis equal; grid off; axis off
```

D.1.2 Raman spectra

```
function plotRS(F,RA,Fmin,Fmax,Fstep,FWHM)
%Plot Raman spectra from Gaussian output
%OUTPUT
%Computational Raman spectrum convoluted with a Lorentzian function of
%specified full width at half maximum (FWHM)
%
%INPUT
%F     = linear array of frequencies of the vibrational modes in cm^-1
%RA    = Raman activitity (or scattering factor) in arbitrary units
%Fmin  = lower boundary of the spectral range to be plotted in cm^-1
%Fmax  = upper boundary of the spectral range to be plotted in cm^-1
%Fstep = step size of the computation of the spectrum in cm^-1
%FWHM  = full width at half maximum of the Lorentzian broadening
```

```
%
% Raymond Rammeloo - 23 August 2018

range = Fmin:Fstep:Fmax;
lorentzian = zeros(length(range),length(F));

%weight peak intensities with their frequencies^-3 and scale to ensure
%equal integrated intensities for varying spectral step size
f_weight = (10^10)*(.1/Fstep)*(1/532 - F*10^-7 ).^3;

for mode = 1:length(F)
    raman_band = 1./( 1 + ( (F(mode) - range)/(FWHM/2)).^2 );
    lorentzian(:,mode) = f_weight(mode)*RA(mode)*raman_band./sum(raman_band);
    %Lorentzian lineshape, integrated intensity is the Raman activity
    %scaled by f^3
end
spectrum = sum(lorentzian,2);
figure; hold on
plot(range,spectrum,'-r')
axis([min(range) max(range) 0 1.05*max(spectrum)])
box on
ylabel('Intensity / a.u.','interpreter','latex','fontsize',12)
xlabel('Raman shift / cm$^{-1}$','interpreter','latex','fontsize',12)
```

D.1.3 Raman tensors

```
function RT = GaussianRT(PD,F,Euler)
%Compute Raman tensors from Gaussian output
%OUTPUT
%RT = array of Raman tensors of the vibrational modes, 3x3xNV in C V^-1 m^2
%
%INPUT
%PD    = linear polarizability derivatives with respect to vibrational
%       normal modes in a 3x3xNV matrix in units of A^2 amu^-1/2
%F     = array of frequencies of the vibrational modes, NVx1 in cm^-1
%Euler = vector of three Euler angles [alpha, beta, gamma] in degrees that
%       define a passive transformation from the frame of reference of the
%       polarizability derivatives to that of the desired output tensors
%       using anticlockwise rotations of the axes
%
% Raymond Rammeloo - 15 August 2018

%Units and constants
c = 299792458*100; %speed of light in cm, as F is given in cm^-1
h = 6.626070040*10^(-34); %Planck constant in m^2 kg s^-1
ep = 8.854187817*10^(-12); %vacuum permittivity in C V^-1 m^-1
amu = 1.660539*10^(-27); %atomic mass unit in kg amu^-1

% Transformation matrix from anti-clockwise rotations of the axes
alpha = Euler(1);
beta = Euler(2);
gamma = Euler(3);
Rz1 = [ cosd(alpha) -sind(alpha) 0
        sind(alpha)  cosd(alpha) 0
        0            0           1        ];
Rx =  [ 1            0           0
        0            cosd(beta) -sind(beta)
        0            sind(beta)  cosd(beta)];
```

```
Rz2 = [ cosd(gamma) -sind(gamma) 0
        sind(gamma)  cosd(gamma) 0
        0           0            1         ];
T = Rz2*Rx*Rz1;

%Pre-define arrays
NV = size(F,1); %number of vibrational modes
RT = nan(3,3,NV); %pre-define output array

%Construct Raman tensor for each mode
for v = 1:NV %loop over vibrational modes
    RT(:,:,v) = 4*pi*ep*sqrt(h/(8*pi^2*c*F(v)*amu))*(10^(-10))^2*...
        (T*PD(:,:,v)*T'); %prefactor to correct units into SI
       %transformation matrix T is applied to change the frame of reference
       %in which the Raman tensor is expressed
end
```

D.2 Sulfate

D.2.1 Geometry optimization

The geometry is optimized from an initial guess until convergence is achieved, *i.e.* the internal energy of the structure is minimized. The initial geometry is specified in the Z-matrix and copied with other instructions from the `.gjf` input file. The optimized atomic positions are given in a standard orientation determined by the program and are plotted in figure D.1. At the end of the log file (the last excerpt given below), the output is summarised in a long row of data, all of which given in the coordinate system of the original input Z-matrix. This includes the optimized atomic x, y, z-position in units of Å, listed as

```
\S,-0.2321981383,0.3560371483,-0.0000000017\
```

and the point group assigned to the structure. Relevant parts of the GAUSSIAN log file are shown below.

```
[...]
 ******************************************
 Gaussian 09:  EM64L-G09RevA.02 11-Jun-2009
               15-Mar-2018
 ******************************************
 %chk=/ddn/data/dch1maf/sulfateopt.chk
 %nprocshared=4
 Will use up to    4 processors via shared memory.
 %mem=450MW
 --------------------------
 #T b3lyp 6-311++G(d,p) opt
 --------------------------
 -------------------
 Title Card Required
 -------------------
 Symbolic Z-matrix:
 Charge = -2 Multiplicity = 1
 S                    -0.2322    0.35604   0.
```

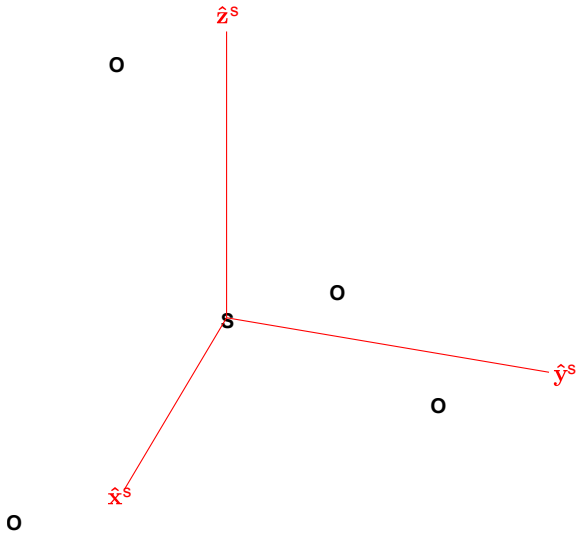

Figure D.1: Optimized geometry of the sulfate anion in GAUSSIAN's computational standard orientation.

```
 O                    -0.89137   1.7859   -0.55667
 O                     1.33569   0.21197  -0.55667
 O                    -0.2322    0.35604   1.67
 O                    -1.14091  -0.92976  -0.55667
[...]
         Item               Value     Threshold  Converged?
 Maximum Force            0.000007     0.000450     YES
 RMS     Force            0.000003     0.000300     YES
 Maximum Displacement     0.000014     0.001800     YES
 RMS     Displacement     0.000008     0.001200     YES
 Optimization completed.
    -- Stationary point found.
                           ----------------------------
                           !   Optimized Parameters   !
                           ! (Angstroms and Degrees)  !
 --------------------------                            --------------------------
 ! Name  Definition              Value          Derivative Info.                !
 --------------------------------------------------------------------------------
 ! R1    R(1,2)                  1.5268         -DE/DX =    0.0                 !
 ! R2    R(1,3)                  1.5268         -DE/DX =    0.0                 !
 ! R3    R(1,4)                  1.5268         -DE/DX =    0.0                 !
 ! R4    R(1,5)                  1.5268         -DE/DX =    0.0                 !
 ! A1    A(2,1,3)              109.4712         -DE/DX =    0.0                 !
 ! A2    A(2,1,4)              109.4712         -DE/DX =    0.0                 !
 ! A3    A(2,1,5)              109.4712         -DE/DX =    0.0                 !
 ! A4    A(3,1,4)              109.4712         -DE/DX =    0.0                 !
 ! A5    A(3,1,5)              109.4712         -DE/DX =    0.0                 !
 ! A6    A(4,1,5)              109.4712         -DE/DX =    0.0                 !
 ! D1    D(2,1,4,3)           -120.0            -DE/DX =    0.0                 !
 ! D2    D(2,1,5,3)            120.0            -DE/DX =    0.0                 !
 ! D3    D(2,1,5,4)           -120.0            -DE/DX =    0.0                 !
 ! D4    D(3,1,5,4)            120.0            -DE/DX =    0.0                 !
 --------------------------------------------------------------------------------
 GradGradGradGradGradGradGradGradGradGradGradGradGradGradGradGradGradGradGrad

                      Distance matrix (angstroms):
```

```
                    1          2          3          4          5
     1  S    0.000000
     2  O    1.526773   0.000000
     3  O    1.526773   2.493209   0.000000
     4  O    1.526773   2.493209   2.493209   0.000000
     5  O    1.526773   2.493209   2.493209   2.493209   0.000000
 Framework group  TD[O(S),4C3(O)]
 Deg. of freedom     1
                          Standard orientation:
 ---------------------------------------------------------------------
 Center     Atomic      Atomic             Coordinates (Angstroms)
 Number     Number       Type              X           Y           Z
 ---------------------------------------------------------------------
      1         16           0        0.000000    0.000000    0.000000
      2          8           0        0.881483    0.881483    0.881483
      3          8           0       -0.881483   -0.881483    0.881483
      4          8           0       -0.881483    0.881483   -0.881483
      5          8           0        0.881483   -0.881483   -0.881483
 ---------------------------------------------------------------------
 Rotational constants (GHZ):      5.0829732      5.0829732      5.0829732
[...]
 1\1\GINC-CN7001\FOpt\RB3LYP\6-311++G(d,p)\O4S1(2-)\DCH1MAF\15-Mar-2018
 \0\\#T b3lyp 6-311++G(d,p) opt\\Title Card Required\\-2,1\S,-0.2321981
 383,0.3560371483,-0.0000000017\O,-0.8348399967,1.6632683994,-0.5089242
 098\O,1.2012182645,0.2243246788,-0.5089242045\O,-0.2321981384,0.356037
 1538,1.5267726084\O,-1.0629726828,-0.8194816387,-0.5089242008\\Version
 =EM64L-G09RevA.02\State=1-A1\HF=-699.1159026\RMSD=6.708e-09\RMSF=3.370
 e-06\Dipole=0.,0.,0.\Quadrupole=0.,0.,0.,0.,0.,0.\PG=TD [O(S1),4C3(O1)
 ]\\@
[...]
```

D.2.2 Raman computation

The Raman computation is performed on the optimized geometry of the molecule and using the same level of theory. It repeats the electronic structure calculation before taking second derivatives of the energy to obtain polarizability derivatives with respect to the vibrational modes. These modes are found by Wilson's matrix method as described in [72]. The keyword `IOp(2/33=1)` is used to obtain the translation vector and rotation matrix, which in this case confirm that the input geometry is left unchanged in the calculation. Using the keyword `IOp(7/33=3)` ensures that the linear polarizability derivatives are given with respect to the vibrational modes in matrix format. The symmetry species, frequencies, Raman scattering activities and normalized atomic displacements (amongst other quantities) are given for each vibrational motion.

The keyword `IOp(2/33=1)` is used to obtain the translation vector and rotation matrix, which in this case confirm that the input geometry is left unchanged in the calculation. Using the keyword `IOp(7/33=3)` ensures that the linear polarizability derivatives are given with respect to the vibrational modes in matrix format. These are specified in the coordinate system of the standard orientation.

The linear polarizability derivatives with respect to the real atomic displacement are included at the end of the output file after `PolarDeriv=` in one long row of scalars. The

polarizability derivative tensors are computed from these values. Their unit is B^2, with 1 B = 0.529 Å, the Bohr radius. These are found in the same output section as presented with the geometry optimization calculation above. Here, it includes additional detail on the computed dipole and polarizability as well as their derivatives.

The polarizability derivatives are listed in order of the atoms as specified in the GJF. Within the set of values for each atom, the derivatives with respect to the x, y and z axis are given, in that order. For each atom and axis, the six components of the symmetric polarizability derivative tensor are listed in the order xx, xy, yy, yz, xz, yz and zz. The total number of polarizability derivatives is thus $N \times 3 \times 6$, with N the number of atoms. The output for the sulfate computation features ninety linear polarizability derivatives as seen below. The first set of six values

```
\PolarDeriv=0.,0.,0.,0.,-8.5166009,0.
```

are the linear polarizability derivatives with respect to displacement of the first atom (sulfur, in this case) along the x-direction. These form the symmetric tensor

$$\frac{\partial \boldsymbol{\alpha}_1}{\partial x_1} = \begin{pmatrix} 0 & 0 & 0 \\ 0 & 0 & -8.5166009 \\ 0 & -8.5166009 & 0 \end{pmatrix} \tag{D.1}$$

in units of (0.529 Å)^2. The remaining tensors are formed in the same way.

Relevant parts of the GAUSSIAN log file are shown below.

```
[...]
 ****************************************
 Gaussian 09:  EM64L-G09RevA.02 11-Jun-2009
               15-Aug-2018
 ****************************************
 %chk=/ddn/data/dch1maf/SulfateRaman180815.chk
 %nprocshared=4
 Will use up to    4 processors via shared memory.
 %mem=450MW
 ---------------------------------------------------------------
 #T b3lyp/6-311++g(d,p) freq=Raman IOp(2/33=1) IOp(7/33=3)
 ---------------------------------------------------------------
 -------------
 Sulfate anion
 -------------
 Symbolic Z-matrix:
 Charge = -2 Multiplicity = 1
 S                     0.        0.        0.
 O                     0.88148   0.88148   0.88148
 O                    -0.88148  -0.88148   0.88148
 O                    -0.88148   0.88148  -0.88148
 O                     0.88148  -0.88148  -0.88148
[...]
                         Standard orientation:
 ---------------------------------------------------------------------
 Center     Atomic      Atomic             Coordinates (Angstroms)
 Number     Number       Type              X           Y           Z
 ---------------------------------------------------------------------
```

```
     1         16           0        0.000000    0.000000    0.000000
     2          8           0        0.881480    0.881480    0.881480
     3          8           0       -0.881480   -0.881480    0.881480
     4          8           0       -0.881480    0.881480   -0.881480
     5          8           0        0.881480   -0.881480   -0.881480
 ---------------------------------------------------------------------
 Translation vector:
                1
     1   0.000000D+00
     2   0.000000D+00
     3   0.000000D+00
 Rotation Matrix:
                1             2             3
     1   0.100000D+01  0.000000D+00  0.000000D+00
     2   0.000000D+00  0.100000D+01  0.000000D+00
     3   0.000000D+00  0.000000D+00  0.100000D+01
[...]
 Dipole derivatives wrt mode   1: -3.16701D-09 -5.15866D-09  8.52832D-09
 Polarizability derivatives wrt mode          1
                1             2             3
     1  -0.136329D+00  0.000000D+00  0.000000D+00
     2   0.000000D+00 -0.236520D+00  0.000000D+00
     3   0.000000D+00  0.000000D+00  0.372849D+00
 Vibrational polarizability contributions from mode   1       0.0000000       0.0000000       0.0000000
 IFr=  0 A012= 0.83D-16 0.19D+01 0.32D+00 Act= 0.22D+01 DepolP= 0.75D+00 DepolU= 0.86D+00
 Dipole derivatives wrt mode   2: -8.19027D-09  6.52856D-09  1.86098D-09
 Polarizability derivatives wrt mode          2
                1             2             3
     1  -0.351819D+00  0.000000D+00  0.000000D+00
     2   0.000000D+00  0.293974D+00  0.000000D+00
     3   0.000000D+00  0.000000D+00  0.578449D-01
 Vibrational polarizability contributions from mode   2       0.0000000       0.0000000       0.0000000
 IFr=  0 A012= 0.56D-16 0.19D+01 0.32D+00 Act= 0.22D+01 DepolP= 0.75D+00 DepolU= 0.86D+00
 Dipole derivatives wrt mode   3: -1.81218D-02  3.48019D+00 -3.34955D+00
 Polarizability derivatives wrt mode          3
                1             2             3
     1   0.000000D+00 -0.229680D+00  0.238638D+00
     2  -0.229680D+00  0.000000D+00 -0.124262D-02
     3   0.238638D+00 -0.124262D-02  0.000000D+00
 Vibrational polarizability contributions from mode   3       0.0000280       1.0338072       0.9576495
 IFr=  0 A012= 0.49D-18 0.20D+01 0.33D+00 Act= 0.23D+01 DepolP= 0.75D+00 DepolU= 0.86D+00
 Dipole derivatives wrt mode   4: -1.72545D+00  3.12391D+00  3.25508D+00
 Polarizability derivatives wrt mode          4
                1             2             3
     1   0.000000D+00  0.223203D+00  0.214208D+00
     2   0.223203D+00  0.000000D+00 -0.118315D+00
     3   0.214208D+00 -0.118315D+00  0.000000D+00
 Vibrational polarizability contributions from mode   4       0.2541192       0.8329716       0.9043940
 IFr=  0 A012= 0.34D-17 0.20D+01 0.33D+00 Act= 0.23D+01 DepolP= 0.75D+00 DepolU= 0.86D+00
 Dipole derivatives wrt mode   5:  4.51155D+00  1.20872D+00  1.23146D+00
 Polarizability derivatives wrt mode          5
                1             2             3
     1   0.000000D+00  0.844417D-01  0.828828D-01
     2   0.844417D-01  0.000000D+00  0.309359D+00
     3   0.828828D-01  0.309359D+00  0.000000D+00
 Vibrational polarizability contributions from mode   5       1.7373376       0.1247060       0.1294412
 IFr=  0 A012= 0.46D-17 0.20D+01 0.33D+00 Act= 0.23D+01 DepolP= 0.75D+00 DepolU= 0.86D+00
 Dipole derivatives wrt mode   6:  2.83632D-08  2.91468D-08  2.86087D-08
```

```
Polarizability derivatives wrt mode          6
               1             2             3
     1  -0.103763D+01  0.000000D+00  0.000000D+00
     2   0.000000D+00 -0.103763D+01  0.000000D+00
     3   0.000000D+00  0.000000D+00 -0.103763D+01
Vibrational polarizability contributions from mode   6       0.0000000       0.0000000       0.0000000
IFr=  0 A012= 0.15D+02 0.29D+02 0.48D+01 Act= 0.48D+02 DepolP= 0.18D-16 DepolU= 0.37D-16
Dipole derivatives wrt mode   7:  1.00543D+01  1.40136D+01  1.40912D+01
Polarizability derivatives wrt mode          7
               1             2             3
     1   0.000000D+00 -0.510462D+00 -0.507652D+00
     2  -0.510462D+00  0.000000D+00 -0.364223D+00
     3  -0.507652D+00 -0.364223D+00  0.000000D+00
Vibrational polarizability contributions from mode   7       2.7450753       5.3327554       5.3919511
IFr=  0 A012= 0.93D-16 0.12D+02 0.20D+01 Act= 0.14D+02 DepolP= 0.75D+00 DepolU= 0.86D+00
Dipole derivatives wrt mode   8: -5.73198D+00  1.71657D+01 -1.29813D+01
Polarizability derivatives wrt mode          8
               1             2             3
     1   0.000000D+00  0.470257D+00 -0.621838D+00
     2   0.470257D+00  0.000000D+00  0.207644D+00
     3  -0.621838D+00  0.207644D+00  0.000000D+00
Vibrational polarizability contributions from mode   8       0.8921957       8.0015416       4.5760446
IFr=  0 A012= 0.26D-18 0.12D+02 0.20D+01 Act= 0.14D+02 DepolP= 0.75D+00 DepolU= 0.86D+00
Dipole derivatives wrt mode   9:  1.90286D+01 -2.23367D+00 -1.13558D+01
Polarizability derivatives wrt mode          9
               1             2             3
     1   0.000000D+00  0.411372D+00  0.809162D-01
     2   0.411372D+00  0.000000D+00 -0.689322D+00
     3   0.809162D-01 -0.689322D+00  0.000000D+00
Vibrational polarizability contributions from mode   9       9.8325108       0.1354849       3.5017861
IFr=  0 A012= 0.53D-17 0.12D+02 0.20D+01 Act= 0.14D+02 DepolP= 0.75D+00 DepolU= 0.86D+00
Diagonal vibrational polarizability:
      15.4612667      15.4612666      15.4612667
Diagonal vibrational hyperpolarizability:
       0.0000002       0.0000004       0.0000003
NorSel:  MapVib=      1      2      3      4      5      6      7      8      9
Harmonic frequencies (cm**-1), IR intensities (KM/Mole), Raman scattering
activities (A**4/AMU), depolarization ratios for plane and unpolarized
incident light, reduced masses (AMU), force constants (mDyne/A),
and normal coordinates:
                          1         2         3         4         5
                          E         E        T2        T2        T2
      Frequencies ---   398.5956  398.5956  561.5002  561.5002  561.5002
   Reduced masses ---    15.9949   15.9949   17.5820   17.5820   17.5820
  Force constants ---     1.4973    1.4973    3.2660    3.2660    3.2660
   IR Intensities ---     0.0000    0.0000   23.3316   23.3316   23.3316
 Raman Activities ---     2.2422    2.2422    2.3038    2.3038    2.3038
   Depol. (Plane) ---     0.7500    0.7500    0.7500    0.7500    0.7500
   Depol. (Unpol) ---     0.8571    0.8571    0.8571    0.8571    0.8571
Coord Atom Element:
  1     1    16          0.00000   0.00000  -0.00118  -0.11258   0.29438
  2     1    16          0.00000   0.00000   0.22708   0.20383   0.07887
  3     1    16          0.00000   0.00000  -0.21856   0.21239   0.08035
  1     2     8         -0.14751  -0.38067   0.00915   0.47426   0.01279
  2     2     8         -0.25591   0.31808  -0.33415  -0.00163   0.33691
  3     2     8          0.40342   0.06259   0.33608  -0.01450   0.33468
  1     3     8          0.14751   0.38067   0.44812   0.04767  -0.14860
  2     3     8          0.25591  -0.31808   0.10482  -0.42822   0.17552
```

```
  3     3     8          0.40342   0.06259  -0.11764  -0.19777  -0.41499
  1     4     8          0.14751   0.38067  -0.44694   0.06486  -0.14562
  2     4     8         -0.25591   0.31808   0.10720  -0.20209  -0.41573
  3     4     8         -0.40342  -0.06259  -0.12002  -0.42390   0.17627
  1     5     8         -0.14751  -0.38067  -0.00797  -0.36173  -0.30700
  2     5     8          0.25591  -0.31808  -0.33178   0.22450  -0.25435
  3     5     8         -0.40342  -0.06259   0.33845   0.21163  -0.25658
                           6         7         8         9
                          A1        T2        T2        T2
      Frequencies ---   864.8256  995.4996  995.4996  995.4996
   Reduced masses ---    15.9949   21.1278   21.1278   21.1278
  Force constants ---     7.0484   12.3363   12.3363   12.3363
    IR Intensities ---     0.0000  496.0319  496.0319  496.0319
 Raman Activities ---    48.4508   13.6697   13.6697   13.6697
   Depol. (Plane) ---     0.0000    0.7500    0.7500    0.7500
   Depol. (Unpol) ---     0.0000    0.8571    0.8571    0.8571
Coord Atom Element:
  1     1    16          0.00000   0.25587  -0.14587   0.48426
  2     1    16          0.00000   0.35664   0.43685  -0.05685
  3     1    16          0.00000   0.35861  -0.33037  -0.28900
  1     2     8         -0.28868  -0.39475   0.03316  -0.11295
  2     2     8         -0.28868  -0.40750  -0.04060  -0.04445
  3     2     8         -0.28868  -0.40775   0.05652  -0.01507
  1     3     8          0.28868  -0.12713  -0.21338  -0.32862
  2     3     8          0.28868  -0.13988  -0.28715  -0.26012
  3     3     8         -0.28868   0.04934   0.27367   0.30390
  1     4     8          0.28868  -0.12860   0.35917  -0.15537
  2     4     8         -0.28868   0.05107  -0.39601   0.10127
  3     4     8          0.28868  -0.14161   0.38253  -0.05749
  1     5     8         -0.28868   0.13902   0.11263  -0.37104
  2     5     8          0.28868  -0.21655  -0.14947   0.31694
  3     5     8          0.28868  -0.21680  -0.05235   0.34632
Harmonic frequencies (cm**-1), IR intensities (KM/Mole), Raman scattering
activities (A**4/AMU), depolarization ratios for plane and unpolarized
incident light, reduced masses (AMU), force constants (mDyne/A),
and normal coordinates:
                      1                     2                     3
                      E                     E                    T2
Frequencies --    398.5956              398.5956              561.5002
Red. masses --     15.9949               15.9949               17.5820
Frc consts  --      1.4973                1.4973                3.2660
IR Inten    --      0.0000                0.0000               23.3316
Raman Activ --      2.2422                2.2422                2.3038
Depolar (P) --      0.7500                0.7500                0.7500
Depolar (U) --      0.8571                0.8571                0.8571
 Atom  AN      X      Y      Z        X      Y      Z        X      Y      Z
    1  16     0.00   0.00   0.00     0.00   0.00   0.00     0.00   0.23  -0.22
    2   8    -0.15  -0.26   0.40    -0.38   0.32   0.06     0.01  -0.33   0.34
    3   8     0.15   0.26   0.40     0.38  -0.32   0.06     0.45   0.10  -0.12
    4   8     0.15  -0.26  -0.40     0.38   0.32  -0.06    -0.45   0.11  -0.12
    5   8    -0.15   0.26  -0.40    -0.38  -0.32  -0.06    -0.01  -0.33   0.34
                      4                     5                     6
                     T2                    T2                    A1
Frequencies --    561.5002              561.5002              864.8256
Red. masses --     17.5820               17.5820               15.9949
Frc consts  --      3.2660                3.2660                7.0484
IR Inten    --     23.3316               23.3316                0.0000
Raman Activ --      2.3038                2.3038               48.4508
```

```
 Depolar (P) --     0.7500                0.7500                0.0000
 Depolar (U) --     0.8571                0.8571                0.0000
  Atom  AN      X      Y      Z        X      Y      Z        X      Y      Z
     1  16    -0.11   0.20   0.21     0.29   0.08   0.08     0.00   0.00   0.00
     2   8     0.47   0.00  -0.01     0.01   0.34   0.33    -0.29  -0.29  -0.29
     3   8     0.05  -0.43  -0.20    -0.15   0.18  -0.41     0.29   0.29  -0.29
     4   8     0.06  -0.20  -0.42    -0.15  -0.42   0.18     0.29  -0.29   0.29
     5   8    -0.36   0.22   0.21    -0.31  -0.25  -0.26    -0.29   0.29   0.29
                    7                     8                     9
                   T2                    T2                    T2
 Frequencies --   995.4996              995.4996              995.4996
 Red. masses --    21.1278               21.1278               21.1278
 Frc consts  --    12.3363               12.3363               12.3363
 IR Inten    --   496.0319              496.0319              496.0319
 Raman Activ --    13.6697               13.6697               13.6697
 Depolar (P) --     0.7500                0.7500                0.7500
 Depolar (U) --     0.8571                0.8571                0.8571
  Atom  AN      X      Y      Z        X      Y      Z        X      Y      Z
     1  16     0.26   0.36   0.36    -0.15   0.44  -0.33     0.48  -0.06  -0.29
     2   8    -0.39  -0.41  -0.41     0.03  -0.04   0.06    -0.11  -0.04  -0.02
     3   8    -0.13  -0.14   0.05    -0.21  -0.29   0.27    -0.33  -0.26   0.30
     4   8    -0.13   0.05  -0.14     0.36  -0.40   0.38    -0.16   0.10  -0.06
     5   8     0.14  -0.22  -0.22     0.11  -0.15  -0.05    -0.37   0.32   0.35
[...]
 1\1\GINC-CN7103\Freq\RB3LYP\6-311++G(d,p)\O4S1(2-)\DCH1MAF\15-Aug-2018
 \0\\#T b3lyp/6-311++g(d,p) freq=Raman IOp(2/33=1) IOp(7/33=3)\\Sulfate
  anion\\-2,1\S,0.,0.,0.\O,0.88148,0.88148,0.88148\O,-0.88148,-0.88148,
 0.88148\O,-0.88148,0.88148,-0.88148\O,0.88148,-0.88148,-0.88148\\Versi
 on=EM64L-G09RevA.02\State=1-A1\HF=-699.1159026\RMSD=6.134e-09\RMSF=1.3
 91e-06\ZeroPoint=0.0144277\Thermal=0.0186031\Dipole=0.,0.,0.\DipoleDer
 iv=2.5175972,0.,0.,0.,2.5175972,0.,0.,0.,2.5175972,-1.1293993,-0.33818
 19,-0.3381819,-0.3381819,-1.1293993,-0.3381819,-0.3381819,-0.3381819,-
 1.1293993,-1.1293993,-0.3381819,0.3381819,-0.3381819,-1.1293993,0.3381
 819,0.3381819,0.3381819,-1.1293993,-1.1293993,0.3381819,-0.3381819,0.3
 381819,-1.1293993,0.3381819,-0.3381819,0.3381819,-1.1293993,-1.1293993
 ,0.3381819,0.3381819,0.3381819,-1.1293993,-0.3381819,0.3381819,-0.3381
 819,-1.1293993\Polar=48.5490159,0.,48.5490159,0.,0.,48.5490159\PolarDe
 riv=0.,0.,0.,0.,-8.5166009,0.,0.,0.,0.0000001,-8.5166009,0.,0.,0.,-8.5
 166009,0.,0.,0.,0.0000001,6.4779517,3.5484643,3.1780441,3.5484643,2.12
 91502,3.1780441,3.1780441,3.5484643,6.4779517,2.1291502,3.5484642,3.17
 80441,3.1780441,2.1291502,3.1780441,3.5484643,3.5484642,6.4779517,-6.4
 779517,-3.5484643,-3.1780441,3.5484643,2.1291502,-3.1780441,-3.1780441
 ,-3.5484643,-6.4779517,2.1291502,3.5484642,-3.1780441,3.1780441,2.1291
 502,3.1780441,-3.5484643,-3.5484642,6.4779517,-6.4779517,3.5484643,-3.
 1780441,-3.5484643,2.1291502,-3.1780441,3.1780441,-3.5484643,6.4779517
 ,2.1291502,-3.5484642,3.1780441,-3.1780441,2.1291502,-3.1780441,-3.548
 4643,3.5484642,-6.4779517,6.4779517,-3.5484643,3.1780441,-3.5484643,2.
 1291502,3.1780441,-3.1780441,3.5484643,-6.4779517,2.1291502,-3.5484642
 ,-3.1780441,-3.1780441,2.1291502,-3.1780441,3.5484643,-3.5484642,-6.47
 79517\HyperPolar=0.,0.,0.,0.,0.,-63.1964848,0.,0.,0.,0.\PG=TD [O(S1),4
 C3(O1)]\NImag=0\\0.65184207,0.,0.65184207,0.,0.,0.65184207,-0.16296052
[...]
```

D.3 Carbon tetrachloride

Raman computations have been performed on the three most abundant isotopologues of carbon tetrachloride. Relevant sections from logs are shown below. A single geometry optimization was performed. Figure D.2 indicates the position of the chlorine isotopes for each of the Raman computations.

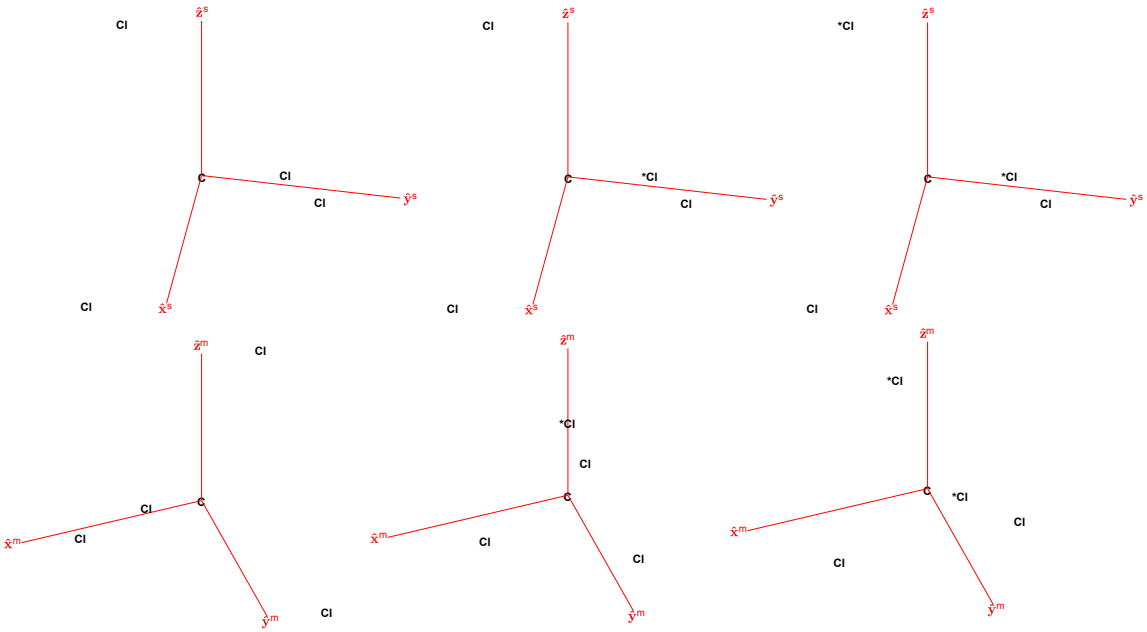

Figure D.2: Optimised geometry of carbon tetrachloride in the computational standard orientation s (top row) and the molecular frame of reference m for the studied isotopologues. The ^{37}Cl isotopes are indicated as *Cl. For $^{12}C^{35}Cl_4$, the computational and molecular frames of reference are identical.

D.3.1 $^{12}C^{35}Cl_4$

```
[...]
 ****************************************
 Gaussian 09:  EM64L-G09RevA.02 11-Jun-2009
               15-Aug-2018
 ****************************************
 %chk=/ddn/data/dch1maf/Carbontetrachloride12C35Cl4Raman180815.chk
 %nprocshared=4
 Will use up to    4 processors via shared memory.
 %mem=450MW
 ---------------------------------------------------------
 #T b3lyp/6-311++g(d,p) freq=Raman IOp(2/33=1) IOp(7/33=3)
 ---------------------------------------------------------
 ------------------------------
 Carbon tetrachloride 12C35Cl4
 ------------------------------
 Symbolic Z-matrix:
 Charge =  0 Multiplicity = 1
 C(iso=12)             0.         0.         0.
 Cl(iso=35)            1.03436    1.03436    1.03436
 Cl(iso=35)           -1.03436   -1.03436    1.03436
 Cl(iso=35)           -1.03436    1.03436   -1.03436
 Cl(iso=35)            1.03436   -1.03436   -1.03436
[...]
 Polarizability derivatives wrt mode          1
                1             2             3
      1  -0.414461D+00  0.000000D+00  0.000000D+00
      2   0.000000D+00  0.732712D-01  0.000000D+00
      3   0.000000D+00  0.000000D+00  0.341190D+00
[...]
 Polarizability derivatives wrt mode          2
                1             2             3
      1  -0.154683D+00  0.000000D+00  0.000000D+00
      2   0.000000D+00  0.436276D+00  0.000000D+00
      3   0.000000D+00  0.000000D+00 -0.281593D+00
[...]
 Polarizability derivatives wrt mode          3
                1             2             3
      1   0.000000D+00  0.496438D+00  0.142373D-01
      2   0.496438D+00  0.000000D+00  0.128026D+00
      3   0.142373D-01  0.128026D+00  0.000000D+00
[...]
 Polarizability derivatives wrt mode          4
                1             2             3
      1   0.000000D+00 -0.126763D+00 -0.366344D-01
      2  -0.126763D+00  0.000000D+00  0.495614D+00
      3  -0.366344D-01  0.495614D+00  0.000000D+00
[...]
 Polarizability derivatives wrt mode          5
                1             2             3
      1   0.000000D+00 -0.229028D-01  0.511370D+00
      2  -0.229028D-01  0.000000D+00  0.319412D-01
      3   0.511370D+00  0.319412D-01  0.000000D+00
[...]
 Polarizability derivatives wrt mode          6
                1             2             3
      1  -0.675438D+00  0.000000D+00  0.000000D+00
```

```
      2   0.000000D+00 -0.675438D+00  0.000000D+00
      3   0.000000D+00  0.000000D+00 -0.675438D+00
[...]
 Polarizability derivatives wrt mode          7
                1             2             3
      1   0.000000D+00 -0.176584D+00 -0.388731D+00
      2  -0.176584D+00  0.000000D+00  0.305786D-01
      3  -0.388731D+00  0.305786D-01  0.000000D+00
[...]
 Polarizability derivatives wrt mode          8
                1             2             3
      1   0.000000D+00 -0.133111D+00  0.285432D-01
      2  -0.133111D+00  0.000000D+00 -0.405828D+00
      3   0.285432D-01 -0.405828D+00  0.000000D+00
[...]
 Polarizability derivatives wrt mode          9
                1             2             3
      1   0.000000D+00 -0.366509D+00  0.176925D+00
      2  -0.366509D+00  0.000000D+00  0.132658D+00
      3   0.176925D+00  0.132658D+00  0.000000D+00
[...]
 Harmonic frequencies (cm**-1), IR intensities (KM/Mole), Raman scattering
 activities (A**4/AMU), depolarization ratios for plane and unpolarized
 incident light, reduced masses (AMU), force constants (mDyne/A),
 and normal coordinates:
                     1                     2                     3
                     E                     E                    T2
 Frequencies --   219.5912              219.5912              314.3246
 Red. masses --    34.9689               34.9689               32.6275
 Frc consts  --     0.9935                0.9935                1.8993
 IR Inten    --     0.0000                0.0000                0.5013
 Raman Activ --     3.0824                3.0824                5.5239
 Depolar (P) --     0.7500                0.7500                0.7500
 Depolar (U) --     0.8571                0.8571                0.8571
  Atom  AN      X      Y      Z        X      Y      Z        X      Y      Z
     1   6     0.00   0.00   0.00     0.00   0.00   0.00     0.08   0.01   0.31
     2  17    -0.38   0.07   0.31    -0.14   0.40  -0.26     0.33   0.41   0.07
     3  17     0.38  -0.07   0.31     0.14  -0.40  -0.26    -0.32  -0.24  -0.12
     4  17     0.38   0.07  -0.31     0.14   0.40   0.26     0.31  -0.41   0.05
     5  17    -0.38  -0.07  -0.31    -0.14  -0.40   0.26    -0.34   0.24  -0.10
                     4                     5                     6
                    T2                    T2                    A1
 Frequencies --   314.3246              314.3246              447.4040
 Red. masses --    32.6275               32.6275               34.9689
 Frc consts  --     1.8993                1.8993                4.1241
 IR Inten    --     0.5013                0.5013                0.0000
 Raman Activ --     5.5239                5.5239               20.5297
 Depolar (P) --     0.7500                0.7500                0.0000
 Depolar (U) --     0.8571                0.8571                0.0000
  Atom  AN      X      Y      Z        X      Y      Z        X      Y      Z
     1   6     0.31  -0.02  -0.08     0.02   0.32  -0.01     0.00   0.00   0.00
     2  17    -0.13   0.24   0.31     0.32  -0.02   0.36    -0.29  -0.29  -0.29
     3  17     0.03   0.41  -0.29     0.35   0.01  -0.35     0.29   0.29  -0.29
     4  17    -0.09  -0.24   0.35    -0.35  -0.03  -0.31     0.29  -0.29   0.29
     5  17     0.08  -0.40  -0.34    -0.32  -0.06   0.31    -0.29   0.29   0.29
                     7                     8                     9
                    T2                    T2                    T2
 Frequencies --   733.4105              733.4105              733.4105
```

```
 Red. masses --    12.9944                12.9944                12.9944
 Frc consts  --     4.1181                 4.1181                 4.1181
 IR Inten    --   195.0500               195.0500               195.0500
 Raman Activ --     3.8478                 3.8478                 3.8478
 Depolar (P) --     0.7500                 0.7500                 0.7500
 Depolar (U) --     0.8571                 0.8571                 0.8571
  Atom  AN      X      Y      Z        X      Y      Z        X      Y      Z
     1   6    -0.07   0.89   0.40     0.93  -0.07   0.30    -0.30  -0.40   0.84
     2  17    -0.05  -0.09  -0.07    -0.09  -0.05  -0.06     0.01   0.01  -0.04
     3  17    -0.02  -0.06   0.00    -0.06  -0.02   0.01     0.08   0.09  -0.10
     4  17     0.03  -0.06   0.01    -0.10   0.06  -0.07    -0.03   0.06  -0.08
     5  17     0.06  -0.10  -0.08    -0.07   0.03   0.02     0.05  -0.02  -0.07
[...]
```

D.3.2 $^{12}C^{35}Cl_3^{37}Cl$

```
[...]
*****************************************
 Gaussian 09:  EM64L-G09RevA.02 11-Jun-2009
               15-Aug-2018
 *****************************************
 %chk=/ddn/data/dch1maf/Carbontetrachloride12C35Cl337ClRaman180815.chk
 %nprocshared=4
 Will use up to    4 processors via shared memory.
 %mem=450MW
 ------------------------------------------------------------
 #T b3lyp/6-311++g(d,p) freq=Raman IOp(2/33=1) IOp(7/33=3)
 ------------------------------------------------------------
 ----------------------------------
 Carbon tetrachloride 12C 35Cl3 37Cl
 ----------------------------------
 Symbolic Z-matrix:
 Charge =  0 Multiplicity = 1
 C(iso=12)             0.         0.         0.
 Cl(iso=37)            1.03436    1.03436    1.03436
 Cl(iso=35)           -1.03436   -1.03436    1.03436
 Cl(iso=35)           -1.03436    1.03436   -1.03436
 Cl(iso=35)            1.03436   -1.03436   -1.03436
[...]
 Polarizability derivatives wrt mode          1
                1             2             3
      1  -0.410254D+00 -0.307446D-02 -0.622561D-03
      2  -0.307446D-02  0.690849D-01  0.369702D-02
      3  -0.622561D-03  0.369702D-02  0.341169D+00
[...]
 Polarizability derivatives wrt mode          2
                1             2             3
      1  -0.157088D+00  0.249391D-02 -0.390951D-02
      2   0.249391D-02  0.433834D+00  0.141560D-02
      3  -0.390951D-02  0.141560D-02 -0.276746D+00
[...]
 Polarizability derivatives wrt mode          3
                1             2             3
      1   0.117550D-01  0.292916D+00  0.292916D+00
      2   0.292916D+00  0.117550D-01  0.292916D+00
      3   0.292916D+00  0.292916D+00  0.117550D-01
[...]
 Polarizability derivatives wrt mode          4
```

```
                1             2             3
      1   0.749840D-02 -0.364062D+00  0.584380D-02
      2  -0.364062D+00  0.122328D-03  0.358218D+00
      3   0.584380D-02  0.358218D+00 -0.762072D-02
[...]
 Polarizability derivatives wrt mode          5
                1             2             3
      1  -0.447045D-02 -0.203443D+00  0.417008D+00
      2  -0.203443D+00  0.872902D-02 -0.213565D+00
      3   0.417008D+00 -0.213565D+00 -0.425858D-02
[...]
 Polarizability derivatives wrt mode          6
                1             2             3
      1  -0.670710D+00  0.944306D-02  0.944306D-02
      2   0.944306D-02 -0.670710D+00  0.944306D-02
      3   0.944306D-02  0.944306D-02 -0.670710D+00
[...]
 Polarizability derivatives wrt mode          7
                1             2             3
      1   0.807438D-02 -0.242997D+00 -0.242997D+00
      2  -0.242997D+00  0.807441D-02 -0.242997D+00
      3  -0.242997D+00 -0.242997D+00  0.807443D-02
[...]
 Polarizability derivatives wrt mode          8
                1             2             3
      1   0.767869D-03  0.134155D-01  0.296307D+00
      2   0.134155D-01 -0.734587D-03 -0.309723D+00
      3   0.296307D+00 -0.309723D+00 -0.332356D-04
[...]
 Polarizability derivatives wrt mode          9
                1             2             3
      1  -0.404918D-03 -0.349892D+00  0.186564D+00
      2  -0.349892D+00 -0.462532D-03  0.163328D+00
      3   0.186564D+00  0.163328D+00  0.867444D-03
[...]
 Harmonic frequencies (cm**-1), IR intensities (KM/Mole), Raman scattering
 activities (A**4/AMU), depolarization ratios for plane and unpolarized
 incident light, reduced masses (AMU), force constants (mDyne/A),
 and normal coordinates:
                     1                     2                     3
                    ?A                    ?A                    ?A
 Frequencies --   218.0804              218.0804              310.4340
 Red. masses --    35.4396               35.4396               33.6189
 Frc consts  --     0.9931                0.9931                1.9088
 IR Inten    --     0.0000                0.0000                0.5345
 Raman Activ --     3.0400                3.0400                5.4116
 Depolar (P) --     0.7500                0.7500                0.7485
 Depolar (U) --     0.8571                0.8571                0.8562
  Atom  AN      X      Y      Z        X      Y      Z        X      Y      Z
     1   6     0.01   0.00  -0.01     0.00  -0.01   0.01     0.18   0.18   0.18
     2  17    -0.37   0.06   0.31    -0.14   0.39  -0.25     0.37   0.37   0.37
     3  17     0.39  -0.06   0.32     0.14  -0.41  -0.26    -0.03  -0.03  -0.40
     4  17     0.38   0.06  -0.31     0.16   0.40   0.27    -0.03  -0.40  -0.03
     5  17    -0.38  -0.07  -0.33    -0.15  -0.41   0.25    -0.40  -0.03  -0.03
                     4                     5                     6
                    ?A                    ?A                    ?A
 Frequencies --   313.1456              313.1456              444.4237
 Red. masses --    32.7920               32.7920               35.3972
```

```
 Frc consts  --     1.8946                 1.8946                 4.1192
 IR Inten    --     0.4916                 0.4916                 0.0013
 Raman Activ --     5.4800                 5.4800                20.2489
 Depolar (P) --     0.7500                 0.7500                 0.0001
 Depolar (U) --     0.8571                 0.8571                 0.0002
  Atom  AN      X      Y      Z        X      Y      Z        X      Y      Z
     1   6     0.23   0.00  -0.23    -0.14   0.26  -0.13     0.01   0.01   0.01
     2  17    -0.24   0.00   0.24     0.14  -0.28   0.14    -0.27  -0.27  -0.27
     3  17     0.22   0.48  -0.22     0.42  -0.03  -0.12     0.29   0.29  -0.30
     4  17    -0.27   0.00   0.26    -0.40   0.26  -0.40     0.29  -0.30   0.29
     5  17     0.22  -0.48  -0.21    -0.13  -0.02   0.43    -0.30   0.29   0.29
                    7                      8                      9
                   ?A                     ?A                     ?A
 Frequencies --   731.8728               733.3236               733.3236
 Red. masses --    12.9721                12.9945                12.9945
 Frc consts  --     4.0938                 4.1172                 4.1172
 IR Inten    --   193.9767               195.0360               195.0360
 Raman Activ --     3.7229                 3.8620                 3.8620
 Depolar (P) --     0.7490                 0.7500                 0.7500
 Depolar (U) --     0.8565                 0.8571                 0.8571
  Atom  AN      X      Y      Z        X      Y      Z        X      Y      Z
     1   6     0.57   0.57   0.57     0.71  -0.68  -0.03    -0.37  -0.43   0.80
     2  17    -0.09  -0.09  -0.09    -0.03   0.03   0.00     0.01   0.02  -0.03
     3  17    -0.05  -0.05   0.00    -0.03   0.03   0.00     0.09   0.09  -0.10
     4  17    -0.05   0.00  -0.05    -0.09   0.09  -0.06    -0.02   0.06  -0.07
     5  17     0.00  -0.05  -0.05    -0.09   0.09   0.06     0.05  -0.02  -0.07
[...]
```

D.3.3 $^{12}C^{35}Cl_2^{37}Cl_2$

```
[...]
 ******************************************
 Gaussian 09:  EM64L-G09RevA.02 11-Jun-2009
               15-Aug-2018
 ******************************************
 %chk=/ddn/data/dch1maf/Carbontetrachloride12C35Cl237Cl2Raman180815.chk
 %nprocshared=4
 Will use up to    4 processors via shared memory.
 %mem=450MW
 ---------------------------------------------------------
 #T b3lyp/6-311++g(d,p) freq=Raman IOp(2/33=1) IOp(7/33=3)
 ---------------------------------------------------------
 ------------------------------------
 Carbon tetrachloride 12C 35Cl2 37Cl2
 ------------------------------------
 Symbolic Z-matrix:
 Charge =  0 Multiplicity = 1
 C(iso=12)             0.         0.         0.
 Cl(iso=37)            1.03436    1.03436    1.03436
 Cl(iso=37)           -1.03436   -1.03436    1.03436
 Cl(iso=35)           -1.03436    1.03436   -1.03436
 Cl(iso=35)            1.03436   -1.03436   -1.03436
[...]
 Polarizability derivatives wrt mode          1
                1             2             3
     1  -0.218208D+00 -0.805324D-02  0.000000D+00
     2  -0.805324D-02 -0.218206D+00  0.000000D+00
     3   0.000000D+00  0.000000D+00  0.435985D+00
```

```
[...]
 Polarizability derivatives wrt mode          2
                1             2             3
      1  -0.377907D+00  0.000000D+00  0.000000D+00
      2   0.000000D+00  0.377908D+00  0.000000D+00
      3   0.000000D+00  0.000000D+00 -0.103937D-05
[...]
 Polarizability derivatives wrt mode          3
                1             2             3
      1   0.000000D+00  0.000000D+00  0.356710D+00
      2   0.000000D+00  0.000000D+00  0.356710D+00
      3   0.356710D+00  0.356710D+00  0.000000D+00
[...]
 Polarizability derivatives wrt mode          4
                1             2             3
      1   0.664138D-02  0.506147D+00  0.000000D+00
      2   0.506147D+00  0.664139D-02  0.000000D+00
      3   0.000000D+00  0.000000D+00  0.283046D-01
[...]
 Polarizability derivatives wrt mode          5
                1             2             3
      1   0.000000D+00  0.000000D+00  0.359716D+00
      2   0.000000D+00  0.000000D+00 -0.359716D+00
      3   0.359716D+00 -0.359716D+00  0.000000D+00
[...]
 Polarizability derivatives wrt mode          6
                1             2             3
      1  -0.666158D+00  0.192043D-01  0.000000D+00
      2   0.192043D-01 -0.666158D+00  0.000000D+00
      3   0.000000D+00  0.000000D+00 -0.665818D+00
[...]
 Polarizability derivatives wrt mode          7
                1             2             3
      1   0.000000D+00  0.000000D+00 -0.296258D+00
      2   0.000000D+00  0.000000D+00 -0.296258D+00
      3  -0.296258D+00 -0.296258D+00  0.000000D+00
[...]
 Polarizability derivatives wrt mode          8
                1             2             3
      1   0.854976D-02 -0.424359D+00  0.000000D+00
      2  -0.424359D+00  0.854977D-02  0.000000D+00
      3   0.000000D+00  0.000000D+00  0.106935D-01
[...]
 Polarizability derivatives wrt mode          9
                1             2             3
      1   0.000000D+00  0.000000D+00  0.303796D+00
      2   0.000000D+00  0.000000D+00 -0.303796D+00
      3   0.303796D+00 -0.303796D+00  0.000000D+00
[...]
 Harmonic frequencies (cm**-1), IR intensities (KM/Mole), Raman scattering
 activities (A**4/AMU), depolarization ratios for plane and unpolarized
 incident light, reduced masses (AMU), force constants (mDyne/A),
 and normal coordinates:
                      1                     2                     3
                     ?A                    ?A                    ?A
 Frequencies --   216.5432              216.6042              308.4505
 Red. masses --    35.9467               35.9120               34.0400
 Frc consts  --     0.9931                0.9927                1.9081
```

```
 IR Inten    --     0.0001                0.0000                0.5378
 Raman Activ --     2.9971                2.9991                5.3442
 Depolar (P) --     0.7500                0.7500                0.7500
 Depolar (U) --     0.8571                0.8571                0.8571
  Atom  AN      X      Y      Z        X      Y      Z        X      Y      Z
     1   6     0.00   0.00  -0.02     0.00   0.00   0.00     0.22   0.22   0.00
     2  17    -0.21  -0.21   0.40    -0.34   0.34   0.00     0.22   0.22   0.47
     3  17     0.21   0.21   0.40     0.34  -0.34   0.00     0.22   0.22  -0.47
     4  17     0.20  -0.20  -0.42     0.36   0.36   0.00    -0.27  -0.27   0.00
     5  17    -0.20   0.20  -0.42    -0.36  -0.36   0.00    -0.27  -0.27   0.00
                     4                     5                     6
                    ?A                    ?A                    ?A
 Frequencies --   310.1098              311.9305              441.3909
 Red. masses --    33.5432               32.9702               35.8682
 Frc consts  --     1.9006                1.8901                4.1172
 IR Inten    --     0.5105                0.4820                0.0016
 Raman Activ --     5.3918                5.4346               19.9704
 Depolar (P) --     0.7479                0.7500                0.0002
 Depolar (U) --     0.8558                0.8571                0.0003
  Atom  AN      X      Y      Z        X      Y      Z        X      Y      Z
     1   6     0.00   0.00   0.32    -0.23   0.23   0.00     0.00   0.00   0.03
     2  17     0.33   0.33  -0.01     0.25  -0.25   0.00    -0.27  -0.27  -0.28
     3  17    -0.33  -0.33  -0.01     0.25  -0.25   0.00     0.27   0.27  -0.28
     4  17     0.34  -0.34  -0.05    -0.22   0.22  -0.48     0.30  -0.30   0.29
     5  17    -0.34   0.34  -0.05    -0.22   0.22   0.48    -0.30   0.30   0.29
                     7                     8                     9
                    ?A                    ?A                    ?A
 Frequencies --   731.2866              732.2742              733.2368
 Red. masses --    12.9642               12.9800               12.9947
 Frc consts  --     4.0848                4.1008                4.1163
 IR Inten    --   193.6126              194.3150              195.0220
 Raman Activ --     3.6863                3.7856                3.8763
 Depolar (P) --     0.7500                0.7487                0.7500
 Depolar (U) --     0.8571                0.8563                0.8571
  Atom  AN      X      Y      Z        X      Y      Z        X      Y      Z
     1   6     0.69   0.69   0.00     0.00   0.00   0.98     0.69  -0.69   0.00
     2  17    -0.08  -0.08  -0.06    -0.04  -0.04  -0.08    -0.03   0.03   0.00
     3  17    -0.08  -0.08   0.06     0.04   0.04  -0.08    -0.03   0.03   0.00
     4  17    -0.03  -0.03   0.00    -0.04   0.04  -0.08    -0.09   0.09  -0.06
     5  17    -0.03  -0.03   0.00     0.04  -0.04  -0.08    -0.09   0.09   0.06
[...]
```

D.4 Toluene

The optimized geometry found for toluene is presented in figure D.3. Relevant output from the Raman computation is given below, which includes the atomic coordinates, polarizability derivatives and normal modes. Though the molecule appears to meet the C_s point group symmetry, GAUSSIAN assigns it to the C_1 point group of lower symmetry.

```
[...]
 ******************************************
 Gaussian 09:  EM64L-G09RevA.02 11-Jun-2009
               15-Aug-2018
 ******************************************
 %chk=/ddn/data/dch1maf/TolueneRaman180815.chk
```

```
 %nprocshared=4
 Will use up to    4 processors via shared memory.
 %mem=400MW
 ---------------------------------------------------------
 #T b3lyp/6-311++g(d,p) freq=Raman IOp(2/33=1) IOp(7/33=3)
 ---------------------------------------------------------
 -------
 Toluene
 -------
 Symbolic Z-matrix:
 Charge =  0 Multiplicity = 1
 C                    -0.19404   1.20058  -0.00915
 C                     1.1998    1.20334   0.00216
 C                     1.90278  -0.00013   0.00857
 C                     1.19945  -1.20353   0.00216
 C                    -0.19427  -1.20045  -0.00915
 C                    -0.91314   0.0002   -0.01177
 H                    -0.73155   2.14369  -0.01835
 H                     1.73637   2.14586   0.00187
 H                     2.9869   -0.0003    0.01436
 H                     1.73586  -2.14614   0.00186
 H                    -0.73202  -2.14344  -0.01834
 C                    -2.42325   0.00008   0.00961
 H                    -2.82945  -0.87886  -0.49686
 H                    -2.80083  -0.01135   1.03819
 H                    -2.82928   0.88997  -0.47739
[...]
 Polarizability derivatives wrt mode          1
                1             2             3
      1  -0.364940D-02  0.187136D+00  0.323784D-02
      2   0.187136D+00 -0.118319D-02 -0.108876D+00
      3   0.323784D-02 -0.108876D+00 -0.897013D-03
[...]
 Polarizability derivatives wrt mode          2
                1             2             3
      1   0.232095D-01 -0.970472D-03 -0.281142D+00
      2  -0.970472D-03 -0.115904D-01  0.777774D-03
      3  -0.281142D+00  0.777774D-03 -0.250156D-01
[...]
 Polarizability derivatives wrt mode          3
                1             2             3
      1  -0.314333D-02  0.849523D-01 -0.338693D-03
      2   0.849523D-01  0.175190D-02 -0.285302D-01
      3  -0.338693D-03 -0.285302D-01 -0.227030D-03
[...]
 Polarizability derivatives wrt mode          4
                1             2             3
      1   0.284071D-02 -0.500696D-01 -0.758978D-03
      2  -0.500696D-01  0.987691D-03 -0.197740D-02
      3  -0.758978D-03 -0.197740D-02  0.525357D-03
[...]
 Polarizability derivatives wrt mode          5
                1             2             3
      1   0.159008D+00 -0.694265D-03 -0.119721D+00
      2  -0.694265D-03 -0.668425D-02 -0.122564D-03
      3  -0.119721D+00 -0.122564D-03 -0.214392D-02
[...]
 Polarizability derivatives wrt mode          6
```

```
                1             2             3
      1   0.710503D+00 -0.744485D-03  0.377970D-01
      2  -0.744485D-03 -0.116210D+00 -0.905754D-05
      3   0.377970D-01 -0.905754D-05  0.106980D+00
[...]
 Polarizability derivatives wrt mode          7
                1             2             3
      1   0.922098D-03  0.483211D+00 -0.181119D-04
      2   0.483211D+00  0.464493D-04  0.212890D-02
      3  -0.181119D-04  0.212890D-02  0.557599D-04
[...]
 Polarizability derivatives wrt mode          8
                1             2             3
      1   0.116577D+00 -0.940957D-03 -0.318950D-03
      2  -0.940957D-03  0.593692D-01  0.298392D-03
      3  -0.318950D-03  0.298392D-03 -0.525668D-02
[...]
 Polarizability derivatives wrt mode          9
                1             2             3
      1  -0.159599D+00  0.131453D-02  0.146825D+00
      2   0.131453D-02 -0.917633D-01  0.494033D-03
      3   0.146825D+00  0.494033D-03 -0.154120D-01
[...]
 Polarizability derivatives wrt mode         10
                1             2             3
      1   0.632918D+00 -0.637923D-03  0.462385D-01
      2  -0.637923D-03  0.826358D+00  0.775602D-04
      3   0.462385D-01  0.775602D-04  0.265886D+00
[...]
 Polarizability derivatives wrt mode         11
                1             2             3
      1  -0.873351D-03  0.378134D-01  0.100989D-02
      2   0.378134D-01 -0.369721D-03 -0.835471D-01
      3   0.100989D-02 -0.835471D-01 -0.102446D-03
[...]
 Polarizability derivatives wrt mode         12
                1             2             3
      1   0.101825D+00 -0.740195D-03  0.195882D-01
      2  -0.740195D-03 -0.144141D-01 -0.260679D-03
      3   0.195882D-01 -0.260679D-03 -0.113443D-01
[...]
 Polarizability derivatives wrt mode         13
                1             2             3
      1  -0.307749D-02  0.663382D-01  0.542697D-03
      2   0.663382D-01 -0.140578D-02  0.912076D-02
      3   0.542697D-03  0.912076D-02 -0.527629D-03
[...]
 Polarizability derivatives wrt mode         14
                1             2             3
      1  -0.253264D-01  0.573740D-03  0.304082D-01
      2   0.573740D-03 -0.982555D-02 -0.308796D-03
      3   0.304082D-01 -0.308796D-03 -0.146754D-02
[...]
 Polarizability derivatives wrt mode         15
                1             2             3
      1  -0.599853D-02  0.884398D-01  0.340919D-03
      2   0.884398D-01 -0.114294D-01  0.237877D-01
      3   0.340919D-03  0.237877D-01 -0.496270D-02
```

```
[...]
 Polarizability derivatives wrt mode         16
                1             2             3
      1   0.115432D+01  0.120144D-02 -0.762434D-02
      2   0.120144D-02  0.961934D+00  0.158833D-03
      3  -0.762434D-02  0.158833D-03  0.419026D+00
[...]
 Polarizability derivatives wrt mode         17
                1             2             3
      1   0.656987D+00  0.589921D-04 -0.648005D-02
      2   0.589921D-04  0.645786D+00 -0.462942D-05
      3  -0.648005D-02 -0.462942D-05  0.294752D+00
[...]
 Polarizability derivatives wrt mode         18
                1             2             3
      1  -0.323814D+00  0.713476D-03 -0.265413D-01
      2   0.713476D-03 -0.495400D-01 -0.230766D-03
      3  -0.265413D-01 -0.230766D-03 -0.165321D-01
[...]
 Polarizability derivatives wrt mode         19
                1             2             3
      1   0.154830D-02  0.170058D+00  0.899264D-04
      2   0.170058D+00 -0.790251D-03  0.922157D-02
      3   0.899264D-04  0.922157D-02 -0.398195D-03
[...]
 Polarizability derivatives wrt mode         20
                1             2             3
      1   0.120841D-02  0.379308D+00 -0.913682D-04
      2   0.379308D+00  0.512557D-04 -0.394528D-02
      3  -0.913682D-04 -0.394528D-02  0.176191D-03
[...]
 Polarizability derivatives wrt mode         21
                1             2             3
      1  -0.333306D+00  0.378409D-03 -0.159226D-01
      2   0.378409D-03  0.470249D+00  0.162610D-04
      3  -0.159226D-01  0.162610D-04 -0.912821D-02
[...]
 Polarizability derivatives wrt mode         22
                1             2             3
      1  -0.556282D+00 -0.233464D-02  0.736688D-01
      2  -0.233464D-02 -0.726808D+00 -0.946254D-04
      3   0.736688D-01 -0.946254D-04 -0.232008D+00
[...]
 Polarizability derivatives wrt mode         23
                1             2             3
      1  -0.241915D-02 -0.482805D-01  0.287610D-03
      2  -0.482805D-01 -0.284757D-02 -0.139078D-02
      3   0.287610D-03 -0.139078D-02 -0.909016D-03
[...]
 Polarizability derivatives wrt mode         24
                1             2             3
      1   0.947851D-03 -0.226929D+00  0.236282D-04
      2  -0.226929D+00  0.173360D-03  0.132850D-01
      3   0.236282D-04  0.132850D-01  0.892845D-04
[...]
 Polarizability derivatives wrt mode         25
                1             2             3
      1   0.113091D+01  0.707917D-02 -0.187621D+00
```

```
      2   0.707917D-02  0.311176D-01 -0.984162D-04
      3  -0.187621D+00 -0.984162D-04 -0.541784D-01
[...]
 Polarizability derivatives wrt mode         26
                1             2             3
      1  -0.269098D-02 -0.445631D+00 -0.209092D-02
      2  -0.445631D+00 -0.189024D-02  0.124528D+00
      3  -0.209092D-02  0.124528D+00  0.277904D-02
[...]
 Polarizability derivatives wrt mode         27
                1             2             3
      1  -0.445956D+00  0.205262D-02  0.589462D+00
      2   0.205262D-02 -0.148343D+00 -0.919539D-02
      3   0.589462D+00 -0.919539D-02  0.258741D+00
[...]
 Polarizability derivatives wrt mode         28
                1             2             3
      1   0.132568D-01  0.311575D+00 -0.329946D-02
      2   0.311575D+00  0.347666D-02 -0.183287D+00
      3  -0.329946D-02 -0.183287D+00 -0.819053D-02
[...]
 Polarizability derivatives wrt mode         29
                1             2             3
      1  -0.138321D+00  0.156057D-02 -0.295264D-02
      2   0.156057D-02  0.117287D+00 -0.206534D-03
      3  -0.295264D-02 -0.206534D-03 -0.465742D-01
[...]
 Polarizability derivatives wrt mode         30
                1             2             3
      1  -0.203581D-02 -0.648919D+00 -0.389675D-04
      2  -0.648919D+00 -0.428774D-04  0.273402D-01
      3  -0.389675D-04  0.273402D-01  0.184226D-02
[...]
 Polarizability derivatives wrt mode         31
                1             2             3
      1   0.122084D+01 -0.682797D-03 -0.149078D-01
      2  -0.682797D-03 -0.771325D+00 -0.819331D-04
      3  -0.149078D-01 -0.819331D-04 -0.596759D-01
[...]
 Polarizability derivatives wrt mode         32
                1             2             3
      1  -0.313666D+01 -0.145695D-01  0.712145D+00
      2  -0.145695D-01 -0.119601D+01  0.463444D-02
      3   0.712145D+00  0.463444D-02 -0.206124D+01
[...]
 Polarizability derivatives wrt mode         33
                1             2             3
      1   0.372423D+00  0.624517D-02  0.166307D+01
      2   0.624517D-02  0.130898D+01  0.342489D-01
      3   0.166307D+01  0.342489D-01 -0.537912D+00
[...]
 Polarizability derivatives wrt mode         34
                1             2             3
      1   0.206608D-02  0.142952D+01 -0.118568D-02
      2   0.142952D+01 -0.383001D-01  0.936296D+00
      3  -0.118568D-02  0.936296D+00  0.257789D-01
[...]
 Polarizability derivatives wrt mode         35
```

```
                1             2             3
      1   0.954793D+00  0.667910D-01  0.354171D-01
      2   0.667910D-01  0.592169D+00  0.164686D-02
      3   0.354171D-01  0.164686D-02  0.522936D-01
[...]
 Polarizability derivatives wrt mode         36
                1             2             3
      1  -0.292491D-01  0.225836D+01 -0.982155D-03
      2   0.225836D+01 -0.949704D-02  0.543187D-01
      3  -0.982155D-03  0.543187D-01  0.103612D-04
[...]
 Polarizability derivatives wrt mode         37
                1             2             3
      1   0.771121D+00  0.795962D-02 -0.147358D-01
      2   0.795962D-02 -0.335133D+01  0.786906D-04
      3  -0.147358D-01  0.786906D-04 -0.745804D-01
[...]
 Polarizability derivatives wrt mode         38
                1             2             3
      1   0.465215D-02 -0.110428D+01 -0.155639D-04
      2  -0.110428D+01 -0.434488D-02  0.210402D-01
      3  -0.155639D-04  0.210402D-01  0.273766D-03
[...]
 Polarizability derivatives wrt mode         39
                1             2             3
      1   0.348791D+01  0.244119D-03  0.238303D-01
      2   0.244119D-03  0.306932D+01 -0.168067D-04
      3   0.238303D-01 -0.168067D-04  0.998807D-01
[...]
 Harmonic frequencies (cm**-1), IR intensities (KM/Mole), Raman scattering
 activities (A**4/AMU), depolarization ratios for plane and unpolarized
 incident light, reduced masses (AMU), force constants (mDyne/A),
 and normal coordinates:
                      1                     2                     3
                      A                     A                     A
 Frequencies --    38.6747               208.5408              343.4871
 Red. masses --     1.0347                 3.0131                2.5038
 Frc consts  --     0.0009                 0.0772                0.1740
 IR Inten    --     0.2468                 2.3783                0.3770
 Raman Activ --     0.9848                 1.6738                0.1688
 Depolar (P) --     0.7498                 0.7493                0.7499
 Depolar (U) --     0.8570                 0.8567                0.8571
  Atom  AN      X      Y      Z        X      Y      Z        X      Y      Z
     1   6     0.00   0.00  -0.02     0.00   0.00   0.19     0.06   0.13   0.01
     2   6     0.00   0.00  -0.02     0.00   0.00  -0.01     0.08  -0.01  -0.01
     3   6     0.00   0.00   0.00     0.00   0.00  -0.20     0.00  -0.07   0.00
     4   6     0.00   0.00   0.02     0.00   0.00  -0.01    -0.08  -0.01   0.01
     5   6     0.00   0.00   0.02     0.00   0.00   0.19    -0.06   0.13  -0.01
     6   6     0.00   0.01   0.00     0.00   0.00   0.15     0.00   0.15   0.00
     7   1     0.00   0.00  -0.04     0.00   0.00   0.25     0.15   0.18   0.02
     8   1     0.00   0.00  -0.04     0.00   0.00  -0.07     0.17  -0.06  -0.02
     9   1     0.00   0.00   0.00     0.01   0.00  -0.45     0.00  -0.14   0.00
    10   1     0.00   0.00   0.04     0.00   0.00  -0.08    -0.17  -0.06   0.02
    11   1     0.00   0.00   0.04     0.00   0.00   0.25    -0.15   0.18  -0.02
    12   6     0.00  -0.01   0.00    -0.01   0.00  -0.21     0.00  -0.23   0.00
    13   1     0.00   0.28  -0.49     0.14   0.00  -0.34     0.33  -0.40   0.03
    14   1     0.00  -0.59  -0.01    -0.32   0.01  -0.33     0.00  -0.35   0.00
    15   1     0.00   0.27   0.50     0.14  -0.01  -0.35    -0.33  -0.40  -0.03
```

	4			5			6		
	A			A			A		
Frequencies --	412.5835			475.3186			528.6652		
Red. masses --	2.9022			2.6971			5.0148		
Frc consts --	0.2911			0.3590			0.8258		
IR Inten --	0.0070			9.8559			0.5886		
Raman Activ --	0.0529			0.6008			6.3302		
Depolar (P) --	0.7477			0.5341			0.3552		
Depolar (U) --	0.8556			0.6963			0.5242		
Atom AN	X	Y	Z	X	Y	Z	X	Y	Z
1 6	0.00	-0.01	0.21	0.01	-0.01	-0.04	0.05	-0.13	0.00
2 6	0.00	0.00	-0.21	0.01	-0.01	-0.13	0.11	-0.12	0.02
3 6	0.00	0.00	0.00	0.02	0.00	0.19	0.29	0.00	-0.02
4 6	0.00	0.00	0.21	0.01	0.01	-0.13	0.11	0.12	0.02
5 6	0.00	-0.01	-0.21	0.01	0.01	-0.04	0.05	0.13	0.00
6 6	0.00	-0.01	0.00	-0.01	0.00	0.28	-0.22	0.00	-0.04
7 1	-0.01	-0.01	0.45	0.02	0.00	-0.32	0.24	-0.02	0.05
8 1	-0.01	0.00	-0.46	0.00	0.00	-0.40	-0.04	-0.03	0.07
9 1	0.00	0.01	0.00	0.02	0.00	0.32	0.30	0.00	-0.02
10 1	0.01	0.00	0.45	0.00	0.00	-0.40	-0.05	0.03	0.07
11 1	0.01	-0.01	-0.45	0.02	0.00	-0.32	0.24	0.02	0.05
12 6	0.00	0.01	0.00	-0.03	0.00	-0.01	-0.37	0.00	0.01
13 1	-0.01	0.02	0.00	0.13	0.00	-0.15	-0.39	0.00	0.02
14 1	0.00	0.01	0.00	-0.36	0.00	-0.14	-0.33	0.00	0.02
15 1	0.01	0.02	0.00	0.12	-0.01	-0.15	-0.39	0.00	0.02

	7			8			9		
	A			A			A		
Frequencies --	636.7566			710.7226			744.7162		
Red. masses --	6.3711			1.9866			1.5077		
Frc consts --	1.5220			0.5912			0.4927		
IR Inten --	0.0980			32.0539			49.1912		
Raman Activ --	4.9034			0.2237			0.9179		
Depolar (P) --	0.7500			0.1758			0.3558		
Depolar (U) --	0.8571			0.2990			0.5248		
Atom AN	X	Y	Z	X	Y	Z	X	Y	Z
1 6	0.24	-0.20	0.00	0.00	0.00	-0.09	0.00	-0.01	0.09
2 6	0.26	0.24	0.00	0.00	0.00	0.16	0.00	-0.01	0.00
3 6	0.00	0.14	0.00	0.00	0.00	-0.10	0.01	0.00	0.11
4 6	-0.26	0.24	0.00	0.00	0.00	0.16	0.00	0.01	0.00
5 6	-0.24	-0.20	0.00	0.00	0.00	-0.09	0.00	0.01	0.09
6 6	0.00	-0.14	0.00	0.00	0.00	0.11	-0.01	0.00	-0.12
7 1	0.10	-0.28	0.00	0.00	0.00	-0.52	0.01	0.00	-0.16
8 1	0.12	0.32	0.00	0.00	0.00	-0.10	-0.01	-0.01	-0.54
9 1	0.00	-0.30	0.00	0.00	0.00	-0.58	0.01	0.00	-0.46
10 1	-0.12	0.32	0.00	0.00	0.00	-0.10	-0.01	0.01	-0.54
11 1	-0.10	-0.28	0.00	0.00	0.00	-0.52	0.01	0.00	-0.16
12 6	0.00	-0.05	0.00	0.00	0.00	0.02	0.01	0.00	-0.03
13 1	0.02	-0.07	0.01	0.04	0.00	-0.01	-0.11	-0.01	0.09
14 1	0.00	-0.06	0.00	-0.09	0.00	-0.02	0.26	0.00	0.07
15 1	-0.02	-0.07	-0.01	0.04	0.00	-0.01	-0.10	0.01	0.09

	10	11	12
	A	A	A
Frequencies --	798.2265	852.7399	910.0940
Red. masses --	4.5133	1.2497	1.3097
Frc consts --	1.6943	0.5354	0.6391
IR Inten --	0.8306	0.0264	0.6840
Raman Activ --	16.6277	0.1766	0.1292
Depolar (P) --	0.0471	0.7499	0.4983

Depolar (U) --		0.0900			0.8571			0.6651		
Atom	AN	X	Y	Z	X	Y	Z	X	Y	Z
1	6	0.08	0.18	0.01	0.00	0.00	-0.08	0.00	-0.01	-0.09
2	6	0.13	0.22	0.00	0.00	0.00	-0.07	0.00	0.00	0.01
3	6	-0.17	0.00	0.02	0.00	0.00	0.00	0.00	0.00	0.10
4	6	0.13	-0.22	0.00	0.00	0.00	0.07	0.00	0.00	0.01
5	6	0.08	-0.18	0.01	0.00	0.00	0.08	0.00	0.01	-0.09
6	6	0.05	0.00	-0.03	0.00	0.00	0.00	0.00	0.00	0.02
7	1	-0.01	0.14	0.00	-0.01	0.00	0.51	-0.01	0.00	0.52
8	1	0.40	0.07	-0.07	-0.01	0.00	0.48	-0.01	0.00	-0.08
9	1	-0.16	0.00	-0.08	0.00	0.00	0.00	0.00	0.00	-0.59
10	1	0.40	-0.07	-0.07	0.01	0.00	-0.48	-0.01	0.00	-0.08
11	1	-0.01	-0.14	0.00	0.01	0.00	-0.51	-0.01	0.00	0.52
12	6	-0.28	0.00	0.01	0.00	0.00	0.00	0.00	0.00	0.03
13	1	-0.31	0.01	0.00	0.01	0.00	0.00	0.10	0.02	-0.08
14	1	-0.29	0.00	0.00	0.00	-0.01	0.00	-0.20	0.00	-0.05
15	1	-0.31	-0.01	0.00	-0.01	-0.01	0.00	0.10	-0.02	-0.08

	13	14	15
	A	A	A
Frequencies --	975.6044	994.0231	999.6828
Red. masses --	1.3685	1.2762	1.4366
Frc consts --	0.7674	0.7429	0.8459
IR Inten --	0.0008	0.0537	0.1552
Raman Activ --	0.0943	0.0292	0.1789
Depolar (P) --	0.7483	0.4930	0.7318
Depolar (U) --	0.8560	0.6604	0.8451

Atom	AN	X	Y	Z	X	Y	Z	X	Y	Z
1	6	0.00	0.00	-0.09	0.00	0.00	0.03	-0.02	0.07	0.00
2	6	0.00	0.00	0.09	0.00	0.00	-0.08	0.03	0.03	0.00
3	6	0.00	0.00	0.00	0.00	0.00	0.09	0.00	-0.04	0.00
4	6	0.00	0.00	-0.09	0.00	0.00	-0.08	-0.03	0.03	0.00
5	6	0.00	0.00	0.09	0.00	0.00	0.03	0.02	0.07	0.00
6	6	0.00	0.00	0.00	0.00	0.00	0.01	0.00	-0.06	0.00
7	1	0.00	0.00	0.48	0.00	0.00	-0.25	-0.04	0.06	0.03
8	1	0.00	0.00	-0.51	0.00	0.00	0.51	0.14	-0.03	0.00
9	1	0.00	0.00	0.00	0.01	0.00	-0.57	0.00	-0.18	0.00
10	1	0.00	0.00	0.51	0.00	0.00	0.51	-0.14	-0.03	0.00
11	1	0.01	0.00	-0.48	0.00	0.00	-0.25	0.04	0.07	-0.03
12	6	0.00	0.00	0.00	0.00	0.00	-0.01	0.00	-0.14	0.00
13	1	0.01	-0.01	0.00	-0.03	-0.01	0.03	-0.60	0.18	-0.06
14	1	0.00	-0.01	0.00	0.06	0.00	0.01	-0.01	0.28	0.00
15	1	-0.01	-0.01	0.00	-0.03	0.01	0.03	0.61	0.17	0.05

	16	17	18
	A	A	A
Frequencies --	1017.1611	1050.3199	1062.9379
Red. masses --	6.1984	2.2230	1.5586
Frc consts --	3.7784	1.4449	1.0375
IR Inten --	0.0818	3.7265	8.2792
Raman Activ --	35.1930	13.6523	1.3724
Depolar (P) --	0.0386	0.0288	0.2364
Depolar (U) --	0.0744	0.0560	0.3825

Atom	AN	X	Y	Z	X	Y	Z	X	Y	Z
1	6	-0.20	0.34	-0.01	-0.05	-0.08	0.00	0.01	-0.02	-0.04
2	6	-0.02	-0.04	0.00	0.03	0.19	0.00	0.00	0.01	0.00
3	6	0.39	0.00	0.00	0.13	0.00	0.00	-0.01	0.00	0.00
4	6	-0.02	0.04	0.00	0.03	-0.19	0.00	0.00	-0.01	0.00
5	6	-0.19	-0.34	-0.01	-0.05	0.08	0.00	0.01	0.02	-0.04
6	6	0.02	0.00	0.03	-0.03	0.00	-0.01	0.00	0.00	0.15

7	1	-0.18	0.37	0.05	-0.35	-0.24	-0.01	0.00	-0.02	0.17
8	1	-0.02	-0.03	-0.02	-0.31	0.39	0.00	-0.01	0.02	0.00
9	1	0.41	0.00	0.01	0.15	0.00	0.01	-0.01	0.00	-0.02
10	1	-0.02	0.02	-0.02	-0.31	-0.39	0.00	-0.01	-0.02	0.00
11	1	-0.17	-0.37	0.05	-0.35	0.24	-0.01	0.00	0.02	0.17
12	6	0.02	0.00	-0.02	0.02	0.00	0.01	-0.01	0.00	-0.15
13	1	-0.05	0.00	0.04	0.05	0.00	-0.02	-0.34	-0.09	0.28
14	1	0.11	0.01	0.01	-0.01	0.00	0.00	0.70	0.00	0.12
15	1	-0.03	0.01	0.04	0.05	0.00	-0.02	-0.33	0.08	0.28

	19	20	21
	A	A	A
Frequencies --	1110.1664	1180.8952	1202.9527
Red. masses --	1.4658	1.1105	1.1408
Frc consts --	1.0644	0.9124	0.9727
IR Inten --	6.2938	0.0536	0.4440
Raman Activ --	0.6091	3.0217	3.5191
Depolar (P) --	0.7500	0.7500	0.7201
Depolar (U) --	0.8571	0.8571	0.8372

Atom	AN	X	Y	Z	X	Y	Z	X	Y	Z
1	6	0.10	-0.02	0.00	-0.01	-0.01	0.00	0.05	0.03	0.00
2	6	-0.05	-0.05	0.00	0.04	-0.02	0.00	-0.05	0.02	0.00
3	6	0.00	0.07	0.00	0.00	0.07	0.00	-0.01	0.00	0.00
4	6	0.05	-0.05	0.00	-0.04	-0.02	0.00	-0.05	-0.02	0.00
5	6	-0.10	-0.02	0.00	0.01	-0.01	0.00	0.05	-0.03	0.00
6	6	0.00	0.03	0.00	0.00	0.00	0.00	0.01	0.00	0.00
7	1	0.46	0.18	0.01	-0.14	-0.09	0.00	0.43	0.24	0.00
8	1	-0.23	0.05	0.00	0.42	-0.24	0.00	-0.44	0.25	-0.01
9	1	0.00	0.52	0.00	0.00	0.68	0.00	-0.01	0.00	0.00
10	1	0.23	0.05	0.00	-0.42	-0.24	0.00	-0.44	-0.25	-0.01
11	1	-0.46	0.18	-0.01	0.14	-0.09	0.00	0.43	-0.24	0.00
12	6	0.00	-0.06	0.00	0.00	0.00	0.00	-0.01	0.00	0.00
13	1	-0.19	0.05	-0.03	-0.01	0.00	0.00	0.00	-0.01	0.01
14	1	0.00	0.10	0.00	0.00	0.01	0.00	-0.01	0.00	0.00
15	1	0.19	0.05	0.03	0.01	0.00	0.00	0.00	0.00	0.01

	22	23	24
	A	A	A
Frequencies --	1227.7948	1328.4489	1355.6884
Red. masses --	2.9933	4.9861	1.3985
Frc consts --	2.6586	5.1845	1.5144
IR Inten --	1.0216	0.0409	0.0015
Raman Activ --	12.9184	0.0492	1.0852
Depolar (P) --	0.0502	0.7449	0.7500
Depolar (U) --	0.0956	0.8538	0.8571

Atom	AN	X	Y	Z	X	Y	Z	X	Y	Z
1	6	0.05	0.00	0.00	-0.17	-0.12	0.00	0.10	0.03	0.00
2	6	-0.09	-0.08	0.00	0.20	-0.13	0.00	-0.01	-0.01	0.00
3	6	0.03	0.00	0.00	0.00	0.20	0.00	0.00	-0.10	0.00
4	6	-0.09	0.08	0.00	-0.20	-0.13	0.00	0.01	-0.01	0.00
5	6	0.05	0.00	0.00	0.17	-0.12	0.00	-0.10	0.03	0.00
6	6	0.36	0.00	0.00	0.00	0.34	0.00	0.00	0.07	0.00
7	1	-0.38	-0.26	-0.01	-0.13	-0.10	0.00	-0.48	-0.30	0.00
8	1	-0.32	0.04	-0.01	-0.38	0.19	-0.01	-0.28	0.14	0.00
9	1	0.02	0.00	0.00	0.00	-0.19	0.00	0.00	0.33	0.00
10	1	-0.32	-0.05	-0.01	0.38	0.19	0.01	0.28	0.14	0.00
11	1	-0.37	0.26	-0.01	0.13	-0.10	0.00	0.48	-0.30	0.00
12	6	-0.14	0.00	0.00	0.00	-0.08	0.00	0.00	-0.03	0.00
13	1	-0.27	0.05	0.00	-0.20	0.08	-0.09	-0.05	0.02	-0.04
14	1	-0.21	0.00	-0.02	0.00	0.28	0.00	0.00	0.09	0.00

```
   15   1    -0.27  -0.05   0.00     0.20   0.07   0.09     0.05   0.02   0.04
                    25                    26                    27
                     A                     A                     A
Frequencies --  1414.0376             1468.2520             1490.1416
Red. masses --     1.2482                1.5993                1.0494
Frc consts  --     1.4705                2.0313                1.3730
IR Inten    --     1.1922                0.0071                7.2707
Raman Activ --    16.0514                4.4963               10.4897
Depolar (P) --     0.3600                0.7500                0.6823
Depolar (U) --     0.5294                0.8571                0.8111
 Atom  AN      X      Y      Z        X      Y      Z        X      Y      Z
    1   6     0.00   0.00   0.00     0.06  -0.04   0.00     0.00   0.00   0.00
    2   6     0.01   0.00   0.00    -0.11   0.01   0.00     0.00   0.00   0.00
    3   6     0.00   0.00   0.00     0.00   0.07   0.00     0.00   0.00   0.00
    4   6     0.00   0.00   0.00     0.11   0.01   0.00     0.00   0.00   0.00
    5   6     0.00   0.00   0.00    -0.06  -0.04   0.00    -0.01   0.00   0.00
    6   6    -0.03   0.00   0.00     0.00   0.10   0.00    -0.01   0.00   0.02
    7   1     0.02   0.01   0.00    -0.06  -0.12   0.01     0.03   0.01   0.00
    8   1     0.01   0.00   0.00     0.25  -0.21   0.00     0.01   0.00   0.00
    9   1     0.00   0.00   0.00     0.00  -0.44   0.00     0.00   0.00   0.00
   10   1     0.01   0.00   0.00    -0.25  -0.21   0.00     0.00   0.00   0.00
   11   1     0.02  -0.01   0.00     0.06  -0.12  -0.01     0.03  -0.01   0.00
   12   6     0.14   0.00  -0.01     0.00  -0.06   0.00     0.02   0.00   0.05
   13   1    -0.49   0.14   0.21     0.14   0.06  -0.29    -0.26   0.41  -0.45
   14   1    -0.56   0.00  -0.25     0.00   0.54   0.01     0.30  -0.01   0.13
   15   1    -0.48  -0.15   0.21    -0.15   0.05   0.29    -0.25  -0.40  -0.48
                    28                    29                    30
                     A                     A                     A
Frequencies --  1502.3096             1527.3007             1623.2737
Red. masses --     1.2828                2.2564                5.2807
Frc consts  --     1.7058                3.1011                8.1984
IR Inten    --    13.2855               13.6049                0.2529
Raman Activ --     2.7472                0.3752                8.8588
Depolar (P) --     0.7498                0.6735                0.7500
Depolar (U) --     0.8570                0.8049                0.8571
 Atom  AN      X      Y      Z        X      Y      Z        X      Y      Z
    1   6     0.05  -0.01   0.00     0.07   0.10   0.00     0.09   0.18   0.00
    2   6    -0.05  -0.02   0.00     0.12  -0.11   0.00     0.07  -0.20   0.00
    3   6     0.00   0.08   0.00    -0.11   0.00   0.00     0.00   0.35   0.00
    4   6     0.05  -0.02   0.00     0.12   0.11   0.00    -0.07  -0.20   0.00
    5   6    -0.05  -0.01   0.00     0.07  -0.10   0.00    -0.09   0.18   0.00
    6   6     0.00   0.08   0.00    -0.15   0.00   0.00     0.00  -0.30   0.00
    7   1    -0.10  -0.11  -0.01    -0.41  -0.16   0.00    -0.28  -0.02   0.00
    8   1     0.09  -0.11   0.00    -0.44   0.20   0.00    -0.24  -0.04   0.00
    9   1     0.00  -0.29   0.00    -0.13   0.00   0.00     0.00  -0.46   0.00
   10   1    -0.09  -0.11   0.00    -0.44  -0.20   0.00     0.24  -0.04   0.00
   11   1     0.09  -0.10   0.01    -0.41   0.16   0.00     0.28  -0.02   0.00
   12   6     0.00   0.03   0.00     0.03   0.00   0.00     0.00   0.02   0.00
   13   1    -0.31  -0.05   0.35     0.03   0.01  -0.01     0.19  -0.01  -0.10
   14   1     0.00  -0.61  -0.01     0.04   0.00   0.01     0.00   0.14   0.00
   15   1     0.32  -0.03  -0.34     0.03  -0.01  -0.02    -0.19  -0.01   0.09
                    31                    32                    33
                     A                     A                     A
Frequencies --  1644.8333             3019.5167             3073.2698
Red. masses --     5.6193                1.0405                1.0946
Frc consts  --     8.9574                5.5894                6.0910
IR Inten    --     9.1017               29.1713               19.4660
Raman Activ --    22.1666              234.9149               82.5544
```

Depolar (P) --		0.7061			0.0589			0.6519		
Depolar (U) --		0.8278			0.1113			0.7893		
Atom	AN	X	Y	Z	X	Y	Z	X	Y	Z
1	6	0.30	0.09	0.00	0.00	0.00	0.00	0.00	0.00	0.00
2	6	-0.27	0.07	0.00	0.00	0.00	0.00	0.00	0.00	0.00
3	6	0.14	0.00	0.00	0.00	0.00	0.00	0.00	0.00	0.00
4	6	-0.27	-0.07	0.00	0.00	0.00	0.00	0.00	0.00	0.00
5	6	0.30	-0.09	0.00	0.00	0.00	0.00	0.00	0.00	0.00
6	6	-0.23	0.00	0.00	0.00	0.00	0.00	0.00	0.00	0.00
7	1	-0.31	-0.26	0.00	-0.01	0.01	0.00	0.01	-0.01	0.00
8	1	0.24	-0.23	0.00	0.00	0.00	0.00	0.00	0.00	0.00
9	1	0.15	0.00	0.00	0.00	0.00	0.00	0.00	0.00	0.00
10	1	0.24	0.23	0.00	0.00	0.00	0.00	0.00	0.00	0.00
11	1	-0.31	0.26	0.00	-0.01	-0.01	0.00	0.01	0.01	0.00
12	6	0.03	0.00	0.00	-0.05	0.00	0.03	0.02	0.00	0.09
13	1	0.02	0.03	-0.03	0.15	0.35	0.21	-0.21	-0.47	-0.25
14	1	0.06	0.00	0.02	0.26	0.01	-0.74	0.21	0.01	-0.56
15	1	0.01	-0.03	-0.03	0.15	-0.35	0.20	-0.20	0.46	-0.23

		34			35			36		
		A			A			A		
Frequencies --		3099.2331			3152.9598			3154.6036		
Red. masses --		1.1023			1.0859			1.0876		
Frc consts --		6.2381			6.3604			6.3772		
IR Inten --		16.7656			8.7464			5.7989		
Raman Activ --		61.3465			17.2393			107.1782		
Depolar (P) --		0.7500			0.1244			0.7499		
Depolar (U) --		0.8571			0.2213			0.8571		
Atom	AN	X	Y	Z	X	Y	Z	X	Y	Z
1	6	0.00	0.00	0.00	0.02	-0.04	0.00	-0.03	0.05	0.00
2	6	0.00	0.00	0.00	0.02	0.03	0.00	-0.01	-0.02	0.00
3	6	0.00	0.00	0.00	-0.02	0.00	0.00	0.00	0.00	0.00
4	6	0.00	0.00	0.00	0.02	-0.03	0.00	0.01	-0.02	0.00
5	6	0.00	0.00	0.00	0.02	0.04	0.00	0.03	0.05	0.00
6	6	0.00	0.00	0.00	0.00	0.00	0.00	0.00	0.00	0.00
7	1	-0.02	0.02	0.00	-0.26	0.45	0.00	0.32	-0.57	0.01
8	1	0.00	0.00	0.00	-0.19	-0.34	0.00	0.15	0.27	0.00
9	1	0.00	0.00	0.00	0.29	0.00	0.00	-0.01	0.00	0.00
10	1	0.00	0.00	0.00	-0.20	0.36	0.00	-0.14	0.25	0.00
11	1	0.02	0.02	0.00	-0.28	-0.49	-0.01	-0.31	-0.54	-0.01
12	6	0.00	0.09	0.00	0.00	0.00	0.00	0.00	0.00	0.00
13	1	-0.25	-0.55	-0.33	-0.01	-0.01	-0.01	-0.01	-0.02	-0.01
14	1	0.00	0.02	0.01	0.00	0.00	0.00	0.00	0.00	0.00
15	1	0.26	-0.58	0.33	-0.01	0.01	-0.01	0.01	-0.02	0.01

		37			38			39		
		A			A			A		
Frequencies --		3167.1936			3175.4530			3187.9875		
Red. masses --		1.0899			1.0938			1.0979		
Frc consts --		6.4416			6.4984			6.5743		
IR Inten --		7.2107			36.0828			14.0259		
Raman Activ --		134.8092			25.6179			293.2483		
Depolar (P) --		0.4631			0.7500			0.1170		
Depolar (U) --		0.6331			0.8571			0.2095		
Atom	AN	X	Y	Z	X	Y	Z	X	Y	Z
1	6	-0.02	0.03	0.00	-0.01	0.02	0.00	0.01	-0.01	0.00
2	6	0.02	0.02	0.00	0.03	0.05	0.00	-0.02	-0.04	0.00
3	6	-0.06	0.00	0.00	0.00	0.00	0.00	-0.06	0.00	0.00
4	6	0.02	-0.02	0.00	-0.03	0.05	0.00	-0.02	0.04	0.00
5	6	-0.02	-0.03	0.00	0.01	0.02	0.00	0.01	0.01	0.00

```
     6   6     0.00   0.00   0.00     0.00   0.00   0.00     0.00   0.00   0.00
     7   1     0.21  -0.36   0.00     0.15  -0.26   0.00    -0.08   0.14   0.00
     8   1    -0.17  -0.29   0.00    -0.32  -0.56   0.00     0.23   0.41   0.00
     9   1     0.65   0.00   0.00     0.00   0.01   0.00     0.70   0.00   0.00
    10   1    -0.17   0.29   0.00     0.32  -0.56   0.00     0.23  -0.41   0.00
    11   1     0.21   0.36   0.00    -0.15  -0.25   0.00    -0.08  -0.14   0.00
    12   6     0.00   0.00   0.00     0.00   0.00   0.00     0.00   0.00   0.00
    13   1     0.01   0.01   0.00     0.00  -0.01   0.00     0.00   0.00   0.00
    14   1     0.00   0.00   0.00     0.00   0.00   0.00     0.00   0.00   0.00
    15   1     0.01  -0.01   0.00     0.00  -0.01   0.00     0.00   0.00   0.00
[...]
```

D.5 Decanoic acid

The optimized geometry found for decanoic acid is presented in figure D.4. Relevant output from the Raman computation is given below, which includes the atomic coordinates in the standard orientation, polarizability derivatives and ninety normal modes. The atomic coordinates in the molecular frame of reference are included in table D.1. Note that the first hydrogen atom of the chain, part of the methyl group, is listed as the last atom in the computational output.

Table D.1: Atomic positions of dodecanoic acid in its optimised geometry, specified in the molecular frame of reference m in which the chain of carbon atoms is in the $x^{\mathsf{m}}z^{\mathsf{m}}$ plane and parallel to $\hat{\mathbf{z}}^{\mathsf{m}}$. Values are rounded to four decimal places.

Atom	x^{m} / Å	y^{m} / Å	z^{m} / Å
C	-0.4995	0	6.7102
C	0.3436	0	5.4315
H	-1.1449	-0.8829	6.7590
H	-1.1449	0.8829	6.7590
C	-0.4972	0	4.1502
H	1.0033	0.8763	5.4296
H	1.0033	-0.8763	5.4296
H	-1.1580	-0.8769	4.1528
H	-1.1580	0.8769	4.1528
C	0.3390	0	2.8653
C	-0.5011	0	1.5835
H	0.9996	-0.8768	2.8641
H	0.9996	0.8768	2.8641
C	0.3387	0	0.3008
H	-1.1615	-0.8769	1.5841
H	-1.1615	0.8769	1.5841
C	-0.4993	0	-0.9822
H	0.9990	0.8766	0.3002
H	0.9990	-0.8766	0.3002
H	-1.1597	-0.8770	-0.9825
H	-1.1597	0.8770	-0.9825
C	0.3503	0	-2.2581
C	-0.4985	0	-3.5288
H	1.0100	-0.8735	-2.2655
H	1.0100	0.8735	-2.2655
H	-1.1624	-0.8715	-3.5639
H	-1.1624	0.8715	-3.5639
C	0.3124	0	-4.8027
O	-0.4898	0	-5.9005
O	1.5147	0	-4.8871
H	0.0905	0	-6.6766
H	0.1299	0	7.6046

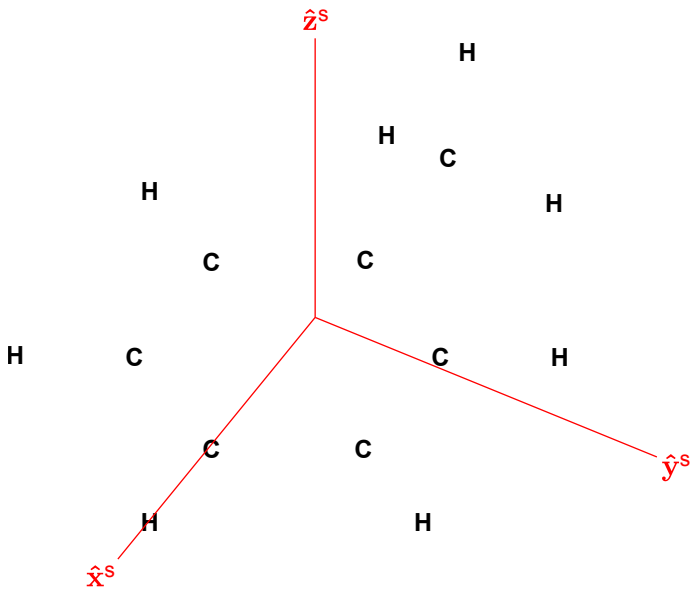

Figure D.3: Optimized geometry of toluene in GAUSSIAN's standard orientation, which matches the desired molecular orientation with the directions of the x and z axes inverted.

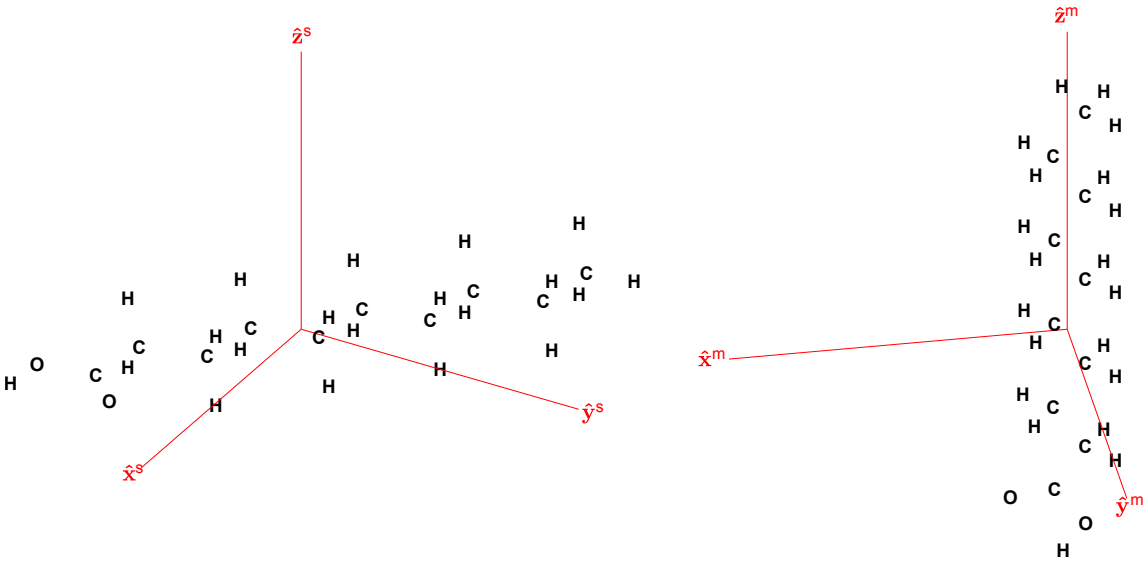

Figure D.4: Optimized geometry of decanoic acid in GAUSSIAN's standard orientation, the computational frame of reference s, (left) and the molecular frame of reference m used in our analysis.

```
[...]
 ****************************************
 %chk=/ddn/data/dch1maf/DecanoicacidRaman180815.chk
 %nprocshared=4
 Will use up to    4 processors via shared memory.
 %mem=450MW
 ---------------------------------------------------------------
 #T b3lyp/6-311++g(d,p) freq=Raman IOp(2/33=1) IOp(7/33=3)
 ---------------------------------------------------------------
 -------------
 Decanoic acid
 -------------
 Symbolic Z-matrix:
 Charge =  0 Multiplicity = 1
 C                    -5.3486    4.08273   0.
 C                    -3.8327    3.86392   0.
 H                    -5.81372   3.63264   0.88289
 H                    -5.81372   3.63264  -0.88289
 C                    -3.43309   2.38433   0.
 H                    -3.39319   4.3559   -0.87628
 H                    -3.39319   4.3559    0.87628
 H                    -3.87389   1.89208   0.87687
 H                    -3.87389   1.89208  -0.87687
 C                    -1.91707   2.15627   0.
 C                    -1.51674   0.67693   0.
 H                    -1.47751   2.64932   0.87675
 H                    -1.47751   2.64932  -0.87675
 C                     0.        0.45296   0.
 H                    -1.95569   0.18355   0.87693
 H                    -1.95569   0.18355  -0.87693
 C                     0.40279  -1.02558   0.
 H                     0.43897   0.94629  -0.8766
 H                     0.43897   0.94629   0.8766
 H                    -0.03555  -1.51953   0.87704
 H                    -0.03555  -1.51953  -0.87704
 C                     1.92094  -1.23769   0.
 C                     2.30726  -2.71616   0.
 H                     2.36456  -0.74939   0.87352
 H                     2.36456  -0.74939  -0.87352
 H                     1.89258  -3.23581   0.87145
 H                     1.89258  -3.23581  -0.87145
 C                     3.7982   -2.9559    0.
 O                     4.08624  -4.28473   0.
 O                     4.65981  -2.11301   0.
 H                     5.05185  -4.36626   0.
 H                    -5.5993    5.14723   0.
[...]
 Polarizability derivatives wrt mode          1
                1             2             3
     1   0.000000D+00  0.000000D+00  0.241826D-01
     2   0.000000D+00  0.000000D+00 -0.999846D-01
     3   0.241826D-01 -0.999846D-01  0.000000D+00
[...]
 Polarizability derivatives wrt mode          2
                1             2             3
     1   0.000000D+00  0.000000D+00  0.140246D-02
     2   0.000000D+00  0.000000D+00 -0.472032D-02
     3   0.140246D-02 -0.472032D-02  0.000000D+00
```

```
[...]
 Polarizability derivatives wrt mode          3
                 1             2             3
      1  -0.481068D-01 -0.159180D-01  0.000000D+00
      2  -0.159180D-01  0.433698D-01  0.000000D+00
      3   0.000000D+00  0.000000D+00  0.335079D-03
[...]
 Polarizability derivatives wrt mode          4
                 1             2             3
      1   0.000000D+00  0.000000D+00 -0.866384D-01
      2   0.000000D+00  0.000000D+00  0.392495D-01
      3  -0.866384D-01  0.392495D-01  0.000000D+00
[...]
 Polarizability derivatives wrt mode          5
                 1             2             3
      1   0.000000D+00  0.000000D+00 -0.680776D-01
      2   0.000000D+00  0.000000D+00  0.571277D-01
      3  -0.680776D-01  0.571277D-01  0.000000D+00
[...]
 Polarizability derivatives wrt mode          6
                 1             2             3
      1   0.000000D+00  0.000000D+00 -0.580321D-01
      2   0.000000D+00  0.000000D+00  0.183003D-01
      3  -0.580321D-01  0.183003D-01  0.000000D+00
[...]
 Polarizability derivatives wrt mode          7
                 1             2             3
      1   0.582496D-01 -0.389480D-01  0.000000D+00
      2  -0.389480D-01  0.176709D-01  0.000000D+00
      3   0.000000D+00  0.000000D+00  0.577627D-02
[...]
 Polarizability derivatives wrt mode          8
                 1             2             3
      1   0.000000D+00  0.000000D+00 -0.270938D-01
      2   0.000000D+00  0.000000D+00  0.110883D-01
      3  -0.270938D-01  0.110883D-01  0.000000D+00
[...]
 Polarizability derivatives wrt mode          9
                 1             2             3
      1   0.000000D+00  0.000000D+00  0.371448D-01
      2   0.000000D+00  0.000000D+00 -0.231577D-02
      3   0.371448D-01 -0.231577D-02  0.000000D+00
[...]
 Polarizability derivatives wrt mode         10
                 1             2             3
      1   0.000000D+00  0.000000D+00 -0.239615D-01
      2   0.000000D+00  0.000000D+00  0.140633D-01
      3  -0.239615D-01  0.140633D-01  0.000000D+00
[...]
 Polarizability derivatives wrt mode         11
                 1             2             3
      1   0.374014D+00 -0.215413D+00  0.000000D+00
      2  -0.215413D+00  0.249267D+00  0.000000D+00
      3   0.000000D+00  0.000000D+00  0.678762D-01
[...]
 Polarizability derivatives wrt mode         12
                 1             2             3
      1   0.178846D+00 -0.195045D+00  0.000000D+00
```

```
      2  -0.195045D+00  0.194483D+00  0.000000D+00
      3   0.000000D+00  0.000000D+00  0.547802D-01
[...]
 Polarizability derivatives wrt mode         13
                1             2             3
      1   0.000000D+00  0.000000D+00 -0.411927D-02
      2   0.000000D+00  0.000000D+00  0.201212D-01
      3  -0.411927D-02  0.201212D-01  0.000000D+00
[...]
 Polarizability derivatives wrt mode         14
                1             2             3
      1   0.331712D-01 -0.890953D-01  0.000000D+00
      2  -0.890953D-01  0.111212D+00  0.000000D+00
      3   0.000000D+00  0.000000D+00  0.160561D-01
[...]
 Polarizability derivatives wrt mode         15
                1             2             3
      1  -0.978904D-01  0.754796D-01  0.000000D+00
      2   0.754796D-01 -0.112191D+00  0.000000D+00
      3   0.000000D+00  0.000000D+00 -0.391894D-01
[...]
 Polarizability derivatives wrt mode         16
                1             2             3
      1  -0.196290D-01 -0.640885D-01  0.000000D+00
      2  -0.640885D-01 -0.226245D-01  0.000000D+00
      3   0.000000D+00  0.000000D+00  0.221196D-02
[...]
 Polarizability derivatives wrt mode         17
                1             2             3
      1  -0.138441D+00  0.407876D-01  0.000000D+00
      2   0.407876D-01  0.144544D-01  0.000000D+00
      3   0.000000D+00  0.000000D+00 -0.281745D-01
[...]
 Polarizability derivatives wrt mode         18
                1             2             3
      1   0.000000D+00  0.000000D+00 -0.279450D+00
      2   0.000000D+00  0.000000D+00  0.120436D+00
      3  -0.279450D+00  0.120436D+00  0.000000D+00
[...]
 Polarizability derivatives wrt mode         19
                1             2             3
      1   0.609782D-01 -0.958423D-01 -0.136737D-05
      2  -0.958423D-01 -0.328657D-01  0.000000D+00
      3  -0.136737D-05  0.000000D+00 -0.289684D-01
[...]
 Polarizability derivatives wrt mode         20
                1             2             3
      1   0.462605D-01  0.173115D+00  0.000000D+00
      2   0.173115D+00 -0.547923D+00  0.000000D+00
      3   0.000000D+00  0.000000D+00 -0.669549D-01
[...]
 Polarizability derivatives wrt mode         21
                1             2             3
      1   0.000000D+00  0.000000D+00 -0.116852D+00
      2   0.000000D+00  0.000000D+00  0.102120D+00
      3  -0.116852D+00  0.102120D+00  0.000000D+00
[...]
 Polarizability derivatives wrt mode         22
```

```
                1             2             3
      1   0.000000D+00  0.000000D+00  0.160536D-02
      2   0.000000D+00  0.000000D+00  0.218371D-02
      3   0.160536D-02  0.218371D-02  0.000000D+00
[...]
 Polarizability derivatives wrt mode         23
                1             2             3
      1   0.000000D+00  0.000000D+00  0.560957D-02
      2   0.000000D+00  0.000000D+00  0.203084D-01
      3   0.560957D-02  0.203084D-01  0.000000D+00
[...]
 Polarizability derivatives wrt mode         24
                1             2             3
      1   0.000000D+00  0.000000D+00 -0.140855D-02
      2   0.000000D+00  0.000000D+00  0.849875D-02
      3  -0.140855D-02  0.849875D-02  0.000000D+00
[...]
 Polarizability derivatives wrt mode         25
                1             2             3
      1   0.000000D+00  0.000000D+00 -0.391952D-01
      2   0.000000D+00  0.000000D+00 -0.409427D-01
      3  -0.391952D-01 -0.409427D-01  0.000000D+00
[...]
 Polarizability derivatives wrt mode         26
                1             2             3
      1   0.000000D+00  0.000000D+00  0.208506D-01
      2   0.000000D+00  0.000000D+00 -0.333464D-01
      3   0.208506D-01 -0.333464D-01  0.000000D+00
[...]
 Polarizability derivatives wrt mode         27
                1             2             3
      1  -0.548196D+00  0.204475D+00  0.000000D+00
      2   0.204475D+00 -0.543167D+00  0.000000D+00
      3   0.000000D+00  0.000000D+00 -0.123747D+00
[...]
 Polarizability derivatives wrt mode         28
                1             2             3
      1  -0.406592D+00  0.281231D+00  0.000000D+00
      2   0.281231D+00 -0.221999D+00  0.000000D+00
      3   0.000000D+00  0.000000D+00  0.428307D-01
[...]
 Polarizability derivatives wrt mode         29
                1             2             3
      1   0.150570D-05 -0.113978D-05 -0.423020D-01
      2  -0.113978D-05  0.000000D+00 -0.738574D-01
      3  -0.423020D-01 -0.738574D-01  0.000000D+00
[...]
 Polarizability derivatives wrt mode         30
                1             2             3
      1   0.000000D+00  0.000000D+00 -0.542367D-02
      2   0.000000D+00  0.000000D+00 -0.490132D-01
      3  -0.542367D-02 -0.490132D-01  0.000000D+00
[...]
 Polarizability derivatives wrt mode         31
                1             2             3
      1   0.315629D+00 -0.194535D-01  0.000000D+00
      2  -0.194535D-01  0.262418D-01  0.000000D+00
      3   0.000000D+00  0.000000D+00  0.555811D-01
```

```
[...]
 Polarizability derivatives wrt mode         32
                1             2             3
     1  -0.856388D-01  0.130327D+00  0.000000D+00
     2   0.130327D+00 -0.116522D+00  0.000000D+00
     3   0.000000D+00  0.000000D+00  0.296134D-01
[...]
 Polarizability derivatives wrt mode         33
                1             2             3
     1  -0.706940D-01 -0.722500D-01  0.000000D+00
     2  -0.722500D-01  0.101558D+00  0.114478D-05
     3   0.000000D+00  0.114478D-05 -0.396099D-01
[...]
 Polarizability derivatives wrt mode         34
                1             2             3
     1   0.113409D-05  0.118515D-05  0.180972D-01
     2   0.118515D-05 -0.154971D-05  0.713324D-01
     3   0.180972D-01  0.713324D-01  0.000000D+00
[...]
 Polarizability derivatives wrt mode         35
                1             2             3
     1  -0.665723D+00  0.158719D+00  0.000000D+00
     2   0.158719D+00  0.736692D-01  0.000000D+00
     3   0.000000D+00  0.000000D+00  0.346326D-01
[...]
 Polarizability derivatives wrt mode         36
                1             2             3
     1   0.138311D+00 -0.351753D-01  0.000000D+00
     2  -0.351753D-01  0.380093D-01  0.000000D+00
     3   0.000000D+00  0.000000D+00  0.150434D-01
[...]
 Polarizability derivatives wrt mode         37
                1             2             3
     1  -0.865614D+00 -0.569818D-01  0.000000D+00
     2  -0.569818D-01  0.733663D+00  0.000000D+00
     3   0.000000D+00  0.000000D+00 -0.130325D-03
[...]
 Polarizability derivatives wrt mode         38
                1             2             3
     1   0.434643D+00 -0.238866D+00  0.000000D+00
     2  -0.238866D+00  0.360440D+00  0.000000D+00
     3   0.000000D+00  0.000000D+00 -0.519203D-01
[...]
 Polarizability derivatives wrt mode         39
                1             2             3
     1  -0.528340D+00  0.219587D+00  0.000000D+00
     2   0.219587D+00 -0.348696D+00  0.000000D+00
     3   0.000000D+00  0.000000D+00  0.761313D-01
[...]
 Polarizability derivatives wrt mode         40
                1             2             3
     1   0.000000D+00  0.000000D+00 -0.359009D-02
     2   0.000000D+00  0.000000D+00  0.222897D+00
     3  -0.359009D-02  0.222897D+00  0.000000D+00
[...]
 Polarizability derivatives wrt mode         41
                1             2             3
     1   0.375101D+00 -0.575345D-01  0.000000D+00
```

```
      2  -0.575345D-01  0.671242D+00  0.000000D+00
      3   0.000000D+00  0.000000D+00 -0.121206D+00
[...]
 Polarizability derivatives wrt mode         42
                1             2             3
      1   0.000000D+00  0.000000D+00  0.184108D+00
      2   0.000000D+00  0.000000D+00  0.149820D+00
      3   0.184108D+00  0.149820D+00  0.000000D+00
[...]
 Polarizability derivatives wrt mode         43
                1             2             3
      1   0.714908D-02 -0.901380D-01  0.000000D+00
      2  -0.901380D-01  0.432581D-02  0.000000D+00
      3   0.000000D+00  0.000000D+00 -0.342551D-01
[...]
 Polarizability derivatives wrt mode         44
                1             2             3
      1   0.000000D+00  0.000000D+00 -0.135778D+00
      2   0.000000D+00  0.000000D+00  0.448564D-01
      3  -0.135778D+00  0.448564D-01  0.000000D+00
[...]
 Polarizability derivatives wrt mode         45
                1             2             3
      1  -0.654157D-01 -0.151483D+00  0.000000D+00
      2  -0.151483D+00  0.599119D-02  0.000000D+00
      3   0.000000D+00  0.000000D+00 -0.334630D-01
[...]
 Polarizability derivatives wrt mode         46
                1             2             3
      1   0.000000D+00  0.000000D+00  0.425795D-01
      2   0.000000D+00  0.000000D+00 -0.473609D-01
      3   0.425795D-01 -0.473609D-01  0.000000D+00
[...]
 Polarizability derivatives wrt mode         47
                1             2             3
      1  -0.170882D+00 -0.256019D+00  0.000000D+00
      2  -0.256019D+00  0.131231D+00  0.000000D+00
      3   0.000000D+00  0.000000D+00 -0.286671D-01
[...]
 Polarizability derivatives wrt mode         48
                1             2             3
      1   0.000000D+00  0.000000D+00 -0.407467D+00
      2   0.000000D+00  0.000000D+00  0.357125D+00
      3  -0.407467D+00  0.357125D+00  0.000000D+00
[...]
 Polarizability derivatives wrt mode         49
                1             2             3
      1   0.000000D+00  0.000000D+00  0.886725D+00
      2   0.000000D+00  0.000000D+00 -0.795746D+00
      3   0.886725D+00 -0.795746D+00  0.000000D+00
[...]
 Polarizability derivatives wrt mode         50
                1             2             3
      1  -0.163136D+00 -0.114607D+00  0.000000D+00
      2  -0.114607D+00  0.636764D-01  0.000000D+00
      3   0.000000D+00  0.000000D+00 -0.827727D-02
[...]
 Polarizability derivatives wrt mode         51
```

```
                1             2             3
     1   0.000000D+00  0.000000D+00 -0.201049D+00
     2   0.000000D+00  0.000000D+00  0.114587D+00
     3  -0.201049D+00  0.114587D+00  0.000000D+00
[...]
 Polarizability derivatives wrt mode         52
                1             2             3
     1   0.000000D+00  0.000000D+00 -0.641560D-01
     2   0.000000D+00  0.000000D+00  0.447670D-01
     3  -0.641560D-01  0.447670D-01  0.000000D+00
[...]
 Polarizability derivatives wrt mode         53
                1             2             3
     1   0.000000D+00  0.000000D+00  0.166290D+00
     2   0.000000D+00  0.000000D+00 -0.144302D+00
     3   0.166290D+00 -0.144302D+00  0.000000D+00
[...]
 Polarizability derivatives wrt mode         54
                1             2             3
     1  -0.165076D+00 -0.100462D+00  0.000000D+00
     2  -0.100462D+00  0.925106D-01  0.000000D+00
     3   0.000000D+00  0.000000D+00  0.872313D-02
[...]
 Polarizability derivatives wrt mode         55
                1             2             3
     1  -0.616641D-01  0.155050D-02  0.000000D+00
     2   0.155050D-02 -0.151815D-01  0.000000D+00
     3   0.000000D+00  0.000000D+00 -0.179739D-01
[...]
 Polarizability derivatives wrt mode         56
                1             2             3
     1   0.165638D+00  0.358998D-01  0.000000D+00
     2   0.358998D-01 -0.995262D-01  0.000000D+00
     3   0.000000D+00  0.000000D+00 -0.106164D-02
[...]
 Polarizability derivatives wrt mode         57
                1             2             3
     1  -0.303664D-01 -0.311138D-02  0.000000D+00
     2  -0.311138D-02 -0.786330D-01  0.000000D+00
     3   0.000000D+00  0.000000D+00  0.695337D-02
[...]
 Polarizability derivatives wrt mode         58
                1             2             3
     1   0.840212D-01 -0.233686D-01  0.000000D+00
     2  -0.233686D-01 -0.136072D+00  0.000000D+00
     3   0.000000D+00  0.000000D+00 -0.352710D-01
[...]
 Polarizability derivatives wrt mode         59
                1             2             3
     1  -0.119125D+00  0.950649D-02  0.000000D+00
     2   0.950649D-02  0.651089D-01  0.000000D+00
     3   0.000000D+00  0.000000D+00 -0.547742D-01
[...]
 Polarizability derivatives wrt mode         60
                1             2             3
     1  -0.136701D+00 -0.513161D+00  0.000000D+00
     2  -0.513161D+00 -0.110164D+00  0.000000D+00
     3   0.000000D+00  0.000000D+00  0.242310D+00
```

```
[...]
 Polarizability derivatives wrt mode         61
                 1             2             3
      1   0.759042D-01 -0.146365D+00  0.000000D+00
      2  -0.146365D+00  0.922664D-02  0.000000D+00
      3   0.000000D+00  0.000000D+00  0.890771D-01
[...]
 Polarizability derivatives wrt mode         62
                 1             2             3
      1   0.124919D+00 -0.154104D+00  0.000000D+00
      2  -0.154104D+00  0.901951D-01  0.000000D+00
      3   0.000000D+00  0.000000D+00  0.663002D-01
[...]
 Polarizability derivatives wrt mode         63
                 1             2             3
      1   0.471986D+00 -0.148728D+01  0.000000D+00
      2  -0.148728D+01  0.111435D+00  0.000000D+00
      3   0.000000D+00  0.000000D+00  0.731068D+00
[...]
 Polarizability derivatives wrt mode         64
                 1             2             3
      1  -0.286246D-01  0.279416D+00  0.000000D+00
      2   0.279416D+00  0.438028D-01  0.000000D+00
      3   0.000000D+00  0.000000D+00 -0.150908D+00
[...]
 Polarizability derivatives wrt mode         65
                 1             2             3
      1   0.675929D-01 -0.536285D+00  0.000000D+00
      2  -0.536285D+00 -0.280868D-02  0.000000D+00
      3   0.000000D+00  0.000000D+00  0.270061D+00
[...]
 Polarizability derivatives wrt mode         66
                 1             2             3
      1   0.000000D+00  0.000000D+00 -0.473629D+00
      2   0.000000D+00  0.000000D+00  0.389060D+00
      3  -0.473629D+00  0.389060D+00  0.000000D+00
[...]
 Polarizability derivatives wrt mode         67
                 1             2             3
      1  -0.958950D-01 -0.105078D+00  0.000000D+00
      2  -0.105078D+00 -0.666339D-02  0.000000D+00
      3   0.000000D+00  0.000000D+00  0.647958D-01
[...]
 Polarizability derivatives wrt mode         68
                 1             2             3
      1  -0.675686D-01 -0.139087D+00  0.000000D+00
      2  -0.139087D+00  0.792216D-01  0.000000D+00
      3   0.000000D+00  0.000000D+00  0.774916D-01
[...]
 Polarizability derivatives wrt mode         69
                 1             2             3
      1  -0.925505D-01  0.493249D-02  0.000000D+00
      2   0.493249D-02  0.234154D-01  0.000000D+00
      3   0.000000D+00  0.000000D+00  0.451469D-02
[...]
 Polarizability derivatives wrt mode         70
                 1             2             3
      1  -0.550323D+00 -0.345708D+00  0.000000D+00
```

```
      2  -0.345708D+00 -0.358023D+00  0.000000D+00
      3   0.000000D+00  0.000000D+00 -0.120920D+00
[...]
 Polarizability derivatives wrt mode         71
                1             2             3
      1   0.497282D+00  0.298260D+00  0.000000D+00
      2   0.298260D+00  0.521764D+00  0.000000D+00
      3   0.000000D+00  0.000000D+00  0.897702D+00
[...]
 Polarizability derivatives wrt mode         72
                1             2             3
      1   0.466735D+00  0.212491D+00  0.000000D+00
      2   0.212491D+00  0.461433D+00  0.000000D+00
      3   0.000000D+00  0.000000D+00  0.717504D+00
[...]
 Polarizability derivatives wrt mode         73
                1             2             3
      1   0.237800D+01  0.807267D+00  0.000000D+00
      2   0.807267D+00  0.258244D+01  0.000000D+00
      3   0.000000D+00  0.000000D+00  0.376882D+01
[...]
 Polarizability derivatives wrt mode         74
                1             2             3
      1  -0.695255D+00 -0.383880D+00  0.000000D+00
      2  -0.383880D+00 -0.690620D+00  0.000000D+00
      3   0.000000D+00  0.000000D+00 -0.118633D+01
[...]
 Polarizability derivatives wrt mode         75
                1             2             3
      1  -0.727981D+00 -0.433114D+00  0.000000D+00
      2  -0.433114D+00 -0.878021D+00  0.000000D+00
      3   0.000000D+00  0.000000D+00 -0.142910D+01
[...]
 Polarizability derivatives wrt mode         76
                1             2             3
      1   0.000000D+00  0.000000D+00  0.227074D+01
      2   0.000000D+00  0.000000D+00  0.256044D+01
      3   0.227074D+01  0.256044D+01  0.000000D+00
[...]
 Polarizability derivatives wrt mode         77
                1             2             3
      1  -0.741939D+00 -0.388883D+00  0.000000D+00
      2  -0.388883D+00 -0.946266D+00  0.000000D+00
      3   0.000000D+00  0.000000D+00 -0.139800D+01
[...]
 Polarizability derivatives wrt mode         78
                1             2             3
      1   0.000000D+00  0.000000D+00  0.564114D+00
      2   0.000000D+00  0.000000D+00  0.675042D+00
      3   0.564114D+00  0.675042D+00  0.000000D+00
[...]
 Polarizability derivatives wrt mode         79
                1             2             3
      1  -0.515660D-05  0.000000D+00 -0.107933D+01
      2   0.000000D+00 -0.539417D-05 -0.121815D+01
      3  -0.107933D+01 -0.121815D+01 -0.513783D-05
[...]
 Polarizability derivatives wrt mode         80
```

```
                1             2             3
      1   0.199880D+01 -0.281462D+00 -0.260531D-05
      2  -0.281462D+00  0.205055D+01 -0.284003D-05
      3  -0.260531D-05 -0.284003D-05  0.201032D+01
[...]
 Polarizability derivatives wrt mode         81
                1             2             3
      1   0.172199D+01  0.631467D+00  0.000000D+00
      2   0.631467D+00  0.179876D+01  0.000000D+00
      3   0.000000D+00  0.000000D+00  0.255458D+01
[...]
 Polarizability derivatives wrt mode         82
                1             2             3
      1   0.000000D+00  0.000000D+00  0.361525D+00
      2   0.000000D+00  0.000000D+00  0.322630D+00
      3   0.361525D+00  0.322630D+00  0.000000D+00
[...]
 Polarizability derivatives wrt mode         83
                1             2             3
      1   0.244606D+00  0.284012D-01  0.000000D+00
      2   0.284012D-01  0.150563D+00  0.000000D+00
      3   0.000000D+00  0.000000D+00  0.502947D+00
[...]
 Polarizability derivatives wrt mode         84
                1             2             3
      1   0.000000D+00  0.000000D+00 -0.933247D+00
      2   0.000000D+00  0.000000D+00 -0.104207D+01
      3  -0.933247D+00 -0.104207D+01  0.000000D+00
[...]
 Polarizability derivatives wrt mode         85
                1             2             3
      1   0.000000D+00  0.000000D+00 -0.666381D+00
      2   0.000000D+00  0.000000D+00 -0.817722D+00
      3  -0.666381D+00 -0.817722D+00  0.000000D+00
[...]
 Polarizability derivatives wrt mode         86
                1             2             3
      1   0.000000D+00  0.000000D+00 -0.813887D+00
      2   0.000000D+00  0.000000D+00 -0.950654D+00
      3  -0.813887D+00 -0.950654D+00  0.000000D+00
[...]
 Polarizability derivatives wrt mode         87
                1             2             3
      1   0.000000D+00  0.000000D+00  0.353097D+00
      2   0.000000D+00  0.000000D+00  0.979859D-01
      3   0.353097D+00  0.979859D-01  0.000000D+00
[...]
 Polarizability derivatives wrt mode         88
                1             2             3
      1   0.000000D+00  0.000000D+00 -0.112709D+01
      2   0.000000D+00  0.000000D+00 -0.324758D+00
      3  -0.112709D+01 -0.324758D+00  0.000000D+00
[...]
 Polarizability derivatives wrt mode         89
                1             2             3
      1   0.114431D+00 -0.134893D+01  0.000000D+00
      2  -0.134893D+01  0.239062D+01  0.000000D+00
      3   0.000000D+00  0.000000D+00 -0.726023D+00
```

```
[...]
 Polarizability derivatives wrt mode         90
                1             2             3
     1  -0.279234D+01  0.147746D+01  0.000000D+00
     2   0.147746D+01 -0.129312D+01  0.000000D+00
     3   0.000000D+00  0.000000D+00 -0.165322D+00
[...]
 Harmonic frequencies (cm**-1), IR intensities (KM/Mole), Raman scattering
 activities (A**4/AMU), depolarization ratios for plane and unpolarized
 incident light, reduced masses (AMU), force constants (mDyne/A),
 and normal coordinates:
                     1                     2                     3
                    A"                    A"                    A'
 Frequencies --    15.9958               24.5456               39.8087
 Red. masses --     2.9835                4.0414                4.4165
 Frc consts  --     0.0004                0.0014                0.0041
 IR Inten    --     0.6735                0.0598                0.2478
 Raman Activ --     0.2222                0.0005                0.0494
 Depolar (P) --     0.7500                0.7500                0.7474
 Depolar (U) --     0.8571                0.8571                0.8555
  Atom  AN      X      Y      Z        X      Y      Z        X      Y      Z
     1   6     0.00   0.00  -0.03     0.00   0.00   0.26     0.14   0.21   0.00
     2   6     0.00   0.00   0.12     0.00   0.00   0.09     0.12   0.05   0.00
     3   1    -0.11  -0.15  -0.17     0.10  -0.02   0.30     0.10   0.26   0.00
     4   1     0.11   0.15  -0.17    -0.10   0.02   0.30     0.10   0.26   0.00
     5   6     0.00   0.00  -0.07     0.00   0.00   0.01    -0.02   0.01   0.00
     6   1     0.11   0.14   0.26    -0.09   0.02   0.06     0.17   0.01   0.00
     7   1    -0.11  -0.14   0.26     0.09  -0.02   0.06     0.17   0.01   0.00
     8   1    -0.10  -0.14  -0.20     0.08  -0.02   0.04    -0.06   0.05   0.00
     9   1     0.10   0.14  -0.20    -0.08   0.02   0.04    -0.06   0.05   0.00
    10   6     0.00   0.00   0.07     0.00   0.00  -0.13    -0.04  -0.11   0.00
    11   6     0.00   0.00  -0.08     0.00   0.00  -0.16    -0.12  -0.13   0.00
    12   1    -0.10  -0.12   0.19     0.08   0.00  -0.16     0.00  -0.14   0.00
    13   1     0.10   0.12   0.19    -0.08   0.00  -0.16     0.00  -0.14   0.00
    14   6     0.00   0.00   0.03     0.00   0.00  -0.21    -0.12  -0.16   0.00
    15   1    -0.08  -0.11  -0.19     0.04   0.00  -0.14    -0.13  -0.11   0.00
    16   1     0.08   0.11  -0.19    -0.04   0.00  -0.14    -0.13  -0.11   0.00
    17   6     0.00   0.00  -0.06     0.00   0.00  -0.17    -0.10  -0.15   0.00
    18   1     0.08   0.08   0.12    -0.03  -0.03  -0.25    -0.12  -0.16   0.00
    19   1    -0.08  -0.08   0.12     0.03   0.03  -0.25    -0.12  -0.16   0.00
    20   1    -0.06  -0.07  -0.13    -0.01   0.03  -0.15    -0.08  -0.17   0.00
    21   1     0.06   0.07  -0.13     0.01  -0.03  -0.15    -0.08  -0.17   0.00
    22   6     0.00   0.00   0.02     0.00   0.00  -0.13    -0.09  -0.08   0.00
    23   6     0.00   0.00   0.00     0.00   0.00  -0.03     0.02  -0.05   0.00
    24   1    -0.05  -0.03   0.06    -0.02   0.05  -0.15    -0.12  -0.05   0.00
    25   1     0.05   0.03   0.06     0.02  -0.05  -0.15    -0.12  -0.05   0.00
    26   1    -0.01  -0.02  -0.02    -0.06   0.05  -0.03     0.06  -0.08   0.00
    27   1     0.01   0.02  -0.02     0.06  -0.05  -0.03     0.06  -0.08   0.00
    28   6     0.00   0.00  -0.02     0.00   0.00   0.10     0.04   0.08   0.00
    29   8     0.00   0.00   0.23     0.00   0.00   0.16     0.16   0.11   0.00
    30   8     0.00   0.00  -0.23     0.00   0.00   0.14    -0.04   0.16   0.00
    31   1     0.00   0.00   0.18     0.00   0.00   0.24     0.17   0.19   0.00
    32   1     0.00   0.00   0.12     0.00   0.00   0.32     0.26   0.24   0.00
                     4                     5                     6
                    A"                    A"                    A"
 Frequencies --    54.1540               67.3893              106.3226
 Red. masses --     1.7417                2.8629                1.7668
 Frc consts  --     0.0030                0.0077                0.0118
```

IR Inten	--	0.0669			0.0114			0.0869		
Raman Activ	--	0.1900			0.1659			0.0778		
Depolar (P)	--	0.7500			0.7500			0.7500		
Depolar (U)	--	0.8571			0.8571			0.8571		
Atom	AN	X	Y	Z	X	Y	Z	X	Y	Z
1	6	0.00	0.00	-0.02	0.00	0.00	0.17	0.00	0.00	0.00
2	6	0.00	0.00	0.11	0.00	0.00	-0.05	0.00	0.00	-0.07
3	1	-0.09	-0.16	-0.15	0.13	0.00	0.24	0.06	0.16	0.12
4	1	0.09	0.16	-0.15	-0.13	0.00	0.24	-0.06	-0.16	0.12
5	6	0.00	0.00	-0.08	0.00	0.00	-0.12	0.00	0.00	0.07
6	1	0.09	0.14	0.23	-0.12	0.01	-0.10	-0.06	-0.11	-0.16
7	1	-0.09	-0.14	0.23	0.12	-0.01	-0.10	0.06	0.11	-0.16
8	1	-0.05	-0.12	-0.17	0.02	-0.03	-0.13	-0.02	0.07	0.10
9	1	0.05	0.12	-0.17	-0.02	0.03	-0.13	0.02	-0.07	0.10
10	6	0.00	0.00	-0.02	0.00	0.00	-0.15	0.00	0.00	0.12
11	6	0.00	0.00	-0.04	0.00	0.00	-0.13	0.00	0.00	-0.10
12	1	-0.04	-0.03	0.02	0.00	0.00	-0.15	-0.05	-0.14	0.22
13	1	0.04	0.03	0.02	0.00	0.00	-0.15	0.05	0.14	0.22
14	6	0.00	0.00	-0.07	0.00	0.00	0.07	0.00	0.00	0.02
15	1	0.02	0.00	-0.03	-0.11	-0.02	-0.20	-0.09	-0.16	-0.23
16	1	-0.02	0.00	-0.03	0.11	0.02	-0.20	0.09	0.16	-0.23
17	6	0.00	0.00	0.08	0.00	0.00	0.06	0.00	0.00	-0.10
18	1	-0.03	-0.09	-0.14	0.12	0.03	0.15	0.08	0.10	0.12
19	1	0.03	0.09	-0.14	-0.12	-0.03	0.15	-0.08	-0.10	0.12
20	1	0.09	0.11	0.18	-0.10	-0.03	-0.01	-0.04	-0.07	-0.16
21	1	-0.09	-0.11	0.18	0.10	0.03	-0.01	0.04	0.07	-0.16
22	6	0.00	0.00	-0.04	0.00	0.00	0.22	0.00	0.00	-0.05
23	6	0.00	0.00	0.15	0.00	0.00	0.10	0.00	0.00	0.14
24	1	0.09	0.14	-0.17	-0.10	-0.09	0.33	-0.01	0.11	-0.11
25	1	-0.09	-0.14	-0.17	0.10	0.09	0.33	0.01	-0.11	-0.11
26	1	0.11	0.15	0.29	0.04	-0.07	0.07	0.10	0.15	0.27
27	1	-0.11	-0.15	0.29	-0.04	0.07	0.07	-0.10	-0.15	0.27
28	6	0.00	0.00	0.02	0.00	0.00	-0.02	0.00	0.00	0.02
29	8	0.00	0.00	-0.09	0.00	0.00	-0.08	0.00	0.00	-0.04
30	8	0.00	0.00	0.02	0.00	0.00	-0.06	0.00	0.00	-0.01
31	1	0.00	0.00	-0.15	0.00	0.00	-0.16	0.00	0.00	-0.09
32	1	0.00	0.00	0.15	0.00	0.00	0.21	0.00	0.00	-0.18

		7			8			9		
		A’			A"			A"		
Frequencies	--	107.5782			118.7883			152.6984		
Red. masses	--	4.2319			2.3168			1.8530		
Frc consts	--	0.0289			0.0193			0.0255		
IR Inten	--	0.7792			0.0068			0.0413		
Raman Activ	--	0.0811			0.0180			0.0291		
Depolar (P)	--	0.3374			0.7500			0.7500		
Depolar (U)	--	0.5045			0.8571			0.8571		
Atom	AN	X	Y	Z	X	Y	Z	X	Y	Z
1	6	0.05	0.20	0.00	0.00	0.00	-0.11	0.00	0.00	0.01
2	6	0.01	-0.03	0.00	0.00	0.00	0.09	0.00	0.00	-0.04
3	1	-0.03	0.27	0.00	-0.13	-0.01	-0.18	0.04	0.12	0.09
4	1	-0.03	0.27	0.00	0.13	0.01	-0.18	-0.04	-0.12	0.09
5	6	-0.15	-0.08	0.00	0.00	0.00	0.17	0.00	0.00	0.01
6	1	0.08	-0.09	0.00	0.10	-0.03	0.13	-0.03	-0.05	-0.08
7	1	0.08	-0.09	0.00	-0.10	0.03	0.13	0.03	0.05	-0.08
8	1	-0.18	-0.05	0.00	0.12	0.07	0.27	-0.07	0.00	-0.02
9	1	-0.18	-0.05	0.00	-0.12	-0.07	0.27	0.07	0.00	-0.02
10	6	-0.15	-0.14	0.00	0.00	0.00	-0.04	0.00	0.00	0.13
11	6	-0.08	-0.12	0.00	0.00	0.00	-0.04	0.00	0.00	-0.10

12	1	-0.15	-0.13	0.00	0.13	0.03	-0.12	-0.09	-0.16	0.26
13	1	-0.15	-0.13	0.00	-0.13	-0.03	-0.12	0.09	0.16	0.26
14	6	-0.05	0.03	0.00	0.00	0.00	-0.15	0.00	0.00	-0.14
15	1	-0.04	-0.15	0.00	0.08	0.02	0.01	0.00	-0.13	-0.18
16	1	-0.04	-0.15	0.00	-0.08	-0.02	0.01	0.00	0.13	-0.18
17	6	0.10	0.07	0.00	0.00	0.00	-0.09	0.00	0.00	0.14
18	1	-0.11	0.08	0.00	-0.06	-0.05	-0.20	-0.05	-0.17	-0.26
19	1	-0.11	0.08	0.00	0.06	0.05	-0.20	0.05	0.17	-0.26
20	1	0.14	0.03	0.00	-0.14	0.00	-0.16	0.07	0.18	0.27
21	1	0.14	0.03	0.00	0.14	0.00	-0.16	-0.07	-0.18	0.27
22	6	0.11	0.15	0.00	0.00	0.00	0.17	0.00	0.00	0.07
23	6	0.08	0.14	0.00	0.00	0.00	0.08	0.00	0.00	-0.07
24	1	0.10	0.15	0.00	-0.16	-0.08	0.29	0.03	-0.06	0.09
25	1	0.10	0.15	0.00	0.16	0.08	0.29	-0.03	0.06	0.09
26	1	0.04	0.16	0.00	0.02	-0.06	0.05	-0.06	-0.11	-0.16
27	1	0.04	0.16	0.00	-0.02	0.06	0.05	0.06	0.11	-0.16
28	6	0.05	-0.02	0.00	0.00	0.00	0.01	0.00	0.00	-0.02
29	8	-0.12	-0.06	0.00	0.00	0.00	-0.03	0.00	0.00	0.01
30	8	0.16	-0.13	0.00	0.00	0.00	-0.03	0.00	0.00	0.00
31	1	-0.13	-0.18	0.00	0.00	0.00	-0.10	0.00	0.00	0.04
32	1	0.22	0.24	0.00	0.00	0.00	-0.14	0.00	0.00	-0.13

	10	11	12
	A"	A'	A'
Frequencies --	160.2403	185.7486	204.1295
Red. masses --	2.1135	5.2097	3.9172
Frc consts --	0.0320	0.1059	0.0962
IR Inten --	0.0006	0.8840	0.6185
Raman Activ --	0.0162	3.8606	1.8383
Depolar (P) --	0.7500	0.1953	0.2738
Depolar (U) --	0.8571	0.3268	0.4299

Atom	AN	X	Y	Z	X	Y	Z	X	Y	Z
1	6	0.00	0.00	0.05	-0.18	0.04	0.00	-0.07	0.20	0.00
2	6	0.00	0.00	-0.06	-0.15	0.19	0.00	-0.10	-0.05	0.00
3	1	0.08	-0.01	0.09	-0.14	-0.01	0.00	-0.16	0.29	0.00
4	1	-0.08	0.01	0.09	-0.14	-0.01	0.00	-0.16	0.29	0.00
5	6	0.00	0.00	-0.13	-0.04	0.20	0.00	-0.15	-0.07	0.00
6	1	-0.05	0.03	-0.07	-0.20	0.23	0.00	-0.05	-0.09	0.00
7	1	0.05	-0.03	-0.07	-0.20	0.23	0.00	-0.05	-0.09	0.00
8	1	-0.15	-0.08	-0.25	-0.04	0.19	0.00	-0.13	-0.08	0.00
9	1	0.15	0.08	-0.25	-0.04	0.19	0.00	-0.13	-0.08	0.00
10	6	0.00	0.00	0.11	-0.03	0.13	0.00	-0.11	0.02	0.00
11	6	0.00	0.00	0.16	-0.11	0.07	0.00	0.10	0.07	0.00
12	1	-0.14	0.00	0.18	0.00	0.10	0.00	-0.17	0.08	0.00
13	1	0.14	0.00	0.18	0.00	0.10	0.00	-0.17	0.08	0.00
14	6	0.00	0.00	-0.11	-0.10	-0.08	0.00	0.13	0.12	0.00
15	1	0.16	0.07	0.29	-0.15	0.11	0.00	0.15	0.02	0.00
16	1	-0.16	-0.07	0.29	-0.15	0.11	0.00	0.15	0.02	0.00
17	6	0.00	0.00	-0.13	-0.05	-0.11	0.00	0.07	0.08	0.00
18	1	-0.16	-0.03	-0.21	-0.07	-0.10	0.00	0.13	0.11	0.00
19	1	0.16	0.03	-0.21	-0.07	-0.10	0.00	0.13	0.11	0.00
20	1	-0.11	-0.03	-0.20	-0.03	-0.12	0.00	0.01	0.12	0.00
21	1	0.11	0.03	-0.20	-0.03	-0.12	0.00	0.01	0.12	0.00
22	6	0.00	0.00	0.06	0.00	-0.07	0.00	0.05	-0.12	0.00
23	6	0.00	0.00	0.06	0.14	-0.05	0.00	-0.02	-0.16	0.00
24	1	-0.12	-0.03	0.14	-0.04	-0.03	0.00	0.11	-0.17	0.00
25	1	0.12	0.03	0.14	-0.04	-0.03	0.00	0.11	-0.17	0.00
26	1	0.02	0.00	0.06	0.17	-0.08	0.00	-0.02	-0.16	0.00
27	1	-0.02	0.00	0.06	0.17	-0.08	0.00	-0.02	-0.16	0.00

```
   28   6     0.00   0.00   0.01     0.17  -0.07   0.00     0.00  -0.09   0.00
   29   8     0.00   0.00  -0.02     0.12  -0.09   0.00     0.18  -0.05   0.00
   30   8     0.00   0.00  -0.01     0.22  -0.13   0.00    -0.10   0.02   0.00
   31   1     0.00   0.00  -0.05     0.12  -0.12   0.00     0.19   0.10   0.00
   32   1     0.00   0.00   0.08    -0.29   0.01   0.00     0.14   0.25   0.00
                    13                    14                    15
                    A"                    A'                    A'
Frequencies --   238.6402              309.6927              362.4443
Red. masses --     1.1251                3.5959                3.9686
Frc consts  --     0.0378                0.2032                0.3072
IR Inten    --     0.0000                0.8213                3.5669
Raman Activ --     0.0089                0.3494                0.4617
Depolar (P) --     0.7500                0.3712                0.1631
Depolar (U) --     0.8571                0.5414                0.2804
 Atom  AN      X      Y      Z        X      Y      Z        X      Y      Z
    1   6     0.00   0.00  -0.01    -0.01  -0.09   0.00     0.18  -0.14   0.00
    2   6     0.00   0.00   0.09     0.03   0.17   0.00     0.15  -0.03   0.00
    3   1     0.00   0.47   0.22     0.10  -0.20   0.00     0.24  -0.21   0.00
    4   1     0.00  -0.47   0.22     0.10  -0.20   0.00     0.24  -0.21   0.00
    5   6     0.00   0.00  -0.04     0.00   0.15   0.00    -0.05  -0.03   0.00
    6   1     0.06   0.07   0.15    -0.02   0.20  -0.01     0.18  -0.07  -0.01
    7   1    -0.06  -0.07   0.15    -0.02   0.20   0.01     0.18  -0.07   0.01
    8   1    -0.02  -0.10  -0.11    -0.08   0.21   0.00    -0.08   0.00   0.00
    9   1     0.02   0.10  -0.11    -0.08   0.21   0.00    -0.08   0.00   0.00
   10   6     0.00   0.00  -0.04    -0.05  -0.10   0.00    -0.11   0.02   0.00
   11   6     0.00   0.00   0.01    -0.11  -0.14   0.00    -0.10   0.08   0.00
   12   1     0.00   0.02  -0.05     0.03  -0.16   0.00    -0.13   0.04   0.00
   13   1     0.00  -0.02  -0.05     0.03  -0.16   0.00    -0.13   0.04   0.00
   14   6     0.00   0.00   0.01    -0.05   0.03   0.00    -0.10   0.20   0.00
   15   1     0.01   0.03   0.03    -0.08  -0.15   0.01    -0.08   0.06   0.00
   16   1    -0.01  -0.03   0.03    -0.08  -0.15  -0.01    -0.08   0.06   0.00
   17   6     0.00   0.00   0.00     0.17   0.09   0.00    -0.14   0.17   0.00
   18   1     0.00   0.01   0.01    -0.14   0.11   0.00    -0.13   0.22   0.00
   19   1     0.00  -0.01   0.01    -0.14   0.11   0.00    -0.13   0.22   0.00
   20   1     0.00  -0.01  -0.01     0.20   0.05  -0.01    -0.20   0.22   0.00
   21   1     0.00   0.01  -0.01     0.20   0.05   0.01    -0.20   0.22   0.00
   22   6     0.00   0.00   0.00     0.17   0.04   0.00    -0.13  -0.01   0.00
   23   6     0.00   0.00   0.00    -0.04  -0.04   0.00    -0.01  -0.04   0.00
   24   1     0.00   0.00   0.00     0.23  -0.03   0.00    -0.11  -0.02  -0.01
   25   1     0.00   0.00   0.00     0.23  -0.03   0.00    -0.11  -0.02   0.01
   26   1     0.00   0.00   0.00    -0.10   0.02   0.00     0.02  -0.07   0.00
   27   1     0.00   0.00   0.00    -0.10   0.02   0.00     0.02  -0.07   0.00
   28   6     0.00   0.00   0.00    -0.06  -0.08   0.00     0.05  -0.05   0.00
   29   8     0.00   0.00   0.00     0.10  -0.04   0.00     0.14  -0.05   0.00
   30   8     0.00   0.00   0.00    -0.15   0.02   0.00     0.08  -0.08   0.00
   31   1     0.00   0.00   0.00     0.11   0.09   0.00     0.15   0.05   0.00
   32   1     0.00   0.00  -0.58    -0.26  -0.15   0.00     0.02  -0.17   0.00
                    16                    17                    18
                    A'                    A'                    A"
Frequencies --   428.6241              485.9920              518.4622
Red. masses --     3.4200                3.1803                1.4842
Frc consts  --     0.3702                0.4426                0.2351
IR Inten    --     2.9665                2.6294               28.7468
Raman Activ --     0.0981                0.2814                1.9445
Depolar (P) --     0.6490                0.3374                0.7500
Depolar (U) --     0.7871                0.5046                0.8571
 Atom  AN      X      Y      Z        X      Y      Z        X      Y      Z
    1   6    -0.01   0.04   0.00     0.13  -0.07   0.00     0.00   0.00   0.00
```

2	6	-0.04	-0.15	0.00	0.08	0.00	0.00	0.00	0.00	0.00
3	1	-0.10	0.15	0.00	0.19	-0.15	0.00	0.00	0.00	0.00
4	1	-0.10	0.15	0.00	0.19	-0.15	0.00	0.00	0.00	0.00
5	6	0.10	-0.08	0.00	-0.16	-0.02	0.00	0.00	0.00	0.00
6	1	-0.02	-0.15	0.01	0.13	-0.06	-0.01	0.00	0.00	0.00
7	1	-0.02	-0.15	-0.01	0.13	-0.06	0.01	0.00	0.00	0.00
8	1	0.21	-0.17	0.00	-0.19	0.02	0.01	0.00	0.00	0.00
9	1	0.21	-0.17	0.00	-0.19	0.02	-0.01	0.00	0.00	0.00
10	6	0.11	0.13	0.00	-0.16	0.15	0.00	0.00	0.00	0.00
11	6	-0.13	0.09	0.00	-0.01	0.17	0.00	0.00	0.00	0.00
12	1	0.11	0.11	0.01	-0.26	0.24	0.00	0.00	0.00	0.00
13	1	0.11	0.11	-0.01	-0.26	0.24	0.00	0.00	0.00	0.00
14	6	-0.17	-0.06	0.00	0.00	-0.11	0.00	0.00	0.00	0.00
15	1	-0.24	0.18	0.00	-0.06	0.19	-0.01	0.00	0.00	0.00
16	1	-0.24	0.18	0.00	-0.06	0.19	0.01	0.00	0.00	0.00
17	6	0.03	0.00	0.00	0.09	-0.14	0.00	0.00	0.00	-0.01
18	1	-0.19	-0.03	0.01	0.07	-0.16	0.01	0.00	0.01	0.01
19	1	-0.19	-0.03	-0.01	0.07	-0.16	-0.01	0.00	-0.01	0.01
20	1	0.11	-0.07	0.00	0.16	-0.20	0.00	0.03	0.01	0.01
21	1	0.11	-0.07	0.00	0.16	-0.20	0.00	-0.03	-0.01	0.01
22	6	0.08	0.14	0.00	0.12	-0.01	0.00	0.00	0.00	-0.03
23	6	-0.01	0.07	0.00	0.05	0.00	0.00	0.00	0.00	0.03
24	1	0.07	0.13	0.01	0.11	-0.01	0.00	0.02	0.08	-0.08
25	1	0.07	0.13	-0.01	0.11	-0.01	0.00	-0.02	-0.08	-0.08
26	1	-0.10	0.13	0.00	0.03	0.01	0.00	-0.34	-0.16	-0.23
27	1	-0.10	0.13	0.00	0.03	0.01	0.00	0.34	0.16	-0.23
28	6	-0.03	-0.09	0.00	0.00	0.00	0.00	0.00	0.00	0.19
29	8	0.13	-0.07	0.00	-0.06	0.00	0.00	0.00	0.00	-0.01
30	8	-0.09	-0.04	0.00	-0.05	0.05	0.00	0.00	0.00	-0.05
31	1	0.15	0.12	0.00	-0.07	-0.09	0.00	0.00	0.00	-0.74
32	1	0.22	0.10	0.00	-0.03	-0.11	0.00	0.00	0.00	0.00

	19	20	21
	A’	A’	A"
Frequencies --	519.9835	636.0402	648.7543
Red. masses --	3.3745	4.4139	1.3822
Frc consts --	0.5376	1.0521	0.3427
IR Inten --	15.0744	24.7927	86.2928
Raman Activ --	0.2521	4.3362	0.5057
Depolar (P) --	0.7500	0.3676	0.7500
Depolar (U) --	0.8571	0.5376	0.8571

Atom	AN	X	Y	Z	X	Y	Z	X	Y	Z
1	6	0.00	-0.01	0.00	0.01	0.00	0.00	0.00	0.00	0.00
2	6	0.01	0.07	0.00	0.00	0.00	0.00	0.00	0.00	0.00
3	1	0.05	-0.06	0.00	0.01	-0.01	0.00	0.00	0.00	0.00
4	1	0.05	-0.06	0.00	0.01	-0.01	0.00	0.00	0.00	0.00
5	6	-0.07	0.02	0.00	-0.02	0.00	0.00	0.00	0.00	0.00
6	1	0.01	0.06	0.00	0.01	-0.01	0.00	0.00	0.00	0.00
7	1	0.01	0.06	0.00	0.01	-0.01	0.00	0.00	0.00	0.00
8	1	-0.12	0.06	0.00	-0.01	0.00	0.00	0.00	0.00	0.00
9	1	-0.12	0.06	0.00	-0.01	0.00	0.00	0.00	0.00	0.00
10	6	-0.05	-0.05	0.00	-0.01	0.03	0.00	0.00	0.00	0.00
11	6	0.15	-0.01	0.00	-0.01	0.01	0.00	0.00	0.00	0.00
12	1	-0.08	-0.01	-0.01	-0.02	0.04	0.00	0.00	0.00	0.00
13	1	-0.08	-0.01	0.01	-0.02	0.04	0.00	0.00	0.00	0.00
14	6	0.12	-0.07	0.00	0.00	-0.05	0.00	0.00	0.00	0.00
15	1	0.19	-0.06	-0.01	-0.04	0.03	0.00	-0.01	0.00	0.00
16	1	0.19	-0.06	0.01	-0.04	0.03	0.00	0.01	0.00	0.00
17	6	-0.10	-0.09	0.00	0.10	-0.01	0.00	0.00	0.00	0.00

18	1	0.21	-0.16	0.00	-0.01	-0.04	0.00	-0.01	-0.01	-0.01
19	1	0.21	-0.16	0.00	-0.01	-0.04	0.00	0.01	0.01	-0.01
20	1	-0.08	-0.09	0.01	0.13	-0.06	0.00	0.01	0.00	0.01
21	1	-0.08	-0.09	-0.01	0.13	-0.06	0.00	-0.01	0.00	0.01
22	6	-0.09	0.19	0.00	0.04	-0.05	0.00	0.00	0.00	0.00
23	6	-0.04	0.18	0.00	-0.23	-0.05	0.00	0.00	0.00	-0.06
24	1	-0.20	0.27	0.01	0.13	-0.15	0.00	-0.03	-0.11	0.08
25	1	-0.20	0.27	-0.01	0.13	-0.15	0.00	0.03	0.11	0.08
26	1	-0.14	0.25	-0.01	-0.22	-0.02	0.02	0.23	0.15	0.14
27	1	-0.14	0.25	0.01	-0.22	-0.02	-0.02	-0.23	-0.15	0.14
28	6	-0.06	-0.08	0.00	-0.16	0.07	0.00	0.00	0.00	-0.11
29	8	0.16	-0.06	0.00	0.05	0.26	0.00	0.00	0.00	0.10
30	8	-0.05	-0.10	0.00	0.16	-0.23	0.00	0.00	0.00	0.06
31	1	0.18	0.24	0.00	0.09	0.71	0.00	0.00	0.00	-0.86
32	1	-0.10	-0.03	0.00	0.00	-0.01	0.00	0.00	0.00	0.00

	22	23	24
	A"	A"	A"
Frequencies --	729.7543	731.4299	744.1485
Red. masses --	1.0617	1.0833	1.1386
Frc consts --	0.3331	0.3415	0.3715
IR Inten --	7.8708	0.1799	4.6597
Raman Activ --	0.0002	0.0093	0.0016
Depolar (P) --	0.7500	0.7500	0.7500
Depolar (U) --	0.8571	0.8571	0.8571

Atom	AN	X	Y	Z	X	Y	Z	X	Y	Z
1	6	0.00	0.00	0.00	0.00	0.00	0.00	0.00	0.00	-0.01
2	6	0.00	0.00	-0.01	0.00	0.00	-0.03	0.00	0.00	-0.05
3	1	0.03	0.01	0.02	0.10	0.01	0.05	0.16	0.00	0.08
4	1	-0.03	-0.01	0.02	-0.10	-0.01	0.05	-0.16	0.00	0.08
5	6	0.00	0.00	-0.02	0.00	0.00	-0.04	0.00	0.00	-0.03
6	1	0.05	0.08	0.06	0.13	0.20	0.15	0.18	0.22	0.17
7	1	-0.05	-0.08	0.06	-0.13	-0.20	0.15	-0.18	-0.22	0.17
8	1	0.13	0.11	0.11	0.20	0.23	0.19	0.05	0.18	0.10
9	1	-0.13	-0.11	0.11	-0.20	-0.23	0.19	-0.05	-0.18	0.10
10	6	0.00	0.00	-0.03	0.00	0.00	-0.03	0.00	0.00	0.02
11	6	0.00	0.00	-0.03	0.00	0.00	-0.01	0.00	0.00	0.05
12	1	-0.15	-0.19	0.16	-0.18	-0.14	0.14	0.01	0.15	-0.07
13	1	0.15	0.19	0.16	0.18	0.14	0.14	-0.01	-0.15	-0.07
14	6	0.00	0.00	-0.03	0.00	0.00	0.02	0.00	0.00	0.02
15	1	0.20	0.21	0.19	-0.02	0.08	0.03	-0.18	-0.20	-0.16
16	1	-0.20	-0.21	0.19	0.02	-0.08	0.03	0.18	0.20	-0.16
17	6	0.00	0.00	-0.03	0.00	0.00	0.03	0.00	0.00	-0.03
18	1	0.20	0.21	0.19	-0.06	-0.15	-0.10	-0.15	-0.03	-0.07
19	1	-0.20	-0.21	0.19	0.06	0.15	-0.10	0.15	0.03	-0.07
20	1	0.14	0.20	0.16	-0.18	-0.18	-0.16	0.16	0.06	0.09
21	1	-0.14	-0.20	0.16	0.18	0.18	-0.16	-0.16	-0.06	0.09
22	6	0.00	0.00	-0.02	0.00	0.00	0.03	0.00	0.00	-0.04
23	6	0.00	0.00	0.00	0.00	0.00	0.01	0.00	0.00	-0.01
24	1	-0.13	-0.09	0.10	0.17	0.13	-0.13	-0.19	-0.18	0.16
25	1	0.13	0.09	0.10	-0.17	-0.13	-0.13	0.19	0.18	0.16
26	1	0.00	0.05	0.03	0.01	-0.08	-0.04	-0.02	0.13	0.06
27	1	0.00	-0.05	0.03	-0.01	0.08	-0.04	0.02	-0.13	0.06
28	6	0.00	0.00	0.02	0.00	0.00	-0.03	0.00	0.00	0.05
29	8	0.00	0.00	-0.01	0.00	0.00	0.01	0.00	0.00	-0.01
30	8	0.00	0.00	0.00	0.00	0.00	0.01	0.00	0.00	-0.02
31	1	0.00	0.00	0.02	0.00	0.00	-0.03	0.00	0.00	0.05
32	1	0.00	0.00	0.01	0.00	0.00	0.03	0.00	0.00	0.06

	25	26	27

		A"			A"			A'		
Frequencies --		777.6215			831.4375			877.0829		
Red. masses --		1.2242			1.2957			3.8554		
Frc consts --		0.4362			0.5277			1.7475		
IR Inten --		1.5541			3.7907			3.4906		
Raman Activ --		0.0675			0.0325			9.5068		
Depolar (P) --		0.7500			0.7500			0.1059		
Depolar (U) --		0.8571			0.8571			0.1915		
Atom	AN	X	Y	Z	X	Y	Z	X	Y	Z
1	6	0.00	0.00	0.02	0.00	0.00	0.03	0.01	-0.02	0.00
2	6	0.00	0.00	0.05	0.00	0.00	0.04	-0.01	-0.02	0.00
3	1	-0.21	0.01	-0.09	-0.24	0.02	-0.09	-0.03	0.04	0.01
4	1	0.21	-0.01	-0.09	0.24	-0.02	-0.09	-0.03	0.04	-0.01
5	6	0.00	0.00	-0.01	0.00	0.00	-0.06	0.03	0.03	0.00
6	1	-0.20	-0.14	-0.13	-0.20	-0.01	-0.07	-0.03	0.01	0.00
7	1	0.20	0.14	-0.13	0.20	0.01	-0.07	-0.03	0.01	0.00
8	1	0.14	-0.04	0.03	0.20	0.10	0.10	0.02	0.03	0.00
9	1	-0.14	0.04	0.03	-0.20	-0.10	0.10	0.02	0.03	0.00
10	6	0.00	0.00	-0.06	0.00	0.00	-0.02	-0.02	-0.02	0.00
11	6	0.00	0.00	0.00	0.00	0.00	0.07	-0.03	0.01	0.00
12	1	-0.18	-0.18	0.14	-0.17	0.06	0.03	0.01	-0.04	0.00
13	1	0.18	0.18	0.14	0.17	-0.06	0.03	0.01	-0.04	0.00
14	6	0.00	0.00	0.06	0.00	0.00	0.00	0.01	0.09	0.00
15	1	-0.10	0.10	0.00	-0.17	-0.16	-0.12	0.00	-0.02	0.00
16	1	0.10	-0.10	0.00	0.17	0.16	-0.12	0.00	-0.02	0.00
17	6	0.00	0.00	0.02	0.00	0.00	-0.06	-0.06	-0.05	0.00
18	1	-0.15	-0.21	-0.14	-0.12	0.13	0.01	0.00	0.09	0.00
19	1	0.15	0.21	-0.14	0.12	-0.13	0.01	0.00	0.09	0.00
20	1	0.05	-0.15	-0.04	0.12	0.20	0.11	-0.13	0.02	0.00
21	1	-0.05	0.15	-0.04	-0.12	-0.20	0.11	-0.13	0.02	0.00
22	6	0.00	0.00	-0.05	0.00	0.00	0.03	0.05	-0.07	0.00
23	6	0.00	0.00	-0.03	0.00	0.00	0.06	0.35	0.05	0.00
24	1	-0.11	-0.20	0.13	-0.06	0.18	-0.05	-0.04	0.03	-0.01
25	1	0.11	0.20	0.13	0.06	-0.18	-0.05	-0.04	0.03	0.01
26	1	-0.02	0.19	0.08	-0.01	-0.23	-0.09	0.43	-0.06	-0.03
27	1	0.02	-0.19	0.08	0.01	0.23	-0.09	0.43	-0.06	0.03
28	6	0.00	0.00	0.07	0.00	0.00	-0.08	-0.14	-0.07	0.00
29	8	0.00	0.00	-0.02	0.00	0.00	0.02	-0.04	0.14	0.00
30	8	0.00	0.00	-0.02	0.00	0.00	0.02	-0.14	-0.14	0.00
31	1	0.00	0.00	0.05	0.00	0.00	-0.03	0.00	0.55	0.00
32	1	0.00	0.00	-0.09	0.00	0.00	-0.12	0.12	0.01	0.00

		28			29			30		
		A'			A"			A"		
Frequencies --		896.4953			896.8882			969.1981		
Red. masses --		1.9855			1.3057			1.2578		
Frc consts --		0.9402			0.6188			0.6961		
IR Inten --		1.8850			0.6590			1.2309		
Raman Activ --		4.4482			0.1521			0.0511		
Depolar (P) --		0.3574			0.7500			0.7500		
Depolar (U) --		0.5266			0.8571			0.8571		
Atom	AN	X	Y	Z	X	Y	Z	X	Y	Z
1	6	0.10	-0.12	0.00	0.00	0.00	0.04	0.00	0.00	0.04
2	6	-0.08	-0.11	0.00	0.00	0.00	0.01	0.00	0.00	-0.03
3	1	-0.13	0.22	0.04	-0.25	0.02	-0.08	-0.22	0.01	-0.07
4	1	-0.13	0.22	-0.04	0.25	-0.02	-0.08	0.22	-0.01	-0.07
5	6	0.02	0.18	0.00	0.00	0.00	-0.07	0.00	0.00	-0.02
6	1	-0.22	0.02	0.00	-0.18	0.12	-0.01	-0.13	0.21	0.03
7	1	-0.22	0.02	0.00	0.18	-0.12	-0.01	0.13	-0.21	0.03

8	1	-0.03	0.20	-0.01	0.07	0.20	0.09	-0.15	0.21	0.02
9	1	-0.03	0.20	0.01	-0.07	-0.20	0.09	0.15	-0.21	0.02
10	6	-0.07	0.03	0.00	0.00	0.00	0.05	0.00	0.00	0.06
11	6	-0.03	-0.04	0.00	0.00	0.00	0.02	0.00	0.00	-0.07
12	1	-0.01	-0.01	-0.01	0.00	0.21	-0.07	0.20	0.04	-0.07
13	1	-0.01	-0.01	0.01	0.00	-0.21	-0.07	-0.20	-0.04	-0.07
14	6	0.05	0.00	0.00	0.00	0.00	-0.07	0.00	0.00	0.04
15	1	0.02	-0.07	0.00	0.13	-0.18	-0.02	0.17	0.09	0.07
16	1	0.02	-0.07	0.00	-0.13	0.18	-0.02	-0.17	-0.09	0.07
17	6	0.01	-0.01	0.00	0.00	0.00	0.05	0.00	0.00	0.01
18	1	0.06	-0.01	0.00	0.18	0.11	0.09	0.10	-0.22	-0.04
19	1	0.06	-0.01	0.00	-0.18	-0.11	0.09	-0.10	0.22	-0.04
20	1	0.01	-0.01	0.00	-0.22	-0.01	-0.07	0.17	-0.20	-0.01
21	1	0.01	-0.01	0.00	0.22	0.01	-0.07	-0.17	0.20	-0.01
22	6	-0.02	0.00	0.00	0.00	0.00	0.02	0.00	0.00	-0.05
23	6	-0.03	0.01	0.00	0.00	0.00	-0.07	0.00	0.00	0.06
24	1	-0.02	0.00	0.00	0.20	-0.10	-0.02	-0.22	0.01	0.06
25	1	-0.02	0.00	0.00	-0.20	0.10	-0.02	0.22	-0.01	0.06
26	1	-0.04	0.02	0.00	0.04	0.21	0.08	-0.07	-0.14	-0.06
27	1	-0.04	0.02	0.00	-0.04	-0.21	0.08	0.07	0.14	-0.06
28	6	0.01	0.01	0.00	0.00	0.00	0.07	0.00	0.00	-0.05
29	8	0.01	-0.02	0.00	0.00	0.00	-0.01	0.00	0.00	0.01
30	8	0.01	0.01	0.00	0.00	0.00	-0.02	0.00	0.00	0.01
31	1	0.00	-0.04	0.00	0.00	0.00	0.01	0.00	0.00	0.00
32	1	0.75	0.04	0.00	0.00	0.00	-0.13	0.00	0.00	-0.12

	31	32	33
	A’	A’	A’
Frequencies --	992.7591	1005.3624	1036.4664
Red. masses --	4.2997	4.0330	3.1949
Frc consts --	2.4968	2.4017	2.0222
IR Inten --	0.4383	7.3362	1.2518
Raman Activ --	1.3306	0.6301	0.2870
Depolar (P) --	0.2109	0.4866	0.7483
Depolar (U) --	0.3483	0.6546	0.8560

Atom	AN	X	Y	Z	X	Y	Z	X	Y	Z
1	6	-0.16	-0.03	0.00	0.04	-0.05	0.00	0.16	0.03	0.00
2	6	0.17	0.00	0.00	-0.04	0.04	0.00	-0.20	0.05	0.00
3	1	-0.29	0.15	0.02	-0.06	0.10	0.02	0.27	-0.11	-0.01
4	1	-0.29	0.15	-0.02	-0.06	0.10	-0.02	0.27	-0.11	0.01
5	6	0.22	-0.01	0.00	-0.06	-0.01	0.00	-0.08	-0.05	0.00
6	1	0.08	0.09	0.00	-0.15	0.13	0.00	-0.20	0.06	0.00
7	1	0.08	0.09	0.00	-0.15	0.13	0.00	-0.20	0.06	0.00
8	1	0.14	0.05	-0.01	-0.19	0.10	0.00	-0.03	-0.12	-0.01
9	1	0.14	0.05	0.01	-0.19	0.10	0.00	-0.03	-0.12	0.01
10	6	-0.19	-0.19	0.00	0.07	-0.14	0.00	0.11	-0.07	0.00
11	6	-0.07	0.20	0.00	0.23	0.11	0.00	-0.03	0.05	0.00
12	1	-0.17	-0.19	-0.01	0.03	-0.08	-0.01	0.21	-0.16	0.00
13	1	-0.17	-0.19	0.01	0.03	-0.08	0.01	0.21	-0.16	0.00
14	6	0.02	0.16	0.00	-0.23	-0.05	0.00	-0.02	0.18	0.00
15	1	0.01	0.12	-0.01	0.25	0.08	-0.01	0.00	0.05	0.01
16	1	0.01	0.12	0.01	0.25	0.08	0.01	0.00	0.05	-0.01
17	6	-0.05	-0.18	0.00	-0.20	0.06	0.00	-0.02	-0.17	0.00
18	1	0.12	0.06	0.00	-0.15	-0.12	0.00	-0.06	0.21	0.00
19	1	0.12	0.06	0.00	-0.15	-0.12	0.00	-0.06	0.21	0.00
20	1	0.01	-0.22	0.01	-0.10	-0.03	0.00	-0.04	-0.16	0.00
21	1	0.01	-0.22	-0.01	-0.10	-0.03	0.00	-0.04	-0.16	0.00
22	6	0.10	-0.03	0.00	0.18	0.12	0.00	0.07	-0.12	0.00
23	6	-0.06	0.03	0.00	0.00	-0.15	0.00	-0.04	0.12	0.00

24	1	0.08	-0.03	0.01	0.27	0.03	0.00	0.04	-0.11	0.01
25	1	0.08	-0.03	-0.01	0.27	0.03	0.00	0.04	-0.11	-0.01
26	1	-0.16	0.13	0.01	0.00	-0.13	0.01	-0.18	0.24	0.01
27	1	-0.16	0.13	-0.01	0.00	-0.13	-0.01	-0.18	0.24	-0.01
28	6	0.02	0.00	0.00	0.02	-0.03	0.00	0.00	0.01	0.00
29	8	0.01	-0.01	0.00	-0.02	0.06	0.00	0.01	-0.03	0.00
30	8	0.02	0.02	0.00	0.00	0.00	0.00	0.01	0.02	0.00
31	1	0.00	-0.08	0.00	-0.03	-0.08	0.00	0.01	-0.01	0.00
32	1	0.10	0.04	0.00	0.31	0.01	0.00	-0.03	-0.02	0.00

	34	35	36
	A"	A’	A’
Frequencies --	1036.6182	1058.3600	1062.8066
Red. masses --	1.1458	2.4902	2.6242
Frc consts --	0.7254	1.6434	1.7464
IR Inten --	0.0553	9.1235	5.8194
Raman Activ --	0.1137	5.7182	0.2993
Depolar (P) --	0.7500	0.4538	0.1996
Depolar (U) --	0.8571	0.6243	0.3328

Atom	AN	X	Y	Z	X	Y	Z	X	Y	Z
1	6	0.00	0.00	-0.04	0.03	-0.04	0.00	-0.11	-0.02	0.00
2	6	0.00	0.00	0.04	-0.02	0.06	0.00	0.14	-0.09	0.00
3	1	0.16	-0.01	0.05	-0.04	0.07	0.02	-0.18	0.05	0.00
4	1	-0.16	0.01	0.05	-0.04	0.07	-0.02	-0.18	0.05	0.00
5	6	0.00	0.00	-0.03	-0.02	-0.06	0.00	-0.10	0.09	0.00
6	1	0.06	-0.19	-0.04	-0.13	0.15	0.00	0.22	-0.17	-0.01
7	1	-0.06	0.19	-0.04	-0.13	0.15	0.00	0.22	-0.17	0.01
8	1	0.24	-0.12	0.03	-0.10	0.01	0.00	-0.20	0.20	0.01
9	1	-0.24	0.12	0.03	-0.10	0.01	0.00	-0.20	0.20	-0.01
10	6	0.00	0.00	0.01	0.04	-0.13	0.00	0.08	0.05	0.00
11	6	0.00	0.00	0.01	0.02	0.13	0.00	0.14	-0.05	0.00
12	1	-0.22	0.22	-0.01	0.03	-0.11	0.00	0.07	0.09	-0.01
13	1	0.22	-0.22	-0.01	0.03	-0.11	0.00	0.07	0.09	0.01
14	6	0.00	0.00	-0.03	-0.04	0.01	0.00	-0.14	0.09	0.00
15	1	0.22	-0.22	-0.01	-0.07	0.21	0.00	0.19	-0.08	0.01
16	1	-0.22	0.22	-0.01	-0.07	0.21	0.00	0.19	-0.08	-0.01
17	6	0.00	0.00	0.04	0.20	-0.01	0.00	0.07	-0.08	0.00
18	1	0.24	-0.12	0.03	-0.06	0.06	0.01	-0.28	0.22	0.00
19	1	-0.24	0.12	0.03	-0.06	0.06	-0.01	-0.28	0.22	0.00
20	1	0.06	-0.20	-0.04	0.33	-0.13	0.00	0.10	-0.14	-0.01
21	1	-0.06	0.20	-0.04	0.33	-0.13	0.00	0.10	-0.14	0.01
22	6	0.00	0.00	-0.05	-0.20	0.07	0.00	-0.04	-0.08	0.00
23	6	0.00	0.00	0.04	0.02	-0.05	0.00	0.00	0.08	0.00
24	1	-0.14	-0.04	0.04	-0.26	0.12	0.00	-0.06	-0.07	0.00
25	1	0.14	0.04	0.04	-0.26	0.12	0.00	-0.06	-0.07	0.00
26	1	-0.07	-0.06	-0.03	0.19	-0.22	-0.01	-0.01	0.08	0.00
27	1	0.07	0.06	-0.03	0.19	-0.22	0.01	-0.01	0.08	0.00
28	6	0.00	0.00	-0.04	-0.02	0.02	0.00	-0.02	0.02	0.00
29	8	0.00	0.00	0.01	0.00	-0.02	0.00	0.01	-0.04	0.00
30	8	0.00	0.00	0.01	-0.01	-0.01	0.00	0.00	0.00	0.00
31	1	0.00	0.00	0.00	0.01	0.08	0.00	0.02	0.06	0.00
32	1	0.00	0.00	0.08	0.20	0.01	0.00	0.00	0.01	0.00

	37	38	39
	A’	A’	A’
Frequencies --	1064.3683	1080.0570	1129.5256
Red. masses --	2.1800	2.8282	2.3475
Frc consts --	1.4551	1.9438	1.7646
IR Inten --	0.0523	43.5909	123.2532
Raman Activ --	13.6136	5.4027	6.2433

Depolar (P) --		0.7416			0.2650			0.2633		
Depolar (U) --		0.8517			0.4190			0.4168		
Atom	AN	X	Y	Z	X	Y	Z	X	Y	Z
1	6	0.05	0.01	0.00	0.00	0.06	0.00	0.03	0.08	0.00
2	6	-0.06	0.06	0.00	-0.02	-0.11	0.00	-0.08	-0.11	0.00
3	1	0.09	-0.02	0.00	0.11	-0.13	-0.03	0.19	-0.17	-0.04
4	1	0.09	-0.02	0.00	0.11	-0.13	0.03	0.19	-0.17	0.04
5	6	0.13	-0.06	0.00	-0.05	0.10	0.00	0.06	0.12	0.00
6	1	-0.12	0.13	0.01	0.14	-0.25	0.00	0.05	-0.20	0.01
7	1	-0.12	0.13	-0.01	0.14	-0.25	0.00	0.05	-0.20	-0.01
8	1	0.26	-0.17	0.00	0.01	0.05	0.00	0.12	0.04	-0.01
9	1	0.26	-0.17	0.00	0.01	0.05	0.00	0.12	0.04	0.01
10	6	-0.14	0.10	0.00	0.03	0.02	0.00	-0.08	-0.06	0.00
11	6	0.10	-0.10	0.00	-0.07	-0.02	0.00	0.04	0.07	0.00
12	1	-0.25	0.21	0.00	0.19	-0.11	0.00	0.03	-0.13	-0.01
13	1	-0.25	0.21	0.00	0.19	-0.11	0.00	0.03	-0.13	0.01
14	6	-0.10	0.07	0.00	0.06	0.13	0.00	-0.05	-0.03	0.00
15	1	0.24	-0.23	0.00	0.04	-0.09	0.01	0.13	-0.02	-0.01
16	1	0.24	-0.23	0.00	0.04	-0.09	-0.01	0.13	-0.02	0.01
17	6	0.03	-0.07	0.00	-0.02	-0.13	0.00	-0.02	0.04	0.00
18	1	-0.18	0.13	0.00	0.10	0.09	-0.01	0.06	-0.12	0.00
19	1	-0.18	0.13	0.00	0.10	0.09	0.01	0.06	-0.12	0.00
20	1	0.11	-0.14	0.00	0.09	-0.20	0.02	0.08	-0.05	0.00
21	1	0.11	-0.14	0.00	0.09	-0.20	-0.02	0.08	-0.05	0.00
22	6	-0.03	0.04	0.00	0.01	0.20	0.00	0.00	0.01	0.00
23	6	0.00	-0.04	0.00	-0.02	-0.20	0.00	-0.01	0.02	0.00
24	1	-0.07	0.06	0.01	-0.11	0.27	0.02	0.14	-0.11	0.00
25	1	-0.07	0.06	-0.01	-0.11	0.27	-0.02	0.14	-0.11	0.00
26	1	0.02	-0.06	0.00	-0.02	-0.19	0.01	0.24	-0.17	0.00
27	1	0.02	-0.06	0.00	-0.02	-0.19	-0.01	0.24	-0.17	0.00
28	6	0.00	0.00	0.00	0.04	-0.05	0.00	-0.10	0.14	0.00
29	8	0.00	0.01	0.00	-0.02	0.08	0.00	0.00	-0.14	0.00
30	8	0.00	0.00	0.00	0.00	-0.01	0.00	0.03	0.02	0.00
31	1	0.00	-0.01	0.00	-0.04	-0.20	0.00	0.06	0.42	0.00
32	1	0.00	0.00	0.00	-0.28	-0.01	0.00	-0.32	-0.01	0.00
		40			41			42		
		A"			A’			A"		
Frequencies --		1140.5094			1149.0965			1208.7051		
Red. masses --		1.5040			3.1159			1.7707		
Frc consts --		1.1526			2.4241			1.5242		
IR Inten --		0.8562			157.9372			0.0106		
Raman Activ --		1.0436			7.7159			1.1832		
Depolar (P) --		0.7500			0.2359			0.7500		
Depolar (U) --		0.8571			0.3818			0.8571		
Atom	AN	X	Y	Z	X	Y	Z	X	Y	Z
1	6	0.00	0.00	0.01	-0.03	-0.08	0.00	0.00	0.00	0.08
2	6	0.00	0.00	-0.01	0.07	0.10	0.00	0.00	0.00	-0.13
3	1	-0.03	0.00	-0.01	-0.17	0.16	0.04	-0.26	-0.02	-0.07
4	1	0.03	0.00	-0.01	-0.17	0.16	-0.04	0.26	0.02	-0.07
5	6	0.00	0.00	0.02	-0.07	-0.11	0.00	0.00	0.00	0.12
6	1	0.00	0.04	0.01	-0.02	0.16	-0.01	0.18	0.18	0.07
7	1	0.00	-0.04	0.01	-0.02	0.16	0.01	-0.18	-0.18	0.07
8	1	-0.06	0.00	-0.01	-0.09	-0.07	0.01	-0.15	-0.20	-0.07
9	1	0.06	0.00	-0.01	-0.09	-0.07	-0.01	0.15	0.20	-0.07
10	6	0.00	0.00	-0.02	0.08	0.09	0.00	0.00	0.00	-0.11
11	6	0.00	0.00	0.03	-0.08	-0.09	0.00	0.00	0.00	0.10
12	1	0.02	-0.08	0.02	0.04	0.09	0.01	-0.20	-0.13	0.07
13	1	-0.02	0.08	0.02	0.04	0.09	-0.01	0.20	0.13	0.07

14	6	0.00	0.00	-0.05	0.08	0.08	0.00	0.00	0.00	-0.08
15	1	-0.13	0.01	-0.02	-0.07	-0.07	0.01	-0.06	-0.21	-0.06
16	1	0.13	-0.01	-0.02	-0.07	-0.07	-0.01	0.06	0.21	-0.06
17	6	0.00	0.00	0.06	-0.09	-0.08	0.00	0.00	0.00	0.05
18	1	-0.04	0.17	0.03	0.07	0.06	-0.01	0.19	0.04	0.05
19	1	0.04	-0.17	0.03	0.07	0.06	0.01	-0.19	-0.04	0.05
20	1	-0.25	0.04	-0.05	-0.06	-0.08	0.01	0.03	-0.17	-0.03
21	1	0.25	-0.04	-0.05	-0.06	-0.08	-0.01	-0.03	0.17	-0.03
22	6	0.00	0.00	-0.09	0.08	0.10	0.00	0.00	0.00	-0.02
23	6	0.00	0.00	0.12	-0.03	-0.07	0.00	0.00	0.00	-0.01
24	1	0.09	-0.34	0.07	0.12	0.05	0.01	-0.14	0.07	0.01
25	1	-0.09	0.34	0.07	0.12	0.05	-0.01	0.14	-0.07	0.01
26	1	-0.46	0.09	-0.06	0.21	-0.24	0.01	0.15	-0.10	0.00
27	1	0.46	-0.09	-0.06	0.21	-0.24	-0.01	-0.15	0.10	0.00
28	6	0.00	0.00	-0.12	-0.12	0.16	0.00	0.00	0.00	0.03
29	8	0.00	0.00	0.02	0.00	-0.15	0.00	0.00	0.00	0.00
30	8	0.00	0.00	0.02	0.05	0.03	0.00	0.00	0.00	0.00
31	1	0.00	0.00	0.00	0.06	0.48	0.00	0.00	0.00	0.00
32	1	0.00	0.00	-0.02	0.27	0.00	0.00	0.00	0.00	-0.16

	43	44	45
	A’	A"	A’
Frequencies --	1235.0539	1243.3966	1272.0192
Red. masses --	1.2961	1.4501	1.3094
Frc consts --	1.1648	1.3209	1.2483
IR Inten --	8.7201	0.0686	9.8392
Raman Activ --	0.1845	0.4294	0.5519
Depolar (P) --	0.7317	0.7500	0.6531
Depolar (U) --	0.8451	0.8571	0.7901

Atom	AN	X	Y	Z	X	Y	Z	X	Y	Z
1	6	-0.01	-0.03	0.00	0.00	0.00	0.07	0.01	0.03	0.00
2	6	0.02	0.05	0.00	0.00	0.00	-0.09	0.00	-0.05	0.00
3	1	-0.06	0.06	0.02	-0.19	-0.02	-0.05	0.04	-0.05	-0.02
4	1	-0.06	0.06	-0.02	0.19	0.02	-0.05	0.04	-0.05	0.02
5	6	-0.05	-0.01	0.00	0.00	0.00	0.04	0.05	-0.02	0.00
6	1	0.07	-0.01	0.00	0.22	0.03	0.04	-0.12	0.07	0.00
7	1	0.07	-0.01	0.00	-0.22	-0.03	0.04	-0.12	0.07	0.00
8	1	0.11	-0.15	0.00	0.10	-0.20	-0.02	-0.19	0.19	0.00
9	1	0.11	-0.15	0.00	-0.10	0.20	-0.02	-0.19	0.19	0.00
10	6	-0.01	0.05	0.00	0.00	0.00	0.01	0.05	-0.02	0.00
11	6	-0.05	0.02	0.00	0.00	0.00	-0.06	0.00	-0.05	0.00
12	1	0.21	-0.16	0.00	-0.17	0.18	-0.01	-0.20	0.19	0.00
13	1	0.21	-0.16	0.00	0.17	-0.18	-0.01	-0.20	0.19	0.00
14	6	-0.04	0.03	0.00	0.00	0.00	0.09	0.03	0.04	0.00
15	1	0.23	-0.22	0.00	0.22	-0.03	0.03	-0.14	0.09	0.00
16	1	0.23	-0.22	0.00	-0.22	0.03	0.03	-0.14	0.09	0.00
17	6	-0.02	0.05	0.00	0.00	0.00	-0.09	-0.05	0.00	0.00
18	1	0.24	-0.21	0.00	-0.06	-0.19	-0.05	0.04	0.01	0.00
19	1	0.24	-0.21	0.00	0.06	0.19	-0.05	0.04	0.01	0.00
20	1	0.23	-0.18	0.00	0.08	0.18	0.05	0.13	-0.15	0.00
21	1	0.23	-0.18	0.00	-0.08	-0.18	0.05	0.13	-0.15	0.00
22	6	-0.05	-0.01	0.00	0.00	0.00	0.06	-0.03	0.03	0.00
23	6	0.00	0.05	0.00	0.00	0.00	0.00	-0.03	0.06	0.00
24	1	0.16	-0.17	-0.01	0.22	-0.03	-0.03	0.24	-0.20	-0.01
25	1	0.16	-0.17	0.01	-0.22	0.03	-0.03	0.24	-0.20	0.01
26	1	0.08	-0.04	-0.01	-0.23	0.19	0.01	0.20	-0.14	-0.01
27	1	0.08	-0.04	0.01	0.23	-0.19	0.01	0.20	-0.14	0.01
28	6	0.01	-0.02	0.00	0.00	0.00	-0.04	-0.01	0.01	0.00
29	8	0.01	0.03	0.00	0.00	0.00	0.00	0.03	0.03	0.00

30	8	-0.02	-0.02	0.00	0.00	0.00	0.01	-0.02	-0.03	0.00	
31	1	-0.01	-0.18	0.00	0.00	0.00	0.00	-0.01	-0.40	0.00	
32	1	0.10	0.00	0.00	0.00	0.00	-0.13	-0.10	0.00	0.00	
			46			47			48		
			A"			A’			A"		
Frequencies --			1281.8996			1299.5284			1313.2939		
Red. masses --			1.3019			1.3878			1.1930		
Frc consts --			1.2605			1.3809			1.2123		
IR Inten --			0.2112			1.7378			0.0148		
Raman Activ --			0.0852			1.8795			6.1649		
Depolar (P) --			0.7500			0.7339			0.7500		
Depolar (U) --			0.8571			0.8465			0.8571		
Atom	AN	X	Y	Z	X	Y	Z	X	Y	Z	
1	6	0.00	0.00	0.05	-0.01	-0.03	0.00	0.00	0.00	0.04	
2	6	0.00	0.00	-0.05	-0.01	0.04	0.00	0.00	0.00	-0.01	
3	1	-0.14	-0.02	-0.04	-0.02	0.04	0.03	-0.11	-0.02	-0.02	
4	1	0.14	0.02	-0.04	-0.02	0.04	-0.03	0.11	0.02	-0.02	
5	6	0.00	0.00	-0.03	-0.04	0.04	0.00	0.00	0.00	-0.06	
6	1	0.25	-0.11	0.02	0.15	-0.11	0.00	0.26	-0.21	0.00	
7	1	-0.25	0.11	0.02	0.15	-0.11	0.00	-0.26	0.21	0.00	
8	1	0.22	-0.13	0.01	0.20	-0.18	0.00	0.12	0.04	0.02	
9	1	-0.22	0.13	0.01	0.20	-0.18	0.00	-0.12	-0.04	0.02	
10	6	0.00	0.00	0.08	-0.04	0.00	0.00	0.00	0.00	0.04	
11	6	0.00	0.00	-0.07	0.04	0.01	0.00	0.00	0.00	0.03	
12	1	0.03	0.17	-0.04	0.09	-0.11	0.00	0.16	-0.04	-0.02	
13	1	-0.03	-0.17	-0.04	0.09	-0.11	0.00	-0.16	0.04	-0.02	
14	6	0.00	0.00	0.01	0.03	-0.04	0.00	0.00	0.00	-0.06	
15	1	-0.04	0.20	0.03	-0.05	0.08	0.00	-0.26	0.16	-0.01	
16	1	0.04	-0.20	0.03	-0.05	0.08	0.00	0.26	-0.16	-0.01	
17	6	0.00	0.00	0.06	0.02	-0.04	0.00	0.00	0.00	0.01	
18	1	-0.21	0.18	0.00	-0.20	0.16	0.00	0.15	0.02	0.02	
19	1	0.21	-0.18	0.00	-0.20	0.16	0.00	-0.15	-0.02	0.02	
20	1	-0.21	0.04	-0.03	-0.17	0.14	0.00	0.13	-0.15	0.00	
21	1	0.21	-0.04	-0.03	-0.17	0.14	0.00	-0.13	0.15	0.00	
22	6	0.00	0.00	-0.08	0.03	0.01	0.00	0.00	0.00	0.06	
23	6	0.00	0.00	0.01	-0.04	0.04	0.00	0.00	0.00	-0.03	
24	1	-0.12	-0.08	0.03	0.01	0.01	0.00	-0.10	0.23	-0.02	
25	1	0.12	0.08	0.03	0.01	0.01	0.00	0.10	-0.23	-0.02	
26	1	0.22	-0.23	-0.01	0.21	-0.14	0.01	-0.20	0.25	0.01	
27	1	-0.22	0.23	-0.01	0.21	-0.14	-0.01	0.20	-0.25	0.01	
28	6	0.00	0.00	0.03	-0.06	0.08	0.00	0.00	0.00	-0.03	
29	8	0.00	0.00	0.00	0.05	0.02	0.00	0.00	0.00	0.00	
30	8	0.00	0.00	0.00	-0.02	-0.05	0.00	0.00	0.00	0.00	
31	1	0.00	0.00	0.00	-0.01	-0.56	0.00	0.00	0.00	0.00	
32	1	0.00	0.00	-0.10	0.10	0.00	0.00	0.00	0.00	-0.07	
			49			50			51		
			A"			A’			A"		
Frequencies --			1323.7340			1328.8484			1329.1819		
Red. masses --			1.0324			1.4536			1.0754		
Frc consts --			1.0659			1.5124			1.1194		
IR Inten --			0.0043			10.6568			0.8283		
Raman Activ --			29.8093			0.6160			1.1246		
Depolar (P) --			0.7500			0.6345			0.7500		
Depolar (U) --			0.8571			0.7764			0.8571		
Atom	AN	X	Y	Z	X	Y	Z	X	Y	Z	
1	6	0.00	0.00	0.01	0.01	0.03	0.00	0.00	0.00	0.03	
2	6	0.00	0.00	-0.02	0.04	-0.05	0.00	0.00	0.00	0.03	
3	1	-0.01	-0.01	-0.01	0.00	-0.05	-0.04	-0.07	0.00	-0.01	

4	1	0.01	0.01	-0.01	0.00	-0.05	0.04	0.07	0.00	-0.01
5	6	0.00	0.00	-0.03	0.03	-0.05	0.00	0.00	0.00	-0.03
6	1	0.01	0.03	0.00	-0.21	0.17	0.00	0.23	-0.27	-0.01
7	1	-0.01	-0.03	0.00	-0.21	0.17	0.00	-0.23	0.27	-0.01
8	1	0.21	-0.12	0.01	-0.19	0.16	0.00	-0.22	0.26	0.01
9	1	-0.21	0.12	0.01	-0.19	0.16	0.00	0.22	-0.26	0.01
10	6	0.00	0.00	0.00	0.01	0.04	0.00	0.00	0.00	-0.02
11	6	0.00	0.00	0.01	-0.05	0.04	0.00	0.00	0.00	0.01
12	1	0.27	-0.23	0.00	0.07	-0.04	0.00	-0.08	0.02	0.00
13	1	-0.27	0.23	0.00	0.07	-0.04	0.00	0.08	-0.02	0.00
14	6	0.00	0.00	-0.01	-0.05	0.00	0.00	0.00	0.00	-0.01
15	1	0.16	-0.18	0.00	0.24	-0.21	0.00	-0.07	0.03	-0.01
16	1	-0.16	0.18	0.00	0.24	-0.21	0.00	0.07	-0.03	-0.01
17	6	0.00	0.00	0.00	0.05	0.00	0.00	0.00	0.00	-0.04
18	1	-0.17	0.19	0.01	0.11	-0.12	0.00	0.11	-0.08	0.00
19	1	0.17	-0.19	0.01	0.11	-0.12	0.00	-0.11	0.08	0.00
20	1	0.27	-0.23	0.00	-0.12	0.14	0.00	0.14	-0.02	0.01
21	1	-0.27	0.23	0.00	-0.12	0.14	0.00	-0.14	0.02	0.01
22	6	0.00	0.00	0.02	0.06	-0.04	0.00	0.00	0.00	-0.01
23	6	0.00	0.00	0.02	0.00	-0.01	0.00	0.00	0.00	0.03
24	1	0.21	-0.14	0.00	-0.23	0.19	0.01	0.27	-0.27	0.00
25	1	-0.21	0.14	0.00	-0.23	0.19	-0.01	-0.27	0.27	0.00
26	1	0.03	-0.05	0.00	0.03	0.01	0.02	0.13	-0.18	-0.01
27	1	-0.03	0.05	0.00	0.03	0.01	-0.02	-0.13	0.18	-0.01
28	6	0.00	0.00	0.00	-0.07	0.09	0.00	0.00	0.00	0.01
29	8	0.00	0.00	0.00	0.04	0.00	0.00	0.00	0.00	0.00
30	8	0.00	0.00	0.00	-0.01	-0.03	0.00	0.00	0.00	0.00
31	1	0.00	0.00	0.00	-0.01	-0.37	0.00	0.00	0.00	0.00
32	1	0.00	0.00	-0.02	-0.12	0.00	0.00	0.00	0.00	-0.02

	52	53	54
	A"	A"	A’
Frequencies --	1336.6065	1338.5524	1362.1968
Red. masses --	1.1109	1.0896	1.4840
Frc consts --	1.1693	1.1503	1.6224
IR Inten --	0.0090	0.0183	21.2232
Raman Activ --	0.1285	1.0180	0.5948
Depolar (P) --	0.7500	0.7500	0.7062
Depolar (U) --	0.8571	0.8571	0.8278

Atom	AN	X	Y	Z	X	Y	Z	X	Y	Z
1	6	0.00	0.00	0.02	0.00	0.00	-0.02	-0.01	-0.03	0.00
2	6	0.00	0.00	0.00	0.00	0.00	-0.03	-0.07	0.06	0.00
3	1	-0.04	-0.01	-0.01	0.05	0.00	0.00	0.03	0.04	0.05
4	1	0.04	0.01	-0.01	-0.05	0.00	0.00	0.03	0.04	-0.05
5	6	0.00	0.00	-0.05	0.00	0.00	0.01	0.01	0.03	0.00
6	1	0.12	-0.10	0.00	-0.16	0.20	0.01	0.26	-0.22	0.00
7	1	-0.12	0.10	0.00	0.16	-0.20	0.01	0.26	-0.22	0.00
8	1	0.12	0.00	0.01	0.22	-0.23	0.00	0.05	-0.03	-0.01
9	1	-0.12	0.00	0.01	-0.22	0.23	0.00	0.05	-0.03	0.01
10	6	0.00	0.00	-0.01	0.00	0.00	0.05	0.05	-0.06	0.00
11	6	0.00	0.00	0.05	0.00	0.00	0.03	0.00	-0.04	0.00
12	1	0.28	-0.29	0.00	0.07	0.05	-0.01	-0.24	0.21	0.00
13	1	-0.28	0.29	0.00	-0.07	-0.05	-0.01	-0.24	0.21	0.00
14	6	0.00	0.00	0.04	0.00	0.00	-0.03	-0.05	0.06	0.00
15	1	0.09	-0.21	-0.01	-0.29	0.20	-0.01	-0.09	0.06	0.01
16	1	-0.09	0.21	-0.01	0.29	-0.20	-0.01	-0.09	0.06	-0.01
17	6	0.00	0.00	-0.02	0.00	0.00	-0.04	-0.02	0.05	0.00
18	1	0.16	-0.25	-0.01	0.29	-0.18	0.01	0.23	-0.19	0.00
19	1	-0.16	0.25	-0.01	-0.29	0.18	0.01	0.23	-0.19	0.00

20	1	-0.25	0.28	0.01	0.07	0.04	0.01	0.13	-0.10	-0.01
21	1	0.25	-0.28	0.01	-0.07	-0.04	0.01	0.13	-0.10	0.01
22	6	0.00	0.00	-0.03	0.00	0.00	0.00	0.04	-0.06	0.00
23	6	0.00	0.00	0.00	0.00	0.00	0.02	0.03	-0.03	0.00
24	1	-0.09	0.00	0.01	0.17	-0.17	0.00	-0.22	0.16	0.01
25	1	0.09	0.00	0.01	-0.17	0.17	0.00	-0.22	0.16	-0.01
26	1	0.05	-0.05	-0.01	0.07	-0.11	-0.01	-0.09	0.11	0.02
27	1	-0.05	0.05	-0.01	-0.07	0.11	-0.01	-0.09	0.11	-0.02
28	6	0.00	0.00	0.01	0.00	0.00	0.01	-0.05	0.07	0.00
29	8	0.00	0.00	0.00	0.00	0.00	0.00	0.02	-0.01	0.00
30	8	0.00	0.00	0.00	0.00	0.00	0.00	0.00	-0.02	0.00
31	1	0.00	0.00	0.00	0.00	0.00	0.00	0.00	-0.21	0.00
32	1	0.00	0.00	-0.03	0.00	0.00	0.00	0.14	0.00	0.00

	55	56	57
	A'	A'	A'
Frequencies --	1388.5865	1398.2189	1401.6268
Red. masses --	1.5326	1.6243	1.5925
Frc consts --	1.7411	1.8710	1.8433
IR Inten --	8.2266	2.0507	3.2715
Raman Activ --	0.0593	0.4255	0.0909
Depolar (P) --	0.1155	0.6871	0.2243
Depolar (U) --	0.2071	0.8145	0.3664

Atom	AN	X	Y	Z	X	Y	Z	X	Y	Z
1	6	0.01	0.03	0.00	-0.04	0.02	0.00	0.01	-0.02	0.00
2	6	0.09	-0.07	0.00	0.06	-0.04	0.00	-0.05	0.04	0.00
3	1	-0.04	-0.05	-0.06	0.11	-0.09	0.02	-0.03	0.05	0.01
4	1	-0.04	-0.05	0.06	0.11	-0.09	-0.02	-0.03	0.05	-0.01
5	6	-0.06	0.04	0.00	-0.09	0.08	0.00	0.06	-0.05	0.00
6	1	-0.26	0.24	0.00	-0.14	0.14	0.00	0.14	-0.13	0.00
7	1	-0.26	0.24	0.00	-0.14	0.14	0.00	0.14	-0.13	0.00
8	1	0.17	-0.16	0.01	0.26	-0.23	-0.01	-0.17	0.16	0.00
9	1	0.17	-0.16	-0.01	0.26	-0.23	0.01	-0.17	0.16	0.00
10	6	-0.05	0.02	0.00	0.10	-0.09	0.00	-0.01	0.02	0.00
11	6	0.07	-0.05	0.00	-0.08	0.07	0.00	-0.05	0.06	0.00
12	1	0.13	-0.12	0.00	-0.30	0.27	0.00	0.05	-0.04	0.00
13	1	0.13	-0.12	0.00	-0.30	0.27	0.00	0.05	-0.04	0.00
14	6	0.02	0.00	0.00	0.04	-0.04	0.00	0.11	-0.09	0.00
15	1	-0.21	0.20	0.00	0.23	-0.21	0.00	0.17	-0.15	-0.01
16	1	-0.21	0.20	0.00	0.23	-0.21	0.00	0.17	-0.15	0.01
17	6	-0.07	0.07	0.00	-0.01	0.01	0.00	-0.09	0.07	0.00
18	1	-0.03	0.04	-0.01	-0.12	0.10	0.00	-0.32	0.28	0.00
19	1	-0.03	0.04	0.01	-0.12	0.10	0.00	-0.32	0.28	0.00
20	1	0.25	-0.22	0.00	0.02	-0.03	0.00	0.26	-0.24	0.00
21	1	0.25	-0.22	0.00	0.02	-0.03	0.00	0.26	-0.24	0.00
22	6	0.02	-0.04	0.00	0.01	-0.01	0.00	0.02	-0.03	0.00
23	6	0.05	-0.04	0.00	-0.02	0.01	0.00	0.02	-0.02	0.00
24	1	-0.11	0.07	0.00	-0.02	0.01	0.00	-0.08	0.05	0.00
25	1	-0.11	0.07	0.00	-0.02	0.01	0.00	-0.08	0.05	0.00
26	1	-0.12	0.13	0.02	0.04	-0.03	0.00	-0.05	0.07	0.01
27	1	-0.12	0.13	-0.02	0.04	-0.03	0.00	-0.05	0.07	-0.01
28	6	-0.04	0.06	0.00	0.01	-0.01	0.00	-0.02	0.02	0.00
29	8	0.01	-0.01	0.00	0.00	0.00	0.00	0.01	0.00	0.00
30	8	0.00	-0.01	0.00	0.00	0.00	0.00	0.00	-0.01	0.00
31	1	0.00	-0.12	0.00	0.00	0.03	0.00	0.00	-0.05	0.00
32	1	-0.10	0.00	0.00	0.12	0.05	0.00	-0.02	-0.02	0.00

	58	59	60
	A'	A'	A'
Frequencies --	1412.6737	1415.6826	1459.3153

Red. masses --		1.2527			1.8549			1.0827		
Frc consts --		1.4729			2.1903			1.3585		
IR Inten --		1.8902			40.1475			16.0341		
Raman Activ --		0.3045			0.2447			6.4702		
Depolar (P) --		0.5998			0.4813			0.7500		
Depolar (U) --		0.7498			0.6498			0.8571		
Atom	AN	X	Y	Z	X	Y	Z	X	Y	Z
1	6	0.13	-0.02	0.00	0.02	0.00	0.00	0.00	0.00	0.00
2	6	-0.01	0.00	0.00	0.00	0.00	0.00	0.00	0.00	0.00
3	1	-0.48	0.20	-0.19	-0.06	0.03	-0.02	0.00	0.00	0.00
4	1	-0.48	0.20	0.19	-0.06	0.03	0.02	0.00	0.00	0.00
5	6	-0.02	0.02	0.00	0.00	0.01	0.00	0.00	0.00	0.00
6	1	0.01	-0.02	0.00	0.01	-0.01	0.00	0.00	0.00	0.00
7	1	0.01	-0.02	0.00	0.01	-0.01	0.00	0.00	0.00	0.00
8	1	0.08	-0.05	0.01	0.02	-0.01	0.00	0.00	0.00	0.00
9	1	0.08	-0.05	-0.01	0.02	-0.01	0.00	0.00	0.00	0.00
10	6	0.02	-0.03	0.00	0.02	-0.01	0.00	0.00	0.00	0.00
11	6	-0.01	0.01	0.00	-0.02	0.02	0.00	0.00	0.00	0.00
12	1	-0.08	0.07	0.00	-0.05	0.04	0.00	0.00	0.00	0.00
13	1	-0.08	0.07	0.00	-0.05	0.04	0.00	0.00	0.00	0.00
14	6	0.00	0.00	0.00	0.01	-0.01	0.00	0.00	0.00	0.00
15	1	0.02	-0.02	0.00	0.07	-0.06	0.00	0.00	-0.01	0.00
16	1	0.02	-0.02	0.00	0.07	-0.06	0.00	0.00	-0.01	0.00
17	6	0.00	0.00	0.00	0.04	-0.04	0.00	0.01	0.00	0.00
18	1	0.01	-0.01	0.00	-0.04	0.02	0.00	0.02	0.02	0.02
19	1	0.01	-0.01	0.00	-0.04	0.02	0.00	0.02	0.02	-0.02
20	1	0.00	0.01	0.00	-0.10	0.09	0.01	-0.04	-0.03	-0.04
21	1	0.00	0.01	0.00	-0.10	0.09	-0.01	-0.04	-0.03	0.04
22	6	0.01	-0.01	0.00	-0.12	0.08	0.00	-0.01	0.02	0.00
23	6	-0.02	0.01	0.00	0.15	-0.10	0.00	-0.05	-0.06	0.00
24	1	-0.03	0.02	0.01	0.35	-0.23	-0.06	-0.02	-0.07	0.05
25	1	-0.03	0.02	-0.01	0.35	-0.23	0.06	-0.02	-0.07	-0.05
26	1	0.04	-0.04	0.00	-0.36	0.30	-0.01	0.35	0.41	0.44
27	1	0.04	-0.04	0.00	-0.36	0.30	0.01	0.35	0.41	-0.44
28	6	0.01	-0.01	0.00	-0.08	0.10	0.00	0.01	-0.01	0.00
29	8	0.00	0.00	0.00	0.02	-0.02	0.00	0.00	0.00	0.00
30	8	0.00	0.00	0.00	0.01	-0.02	0.00	-0.01	0.00	0.00
31	1	0.00	0.03	0.00	0.00	-0.20	0.00	0.00	0.04	0.00
32	1	-0.53	-0.16	0.00	-0.07	-0.02	0.00	0.00	0.00	0.00
		61			62			63		
		A'			A'			A'		
Frequencies --		1483.5856			1483.9213			1487.3552		
Red. masses --		1.0745			1.0761			1.0695		
Frc consts --		1.3935			1.3961			1.3940		
IR Inten --		0.0239			0.2385			0.1303		
Raman Activ --		0.6401			0.9129			57.1249		
Depolar (P) --		0.4858			0.3205			0.5717		
Depolar (U) --		0.6539			0.4854			0.7275		
Atom	AN	X	Y	Z	X	Y	Z	X	Y	Z
1	6	0.00	0.00	0.00	0.00	0.01	0.00	0.00	0.00	0.00
2	6	0.01	0.01	0.00	-0.02	-0.02	0.00	0.01	0.02	0.00
3	1	0.00	-0.02	-0.01	-0.04	-0.06	-0.05	0.02	0.01	0.02
4	1	0.00	-0.02	0.01	-0.04	-0.06	0.05	0.02	0.01	-0.02
5	6	-0.03	-0.03	0.00	0.01	0.01	0.00	-0.02	-0.03	0.00
6	1	-0.07	-0.08	-0.09	0.14	0.14	0.16	-0.10	-0.11	-0.12
7	1	-0.07	-0.08	0.09	0.14	0.14	-0.16	-0.10	-0.11	0.12
8	1	0.22	0.24	0.26	-0.07	-0.08	-0.09	0.17	0.19	0.20
9	1	0.22	0.24	-0.26	-0.07	-0.08	0.09	0.17	0.19	-0.20

10	6	0.03	0.03	0.00	0.02	0.03	0.00	0.01	0.01	0.00
11	6	0.00	0.00	0.00	-0.04	-0.04	0.00	-0.01	-0.01	0.00
12	1	-0.19	-0.21	0.23	-0.14	-0.17	0.18	-0.10	-0.11	0.12
13	1	-0.19	-0.21	-0.23	-0.14	-0.17	-0.18	-0.10	-0.11	-0.12
14	6	-0.02	-0.03	0.00	0.02	0.01	0.00	0.02	0.03	0.00
15	1	-0.01	-0.01	-0.01	0.25	0.28	0.30	0.08	0.09	0.10
16	1	-0.01	-0.01	0.01	0.25	0.28	-0.30	0.08	0.09	-0.10
17	6	0.02	0.02	0.00	0.01	0.02	0.00	-0.03	-0.03	0.00
18	1	0.16	0.18	0.20	-0.10	-0.11	-0.12	-0.17	-0.19	-0.21
19	1	0.16	0.18	-0.20	-0.10	-0.11	0.12	-0.17	-0.19	0.21
20	1	-0.14	-0.16	-0.17	-0.09	-0.10	-0.11	0.20	0.23	0.24
21	1	-0.14	-0.16	0.17	-0.09	-0.10	0.11	0.20	0.23	-0.24
22	6	0.00	-0.01	0.00	-0.01	-0.01	0.00	0.01	0.01	0.00
23	6	0.00	0.00	0.00	-0.01	0.00	0.00	0.00	0.00	0.00
24	1	0.04	0.05	-0.05	0.07	0.10	-0.10	-0.08	-0.11	0.11
25	1	0.04	0.05	0.05	0.07	0.10	0.10	-0.08	-0.11	-0.11
26	1	-0.01	-0.02	-0.02	0.01	0.01	0.01	0.01	0.02	0.02
27	1	-0.01	-0.02	0.02	0.01	0.01	-0.01	0.01	0.02	-0.02
28	6	0.00	0.00	0.00	0.00	0.00	0.00	0.00	0.00	0.00
29	8	0.00	0.00	0.00	0.00	0.00	0.00	0.00	0.00	0.00
30	8	0.00	0.00	0.00	0.00	0.00	0.00	0.00	0.00	0.00
31	1	0.00	0.00	0.00	0.00	0.00	0.00	0.00	0.00	0.00
32	1	0.02	0.01	0.00	0.05	0.01	0.00	0.00	0.00	0.00

	64	65	66
	A’	A’	A"
Frequencies --	1489.4918	1496.0780	1498.6320
Red. masses --	1.0743	1.0775	1.0398
Frc consts --	1.4043	1.4209	1.3759
IR Inten --	0.2456	1.6163	7.9835
Raman Activ --	1.9350	7.0217	7.8895
Depolar (P) --	0.6897	0.6511	0.7500
Depolar (U) --	0.8163	0.7887	0.8571

Atom	AN	X	Y	Z	X	Y	Z	X	Y	Z
1	6	0.00	0.02	0.00	-0.01	-0.03	0.00	0.00	0.00	-0.05
2	6	-0.04	-0.03	0.00	0.02	0.00	0.00	0.00	0.00	-0.02
3	1	-0.10	-0.17	-0.14	0.14	0.25	0.21	-0.26	0.42	0.05
4	1	-0.10	-0.17	0.14	0.14	0.25	-0.21	0.26	-0.42	0.05
5	6	0.00	0.00	0.00	0.02	0.03	0.00	0.00	0.00	0.00
6	1	0.23	0.22	0.26	-0.12	-0.08	-0.11	0.04	0.00	0.00
7	1	0.23	0.22	-0.26	-0.12	-0.08	0.11	-0.04	0.00	0.00
8	1	-0.02	-0.02	-0.02	-0.13	-0.15	-0.17	0.02	-0.02	0.00
9	1	-0.02	-0.02	0.02	-0.13	-0.15	0.17	-0.02	0.02	0.00
10	6	0.02	0.02	0.00	0.01	0.01	0.00	0.00	0.00	0.00
11	6	0.01	0.01	0.00	-0.02	-0.02	0.00	0.00	0.00	0.00
12	1	-0.11	-0.13	0.14	-0.07	-0.07	0.08	0.01	0.00	0.00
13	1	-0.11	-0.13	-0.14	-0.07	-0.07	-0.08	-0.01	0.00	0.00
14	6	-0.02	-0.02	0.00	-0.02	-0.03	0.00	0.00	0.00	0.00
15	1	-0.07	-0.08	-0.09	0.12	0.13	0.15	0.00	0.00	0.00
16	1	-0.07	-0.08	0.09	0.12	0.13	-0.15	0.00	0.00	0.00
17	6	-0.02	-0.02	0.00	0.00	0.00	0.00	0.00	0.00	0.00
18	1	0.11	0.13	0.14	0.13	0.15	0.16	0.00	0.00	0.00
19	1	0.11	0.13	-0.14	0.13	0.15	-0.16	0.00	0.00	0.00
20	1	0.12	0.13	0.15	0.00	0.01	0.01	0.00	0.00	0.00
21	1	0.12	0.13	-0.15	0.00	0.01	-0.01	0.00	0.00	0.00
22	6	0.02	0.03	0.00	0.02	0.03	0.00	0.00	0.00	0.00
23	6	0.01	0.00	0.00	0.01	0.00	0.00	0.00	0.00	0.00
24	1	-0.14	-0.19	0.19	-0.15	-0.21	0.21	0.00	0.00	0.00
25	1	-0.14	-0.19	-0.19	-0.15	-0.21	-0.21	0.00	0.00	0.00

26	1	-0.02	-0.01	-0.02	-0.03	-0.02	-0.03	0.00	0.00	0.00
27	1	-0.02	-0.01	0.02	-0.03	-0.02	0.03	0.00	0.00	0.00
28	6	0.00	0.00	0.00	0.00	0.00	0.00	0.00	0.00	0.00
29	8	0.00	0.00	0.00	0.00	0.00	0.00	0.00	0.00	0.00
30	8	0.00	0.00	0.00	0.00	0.00	0.00	0.00	0.00	0.00
31	1	0.00	0.00	0.00	0.00	-0.01	0.00	0.00	0.00	0.00
32	1	0.14	0.04	0.00	-0.21	-0.06	0.00	0.00	0.00	0.71

	67	68	69
	A'	A'	A'
Frequencies --	1503.3772	1510.0484	1514.6455
Red. masses --	1.0866	1.0938	1.0982
Frc consts --	1.4469	1.4695	1.4844
IR Inten --	1.7767	0.9293	15.0552
Raman Activ --	0.3751	0.5951	0.1027
Depolar (P) --	0.7254	0.6665	0.5184
Depolar (U) --	0.8409	0.7999	0.6829

Atom	AN	X	Y	Z	X	Y	Z	X	Y	Z
1	6	-0.01	-0.03	0.00	-0.01	-0.02	0.00	0.00	-0.01	0.00
2	6	-0.01	-0.03	0.00	-0.02	-0.04	0.00	-0.02	-0.03	0.00
3	1	0.15	0.26	0.22	0.12	0.20	0.18	0.06	0.10	0.09
4	1	0.15	0.26	-0.22	0.12	0.20	-0.18	0.06	0.10	-0.09
5	6	0.00	0.02	0.00	-0.02	-0.02	0.00	-0.02	-0.02	0.00
6	1	0.05	0.11	0.10	0.14	0.20	0.21	0.10	0.14	0.14
7	1	0.05	0.11	-0.10	0.14	0.20	-0.21	0.10	0.14	-0.14
8	1	-0.05	-0.05	-0.06	0.13	0.14	0.15	0.14	0.15	0.17
9	1	-0.05	-0.05	0.06	0.13	0.14	-0.15	0.14	0.15	-0.17
10	6	0.03	0.03	0.00	-0.01	-0.01	0.00	-0.03	-0.03	0.00
11	6	0.03	0.02	0.00	0.01	0.01	0.00	-0.03	-0.03	0.00
12	1	-0.15	-0.17	0.18	0.05	0.05	-0.06	0.15	0.17	-0.19
13	1	-0.15	-0.17	-0.18	0.05	0.05	0.06	0.15	0.17	0.19
14	6	0.00	0.01	0.00	0.02	0.02	0.00	-0.02	-0.03	0.00
15	1	-0.14	-0.15	-0.17	-0.05	-0.04	-0.05	0.16	0.17	0.19
16	1	-0.14	-0.15	0.17	-0.05	-0.04	0.05	0.16	0.17	-0.19
17	6	-0.02	-0.02	0.00	0.03	0.03	0.00	-0.02	-0.02	0.00
18	1	-0.02	-0.02	-0.03	-0.12	-0.14	-0.15	0.15	0.17	0.18
19	1	-0.02	-0.02	0.03	-0.12	-0.14	0.15	0.15	0.17	-0.18
20	1	0.11	0.11	0.12	-0.16	-0.16	-0.19	0.12	0.13	0.15
21	1	0.11	0.11	-0.12	-0.16	-0.16	0.19	0.12	0.13	-0.15
22	6	-0.02	-0.04	0.00	0.02	0.03	0.00	-0.01	-0.02	0.00
23	6	-0.01	0.00	0.00	0.01	0.00	0.00	-0.01	0.00	0.00
24	1	0.15	0.21	-0.21	-0.13	-0.17	0.18	0.08	0.11	-0.11
25	1	0.15	0.21	0.21	-0.13	-0.17	-0.18	0.08	0.11	0.11
26	1	0.03	0.03	0.04	-0.03	-0.02	-0.03	0.02	0.02	0.02
27	1	0.03	0.03	-0.04	-0.03	-0.02	0.03	0.02	0.02	-0.02
28	6	0.00	0.00	0.00	0.00	0.00	0.00	0.00	0.00	0.00
29	8	0.00	0.00	0.00	0.00	0.00	0.00	0.00	0.00	0.00
30	8	0.00	0.00	0.00	0.00	0.00	0.00	0.00	0.00	0.00
31	1	0.00	0.01	0.00	0.00	0.00	0.00	0.00	0.00	0.00
32	1	-0.21	-0.07	0.00	-0.16	-0.05	0.00	-0.08	-0.03	0.00

	70	71	72
	A'	A'	A'
Frequencies --	1811.7485	2990.7263	2991.1097
Red. masses --	9.6128	1.0577	1.0573
Frc consts --	18.5907	5.5738	5.5732
IR Inten --	301.3317	1.7510	0.7403
Raman Activ --	8.7783	21.2957	14.9391
Depolar (P) --	0.2048	0.0626	0.0418
Depolar (U) --	0.3399	0.1178	0.0802

Atom	AN	X	Y	Z	X	Y	Z	X	Y	Z
1	6	0.00	0.00	0.00	0.00	0.00	0.00	0.00	0.00	0.00
2	6	0.00	0.00	0.00	-0.01	-0.01	0.00	0.00	0.00	0.00
3	1	0.00	0.00	0.00	0.01	0.01	-0.02	0.01	0.01	-0.02
4	1	0.00	0.00	0.00	0.01	0.01	0.02	0.01	0.01	0.02
5	6	0.00	0.00	0.00	0.03	0.04	0.00	0.01	0.01	0.00
6	1	0.00	0.00	0.00	0.05	0.06	-0.10	-0.01	-0.01	0.02
7	1	0.00	0.00	0.00	0.05	0.06	0.10	-0.01	-0.01	-0.02
8	1	0.00	0.00	0.00	-0.20	-0.23	0.43	-0.08	-0.09	0.17
9	1	0.00	0.00	0.00	-0.20	-0.23	-0.43	-0.08	-0.09	-0.17
10	6	0.00	0.00	0.00	-0.01	-0.01	0.00	-0.03	-0.03	0.00
11	6	0.00	0.00	0.00	-0.03	-0.03	0.00	0.02	0.02	0.00
12	1	0.00	0.00	0.00	0.03	0.03	0.07	0.16	0.18	0.35
13	1	0.00	0.00	0.00	0.03	0.03	-0.07	0.16	0.18	-0.35
14	6	0.00	0.00	0.00	0.01	0.01	0.00	0.01	0.01	0.00
15	1	0.00	0.00	0.00	0.15	0.17	-0.32	-0.11	-0.13	0.24
16	1	0.00	0.00	0.00	0.15	0.17	0.32	-0.11	-0.13	-0.24
17	6	0.00	-0.01	0.00	0.01	0.01	0.00	-0.02	-0.03	0.00
18	1	0.00	0.00	0.00	-0.05	-0.06	0.11	-0.07	-0.08	0.15
19	1	0.00	0.00	0.00	-0.05	-0.06	-0.11	-0.07	-0.08	-0.15
20	1	-0.02	0.01	0.00	-0.05	-0.05	0.11	0.15	0.17	-0.32
21	1	-0.02	0.01	0.00	-0.05	-0.05	-0.11	0.15	0.17	0.32
22	6	0.01	0.01	0.00	0.00	0.00	0.00	0.00	0.00	0.00
23	6	-0.05	-0.02	0.00	0.00	0.00	0.00	0.00	0.00	0.00
24	1	0.04	-0.01	0.01	0.01	0.01	0.02	-0.01	-0.01	-0.02
25	1	0.04	-0.01	-0.01	0.01	0.01	-0.02	-0.01	-0.01	0.02
26	1	-0.16	-0.01	-0.07	0.00	0.00	0.00	-0.01	-0.01	0.01
27	1	-0.16	-0.01	0.07	0.00	0.00	0.00	-0.01	-0.01	-0.01
28	6	0.56	0.44	0.00	0.00	0.00	0.00	0.00	0.00	0.00
29	8	-0.04	-0.04	0.00	0.00	0.00	0.00	0.00	0.00	0.00
30	8	-0.33	-0.30	0.00	0.00	0.00	0.00	0.00	0.00	0.00
31	1	0.02	0.48	0.00	0.00	0.00	0.00	0.00	0.00	0.00
32	1	0.00	0.00	0.00	0.00	-0.03	0.00	0.00	-0.01	0.00

	73	74	75
	A'	A'	A'
Frequencies --	2994.1316	2996.9887	3004.7772
Red. masses --	1.0577	1.0589	1.0595
Frc consts --	5.5865	5.6036	5.6358
IR Inten --	4.4914	0.1242	16.1065
Raman Activ --	406.5274	37.8800	52.8608
Depolar (P) --	0.0277	0.0574	0.0584
Depolar (U) --	0.0538	0.1086	0.1103

Atom	AN	X	Y	Z	X	Y	Z	X	Y	Z
1	6	0.00	0.00	0.00	0.00	0.00	0.00	0.00	-0.01	0.00
2	6	0.00	0.00	0.00	0.02	0.02	0.00	0.03	0.03	0.00
3	1	0.01	0.01	-0.02	0.00	-0.01	0.01	0.01	0.01	-0.03
4	1	0.01	0.01	0.02	0.00	-0.01	-0.01	0.01	0.01	0.03
5	6	0.01	0.01	0.00	-0.02	-0.02	0.00	0.00	0.00	0.00
6	1	-0.01	-0.01	0.02	-0.10	-0.11	0.21	-0.17	-0.19	0.36
7	1	-0.01	-0.01	-0.02	-0.10	-0.11	-0.21	-0.17	-0.19	-0.36
8	1	-0.06	-0.07	0.13	0.11	0.13	-0.24	-0.01	-0.02	0.03
9	1	-0.06	-0.07	-0.13	0.11	0.13	0.24	-0.01	-0.02	-0.03
10	6	-0.02	-0.02	0.00	-0.02	-0.03	0.00	-0.01	-0.01	0.00
11	6	0.02	0.02	0.00	-0.01	-0.01	0.00	-0.02	-0.02	0.00
12	1	0.11	0.12	0.23	0.13	0.15	0.29	0.04	0.05	0.09
13	1	0.11	0.12	-0.23	0.13	0.15	-0.29	0.04	0.05	-0.09
14	6	-0.02	-0.02	0.00	0.02	0.02	0.00	-0.03	-0.03	0.00
15	1	-0.11	-0.12	0.23	0.08	0.09	-0.16	0.11	0.12	-0.23

16	1	-0.11	-0.12	-0.23	0.08	0.09	0.16	0.11	0.12	0.23
17	6	0.03	0.03	0.00	0.02	0.02	0.00	-0.01	-0.02	0.00
18	1	0.13	0.15	-0.28	-0.13	-0.15	0.28	0.15	0.17	-0.32
19	1	0.13	0.15	0.28	-0.13	-0.15	-0.28	0.15	0.17	0.32
20	1	-0.17	-0.19	0.36	-0.10	-0.11	0.20	0.09	0.10	-0.19
21	1	-0.17	-0.19	-0.36	-0.10	-0.11	-0.20	0.09	0.10	0.19
22	6	0.00	0.00	0.00	0.00	0.00	0.00	0.00	0.01	0.00
23	6	0.00	0.00	0.00	0.00	0.00	0.00	0.00	0.00	0.00
24	1	0.01	0.01	0.02	0.02	0.02	0.04	-0.03	-0.03	-0.06
25	1	0.01	0.01	-0.02	0.02	0.02	-0.04	-0.03	-0.03	0.06
26	1	0.01	0.01	-0.02	0.00	0.00	-0.01	0.00	0.00	0.01
27	1	0.01	0.01	0.02	0.00	0.00	0.01	0.00	0.00	-0.01
28	6	0.00	0.00	0.00	0.00	0.00	0.00	0.00	0.00	0.00
29	8	0.00	0.00	0.00	0.00	0.00	0.00	0.00	0.00	0.00
30	8	0.00	0.00	0.00	0.00	0.00	0.00	0.00	0.00	0.00
31	1	0.00	0.00	0.00	0.00	0.00	0.00	0.00	0.00	0.00
32	1	0.00	-0.01	0.00	-0.01	0.04	0.00	-0.01	0.04	0.00

	76	77	78
	A"	A’	A"
Frequencies --	3007.2660	3009.5867	3010.4341
Red. masses --	1.0989	1.0593	1.1000
Frc consts --	5.8552	5.6532	5.8735
IR Inten --	0.3538	148.0822	0.7520
Raman Activ --	245.9549	53.1658	16.2520
Depolar (P) --	0.7500	0.0468	0.7500
Depolar (U) --	0.8571	0.0894	0.8571

Atom	AN	X	Y	Z	X	Y	Z	X	Y	Z
1	6	0.00	0.00	0.00	-0.01	-0.01	0.00	0.00	0.00	0.00
2	6	0.00	0.00	-0.02	0.03	0.03	0.00	0.00	0.00	0.02
3	1	0.01	0.01	-0.01	0.04	0.04	-0.09	-0.01	-0.01	0.02
4	1	-0.01	-0.01	-0.01	0.04	0.04	0.09	0.01	0.01	0.02
5	6	0.00	0.00	0.05	0.02	0.02	0.00	0.00	0.00	-0.04
6	1	-0.06	-0.06	0.11	-0.18	-0.20	0.38	0.07	0.08	-0.14
7	1	0.06	0.06	0.11	-0.18	-0.20	-0.38	-0.07	-0.08	-0.14
8	1	0.15	0.17	-0.30	-0.09	-0.10	0.20	-0.13	-0.14	0.25
9	1	-0.15	-0.17	-0.30	-0.09	-0.10	-0.20	0.13	0.14	0.25
10	6	0.00	0.00	-0.05	0.02	0.02	0.00	0.00	0.00	0.01
11	6	0.00	0.00	0.04	0.01	0.02	0.00	0.00	0.00	0.03
12	1	0.17	0.19	0.34	-0.12	-0.13	-0.25	-0.04	-0.04	-0.08
13	1	-0.17	-0.19	0.34	-0.12	-0.13	0.25	0.04	0.04	-0.08
14	6	0.00	0.00	-0.02	0.01	0.02	0.00	0.00	0.00	-0.05
15	1	0.14	0.16	-0.27	-0.09	-0.10	0.19	0.10	0.11	-0.19
16	1	-0.14	-0.16	-0.27	-0.09	-0.10	-0.19	-0.10	-0.11	-0.19
17	6	0.00	0.00	0.01	0.01	0.01	0.00	0.00	0.00	0.05
18	1	-0.07	-0.08	0.14	-0.09	-0.10	0.18	-0.16	-0.18	0.32
19	1	0.07	0.08	0.14	-0.09	-0.10	-0.18	0.16	0.18	0.32
20	1	0.03	0.04	-0.06	-0.04	-0.05	0.08	0.15	0.17	-0.29
21	1	-0.03	-0.04	-0.06	-0.04	-0.05	-0.08	-0.15	-0.17	-0.29
22	6	0.00	0.00	0.00	0.00	0.00	0.00	0.00	0.00	-0.01
23	6	0.00	0.00	0.00	0.00	0.00	0.00	0.00	0.00	0.00
24	1	0.00	0.00	0.01	0.02	0.02	0.04	0.03	0.03	0.05
25	1	0.00	0.00	0.01	0.02	0.02	-0.04	-0.03	-0.03	0.05
26	1	0.00	0.00	0.00	0.00	0.00	0.00	0.00	0.00	0.00
27	1	0.00	0.00	0.00	0.00	0.00	0.00	0.00	0.00	0.00
28	6	0.00	0.00	0.00	0.00	0.00	0.00	0.00	0.00	0.00
29	8	0.00	0.00	0.00	0.00	0.00	0.00	0.00	0.00	0.00
30	8	0.00	0.00	0.00	0.00	0.00	0.00	0.00	0.00	0.00
31	1	0.00	0.00	0.00	0.00	0.00	0.00	0.00	0.00	0.00

32	1	0.00	0.00	0.00	0.00	0.00	0.00	0.00	0.00	0.00

	79	80	81
	A"	A’	A’
Frequencies --	3016.6605	3017.2084	3026.5803
Red. masses --	1.1024	1.0357	1.0602
Frc consts --	5.9106	5.5549	5.7221
IR Inten --	1.8518	51.5287	2.8285
Raman Activ --	55.6258	185.2765	197.3676
Depolar (P) --	0.7500	0.0039	0.0286
Depolar (U) --	0.8571	0.0078	0.0557

Atom	AN	X	Y	Z	X	Y	Z	X	Y	Z
1	6	0.00	0.00	-0.01	0.05	0.00	0.00	0.00	0.00	0.00
2	6	0.00	0.00	0.04	0.00	0.00	0.00	0.00	0.00	0.00
3	1	-0.02	-0.02	0.04	-0.24	-0.25	0.49	0.00	0.00	0.00
4	1	0.02	0.02	0.04	-0.24	-0.25	-0.49	0.00	0.00	0.00
5	6	0.00	0.00	-0.04	0.01	0.01	0.00	0.00	0.00	0.00
6	1	0.11	0.12	-0.22	-0.02	-0.02	0.05	0.00	0.00	0.00
7	1	-0.11	-0.12	-0.22	-0.02	-0.02	-0.05	0.00	0.00	0.00
8	1	-0.11	-0.12	0.22	-0.03	-0.04	0.07	0.00	0.00	0.00
9	1	0.11	0.12	0.22	-0.03	-0.04	-0.07	0.00	0.00	0.00
10	6	0.00	0.00	-0.02	0.00	0.00	0.00	0.00	0.00	0.00
11	6	0.00	0.00	0.04	0.00	0.00	0.00	0.00	0.00	0.00
12	1	0.08	0.08	0.15	-0.01	-0.01	-0.02	0.00	0.00	0.01
13	1	-0.08	-0.08	0.15	-0.01	-0.01	0.02	0.00	0.00	-0.01
14	6	0.00	0.00	0.01	0.00	0.00	0.00	0.00	0.00	0.00
15	1	0.14	0.15	-0.27	-0.01	-0.01	0.02	0.00	0.00	0.00
16	1	-0.14	-0.15	-0.27	-0.01	-0.01	-0.02	0.00	0.00	0.00
17	6	0.00	0.00	-0.06	0.00	0.00	0.00	0.00	0.00	0.00
18	1	0.04	0.04	-0.07	0.00	0.00	0.01	0.01	0.02	-0.03
19	1	-0.04	-0.04	-0.07	0.00	0.00	-0.01	0.01	0.02	0.03
20	1	-0.17	-0.19	0.33	0.00	0.00	0.01	0.01	0.01	-0.01
21	1	0.17	0.19	0.33	0.00	0.00	-0.01	0.01	0.01	0.01
22	6	0.00	0.00	0.01	0.00	0.00	0.00	-0.02	-0.03	0.00
23	6	0.00	0.00	0.00	0.00	0.00	0.00	0.04	0.05	0.00
24	1	-0.04	-0.05	-0.09	0.00	0.00	0.00	0.14	0.16	0.30
25	1	0.04	0.05	-0.09	0.00	0.00	0.00	0.14	0.16	-0.30
26	1	-0.01	-0.01	0.01	0.00	0.00	0.00	-0.22	-0.27	0.49
27	1	0.01	0.01	0.01	0.00	0.00	0.00	-0.22	-0.27	-0.49
28	6	0.00	0.00	0.00	0.00	0.00	0.00	0.00	0.00	0.00
29	8	0.00	0.00	0.00	0.00	0.00	0.00	0.00	0.00	0.00
30	8	0.00	0.00	0.00	0.00	0.00	0.00	0.00	0.00	0.00
31	1	0.00	0.00	0.00	0.00	0.00	0.00	0.00	0.00	0.00
32	1	0.00	0.00	0.00	-0.10	0.50	0.00	0.00	0.00	0.00

	82	83	84
	A"	A’	A"
Frequencies --	3028.7688	3036.2056	3041.0354
Red. masses --	1.1044	1.0597	1.1052
Frc consts --	5.9694	5.7557	6.0217
IR Inten --	2.3440	41.2012	0.0162
Raman Activ --	4.9306	4.7492	41.0942
Depolar (P) --	0.7500	0.0691	0.7500
Depolar (U) --	0.8571	0.1292	0.8571

Atom	AN	X	Y	Z	X	Y	Z	X	Y	Z
1	6	0.00	0.00	0.02	0.00	0.00	0.00	0.00	0.00	-0.02
2	6	0.00	0.00	-0.05	0.00	0.00	0.00	0.00	0.00	0.05
3	1	0.05	0.05	-0.09	0.00	0.00	0.00	-0.07	-0.07	0.13
4	1	-0.05	-0.05	-0.09	0.00	0.00	0.00	0.07	0.07	0.13
5	6	0.00	0.00	0.00	0.00	0.00	0.00	0.00	0.00	0.04

6	1	-0.16	-0.18	0.32	0.00	0.00	0.00	0.14	0.16	-0.28
7	1	0.16	0.18	0.32	0.00	0.00	0.00	-0.14	-0.16	-0.28
8	1	0.00	0.00	0.01	0.00	0.00	0.00	0.12	0.14	-0.24
9	1	0.00	0.00	0.01	0.00	0.00	0.00	-0.12	-0.14	-0.24
10	6	0.00	0.00	0.05	0.00	0.00	0.00	0.00	0.00	0.01
11	6	0.00	0.00	0.03	0.00	0.00	0.00	0.00	0.00	-0.03
12	1	-0.14	-0.16	-0.28	0.00	0.00	0.01	-0.05	-0.04	-0.08
13	1	0.14	0.16	-0.28	0.00	0.00	-0.01	0.05	0.04	-0.08
14	6	0.00	0.00	-0.03	0.00	0.00	0.00	0.00	0.00	-0.05
15	1	0.08	0.09	-0.16	0.01	0.01	-0.01	-0.08	-0.08	0.15
16	1	-0.08	-0.09	-0.16	0.01	0.01	0.01	0.08	0.08	0.15
17	6	0.00	0.00	-0.04	-0.01	-0.01	0.00	0.00	0.00	-0.02
18	1	-0.10	-0.11	0.20	0.02	0.03	-0.04	-0.14	-0.16	0.28
19	1	0.10	0.11	0.20	0.02	0.03	0.04	0.14	0.16	0.28
20	1	-0.11	-0.13	0.22	0.03	0.04	-0.07	-0.07	-0.08	0.14
21	1	0.11	0.13	0.22	0.03	0.04	0.07	0.07	0.08	0.14
22	6	0.00	0.00	0.02	-0.04	-0.04	0.00	0.00	0.00	0.02
23	6	0.00	0.00	0.00	-0.02	-0.03	0.00	0.00	0.00	-0.01
24	1	-0.05	-0.06	-0.10	0.23	0.26	0.48	-0.07	-0.08	-0.14
25	1	0.05	0.06	-0.10	0.23	0.26	-0.48	0.07	0.08	-0.14
26	1	-0.01	-0.02	0.03	0.14	0.17	-0.30	-0.05	-0.05	0.09
27	1	0.01	0.02	0.03	0.14	0.17	0.30	0.05	0.05	0.09
28	6	0.00	0.00	0.00	0.00	0.00	0.00	0.00	0.00	0.00
29	8	0.00	0.00	0.00	0.00	0.00	0.00	0.00	0.00	0.00
30	8	0.00	0.00	0.00	0.00	0.00	0.00	0.00	0.00	0.00
31	1	0.00	0.00	0.00	0.00	0.00	0.00	0.00	0.00	0.00
32	1	0.00	0.00	0.01	0.00	0.00	0.00	0.00	0.00	-0.01

	85	86	87
	A"	A"	A"
Frequencies --	3049.7286	3053.5077	3076.3471
Red. masses --	1.1024	1.1039	1.1041
Frc consts --	6.0409	6.0643	6.1564
IR Inten --	38.8602	91.0493	46.4576
Raman Activ --	23.3674	32.8893	2.8199
Depolar (P) --	0.7500	0.7500	0.7500
Depolar (U) --	0.8571	0.8571	0.8571

Atom	AN	X	Y	Z	X	Y	Z	X	Y	Z
1	6	0.00	0.00	0.01	0.00	0.00	-0.01	0.00	0.00	0.01
2	6	0.00	0.00	-0.02	0.00	0.00	0.01	0.00	0.00	0.00
3	1	0.04	0.04	-0.08	-0.04	-0.04	0.07	0.03	0.03	-0.05
4	1	-0.04	-0.04	-0.08	0.04	0.04	0.07	-0.03	-0.03	-0.05
5	6	0.00	0.00	-0.03	0.00	0.00	0.02	0.00	0.00	0.00
6	1	-0.06	-0.07	0.12	0.04	0.05	-0.09	0.01	0.01	-0.02
7	1	0.06	0.07	0.12	-0.04	-0.05	-0.09	-0.01	-0.01	-0.02
8	1	-0.09	-0.10	0.17	0.08	0.08	-0.15	0.00	0.00	0.00
9	1	0.09	0.10	0.17	-0.08	-0.08	-0.15	0.00	0.00	0.00
10	6	0.00	0.00	-0.03	0.00	0.00	0.04	0.00	0.00	0.00
11	6	0.00	0.00	-0.03	0.00	0.00	0.04	0.00	0.00	0.00
12	1	0.10	0.11	0.20	-0.11	-0.12	-0.21	0.00	0.01	0.01
13	1	-0.10	-0.11	0.20	0.11	0.12	-0.21	0.00	-0.01	0.01
14	6	0.00	0.00	-0.01	0.00	0.00	0.04	0.00	0.00	-0.01
15	1	-0.08	-0.09	0.16	0.12	0.13	-0.24	-0.01	-0.01	0.03
16	1	0.08	0.09	0.16	-0.12	-0.13	-0.24	0.01	0.01	0.03
17	6	0.00	0.00	0.01	0.00	0.00	0.03	0.00	0.00	-0.02
18	1	-0.04	-0.04	0.07	0.12	0.14	-0.24	-0.03	-0.04	0.07
19	1	0.04	0.04	0.07	-0.12	-0.14	-0.24	0.03	0.04	0.07
20	1	0.02	0.02	-0.05	0.07	0.09	-0.15	-0.07	-0.08	0.14
21	1	-0.02	-0.02	-0.05	-0.07	-0.09	-0.15	0.07	0.08	0.14

```
    22   6     0.00   0.00   0.04     0.00   0.00   0.01     0.00   0.00  -0.08
    23   6     0.00   0.00  -0.06     0.00   0.00  -0.05     0.00   0.00  -0.05
    24   1    -0.12  -0.13  -0.23    -0.04  -0.04  -0.08     0.23   0.26   0.46
    25   1     0.12   0.13  -0.23     0.04   0.04  -0.08    -0.23  -0.26   0.46
    26   1    -0.18  -0.22   0.37    -0.15  -0.18   0.30    -0.13  -0.17   0.27
    27   1     0.18   0.22   0.37     0.15   0.18   0.30     0.13   0.17   0.27
    28   6     0.00   0.00   0.00     0.00   0.00   0.00     0.00   0.00   0.00
    29   8     0.00   0.00   0.00     0.00   0.00   0.00     0.00   0.00   0.00
    30   8     0.00   0.00   0.00     0.00   0.00   0.00     0.00   0.00   0.00
    31   1     0.00   0.00   0.00     0.00   0.00   0.00     0.00   0.00   0.00
    32   1     0.00   0.00   0.00     0.00   0.00   0.00     0.00   0.00   0.00
                     88                     89                     90
                     A"                     A'                     A'
 Frequencies --  3077.5245              3081.9525              3759.3043
 Red. masses --     1.1025                 1.1009                 1.0645
 Frc consts  --     6.1521                 6.1607                 8.8632
 IR Inten    --    88.0220                45.7924                65.1459
 Raman Activ --    28.8920               108.6398               172.6592
 Depolar (P) --     0.7500                 0.5776                 0.2568
 Depolar (U) --     0.8571                 0.7323                 0.4086
  Atom  AN      X      Y      Z        X      Y      Z        X      Y      Z
     1   6     0.00   0.00  -0.09    -0.01  -0.09   0.00     0.00   0.00   0.00
     2   6     0.00   0.00  -0.03    -0.01  -0.01   0.00     0.00   0.00   0.00
     3   1    -0.28  -0.28   0.52     0.15   0.13  -0.29     0.00   0.00   0.00
     4   1     0.28   0.28   0.52     0.15   0.13   0.29     0.00   0.00   0.00
     5   6     0.00   0.00  -0.01     0.00   0.00   0.00     0.00   0.00   0.00
     6   1    -0.09  -0.10   0.18     0.03   0.03  -0.06     0.00   0.00   0.00
     7   1     0.09   0.10   0.18     0.03   0.03   0.06     0.00   0.00   0.00
     8   1    -0.03  -0.04   0.07     0.00   0.01  -0.01     0.00   0.00   0.00
     9   1     0.03   0.04   0.07     0.00   0.01   0.01     0.00   0.00   0.00
    10   6     0.00   0.00  -0.01     0.00   0.00   0.00     0.00   0.00   0.00
    11   6     0.00   0.00   0.00     0.00   0.00   0.00     0.00   0.00   0.00
    12   1     0.02   0.02   0.03     0.00   0.00   0.01     0.00   0.00   0.00
    13   1    -0.02  -0.02   0.03     0.00   0.00  -0.01     0.00   0.00   0.00
    14   6     0.00   0.00   0.00     0.00   0.00   0.00     0.00   0.00   0.00
    15   1    -0.01  -0.01   0.02     0.00   0.00   0.00     0.00   0.00   0.00
    16   1     0.01   0.01   0.02     0.00   0.00   0.00     0.00   0.00   0.00
    17   6     0.00   0.00   0.00     0.00   0.00   0.00     0.00   0.00   0.00
    18   1    -0.01  -0.01   0.01     0.00   0.00   0.00     0.00   0.00   0.00
    19   1     0.01   0.01   0.01     0.00   0.00   0.00     0.00   0.00   0.00
    20   1    -0.01  -0.01   0.02     0.00   0.00   0.00     0.00   0.00   0.00
    21   1     0.01   0.01   0.02     0.00   0.00   0.00     0.00   0.00   0.00
    22   6     0.00   0.00  -0.01     0.00   0.00   0.00     0.00   0.00   0.00
    23   6     0.00   0.00   0.00     0.00   0.00   0.00     0.00   0.00   0.00
    24   1     0.02   0.03   0.04     0.00   0.00   0.00     0.00   0.00   0.00
    25   1    -0.02  -0.03   0.04     0.00   0.00   0.00     0.00   0.00   0.00
    26   1    -0.01  -0.02   0.03     0.00   0.00   0.00     0.00   0.00   0.00
    27   1     0.01   0.02   0.03     0.00   0.00   0.00     0.00   0.00   0.00
    28   6     0.00   0.00   0.00     0.00   0.00   0.00     0.00   0.00   0.00
    29   8     0.00   0.00   0.00     0.00   0.00   0.00     0.06  -0.01   0.00
    30   8     0.00   0.00   0.00     0.00   0.00   0.00     0.00   0.00   0.00
    31   1     0.00   0.00   0.00     0.00   0.00   0.00    -0.99   0.11   0.00
    32   1     0.00   0.00  -0.02    -0.19   0.83   0.00     0.00   0.00   0.00
[...]
```

Appendix E

Raman scattering Matlab code

E.1 Shape parameters

The shape parameters are used in the local field correction as developed in section 5.3.2. The file name is `shapefactor.m`; as with all MATLAB functions, the file name is identical to the name of the function.

```
function [S] = shapefactor(r_1,r_2,r_3)
% The function SHAPEFACTOR computes the shape factors of an ellipsoid as
% used in local field corrections through numerical integration and scaling
% to ensure S_1 + S_2 + S_3 = 1.
%
% Raymond Rammeloo - 5 November 2018
%
% INPUT
% r_1, r_2, r_3  The three semiaxes of the ellipsoid, in a any unit.
%
% OUTPUT
% S              The shape factor for each axis of the ellipsoid in a
%                vector of size 3x1 as S = [S_1; S_2; S_3]

%Specify integration variable and range
u = 0:0.001:1000;

%Compute fuction and its numerical integration by summation
f_1 = .5*r_1*r_2*r_3./((u+r_1^2).*sqrt((u+r_1^2).*(u+r_2^2).*(u+r_3^2)));
S_1 = sum(f_1);
f_2 = .5*r_1*r_2*r_3./((u+r_2^2).*sqrt((u+r_1^2).*(u+r_2^2).*(u+r_3^2)));
S_2 = sum(f_2);
f_3 = .5*r_1*r_2*r_3./((u+r_3^2).*sqrt((u+r_1^2).*(u+r_2^2).*(u+r_3^2)));
S_3 = sum(f_3);

%Scale output vector so that S_1 + S_2 + S_3 = 1 is satisfied
S = [S_1; S_2; S_3]./(S_1 + S_2 + S_3);
```

E.2 The `pirs` function

This function performs the computational method developed in chapter 5. Its file name is `pirs.m`. It comprises the computation of shape factors. To save time, the function

may be adjusted to take the shape parameters (S_x, S_y, S_z) rather than the molecular radii (r_x, r_y, r_z) as input.

```
function [I_x, I_y, I_x_map, I_y_map, I_tot_map] = ...
         pirs(n,k_i_theta,psi,lambda_0_laser,z,MOL_ORIENTATION,...
         RAMANSHIFT,RAMANTENSOR_m,MOL_RADII_m,POLARTENSOR_m,NA,...
         OBJ_ORIENTATION,g,fig)
%
% The function PIRS models the detected polarised intensities from a Raman
% scatterer located at or near an interface in a user-specified
% experimental geometry. The detected intensities are given by the squared
% sum of the complex field amplitudes along the X and Y directions for all
% modelled rays within the observed field of view. The effects of the
% interface on the electromagnetic radiation is approximated by an
% optically thin film bounded by two infinite half-spaces (media) when the
% scatterer is located at the interface. However, when the scatterer is
% located away from said interface, two infinite half-spaces are considered
% and the refractive index of the intermediate layer should be the same as
% that of the lower medium. Local field correction is applied to the
% incident field, the induced dipole moment and the radiated Raman field.
% Lorentz reciprocity is used to obtain the far-field radiation of the
% effective Raman-induced dipole in both half-spaces.
%
% (c) Raymond X. Rammeloo, 2016-2019
% Version of 18 November 2019
%
% --- INPUT VARIABLES -----------------------------------------------------
% n         = 3x2 array containing the refractive indices of the three
%           layers at the incident wavelength (first column) and at the
%           Raman scattering wavelength (second column). The numbering is
%           along the +z-direction of the laser of reference (L-frame):
%               1 = substrate hemisphere material (z < 0),
%               2 = interfacial thin film (z = 0),
%               3 = lower material/medium (z > 0).
%           If only one column is provided, the same refractive indices are
%           used for both incident and Raman scattered light.
%
% k_i_theta = propagation angle of the incident laser beam in the L-frame,
%           taken from the +Z-direction in a right-handed rotation about
%           the +Y-axis, in the range 0-180 degrees.
%
% psi       = linear polarization direction of the incident laser beam,
%           measured anti-clockwise from the plane of incidence in the
%           range 0-90 degrees, with:
%                0 degrees = p-polarisation,
%               90 degrees = s-polarisation.
%
% lambda_0_laser = vacuum wavelength of the incident laser in nm.
%
% z         = position of the scattering molecule in the laser-frame as
%           (X,Y,Z) = (0,0,z) with z >= 0 in nm. If z = 0, a thin film may
%           be accommodated with a refractive index (n2) that differs from
%           those of the bounding media (n1, n3). However, if z > 0, n2
%           must be equal to n3 or an unphysical result is obtained.
%
% MOL_ORIENTATION = orientation of the scattering molecule in the L-frame,
%           a vector containing the 3 classical Euler angles alpha, beta
%           and gamma in degrees which specify the molecular orientation by
```

```
%           successive anticlockwise rotations of the molecular frame of
%           reference (m-frame) to the L-frame of reference with respect to
%           a space-fixed vector.
%
% RAMANSHIFT = the Stokes Raman shift of the modelled mode in 1/cm.
%
% RAMANTENSOR_m = the 3x3 Raman polarisability tensor of the scattering
%           moiety in the m-frame. It may be specified in any unit, the SI
%           has it in C/V*m^2.
%
% MOL_RADII_m = semi-axes of the molecular ellipsoid that specify the
%           ellipsoidal shape of the scattering molecule in nm. It is used
%           to implement the local field correction.
%
% POLARTENSOR_m = the 3x3 polarisability tensor of the scattering molecule
%           in the m-frame in C/V*m^2. It is used to implement the local
%           field correction.
%
% NA        = the numerical aperture of the microscope objective that
%           collects and collimates the Raman-scattered light.
%
% OBJ_ORIENTATION = the orientation of microscope objective in the L-frame,
%           a vector containing the 3 classical Euler angles alpha, beta
%           and gamma in degrees that specify the transformation from the
%           observation frame of reference (O-frame) to the L-frame by
%           successive anticlockwise rotations of the axes with respect to
%           a vector fixed in space.
%
% g         = number of nodes in the modelling grid along each axis X, Y of
%           the O-frame. The field due to the induced dipole is computed at
%           each grid node on the circular aperture of the objective lens.
%           The value of g should be chosen large enough to capture the
%           variation of the emited Raman field across said aperture.
%
% fig       = set to 1 to produce a figure of the polarised intensity
%           distributions over the modelling grid.
%
% --- OUTPUT ----------------------------------------------------------
% I_x       = the modelled irradiance recorded along the x-polarisation
%           axis in the O-frame in arbitrary units. It is computed from the
%           sum of the squared complex amplitudes of the collimated dipole
%           field along the O-frame x-axis at each modelling grid node.
%
% I_y       = as I_x but along the y-axis of the O-frame.
%
% I_x_map   = the intensities I_x in a square array of size g x g,
%           representing a top-view intensity map, looking down the z-axis
%           of the O-frame towards the origin where the Raman-scattering
%           molecule is located.
%
% I_y_map   = as I_x_map but with the I_y intensities in the array.
%
% --- FIGURE ----------------------------------------------------------
% One figures is produced if input variable fig is set to 1. The modelled
% polarised intensity distributions I_X_map and I_Y_map as well as their
% sum I_tot_map are plotted as a colour intensity map of the field of view
% after collimation by the objective.
```

```
%% -- I. CHECK FOR ERRORS IN INPUT VARIABLES -----------------------------
% The computation is stopped and an error message is presented if the input
% lies out of the intended range. The Euler angles are left without
% constraint.

% (1) Ensure six refractive indices are specified
if size(n,2) == 1
   n = [n n];
end

% (2) Check whether k_i_theta is in the correct range
% Note: || is the logic OR operator in Matlab.
if k_i_theta < 0 || k_i_theta > 180
     error(['Propagation angle of incident laser out of range.'...
                          'Value is restricted to 0 <= k_i_theta <= 180.'])
end

% (3) Check if thin-film approximation is correctly applied
if z == 0
elseif z < 0
     error('Molecular position z < 0, but is restricted to z >= 0.')
elseif n(2,1) == n(3,1) && n(2,2) == n(3,2)
else
    error(['Thin-film approximation does not apply.'...
                                     'For z > 0, n2 must be equal to n3.'])
end

% (4) Check if NA is positive and does not exceed maximum value of n_air
if NA < 0
    error('NA is negative, but must be 0 <= NA <= n_air.')
elseif NA > 1.0003
    error(['NA is larger than n of immersion medium (air).'...
                                       'Value must be 0 <= NA <= n_air.'])
end

% (5) Check whether g is a positive integer
if rem(g,1) ~= 0 || g <= 0
    error('Grid size g must be a positive integer.')
end

%% -- II. CALCULATE APPLIED FIELD AT MOLECULE IN LASER FRAME (E_app_L) ----
% A linearly polarised incoming laser beam at unity intensity is propagated
% to the location (0,0,z) of the molecule. The coupling factors F depend on
% the propagation angle of the laser beam in the L-frame.

% (1) Compute the p- and s-polarised components of incident field with the
% linearly polarised amplitude set to unity.
E_i_p = cosd(psi);
E_i_s = sind(psi);

% (2) Compute the coupling factors F, depending on the range of k_i_theta.
% The angles of incidence and transmission are in radians as required for
% complex calculations. The thin-film approximation is used in the F_z
% coupling factor. This is only relevant for z = 0 and n2 not equal to n3.
if k_i_theta <= 90
   % Zones I and II, laser incident on molecule through medium 1
   theta_i = pi/180*k_i_theta;
   theta_t = asin(n(1,1)/n(3,1)*sin(theta_i));
```

```
   t_p = (2*n(1,1)*cos(theta_i))/...
                              (n(3,1)*cos(theta_i) + n(1,1)*cos(theta_t));
   t_s = (2*n(1,1)*cos(theta_i))/...
                              (n(1,1)*cos(theta_i) + n(3,1)*cos(theta_t));
   PHASE = 2*pi*n(3,1)/lambda_0_laser*z*cos(theta_t);
   F_x = t_p*cos(theta_t)*exp(1i*PHASE); % 1i is the complex number
   F_y = t_s*exp(1i*PHASE);
   F_z = -(n(3,1)/n(2,1))^2*t_p*sin(theta_t)*exp(1i*PHASE);
else % k_i_theta > 90
   % Zone III, laser incident on molecule through medium 3
   theta_i = (180 - k_i_theta)*pi/180;
   theta_t = asin(n(3,1)/n(1,1)*sin(theta_i));
   r_p = (n(1,1)*cos(theta_i)-n(3,1)*cos(theta_t))/...
                                (n(1,1)*cos(theta_i)+n(3,1)*cos(theta_t));
   r_s = (n(3,1)*cos(theta_i)-n(1,1)*cos(theta_t))/...
                                (n(3,1)*cos(theta_i)+n(1,1)*cos(theta_t));
   PHASE = 2*pi*n(3,1)/lambda_0_laser*z*cos(theta_i);
   F_x = (-exp(-1i*PHASE) + r_p*exp(1i*PHASE))*cos(theta_i);
   F_y = exp(-1i*PHASE) + r_s*exp(1i*PHASE);
   F_z = -(n(3,1)/n(2,1))^2*(exp(-1i*PHASE) + r_p*exp(1i*PHASE))*...
                                                              sin(theta_i);
end

% (3) Compute the macroscopic applied field at the location of the molecule
% in the L-frame. Note that above the critical angle, E_app is an
% evanescent field. The p-polarised component then produces independent
% E_app_x and E_app_z components, with s always along y.
E_app_L = [F_x   0 ;
            0   F_y;
           F_z   0 ]*[E_i_p; E_i_s];

%% -- III. PROJECT APPLIED FIELD ONTO FRAME OF MOLECULE (E_app_m) ---------
% Given the orientation of the molecule through the input, we can find the
% transformation matrix between the L-frame of reference and the m-frame
% for a vector fixed in space. This matrix is then used to express the
% electric field at the molecule in the m-frame of reference.

% (1) Define the three Euler angles that give the orientation of the
% scatterer in the laboratory frame of reference in radians.
alpha = pi/180*MOL_ORIENTATION(1);
beta  = pi/180*MOL_ORIENTATION(2);
gamma = pi/180*MOL_ORIENTATION(3);

% (2) Define the transformation matrix T_L_to_m from molecule to laboratory
% frame of reference using these Euler angles. The inverse matrix T_L_to_m'
% effects the transformation from L to m-frame.
T_L_to_m = [cos(gamma)*cos(alpha)-sin(gamma)*cos(beta)*sin(alpha), ...
               cos(gamma)*sin(alpha)+sin(gamma)*cos(beta)*cos(alpha), ...
                                                    sin(gamma)*sin(beta);
           -sin(gamma)*cos(alpha)-cos(gamma)*cos(beta)*sin(alpha), ...
               cos(gamma)*cos(beta)*cos(alpha)-sin(gamma)*sin(alpha), ...
                                                    cos(gamma)*sin(beta);
                   sin(beta)*sin(alpha), -sin(beta)*cos(alpha), cos(beta)];

%(3) The applied field is now transformed onto the axes of the molecule to
% find the field E_app_m causing Raman scattering.
E_app_m = T_L_to_m*E_app_L;
```

```
%% -- IV. CALCULATION OF EFFECTIVE INDUCED DIPOLE IN L-FRAME (p_eff_L) ----
% The induced dipole arises from the Raman effect. We know the electric
% field at the molecule and its Raman tensor, both expressed in the
% scatterer frame of reference. The local field correction is applied using
% the molecular ellipsoidal shape and its polarisability in the m-frame.
% The shape parameters as well as the cavity and reaction field tensors are
% computed before the local field correction can be applied to obtain the
% effective Raman tensor in the m-frame. The induced dipole is then
% computed and transformed from the m-frame to the L-frame. The components
% of the obtained dipole vector p_eff_L are complex and may not be in
% phase.

% (1) Compute shape parameters S through numerical intergration and scaling
% to ensure S_x + S_y + S_z = 1. Shape parameters are included as a
% diagonal matrix for ease of computation of the local field correction.
r_x = MOL_RADII_m(1); % semi-axes of molecular ellipsoid in nm
r_y = MOL_RADII_m(2);
r_z = MOL_RADII_m(3);
u = 0:0.001:1000; % dummy integration variable
S_x = sum(.5*r_x*r_y*r_z./...
                        ((u+r_x^2).*sqrt((u+r_x^2).*(u+r_y^2).*(u+r_z^2))));
S_y = sum(.5*r_x*r_y*r_z./...
                        ((u+r_y^2).*sqrt((u+r_x^2).*(u+r_y^2).*(u+r_z^2))));
S_z = sum(.5*r_x*r_y*r_z./...
                        ((u+r_z^2).*sqrt((u+r_x^2).*(u+r_y^2).*(u+r_z^2))));
S = [S_x 0 0; 0 S_y 0; 0 0 S_z]./(S_x + S_y + S_z);

% (2) Compute cavity and reaction field tensors C_in and R_in for the
% incident light. The permittivity of medium 2 (surrounding the cavity) is
% given as a tensor for ease of computation.
IM = [1 0 0; 0 1 0; 0 0 1]; % 3x3 identity matrix
epsilon_in = IM*n(2,1)^2;
epsilon_0 = 8.854187817*10^(-12); % vacuum permittivity in C/V/m
C_in = epsilon_in/(epsilon_in - S*(epsilon_in - IM));
R_in = 3*S*(IM - S)*(epsilon_in - IM)/...
                    (4*pi*epsilon_0*r_x*r_y*r_z*10^(-27)*...
                                    (epsilon_in - S*(epsilon_in - IM)));

% (3) Compute reaction field tensor R_scat for scattered light
epsilon_scat = IM*n(2,2)^2;
R_scat = 3*S*(IM - S)*(epsilon_scat - IM)/...
                      (4*pi*epsilon_0*r_x*r_y*r_z*10^(-27)*....
                                    (epsilon_scat - S*(epsilon_scat - IM)));

% (4) The effective Raman tensor, considering the local field effect can
% now be given
RAMANTENSOR_eff_m = (IM + POLARTENSOR_m*R_scat)*RAMANTENSOR_m*...
                                          (C_in/(IM - R_in*POLARTENSOR_m));

% (5) The effective Raman-induced dipole in the L-frame p_eff_L is now
% given as a 3x1 column vector
p_eff_L = T_L_to_m'*RAMANTENSOR_eff_m*E_app_m;

%% -- V. DEFINE MODELLING GRID AT OBJECTIVE ENTRANCE ----------------------
% The collected Raman scattered radiation is modelled on a grid of nodes at
% the circular entrance to the microscope objective. The physical size of
% this grid is limited by the NA of the objective, while the modelling size
% is given as input variable g.
```

```
% (1) Find all grid coordinates falling withing the field of view in the
% O-frame of reference. The coordinates of the grid run from -R_obj to
% +R-obj along the x and y directions while z = 1 for each grid node Q.
% R_obj is de radius of the objective in units of its working distance. The
% number of nodes g along x and y is given as input, resuling in a square
% grid to represent the circular aperture. All nodes for which
% x^2 + y^2 =< R_obj^2 fall within view of the objective, those outside the
% view are discarded. Each grid node in our view Q_O, given by GRID through
% the appropriate index in RAY_index, is specified in O-frame coordinates.
% The unit of length is the working distance of the objective, so z = 1 for
% each Q.
n_air = 1.0003;
if g == 1
   Q_O = [0 0 1]';
   RAY_index = 1;
   NQ = 1;
else
   R_obj = tan(asin(NA/n_air));
   GRID_X = repmat(R_obj.*(2.*((1:g)-1)/(g-1)-1),g,1);
   GRID_Y = repmat((R_obj.*(2.*((1:g)-1)/(g-1)-1))',1,g);
   [RAY_index] = find(GRID_X.^2 + GRID_Y.^2 <= R_obj^2);
   NQ = numel(RAY_index);
   Q_O = [GRID_X(RAY_index) GRID_Y(RAY_index) ones(length(RAY_index),1)]';
end

% (2) The grid nodes Q are now expressed in L-frame coordinates through a
% transformation over the Euler angles of OBJ_ORIENTATION, which specify
% the O-frame relative to the L-frame. We define the transformation matrix
% T_L_to_m from m-frame to L-frame using these Euler angles. The inverse
% matrix T_L_to_m' effects the transformation from L-frame to m-frame.
alpha = pi/180*OBJ_ORIENTATION(1);
beta  = pi/180*OBJ_ORIENTATION(2);
gamma = pi/180*OBJ_ORIENTATION(3);
T_L_to_O = [cos(gamma)*cos(alpha)-sin(gamma)*cos(beta)*sin(alpha), ...
               cos(gamma)*sin(alpha)+sin(gamma)*cos(beta)*cos(alpha), ...
                                                    sin(gamma)*sin(beta);
           -sin(gamma)*cos(alpha)-cos(gamma)*cos(beta)*sin(alpha), ...
               cos(gamma)*cos(beta)*cos(alpha)-sin(gamma)*sin(alpha), ...
                                                    cos(gamma)*sin(beta);
                   sin(beta)*sin(alpha), -sin(beta)*cos(alpha), cos(beta)];
Q_L = T_L_to_O'*Q_O;

% (3) The grid nodes in L-frame spherical coordinates are given in Q_Lsph
% as [rho; theta; phi] for each grid node within view of the objective. The
% quandrant of the arctan function is taken into acccount with Matlab
% in-built function atan2, in which the range of phi is from -pi to +pi.
% This range is brought into our range of 0-2pi by adjusting the negative
% range of phi from (-pi to 0) to (+2pi to +pi).
Q_Lsph = [sqrt(sum(Q_L.^2,1));
          acos(Q_L(3,:)./sqrt(sum(Q_L.^2,1)));
          atan2(Q_L(2,:),Q_L(1,:))];
Q_Lsph(3,Q_Lsph(3,:) < 0)=2*pi+Q_Lsph(3,Q_Lsph(3,:) < 0);

%% -- VI. COMPUTE THE DIPOLE FIELD AT OBJECTIVE (E_dip_O)------------------
% The Lorentz reciprocity theorem is employed to calculate the dipole
% field amplitude E_dip_Q = [E_p; E_s; 0] at each grid node relative to the
% plane of incidence that includes the L-frame z-axis and the node Q. The
```

```
% coupling factors of the dipole far-field into the surrounding media are
% derived from the coupling of a plane wave incident from point Q onto the
% dipole components parallel and orthogonal to this plane of incidence. The
% cavity field is also taken into account at this stage as a further local
% field correction for the Raman emission. The computation is performed for
% each grid node Q in a for-loop. The form of the coupling factors depends
% on the polar angle Q_theta, that expresses from which side of the
% interface the light is coming (following reciprocity, this is the
% direction in which the scattered radiation is propagating). The
% wavelength of the Raman-scattered light and the refractive indices at
% that wavelength are employed.

% (1) The vacuum wavelength and angular frequency of the Raman-scattered
% light depends on the incident laser wavelength and the Raman shift, both
% given as input. These values are used for to compute the coupling
% factors.
c = 299792458; % vacuum speed of light in m/s
lambda_0_scat = n_air/(n_air/lambda_0_laser - 10^(-7)*RAMANSHIFT); % in nm
omega_Raman = 2*pi*c/lambda_0_scat; % in 1/s

% (2) Start loop over all grid nodes Q to computed E_dip_0 at each Q
E_dip_0 = zeros(3,NQ); % pre-allocate array for speed
for k = 1:NQ
   Q_rho_L = Q_Lsph(1,k);
   Q_theta_L = Q_Lsph(2,k);
   Q_phi_L = Q_Lsph(3,k);

% (3) Compute the coupling factors for a plane wave incident onto the
% molecule, which are then used through reciprocity to obtain the coupling
% factors for the far-field radiation of the Raman-induced dipole. The
% scattered wavelength and refractive indices at that wavelength are used.
 if Q_theta_L < pi/2
   % Zone III, the far-field radiation of the dipole into medium 3,
   % obtained from a plane wave incident from medium 3 through reciprocity
   theta_i = Q_theta_L;
   theta_t = asin(n(3,2)/n(1,2)*sin(theta_i));
   r_p = (n(1,2)*cos(theta_i) - n(3,2)*cos(theta_t))/...
                              (n(1,2)*cos(theta_i) + n(3,2)*cos(theta_t));
   r_s = (n(3,2)*cos(theta_i) - n(1,2)*cos(theta_t))/...
                              (n(3,2)*cos(theta_i) + n(1,2)*cos(theta_t));
   PHASE = 2*pi*n(3,2)/lambda_0_scat*z*cos(theta_i);
   F_x = (-exp(-1i*PHASE) + r_p*exp(1i*PHASE))*cos(theta_i);
   F_y = exp(-1i*PHASE) + r_s*exp(1i*PHASE);
   F_z = (n(3,2)/n(2,2))^2*(exp(-1i*PHASE) + r_p*exp(1i*PHASE))*...
                                                              sin(theta_i);
 else % Q_theta_L >= pi/2
   % Zones I and II, the far-field radiation of the dipole into medium 1,
   % obtained from a plane wave incident from medium 1 through reciprocity
   theta_i = pi - Q_theta_L;
   theta_t = asin(n(1,2)/n(3,2)*sin(theta_i));
   t_p = (2*n(1,2)*cos(theta_i))/...
                              (n(3,2)*cos(theta_i) + n(1,2)*cos(theta_t));
   t_s = (2*n(1,2)*cos(theta_i))/...
                              (n(1,2)*cos(theta_i) + n(3,2)*cos(theta_t));
   PHASE = 2*pi*n(3,2)/lambda_0_scat*z*cos(theta_t);
   F_x = t_p*cos(theta_t)*exp(1i*PHASE);
   F_y = t_s*exp(1i*PHASE);
   F_z = (n(3,2)/n(2,2))^2*t_p*sin(theta_t)*exp(1i*PHASE);
```

```
 end

% (4) The dipole field E_dip_Q = [E_p; E_s] along the p and s directions of
% the Q-frame are computed using the coupling factors just derived through
% Lorentz reciprocity, using the appropriate prefactor and using the
% projection of p_eff_L onto the plane of incidence spanned by Q and the z-
% axis of the L-frame. The p and s directions are defined relative to this
% plane.
   T_L_to_q = [ cos(Q_phi_L) sin(Q_phi_L) 0;
               -sin(Q_phi_L) cos(Q_phi_L) 0;
                           0          0     1];
   C_scat_m = epsilon_scat/(epsilon_scat - S*(epsilon_scat - IM));
   C_scat_q = T_L_to_q*T_L_to_m'*C_scat_m*T_L_to_m*T_L_to_q';
   E_dip_Q = 1/(4*pi*epsilon_0*Q_rho_L)*(omega_Raman/c)^2*...
                                [-F_x  0  -F_z;
                                   0  F_y   0 ]*C_scat_q'*T_L_to_q*p_eff_L;

% (5) The field due to the Raman-induced dipole at Q is now given in
% Cartesian coordinates of the Q-frame as E_dip_Q = [E_p; E_s; 0]. This
% expression is transformed to the L-frame with transformation matrix
% T_Q_to_L, specified by the spherical coordinates of Q in the L-frame. The
% result is then transformed to the O-frame with T_L_to_O, which was
% computed in section V and which is the same matrix for each point Q,
% whereas T_Q_to_L varies with the location of Q.
   T_Q_to_L = [cos(Q_phi_L) -sin(Q_phi_L) 0;
               sin(Q_phi_L)  cos(Q_phi_L) 0;
                      0             0     1]*...
                                    [ cos(Q_theta_L) 0 sin(Q_theta_L);...
                                             0       1        0      ;...
                                     -sin(Q_theta_L) 0 cos(Q_theta_L)];
   E_dip_O(:,k) =  T_L_to_O*T_Q_to_L*[E_dip_Q; 0];
end

%% -- VII. COLLIMATE DIPOLE FIELD AT OBJECTIVE (E_col_O) ------------------
% Effect collimation of the dipole field at each Q by rotating over angle
% col_angle about axis col_axis to bring the propagation direction of the
% dipole field along the +z-axis of the O-frame.

% (1) Specify unit vectors zu_O and Qu_O
zu_O = [0 0 1]'; % unit vector +z in O-frame
E_col_O = zeros(3,NQ); % pre-allocate array for speed
for k = 1:NQ % Loop over all grid nodes Q
    Qu_O = Q_O(:,k)/norm(Q_O(:,k)); % unit vector pointing from origin to
                                    % point Q in the O-frame

% (2) Compute collimation angle and axis for each point Q
    col_angle = acos(dot(zu_O,Qu_O));
    if col_angle == 0
    col_axis = [0 0 0]';
    else
    col_axis = cross(Qu_O,zu_O)/sin(col_angle); % axis specified in O-frame
    end

% (3) Perform rotation that represents the collimation action with
% Rodrigues' rotation formula
    E_col_O(:,k) = E_dip_O(:,k)*cos(col_angle) +...
                cross(col_axis,E_dip_O(:,k))*sin(col_angle) +...
                   col_axis*dot(col_axis,E_dip_O(:,k))*(1-cos(col_angle));
```

```
end

% (4) Any NaN (not a number) entries in the result are set to zero, as this
% implies that no dipole was induced in the first place
E_col_O(isnan(E_col_O)) = 0;

%% -- VIII. COLLECTION POLARISATION & DETECTION (OUTPUT) ------------------
% The collection polarisation can be set along either the x or y axis of
% the O-frame, both of which are calculated. The detected intensity at each
% grid node is given by the squared absolute amplitude along the selected
% direction. For complex amplitudes, the function abs takes the complex
% modulus. The intensity is scaled to the number of grid nodes NQ for
% comparison of modelling results obtained with different grid sizes.

% (1) The intensity map on the square modelling grid, viewed from the
% objective towards the molecule (i.e. down the z-axis of the O-frame).
I_x_map = zeros(g,g);
I_x_map(RAY_index) = 0.5*n_air*epsilon_0*c*(abs(E_col_O(1,:)).^2);
I_y_map = zeros(g,g);
I_y_map(RAY_index) = 0.5*n_air*epsilon_0*c*(abs(E_col_O(2,:)).^2);
I_tot_map = I_x_map + I_y_map;

% (2) The sum over all grid nodes gives the total polarised intensity. This
% is divided by the number of grid nodes in the field of view to facilitate
% comparison between modelling runs of varying grid size.
I_x = sum(sum(I_x_map))/NQ;
I_y = sum(sum(I_y_map))/NQ;

%% -- IX. FIGURE (OUTPUT) -------------------------------------------------
% The figure is produced only if fig == 1. It presents the three intensity
% maps in one figure with a single intensity colorbar.
if fig == 1
caxis_max = max(max([I_x_map; I_y_map; I_tot_map]));
set(groot,'defaulttextinterpreter','latex');
figure('name','I_map','Color','w',...
                                'units','centimeters','position',[3 3 20 7])
s1 = subplot(1,3,1);
    imagesc(I_x_map)
    colormap(hot)
    xlabel('$x^\mathsf{O}$-axis')
    ylabel('$y^\mathsf{O}$-axis')
    title(['$I_x = $ ' num2str(I_x,3)])
    caxis([0 caxis_max]);
    set(s1,'XTick',[],'YTick',[])
    set(s1,'units','centimeters','position',[1.5 1 5 5])
s2 = subplot(1,3,2);
    imagesc(I_y_map)
    title(['$I_y = $ ' num2str(I_y,3)])
    caxis([0 caxis_max]);
    set(s2,'XTick',[],'YTick',[])
    set(s2,'units','centimeters','position',[7 1 5 5])
s3 = subplot(1,3,3);
    imagesc(I_tot_map)
    title(['$I_x + I_y = $ ' num2str(I_x+I_y,3)])
    caxis([0 caxis_max]);
    set(s3,'XTick',[],'YTick',[])
    set(s3,'units','centimeters','position',[12.5 1 5 5])
colorbar('units','centimeters','Position',[18 1 .5 5],...
```

```
                                    'axislocation','out','ticklength',0.03)
end
```

E.3 Example script

The example given below was used to compute the relative intensities of Raman-scattering of the sulfate v_1 mode as a function of laser polarisation angle ψ. The results are presented in figure 6.9. The file name of the script is `example_script_sulfate_psi.m`.

```
% Sulfate anion v_1 Raman mode at fused silica surface

%% (1) Compute intensities for varying incident polarisation angle psi

n_sul = 1.3368; % 0.3 molar ammonium sulfate in water used in KTH
nn = [1.4607 1.4594
      n_sul  n_sul
      n_sul  n_sul];
k_i_theta = 75; % in degrees
NA = 0.55;
RAMANTENSOR_m = -16.1e-42*eye(3); % sulfate v_1 mode, result from Gaussian
lambda_0_laser = 532; % in nm
MOL_ORIENTATION = [0 0 0]; % isotropic scatterer, so orientation irrelevant
RAMANSHIFT = 980; % in 1/cm
MOL_RADII_m = 0.30268*[1 1 1]; % in nm
POLARTENSOR_m = -1.649e-41*48.549*eye(3); % in SI units
OBJ_ORIENTATION = [0, 180, 0]; % in degrees
fig = 0;
z = 0;
g = 15; % optimised value for speed and sufficient precision

psi = 0:1:90; % in degrees

%Compute absolute and relative intensities at each value of psi
IM_psi = zeros(2,numel(psi)); % pre-allocate for speed
IM_psi_rel = zeros(2,numel(psi));
for m = 1:numel(psi) %loop over psi
   [IM_psi(1,m), IM_psi(2,m), ~] = pirs(nn,k_i_theta,psi(m),...
     lambda_0_laser,z,MOL_ORIENTATION,RAMANSHIFT,...
      RAMANTENSOR_m,MOL_RADII_m,POLARTENSOR_m,NA,OBJ_ORIENTATION,g,fig);
   IM_psi_rel(:,m) = IM_psi(:,m)./sum(IM_psi(:,m));
end

%% (2) Figure of absolute and relative intensities vs psi
set(groot,'defaulttextinterpreter','latex');
figure
subplot(1,2,1)
hold on; box on;
plot(psi,IM_psi(1,:),'-','color',[255,0,0]./255,'linewidth',2); %x
plot(psi,IM_psi(2,:),'-','color',[0,0,0]./255,'linewidth',2); %y
axis([min(psi) max(psi) 0 max(max(IM_psi))])
xlabel('Incident polarisation angle $\psi$ / $^\circ$',...
    'interpreter','latex','fontsize',12)
ylabel('Modelled intensity / a.u.','interpreter','latex','fontsize',12)
legend({'$I_x$','$I_y$'},'location','east',...
    'interpreter','latex','fontsize',12)
subplot(1,2,2)
```

```
hold on; box on;
plot(psi,IM_psi_rel(1,:),'-','color',[255,0,0]./255,'linewidth',2); %x
plot(psi,IM_psi_rel(2,:),'-','color',[0,0,0]./255,'linewidth',2); %y
axis([min(psi) max(psi) 0 1])
xlabel('Incident polarisation angle $\psi$ / $^\circ$',...
    'interpreter','latex','fontsize',12)
ylabel('Relative intensity','interpreter','latex','fontsize',12)
legend({'$I_x$','$I_y$'},'location','east',...
    'interpreter','latex','fontsize',12)

%% (3) Figure of relative intensities from model and experiment
% data 20170324/022-035
psi_exp = (0:15:90)';
IE_psi = 1000*[0.3749 0.3724 0.2916 0.2004 0.1736 0.0817 0.0267;
               0.1970 0.2930 0.5446 0.9009 1.3099 1.6524 1.8460];
IE_psi_rel = [0.6555 0.5596 0.3487 0.1819 0.1170 0.0471 0.0143;
              0.3445 0.4404 0.6513 0.8181 0.8830 0.9529 0.9857];

figure
hold on; box on;
plot(psi,IM_psi_rel(1,:),'-r','linewidth',1); %x
plot(psi,IM_psi_rel(2,:),'-k','linewidth',1); %y
plot(psi_exp,IE_psi_rel(1,:),'xr','linewidth',2); %x
plot(psi_exp,IE_psi_rel(2,:),'ok','linewidth',2); %y
axis([0 90 0 1])
xlabel('Incident polarisation angle $\psi$ / $^\circ$',...
    'interpreter','latex','fontsize',12)
ylabel('Relative intensity','interpreter','latex','fontsize',12)
legend({'$I_x$ model','$I_y$ model','$I_x$ exp.','$I_y$ exp.'},...
    'location','east','interpreter','latex','fontsize',12)
```

Appendix F

Image analysis

Microscopy images of section 7.1 are analysed by the following method. In these images, the contact spot between a mating flat and spherical surface is seen (figure 7.2) as a circular dark area. In this area, the white light illumination passes through the glass-on-glass contact, whereas it reflects off the glass-air interfaces formed outside the contact area. The size of the contact spot is a measure of the contact pressure, which we aim to derive reproducibly here.

The method centres on fitting a circle through the edges of the observed contact spot. This may be performed by manually selecting points in the images or by an automated procedure. Both are implemented in the MATLAB script presented below. The manual procedure is favoured for images that include distortions, such as those analysed here. Figure F.1 presents the fitting result for contact spot 7 of the dataset presented in chapter 7. The circular fit was consistently applied around the first inflection point from the centre of the circle towards its edge in all seven contact spots. Once a radius is found, expressed in pixels, it is converted to physical dimensions by a magnification factor. In our analysis, a value of 1.64 μm per pixel was used.

Matlab script

```
% A script to analyse microscope images of the contact area between a
% sphere and a flat surface
% INPUT  - a bmp file from the microscope camera
%        - when running the script, you will be prompted to provide the
%          area of the image that includes the central dark spot. First
%          click at the approximate centre of the contact spot and with a
%          second click provide an outer radius from said centre to define
%          the image area used in the algorithm.
% OUTPUT - figure with the image, selected area and fitted circle
%        - figure with the X and Y cross-sections of the image through the
%          centre of the contact area
%        - derived contact pressure
%
% (c) Raymond X. Rammeloo, 2018

%% Process image data
%import bitmap file manually into Matlab workspace
```

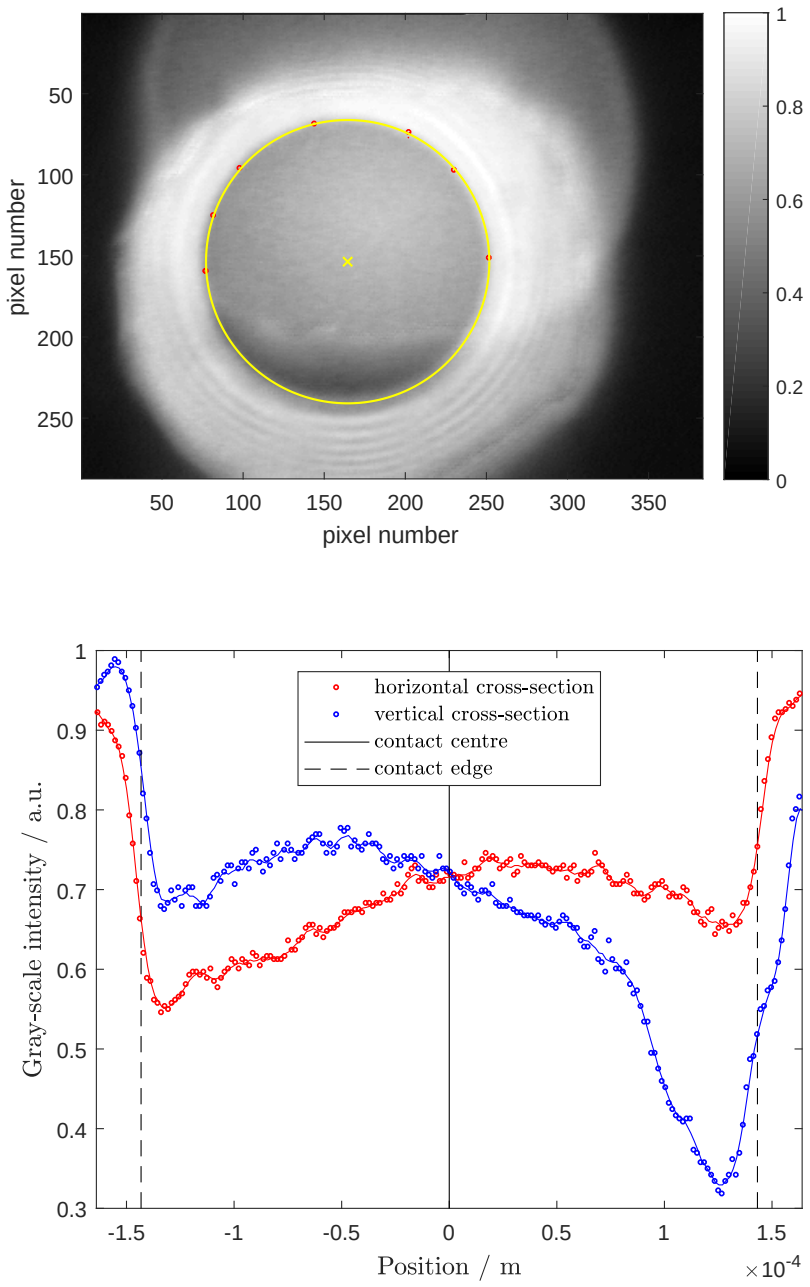

Figure F.1: Analysis of the microscopy image of contact spot 7 from the dataset analysed in chapter 7. Top image: a circle (yellow) is fitted through eight manually selected points (red) at the edges of the contact area. Bottom plot: horizontal and vertical cross-sections through the centre of the fitted circle are computed to assess their accuracy.

```
data = spot7;
%format to double-precision numbers rather than bits
image = double(data)./255;
%produce gray scale image using the blue colour only and scale the
%intensity to a maximum of 1
I = sqrt(image(:,:,3).^2)./max(max(sqrt(image(:,:,3).^2)));

%% Choose manual or automatic circle fitting
manual = 1; %1 for manual, 0 for automatic
MAGNIFICATION = 1.64e-6; % meter per pixel from calibration of camera image

%% Extract circular contact spot from microscope image
fig1 = figure('name','Contact image analysis');
imagesc(I)
axis image; caxis([0 max(max(I))])
colormap gray; colorbar
set(fig1,'windowstyle','docked')
hold on

if manual ==0
%Select relevant area of image in which the central dark spot is situated
%with the crosshairs:
% - first, the approximate centre of the central dark spot
% - second, a point that defines a circular ring encompassing the processed
% part of the image
[X, Y] = ginput(2);
selection_centre = [round(X(1)) round(Y(1))];
selection_edge = [ceil(X(2)) ceil(Y(2))];
selection_radius = norm(selection_edge-selection_centre);
selection = [selection_centre(1) + selection_radius*cos(0:0.01:2*pi) ;
             selection_centre(2) + selection_radius*sin(0:0.01:2*pi)]';
%Draw selected area in figure
plot(selection(:,1),selection(:,2),'-r','LineWidth',1)
%Obtain X and Y pixel coordinates
[data_xx, data_yy] = meshgrid(1:size(I,2),1:size(I,1));
selection = zeros(size(I));
selection(((data_xx-selection_centre(1)).^2 ...
             + (data_yy-selection_centre(2)).^2) < selection_radius^2) = 1;
selection_X = data_xx(selection == 1);
selection_Y = data_yy(selection == 1);

%Assign points that are below an intensity threshold that includes the
%central dark spot and plot these in the image
INTmin = min(min(I(selection == 1)));
INTmax = max(max(I(selection == 1)));
intensity_threshold = INTmin + 0.2*(INTmax - INTmin);
[Y_threshold, X_threshold] = find( I < intensity_threshold );
%Remove coordinates of pixels that lie outside the selected circle
disregard = find(((X_threshold-selection_centre(1)).^2 ...
             + (Y_threshold-selection_centre(2)).^2) > selection_radius^2);
X_threshold(disregard) = [];
Y_threshold(disregard) = [];
plot(X_threshold,Y_threshold,'.r','Markersize',1);

elseif manual == 1
% Manual selection of 8 points on the edge of the dark spot at the user's
% discretion
[X_threshold,Y_threshold] = ginput(8);
```

```
plot(X_threshold,Y_threshold,'.r','Markersize',1);
end

%Determine the convex hull (or envelope) that encompasses all points below
%the threshold and use this to determine the edge of the contact area
EDGE_POINTS = convhull(X_threshold,Y_threshold);
EDGE_X = X_threshold(EDGE_POINTS);
EDGE_Y = Y_threshold(EDGE_POINTS);
plot(EDGE_X,EDGE_Y,'or','Markersize',2);

%Fit a circle through the edge coordinates and extract its radius (based on
%the circfit function by Izhak Bucher of 25/10/1991)
a = [EDGE_X EDGE_Y ones(size(EDGE_X))] \ [-(EDGE_X.^2 + EDGE_Y.^2)];
X_centre = -.5*a(1); %position in pixel units
Y_centre = -.5*a(2);
R = sqrt((a(1)^2 + a(2)^2)/4 - a(3)); %radius in pixel units

%Draw fitted circle and its centre into image
CIRCLE = [X_centre + R*cos(0:0.01:2*pi) ; Y_centre + R*sin(0:0.01:2*pi)]';
plot(CIRCLE(:,1),CIRCLE(:,2),'-y','LineWidth',1)
plot(X_centre,Y_centre,'xy','Markersize',6,'Linewidth',1)

%% Plot cross-section of contact through its centre
fig2 = figure('name','contact cross-section');
set(fig2,'windowstyle','docked')
hold on; box on
[pixels_Y, pixels_X] = size(I);
%centre of the horizontal axis is the centre of the fitted circle
Xaxis_horizontal = ((1:pixels_X)' - X_centre).*MAGNIFICATION;
Xaxis_vertical = ((1:pixels_Y)' - Y_centre).*MAGNIFICATION;
%horizontal cross-section, along X-direction
plot(Xaxis_horizontal,I(round(Y_centre),:),'or','Markersize',2);
%vertical cross-section, along Y-direction
plot(Xaxis_vertical,I(:,round(X_centre)),'ob','Markersize',2);
%include vertical lines to indicate centre and edge of the fitted circle
plot([0 0],[0 1],'-k')
plot([-R*MAGNIFICATION -R*MAGNIFICATION],[0 1],'--k')
plot([R*MAGNIFICATION R*MAGNIFICATION],[0 1],'--k')
%include smoothed lines, 5-point moving average
plot(Xaxis_horizontal,smooth(I(round(Y_centre),:),5,'moving'),'-r');
plot(Xaxis_vertical,smooth(I(:,round(X_centre)),5,'moving'),'-b');
axis([-100*MAGNIFICATION 100*MAGNIFICATION 0.5 1])
xlabel('Position / m','fontsize',10,'interpreter','latex')
ylabel('Gray-scale intensity / a.u.','fontsize',10,'interpreter','latex')
legend({'horizontal cross-section','vertical cross-section'...
    'contact centre','contact edge'},'fontsize',10,...
    'interpreter','latex','Location','south')

%% Compute mean and central normal contact pressure for the sphere-on-flat
%Compute diameter of the contact spot in meters
CONTACT_DIAMETER = 2*R*MAGNIFICATION; % in meter

%Use Hertzian contact mechanics to compute the normal mean and central
%pressure in the contact
E = 34.451e9; %composite modulus of SF10 and fused silica in contact / Pa
R_sphere = 5e-3; %radius of curvature of the fused silica sphere / m
P_mean = (2*E*CONTACT_DIAMETER) / (3*pi*R_sphere); %mean pressure / Pa
P_centre = CONTACT_DIAMETER*E / (pi*R_sphere); %pressure in centre / Pa
```

Appendix G

Supplementary results

G.1 Chapter 4

G.1.1 Phenyl breathing mode in the bond-polarisability model

Of particular interest is the symmetric breathing mode of the benzene ring, in its pure form or in a phenyl derivative such as toluene. It gives rise to a strong polarised Raman band that Raman himself used to demonstrate the effect [59]. The polarisability of each C−H bond can be given in the bond frame of reference b as

$$\boldsymbol{\alpha}^{\mathsf{b}}_{\mathrm{C-H}} = \begin{pmatrix} \alpha_{\parallel} & 0 & 0 \\ 0 & \alpha_{\perp,ip} & 0 \\ 0 & 0 & \alpha_{\perp,oop} \end{pmatrix} \tag{G.1}$$

with component $\alpha_{\parallel}$ parallel to the bond axis $\hat{\mathbf{x}}^{\mathsf{b}}$ and the two components $\alpha_{\perp}$ in plane or out-of-plane with respect to the plane of the molecule (see figure G.1). The choice of axes is such that the transformation from the bond frame of reference to that of the functional group involves just one elementary rotation.

The bond polarisability tensor $\boldsymbol{\alpha}^{\mathsf{g}}_{\mathrm{C-H}}$ in the functional group frame of reference g is given through equation 4.2 where the transformation $\mathbf{T}_{\mathsf{b}\to\mathsf{g}}$ is effected by an active

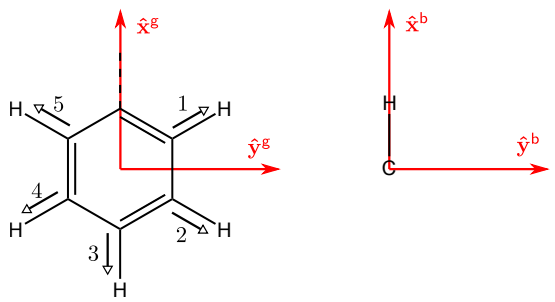

Figure G.1: The symmetric phenyl ring breathing mode (open arrows) and choice of axes in the functional group (left) and bond (right) frames of reference.

anticlockwise rotation about the common z axis

$$\mathbf{T}_{\mathsf{b}\to\mathsf{g}} = \mathbf{R}_z(\phi)^{-1} = \mathbf{R}_z(-\phi) = \begin{pmatrix} \cos\phi & -\sin\phi & 0 \\ \sin\phi & \cos\phi & 0 \\ 0 & 0 & 1 \end{pmatrix} \tag{G.2}$$

with rotation matrix defined in equation 2.12. This definition effects an anticlockwise rotation of the axes with a vector fixed in space, so its inverse (equivalent to a negative rotation angle) has to be employed to effect an anticlockwise rotation of a vector in a fixed set of axes. The angle ϕ takes the place of the first or third Euler angle (the other two being zero) and specifies the orientation of the bond in the plane of the molecule. The bond polarisability in the molecular frame of reference can now be given as

$$\begin{aligned} \boldsymbol{\alpha}^{\mathsf{g}}_{\mathrm{C-H}} &= \mathbf{R}_z(-\phi)\boldsymbol{\alpha}^{\mathsf{b}}_{\mathrm{C-H}}\mathbf{R}_z(\phi) \\ &= \begin{pmatrix} \cos\phi & -\sin\phi & 0 \\ \sin\phi & \cos\phi & 0 \\ 0 & 0 & 1 \end{pmatrix} \begin{pmatrix} \alpha_{\parallel} & 0 & 0 \\ 0 & \alpha_{\perp,ip} & 0 \\ 0 & 0 & \alpha_{\perp,oop} \end{pmatrix} \begin{pmatrix} \cos\phi & \sin\phi & 0 \\ -\sin\phi & \cos\phi & 0 \\ 0 & 0 & 1 \end{pmatrix} \\ &= \begin{pmatrix} \alpha_{\parallel}\cos^2\phi + \alpha_{\perp,ip}\sin^2\phi & (\alpha_{\parallel} - \alpha_{\perp,ip})\sin\phi\cos\phi & 0 \\ (\alpha_{\parallel} - \alpha_{\perp,ip})\sin\phi\cos\phi & \alpha_{\parallel}\sin^2\phi + \alpha_{\perp,ip}\cos^2\phi & 0 \\ 0 & 0 & \alpha_{\perp,oop} \end{pmatrix} \end{aligned} \tag{G.3}$$

The orientation of the C−H bonds in the molecule are given by its equilibrium geometry. The values for the five bonds (numbered from 1 to 5 in figure G.1) are $\phi_1 = 60°$, $\phi_2 = 120°$, $\phi_3 = 180°$, $\phi_4 = 240°$ and $\phi_5 = 300°$. The normal coordinate Q_{br} of the breathing mode br describes the simultaneous stretching of the five C−H bonds

$$Q_{\mathsf{br}}(t) = q_1(t) + q_2(t) + q_3(t) + q_4(t) + q_5(t) \tag{G.4}$$

where the motions of all bonds are in-phase with equal amplitudes. This means that the values of the bond length coordinates q are assumed to be identical at all times t

$$q_1(t) = q_2(t) = q_3(t) = q_4(t) = q_5(t) \tag{G.5}$$

which requires that

$$q_1 = q_2 = q_3 = q_4 = q_5 = \frac{Q_{\mathsf{br}}}{\sqrt{5}} \tag{G.6}$$

to ensure normalisation of the normal mode amplitude Q_{br}. The polarisability tensor for the vibrational mode is now computed through the sum of the individual bond polaris-

abilities in the group frame of reference, obtaining

$$\begin{aligned}\boldsymbol{\alpha}^{\mathsf{g}}_{\mathsf{br}} &= \frac{Q_{\mathsf{br}}}{\sqrt{5}}\left(\boldsymbol{\alpha}^{\mathsf{m}}_1 + \boldsymbol{\alpha}^{\mathsf{m}}_2 + \boldsymbol{\alpha}^{\mathsf{m}}_3 + \boldsymbol{\alpha}^{\mathsf{m}}_4 + \boldsymbol{\alpha}^{\mathsf{m}}_5\right) \\ &= \frac{Q_{\mathsf{br}}}{\sqrt{5}}\begin{pmatrix} 2\alpha_{\parallel} + 3\alpha_{\perp,ip} & 0 & 0 \\ 0 & 3\alpha_{\parallel} + 2\alpha_{\perp,ip} & 0 \\ 0 & 0 & 5\alpha_{\perp,oop} \end{pmatrix}\end{aligned} \tag{G.7}$$

which forms a tensor of elliptical symmetry. It has three unique non-zero components ($\alpha_{xx} \neq \alpha_{yy} \neq \alpha_{zz}$) and no off-diagonal components. The polarisability of bond 3 does not contribute to α_{xy} while the pair of bonds 1 and 4 cancel the contribution of 2 and 5. Finally, the Raman tensor can now be given as

$$\boldsymbol{\alpha'}^{\mathsf{g}}_{\mathsf{br}} = \frac{\partial \boldsymbol{\alpha}^{\mathsf{g}}_{\mathsf{br}}}{\partial Q_{\mathsf{br}}} = \frac{1}{\sqrt{5}}\begin{pmatrix} 2\alpha'_{\parallel} + 3\alpha'_{\perp,ip} & 0 & 0 \\ 0 & 3\alpha'_{\parallel} + 2\alpha'_{\perp,ip} & 0 \\ 0 & 0 & 5\alpha'_{\perp,oop} \end{pmatrix} \tag{G.8}$$

Considered in isolation, the phenyl moiety has the symmetry properties of the C_{2v} point group. A fully symmetric vibrational mode belongs to to its A_1 symmetry species. The vectors xx, yy and zz form a suitable basis for this irreducible representation (see the character table in appendix A). Thus, the Raman tensor of such modes have non-zero and unequal diagonal elements only, as shown above. As no off-diagonal elements are present, a fully polarised Raman band is expected in the spectrum of a molecule containing a phenyl group. However, the equilibrium geometry of such a molecule may be of lower symmetry. Furthermore, side groups may distort the bond polarisabilities so that these are no longer identical. Non-zero off-diagonal components then arise in the Raman tensor of such vibrational modes, giving rise to bands that show a degree of depolarisation.

In toluene, the motions in the phenyl and methyl groups are coupled. Though this affects the molecular vibrational frequencies, the methyl group rotates freely in the liquid state at room temperature [203]. This ensures that the point group symmetry of the molecule is best described as C_{2v}, even though at any instant in time it is of lower symmetry. Toluene has C_s symmetry when one of the C−H bonds of the methyl group is in the plane of the aromatic ring or perpendicular to it. These are also known as an eclipsed and staggered conformation, respectively. The staggered conformation has been found to be the equilibrium geometry of the electronic ground state in a number of studies [203].

G.1.2 Toluene computational results

Toluene is known to be a strong Raman scatterer and one of the demonstration materials favoured by C.V. Raman himself [59]. The computation on toluene serves a limited purpose here: to characterise its Raman spectrum and identify strong and highly polarised modes around 1000 cm^{-1}. These are used to calibrate the linear polarisation directions in the Raman system as explained in chapter 3.

The computational frame of reference of the standard orientation s is transformed to our molecular frame m, given in figure A.1, by changing the directionality of the x and z axes through transformation matrix

$$\mathbf{T}_{\mathsf{s}\to\mathsf{m}} = \begin{pmatrix} -1 & 0 & 0 \\ 0 & 1 & 0 \\ 0 & 0 & -1 \end{pmatrix} \tag{G.9}$$

which is its own transverse. The transformation results in a sign change of the xy, yx, yz and zy components of the Raman tensors while leaving the other components unaffected. A small deviation of the carbon plane from the $x^{\mathsf{m}}y^{\mathsf{m}}$ plane remains.

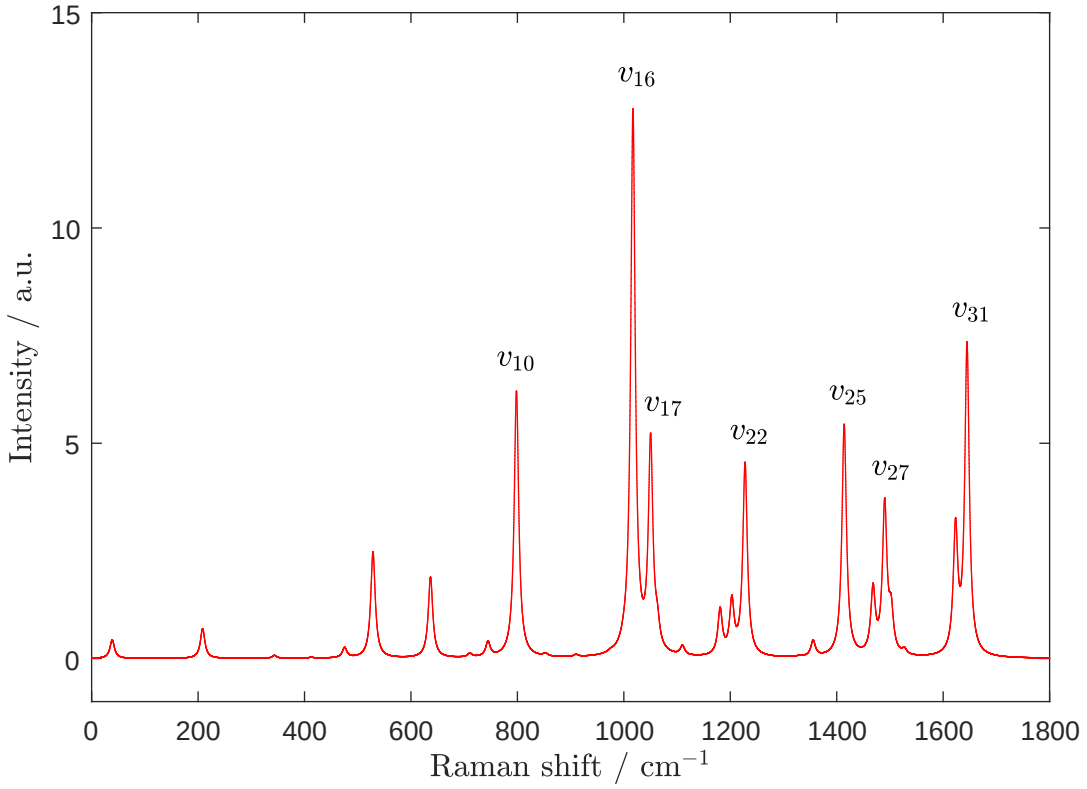

Figure G.2: Computed Raman spectrum of toluene in the gas phase at B3LYP/6-311++G(d,p) theory and convoluted with a Lorentzian of 10 cm^{-1} full width at half maximum. The spectrum is shown up to 1800 cm^{-1}, ignoring the strong Raman bands between 3000 and 3200 cm^{-1}.

The computed Raman spectrum of toluene (figure G.2) includes seven strong non-degenerate bands below 1800 cm^{-1}. There are 39 modes, numbered from low to high frequency following the numbering of Gaussian. None of the computed modes are fully polarised. The normal motion of the atoms is included with appendix D.4. These reveal

that most modes are localised to either the aromatic ring or the methyl group. The frequencies are overestimated by around 2% according to reference [203], which was confirmed in our own experiments (not shown).

Eight out of its 39 normal modes lie in the range 3000-3200 cm^{-1}. These mainly involve motions of the hydrogen atoms. Motion of their diffuse electron clouds increases the polarisability derivative and these modes are predicted to be strongly Raman active. In fact, the mode of highest frequency (v_{39}) is the strongest Raman scattering as well as being highly polarised (table G.1). Its form is similar to the ring breathing mode derived in the bond-polarisability model in equation G.1. Our computation suggests that it is advantageous to use the high-shift rather than the low-shift region, in particular when interfacial experiments are performed where overlap with substrate bands is expected (compare figure 3.6).

Table G.1 lists the seven strongest Raman bands of toluene below 1800 cm^{-1} alongside mode 39. Though assigned to the A species of C_1 by GAUSSIAN, the form of its Raman tensors is close to that of the A' species of C_s, the expected point group of toluene. The symmetry properties of most vibrational modes are clearly of a higher order than C_1, which causes some components of the Raman tensor to be practically zero, *i.e.* zero within precision of the computation or of negligible magnitude compared to the other components of the tensor.

Mode v_{10} is a ring breathing mode involving atomic motion in the plane of the molecule. Its depolarisation ratio ρ is 0.0471. Mode v_{16} is a ring deformation, with alternate carbon atoms moving towards the centre of mass. It is the strongest band in this spectral region and is nearly fully polarised at $\rho = 0.0386$. Any depolarisation arises from the non-zero xz and zx components of its Raman tensor. The modes v_{22}, v_{25} and v_{27} have small but non-zero xy and yx components (as well as yz and zy in the latter), though these are expected to be zero on the grounds of symmetry for the C_s point group. In all tensors of table G.1, the off-diagonal components are small compared to the components on the diagonal. Taking only the diagonal into account would produce a form expected of the fully symmetric species of the C_{2v} point group (see table C.1). Some vibrational modes thus exhibit a higher symmetry than the molecule itself and the forms of their Raman tensors resemble those of another species.

Mode v_{16} is the polarised band observed at about 1000 cm^{-1} experimentally. Its Raman tensor is very close to the form expected for an A_1 mode of the C_{2v} point group as derived in the bond-polarisability model (equation G.8). The off-diagonal non-zero elements arise from slight differences in the polarisabilities of the C−H bonds in the phenyl moiety which don't completely cancel when combined in the pattern of the vibrational motion. Its low depolarisation and relative strength make this Raman band suitable for calibration of the directions of linear polarisation. Though many other materials could be used for this purpose, toluene gives rise to strong Raman scattering as the components in its Raman tensors are high for a number of modes. Furthermore, toluene has the advantages of being readily available at high purity in nearly every laboratory.

Table G.1: Selected vibrational modes of toluene and their Raman tensors in the molecular frame of reference at B3LYP/6-311++G(d,p) theory level. All modes belong to the A symmetry species of the C_1 point group, though resemble the Raman tensors of the A' species of C_s. Their numbering follows the GAUSSIAN log.

Mode #	$\bar{\nu}$ / cm^{-1}	S / $\mathrm{Å}^4\ \mathrm{amu}^{-1}$	$\boldsymbol{\alpha}_{\mathsf{v}}^{\mathsf{m}}$ / 10^{-42} C V^{-1} m^2
v_{10}	798	16.6	$\begin{pmatrix} 10.2 & 0 & 0.7 \\ 0 & 13.4 & 0 \\ 0.7 & 0 & 4.3 \end{pmatrix}$
v_{16}	1017	35.2	$\begin{pmatrix} 16.5 & 0 & -0.1 \\ 0 & 13.8 & 0 \\ -0.1 & 0 & 6.0 \end{pmatrix}$
v_{17}	1050	13.7	$\begin{pmatrix} 9.26 & 0 & -0.09 \\ 0 & 9.10 & 0 \\ -0.09 & 0 & 4.15 \end{pmatrix}$
v_{22}	1228	12.9	$\begin{pmatrix} -7.25 & 0.03 & 0.96 \\ 0.03 & -9.48 & 0 \\ 0.96 & 0 & -3.02 \end{pmatrix}$
v_{25}	1414	16.0	$\begin{pmatrix} 13.7 & 0.1 & -2.3 \\ 0.1 & 0.4 & 0 \\ -2.3 & 0 & -0.7 \end{pmatrix}$
v_{27}	1490	10.5	$\begin{pmatrix} -5.28 & -0.02 & 6.98 \\ -0.02 & -1.76 & 0.11 \\ 6.98 & 0.11 & 3.06 \end{pmatrix}$
v_{31}	1645	22.2	$\begin{pmatrix} 13.8 & 0 & -0.2 \\ 0 & -8.7 & 0 \\ -0.2 & 0 & -0.7 \end{pmatrix}$
v_{39}	3188	293	$\begin{pmatrix} 28.2 & 0 & 0.2 \\ 0 & 24.8 & 0 \\ 0.2 & 0 & 0.8 \end{pmatrix}$

G.2 Chapter 7

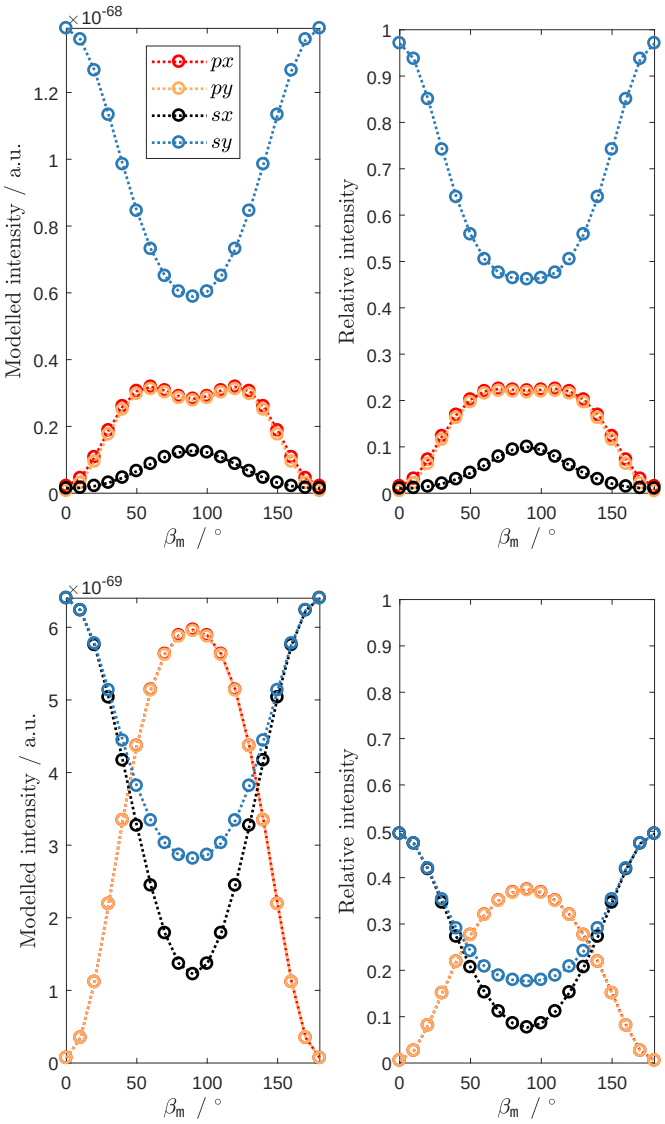

Figure G.3: Symmetric (top) and antisymmetric CH_2 stretch Raman intensities modelled for zinc arachidate in the SF10-silica contact as a function of the tilt angle of its alkyl chain (further details in section 7.3. The range $0° \leq \beta_m \leq 90°$ fully specifies the intensities, modelling over $90° < \beta_m \leq 180°$ is redundant. The position of the headgroup can thus not be deduced from this analysis.

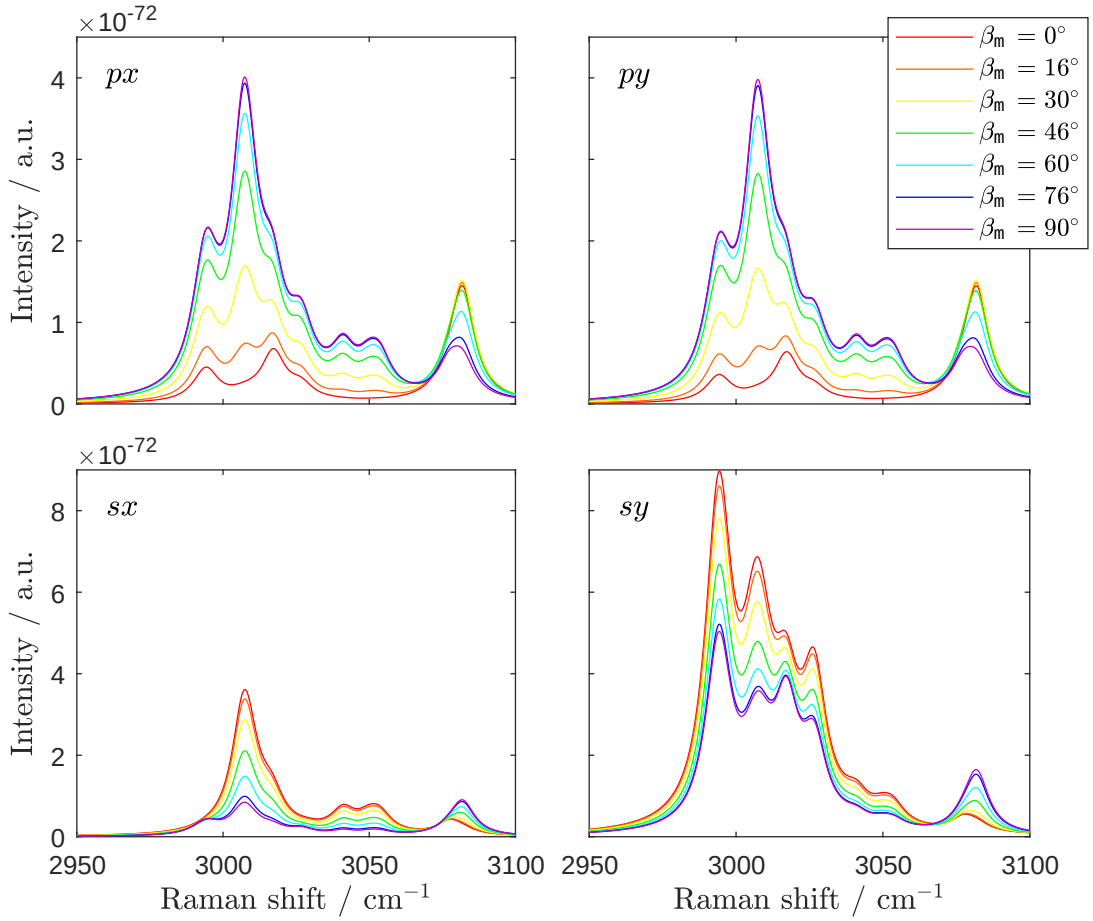

Figure G.4: Modelled harmonic Raman spectra of the ν(CH) band for zinc arachidate in the SF10-silica contact for various molecular tilt angles β_{m} with respect to the interface normal. The local field correction is omitted here (compare figure 7.8 where it is included). The spectral intensities are summed over the full full range of molecular azimuthal and twist angles. Modelling parameters conform to the contact Raman experiment while employing computational Raman tensors of decanoic acid (modes 71-89). Each modelled Raman line is convoluted with a Lorentzian of 10 cm^{-1} fwhm to generate the spectra.